THE UNIVERSITY OF CHICAGO

GROUP 6 METAL-OXO AND -ALKYLIDYNE COMPLEXES WITH HIGH REACTIVITY DERIVED FROM π-ANTIBONDING ORBITALS

A DISSERTATION SUBMITTED TO

THE FACULTY OF THE DIVISION OF THE PHYSICAL SCIENCES

IN CANDIDACY FOR THE DEGREE OF

DOCTOR OF PHILOSOPHY

DEPARTMENT OF CHEMISTRY

BY

HUNTER BAKSA VIBBERT

CHICAGO, ILLINOIS

DECEMBER 2018

TABLE OF CONTENTS

Page

LIST OF FIGURES

LIST OF TABLES

LIST OF EQUATIONS

ACKNOWLEDGMENTS

The number of people who have helped, supported, and mentored me throughout my education is in no small part how I have been able to succeed in finishing this dissertation. First, I would like to thank my advisor, Mike Hopkins. He has been an unbelievably supportive and good mentor to me throughout graduate school. His interest has taught me how to be a successful scientist, how to approach difficult problems, and how to be a better person. I'd also like to thank my undergraduate mentors, Prof. Mike Ladisch, Prof. Dave McMillin, and Dr. Eduardo Ximenes. Working with Mike Ladisch and Eduardo Ximenes as a late high-school and college student cemented in me the love of science and research. Dave (with Dan and Bork) patiently taught me the old-school approach to inorganic photochemistry. I really wouldn't be here without all of you. I'd like to thank my dissertation committee Profs. John Anderson and Rich Jordan who really helped me throughout my time here.

My family has been an exceptionally important in helping me finish my Ph.D. My parents were always good at cheering me up when I was down or frustrated, and it was always a welcome break when they'd come to visit and we'd go find some coffee and explore different parts of the city. Without their support, there is no doubt that I wouldn't be where I am now. A huge part of my Chicago experience has also been in visiting my Aunt and Uncle. Visiting them has always been fun, and they've been amazingly supportive of me during all of my education. I'd like to thank the rest of my family too! Your support during the entirety of my education has really helped me push through the ups and downs to get where I am.

One of the definite pros of the Chicago experience were my labmates in Mike's group. The group is the smallest it's been since I've been here, but I know that it's current inhabitants, Andrew, Kate, and Ayush will do amazing things. Judith and Wayne were among my closest

friends in the group—I'll always look back on our lunches and adventures (expect when Wayne nearly killed me with a bowl of Ramen) as some of my best times in grad school. I want to thank Dan O, Davis, and Nathan for helping me integrate into the lab and get my project off the ground when I started, and it was always fun to talk to Mark about football and get coffee and literally any time of day.

I'd also like to thank all of my friends who helped me navigate grad school as well. It was always great fun to play games with and watch far too much football with Jon, Alex, Wayne, Chris, and Judith. I also had a great time playing in the UChicago Wind Ensemble playing with Mary, Erica, and Jacob. It was always good to shake off science for a day and think about music! I've had a lot of fun getting to know all of the other remarkable people at Chicago: Donglin, Joe, Becca, Pavel, Landon, EW, and Johnny among many, many others.

I really want to especially thank Judith Kamm. She is the one person that could always cheer me up, no matter my mood. Our adventures around the city are some of my fondest memories in Chicago. I'll never be able to put a finger on how much her love and support has really helped me, but I certainly wouldn't be where I am today without her.

ABSTRACT

Photoredox catalysis has become a useful synthetic technique to make and break chemical bonds in chemical structures relevant to medicinal chemistry and renewable energy. Few general approaches, however, have been reported that can prepare synthetically useful organic radicals whose parent molecules are reduced negative of –2.6 V (vs $FeCp_2^{0/+}$). One such approach to accessing these molecules is to design photoredox chromophores that can directly prepare these radical species. The central hypothesis investigated here is that the electronic structure of tungsten-alkylidyne (or benzylidyne) complexes lends them to serve as highly reducing, visible-light photoreductants.

This work describes the electronic-structure description, optimization of synthetic routes, excited-state characterization, and net reactions of tungsten-alkylidyne complexes of the general form $W(CAr)L_4X$ (Ar = aryl, L = bidentate phosphine, X = halide/pseudo-halide). First, we elaborate the general synthetic routes to these complexes for the purpose of electronic-structure design. The electronic-structure design was accomplished *via* Density Functional Theory (DFT) with experimental correlations. This was used to design highly reducing tungsten photoredox catalysts. The photophysics of these complexes were studied to assess their reactivity as photoredox chromophores, and the experimental room temperature measurement of the excited-state oxidation potentials for two tungsten derivatives demonstrated the highly reducing nature of these complexes. Finally, net photoredox reactions were explored. Among those were the C–H arylation of difficult-to-reduce aryl halide (I, Br, and Cl) molecules. These reactions could be affected using low chromophore loadings and a simple industrially relevant base.

A second conceptually related project stemmed from the observation that some of the electrochemical first reduction potentials of a series of molybdenum(IV)-oxo complexes of the general type, $[Mo(O)L_4X]^+$ were reversible. We were able to isolate and study an unusual example of a low-spin d^3 molybdenum-oxo complex *via* single-electron reduction. This complex was observed to possess an elongated bond relative to the d^2 redox congener by single crystal X-ray crystallography that could be corroborated by vibrational spectroscopy and DFT.

CHAPTER 1

Introduction

Photoredox catalysis has proven a valuable strategy to generate or break bonds in chemical structures relevant to medicinal chemistry[1-5] and renewable energy.[6, 7] Few general approaches have been reported that can break bonds of hard-to-reduce compounds to form synthetically useful radicals. In order to continue the development of new methodologies in photoredox catalysis, there is a need for different approaches. In the design of these methods, it will be important to develop highly tunable, modular photoredox catalysts that can enable new bond-breaking and bond-forming reactions.

Photoredox chemistry enhances reactivity because the electronic excitation of chromophores generates molecules that are significantly more reducing and oxidizing than those in their ground-states, exemplified by $[Ru(bpy)_3]^{2+}$ or *fac*-$Ir(ppy)_3$ (Figure 1.1). The extent to which the redox potential is increased is related to the energy of the catalyst's excited state. The visible-light absorption maximum of $[Ru(bpy)_3]^{2+}$ (λ_{max} = 452 nm, Table 1.1), for instance, is assigned as a metal-to-ligand charge transfer (MLCT) where the HOMO is localized on the Ru^{2+} center and the LUMO is primarily localized on the bpy π^*-orbitals.[8] One limitation with $[Ru(bpy)_3]^{2+}$ is that substituent variation (on bpy) provides little difference in excited-state energy. For example, $[Ru(pyrbpy)_3]^{2+}$ (pyrbpy = 4,4′-pyrrolidyl-2,2′-bipyridine), the most reducing ruthenium(II) chromophore reported, possesses only a 0.01 eV difference in excited-state energy over $[Ru(bpy)_3]^{2+}$ (Table 1.1). We wish to develop chromophores that are highly tunable about their ground and excited-state properties to break difficult-to-activate bonds.

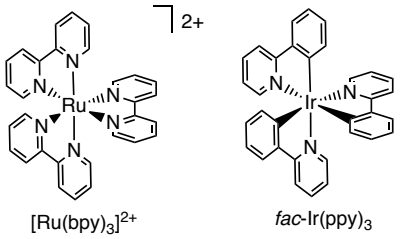

Figure 1.1. Common photoredox chromophores: $[Ru(bpy)_3]^{2+}$ and *fac*-$Ir(ppy)_3$.

Two reaction pathways are normally operative in reductive photoredox catalysis, shown in Figure 1.2. Common to both is the generation of an excited-state catalyst, which can either reduce the substrate directly or oxidize a sacrificial donor to produce a reduced chromophore, which then reduces the substrate. Subsequently, the catalytic cycle is closed by another oxidation or reduction. Often, the closure of catalytic cycles is achieved through the application of sacrificial electron-donor reagents, like triethylamine.[4] Sacrificial reagents are often used because they generate more reducing catalysts or provide a convenient way to regenerate oxidized catalysts. We aim to develop highly-reducing catalysts that can circumvent the need for sacrificial electron-donor molecules, and thus asked the question: What is the upper bound of potentials provided by conventional photoredox catalysts?

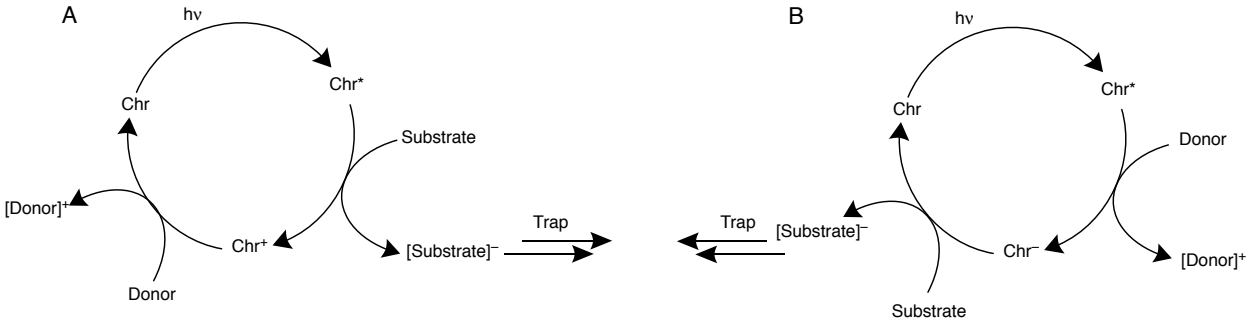

Figure 1.2. Typical pathways in photoredox catalysis using a sacrificial reagent where the (A) chromophore acts as a photoreductant, or (B) chromophore acts as a photooxidant.

Among the metrics used to establish the upper-bound for photoredox chromophores are the excited-state oxidation and ground-state reduction potential. A list of relevant conventional

and unconventional catalysts is shown in Table 1.1. Among the conventional photoredox catalysts, *i.e.* those that are commercially available, the upper-bound of accessible reduction potentials is defined by [*fac*-Ir(ppy)$_3$]$^-$. The potential of –2.59 V vs $FeCp_2$ is not sufficient to reduce a number of desirable molecules,[9-11] including aryl halides.[12, 13] For aryl halides, reduction induces halide loss. The resulting generated aryl radicals can be synthetically elaborated by dimerization or using radical traps such as pyrroles or arenes; these create new bonds that are important in medicinal chemistry.[14, 15] For comparison, iodobenzene, the simplest derivative, is reduced at –2.69 V[16, 17] which is 0.1 V thermodynamically disfavored from [*fac*-Ir(ppy)$_3$]$^-$. Those examples of chromophores that exceed the –2.59 V threshold set by [*fac*-Ir(ppy)$_3$]$^-$ do not possess widely tunable excited-state redox potentials, owing to the nature of their electronic structures.[18-21 22, 23]

Table 1.1. Ground- and excited-state potentials of selected photoredox catalysts (V vs $FeCp_2$).

Chromophore	$E^{*/ox}$ (V)[17]	E^{red} (V)[17]	λ_{abs} (nm)	Ref.
$[CeCl_6]^{3-}$	–3.45	N/A	329	18
$[Cu(PNP)_2]_2$	–3.15	N/A	440	24
$W(CNdipp)_6$	–3.00	< –2.5	465	20, 21
$Ce[(Me_3Si)_2NC(N^iPr_2)]_3$	–2.92	N/A	420	25
$Cu(cbz)(PPh_3)_2$	–2.79	N/A	360	26
$Mo(CNAr_3NC)_3$	–2.60	N/A	425	22
fac-Ir(ppy)$_3$	–2.13	–2.60	375	27
$[Ru(pyrbpy)_3]^{2+}$	–1.96	–1.92	481	28, 29
$[Cu(dip)_2]^+$	–1.53	–2.16	454	30
$[Ru(bpy)_3]^{2+}$	–1.25	–1.71	452	8, 31

Tungsten-alkylidyne catalysts are one family of complexes that possess modifiable and highly reducing excited-state potentials (Figure 1.3). These complexes are particularly intriguing candidates as photocatalysts for several reasons. First, they possess a symmetry-orthogonal electronic structure[32] that could be used to enable the design of highly active photoredox catalysts. The HOMO of these complexes is principally of d_{xy} character and formally

nonbonding (δ-symmetry). The LUMO of tungsten(IV)-alkylidyne complexes is of π^*(WCAr) character. The symmetry-orthogonal nature of the HOMO and LUMO suggests that these orbitals could be independently controlled. Secondly, they possess a modular structure;[33] ligand components for CAr, L, and X can be varied widely.[33-36] Finally, these complexes were observed to undergo only small structural distortions upon oxidation,[37] suggesting that they possessed correspondingly small reorganization barriers. For these reasons, tungsten-alkylidyne complexes are excellent candidates to study.

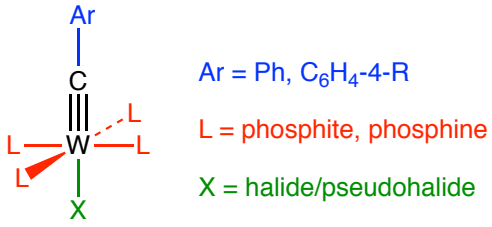

Figure 1.3. General structure of a tungsten-alkylidyne complex.

In this work, the central hypothesis is that tungsten-alkylidyne complexes are highly-reducing photoredox catalysts. We aim to use a combination of computational chemistry, synthesis, and physical measurements as complementary approaches to probe the central hypothesis.

As previously discussed, tungsten-alkylidyne complexes are excellent candidates for the development of highly-reducing photoredox catalysts. Therefore, a systematic study of the CAr, L, and X modular ligands is required. Because general synthetic approaches to W(CAr)L_4X complexes have been described by our group[38] and others,[39, 40] density functional theory (DFT) is ideal as a first step for catalyst screening. Prior computational efforts in our group have demonstrated that the ground-state oxidation potentials of W(CAr)L_4X complexes are linearly dependent on the calculated HOMO orbital energy.[33] Thus, this prior work has enabled the computational prediction of molecules with more reducing ground-state properties.

Once a systematic computational study of CAr, L, and X ligands is completed, the combinations predicted to give the most reducing compounds can be synthesized. We aim to measure the excited-state oxidation potentials of representative derivatives, thus establishing that W(CAr)L_4X compounds are highly reducing chromophores. Demonstration of their ability to participate in photoredox events can be established by transient spectroscopies.[41-43] Measurement of the excited-state potential can be realized through an electron-transfer quenching analysis.[44]

Keeping in mind original goals, we focus our attention on demonstrating that W(CAr)L_4X compounds are highly reducing catalysts in transformations with substrates that cannot be activated by conventional photoredox chromophores. We expect the excited-state oxidation potentials generated by these catalysts to be thermodynamically favorable to reduce a variety of aryl and heteroaryl halide (iodide, bromide, and chloride)[12, 13] and triflate[45] molecules. We additionally expect favorable thermodynamic driving forces in the reduction of carbon dioxide[46] and selected alkyl halides (benzyl, secondary, tertiary).[11]

Chapters 2, 3, 4, and 5 describe efforts towards answering the first proposed question. In Chapter 2, the fundamental synthetic methods used to prepare W(CAr)L_4X compounds are addressed. It was found that a modified ligand substitution approach to the Fischer-Mayr-Berke synthetic route could provide gram-scale quantities of catalyst, from $W(CO)_6$, in less than one week. In Chapter 3, we provide a detailed computational description of the tungsten-alkylidyne complexes that results in the discovery of a correlation between the experimentally determined absorption energy and the HOMO-LUMO gap. Application of both the absorption and oxidation potential correlation enabled the coarse prediction of excited-state oxidation potentials. Chapter 4 describes the photophysical and electrochemical characterization of these complexes. Additionally, the excited-state oxidation potentials for two complexes are measured and

compared to the potentials provided from the Rehm-Weller formalism. Chapter 5 develops the argument that $W(CAr)L_4X$ compounds are photocatalysts. We discovered that these molecules efficiently catalyzed the radical C–H arylation of pyrroles and benzene. The reaction was found to be tolerant of multiple substrates and functionalities. Preparation of one C–H arylated substrate on a quarter-gram scale demonstrated these chromophores were suitable for bulk scale synthetic procedures.

In the course of this work, a separate family of multiply bonded molybdenum- and tungsten-oxo compounds were studied. These are described in Chapter 6. While late metal-oxos with d-electron counts greater than two are known,[47-52] few general approaches exist to isolate and study early metal-oxo compounds with more than two d-electrons. Low oxidation-state early metal-oxo compounds, especially in group 6, are broadly relevant to the development of water reduction catalysts, as notable derivatives have been observed to catalyze the electro-reduction of water to dihydrogen.[53-55] We aimed to develop low oxidation-state molybdenum-oxo catalysts whose reactivity can be controlled to be studied (Figure 1.4).

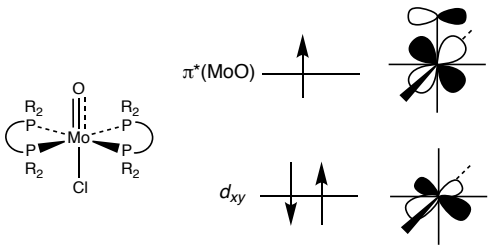

Figure 1.4. Representative molybdenum(III)-oxo compound. R = alkyl, aryl.

The electronic structure of molybdenum-oxo compounds in tetragonal environments suggests that the molybdenum-oxygen bond will be most stable (bond order = 3) for d-electron counts of zero, one, or two.[56-58] With d-electron counts above two, however, the formal bond order of the complex should reduce by 0.5 for each additional electron. In complexes where L is sterically unencumbered, the generation of a molybdenum(III)-oxo is expected to result in the

formation of a highly reactive species. We probed the hypothesis that tuning the steric bulk around the oxo ligand can enable the isolation and study of low-oxidation state molybdenum(III)-oxos, using a combination of computational chemistry, electrochemical methods, and synthetic chemistry, with the isolated compound being studied by X-ray crystallography, vibrational spectroscopy, and UV-vis-NIR spectroscopy.

1.1. References.

1. Douglas, J. J.; Sevrin, M. J.; Stephenson, C. R. J. *Org. Process Res. Dev.* **2016**, *20*, 1134-1147.

2. Loh, Y. Y.; Nagao, K.; Hoover, A. J.; Hesk, D.; Rivera, N. R.; Colletti, S. L.; Davies, I. W.; MacMillan, D. W. C. *Science* **2017**, *358*, 1182-1187.

3. Boubertakh, O.; Goddard, J. P. *Eur. J. Org. Chem.* **2017**, *2017*, 2072-2084.

4. Prier, C. K.; Rankic, D. A.; MacMillan, D. W. C. *Chem. Rev.* **2013**, *113*, 5322-5363.

5. Shaw, M. H.; Twilton, J.; MacMillan, D. W. C. *J. Org. Chem.* **2016**, *81*, 6898-6926.

6. Benson, E. E.; Kubiak, C. P.; Sathrum, A. J.; Smieja, J. M. *Chem. Soc. Rev.* **2009**, *38*, 89-99.

7. Liu, Q.; Wu, L.; Jackstell, R.; Beller, M. *Nature Commun.* **2015**, *6*, 5933-5948.

8. Thompson, D. W.; Ito, A.; Meyer, T. J. *Pure. Appl. Chem.* **2013**, *85*, 1257-1305.

9. Cardinale, A.; Isse, A. A.; Gennaro, A.; Robert, M.; Savéant, J.-M. *J. Am. Chem. Soc.* **2002**, *124*, 13533-13539.

10. Adcock, W.; Clark, C. I.; Houmam, A.; Krstic, A. R.; Pinson, J.; Savéant, J.-M.; Taylor, D. K.; Taylor, J. F. *J. Am. Chem. Soc.* **1994**, *116*, 4653-4659.

11. Savéant, J.-M. *J. Am. Chem. Soc.* **1992**, *114*, 10595-10602.

12. Andrieux, C. P.; Le Gorande, A.; Savéant, J.-M. *J. Am. Chem. Soc.* **1992**, *114*, 6892-6904.

13. Costentin, C.; Robert, M.; Savéant, J.-M. *J. Am. Chem. Soc.* **2004**, *126*, 16051-16057.

14. Young, I. S.; Thornton, P. D.; Thompson, A. *Nat. Prod. Rep.* **2010**, *27*, 1801-1839.

15. Shida, T. *Electronic absorption spectra of radical ions*. Elsevier Science Publishers: New York, New York, 1988.

16. Pause, L.; Robert, M.; Savéant, J.-M. *J. Am. Chem. Soc.* **1999**, *121*, 7158-7159.

17. Potential recorded vs SCE, converted relative to $FeCp_2$ from Connelly, N.G.; Geiger, W.E. *Chem. Rev.* **1996**, *96*, 877-910. .

18. Yin, H.; Jin, Y.; Hertzog, J. E.; Mullane, K. C. *J. Am. Chem. Soc.* **2016**, *138*, 16266-16273.

19. Jenks, T. C.; Bailey, M. D.; Hovey, J. L.; Fernando, S.; Basnayake, G.; Cross, M. E.; Li, W.; Allen, M. J. *Chem. Sci.* **2018**, *9*, 1273-1278.

20. Sattler, W.; Henling, L. M.; Winkler, J. R.; Gray, H. B. *J. Am. Chem. Soc.* **2015**, *137*, 1198-1205.

21. Sattler, W.; Ener, M. E.; Blakemore, J. D.; Rachford, A. A.; LaBeaume, P. J.; Thackeray, J. W.; Cameron, J. F.; Winkler, J. R.; Gray, H. B. *J. Am. Chem. Soc.* **2013**, *135*, 10614-10617.

22. Büldt, L. A.; Guo, X.; Prescimone, A.; Wenger, O. S. *Angew. Chem. Int. Ed.* **2016**, *55*, 11247-11250.

23. McTiernan, C. D.; Morin, M.; McCallum, T.; Scaiano, J. C.; Barriault, L. *Catal. Sci. Technol.* **2016**, *6*, 201-207.

24. Harkins, S. B.; Peters, J. C. *J. Am. Chem. Soc.* **2005**, *127*, 2030-2031.

25. Yin, H.; Carroll, P. J.; Manor, B. C.; Anna, J. M.; Schelter, E. J. *J. Am. Chem. Soc.* **2016**, *138*, 5984-5993.

26. Lotito, K. J.; Peters, J. C. *Chem. Commun.* **2010**, *46*, 3690-3692.

27. Flamigni, L.; Barbieri, A.; Sabatini, C.; Ventura, B.; Barigelletti, F. *Topics in Current Chemistry*; 2007; Vol. 281, pp 143-203.

28. Martineau, D.; Beley, M.; Gros, P. C.; Cazzanti, S.; Caramori, S.; Bignozzi, C. A. *Inorg. Chem.* **2007**, *46*, 2272-2277.

29. Martineau, D.; Beley, M.; Gros, P. C. *J. Org. Chem.* **2006**, *71*, 566-571.

30. Garakyaraghi, S.; Crapps, P. D.; McCusker, C. E.; Castellano, F. N. *Inorg. Chem.* **2016**, *55*, 10628-10636.

31. Bock, C. R.; Connor, J. A.; Gutierrez, A. R.; Meyer, T. J.; Whitten, D. G.; Sullivan, B. P.; Nagle, J. K. *J. Am. Chem. Soc.* **1979**, *101*, 4815-4824.

32. Da Re, R. E.; Hopkins, M. D. *Coord. Chem. Rev.* **2005**, *249*, 1396-1409.

33. Haines, D. E.; O'Hanlon, D. C.; Manna, J.; Jones, M. K.; Shaner, S. E.; Sun, J.; Hopkins, M. D. *Inorg. Chem.* **2013**, *52*, 9650-9658.

34. Rudshteyn, B.; Vibbert, H. B.; May, R.; Wasserman, E.; Warnke, I.; Hopkins, M. D.; Batista, V. S. *ACS Catal.* **2017**, *7*, 6134-6143.

35. Moravec, D. B.; Hopkins, M. D. *J. Phys. Chem. A.* **2013**, *117*, 1744-1755.

36. O'Hanlon, D. C.; Cohen, B. W.; Moravec, D. B.; Dallinger, R. F.; Hopkins, M. D. *J. Am. Chem. Soc.* **2014**, *136*, 3127-3136.

37. Lovaasen, B. M.; Lockard, J. V.; Cohen, B. W.; Yang, S.; Zhang, X.; Simpson, C. K.; Chen, L. X.; Hopkins, M. D. *Inorg. Chem.* **2012**, *51*, 5660-5670.

38. Sun, J.; Simpson, C. K.; Hopkins, M. D.; Hock, A. S.; Schrock, R. R. *Inorg. Synth.*; Girolami, G. S., Sattelberger, A. P., Ed.; John Wiley & Sons, Inc.: Hoboken, NJ, 2014; Vol. 36, pp 134-138.

39. Mayr, A.; McDermott, G. A.; Dorries, A. M. *Organometallics* **1985**, *4*, 608-610.

40. Furno, F.; Fox, T.; Schmalle, H. W.; Berke, H. *Organometallics* **2000**, *19*, 3620-3630.

41. Pedersen, S. U.; Bo Christensen, T.; Thomasen, T.; Daasbjerg, K. *J. Electroanal. Chem.* **1998**, *454*, 123-143.

42. Shida, T. *Electronic absorption spectra of radical anions*. ElSevier Science: 1988.

43. Dereka, B.; Koch, M.; Vauthey, E. *Acc. Chem. Res.* **2017**, *50*, 426-434.

44. Balzani, V.; Bolletta, F.; Scandola, F. *J. Am. Chem. Soc.* **1980**, *102*, 2152-2163.

45. Jutand, A.; Négri, S. *Eur. J. Org. Chem.* **1998**, 1811-1821.

46. Berto, T. C.; Zhang, L.; Hamers, R. J.; Berry, J. F. *ACS Catal.* **2015**, *5*, 703-707.

47. Rohde, J.-U.; In, J.-H.; Lim, M. H.; Brennessel, W. W.; Bukowski, M. R.; Stubna, A.; Münck, E.; Nam, W.; Que, L. *Science* **2003**, *299*, 1037-1039.

48. Marshman, R. W.; Shapley, P. A. *J. Am. Chem. Soc.* **1990**, *112*, 8369-8378.

49. Marmion, M. E.; Takeuchi, K. J. *J. Am. Chem. Soc.* **1986**, *108*, 510-511.

50. Lim, M. H.; Rohde, J.-U.; Stubna, A.; Bukowski, M. R.; Costas, M.; Ho, R. Y. N.; Münck, E.; Nam, W.; Que, L. *Proc. Natl. Acad. Sci.* **2003**, *100*, 3665-3670.

51. Barthazy, P.; Wörle, M.; Mezzetti, A. *J. Am. Chem. Soc.* **1999**, *121*, 480-481.

52. Barthazy, P.; Wörle, M.; Rüegger, H.; Mezzetti, A. *Inorg. Chem.* **2000**, *39*, 4903-4912.

53. Karunadasa, H. I.; Chang, C. J.; Long, J. R. *Nature* **2010**, *464*, 1329-1333.

54. Thoi, S. V.; Karunadasa, H. I.; Surendranath, Y.; Long, J. R.; Chang, C. J. *Energy Environ. Sci.* **2012**, *5*, 7762-7770.

55. Pal, R.; Laureanti, J. A.; Groy, T. L.; Jones, A. K.; Trovitch, R. J. *Chem. Commun.* **2016**, *52*, 11555-11558.

56. Ballhausen, C. J.; Gray, H. B. *Inorg. Chem.* **1962**, *1*, 111-122.

57. Gray, H. B.; Hare, C. R. *Inorg. Chem.* **1962**, *1*, 363-368.

58. Winkler, J. R.; Gray, H. B., Electronic structures of oxo-metal ions. In *Molecular Electronic Structures of Transition Metal Complexes. I. Structure and Bonding*, Mingos, D., Day, P., Dahl, J., Eds. Springer: Berlin, Heidelberg, 2011; Vol. 142, pp 17-28.

CHAPTER 2

Improved syntheses of d^2 tungsten-alkylidyne complexes

Note: Portions of this work have been published in an alternative format in Rudshetyn, B.; Vibbert, H.B.; May, R.; Wasserman, E.; Warnke, I.; Hopkins, M.D. *ACS Catalysis* **2017**, *7*, 6134-6143.

2.1. Introduction.

Tungsten-alkylidyne compounds of the general form $W(CAr)L_4X$ (Ar = aryl; L = neutral ligand; X = halide/pseudohalide) were first recognized to be luminescent in fluid solution by Mayr and coworkers nearly 35 years ago.[1] Despite considerable progress since that time towards understanding the ground- and excited-state properties relevant to their photophysical properties, there remain important unanswered questions. The research in this dissertation aims to address some of these questions, central to which is the availability of derivatives in which the CAr, L, and X groups are systematically varied. This chapter focuses on the synthesis and characterization of $W(CAr)L_4X$ complexes that will be studied in Chapters 3, 4, and 5. The synthetic methods described in this chapter circumvent problems of previous methods in terms of functional group tolerance and/or product yields. This has allowed the synthesis of previously inaccessible tungsten-alkylidyne photoredox chromophores in relatively high overall yields and on large scales. In Chapter 3, predictions are made for these compounds based on theoretical calculations, while Chapters 4 and 5 focus on their optical and redox properties and applications to organic synthesis.

Two complementary approaches exist to synthesize $W(CAr)L_4X$-type complexes: one based on alkyne-metathesis reactions, employing advances made by Schrock and former

Hopkins-group member Margaret Stevenson (Schrock–Stevenson); and another based on the classical Fischer carbyne synthesis, with modifications by Mayr and Berke (Fischer–Mayr–Berke). The Schrock-Stevenson route is shown in Figure 2.1. Due to the present commercial availability of starting materials, the Schrock–Stevenson route begins from WCl_4 and involves many steps.[2, 3] The alkylidyne ligand is installed through an alkyne metathesis reaction between $W_2(O^tBu)_6$[4, 5] and an aryl-alkyne in the presence of catalytic 3-hexyne[6] to provide a d^0 Schrock-type alkylidyne, $W(CAr)(O^tBu)_3$ in high yield.[7, 8] Conversion of $W(CAr)(O^tBu)_3$ into the desired $W(CAr)L_4X$ product involves treatment with BCl_3 and 1,2-bis(dimethoxyethane) (DME) to give $W(CAr)Cl_3(DME)$, and then reduction with Na/Hg (0.2% w/w) in the presence of the desired phosphine ligand.[3, 9] The Schrock-Stevenson route has facilitated the preparation of several d^2 tungsten-alkylidyne complexes with differing L and CAr ligands. This method is particularly well-suited for the installation of different equatorial phosphine ligands. One limitation is that not all desirable aryl substituents are stable to BCl_3 (e.g. NR_2, OR) and/or Na/Hg (e.g. halides), either requiring use of protecting groups[10-13] or prohibiting synthesis. Using the Schrock-Stevenson route, $W(CPh)(dppe)_2Cl$ can be prepared from WCl_4 with a total synthetic yield of 23% (Figure 2.1).

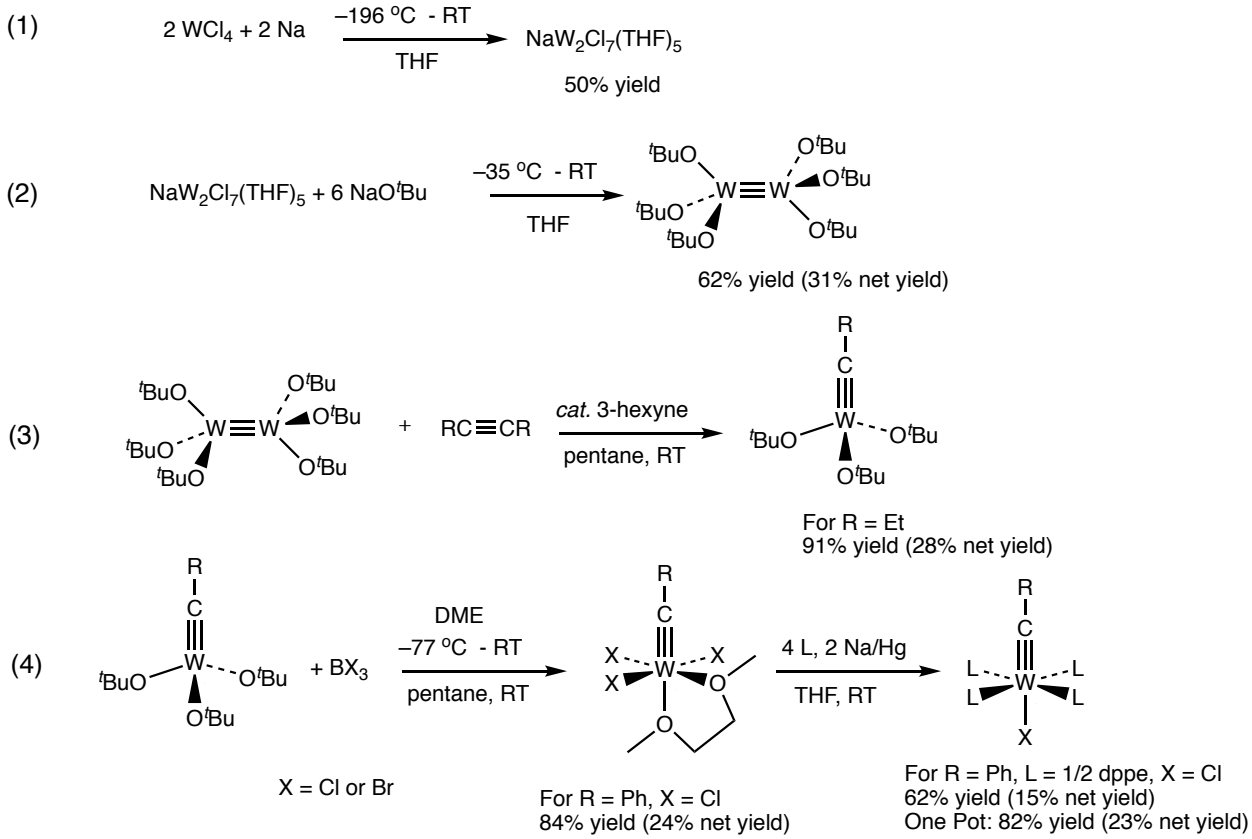

Figure 2.1. Schrock-Stevenson synthetic route. Reported yields are from Refs. 3, 5, 8.

The Fischer–Mayr-Berke route (Figure 2.2) is based on the work of Fischer, who originally prepared $W(CAr)(CO)_4X$ compounds.[14, 15] This synthesis was later improved by Mayr and coworkers.[16] Although $W(CAr)(CO)_4X$ is unstable above –40 °C, they found that certain $W(CAr)L_2(CO)_2Cl$ derivatives are stable at room temperature. In our hands, for example, $W(CPh)(pic)_2(CO)_2Cl$ (pic = 4-picoline), is stable in air for > 1 year. The $W(CAr)L_2(CO)_2X$ compounds are useful starting materials for the preparation of many other tungsten-alkylidyne complexes and can be produced on very large scales (> 40 g, reported by Mayr).[17] Of relevance to the present work is that reaction of $W(CAr)L_2(CO)_2X$ with $P(OMe)_3$ or PMe_3 provides the corresponding $W(CAr)L_3(CO)Cl$ compounds.[18,19] subsequent reaction of $W(CPh)\{P(OMe)_3\}_3(CO)Cl$ with bidentate phosphines (PP) provides $W(CAr)(PP)_2X$

compounds[20] (as does reaction with W(CAr){P(OMe)$_3$}$_4$Cl).[18, 20, 21] The Fischer-Mayr route has been used to prepare compounds with substituted aryls that are not readily accessible through the Schrock–Stevenson method, including NH_2,[22] NMe_2,[23, 24] NC,[22] and halides[25]. However, installation of equatorial phosphine ligands is more difficult with the Fischer-Mayr-Berke route because it requires forcing conditions for >3 days.

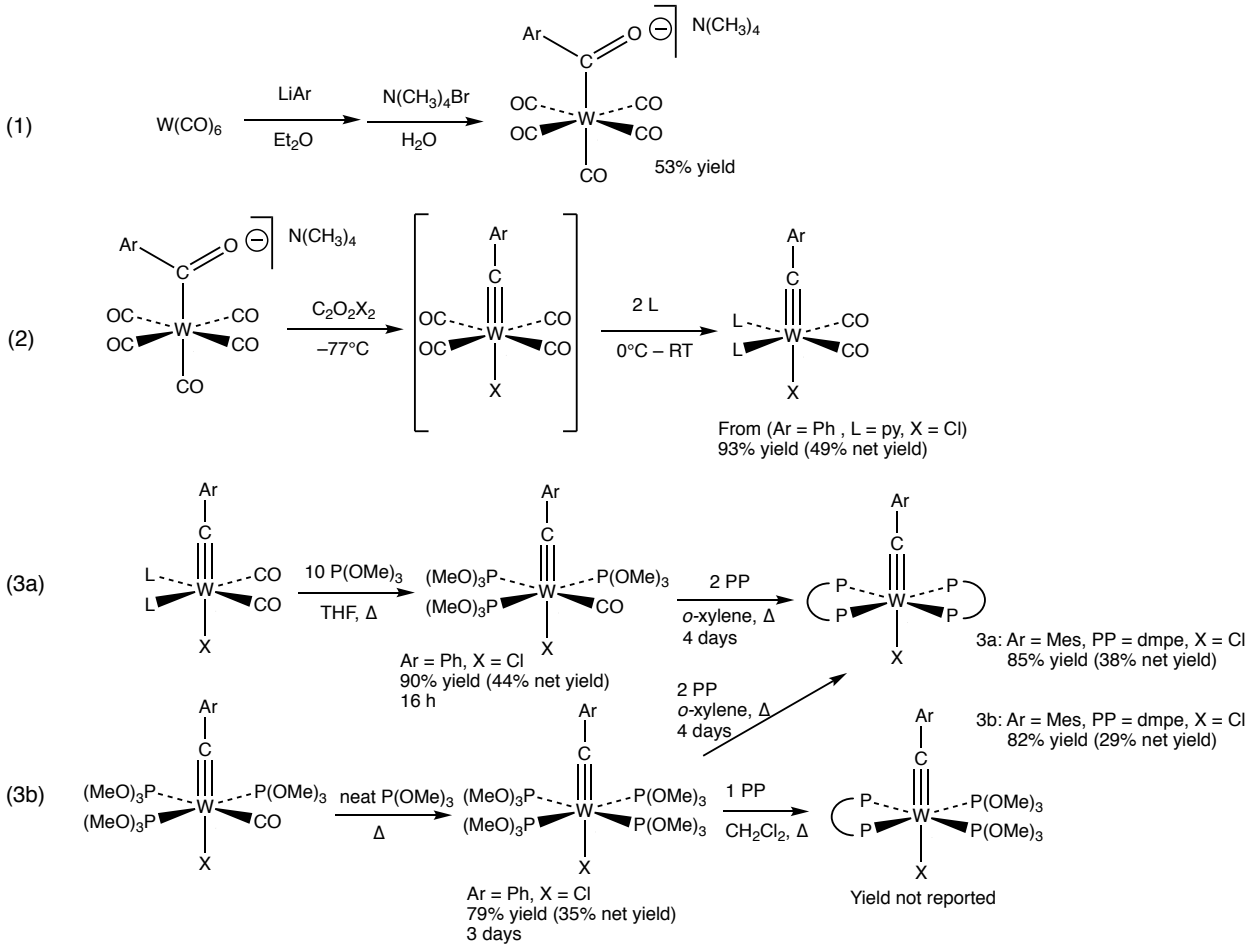

Figure 2.2. Fischer-Mayr-Berke synthetic route. Reported yields are from Refs. 14, 17, 18, 20.

In addition to the considerations above, which provide routes for varying the CAr and L ligands, variation of the X ligand in W(CAr)L$_4$X complexes is also important. One convenient method to approach variation of X is to first install triflate (OSO_2CF_3 = OTf). The triflate ligand can be readily substituted with F, Bu^n, $OSi(CH_3)_3$, CN, and OPh.[10]

In this chapter, improvements to the Fischer-Mayr-Berke route are developed. To circumvent long reaction times and or low yields associated with liberation of CO in ligand substitution reactions of W(CAr){P(OMe)$_3$}$_3$(CO)Cl, the improved starting material W(CAr){P(OMe)$_3$}$_4$Cl was directly prepared from W(CAr)(pic)$_2$(CO)$_2$Cl. W(CAr){P(OMe)$_3$}$_4$Cl complexes were found to react with a number of different bidentate phosphines, providing W(CAr)(PP)$_2$Cl in high yields (*ca.* 80%) with overnight reactions and on gram-scale quantities. Additionally, a quicker, higher yielding route was discovered to fluoro derivatives of the form, W(CAr)L$_4$F.

2.2. Results and Discussion.

2.2.1. Synthetic approaches for W(CC$_6$H$_4$-4-R)L$_4$Cl (D = NR′$_2$ or OR′). As will be discussed further in Chapter 3, tungsten-alkylidyne complexes with electron-donor substituents on the CAr ligand are desired because they were predicted to profoundly impact W(CAr)L$_4$X ground- and excited-state properties. The synthesis of one such compound, W(CC$_6$H$_4$-4-pyr)(PP)$_2$Cl (pyr = N-pyrroldyl), was attempted with the Schrock-Stevenson methodology (Figure 2.1). The procedure required the synthesis of 4-(1-hexynyl)-*N*-phenylpyrrolidine *via* Sonogashira coupling; reaction of the acetylene with W$_2$(O^{t}Bu)$_6$ cleanly provided the d^0 compound W(CC$_6$H$_4$-4-pyr)(O^{t}Bu)$_3$. Recrystallization provided one large (*ca.* 1 cm wide) crystal of product. The crystal structure of the compound (Figure 2.3) shows that the pyrrolidine substituent lies nearly co-planar to the arene ring. Subsequent reaction of W(CC$_6$H$_4$-4-pyr)(O^{t}Bu)$_3$ with BCl$_3$, however, was not clean, and W(CC$_6$H$_4$-4-pyr)(DME)Cl$_3$ could not be isolated. Upon further consideration, it was found that reaction between *N*-phenylpyrrolidine and BCl$_3$ was reported to induce ring-opening reactions.[26] Furthermore, in considering the possibility of applying the Schrock-Stevenson route to W(CC$_6$H$_4$-4-OCH$_3$)L$_4$X complexes, it

was found that the reaction of BCl_3 or BBr_3 with anisole is known to induce O–C bond scission.[26] Because of these undesirable reactions, the Schrock-Stevenson method was not further pursued for these compounds.

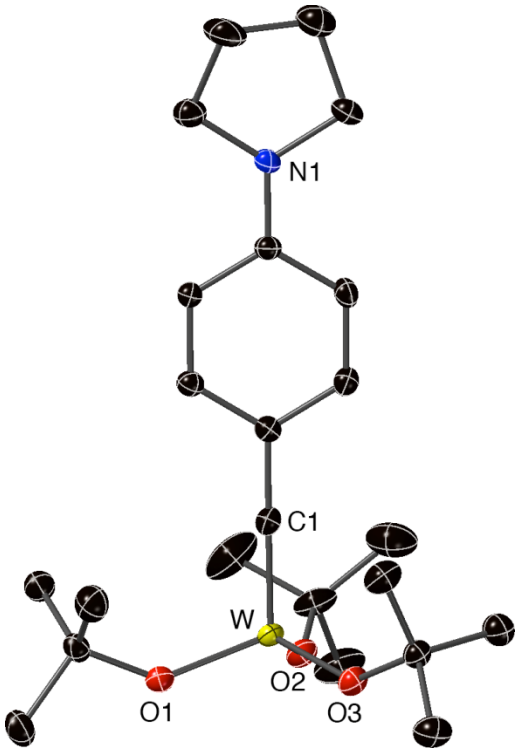

Figure 2.3. Molecular structure of $W(CC_6H_4\text{-}4\text{-}pyr)(O^tBu)_3$ (50% probability ellipsoids). Hydrogen atoms not shown. Relevant structural parameters WC1 = 1.772(3); WO(avg) =1.872[2]; CN1C torsion = 177.9(3); R1 = 0.0394.

Mayr and others demonstrated that the Fischer-Mayr-Berke route would allow installation of strongly-donating groups into the *para*-position of the alkylidyne group.[22, 25, 27-29] Thus, syntheses of $W(CC_6H_4\text{-}4\text{-}NR_2)(PP)_2Cl$ and $W(CC_6H_4\text{-}4\text{-}OR)(PP)_2Cl$ complexes were attempted using that approach (Figure 2.2). We found that compounds of the type $W(CAr)(pic)_2(CO)_2Cl$ with -4-pyrrolidyl, -4-NH_2, -4-OCH_3, and -4-OTBDMS Ar groups could be prepared. The $W(CAr)(pic)_2(CO)_2Cl$ derivatives were indefinitely stable in air. One improvement to the reported approach was discovered; it was found that the purification of the final product by low-temperature column chromatography specified in the literature[16] could be

replaced by filtering a solution of the product, in air, through a pad of silica. With this method, crystalline samples of $W(CAr)(pic)_2(CO)_2Cl$ were obtained with comparable yields to those reported by Mayr *et al*. This synthetic and purification method was found to be highly reproducible and easily implemented; a set of undergraduate laboratory experiments (CHEM 227) was designed around the synthesis $W(CPh)(pic)_2(CO)_2Cl$ utilizing the simplified purification technique.

From $W(CAr)(pic)_2(CO)_2Cl$ compounds, the Fischer-Mayr-Berke method uses sequential ligand exchange to produce $W(CAr)L_4Cl$ complexes. First, $W(CAr)\{P(OMe)_3\}_3(CO)Cl$ is prepared by reaction of $W(CAr)(pic)_2(CO)_2Cl$ with excess $P(OMe)_3$ at reflux; treatment of that product with bidentate phosphines in refluxing, high-boiling solvent for several days provides $W(CAr)(PP)_2Cl$. Application of this method to the synthesis of $W(CAr)\{P(OMe)_3\}_3(CO)Cl$ with -4-pyr, -4-NH_2, -4-OTBDMS substituents produced the desired $W(CAr)\{P(OMe)_3\}_3(CO)Cl$ complexes, although each sample was noted to contain small amounts (*ca.* 5%) of $W(CAr)\{P(OMe)_3\}_4Cl$ by $^{31}P\{^1H\}$ NMR spectroscopy. It is known that $W(CAr)\{P(OMe)_3\}_4Cl$ is also be a precursor for $W(CAr)(PP)_2Cl$ complexes,[18, 20] and so no attempts were made to remove these impurities. Reactions between $W(CAr)\{P(OMe)_3\}_3(CO)Cl$ and 2.5 equiv. dmpe in refluxing *o*-xylene provided $W(CAr)(dmpe)_2Cl$ after 2-3 days. However, during the prolonged reflux a dark precipitate was observed to coat the bottom of the reaction flask. Removal of this impurity required a recrystallization method which required optimization for each compound, and final yields were lower than desired (66% yield for $W(CC_6H_4\text{-}4\text{-pyr})(dmpe)_2Cl$). This difficulty, coupled with the extended reaction time required for each synthesis, prompted us to explore other precursors for these products.

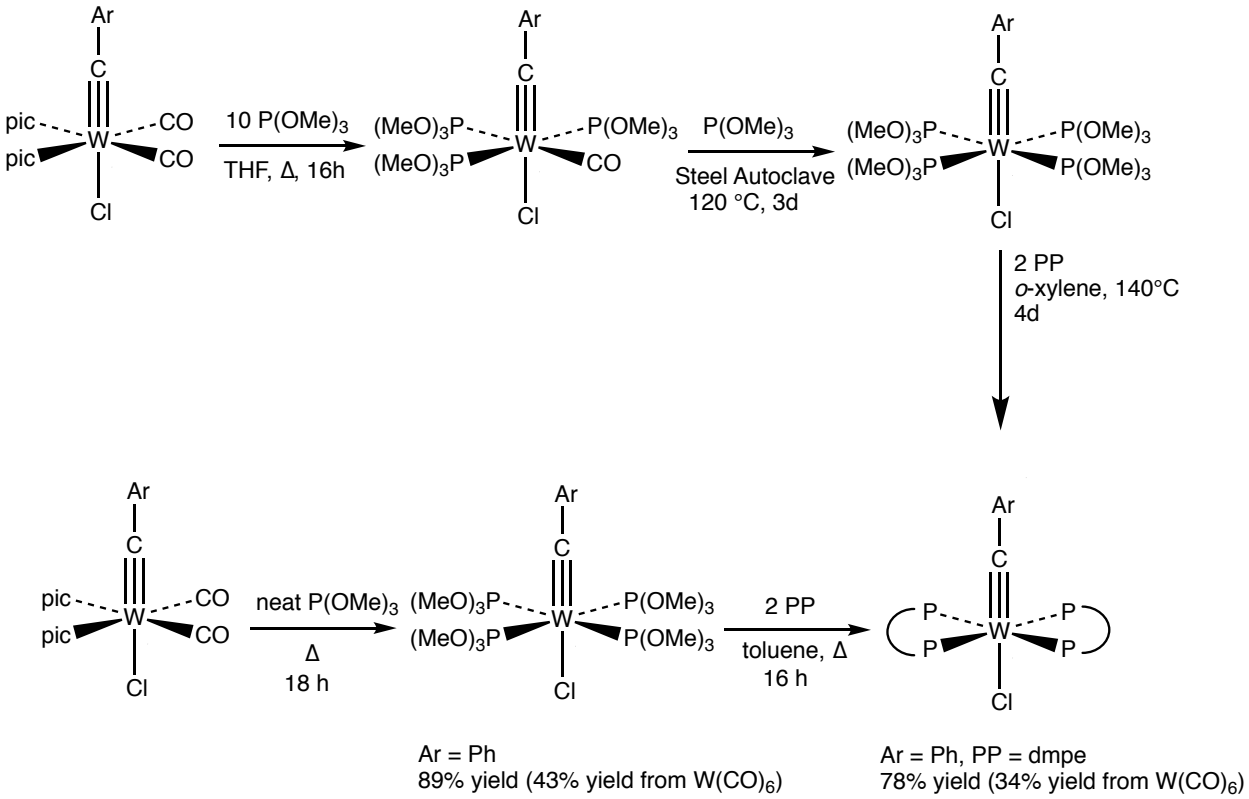

Figure 2.4. Comparison between the prior route,[20, 21] optimized synthesis, and subsequent reaction of W(CAr){P(OMe)$_3$}$_4$Cl. Yields reported in Section 2.4.

We hypothesized that the long reaction times and forcing conditions required in the above synthesis of W(CAr)(dmpe)$_2$Cl from W(CAr){P(OMe)$_3$}$_3$(CO)Cl were due to the slow liberation of the final CO ligand. Surmising that W(CAr){P(OMe)$_3$}$_4$Cl would be an improved starting material, we sought to prepare this compound directly from W(CAr)(pic)$_2$(CO)$_2$Cl rather than in two steps (Figure 2.4). The reflux of W(CAr)(pic)$_2$(CO)$_2$Cl (Ar =Ph, C$_6$H$_4$-4-pyr and C$_6$H$_4$-4-OCH$_3$) in neat trimethylphosphite for 18-24 h resulted in complete and clean conversion to W(CAr){P(OMe)$_3$}$_4$Cl (Ar = C$_6$H$_4$-4-OCH$_3$ or C$_6$H$_4$-4-pyr). A ^{31}P{^{1}H} NMR spectrum of the crude product of W(CC$_6$H$_4$-4-OCH$_3$){P(OMe$_3$)}$_4$Cl (Figure 2.5) is indicative of its purity; indeed, it was used for further derivatization without recrystallization.

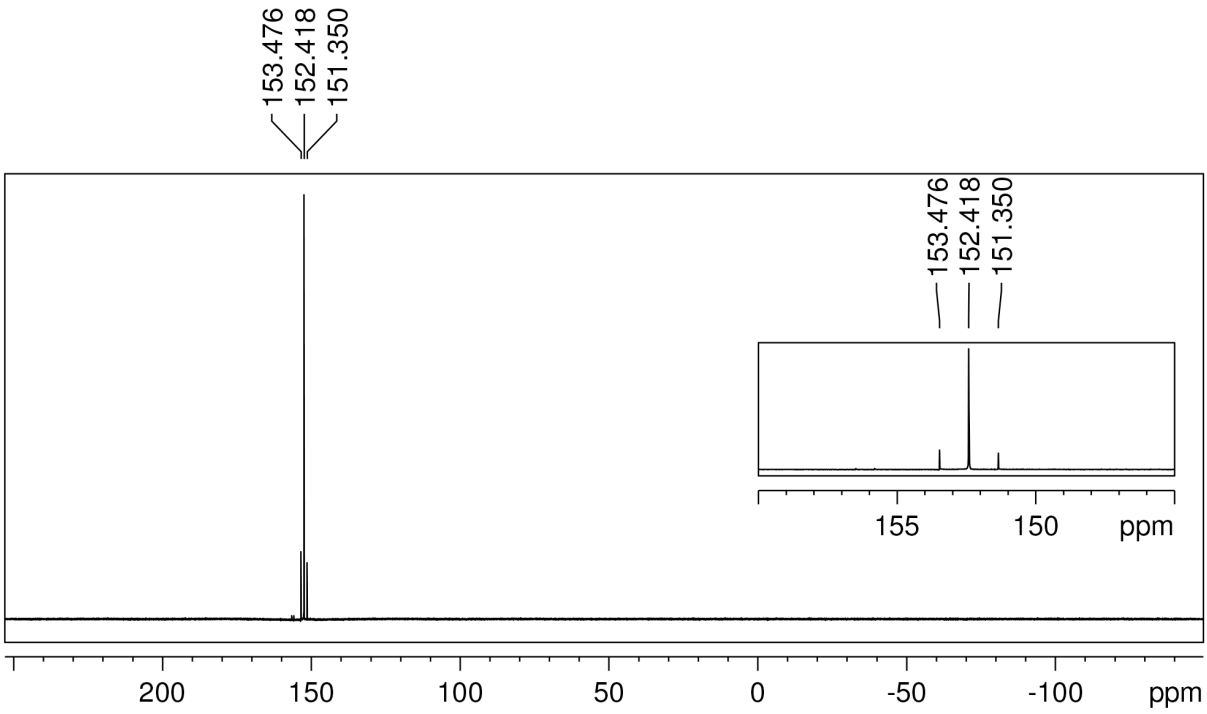

Figure 2.5. Crude $^{31}P\{^{1}H\}$ NMR of $W(CC_6H_4\text{-}4\text{-}OCH_3)\{P(OMe)_3\}_4Cl$ in C_6D_6.

Use of $W(CAr)\{P(OMe)_3\}_4Cl$ (Ar = C_6H_4-4-pyr and C_6H_4-4-OCH_3) starting materials provided $W(CAr)(PP)_2Cl$ products more quickly, cleanly, and in higher yields than did the $W(CAr)\{P(OMe)_3\}_3(CO)Cl$ precursors. Treatment of $W(CAr)\{P(OMe)_3\}_4Cl$ with 2.1 equiv. of PP ligands in refluxing toluene for 16 h provided the Ar-functionalized complexes $W(CC_6H_4\text{-}4\text{-}OCH_3)(dmpe)_2Cl$, $W(CC_6H_4\text{-}4\text{-}OCH_3)(dppe)_2Cl$, $W(CC_6H_4\text{-}4\text{-pyr})(dmpe)_2Cl$, $W(CC_6H_4\text{-}4\text{-pyr})(depe)_2Cl$, and $W(CC_6H_4\text{-}4\text{-pyr})(dppe)_2Cl$, in yields of 69–88% (Table 2.1). The compounds were characterized by ^{1}H-, $^{31}P\{^{1}H\}$-, $^{13}C\{^{1}H\}$ NMR and HR-ESI-MS. The route also proved better for the synthesis of simple $W(CPh)(PP)_2Cl$ compounds than the Schrock-Stevenson. The latter method provides $W(CPh)(dmpe)_2Cl$ in 19% overall yield based on WCl_4, whereas the approach here involving $W(CPh)\{P(OMe)_3\}_4Cl$ provided the compound in 34% overall yield from $W(CO)_6$.

Table 2.1. Product yields obtained from the starting material W(CAr){P(OMe)$_3$}$_4$Cl.

Compound	Yield (%)[a]
W(CPh)(dmpe)$_2$Cl	78
W(CPh)(depe)$_2$Cl	79
W(CC$_6$H$_4$-4-OCH$_3$)(dmpe)$_2$Cl	73
W(CC$_6$H$_4$-4-OCH$_3$)(dppe)$_2$Cl	83
W(CC$_6$H$_4$-4-pyr)(dmpe)$_2$Cl	88
W(CC$_6$H$_4$-4-pyr)(depe)$_2$Cl	82
W(CC$_6$H$_4$-4-pyr)(dppe)$_2$Cl	69

[a]Full characterization data are shown in Chapter 2.4.

2.2.2. Attempted synthesis of W(CC$_6$H$_4$-4-OH)(dmpe)$_2$Cl. As will be further discussed in Chapter 3, we were interested in studying the properties of d^2 [W(CAr)L$_4$X]$^-$ complexes, which possess anionic substituents such as O$^-$ or NH$^-$ on the CAr ligand, because we believe these groups will both strongly destabilize the π*(WCAr) orbital and decrease the ground-state oxidation potential. One target, [W(CC$_6$H$_4$-4-O)(PP)$_2$Cl]$^-$, could potentially be prepared *via* deprotonation of W(CC$_6$H$_4$-4-OH)(dmpe)$_2$Cl. The synthesis of W(CC$_6$H$_4$-4-OH)(dmpe)$_2$Cl, however, cannot be directly prepared by the Schrock-Stevenson or Fischer-Mayr-Berke synthetic routes because the OH group would react with BCl$_3$ (Schrock-Stevenson) and organolithium reagents (Fischer-Mayr-Berke). As a result, preparation of a silane-protected derivative was pursued. The compound W(CC$_6$H$_4$-4-OTBDMS)(dmpe)$_2$Cl (TBDMS = *tert*-butyl dimethylsilyl) was prepared by the Fischer-Mayr-Berke method due to the stability of this silane protecting group to the requisite conditions.

The attempt to prepare W(CC$_6$H$_4$-4-OH)(dmpe)$_2$Cl *via* the protiodesilylation reaction between W(CC$_6$H$_4$-4-OTBDMS)(dmpe)$_2$Cl and [^{n}Bu$_4$N]F resulted in a quick reaction, as indicated by UV-vis (Figure 2.6), ^{1}H- (Figures 2.7-2.9), and ^{31}P-NMR (Figure 2.10) spectroscopic monitoring. However, all probes indicated that the reaction slowly evolved

through a series of products. The UV-vis spectrum showed rapid growth of a shoulder that then diminished in intensity, a broad feature in the ^{1}H NMR spectrum at ~5.1 ppm consistent with the OH resonance appeared and then disappeared, concomitant with evolution of aromatic and dmpe resonances, and the $^{31}P\{^{1}H\}$ NMR spectrum showed a single new feature together with a weak doublet consistent with a W(CAr)(dmpe)$_2$F compounds. These complexities led us to abandon synthesis of the target compound. Future attempts might be able to circumvent these issues by the introduction of more sterically demanding ligands for L.

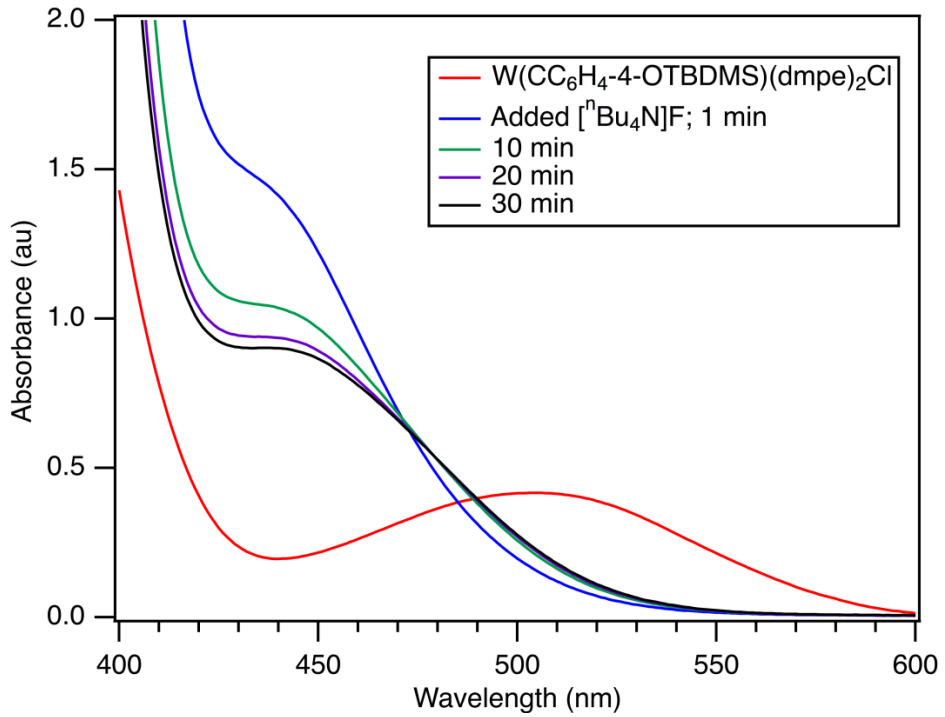

Figure 2.6. Reaction progress of de-protection reaction for W(CC$_6$H$_4$-4-OTBDMS)(dmpe)$_2$Cl.

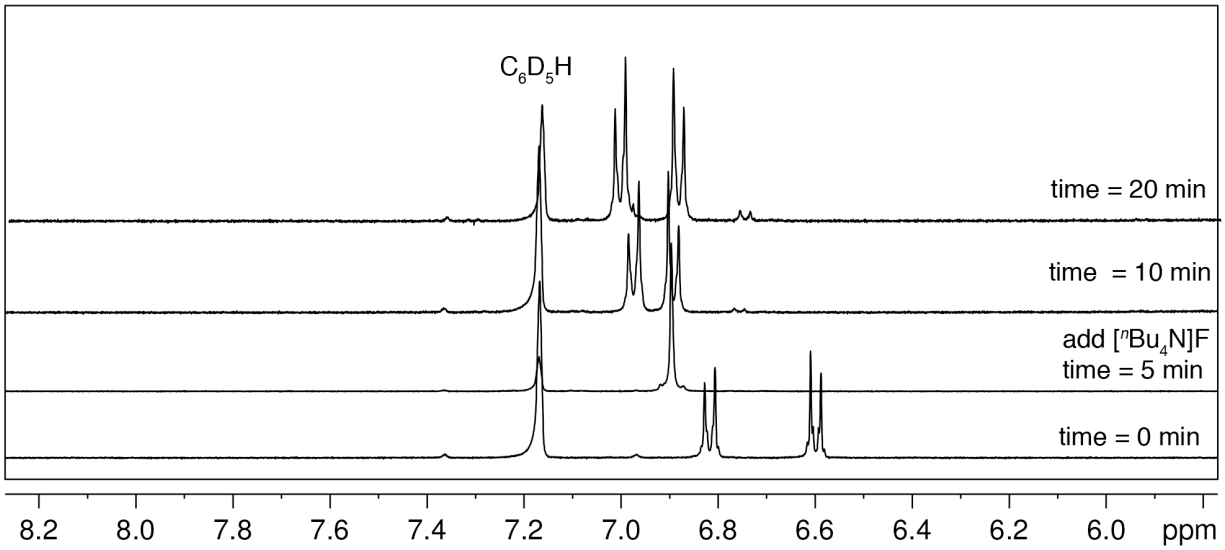

Figure 2.7. ^{1}H NMR aryl region reaction progress for the synthesis of W(CC_6H_4-4-OH)(dmpe)$_2$Cl in C_6D_6.

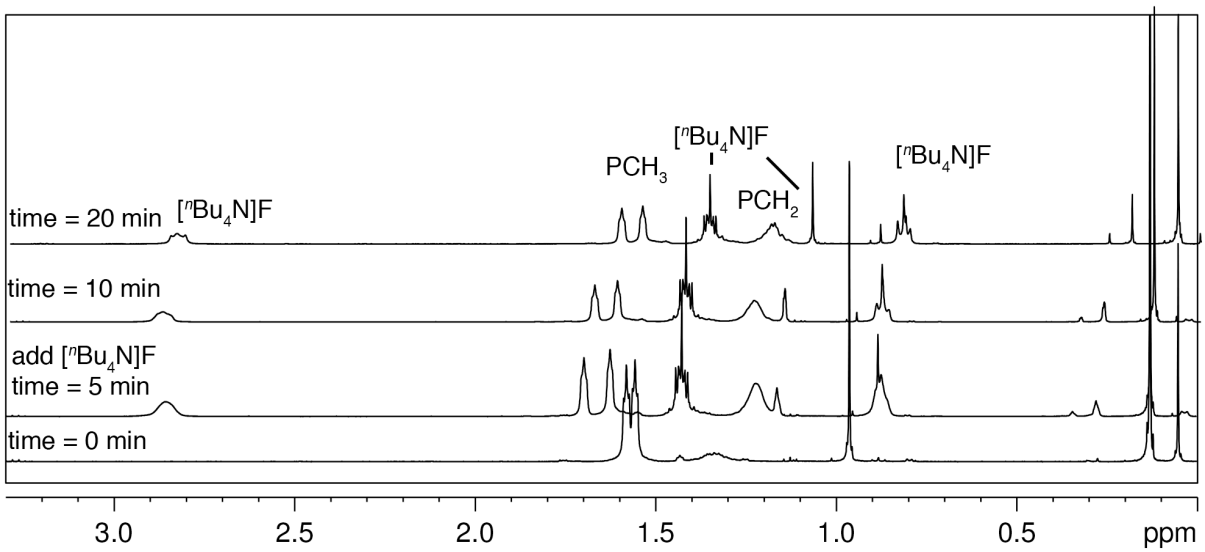

Figure 2.8. ^{1}H NMR alkyl region reaction progress for the synthesis of W(CC_6H_4-4-OH)(dmpe)$_2$Cl in C_6D_6.

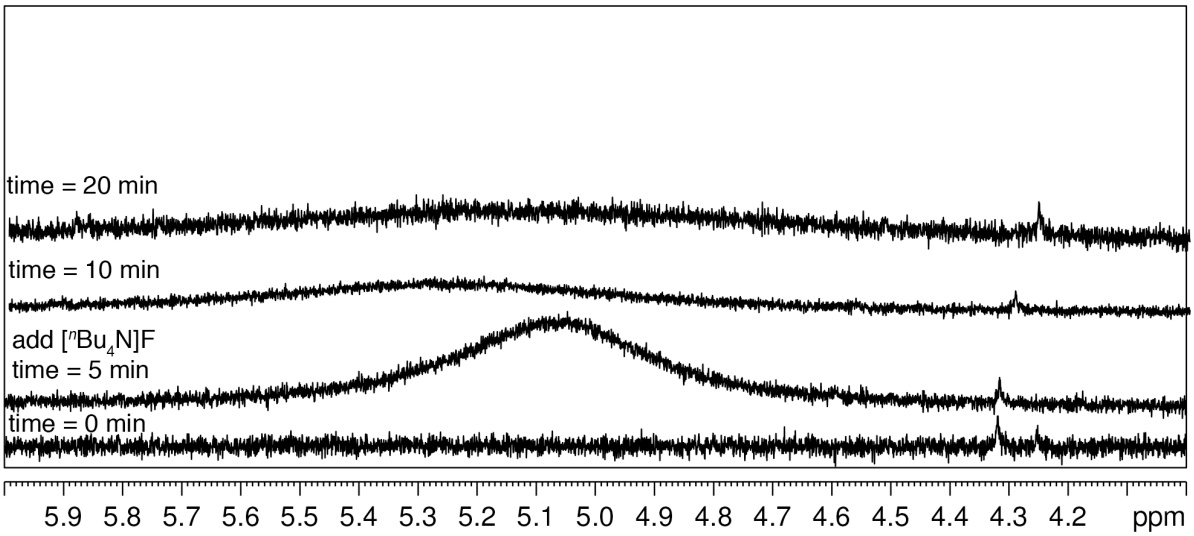

Figure 2.9. ^{1}H NMR OH region reaction progress for the synthesis of W(CC_6H_4-4-OH)$(dmpe)_2Cl$ in C_6D_6.

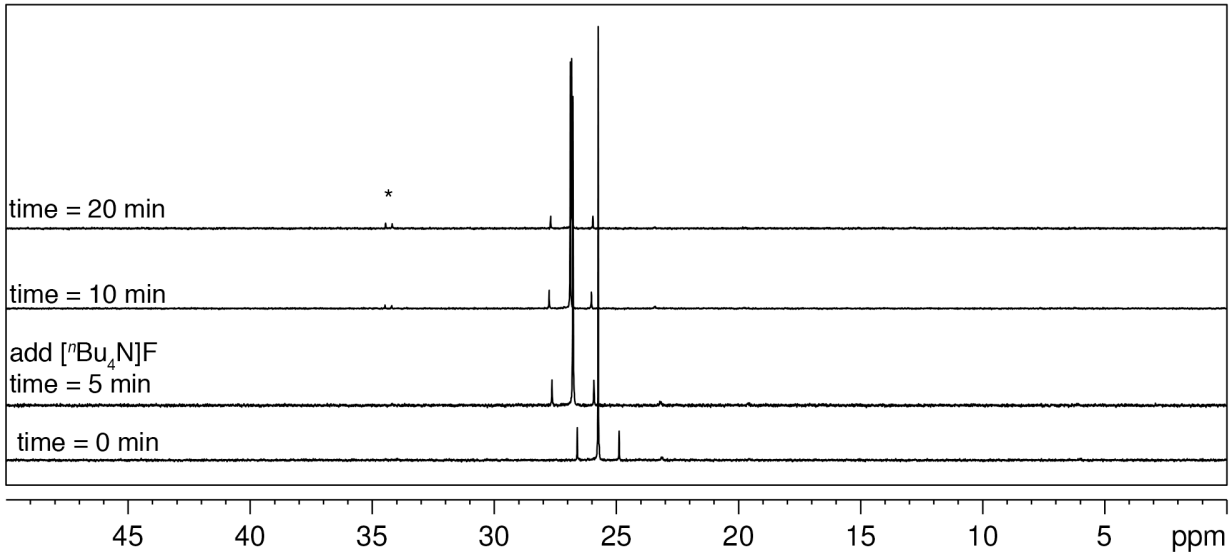

Figure 2.10. $^{31}P\{^{1}H\}$NMR for the synthesis of W(CC_6H_4-4-OH)$(dmpe)_2Cl$ in C_6D_6. The asterisk (*) indicates the ingrowth of an impurity resonance attributed to W(CC_6H_4-4-OH)$(dmpe)_2F$.

2.2.3. Optimization of synthetic approaches for W(CAr)L$_4$F. The development of W(CAr)L$_4$F compounds is of interest because these strong donors destabilize the π*(WCAr) orbital (Chapter 3). The one example of such a compound, W(CH)$(dmpe)_2F$, was prepared in

40% yield by treatment of W(CH)(dmpe)$_2$(OTf) with KF•18-crown-6 in THF for 30 d.[10] This approach was taken because KF can be made rigorously anhydrous, which was important due to the sensitivity of the methylidyne ligand to water. In view of the lengthy reaction time and low yield, alternative synthetic methods for W(CAr)L$_4$F were sought. One approach was to avoid the necessity to prepare W(CAr)(PP)$_2$(OTf) by direct reaction of W(CAr)(PP)$_2$Cl with F^- sources, which was tested with W(CPh)(dmpe)$_2$Cl (Table 2.2). The fluoride sources and conditions used were KF in refluxing DMF, which provided no product after 5 d; [^{n}NBu$_4$]F·3H$_2$O in refluxing THF; which provided a trace of product after 2 d; and a gross excess of CsF (1.0 g, 6.58 mmol; W(CPh)(dmpe)$_2$Cl, 0.1g, 0.164 mmol) in a refluxing 1:1 mixture of THF and CH$_3$CN (20 mL), which resulted in approximately 83% conversion overnight, together with trace impurities (Figure 2.11). Unfortunately, the reaction was not observed to progress further during multiple days of subsequent reflux, so this method was not pursued further.

Table 2.2. Synthesis of W(CPh)(dmpe)$_2$F from W(CPh)(dmpe)$_2$Cl *via* reaction with F^- sources.

Conditions	Conversion %[a]	Notes
KF, DMF, Δ	0	5 days
[^{n}NBu$_4$]F·3H$_2$O, THF Δ	tr	2 days
xss CsF, THF/CH$_3$CN, Δ	83%	1 day

[a] Conversion monitored by $^{31}P\{^1H\}$ NMR spectroscopy.

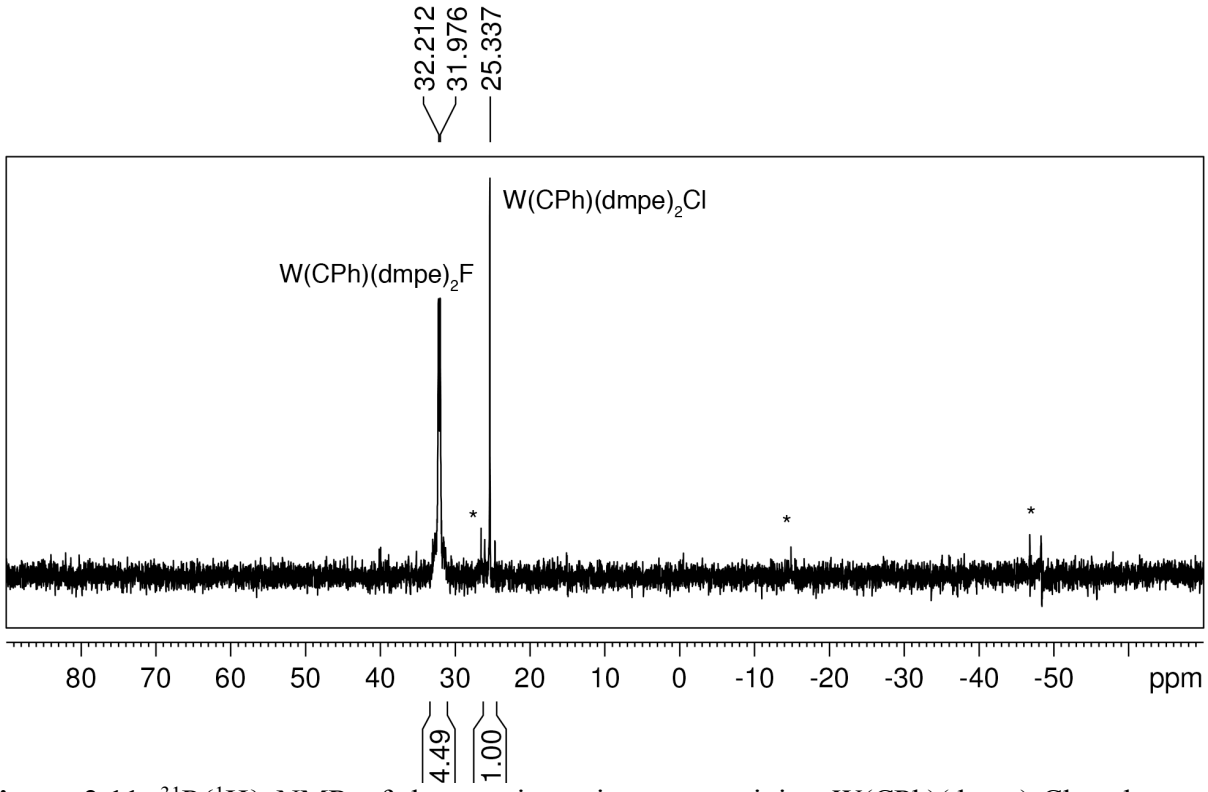

Figure 2.11. $^{31}P\{^{1}H\}$ NMR of the reaction mixture containing W(CPh)(dmpe)$_2$Cl and excess CsF in a 1:1 mixture of THF and CH_3CN. Asterisks (*) indicate an unidentified impurity in the reaction mixture.

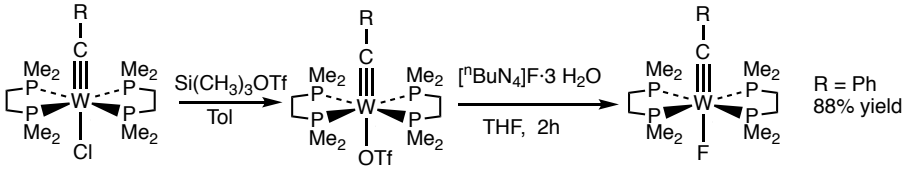

Figure 2.12. Optimization of the synthesis of W(CAr)(dmpe)$_2$F *via* –OTf.

The second approach to preparing W(CAr)(PP)$_2$F compounds was to react W(CAr)(PP)$_2$(OTf) with a more soluble fluoride source than the originally employed KF•18-crown-6. The reaction between [^{n}NBu$_4$]F·3H$_2$O and W(CPh)(dmpe)$_2$(OTf) in THF resulted in complete conversion to W(CPh)(dmpe)$_2$F after 2 h, as judged by $^{31}P\{^{1}H\}$ NMR spectroscopy (Figure 2.12). The isolated yield was 88% after recrystallization. This method was also used to prepare W(CC$_6$H$_4$-4-pyr)(dmpe)$_2$F. Unlike for W(CPh)(dmpe)$_2$F, which was prepared from isolated and purified W(CPh)(dmpe)$_2$(OTf), W(CC$_6$H$_4$-4-pyr)(dmpe)$_2$(OTf) was prepared *in-situ*

from the reaction between $W(CC_6H_4\text{-}4\text{-}pyr)(dmpe)_2Cl$ and $Me_3Si(OTf)$. Interestingly, this product exhibited a broad $^{31}P\{^1H\}$ NMR resonance (Figure 2.13). Nonetheless, addition of $[^nBu_4N]F\cdot 3H_2O$ to this mixture resulted in a rapid conversion to $W(CC_6H_4\text{-}4\text{-}pyr)(dmpe)_2F$; the yield from $W(CC_6H_4\text{-}4\text{-}pyr)(dmpe)_2Cl$ in this one-pot method was 65%. This improved reaction should facilitate synthesis of $W(CAr)(PP)_2F$ compounds.

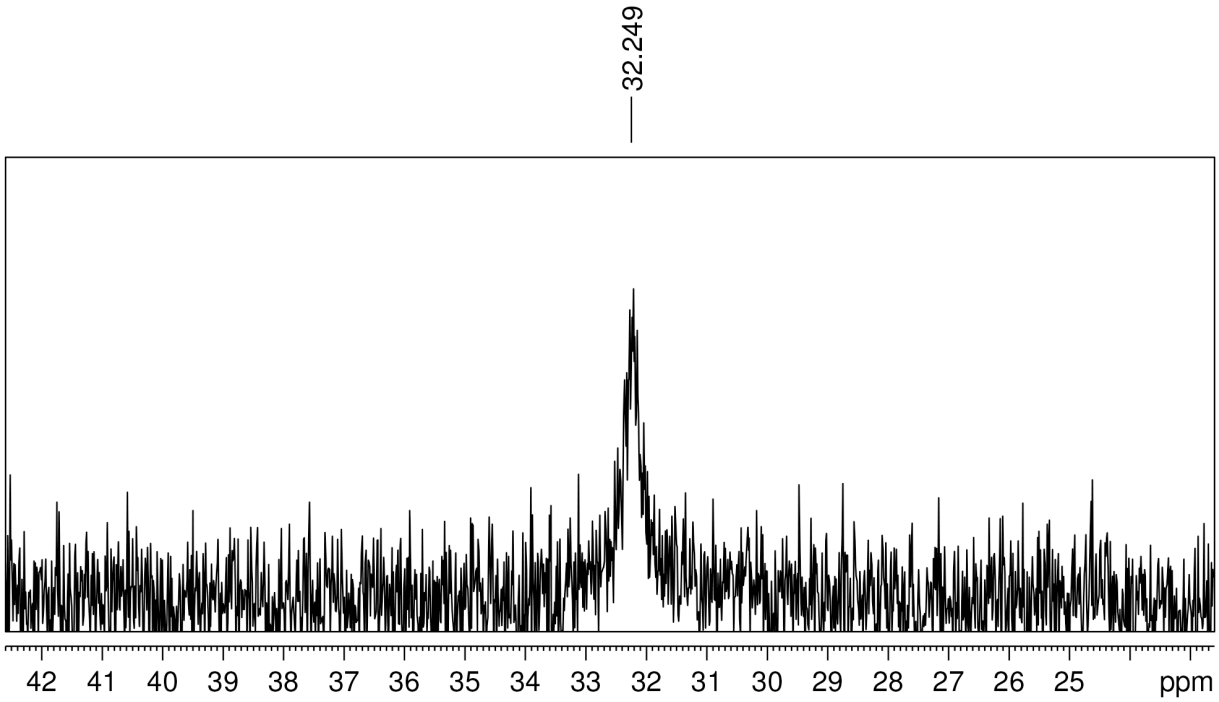

Figure 2.13. Crude reaction mixture of the reaction between $W(CC_6H_4\text{-}4\text{-}pyr)(dmpe)_2Cl$ and $Si(CH_3)_3(OTf)$.

2.2.4. Molecular structures of W(CAr)L_4X compounds. X-ray crystallography was used to characterize the structures of W(CPh)(dmpe)$_2$Cl, W(CPh)(dmpe)$_2$F, W(CC_6H_4-4-pyr)(dmpe)$_2$Cl, and W(CPh)(depe)$_2$Cl. The structures are shown in Figures 2.14–2.17 and selected bond distances and bond angles are set forth in Table 2.3. All of the W(CAr)L_4X compounds exhibit a pseudo-octahedral structure with the alkylidyne (CAr) ligand *cis* to the phosphine groups and *trans* to the halide as expected from the crystallography of other tungsten-alkylidyne compounds.[11] The alkylidyne substituent bisects the backbone of the phosphines in the case of the W(CAr)L_4Cl structures, while it bisects the cleft between the phosphine groups for W(CPh)(dmpe)$_2$F. Presumably, the energy difference between these configurations is small. Amongst these complexes and previously reported W(CPh)(dppe)$_2$Cl[11] the core bond distances are essentially identical. The W≡C bond for all compounds are within ± 3σ of one another and the W–P bond lengths span the narrow range 2.4295-2.4881 Å. The W–X distances of the chloride compounds are ordered such that W–Cl (dppe) is shorter than W–Cl(dmpe), although there is virtually no difference in the bond length between W(CC_6H_4-4-pyr)(dmpe)$_2$Cl, W(CPh)(dmpe)$_2$Cl, and W(CPh)(depe)$_2$Cl.

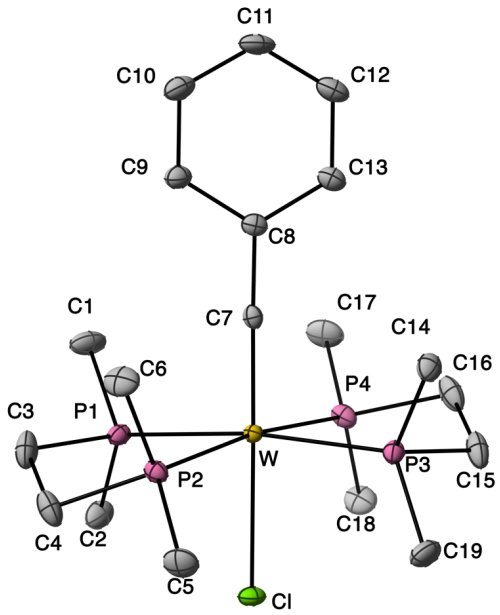

Figure 2.14. Molecular structure of W(CPh)(dmpe)$_2$Cl as determined by X-ray crystallography (50% probability ellipsoids). Hydrogen atoms are not shown.

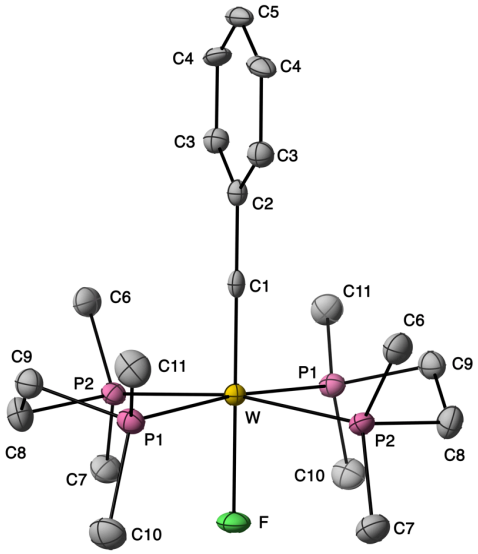

Figure 2.15. Molecular structure of W(CPh)(dmpe)$_2$F as determined by X-ray crystallography (50% probability ellipsoids). Hydrogen atoms are not shown.

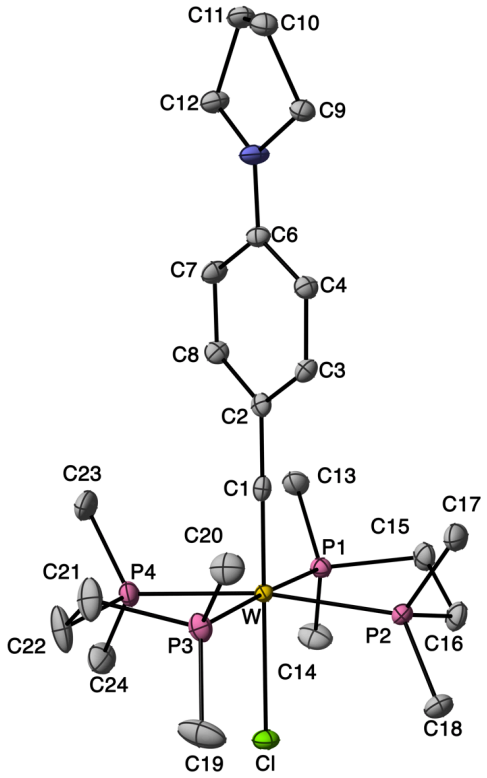

Figure 2.16. Molecular structure of W(CC_6H_4-4-pyr)$(dmpe)_2Cl$ as determined by X-ray crystallography (50% probability ellipsoids). Hydrogen atoms, interstitial THF, and the disorder within one of the dmpe ligands are not shown.

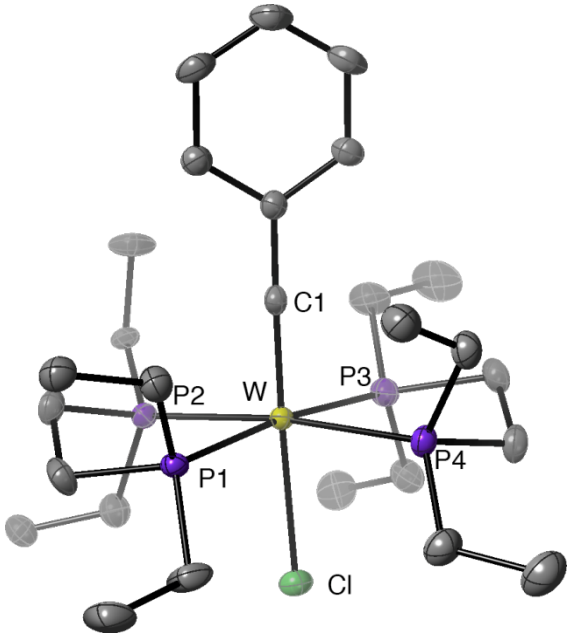

Figure 2.17. Molecular structure of W(CPh)$(depe)_2Cl$ as determined by X-ray crystallography (50% probability ellipsoids). Hydrogen atoms and disorder are not shown.

Table 2.3. Selected bond distances and angles for W(CAr)L_4X compounds.

Bond/Angle	W(CPh)$(dppe)_2Cl$[a]	W(CPh)$(dmpe)_2Cl$[b]	W(CPh)$(depe)_2Cl$	W(CPh)$(dmpe)_2F$[b]	W(CC_6H_4-4-pyr)$(dmpe)_2Cl$[b]
W≡C	1.833(5)	1.829(2)	1.817(4)	1.814(7)	1.8197(18)
W–X	2.5373(14)	2.5834(5)	2.577(1)	2.100(4)	2.5832(4)
W–P(1)	2.4819(14)	2.4332(6)	2.460(1)	2.4308(13)	2.4295(5)
W–P(2)	2.4898(14)	2.4445(6)	2.468(1)	2.4276(13)	2.4367(5)
W–P(3)	2.5056(14)	2.4432(6)	2.460(1)	2.4308(13)	2.4320(5)
W–P(4)	2.4749(14)	2.4272(6)	2.436(1)	2.4276(13)	2.4286(5)
W–P(avr)	2.4881[14]	2.4370[6]	2.456[1]	2.4292[13]	2.4319[5]
C(1)–C(2)	1.441(8)	1.433(3)	1.448(7)	1.474(9)	1.442(2)
C(1)–W–X	177.05(17)	178.38(6)	178.3(3)	180.0	179.74(6)
C(2)–C(1)–W	178.3(4)	176.76(16)	177.9(9)	180.0	179.49(14)
P(1)–W–P(2)	79.62(5)	80.809(19)	80.11(4)	80.25(4)	81.190(16)
P(2)–W–P(3)	99.74(5)	98.565(19)	97.87(4)	99.18(4)	99.156(16)
P(3)–W–P(4)	80.00(5)	80.741(19)	80.50(4)	80.24(4)	81.067(17)
P(4)–W–P(1)	100.33(5)	98.97(2)	100.74(4)	99.18(4)	98.150(16)
P(1)–W–P(3)	177.98(5)	172.655(18)	173.05(4)	173.90(7)	177.238(16)
P(2)–W–P(4)	170.98(5)	172.933(18)	173.38(4)	169.45(6)	170.802(16)
C(1)–W–P(1)	90.04(16)	93.56(6)	92.70(1)	93.05(3)	92.29(5)
C(1)–W–P(2)	94.45(16)	98.03(6)	95.35(1)	95.28(3)	95.63(5)
C(1)–W–P(3)	91.91(16)	93.77(6)	94.11(1)	95.28(3)	90.40(5)
C(1)–W–P(4)	94.57(16)	89.04(6)	91.17(1)	93.05(3)	93.56(5)
C(1)–W–P(avr)	92.74[16]	93.60[6]	93.33[1]	94.16[3]	92.97[5]

[a]Ref. 11. [b]Ref. 30

2.3. Conclusions.

In this chapter, work towards optimizing the synthetic procedures for $W(CAr)L_4X$ complexes and their precursors was presented. A synthetic procedure which is tolerant of electron-donating alkylidyne CAr groups was improved from the Fischer-Mayr-Berke route, in which $W(CAr)\{P(OMe)_3\}_4Cl$ was prepared directly and more quickly from $W(CAr)(pic)_2(CO)_2Cl$ than in two steps from this precursor. The synthetic methods are reproducible, improved overall yields, and allow synthesis of multi-gram quantities of material. Additionally, an improved synthesis of $W(CAr)(PP)_2F$ complexes was developed that requires shorter reaction time and is higher yielding than that previously reported. These synthetic procedures have been applied to the preparation of fifteen tungsten-alkylidyne complexes. The procedures developed in this chapter are instrumental to the design and development of these complexes as potent photoredox chromophores (Chapter 3, 4, and 5).

2.4. Experimental Section.

2.4.1. Synthesis of $W(CAr)L_4X$ complexes.

General Procedures. All manipulations were performed under a nitrogen atmosphere using standard Schlenk and glovebox techniques, unless otherwise noted. Solvents used for synthesis and electrochemistry were HPLC grade and purified by passing them under nitrogen pressure through an anaerobic, stainless-steel system consisting of either two 4.5 in × 24 in (1 gal) columns of activated A2 alumina (CH_3CN, Et_2O, CH_2Cl_2, THF), or one column of activated A2 alumina and one column of activated BASF R3-11 catalyst (toluene, pentane).[31] *o*-Xylene and *n*-hexane were degassed on a vacuum line via five freeze–pump–thaw cycles and stored over 3A molecular sieves. Solvents used for NMR spectroscopy (C_6D_6, CD_2Cl_2) were stored in a

glovebox over 3A molecular sieves. The synthesis of $W(C^tBu)(PMe_3)_4Cl$,[10] $W(CPh)(PMe_3)_4Cl$,[10] $W(CPh)(dmpe)_2(OTf)$,[10] $W(CMes)(dmpe)_2Cl$,[20, 21] and $W(CPh)(dppe)_2Cl$[3] have been previously described and were unmodified in these studies. All other reagents were procured from commercial sources and used as received. ^1H-, $^{13}C\{^1H\}$-, $^{13}C\{^1H,^{31}P\}$-, $^{31}P\{^1H\}$-, ^{19}F- and $^{19}F\{^1H\}$-NMR spectra were measured at room temperature with a Bruker AF-500 or DRX-400 NMR spectrometer. Chemical shifts were measured relative to solvent resonances (^1H, ^{13}C)[32] or external standards (^{31}P, 85% v/v H_3PO_4; ^{19}F, C_6F_6); key ^{13}C and ^{31}P-NMR chemical shifts are set out in Tables 2.4 and 2.5. ESI-MS spectra were measured with an Agilent 6224 TOF-MS. Infrared spectra were measured with a Thermo NEXUS 670 FT-IR. Elemental analyses were performed by Robertson Microlit Laboratories (Ledgewood, NJ).

Synthesis of $[NMe_4][W\{C(O)Ph\}(CO)_5]$. This synthesis followed the literature procedure for this compound,[14] with two modifications: use of commercial and rather than freshly prepared PhLi, and recrystallization of this compound in air. To a suspension of $W(CO)_6$ (5.0 g, 14.21 mmol) in Et_2O (50 mL) was added a solution of PhLi (2 M in Bu_2O, 7.00 mL, 14.00 mmol). Over the course of 1 h the color of the reaction mixture changed to dark yellow and the $W(CO)_6$ dissolved. The volatile components were then removed under vacuum and the remaining dark yellow film of $Li[W\{C(O)Ph\}(CO)_5]$ was dissolved in N_2-purged deionized water (100 mL). The solution was filtered to remove a small amount of unreacted $W(CO)_6$. The filtrate was cooled to 0 °C, and a solution of NMe_4Br (3.08 g, 20.0 mmol) in N_2-purged deionized water (25 mL) was added *via* syringe with stirring. Over the course of 10 min, the reaction mixture became cloudy; filtration provided an orange solid. The solid was collected in air, extracted in air into CH_2Cl_2 (25 mL), and the resulting solution filtered. Addition of Et_2O (250 mL) resulted in precipitation of the dark orange product, which was collected by filtration

and dried under vacuum (4.32 g, 7.84 mmol, 56% yield). The ^{1}H- and ^{13}C{^{1}H}- NMR spectra of this compound matched that of literature.[28] The complex can be stored on the benchtop in a vacuum desiccator.

Synthesis of W(CPh)(pic)$_2$(CO)$_2$Cl. (pic = 4-picoline). The synthesis followed the literature procedure for the synthesis of W(CPh)(py)$_2$(CO)$_2$Br,[17] with two modifications; oxalyl chloride replaced oxalyl bromide and the product was purified by a simpler method than low-temperature column chromatography. A stirred solution of [NMe$_4$][W{C(O)Ph}(CO)$_5$] (3.0 g, 5.43 mmol) in CH_2Cl_2 (50 mL) was cooled to –77 °C using a dry-ice/isopropanol bath. Oxalyl chloride (3.0 mL, 2 M solution in CH_2Cl_2, 6.00 mmol) was added over the course of 30 s by syringe, resulting in an immediate color change of the reaction mixture from yellow to black. The reaction mixture was stirred at –77 °C for 30 min, during which time the black solution lightened slightly. The flask was removed to an ice bath and the reaction mixture was allowed to warm to 0 °C with stirring. Over the course of 15 min, the reaction mixture became opaque and the color changed from black to tan. 4-Picoline (pic, 1.1 mL, 11.80 mmol) was added via syringe. Immediately, the reaction mixture changed in appearance to a homogenous, dark yellow solution. The reaction vessel was removed from the ice bath and allowed to warm to room temperature, while stirring. After 2 h, the volatile components were removed under vacuum, the flask was opened to air, and the residue was washed with pentane (50 mL) and extracted into CH_2Cl_2 (25 mL). The resulting solution filtered through a pad of silica gel (3 cm × 1.5 cm) on a sintered-glass filter. The silica pad was washed with CH_2Cl_2 (65 mL) and the dark yellow filtrate was reduced in volume under vacuum to 20 mL. Addition of pentane (200 mL) resulted in precipitation of the product as bright canary-yellow needles, which were collected by filtration and dried under vacuum (2.60 g, 4.72 mmol, 87% yield). ^{1}H NMR (500.13 MHz, CD_2Cl_2, Figure

2.18): δ 8.91 (d, 4H, *m*-$NC_5\underline{H}_4CH_3$); 7.37 (m, 2H, *m*-C_6H_5); 7.32 (m, 3H, *o*-C_6H_5 and *p*-C_6H_5); 7.17 (d, 4H, *o*-$NC_5\underline{H}_4CH_3$); 2.41 (s, 6H, $NC_5H_4C\underline{H}_3$). $^{13}C\{^1H\}$ NMR (125.75 MHz, CD_2Cl_2, Figure 2.19): δ 262.91 (s with ^{183}W satellites, $^1J_{WC}$ =198 Hz, WC); 221.94 (s with ^{183}W satellites, $^1J_{WC}$ = 167.63 Hz, CO); 152.56 ($N\underline{C}_5H_4CH_3$ or C_6H_4); 151.01 ($N\underline{C}_5H_4CH_3$ or C_6H_4); 149.76 ($N\underline{C}_5H_4CH_3$ or C_6H_4); 129.55 ($N\underline{C}_5H_4CH_3$ or C_6H_4); 128.40 ($N\underline{C}_5H_4CH_3$ or C_6H_4); 127.73 ($N\underline{C}_5H_4CH_3$ or C_6H_4); 126.32 ($N\underline{C}_5H_4CH_3$ or C_6H_4); 21.31 ($NC_5H_4\underline{C}H_3$).

Alternative synthesis of W(CPh){P(OMe)$_3$}$_4$Cl from W(CPh)(pic)$_2$(CO)$_2$Cl. A solution of $W(CPh)(pic)_2(CO)_2Cl$ (2.50 g, 4.53 mmol) in neat trimethylphosphite (25 mL) was stirred at room temperature for 5 min and then slowly heated to reflux with stirring. After 18 h, the reaction mixture was allowed to cool to room temperature and the volatile components were removed under vacuum. The resulting solid was extracted into Et_2O and the resulting solution filtered through Celite to remove a dark-colored impurity. The filtrate was cooled at –40 °C to produce small yellow prisms, which were collected by filtration and dried under vacuum (3.24 g, 4.03 mmol, 89% yield). The ^1H- and $^{13}C\{^1H\}$- NMR spectra of this compound matched that of a purified sample prepared *via* reduction of $W(CPh)Cl_3(DME)$.[10]

Alternative synthesis of W(CPh)(dmpe)$_2$Cl from W(CPh){P(OMe)$_3$}$_4$Cl. To a stirred, room temperature solution of $W(CPh)\{P(OMe)_3\}_4Cl$ (1.0 g, 1.24 mmol) in toluene (40 mL) was added 1,2-bis(dimethylphosphino)ethane (dmpe, 0.391 g, 2.61 mmol). The yellow solution was heated to reflux for 16 h, during which the color of the reaction mixture changed from yellow to purple. The reaction mixture was allowed to cool to room temperature and the volatile components were removed under vacuum. The remaining purple solid was extracted into pentane (100 mL) and the resulting filtered through Celite, which was then washed with pentane (3 × 25 mL). The filtrate was reduced to dryness under vacuum. The purple solid was extracted into Et_2O

(35 mL) and cooled to −30 °C overnight; this provided a bright purple microcrystalline solid, which was collected by filtration and dried under vacuum. (0.590 g, 0.970 mmol, 78% yield). The ^{1}H- and ^{13}C{^{1}H}- NMR spectra of this compound matched that of a purified sample prepared *via* reduction of W(CPh)Cl$_3$(DME).[10]

Alternative synthesis of W(CPh)(depe)$_2$Cl from W(CPh){P(OMe)$_3$}$_4$Cl. To a stirred, room temperature solution of W(CPh){P(OMe)$_3$}$_4$Cl (1.0 g, 1.24 mmol) in toluene (40 mL) was added 1,2-bis(diethylphosphino)ethane (depe, 0.537 g, 2.60 mmol). The yellow solution was heated to reflux. Over the course of 16 h, the color of the reaction mixture changed from yellow to purple. The reaction mixture was allowed to cool to room temperature and the volatile components were removed under vacuum. The remaining purple solid was extracted into pentane (50 mL) and filtered through Celite, which was then washed with pentane (3 × 25 mL). The filtrate was reduced to dryness under vacuum. The purple solid was extracted into pentane (30 mL) and the resulting solution cooled to −30 °C; this provided a bright pink microcrystalline solid, which was collected by filtration and dried under vacuum (0.703 g, 0.975 mmol, 79% yield). The ^{1}H- and ^{13}C{^{1}H}- NMR spectra of this compound matched that of a purified sample prepared *via* reduction of W(CPh)Cl$_3$(DME).[10]

Synthesis of W(CPh)(dmpe)$_2$F. To a stirred, room temperature solution of W(CPh)(dmpe)$_2$(OTf) (0.111 g, 0.153 mmol) in THF (25 mL) was added [NBu$^n_4$]F·2H$_2$O (0.090 g, 0.344 mmol). The color of the reaction mixture changed from pink to bright red over the course of 2 h, after which the volatile components were removed under vacuum. The resulting red solid was extracted into a minimum amount of pentane, filtered through Celite, and reduced to dryness under vacuum to produce a bright red film. The crude product was recrystallized from Et$_2$O (5 mL) at −50 °C to yield bright red microcrystals of suitable quality for X-ray diffraction

studies; these were collected by filtration and dried under vacuum (0.075 g, 0.126 mmol, 88% yield). ^{1}H NMR (C_6D_6, 500.1 MHz, Figure 2.20): δ 6.99 (t, 2 H, *m*-C_6H_5); 6.92 (t, 1 H, *p*-C_6H_5); 6.79 (d, 2 H, *o*-C_6H_5); 1.62 (s, 12 H, PCH_3); 1.50 (br m, 4 H, PCH_2); 1.40 (br m, 4 H, PCH_2); 1.30 (s, 12 H, PCH_3). $^{13}C\{^{1}H\}$ NMR (C_6D_6, 125.8 MHz, Figure 2.21-2.22): δ 252.67 (d quin, WC, $^{2}J_{CF}$ = 103 Hz, $^{2}J_{CP}$ = 10 Hz); 155.42 (d, C_6H_5, $^{3}J_{CF}$ = 16 Hz); 128.62 (C_6H_5); 127.60 (C_6H_5); 121.52 (C_6H_5); 34.10 (m, PCH_2); 21.55 (m, PCH_3); 13.82 (m, PCH_3). $^{31}P\{^{1}H\}$ NMR (C_6D_6, 202.45 MHz, Figure 2.23): δ 32.75 (d with satellites, $^{1}J_{WP}$ = 283 Hz, $^{2}J_{PF}$ = 49 Hz). $^{19}F\{^{1}H\}$ NMR (C_6D_6, 470.6 MHz, Figure 2.24): δ –284.22 (quin with satellites, $^{1}J_{WF}$ = 61 Hz, $^{2}J_{PF}$ = 49 Hz). ESI-MS (THF, 298 K): *m*/*z* 593.2 (M^+, rel. int. 100, calc 593.1), 575.2 ($[M–F]^+$, rel. int. 49, calc 575.1), 441.1 ($[M–dmpe]^+$, rel. int. 47, calc 441.1). Anal. Calc. (Found) for $C_{19}H_{37}ClFP_4W$: C 38.53 (38.32); H 6.30 (6.07).

Synthesis of [NMe$_4$][W{C(O)C$_6$H$_4$-4-OCH$_3$}(CO)$_5$]. A stirred, room temperature solution of 4-iodoanisole (3.02 g, 12.91 mmol) in Et_2O (100 mL) was cooled to 0 °C and ^{n}BuLi (8.12 mL, 1.6 M in hexane, 13.00 mmol) was added via syringe. After 2 h the colorless reaction mixture was transferred via cannula to a stirred, room-temperature suspension of $W(CO)_6$ (5.0 g, 14.21 mmol) in Et_2O (50 mL). Over the course of 1 h, the color of the reaction mixture changed to dark yellow and the $W(CO)_6$ dissolved. The volatile components were then removed under vacuum and the remaining dark yellow film of Li[W{C(O)C$_6$H$_4$-4-OCH$_3$}(CO)$_5$] was dissolved in N_2-purged deionized water (100 mL). The solution was filtered to remove a small amount of unreacted $W(CO)_6$. The filtrate was cooled to 0 °C, and a solution of NMe_4Br (2.00 g, 12.98 mmol) in N_2-purged deionized water (25 mL) was added *via* syringe with stirring. Over the course of 10 min, the reaction mixture became cloudy; filtration provided an orange solid. The solid was extracted into CH_2Cl_2 (25 mL), and the resulting solution was filtered. Addition of

Et_2O (250 mL) resulted in precipitation of the dark orange product, which was collected by filtration and dried under vacuum (4.22 g, 7.91 mmol, 61% yield). ^{1}H NMR (400.13 MHz, CD_3CN, Figure 2.25): δ 7.54 (d, 2H, *m*-C_6H_4); 6.85 (d, 2H, *o*-C_6H_4); 3.78 (s, 3H, OCH_3); 3.07 (s, 12H, $N(CH_3)_4$). $^{13}C\{^1H\}$ NMR (100.61 MHz, CD_3CN, Figure 2.26): δ 276.47 (W<u>C</u>(O)Ar); 208.86 (CO); 204.66 (s with ^{183}W satellites, $^1J_{WC}$ = 121 Hz, CO); 161.18 (C_6H_4); 150.60 (C_6H_4); 129.09 (C_6H_4); 113.31 (C_6H_4); 56.12 (t, $^1J_{NC}$ = 4 Hz, $N(CH_3)_4$); 55.91 (OCH_3).

Synthesis of W(CC$_6$H$_4$-4-OCH$_3$)(pic)$_2$(CO)$_2$Cl (pic = 4-picoline). A stirred solution of [NMe$_4$][W{C(O)C$_6$H$_4$-4-OCH$_3$}(CO)$_5$] (3.0 g, 5.62 mmol) in CH_2Cl_2 (50 mL) was cooled to –77 °C using a dry-ice/isopropanol bath. Oxalyl chloride (3.37 mL, 2 M solution in CH_2Cl_2, 6.75 mmol) was added over the course of 30 s by syringe, resulting in an immediate color change of the reaction mixture from yellow to bright red. The reaction mixture was stirred at –77 °C for 30 min, during which time the bright-red solution lightened slightly. The flask was removed to an ice bath and the reaction mixture was allowed to warm to 0 °C with stirring. Over the course of 15 min, the reaction mixture became opaque and the color changed from bright red to orange. 4-Picoline (pic, 1.1 mL, 11.80 mmol) was added via syringe. Immediately, the color of the reaction mixture changed in appearance to a homogenous, dark yellow solution. The reaction vessel was removed from the ice bath and allowed to warm to room temperature, while stirring. After 2 h, the volatile components were removed under vacuum, the flask was opened to air, and the residue was washed with pentane (50 mL), extracted into CH_2Cl_2 (25 mL), and the resulting solution filtered through a pad of silica gel (3 cm × 1.5 cm) on a sintered-glass filter. The silica pad was washed with CH_2Cl_2 (65 mL) and the dark yellow filtrate was reduced in volume under vacuum to 20 mL. Addition of pentane (200 mL) resulted in precipitation of the product as bright canary-yellow needles, which were collected by filtration and dried under vacuum (2.67 g, 4.61

mmol, 82% yield). ^{1}H NMR (500.13 MHz, CD_2Cl_2, Figure 2.27): δ 8.87 (d, 4H, *m*-$NC_5\underline{H}_4CH_3$); 7.31 (d, 2H, *m*-C_6H_4); 7.13 (d, 4H, *o*-$NC_5\underline{H}_4CH_3$); 6.81 (d, 2H, *o*-C_6H_4); 3.79 (s, 3H, OCH_3); 2.37 (s, 6H, $NC_5H_4C\underline{H}_3$). $^{13}C\{^{1}H\}$ NMR (125.75 MHz, CD_2Cl_2, Figure 2.28): δ 263.72 (s with ^{183}W satellites, $^{1}J_{WC}$ =196 Hz, WC); 222.25 (s with ^{183}W satellites, $^{1}J_{WC}$ = 170 Hz, CO); 159.69 ($N\underline{C}_5H_4CH_3$ or C_6H_4); 152.68 ($N\underline{C}_5H_4CH_3$ or C_6H_4); 151.06 ($N\underline{C}_5H_4CH_3$ or C_6H_4); 143.34 ($N\underline{C}_5H_4CH_3$ or C_6H_4); 131.36 ($N\underline{C}_5H_4CH_3$ or C_6H_4); 126.34 ($N\underline{C}_5H_4CH_3$ or C_6H_4); 113.89 ($N\underline{C}_5H_4CH_3$ or C_6H_4); 55.83 (OCH_3); 21.39 ($NC_5H_4\underline{C}H_3$). IR (CH_2Cl_2, cm^{-1}): 1972 (ν_{CO}); 1878 (ν_{CO}).

Synthesis of W(CC$_6$H$_4$-4-OCH$_3$){P(OMe)$_3$}$_4$Cl. A solution of W(CC_6H_4-4-OCH_3)$(pic)_2(CO)_2Cl$ (1.41 g, 2.43 mmol) in neat trimethylphosphite (25 mL) was stirred at room temperature for 5 min and then slowly heated to reflux with stirring. After 24 h the reaction mixture was allowed to cool to room temperature and the volatile components were removed under vacuum. The resulting solid was extracted into Et_2O and filtered through Celite to remove a dark-colored impurity. The filtrate was cooled at –40 °C to produce a canary-yellow microcrystalline solid, which was collected by filtration and dried under vacuum (1.86 g, 2.24 mmol, 92% yield). ^{1}H NMR (500.13 MHz, CD_2Cl_2, Figure 2.29): δ 7.57 (d, 2H, *m*-C_6H_4); 6.69 (d, 2H, *o*-C_6H_4); 3.80 (virtual t, 36H, $P(OMe)_3$); 3.29 (s, 3H, OCH_3). $^{13}C\{^{1}H\}$ NMR (125.75 MHz, C_6D_6, Figure 2.30-2.31): δ 249.98 (quin, $^{2}J_{CP}$ = 18 Hz, WC); 157.41 (C_6H_4); 146.99 (t, J_{CP} = 2.5 Hz, C_6H_4); 131.94 (quin, J_{CP} = 3 Hz, C_6H_4); 112.89 (C_6H_4); 54.68 (OCH_3); 52.18 ($P(OMe)_3$). $^{31}P\{^{1}H\}$ NMR (C_6D_6, 202.45 MHz, Figure 2.32): δ 150.75 (s with ^{183}W satellites, $^{1}J_{WP}$ = 430 Hz). MALDI-MS (anthracene matrix, *m/z*): 834.11 (M^+, Calc. 834.09); 799.22 (M^+–Cl, Calc. 799.12); 710.05 (M^+–$P(OMe)_3$, Calc. 710.06).

Synthesis of W(CC$_6$H$_4$-4-OCH$_3$)(dmpe)$_2$Cl. To a stirred, room temperature solution of W(CC$_6$H$_4$-4-OCH$_3$){P(OMe)$_3$}$_4$Cl (0.200 g, 0.239 mmol) in toluene (40 mL) was added 1,2-bis(dimethylphosphino)ethane (dmpe, 0.075 g, 0.503 mmol). The yellow solution was heated to reflux. Over the course of 16 h, the color of the reaction mixture changed from yellow to pink. The reaction mixture was allowed to cool to room temperature and the volatile components were removed under vacuum. The remaining pink film was extracted into pentane (50 mL) and filtered through Celite, which was then washed with pentane (3 × 25 mL). The filtrate was reduced to dryness under vacuum, and the crude product was recrystallized by cooling a THF solution layered with pentane (1:1) to −30 °C; this provided a bright-red microcrystalline solid, which was collected by filtration and dried under vacuum (0.112 g, 0.176 mmol, 73% yield). ^{1}H NMR (C$_6$D$_6$, 500.13 MHz, Figure 2.33): δ 6.82 (d, 2H, *m*-C$_6$H$_4$); 6.56 (d, 2H, *o*-C$_6$H$_4$); 3.27 (s, 3H, OCH$_3$); 1.59 (overlapping s and br m, 14H, PCH$_3$ and PCH$_2$); 1.57 (overlapping s and br m, 14H, PCH$_2$ and PCH$_3$); 1.36 (m, 4H, PCH$_2$). ^{13}C{^{1}H} NMR (C$_6$D$_6$, 125.77 MHz, Figure 2.34-2.35): δ 251.34 (quin, $^2J_{PC}$ =11 Hz, WC); 156.21 (C$_6$H$_4$); 147.67 (C$_6$H$_4$); 130.20 (quin, J_{CP} = 3 Hz, C$_6$H$_4$); 113.34 (C$_6$H$_4$); 54.76 (OCH$_3$); 34.16 (PCH$_2$); 22.13 (PCH$_3$); 16.07 (PCH$_3$). ^{31}P{^{1}H} NMR (C$_6$D$_6$, 202.45 MHz, Figure 2.36): 26.56 (s with ^{183}W satellites, $^1J_{WP}$ = 279 Hz). LDI-MS (*m/z*): 638.13 (M$^+$, Calc. 638.11).

Synthesis of W(CC$_6$H$_4$-4-OCH$_3$)(dppe)$_2$Cl. To a stirred, room temperature solution of W(CC$_6$H$_4$-4-OCH$_3$){P(OMe)$_3$}$_4$Cl (0.500 g, 0.708 mmol) in toluene (40 mL) was added 1,2-bis(diphenylphosphino)ethane (dppe, 0.620 g, 1.58 mmol). The yellow solution was heated to reflux. Over the course of 16 h, the color of the reaction mixture changed from yellow to red. The reaction mixture was allowed to cooled to room temperature and the volatile components were removed under vacuum. The crude red solid was triturated with Et$_2$O for 2 h, collected by

filtration, and dried under vacuum to provide a light red solid (0.667 g, 0.587 mmol, 83% yield). ^{1}H NMR (C_6D_6, 500.13 MHz, Figure 2.37): δ 7.61 (br s, 8H, *o*-PPh_2); 7.49 (br s, 8H, *o*-PPh_2); 7.00 (overlapping t, 8H, *p*-PPh_2); 6.95 (t, 8H, *m*-PPh_2); 6.87 (t, 8H, *m*-PPh_2); 6.24 (d, 2H, *m*-C_6H_4); 5.84 (d, 2H, *o*-C_6H_4); 3.20 (s, 3H, OCH_3); 2.75 (br m, 4H, PCH_2); 2.42 (br m, 4H, PCH_2). ^{13}C{^{1}H} NMR (C_6D_6, 125.77 MHz, Figure 2.38): δ 249.76 (WC); 156.07 (C_6H_4 or PPh_2); 145.97 (C_6H_4 or PPh_2); 141.24 (C_6H_4 or PPh_2); 139.27 (C_6H_4 or PPh_2); 134.56 (C_6H_4 or PPh_2); 134.39 (C_6H_4 or PPh_2); 132.01 (C_6H_4 or PPh_2); 128.84 (C_6H_4 or PPh_2); 128.55 (C_6H_4 or PPh_2); 127.45 (C_6H_4 or PPh_2); 111.86 (C_6H_4 or PPh_2); 54.49 (OCH_3); 32.93 (PCH_2). **Note:** One ^{13}C{^{1}H} NMR resonance that is likely at 127.78 ppm was observed to considerably overlap with the solvent (C_6D_6) resonance and could not be accurately assigned. ^{31}P{^{1}H} NMR (C_6D_6, 202.45 MHz, Figure 2.39): 46.35 (s with ^{183}W satellites, $^{1}J_{WP}$ = 281 Hz). HR-MS (THF, 70V, *m/z*): 1134.24 (M^+, Calc. 1134.24).

Synthesis of [NMe_4][W(CC_6H_4-4-OTBDMS)$(CO)_5$] (TBDMS = *tert*-butyldimethylsilyl). A stirred, room temperature solution of 1-bromo-4-[(*tert*-butyldimethylsilyl)oxy]benzene (4.00 g, 13.92 mmol) in Et_2O (100 mL) was cooled to 0 °C and ^{n}BuLi (5.6 mL, 2.5 M in hexane, 14.00 mmol) was added via syringe. After 2 h the colorless reaction mixture was transferred via cannula to a stirred, room-temperature suspension of $W(CO)_6$ (5.0 g, 14.21 mmol) in Et_2O (50 mL). Over the course of 1 h, the color of the reaction mixture changed to dark yellow and the $W(CO)_6$ dissolved. The volatile components were then removed under vacuum and the remaining dark yellow oil of Li[W{C(O)C_6H_4-4-OTBDMS}$(CO)_5$] was dissolved in N_2-purged deionized water (100 mL). The solution was filtered to remove a small amount of unreacted $W(CO)_6$. The filtrate was cooled to 0 °C, and a solution of NMe_4Br (5.36 g, 34.8 mmol) in N_2-purged deionized water (25 mL) was added *via*

syringe with stirring. Over the course of 10 min, the reaction mixture became cloudy and a dark yellow oil separated from the reaction mixture. The dark yellow oil was extracted with CH_2Cl_2 (25 mL), dried with $MgSO_4$ and filtered. An attempt to recrystallize the oil from THF/pentane was unsuccessful. (4.29 g, 7.67 mmol, 55% crude yield). ^{1}H NMR (400.13 MHz, CD_2Cl_2, Figure 2.40): δ 7.54 (d, 2H, *m*-C_6H_4); 6.81 (d, 2H, *o*-C_6H_4); 3.22 (s, 12H, $N(CH_3)_4$); 1.00 (s, 9H, ^{t}Bu); 0.22 (s, 6H, $SiCH_3$). $^{13}C\{^1H\}$ NMR (100.61 MHz, CD_2Cl_2, Figure 2.41): δ 281.00 (W<u>C</u>(O)Ar); 207.91 (CO); 203.57 (s with ^{183}W satellites, $^1J_{WC}$ = 127 Hz, CO); 156.1 (C_6H_4); 150.22 (C_6H_4); 128.17 (C_6H_4); 118.70 (C_6H_4); 67.70 ($SiCH_3$,); 55.82 (t, $^1J_{NC}$ = 4 Hz, $N(CH_3)_4$); 25.53 (Si^{t}Bu). **Note:** The ^{1}H and $^{13}C\{^1H\}$ NMR spectra were each observed to contain two impurities that are labeled with an asterisk. The product was used in subsequent reactions without additional purification.

Synthesis of W(CC$_6$H$_4$-4-OTBDMS)(pic)$_2$(CO)$_2$Cl (pic = 4-picoline). A stirred solution of $[NMe_4][W\{C(O)C_6H_4\text{-}4\text{-}OTBDMS\}(CO)_5]$ (4.29 g, 7.67 mmol) in CH_2Cl_2 (50 mL) was cooled to –77 °C using a dry-ice/isopropanol bath. Oxalyl chloride (4.21 mL, 2 M solution in CH_2Cl_2, 8.43 mmol) was added over the course of 30 s by syringe, resulting in an immediate color change of the reaction mixture from yellow to bright red. The reaction mixture was stirred at –77 °C for 30 min, during which time the bright-red solution lightened slightly. The flask was removed to an ice bath and the reaction mixture was allowed to warm to 0 °C with stirring. Over the course of 15 min, the reaction mixture became opaque and the color changed from bright red to orange. 4-Picoline (pic, 1.65 mL, 17.00 mmol) was added via syringe. Immediately, the color of the reaction mixture changed in appearance to a homogenous, dark yellow solution. The stirred reaction mixture was allowed to warm to room temperature. After 2 h, the volatile components were removed under vacuum, the flask was opened to air, and the residue was

washed with pentane (50 mL), extracted into CH_2Cl_2 (25 mL), and the resulting solution filtered through a pad of silica gel (3 cm × 1.5 cm) on a sintered-glass filter. The silica pad was washed with CH_2Cl_2 (65 mL) and the dark yellow filtrate was reduced in volume under vacuum to 20 mL. Addition of pentane (200 mL) resulted in precipitation of the product as a yellow powder, which was collected by filtration and dried under vacuum (3.39 g, 4.98 mmol, 65% yield). ^{1}H NMR (500.13 MHz, CD_2Cl_2, Figure 2.42): δ 8.87 (d, 4H, *m*-$NC_5\underline{H}_4CH_3$); 7.24 (d, 2H, *m*-C_6H_4); 7.12 (d, 4H, *o*-$NC_5\underline{H}_4CH_3$); 6.74 (d, 2H, *o*-C_6H_4); 2.37 (s, 6H, $NC_5H_4C\underline{H}_3$); 0.98 (s, 9H, Si^{t}Bu); 0.20 (s, 6H, $SiCH_3$). $^{13}C\{^1H\}$ NMR (125.75 MHz, CD_2Cl_2, Figure 2.43): δ 263.76 (WC); 222.63 (CO); 152.64 ($N\underline{C}_5H_4CH_3$ or C_6H_4); 150.99 ($N\underline{C}_5H_4CH_3$ or C_6H_4); 131.24 ($N\underline{C}_5H_4CH_3$ or C_6H_4); 126.28 ($N\underline{C}_5H_4CH_3$ or C_6H_4); 120.05 ($N\underline{C}_5H_4CH_3$ or C_6H_4); 25.78 (Si^{t}Bu); 21.33 ($SiCH_3$). **Note:** $^{13}C\{^1H\}$ NMR resonances due to $\underline{C}(CH_3)_3$,*ipso*-C_6H_4, *para*-C_6H_4, and *ipso*-pic resonances are not visible due to the signal-to-noise obtained from this experiment.

Synthesis of W(CC_6H_4-O-TBDMS)(dmpe)$_2$Cl. To a stirred, room-temperature solution of W(CC_6H_4-4-OTBDMS)(pic)$_2$(CO)$_2$Cl (1.25g, 1.88 mmol) in THF (35 mL) was added trimethylphosphite (2.33 g, 18.8 mmol). A reflux condenser was affixed to the flask and the reaction mixture was refluxed for 16 h, during which time it darkened in color. The mixture was allowed to cool to room temperature and the volatile components were removed under vacuum, leaving a dark-yellow oil. The dark yellow oil was dissolved in *o*-xylene (60 mL) containing 1,2-bis(dimethylphosphino)ethane (0.564 g, 3.76 mmol). A reflux condenser was affixed to the flask and the golden yellow solution was heated to reflux. Over the course of 48 h, the color of the reaction mixture changed to dark orange and a visible dark precipitate was observed to coat the bottom of the reaction flask. The reaction mixture was allowed to cool to room temperature, and the volatile components were removed under vacuum. The remaining dark orange film was

extracted into pentane (200 mL) and the resulting solution filtered through Celite, which was then washed with pentane (3 × 25 mL). The filtrate was reduced to dryness under vacuum, and the crude product was recrystallized by cooling a THF solution layered with pentane (1:1) to −50 °C. The precipitate was collected by filtration and dried under vacuum to obtain an orange powder (0.430 g, 0.582 mmol, 31% yield). ^{1}H NMR (C_6D_6, 500.13 MHz, Figure 2.44): δ 6.81 (d, 2H, *m*-C_6H_4); 6.59 (d, 2H, *o*-C_6H_4); 1.57 (overlapping s, 28H, PCH_3 or PCH_2); 1.32 (br s, 4H, PCH_2); 0.95 (s, 9H, Si^{t}Bu); 0.05 (s, 6H, $SiCH_3$). ^{31}P{^{1}H} NMR (C_6D_6, 202.45 MHz, Figure 2.45): δ 25.73 (s with satellites, $^{1}J_{WP}$ = 278 Hz).

Synthesis of *N*-(4-bromophenyl)pyrrolidine. This procedure is adapted from the synthesis of *N*-(4-iodophenyl)pyrrolidine.[33] The synthesis was conducted in air; inert-atmosphere techniques were not used. To a stirred, room temperature solution of 4-bromoaniline (10.00 g, 58.13 mmol) in benzene (10 mL) was added NEtPr$^{i}_2$ (8.26 g, 63.95 mmol). The solution was stirred vigorously for 10 min, 1,4-dibromobutane (13.81 g, 63.95 mmol) was added, and the reaction mixture was heated to reflux. Over the course of 15 h, the reaction mixture changed from a dark brown solution to a white slurry. The reaction mixture was allowed to cool to room temperature and filtered to collect a white solid. The solid was washed with 2 M NaOH (250 mL) and recrystallized from EtOH (50 mL) at 0 °C, which provided colorless needles that were collected by filtration and dried under vacuum (6.17 g, 27.28 mmol, 47% yield). ^{1}H NMR (400.13 MHz, CD_2Cl_2): δ 7.26 (d, 2H, *m*-C_6H_4); 6.44 (d, 2H, *o*-C_6H_4); 3.24 (m, 4H, $NC\underline{H}_2CH_2$); 2.01 (m, 4H, $NCH_2C\underline{H}_2$). ^{13}C{^{1}H} NMR (100.61 MHz, CD_2Cl_2): δ 147.38 (C_6H_4); 131.87 (C_6H_4); 113.49 (C_6H_4); 106.93 (C_6H_4); 48.00 ($N\underline{C}H_2CH_2$); 25.81 ($NCH_2\underline{C}H_2$).

Synthesis of [NMe$_4$][W{C(O)C$_6$H$_4$-4-pyr}(CO)$_5$] (pyr = *N*-pyrrolidyl). A stirred, room temperature solution of *N*-(4-bromophenyl)pyrrolidine (3.25 g, 14.4 mmol) in Et_2O (100 mL)

was cooled to 0 °C and ^{n}BuLi (9.0 mL, 1.8 M in hexane, 16.2 mmol) was added via syringe. After 2 h the reaction mixture was transferred via cannula to a stirred, room temperature suspension of $W(CO)_6$ (5.56 g, 15.81 mmol) in Et_2O (50 mL). Over the course of 1 h, the color of the reaction mixture changed to dark yellow. The volatile components were removed under vacuum and the remaining dark yellow film of Li[W{C(O)C_6H_4-4-pyr}$(CO)_5$] was dissolved in N_2-purged deionized water (100 mL). The solution was filtered to remove a small amount of unreacted $W(CO)_6$. The filtrate was cooled to 0 °C, and a solution of NMe_4Br (4.87 g, 63.24 mmol) in N_2-purged deionized water (25 mL) was added via syringe with stirring. Over the course of 10 min, the reaction mixture became cloudy; filtration provided an orange solid. The solid was extracted into CH_2Cl_2 (25 mL), and the resulting mixture was filtered. Addition of Et_2O (250 mL) resulted in precipitation of the product, which was collected via filtration (2.01 g, 3.51 mmol, 25% yield). ^{1}H NMR (400.13 MHz, CD_2Cl_2, Figure 2.46): δ 7.62 (d, 2H, *m*-C_6H_4); 6.49 (d, 2H, *o*-C_6H_4); 3.31 (m, 4H, NC<u>H</u>$_2$CH$_2$); 3.27 (s, 12H, N$(CH_3)_4$); 2.00 (m, 4H, NCH$_2$C<u>H</u>$_2$). ^{13}C{^{1}H} NMR (100.61 MHz, CD_2Cl_2, Figure 2.47): δ 278.82 (W<u>C</u>(O)Ar); 208.30 (CO); 204.53 (CO); 149.34 (C_6H_4); 144.81 (C_6H_4); 129.66 (C_6H_4); 110.17 (C_6H_4); 56.43 (N$(CH_3)_4$); 47.94 (N<u>C</u>H$_2$CH$_2$); 25.77 (NCH$_2$<u>C</u>H$_2$). IR (CH_2Cl_2, cm^{-1}): 2042 (ν_{CO}); 1948 (ν_{CO}); 1883 (ν_{CO}).

Synthesis of W(CC$_6$H$_4$-4-pyr)(pic)$_2$(CO)$_2$Cl. A stirred solution of [NMe_4][W{C(O)C_6H_4-4-pyr}$(CO)_5$] (1.50 g, 2.62 mmol) in CH_2Cl_2 (50 mL) was cooled to –77 °C using a dry-ice/isopropanol bath. Oxalyl chloride (1.4 mL, 2.8 mmol, 2 M solution in CH_2Cl_2) was added over the course of 1 min by syringe, resulting in an immediate color change of the reaction mixture from yellow to dark purple. Over the course of 30 min, the color of the reaction mixture changed further from dark purple to dark red. The flask was removed to a $CaCl_2$/ice bath and the reaction mixture was allowed to warm with stirring. Over the course of 15

min, the reaction mixture became opaque and the color changed from dark red to tan. 4-Methylpyridine (pic, 0.41 mL, 6.55 mmol) was added via syringe. Immediately, the color of the reaction mixture changed in appearance to a homogenous, emerald green solution. The reaction vessel was removed from the cooling bath and allowed to warm to room temperature, while stirring. After 2 h, the volatile components were removed under vacuum, the flask was opened to air, and the residue was washed with pentane (50 mL), dissolved in CH_2Cl_2 (25 mL), and filtered through a pad of silica gel (3 cm × 1.5 cm). The silica pad was washed with CH_2Cl_2 (30 mL) and the dark yellow filtrate was reduced in volume under vacuum to 20 mL. Addition of pentane (200 mL) resulted in precipitation of the product, which was collected by filtration and dried under vacuum (1.27 g, 2.05 mmol, 78 % yield). ^{1}H NMR (500.13 MHz, CD_2Cl_2, Figure 2.48): δ 8.90 (d, 4H, *m*-$NC_5\underline{H}_4CH_3$); 7.25 (d, 2H, *m*-C_6H_4); 7.12 (d, 4H, *o*-$NC_5\underline{H}_4CH_3$); 6.43 (d, 2H, *o*-C_6H_4); 3.30 (m, 4H, $NC\underline{H}_2CH_2$); 2.37 (s, 6H, $NC_5H_4C\underline{H}_3$); 2.01 (m, 4H, $NCH_2C\underline{H}_2$). ^{13}C{^{1}H} NMR (125.75 Hz, CD_2Cl_2, Figure 2.49): δ 267.40 (WC, $^1J_{WC}$ =196 Hz); 222.63 (CO, $^1J_{WC}$ = 172 Hz); 152.50 ($N\underline{C}_5H_4CH_3$ or C_6H_4); 150.73 ($N\underline{C}_5H_4CH_3$ or C_6H_4); 147.60 ($N\underline{C}_5H_4CH_3$ or C_6H_4); 137.87 ($N\underline{C}_5H_4CH_3$ or C_6H_4); 131.28 ($N\underline{C}_5H_4CH_3$ or C_6H_4); 125.99 ($N\underline{C}_5H_4CH_3$ or C_6H_4); 111.08 ($N\underline{C}_5H_4CH_3$ or C_6H_4); 47.81 ($N\underline{C}H_2CH_2$); 25.73 ($NCH_2\underline{C}H_2$); 21.15 ($NC_5H_4\underline{C}H_3$). IR (CH_2Cl_2, cm^{-1}): 1962 (ν_{CO}); 1872 (ν_{CO}).

Synthesis of W(CC$_6$H$_4$-4-pyr){P(OMe)$_3$}$_3$(CO)Cl. To a stirred, room-temperature solution of W(CC$_6$H$_4$-4-pyr)(pic)$_2$(CO)$_2$Cl (0.600 g, 0.969 mmol) in THF (35 mL) was added trimethylphosphite (1.1 mL, 9.69 mmol). The reaction mixture was refluxed for 16 h, during which time it darkened in color. The mixture was allowed to cool to room temperature and the volatile components were removed under vacuum, leaving a dark-yellow oil. The oil was dissolved in CH_2Cl_2 (30 mL), filtered through Celite, and the filtrate concentrated to dryness

under vacuum. The remaining dark yellow solid was extracted into a minimum volume of Et_2O and filtered through Celite. The Celite was washed with Et_2O (3 × 5 mL) and the combined filtrate cooled to −50 °C, which produced large yellow crystals that were collected by filtration and dried under vacuum (0.710 g, 0.912 mmol, 94% crude yield). **Note**: The product obtained contains a small amount of $W(CC_6H_4\text{-}4\text{-pyr})\{P(OMe)_3\}_4Cl$ (*ca*. 1.5% by ^{31}P NMR integration), but was suitable for use in the synthesis of $W(CC_6H_4\text{-}4\text{-pyr})(dmpe)_2Cl$. ^1H NMR (CD_2Cl_2, 500.13 Hz, Figure 2.50): δ 7.16 (d, 2H, *m*-C_6H_4); 6.29 (d, 2H, *o*-C_6H_4); 3.70 (m, 27H, POMe); 3.24 (m, 4H, $NC\underline{H}_2CH_2$); 1.97 (m, 4H, $NCH_2C\underline{H}_2$). $^{31}P\{^1H\}$ NMR (CD_2Cl_2, 202.45 Hz, Figure 2.51): 149.22 (d with ^{183}W satellites, $^1J_{WP}$ = 424 Hz, $^2J_{PP}$ = 40 Hz, 2P); 145.51 (t with ^{183}W satellites, $^1J_{WP}$ = 366 Hz, $^2J_{PP}$ = 40 Hz). IR (CH_2Cl_2, cm^{-1}): 1933 (s, ν_{CO}). For the impurity $W(CC_6H_4\text{-}4\text{-pyr})\{P(OMe)_3\}_4Cl$: ^{31}P NMR (CD_2Cl_2, 202.45 Hz): δ 152.70 (s).

Synthesis of $W(CC_6H_4\text{-}4\text{-pyr})\{P(OMe)_3\}_4Cl$ $W(CC_6H_4\text{-}4\text{-pyr})(pic)_2(CO)_2Cl$ (1.70 g, 2.75 mmol) was dissolved in neat trimethylphosphite (25 mL) and stirred at room temperature for 5 min. Upon mixing, the bright-yellow solution darkened slightly. The reaction mixture was slowly heated to reflux. After 20 h, the reaction mixture was allowed to cool to room temperature and the volatile components were removed under vacuum. The mixture was extracted into a mixture of Et_2O and THF (2:1, 20 mL) and filtered through Celite to remove a dark colored impurity. The volatile components of the solution were removed under vacuum and the remaining solid was recrystallized from layered THF/pentane (1:2) at –30 °C, which provided a yellow microcrystalline solid that was collected by filtration and dried under vacuum (2.21 g, 2.53 mmol, 92% yield). ^1H NMR (C_6D_6, 500.13 MHz, Figure 2.52): δ 7.63 (d, 2H, *o*-C_6H_4); 6.36 (d, 2H, *o*-C_6H_4); 3.86 (virtual t, 36H, $P(OMe)_3$); 2.91 (m, 4H, $N(C\underline{H}_2CH_2)_2$); 1.44 (m, 4H, $N(CH_2C\underline{H}_2)_2$). $^{13}C\{^1H\}$ NMR (125.75 MHz, C_6D_6, Figure 2.53-2.54): δ 252.83 (quin, $^2J_{CP}$ = 18

Hz, WC); 145.53 (C_6H_4); 142.56 (C_6H_4); 132.08 (quin, J_{CP} = 3Hz, C_6H_4); 110.58 (C_6H_4); 52.17 ($P(OMe)_3$); 47.44 ($N(\underline{C}H_2CH_2)_2$); 25.48 ($N(CH_2\underline{C}H_2)_2$). $^{31}P\{^1H\}$ NMR (C_6D_6, 202.45 MHz, Figure 2.55): δ152.25 (s with ^{183}W satellites, $^1J_{WP}$ = 430 Hz).

Synthesis of W(CC$_6$H$_4$-4-pyr)(dmpe)$_2$Cl *via* W(CC$_6$H$_4$-4-pyr){P(OMe)$_3$}(CO)Cl. To a stirred, room temperature solution of W(CC$_6$H$_4$-4-pyr){P(OMe)$_3$}$_3$(CO)Cl (0.200 g, 0.257 mmol, containing a ~1.5% W(CC$_6$H$_4$-4-pyr){P(OMe)$_3$}$_4$Cl impurity) in *o*-xylene (100 mL) was added 1,2-bis(dimethylphosphino)ethane (dmpe, 0.096 g, 0.642 mmol). The golden yellow solution was heated to reflux, And over the course of 48 h, the color of the reaction mixture changed from golden yellow to dark orange. The reaction mixture was allowed to cool to room temperature, and the volatile components were removed under vacuum. The remaining dark orange film was extracted into pentane (200 mL) and filtered through Celite, which was then washed with pentane (3 × 25 mL). The filtrate was reduced to dryness under vacuum, and the crude product was recrystallized by cooling a THF solution layered with pentane (1:1) to −50 °C; this provided an orange powder (0.115 g, 0.169 mmol, 66% yield).

Alternative synthesis of W(CC$_6$H$_4$-4-pyr)(dmpe)$_2$Cl *via* W(CC$_6$H$_4$-4-pyr){P(OMe)$_3$}$_4$Cl. This compound was previously prepared from W(CC$_6$H$_4$-4-pyr)(CO){P(OMe)$_3$}$_3$Cl. To a stirred, room temperature solution of W(CC$_6$H$_4$-4-pyr){P(OMe)$_3$}$_4$Cl (1.0 g, 1.14 mmol) in toluene (60 mL) was added 1,2-bis(dimethylphosphino)ethane (dmpe, 0.360 g, 2.40 mmol). The yellow solution was heated to reflux. Over the course of 16 h, the color of the reaction mixture changed from yellow to orange. The reaction mixture was allowed to cool to room temperature, and the volatile components were removed under vacuum. The remaining orange film was extracted into pentane (40 mL) and the resulting solution filtered through Celite, which was then washed with pentane (3 × 25 mL). The

filtrate was reduced to dryness under vacuum; this provided an orange powder, which was collected by filtration and dried under vacuum (0.685 g, 1.01 mmol, 88% yield). ^{1}H NMR (C_6D_6, 500.13 MHz, Figure 2.56): δ 6.94 (d, 2H, *m*-C_6H_4); 6.24 (d, 2H, *o*-C_6H_4); 2.87 (m, 4H, NCH_2CH_2); 1.68 (s, 12H, PCH_3); 1.61 (overlapping s and br m, 16H, PCH_2 and PCH_3); 1.46 (m, 4H, NCH_2CH_2); 1.39 (br m, 4H, PCH_2). ^{13}C{^{1}H,^{31}P} NMR (C_6D_6, 125.77 MHz, Figure 2.57): δ 253.73 (WC); 144.72 (C_6H_4); 143.44 (C_6H_4); 130.48 (C_6H_4); 111.57 (C_6H_4); 47.66 (NCH_2CH_2); 34.30 (PCH_2); 25.47 (NCH_2CH_2); 22.38 (PCH_3); 16.25 (PCH_3). ^{31}P{^{1}H} NMR (C_6D_6, 202.45 MHz, Figure 2.58): δ 26.36 (s with satellites, $^{1}J_{WP}$ = 279 Hz). Anal. Calc. (Found) for $C_{24}H_{45}ClNP_4W$: C 41.73 (41.84); H 6.57 (6.76); N 2.03 (1.83).

Synthesis of W(CC$_6$H$_4$-4-pyr)(depe)$_2$Cl. To a stirred, room temperature solution of W(CC$_6$H$_4$-4-pyr){P(OMe)$_3$}$_4$Cl (0.3 g, 0.343 mmol) in toluene (20 mL) was added 1,2-bis(diethylphosphino)ethane (depe, 0.150 g, 0.721 mmol). The yellow solution was heated to reflux. Over the course of 16 h, the color of the reaction mixture changed from yellow to orange. The reaction mixture was allowed to cool to room temperature and the volatile components were removed under vacuum. The remaining orange film was extracted into pentane (25 mL) and the resulting solution filtered through Celite, which was then washed with pentane (3 × 25 mL). The filtrate was reduced to dryness under vacuum, and the crude product was extracted into pentane (20 mL) and cooled to −30 °C; this provided an orange microcrystalline solid, which was collected by filtration and dried under vacuum (0.222 g, 0.281 mmol, 82% yield). ^{1}H NMR (C_6D_6, 500.13 MHz, Figure 2.59): δ 6.88 (d, 2H, *m*-C_6H_4); 6.23 (d, 2H, *o*-C_6H_4); 2.83 (m, 4H, NCH_2CH_2); 2.33 (m, 4H, PCH_2CH_3); 2.10 (m, 8H, PCH_2CH_3); 2.01 (m, 4H, PCH_2CH_3); 1.71 (br m, 4H, PCH_2); 1.52 (br m, 4H, PCH_2); 1.42 (m, 4H, NCH_2CH_2); 1.14 (br m, 24H, PCH_3). ^{13}C{^{1}H} NMR (125.75 MHz, C_6D_6, Figure 2.60-2.61): δ 249.47 (quin, $^{2}J_{CP}$ = 11 Hz, WC);

144.04 (C_6H_4); 143.89 (C_6H_4); 129.81 (quin, J_{CP} = 3Hz, C_6H_4); 111.08 (C_6H_4); 47.43 (N($\underline{C}H_2CH_2)_2$); 26.82 (quin, $^1J_{CP}$ = 9 Hz, PCH_2); 25.43 (overlapping quin and s, P$\underline{C}H_2CH_3$ and (N($CH_2\underline{C}H_2)_2$)); 19.32 (quin, $^1J_{CP}$ = 5 Hz, PCH_2); 9.80 (PCH_3); 9.08 (PCH_3). $^{31}P\{^1H\}$ NMR (C_6D_6, 202.45 MHz, Figure 2.62): δ 43.79 (s with ^{183}W satellites, $^1J_{WP}$ = 273 Hz). HR-MS (THF, 70V, *m/z*): 789.29 (M^+, calc. 789.29).

Synthesis of W(CC$_6$H$_4$-4-pyr)(dppe)$_2$Cl. To a stirred, room temperature solution of W(CC$_6$H$_4$-4-pyr){P(OMe)$_3$}$_4$Cl (0.200 g, 0.238 mmol) in toluene (40 mL) was added 1,2-bis(diphenylphosphino)ethane (dppe, 0.199 g, 0.500 mmol). The yellow solution was heated to reflux. Over the course of 16 h, the color of the reaction mixture converted from yellow to orange. The reaction mixture was allowed to cool to room temperature and the volatile components were removed under vacuum. The crude orange solid was dissolved in THF (10 mL) and the resulting solution filtered through a pad of Celite to remove a small amount of a light grey impurity. The volatile components of the resulting solution were removed by vacuum and the crude orange solid was triturated with Et_2O for 2 h, collected by filtration, and dried by vacuum overnight to obtain a pale orange powder (0.168 g, 0.165 mmol, 69% yield). ^1H NMR (C_6D_6, 500.13 MHz, Figure 2.63): δ 7.73 (br s, 8H, *o*-PPh_2); 7.48 (br s, 8H, *o*-PPh_2); 6.98 (m, 24H, *m,p*-PPh_2); 6.05 (d, 2H, *m*-C_6H_4); 5.94 (d, 2H, *o*-C_6H_4); 2.78 (overlapping m and br s, 8H, N$\underline{C}H_2CH_2$ and PCH_2); 2.48 (br s, 4H, PCH_2); 1.36 (m, 4H, $NCH_2C\underline{H}_2$). $^{13}C\{^1H\}$ NMR (C_6D_6, 500.13 MHz, Figure 2.64-2.66): δ 251.65 (quin, $^2J_{CP}$ = 12 Hz, WC); 144.29 (C_6H_4 or PPh_2); 141.817 (C_6H_4 or PPh_2); 141.71 (C_6H_4 or PPh_2); 139.45 (C_6H_4 or PPh_2); 134.62 (C_6H_4 or PPh_2); 132.18 (C_6H_4 or PPh_2); 128.73 (C_6H_4 or PPh_2); 128.40 (C_6H_4 or PPh_2); 127.75 (C_6H_4 or PPh_2); 127.36 (C_6H_4 or PPh_2); 109.77 (C_6H_4 or PPh_2); 47.31 (N($\underline{C}H_2CH_2)_2$) ; 32.03 (quin, $^1J_{CP}$ = 10 Hz, PCH_2); 25.35 (N($\underline{C}H_2CH_2)_2$). **Note:** One $^{13}C\{^1H\}$ NMR resonance that is likely at 128.34 ppm

was observed to considerably overlap with the solvent (C_6D_6), but could not accurately identified. Two $^{13}C\{^1H\}$ resonances were observed to overlap (141.82 ppm and 141.71 ppm). $^{31}P\{^1H\}$ NMR (C_6D_6, 500.13 MHz, Figure 2.67): δ 49.16 (s with ^{183}W satellites, $^1J_{WP}$ = 283 Hz). HR-MS (THF, 70V, *m/z*): 1173.29 (M^+, calc. 1173.29).

Synthesis of W(CC$_6$H$_4$-4-pyr)(dmpe)$_2$F. To a stirred, room-temperature solution of W(CC$_6$H$_4$-4-pyr)(dmpe)$_2$Cl[30] (0.200 g, 0.295 mmol) in toluene (5 mL) was added SiMe$_3$(O$_3$SCF$_3$) (0.098 g, 0.442 mmol), resulting in an immediate darkening of the initially dark orange solution. After 16 h the dark-orange reaction mixture was filtered through a pad of Celite to remove a small amount of dark-colored solid and the filtrate reduced to dryness under vacuum. The resulting dark yellow film was extracted into THF (5 mL) at room temperature, to which was added with stirring [^{n}Bu$_4$N]F•3.5H$_2$O (0.098 g, 0.310 mmol). After 18 h, the volatile components of the solution were removed under vacuum, the remaining light-yellow film was extracted into pentane (100 mL), and the solution filtered through Celite. The volatile components were removed under vacuum, the resulting light-yellow film was extracted into Et$_2$O (5 mL) and recrystallized at −30 °C to provide a light-yellow powder, which was collected by filtration and dried under vacuum (0.126 g, 0.190 mmol, 65% yield). ^1H NMR (C_6D_6, 500.13 MHz, Figure 2.68): δ 6.88 (d, 2H, *m*-C$_6$H$_4$); 6.30 (d, 2H, *o*-C$_6$H$_4$); 2.91 (m, 4H, N(C$\underline{H}_2$CH$_2$)$_2$); 1.75 (s, 12H, PCH$_3$); 1.54 (overlapping m, 12H, PCH$_2$/N(CH$_2$C$\underline{H}_2$)$_2$); 1.45 (s, 12H, PCH$_3$). $^{13}C\{^1H\}$ NMR (C_6D_6, 125.77 MHz, Figure 2.69-2.70): δ 253.68 (d quin, $^1J_{CF}$ = 82 Hz; $^2J_{PC}$ =11 Hz, WC); 145.50 (C$_6$H$_4$); 144.04 (C$_6$H$_4$); 130.05 (t, *J* = 3 Hz, C$_6$H$_4$); 111.32 (C$_6$H$_4$); 47.80 (N($\underline{C}$H$_2$CH$_2$)$_2$); 34.29 (PCH$_2$); 25.48 (N(CH$_2$$\underline{C}H_2$)$_2$) 22.00 (PCH$_3$); 14.00 (PCH$_3$). $^{31}P\{^1H\}$ NMR (C_6D_6, 202.45 MHz, Figure 2.71): 33.42 (d with ^{183}W satellites, $^1J_{WP}$ = 283 Hz, $^2J_{PF}$ = 49 Hz). ^{19}F

NMR (C_6D_6, 470.6 MHz, Figure 2.72): –293.01 (quin with ^{183}W satellites, $^1J_{WF}$ = 56 Hz, $^2J_{PF}$ = 49 Hz). HR-MS (THF, 70V, *m/z*): 661.20 (M^+, calc. 661.19).

Synthesis of [NMe$_4$][W{C(O)C$_6$H$_4$-4-N(SiMe$_3$)$_2$}(CO)$_5$]. A stirred solution of 4-bromo-*N*,*N*-bis(trimethylsilyl)aniline (5.03 g, 15.89 mmol) in Et_2O (100 mL) was cooled to 0 °C, and ^{n}BuLi (11.54 mL, 1.6 M in hexane, 18.4 mmol) was added via syringe. The reaction mixture was stirred for 2 h and then transferred via cannula to a stirred, room temperature suspension of $W(CO)_6$ (6.20 g, 17.60 mmol) in Et_2O (50 mL). Over the course of 1 h, the color of the reaction mixture changed to bright yellow. The volatile components were removed under vacuum and the remaining dark yellow film of Li[W{C(O)C$_6$H$_4$-4-N(SiMe$_3$)$_2$}(CO)$_5$] was dissolved in N_2-purged deionized water (100 mL) and filtered to remove a small amount of unreacted $W(CO)_6$. The filtrate was cooled to 0 °C and a solution of [NMe$_4$]Br (6.58 g, 42.75 mmol) in N_2-purged deionized water (25 mL) was added via syringe with stirring. Over the course of 10 min, the reaction mixture became cloudy; filtration provided a dark yellow powder. The powder was extracted into CH_2Cl_2 (25 mL), and the resulting mixture filtered. Addition of Et_2O (350 mL) resulted in precipitation of the product, which was collected via filtration (4.42 g, 6.03 mmol, 38% yield). ^{1}H NMR (CD_2Cl_2, 400.13 MHz, Figure 2.73): δ 7.41 (d, 2H, *m*-C$_6$H$_4$); 6.87 (d, 2H, *o*-C$_6$H$_4$); 3.31 (s, 12H, NMe$_4$); 0.07 (s, 18H, N(SiMe$_3$)$_2$). ^{13}C{^{1}H} NMR (CD_2Cl_2, 100.61 MHz, Figure 2.74): δ 283.81 (W<u>C</u>(O)Ar); 208.37 (CO); 203.94 (CO, $^1J_{WC}$ = 127.7 Hz); 152.81 (C$_6$H$_4$); 149.36 (C$_6$H$_4$); 129.21 (C$_6$H$_4$); 126.64 (C$_6$H$_4$); 56.63 (N(CH$_3$)$_4$); 2.18 (N(SiMe$_3$)$_2$).

Synthesis of W(CC$_6$H$_4$-4-NH$_2$)(pic)$_2$(CO)$_2$Cl (pic = 4-methylpyridine). A one-pot synthesis of this complex has been previously described.[22] A stirred solution of [NMe$_4$][W{C(O)C$_6$H$_4$-4-N(SiMe$_3$)$_2$}(CO)$_5$] (2.00 g, 3.02 mmol) in CH_2Cl_2 (60 mL) was cooled to −77 °C using a dry-ice/isopropanol bath. Oxalyl chloride (1.5 mL, 2 M solution in CH_2Cl_2,

3.00 mmol) was added over the course of 1 min by syringe, resulting in an immediate color change of the reaction mixture from orange to dark purple. Over the course of 30 min, the color of the reaction mixture changed further from dark purple to dark red. The flask was moved to a $CaCl_2$/ice bath and the reaction mixture allowed to warm with stirring. Over the course of 15 min, the reaction mixture became opaque and the color changed from dark red to tan. 4-Methylpyridine (0.41 mL, 6.55 mmol) was added via syringe. Immediately, the reaction mixture changed in appearance to a homogeneous, dark yellow solution. The reaction vessel was removed from the cooling bath and allowed to warm to room temperature with stirring. After 2 h, the volatile components were removed under vacuum, the flask was opened to air, and the residue was washed with pentane (50 mL), dissolved in CH_2Cl_2 (25 mL), and filtered through a pad of silica gel (3 cm × 1.5 cm). The silica pad was washed with CH_2Cl_2 (50 mL) and the dark yellow filtrate was reduced in volume under vacuum to 20 mL. Addition of pentane (200 mL) resulted in precipitation of the product, which was collected by filtration and dried under vacuum (1.40 g, 2.05 mmol, 82% yield). ^{1}H NMR (500.13 MHz, CD_2Cl_2, Figure 2.75): δ 8.88 (d, 4H, *m*-$NC_5\underline{H}_4CH_3$); 7.18 (d, 2H, *m*-C_6H_4); 7.11 (d, *o*-$NC_5\underline{H}_4CH_3$, 4H); 6.55 (d, 2H, *o*-C_6H_4); 3.94 (br s, 2H, NH_2); 2.37 (s, 6H, $NC_5H_4C\underline{H}_3$). $^{13}C\{^1H\}$ NMR (125.75 MHz, CD_2Cl_2, Figure 2.76): δ 265.58 (WC); 222.40 (CO); 152.62 ($N\underline{C}_5H_4CH_3$ or $\underline{C}_6H_4$); 150.81 ($N\underline{C}_5H_4CH_3$ or $\underline{C}_6H_4$); 147.15 ($N\underline{C}_5H_4CH_3$ or $\underline{C}_6H_4$); 140.95 ($N\underline{C}_5H_4CH_3$ or $\underline{C}_6H_4$); 131.34 ($N\underline{C}_5H_4CH_3$ or $\underline{C}_6H_4$); 126.25 ($N\underline{C}_5H_4CH_3$ or $\underline{C}_6H_4$); 114.14 ($N\underline{C}_5H_4CH_3$ or $\underline{C}_6H_4$); 21.28 ($NC_5H_4\underline{C}H_3$).

Synthesis of $W(CC_6H_4\text{-}4\text{-}NH_2)\{P(OMe)_3\}_3(CO)Cl$. To a stirred, room temperature solution of $W(CC_6H_4\text{-}4\text{-}NH_2)(pic)_2(CO)_2Cl$ (0.400 g, 0.707 mmol) in THF (50 mL) was added trimethylphosphite (0.322 mL, 2.50 mmol). The reaction mixture was refluxed for 12 h, during which time it darkened in color. The mixture was allowed to cool to room temperature, and the

volatile components were removed under vacuum, leaving a dark-yellow oil. The oil was dissolved in CH_2Cl_2 (30 mL), filtered through Celite, and concentrated to dryness under vacuum. The remaining dark yellow solid was extracted into a minimum volume of Et_2O and the resulting solution filtered through Celite. The Celite was washed with Et_2O (3 × 5 mL) and the combined filtrate cooled to –50 °C, which produced large yellow crystals. The crystals were collected by filtration and dried under vacuum (0.250 g, 0.345 mmol, 49% crude yield). **Note:** The product obtained contains a small amount of $W(CC_6H_4\text{-}4\text{-}NH_2)\{P(OMe)_3\}_4Cl$ (*ca.* 7% by ^{31}P NMR integration), but was suitable for use in the synthesis of $W(CC_6H_4\text{-}4\text{-}NH_2)(dmpe)_2Cl$ because both compounds are precursors for this product. ^1H NMR (500.13 Hz, CD_2Cl_2, Figure 2.77): δ 7.09 (d, 2H, *m*-C_6H_4); 6.42 (d, 2H, *o*-C_6H_4); 3.83 (br s, 2H, NH_2); 3.73 (m, 27H, POMe). $^{31}P\{^1H\}$ NMR (CD_2Cl_2, 161.97 MHz, Figure 2.78): δ 149.45 (d with satellites, $^1J_{WP}$ = 427 Hz, $^2J_{PP}$ = 39 Hz, 2P); 146.10 (t with satellites, $^1J_{WP}$ = 367.67 Hz, $^2J_{PP}$ = 37 Hz, 1P). $W(CC_6H_4\text{-}4\text{-}NH_2)\{P(OMe)_3\}_4Cl$ ^{31}P NMR (CD_2Cl_2, 161.97 MHz): δ 153.01 (s with satellites, $^1J_{WP}$ = 443 Hz).

Synthesis of $W(CC_6H_4\text{-}4\text{-}NH_2)(dmpe)_2Cl$. To a stirred, room temperature solution of $W(CC_6H_4\text{-}4\text{-}NH_2)\{P(OMe)_3\}_3(CO)Cl$ (0.144 g, 0.199 mmol, containing a ~7% $W(CC_6H_4\text{-}4\text{-}NH_2)\{P(OMe)_3\}_4Cl$ impurity) in *o*-xylene (100 mL) was added 1,2-bis(dimethylphosphino)ethane (0.075 g, 0.497 mmol). The golden yellow solution was heated to reflux, and over the course of 72 h, the color of the reaction mixture changed to dark orange. The reaction mixture was allowed to cool to room temperature, and the volatile components were removed under vacuum. The remaining dark orange film was extracted into pentane (100 mL), the resulting solution filtered through Celite, and the Celite was then washed with pentane (3 × 10 mL). The filtrate was reduced to dryness under vacuum, and the crude product was

recrystallized by layering a THF solution with pentane (1:1) and cooling to −50 °C, which provided a light-yellow powder (0.055 g, 0.09 mmol, 44% yield). **Note:** The ^{1}H NMR spectrum of the compound was observed to contain impurity signals at 3.7 and 0.8 ppm that could not be removed *via* recrystallization. ^{1}H NMR (500.13 Hz, C_6D_6, Figure 2.79): δ 6.77 (d, 2H, *m*-C_6H_4); 6.10 (d, 2H, *o*-C_6H_4); 2.59 (br s, 2H, NH_2); 1.59–1.55 (overlapping s and br m, 28H, PCH_3 and PCH_2); 1.34 (m, 4H, PCH_2). ^{31}P{^{1}H} NMR (C_6D_6, 202.45 MHz, Figure 2.80): δ 26.19 (s with satellites, $^{1}J_{WP}$ = 278 Hz). HR-MS (THF, 0V, *m/z*): 623.2 (M^+, calc 623.1).

Table 2.4. $^{31}P\{^{1}H\}$ NMR chemical shifts in C_6D_6.

Compound	$^{31}P\{^{1}H\}$	$^{1}J_{WP}$
W(CPh){P(OMe)$_3$}$_4$Cl	150.91[a]	430
W(CC$_6$H$_4$-4-OCH$_3$){P(OMe)$_3$}$_4$Cl	150.75	430
W(CC$_6$H$_4$-4-pyr){P(OMe)$_3$}$_4$Cl	152.25	430
W(C^{t}Bu)(PMe$_3$)$_4$Cl	−22.56[a]	285
W(CPh)(PMe$_3$)$_4$Cl	−22.69[a]	281
W(CPh)(dmpe)$_2$Cl	25.38[a]	277
W(CPh)(dmpe)$_2$OTf	32.27[a]	281
W(CC$_6$H$_4$-4-OCH$_3$)(dmpe)$_2$Cl	26.56	279
W(CC$_6$H$_4$-4-OTBDMS)(dmpe)$_2$Cl	25.73	278
W(CC$_6$H$_4$-4-pyr)(dmpe)$_2$Cl	26.36	279
W(CPh)(dmpe)$_2$F	32.75	283
W(CC$_6$H$_4$-4-pyr)(dmpe)$_2$F	33.42	283
W(CPh)(depe)$_2$Cl	41.90[a]	279
W(CC$_6$H$_4$-4-pyr)(depe)$_2$Cl	43.79	273
W(CPh)(dppe)$_2$Cl	45.23[b]	281
W(CC$_6$H$_4$-4-OCH$_3$)(dppe)$_2$Cl	46.35	281
W(CC$_6$H$_4$-4-pyr)(dppe)$_2$Cl	49.16	283

[a]Initially reported in Ref. 10. [b]Initially reported in Ref. 11.

Table 2.5. $^{13}C\{^{1}H\}$ NMR chemical shifts in C_6D_6.

Compound	$^{13}C\{^{1}H\}$
W(CPh)(pic)$_2$(CO)$_2$Cl	262.9
W(CC$_6$H$_4$-4-OCH$_3$)(pic)$_2$(CO)$_2$Cl	263.7
W(CC$_6$H$_4$-4-pyr)(pic)$_2$(CO)$_2$Cl	267.4
W(CC$_6$H$_4$-4-OCH$_3$){P(OMe)$_3$}$_4$Cl	250.0
W(CC$_6$H$_4$-4-pyr){P(OMe)$_3$}$_4$Cl	252.8
W(CPh)(dmpe)$_2$Cl	252.3[a]
W(CPh)(dmpe)$_2$OTf	268.8[a]
W(CC$_6$H$_4$-4-OCH$_3$)(dmpe)$_2$Cl	251.3
W(CC$_6$H$_4$-4-pyr)(dmpe)$_2$Cl	253.7
W(CPh)(dmpe)$_2$F	252.7
W(CC$_6$H$_4$-4-pyr)(dmpe)$_2$F	253.7
W(CPh)(depe)$_2$Cl	247.8
W(CC$_6$H$_4$-4-pyr)(depe)$_2$Cl	249.5
W(CC$_6$H$_4$-4-OCH$_3$)(dppe)$_2$Cl	249.8
W(CC$_6$H$_4$-4-pyr)(dppe)$_2$Cl	253.7

[a]Initially reported in Ref. 10.

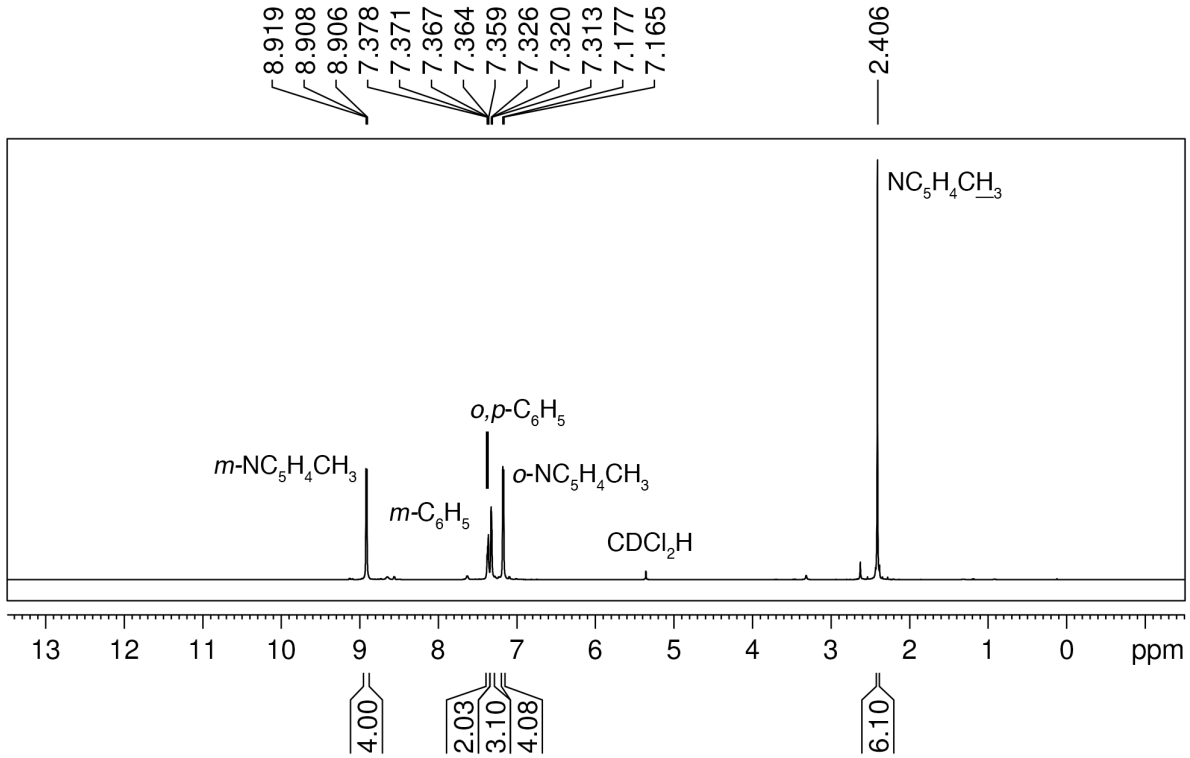

Figure 2.18. ^{1}H NMR spectrum of $W(CPh)(pic)_2(CO)_2Cl$ in CD_2Cl_2.

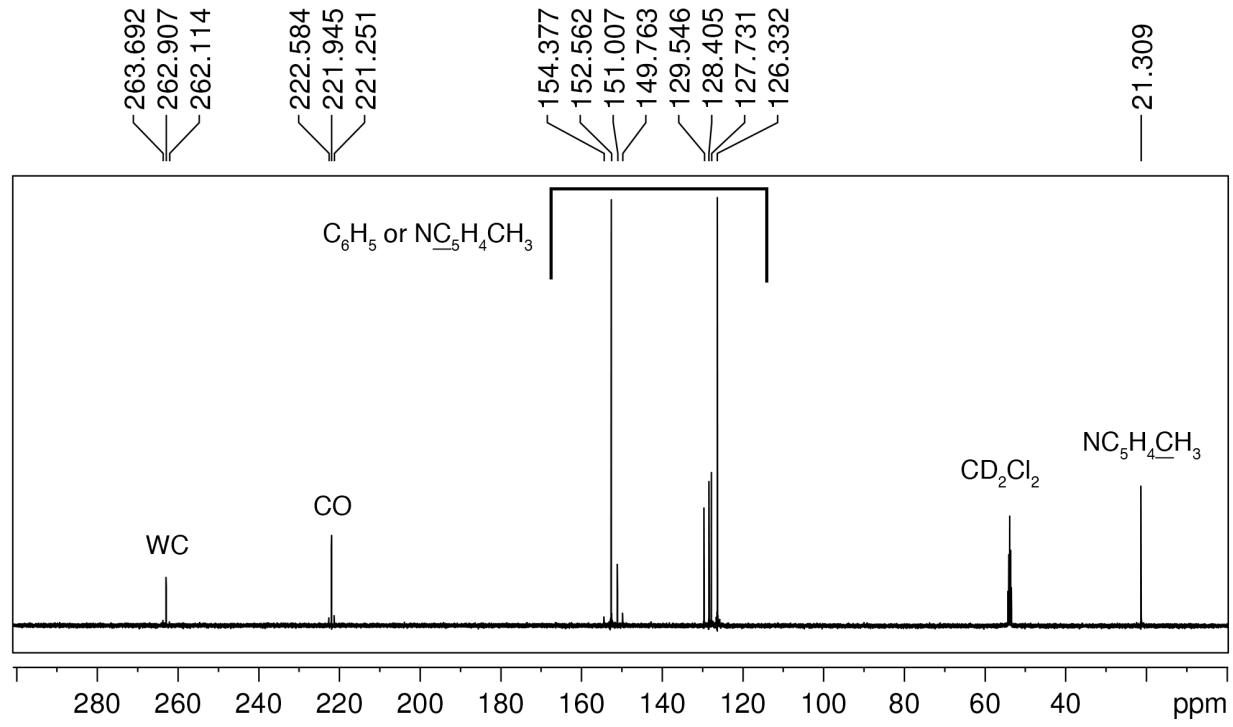

Figure 2.19. $^{13}C\{^{1}H\}$ NMR spectrum of $W(CPh)(pic)_2(CO)_2Cl$ in CD_2Cl_2.

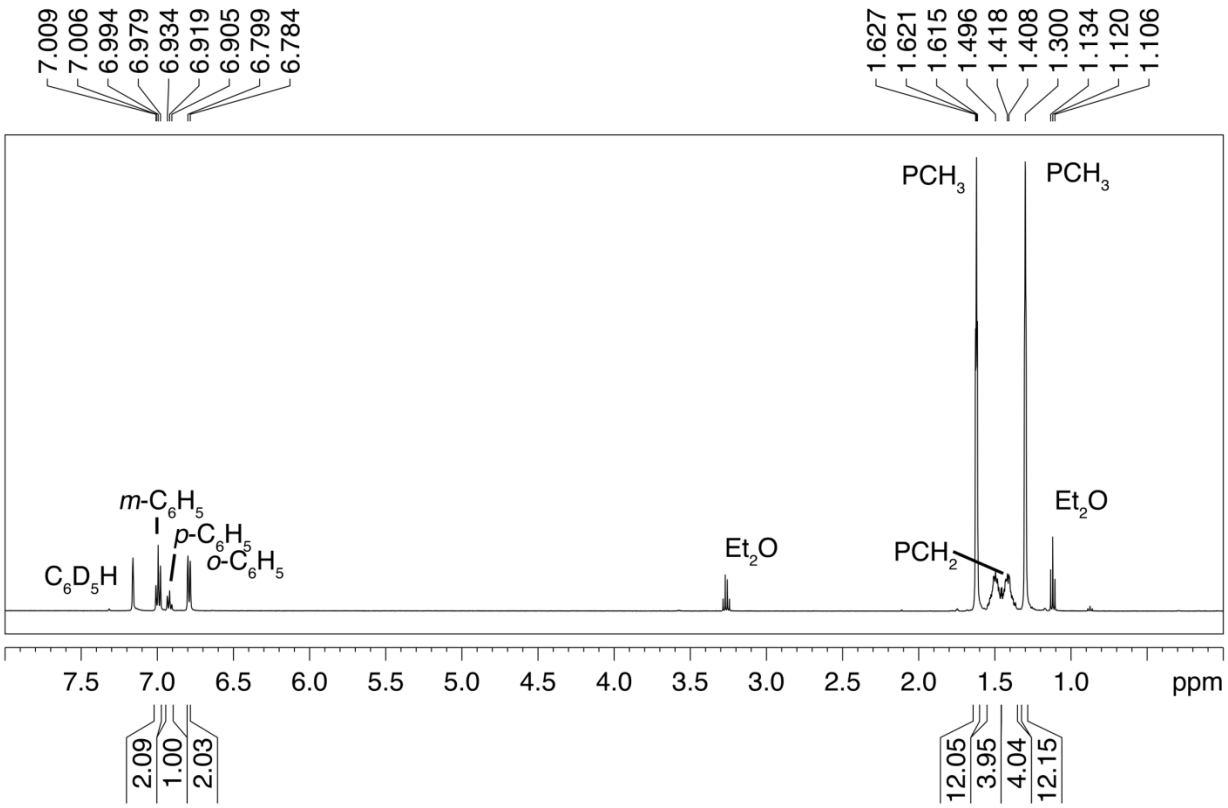

Figure 2.20. ^{1}H NMR spectrum of W(CPh)(dmpe)$_2$F in C_6D_6.

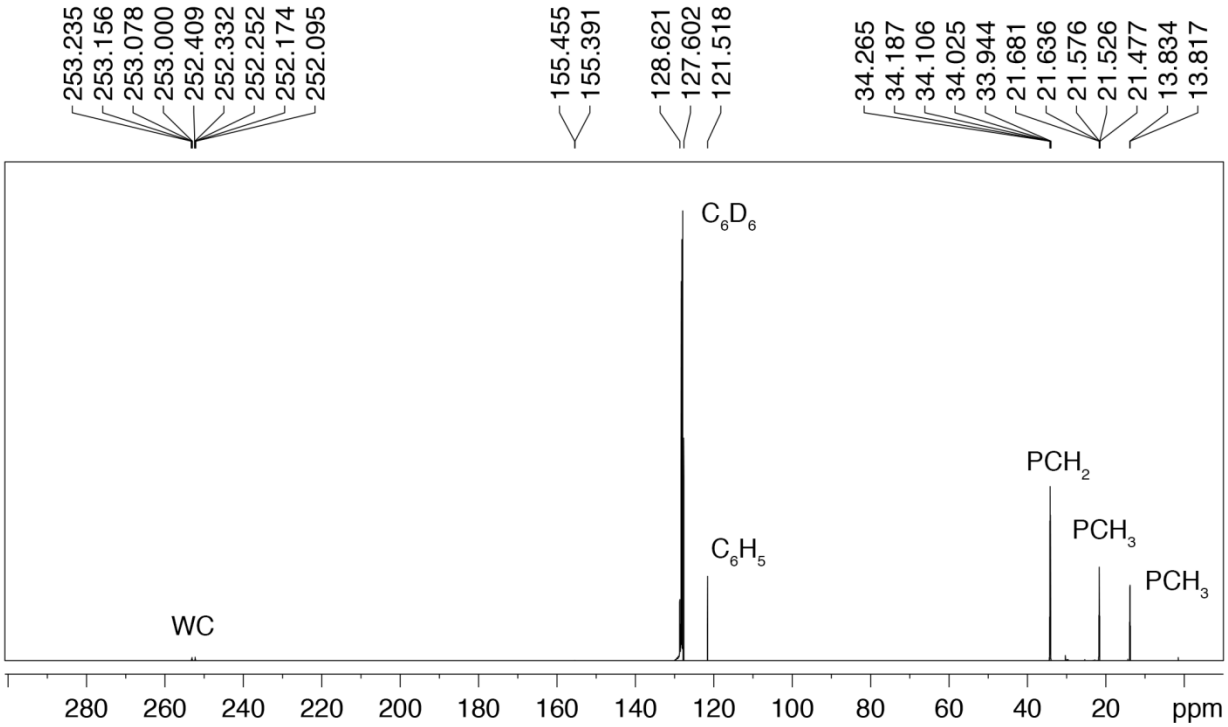

Figure 2.21. ^{13}C{^{1}H} NMR spectrum of W(CPh)(dmpe)$_2$F in C_6D_6.

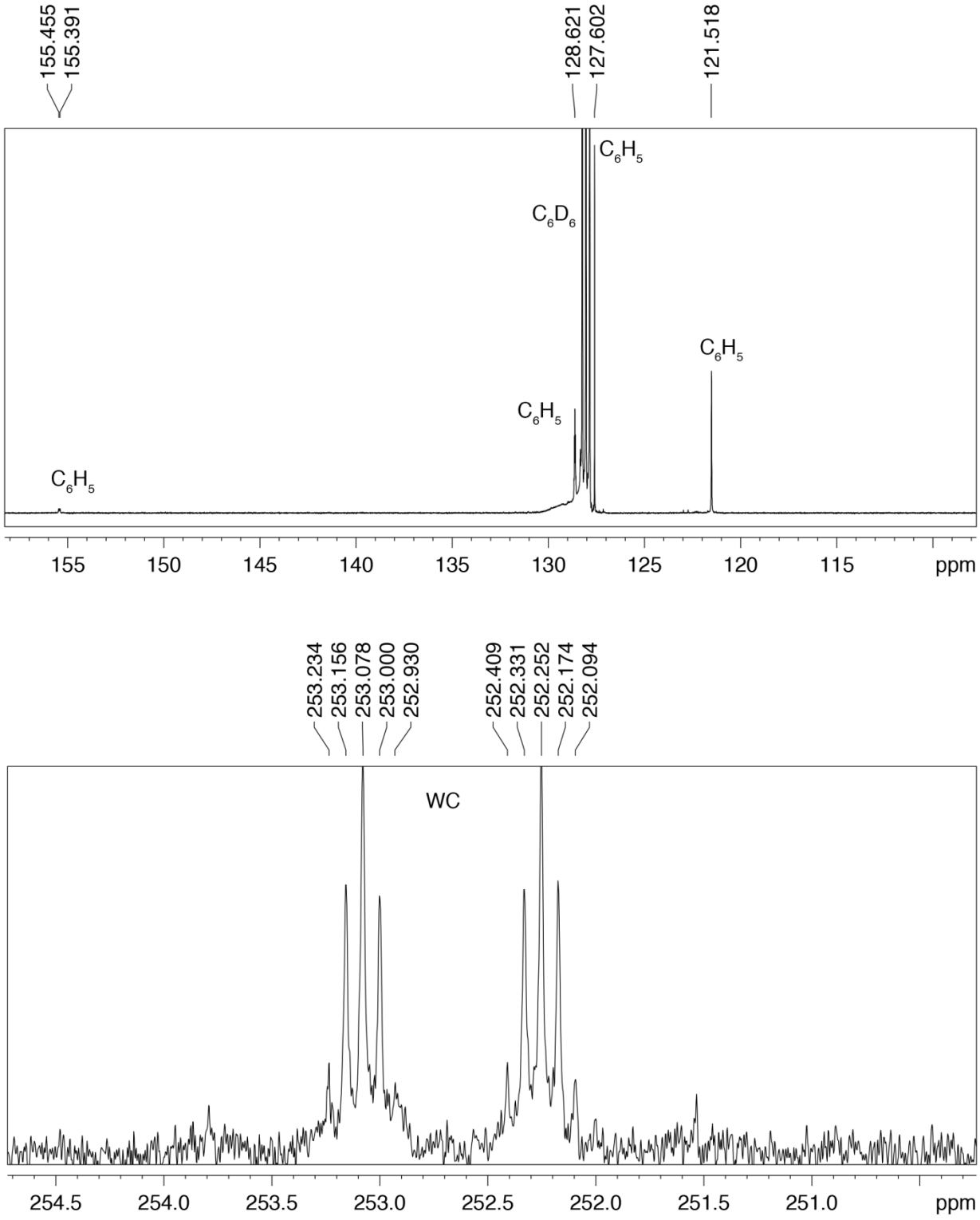

Figure 2.22. Expansions of the $^{13}C\{^{1}H\}$ NMR spectrum of W(CPh)(dmpe)$_2$F in C_6D_6, showing aryl and W<u>C</u> resonances.

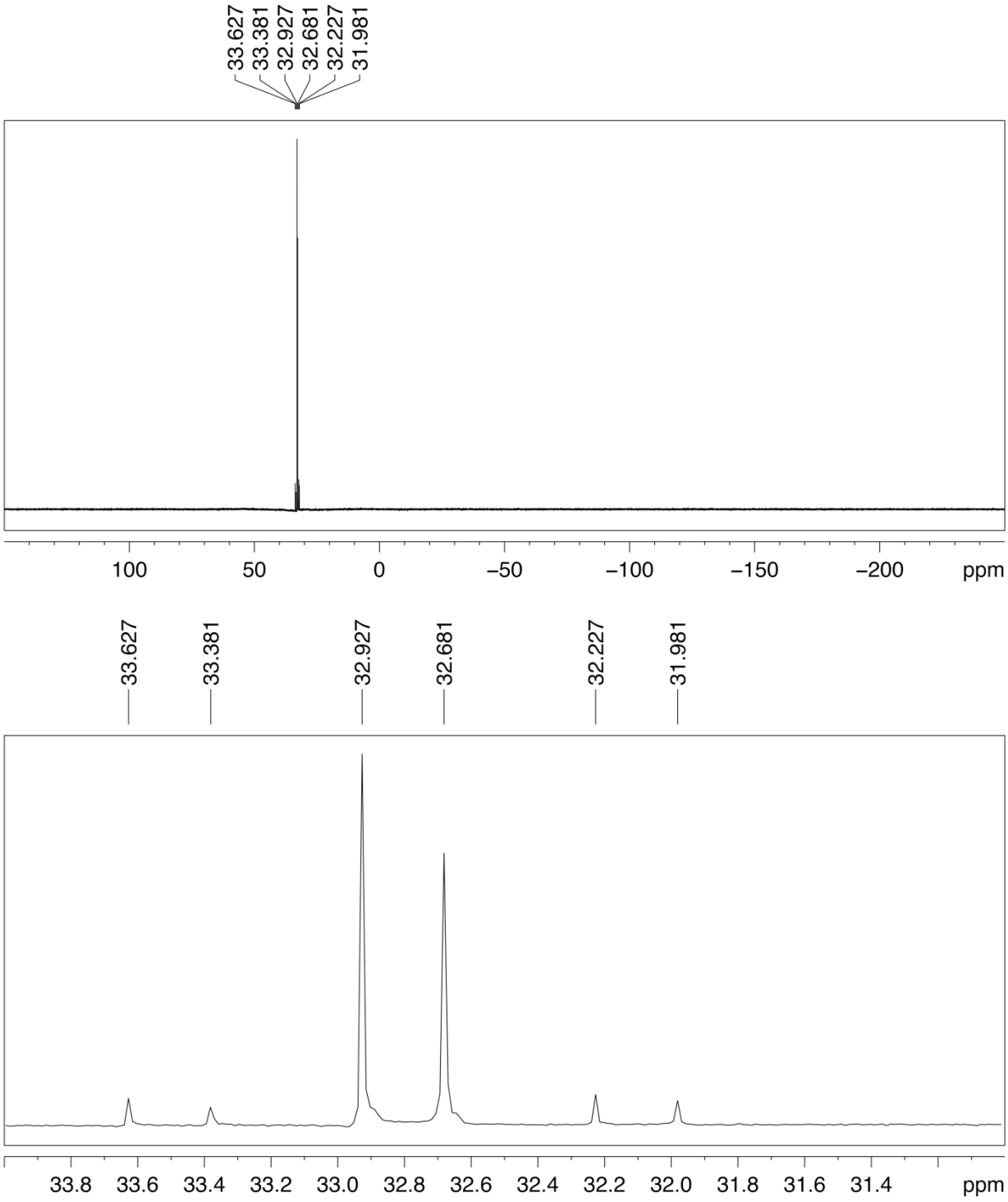

Figure 2.23. $^{31}P\{^{1}H\}$ NMR spectrum of $W(CPh)(dmpe)_2F$ in C_6D_6. The bottom spectrum is an expansion of the top spectrum.

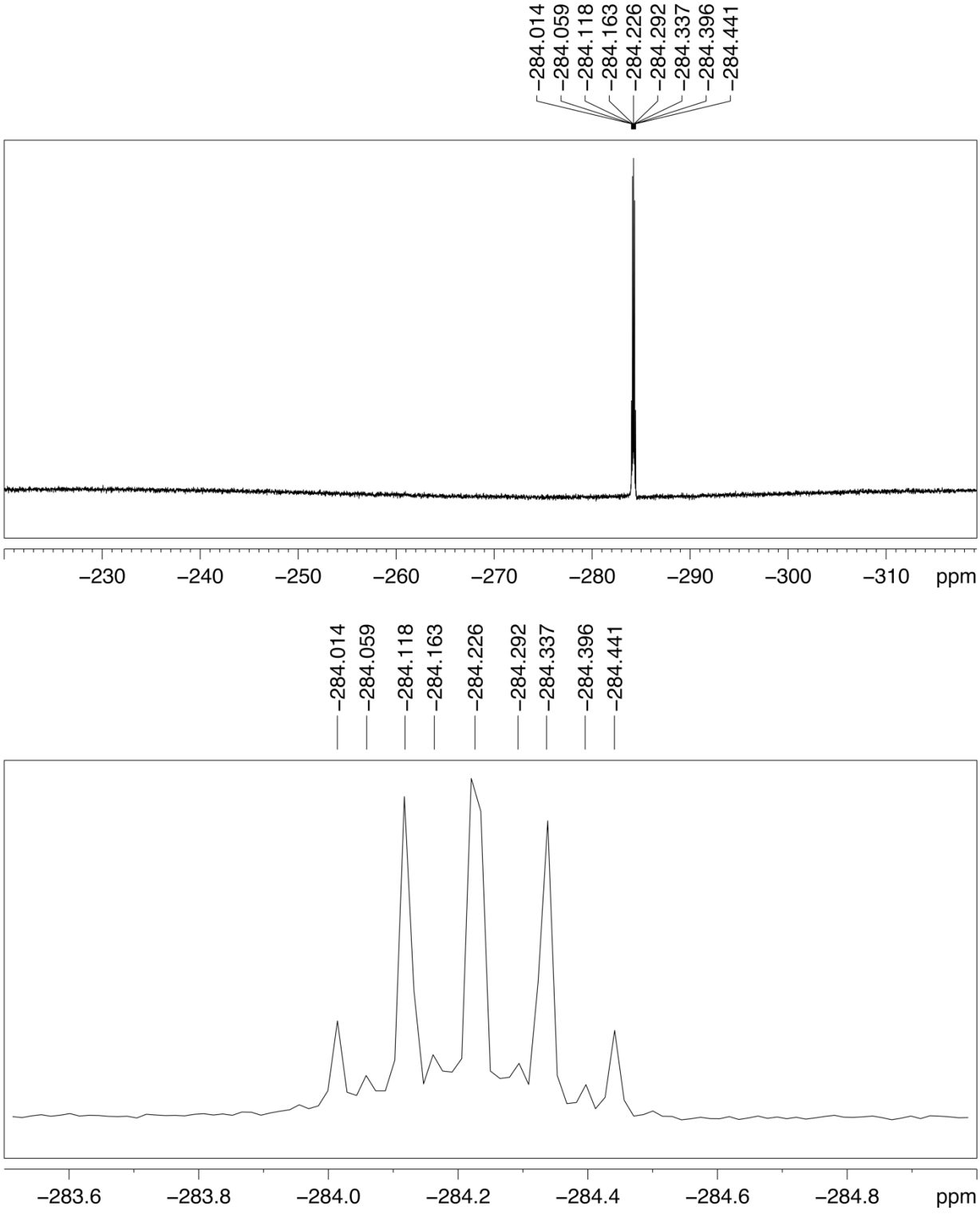

Figure 2.24. $^{19}F\{^{1}H\}$ NMR spectrum of $W(CPh)(dmpe)_2F$ in C_6D_6. The bottom spectrum is an expansion of the top spectrum.

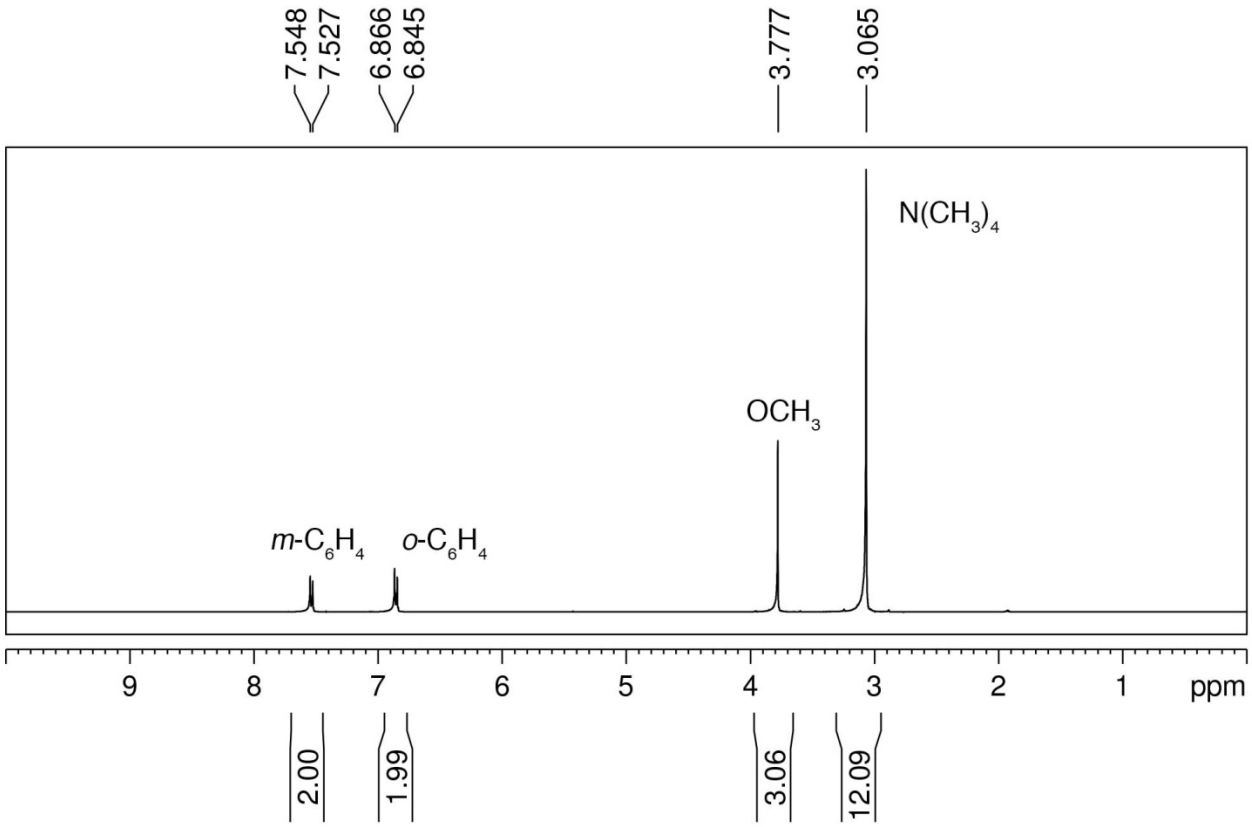

Figure 2.25. ^{1}H NMR spectrum of $[NMe_4][W\{C(O)C_6H_4\text{-}4\text{-}OCH_3\}(CO)_5]$ in CD_3CN.

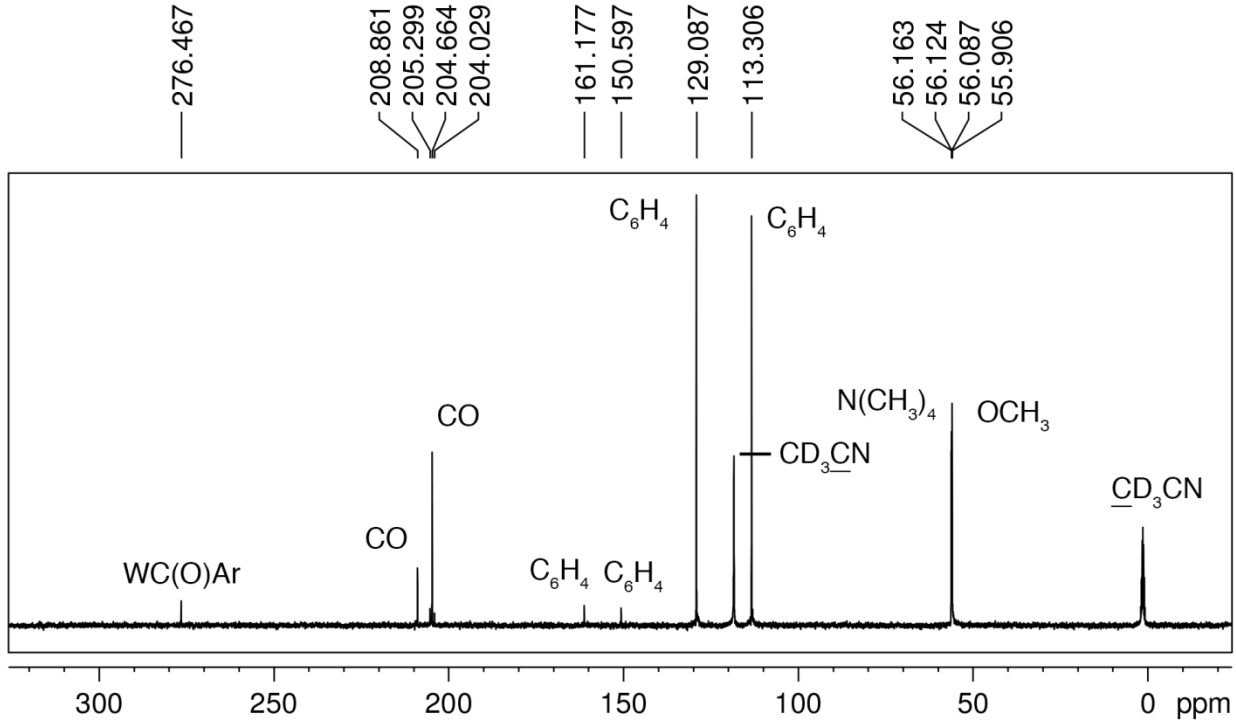

Figure 2.26. $^{13}C\{^{1}H\}$ NMR spectrum of $[NMe_4][W\{C(O)C_6H_4\text{-}4\text{-}OCH_3\}(CO)_5]$ in CD_3CN.

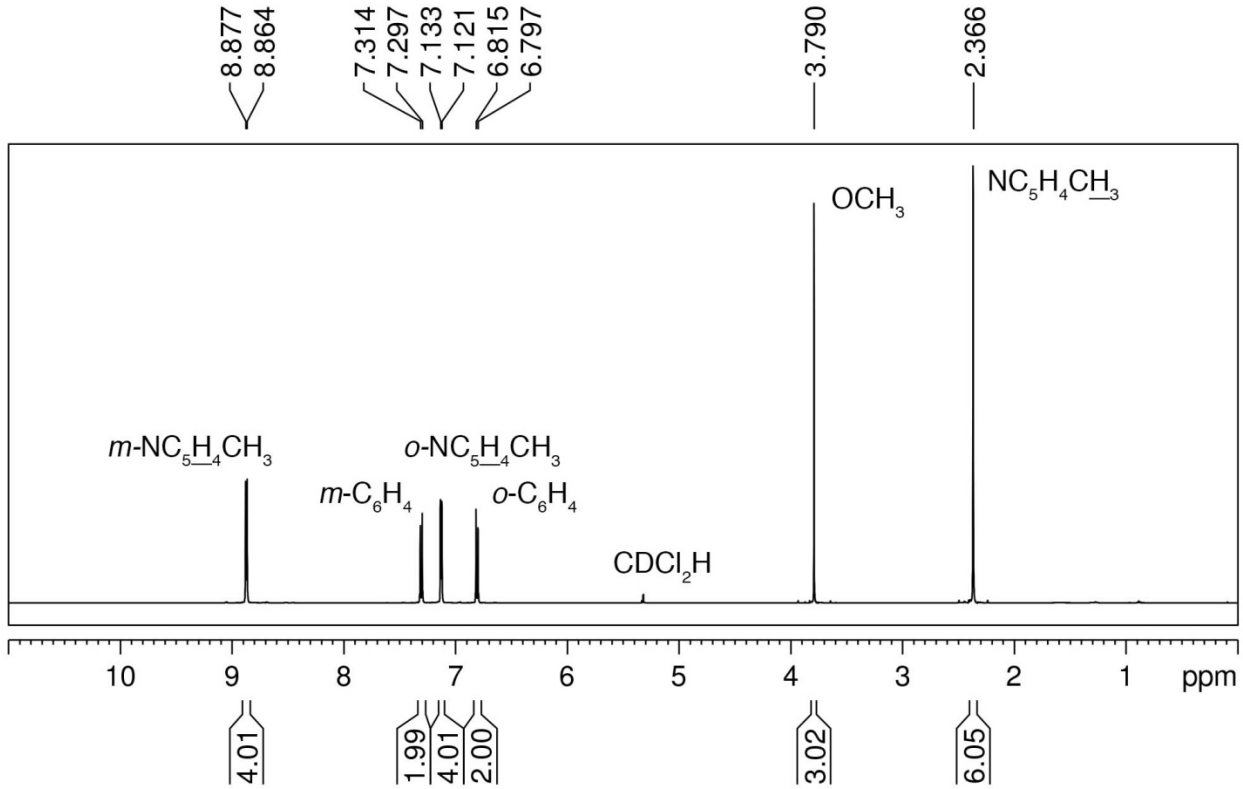

Figure 2.27. ^{1}H NMR spectrum of $W(CC_6H_4\text{-}4\text{-}OCH_3)(pic)_2(CO)_2Cl$ in CD_2Cl_2.

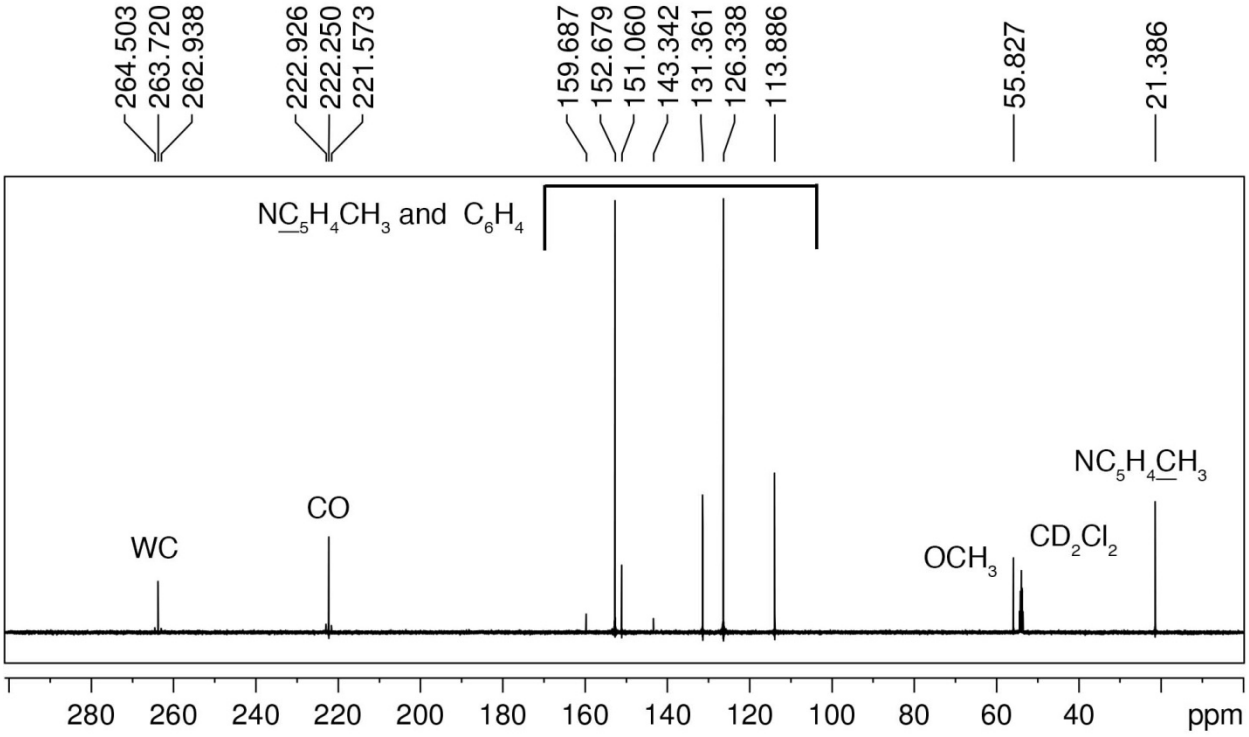

Figure 2.28. $^{13}C\{^{1}H\}$ NMR spectrum of $W(CC_6H_4\text{-}4\text{-}OCH_3)(pic)_2(CO)_2Cl$ in CD_2Cl_2.

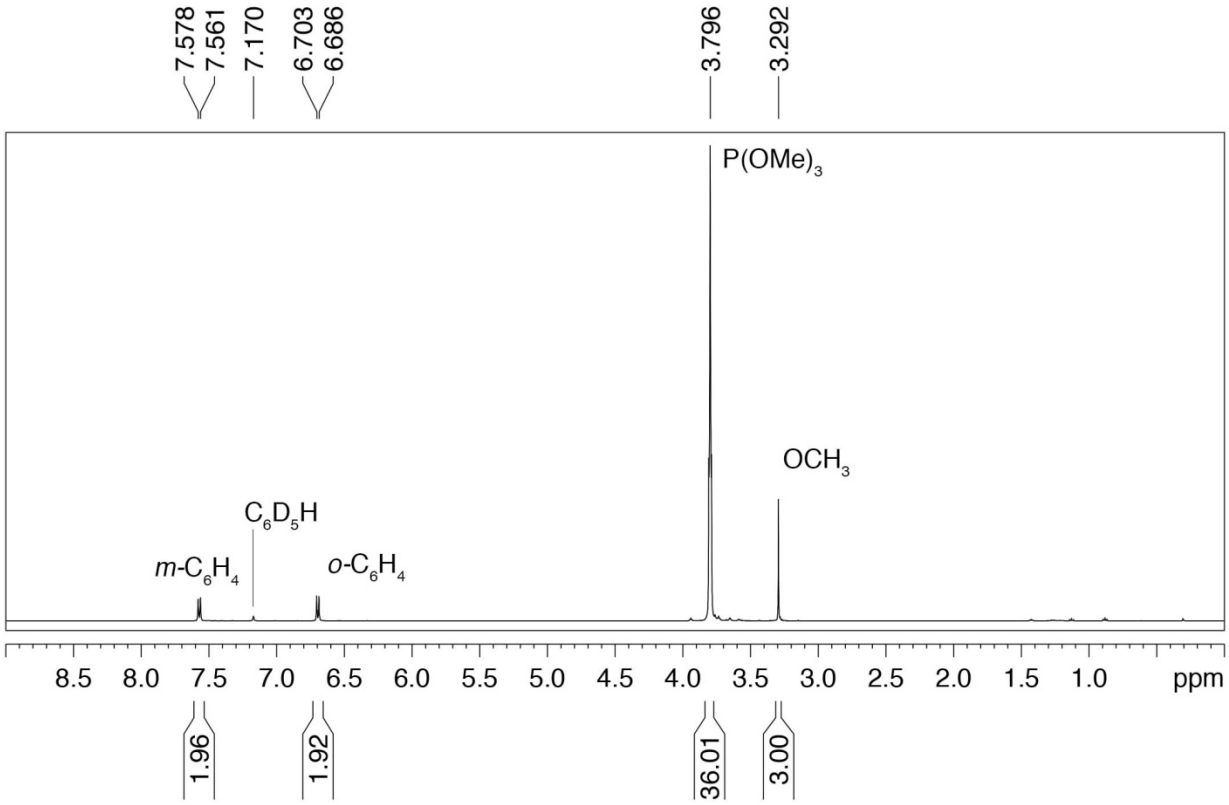

Figure 2.29. ^{1}H NMR spectrum of $W(CC_6H_4\text{-}4\text{-}OCH_3)\{P(OMe)_3\}_4Cl$ in C_6D_6.

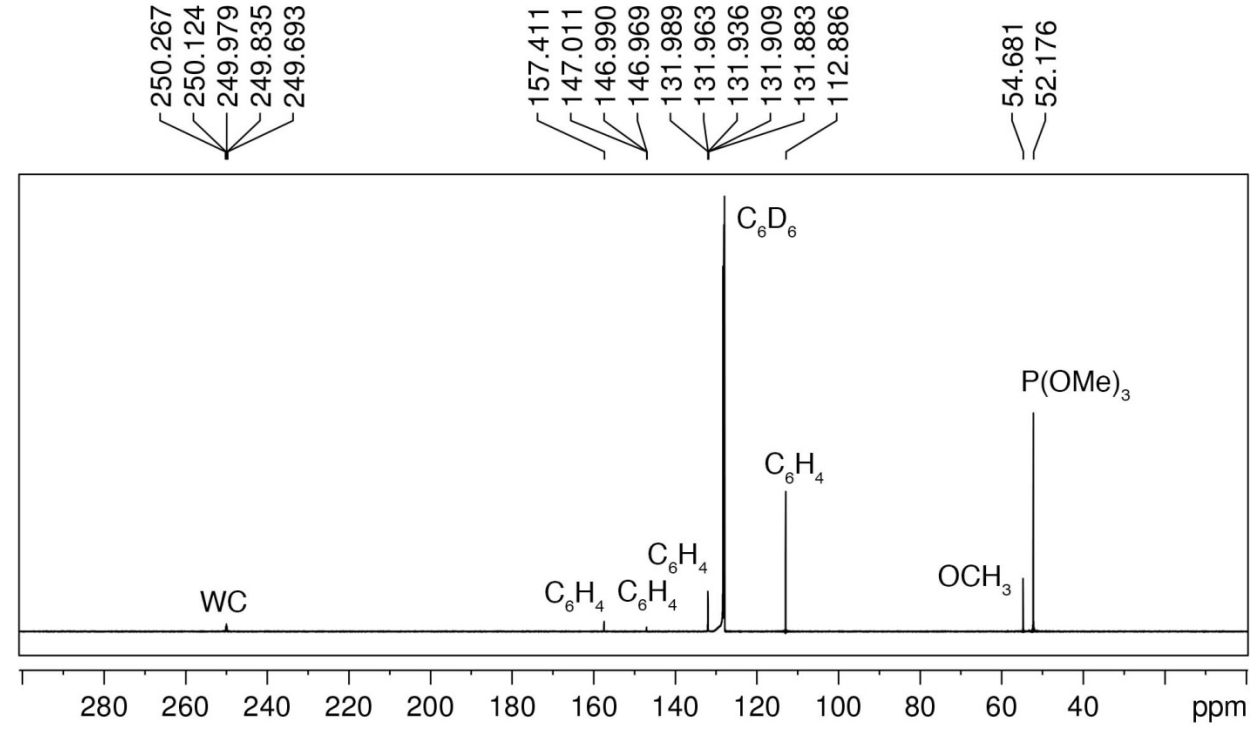

Figure 2.30. $^{13}C\{^{1}H\}$ NMR spectrum of $W(CC_6H_4\text{-}4\text{-}OCH_3)\{P(OMe)_3\}_4Cl$ in C_6D_6

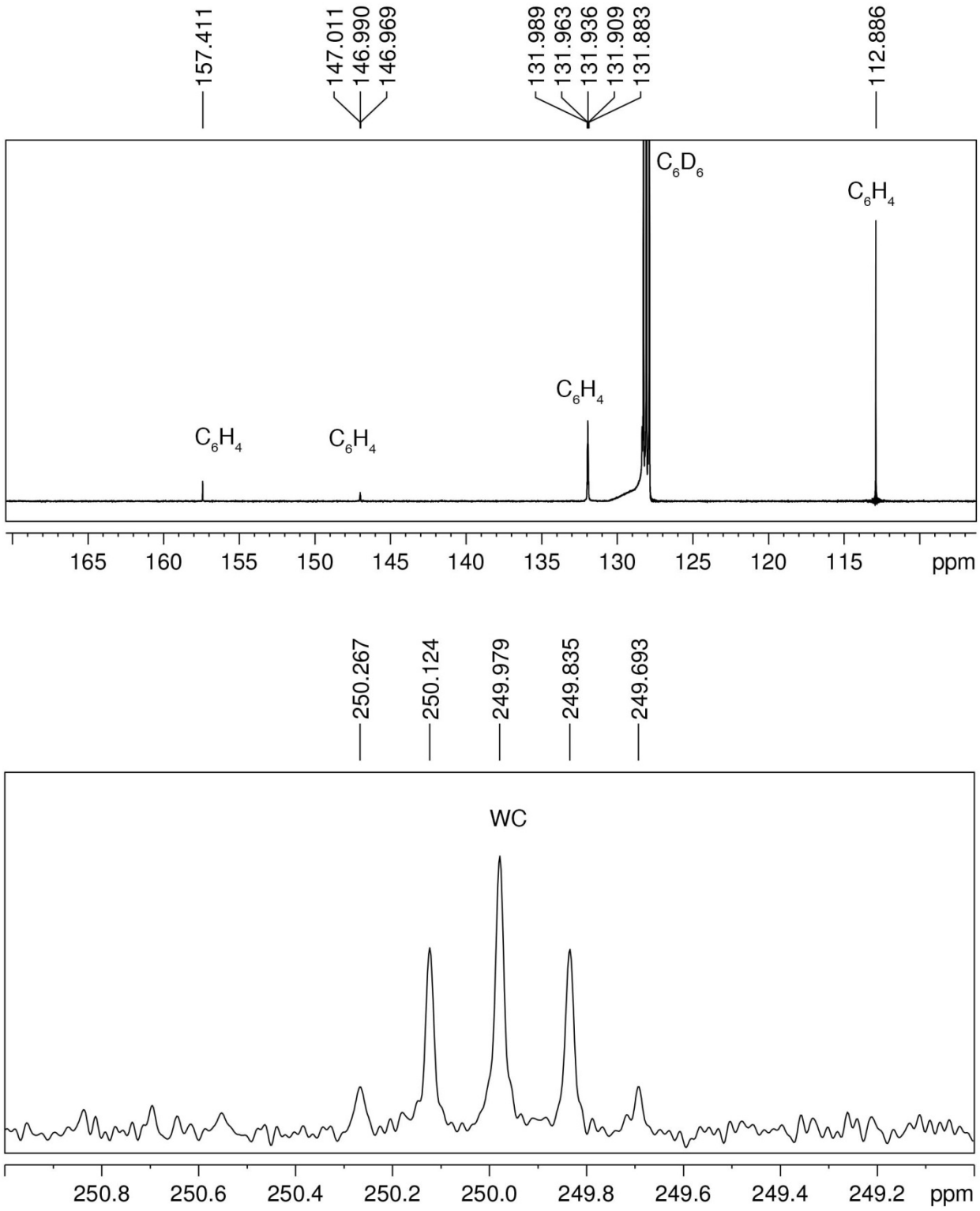

Figure 2.31. Expansions of the $^{13}C\{^{1}H\}$ NMR spectrum of $W(CC_6H_4\text{-}4\text{-}OCH_3)\{P(OMe)_3\}_4Cl$ in C_6D_6 showing aryl and WC resonances.

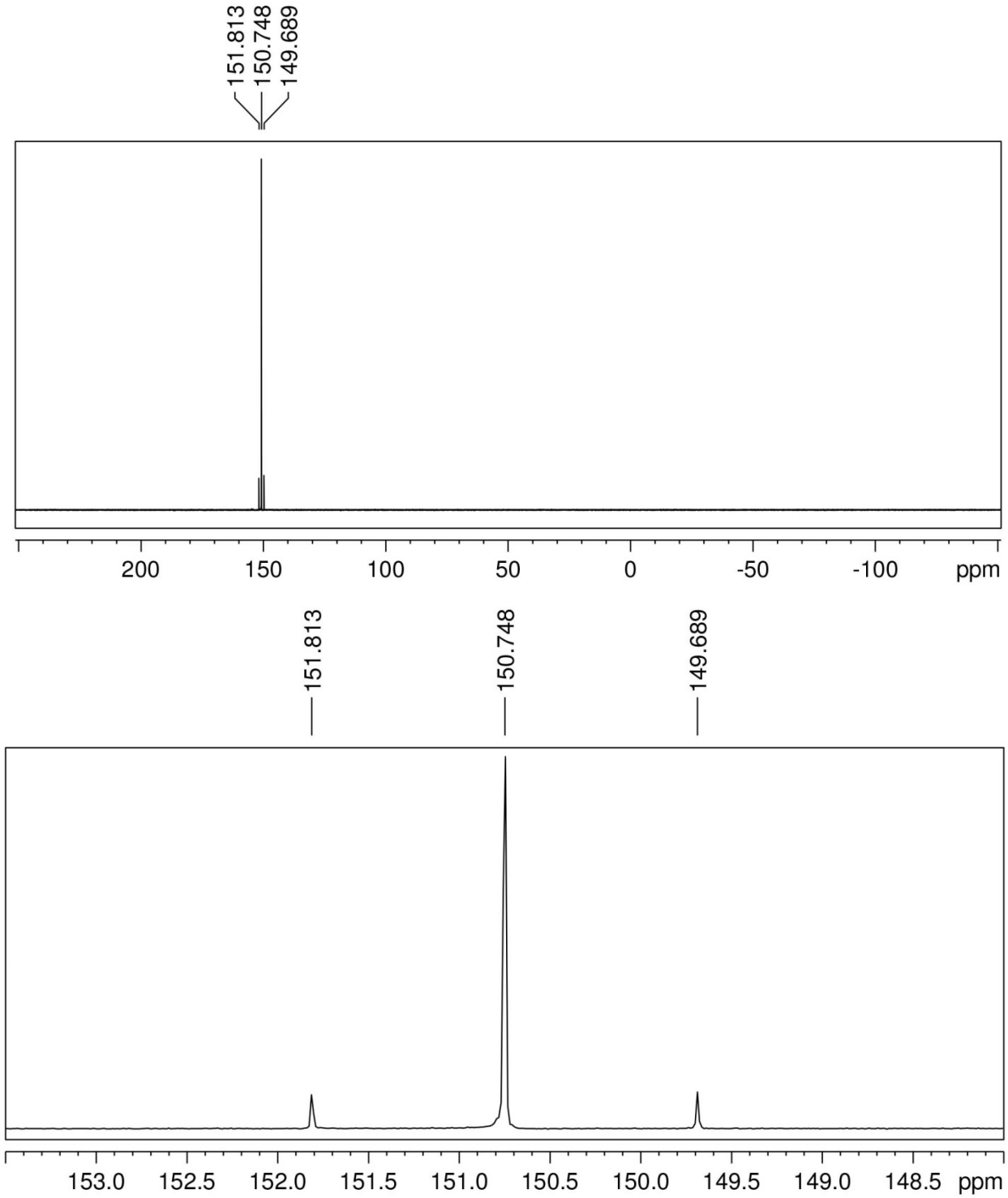

Figure 2.32. $^{31}P\{^{1}H\}$ NMR spectrum of $W(CC_6H_4\text{-}4\text{-}OCH_3)\{P(OMe)_3\}_4Cl$ in C_6D_6. The bottom spectrum is an expansion of the top spectrum.

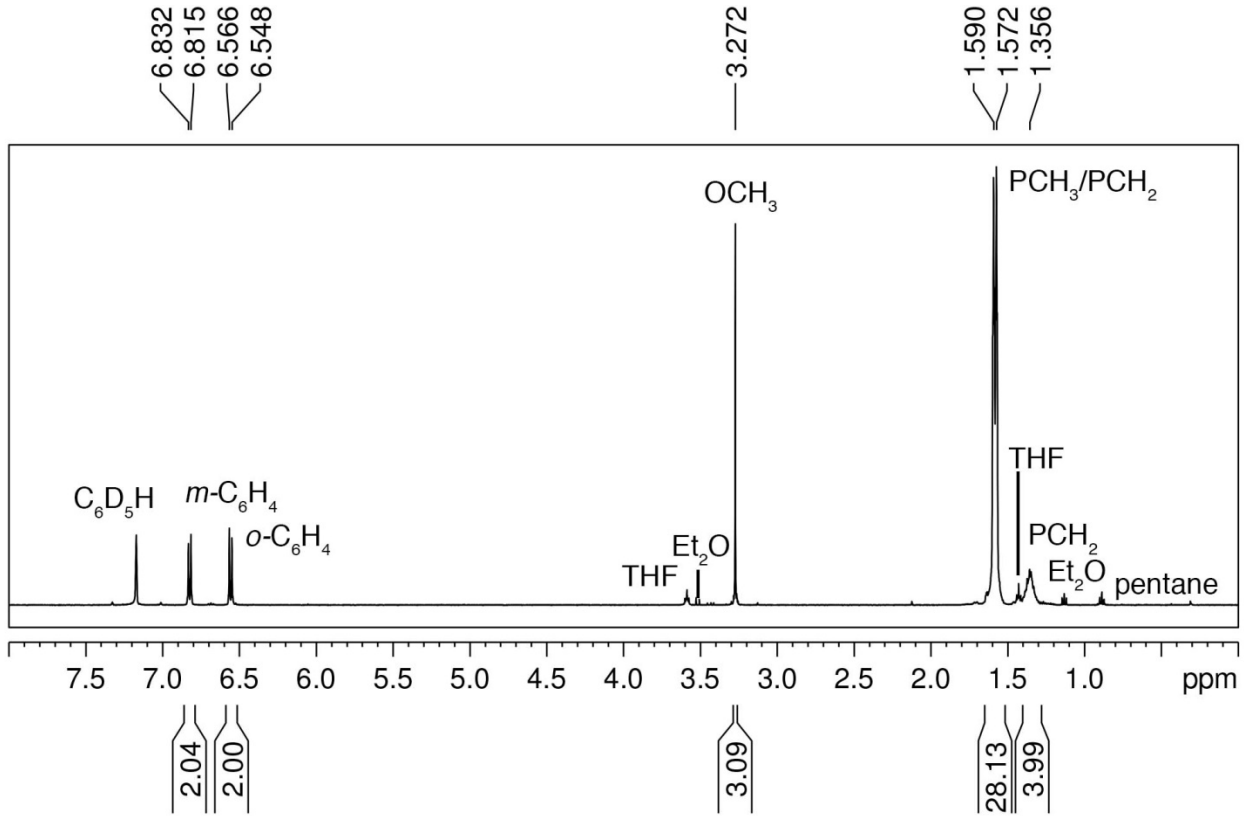

Figure 2.33. ^{1}H NMR spectrum of $W(CC_6H_4\text{-}4\text{-}OCH_3)(dmpe)_2Cl$ in C_6D_6.

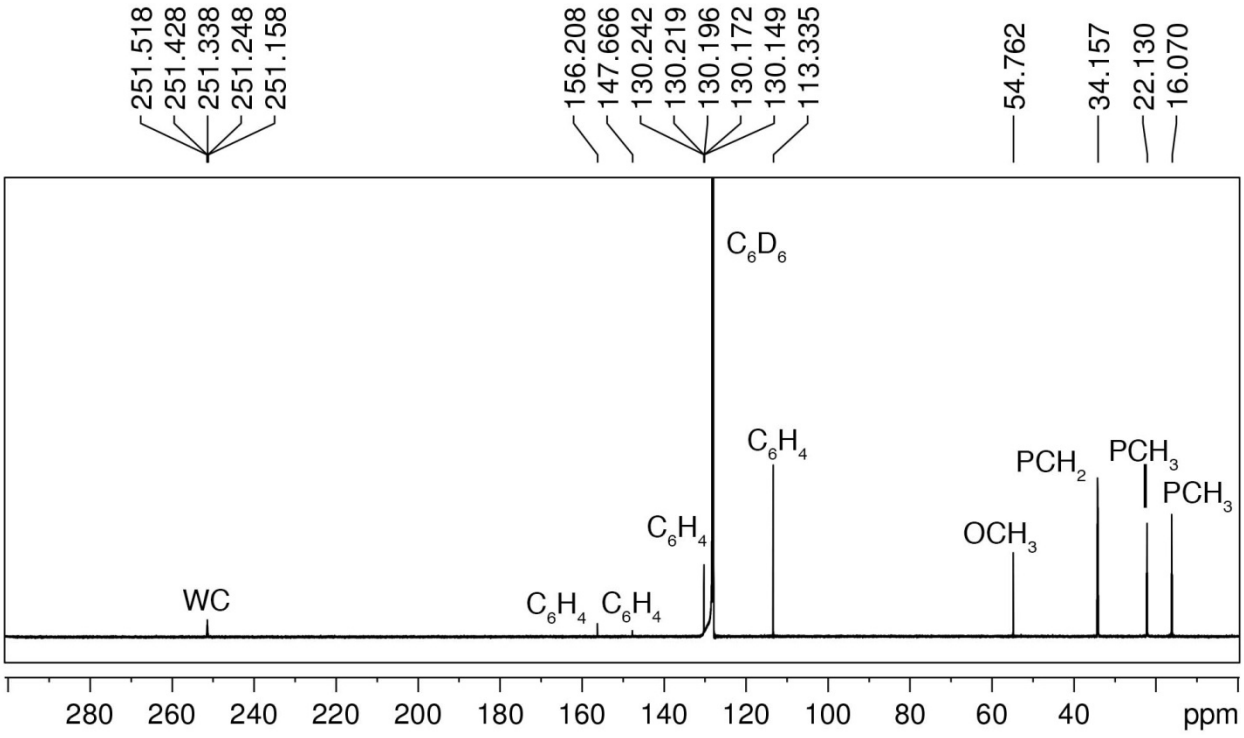

Figure 2.34. $^{13}C\{^{1}H\}$ NMR spectrum of $W(CC_6H_4\text{-}4\text{-}OCH_3)(dmpe)_2Cl$ in C_6D_6.

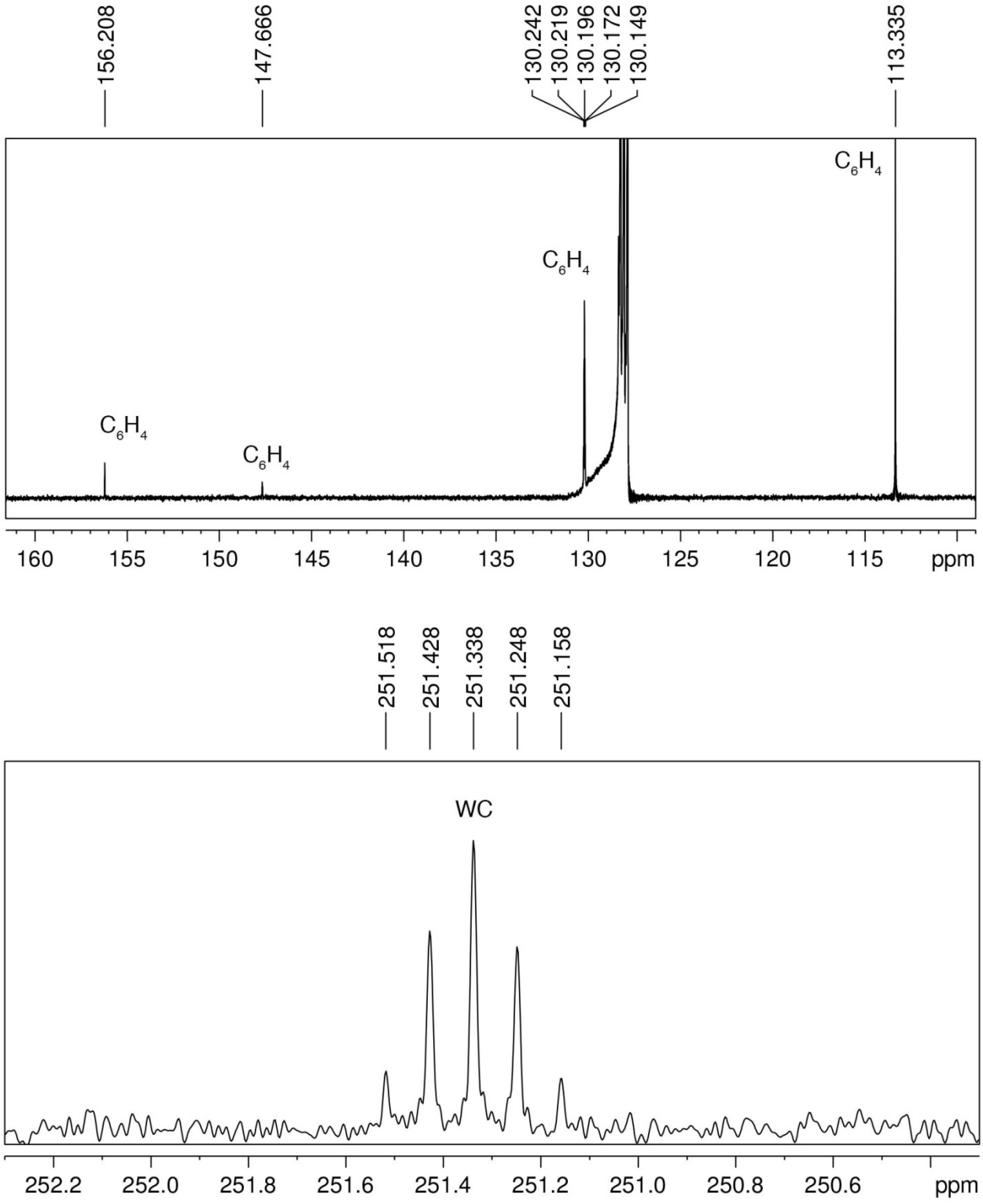

Figure 2.35. Expansions of the $^{13}C\{^{1}H\}$ NMR spectrum of $W(CC_6H_4\text{-}4\text{-}OCH_3)(dmpe)_2Cl$ in C_6D_6 showing aryl and WC resonances.

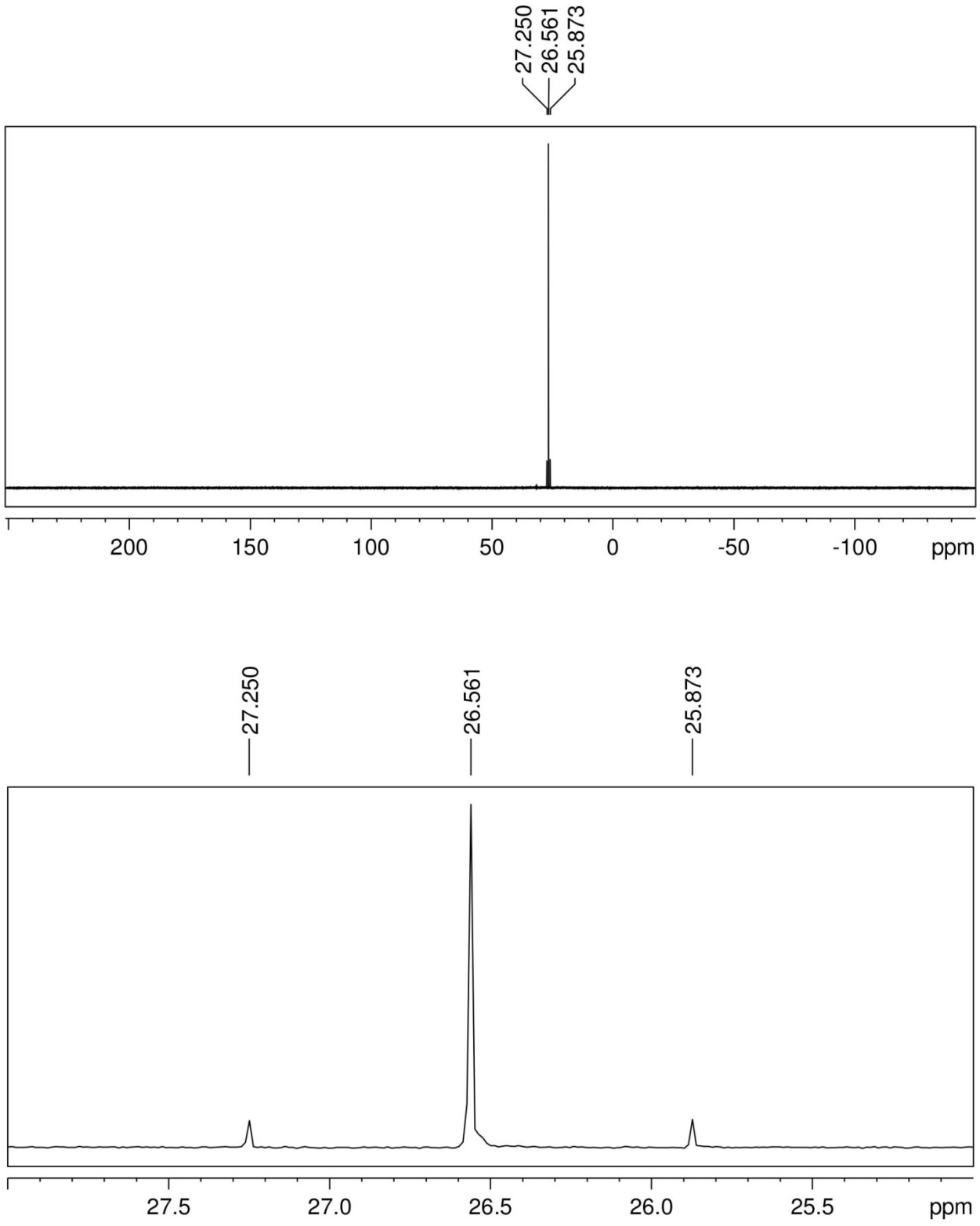

Figure 2.36. $^{31}P\{^{1}H\}$ NMR spectrum of $W(CC_6H_4\text{-}4\text{-}OCH_3)(dmpe)_2Cl$ in C_6D_6. The bottom spectrum is an expansion of the top spectrum.

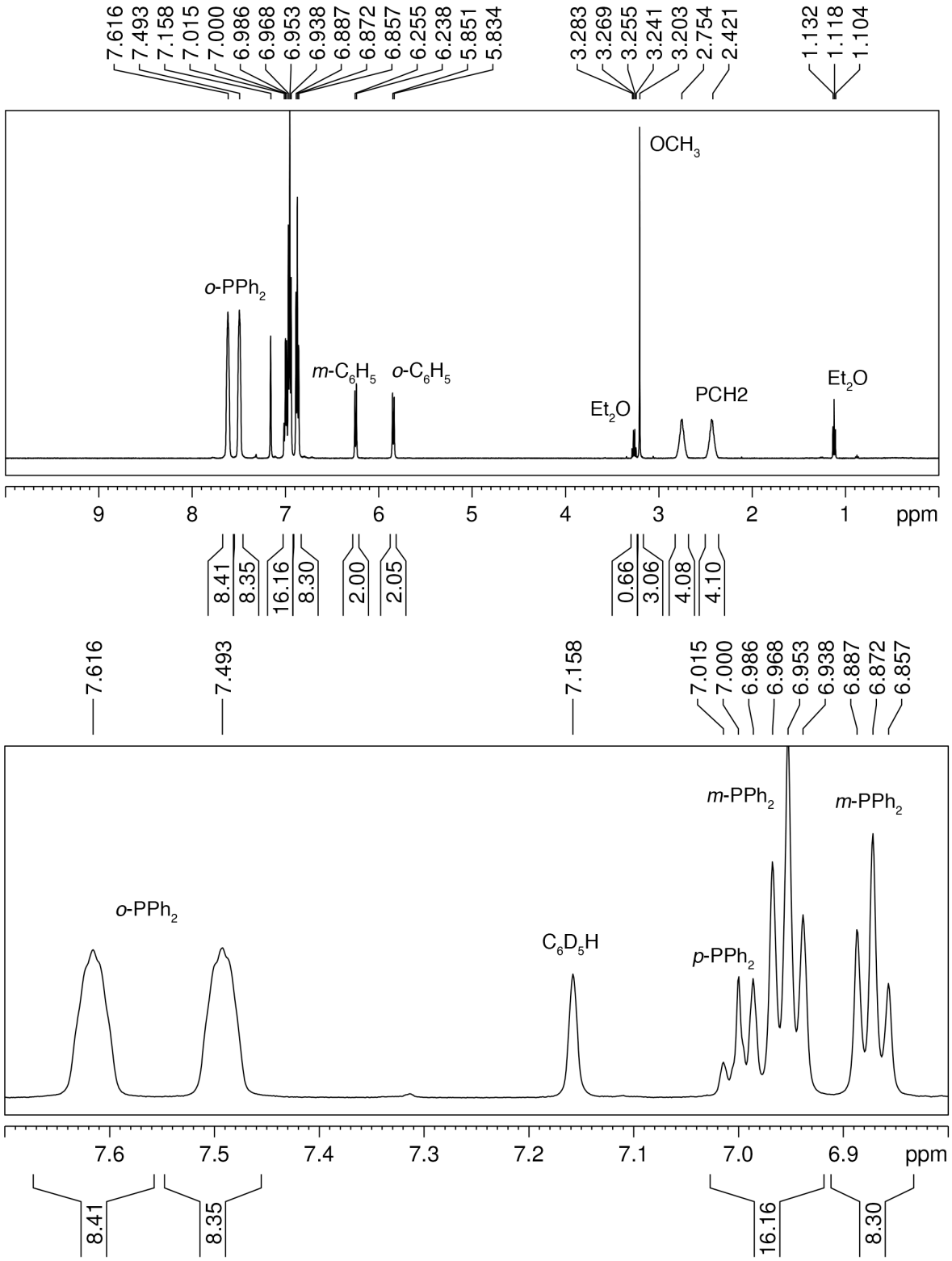

Figure 2.37. ^{1}H NMR spectrum of W(CC_6H_4-4-OCH_3)(dppe)$_2$Cl in C_6D_6. The bottom spectrum is an expansion of the top spectrum.

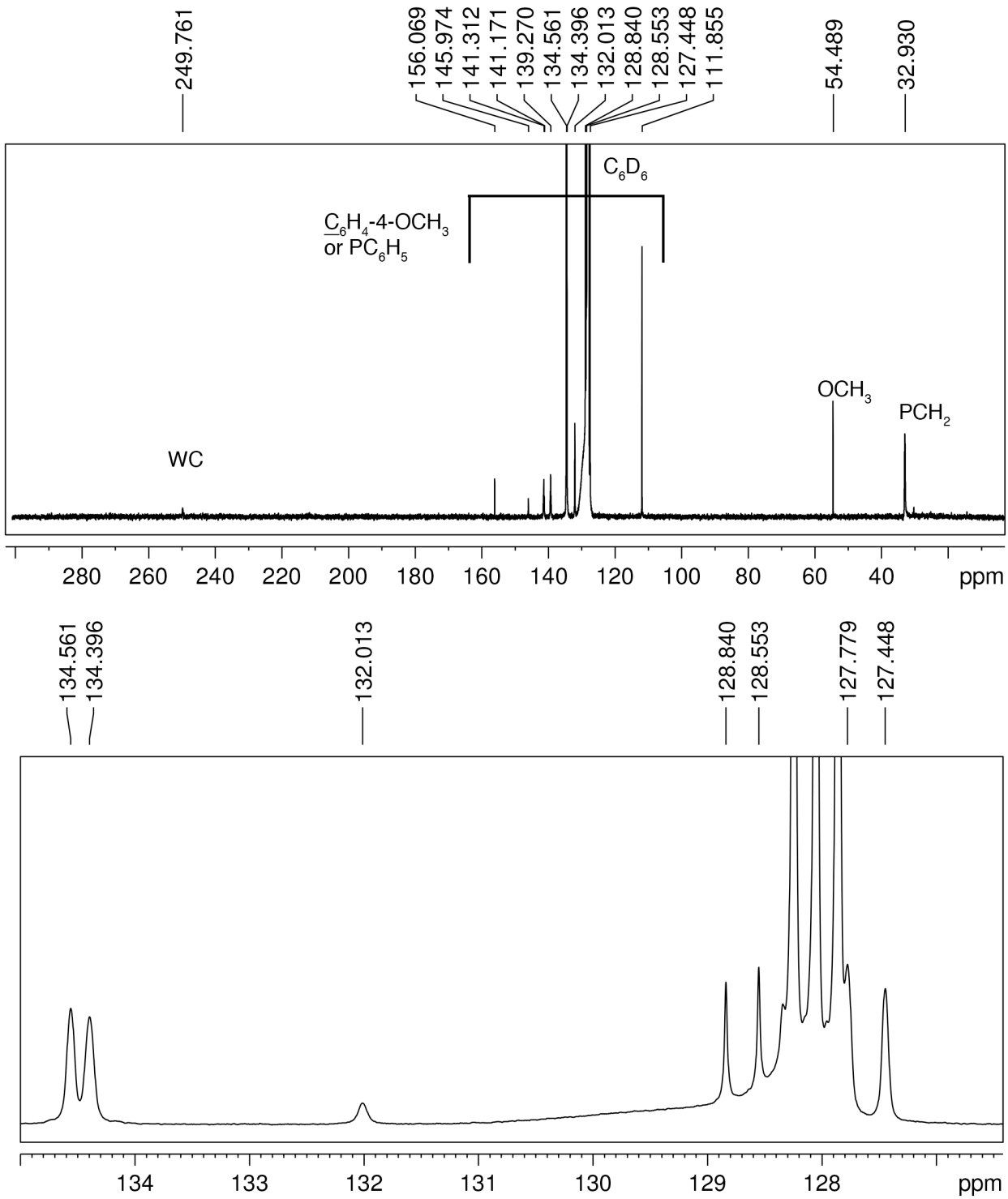

Figure 2.38. $^{13}C\{^{1}H\}$ NMR spectrum of $W(CC_6H_4\text{-}4\text{-}OCH_3)(dppe)_2Cl$ in C_6D_6. The bottom spectrum is an expansion of the top spectrum.

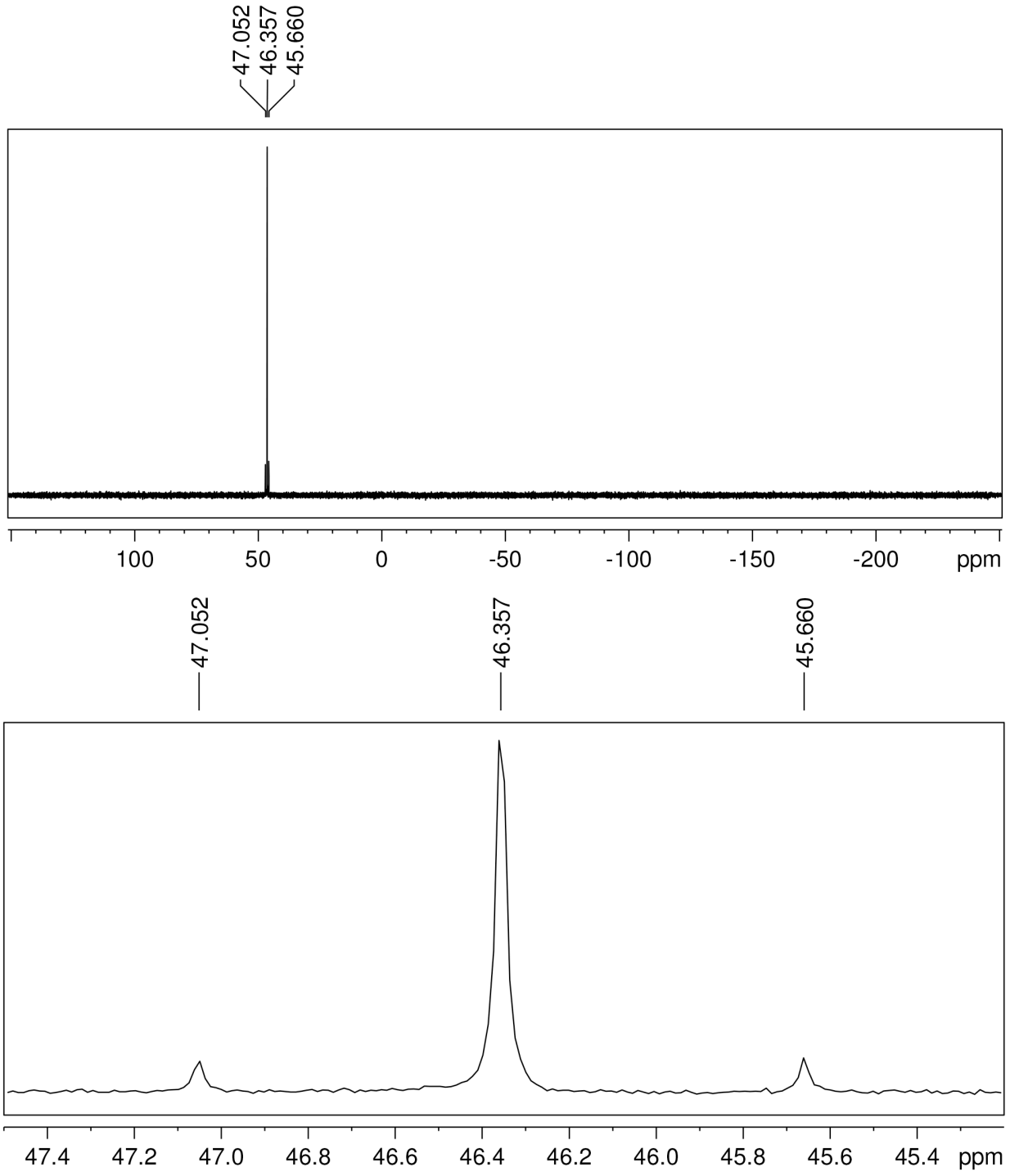

Figure 2.39. $^{31}P\{^{1}H\}$ NMR spectrum of $W(CC_6H_4\text{-}4\text{-}OCH_3)(dppe)_2Cl$ in C_6D_6. The bottom spectrum is an expansion of the top spectrum

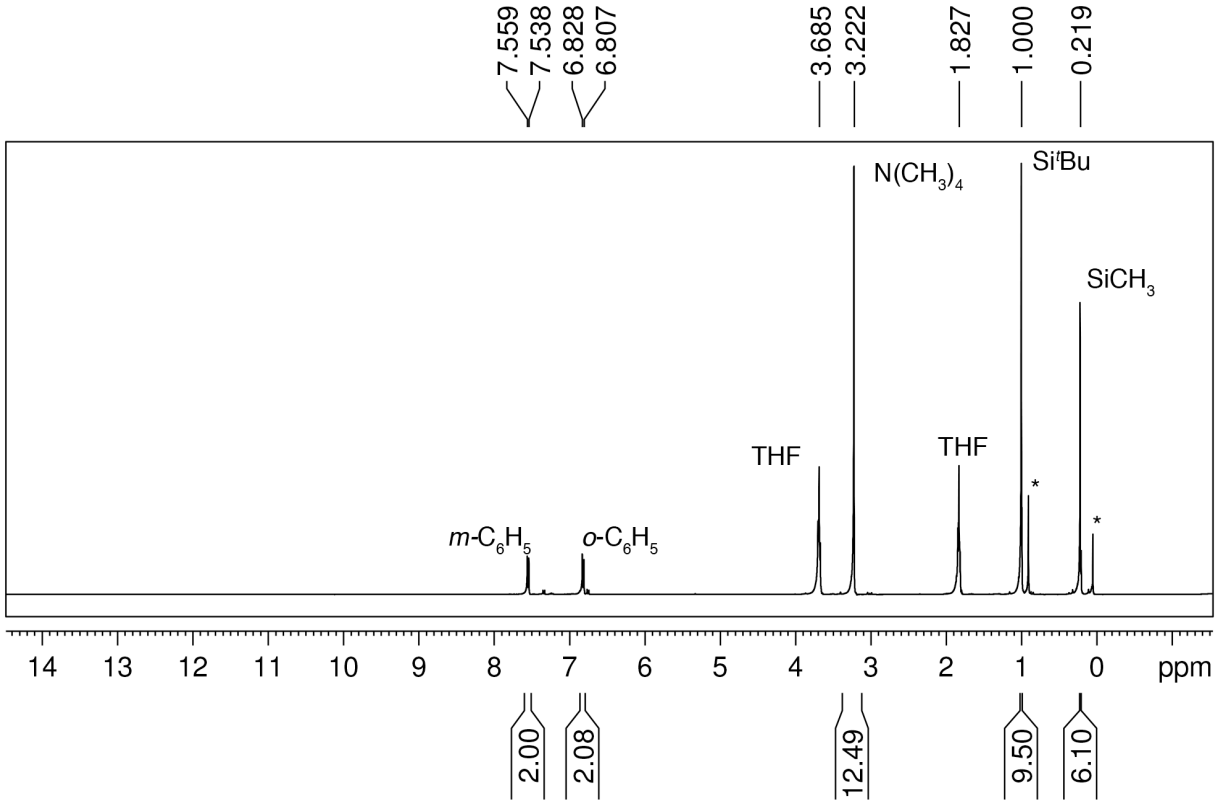

Figure 2.40. ^{1}H NMR spectrum of $[NMe_4][W\{C(O)C_6H_4\text{-}4\text{-}OTBDMS\}(CO)_5]$ in CD_2Cl_2.

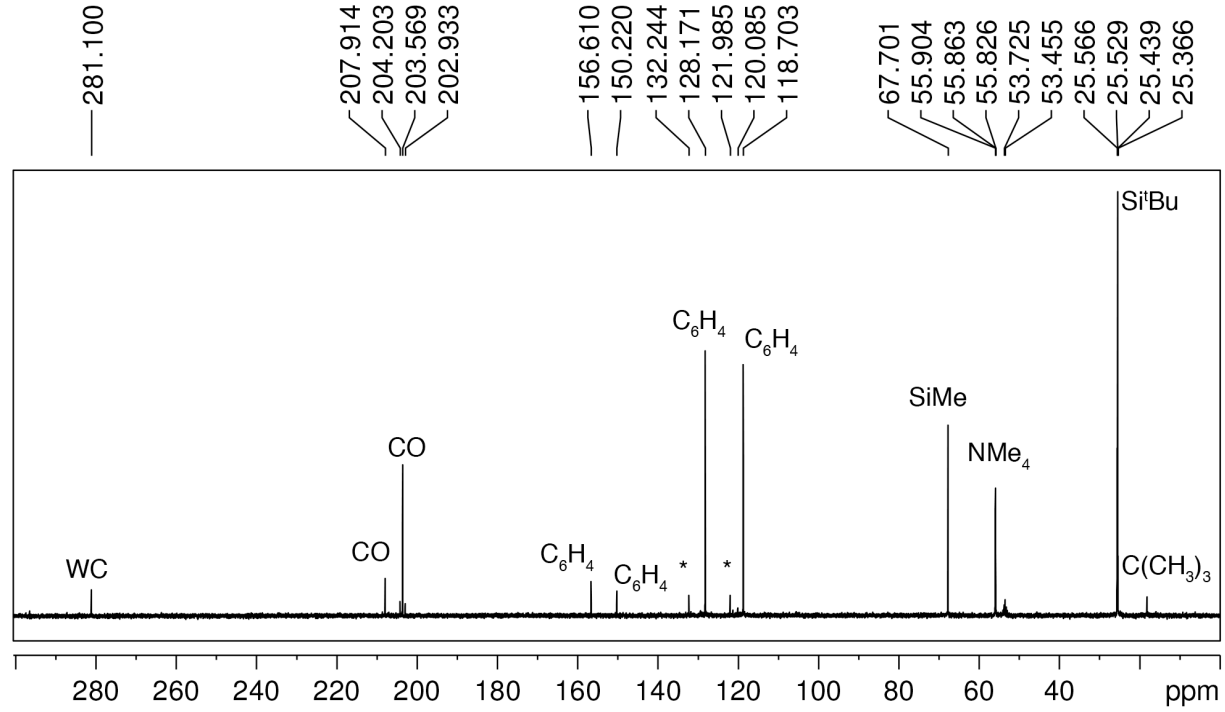

Figure 2.41. $^{13}C\{^{1}H\}$ NMR spectrum of $[NMe_4][W\{C(O)C_6H_4\text{-}4\text{-}OTBDMS\}(CO)_5]$ in CD_2Cl_2. The asterisks (*) indicate unidentified impurities.

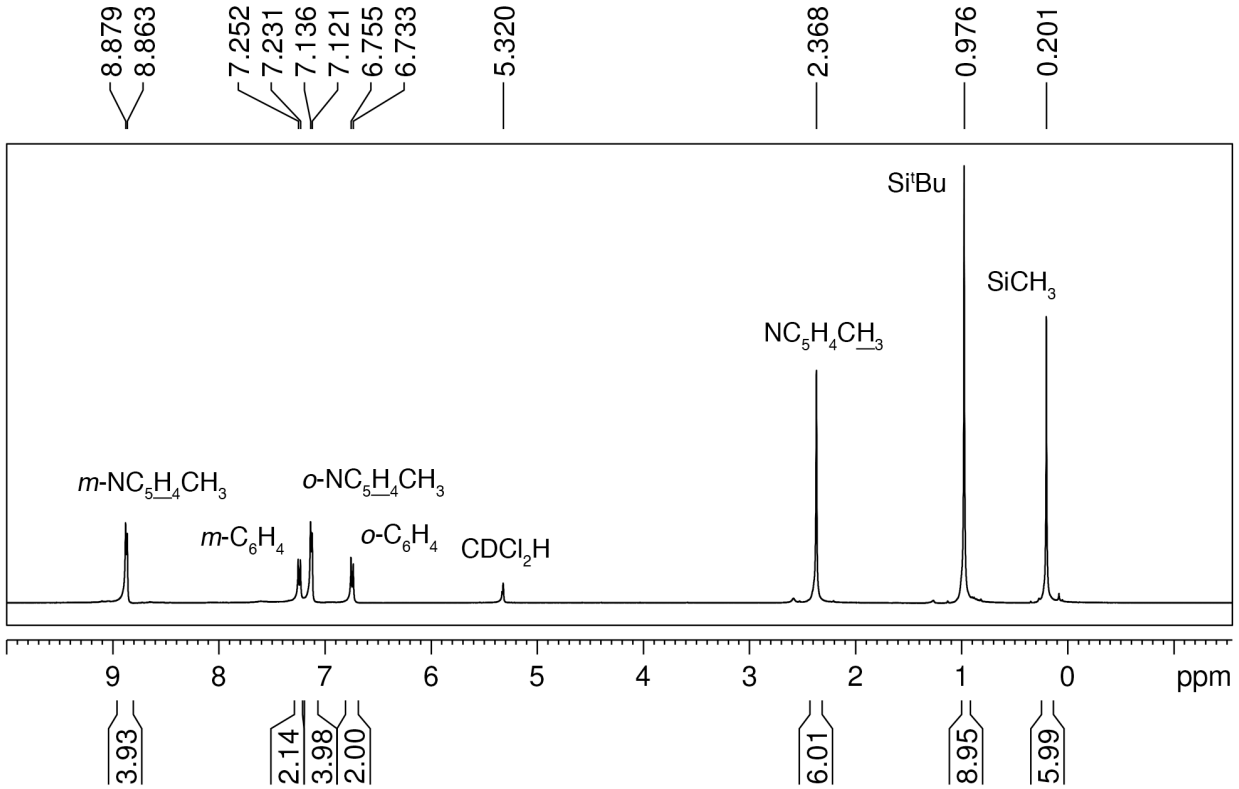

Figure 2.42. ^{1}H NMR spectrum of W(CC_6H_4-4-OTBDMS)$(pic)_2(CO)_2Cl$ in CD_2Cl_2.

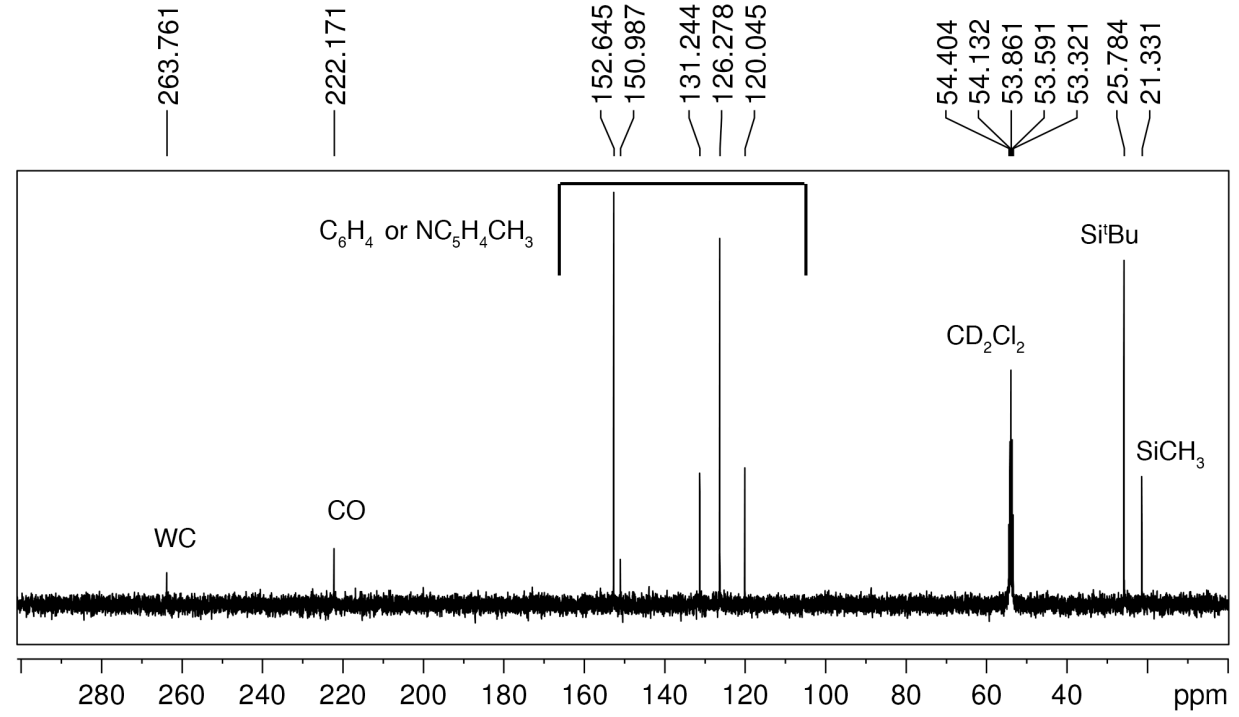

Figure 2.43. $^{13}C\{^{1}H\}$ NMR spectrum of W(CC_6H_4-4-OTBDMS)$(pic)_2(CO)_2Cl$ in CD_2Cl_2.

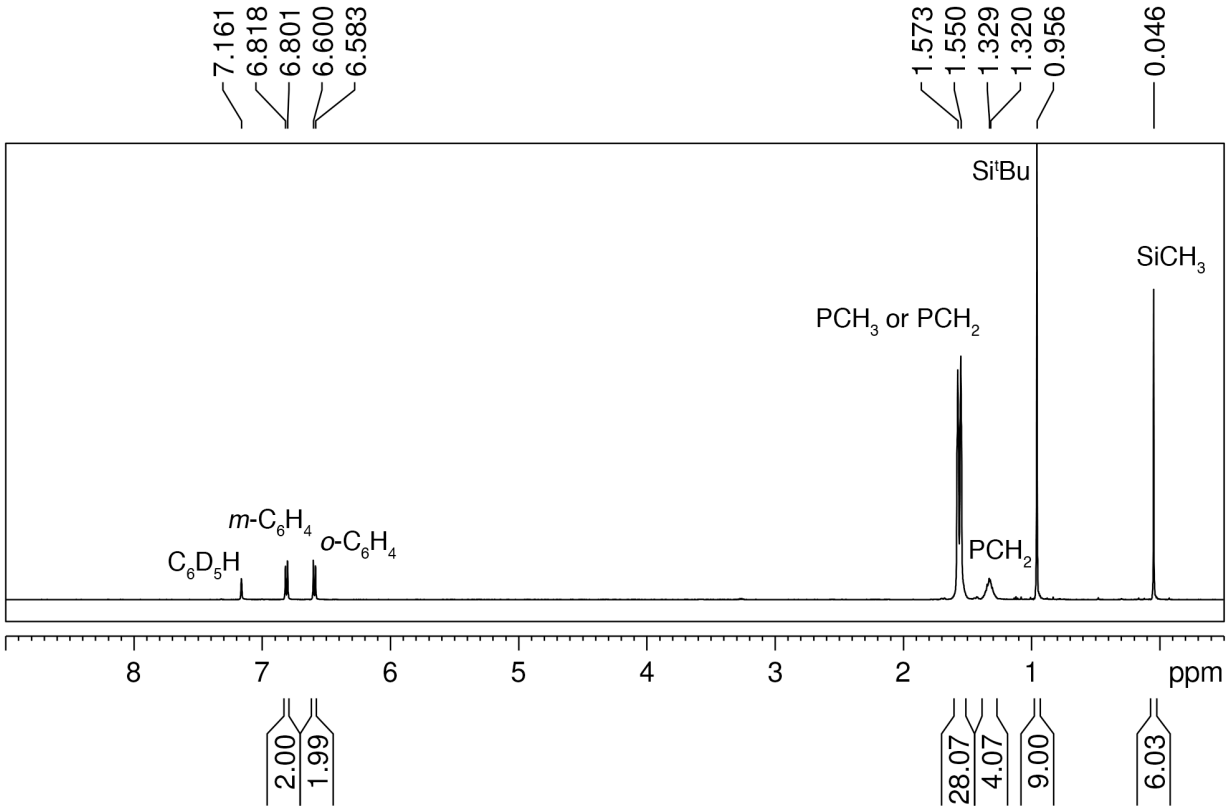

Figure 2.44. ^{1}H NMR spectrum of W(CC$_6$H$_4$-4-OTBDMS)(dmpe)$_2$Cl in C$_6$D$_6$.

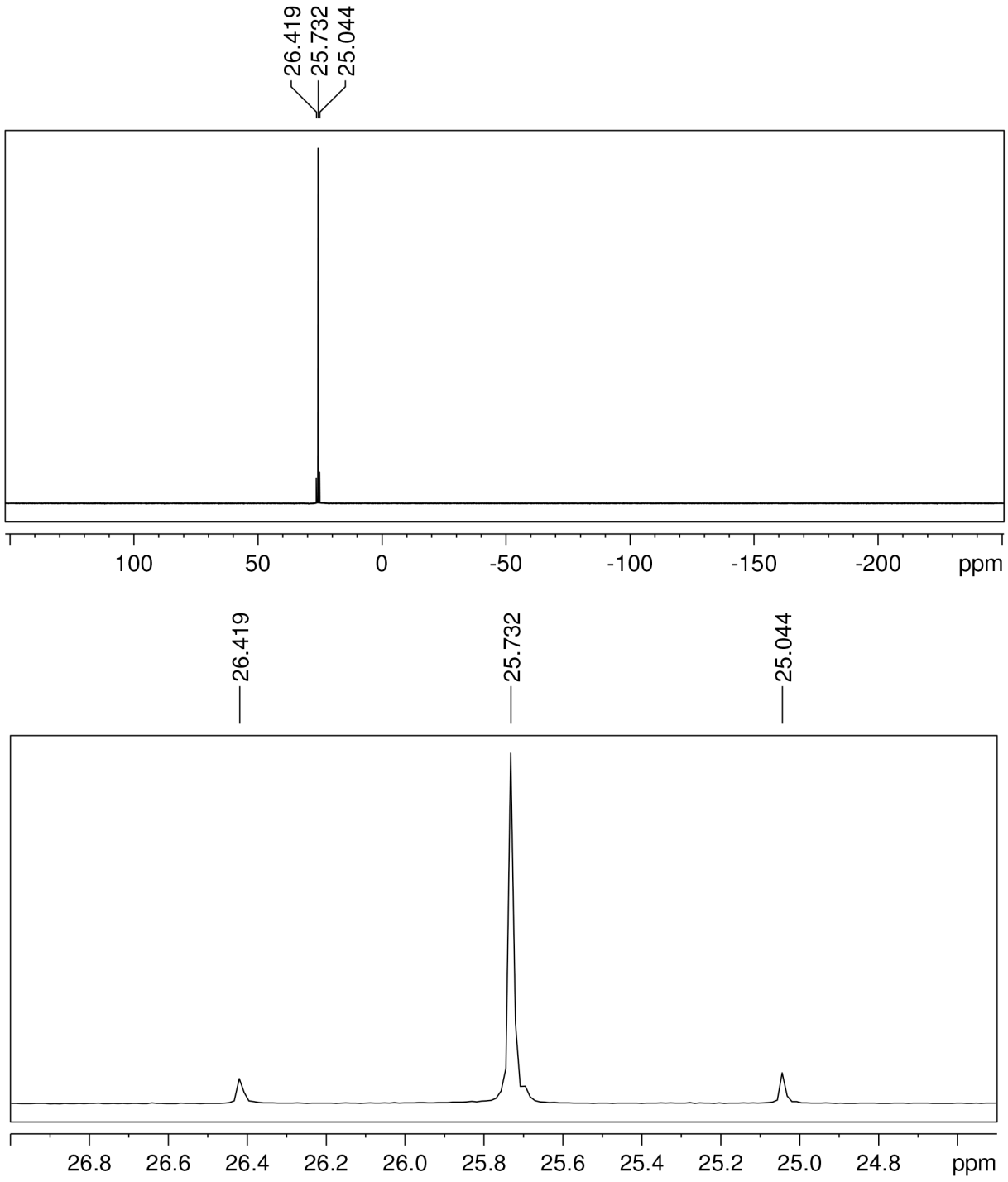

Figure 2.45. $^{31}P\{^{1}H\}$ NMR spectrum of $W(CC_6H_4\text{-}4\text{-}OTBDMS)(dmpe)_2Cl$ in C_6D_6. The bottom spectrum is an expansion of the top spectrum.

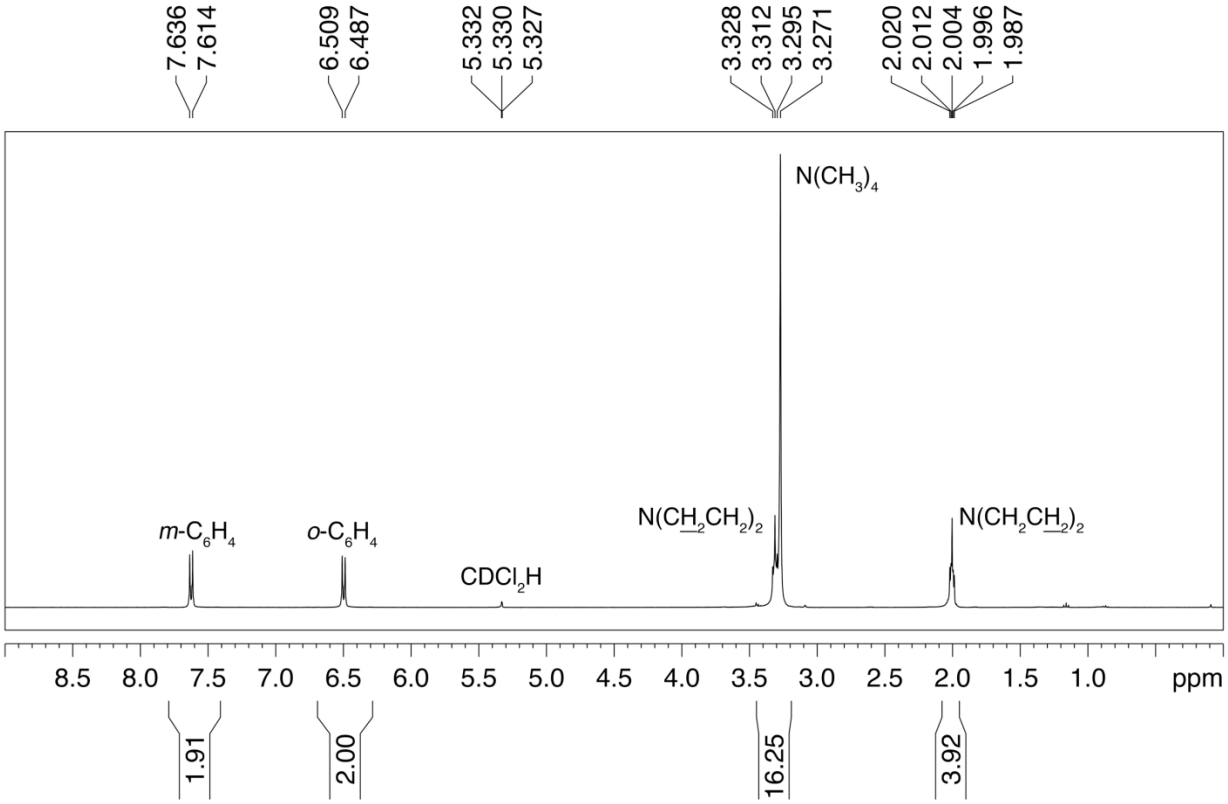

Figure 2.46. ^{1}H NMR spectrum of [NMe$_4$][W{C(O)C$_6$H$_4$-4-pyr}(CO)$_5$] in CD_2Cl_2.

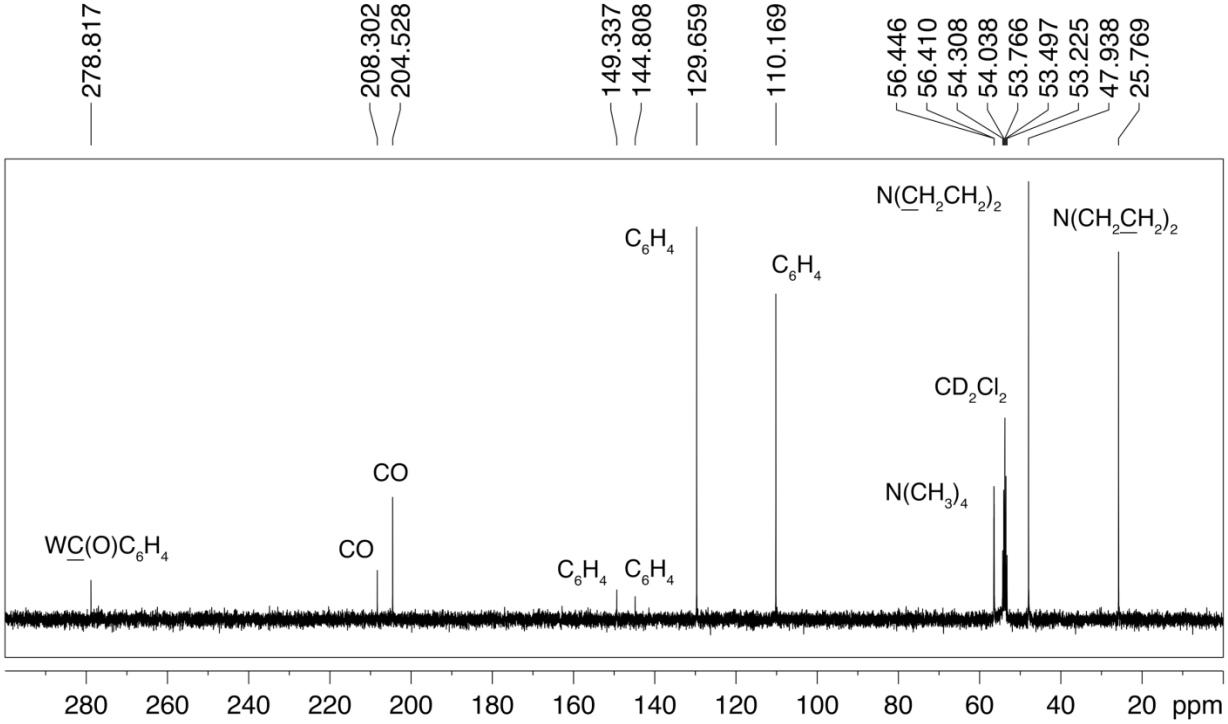

Figure 2.47. ^{13}C{^{1}H} NMR spectrum of [NMe$_4$][W{C(O)C$_6$H$_4$-4-pyr}(CO)$_5$] in CD_2Cl_2.

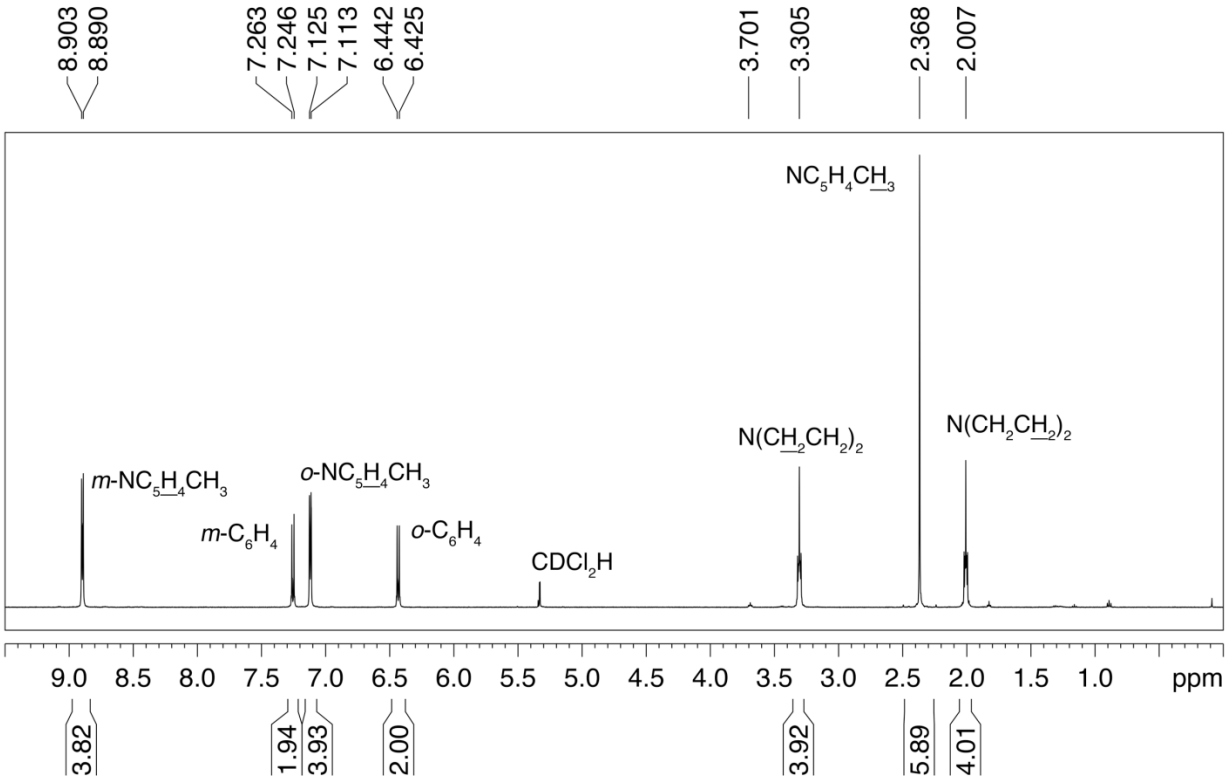

Figure 2.48. ^{1}H NMR spectrum of $W(CC_6H_4\text{-}4\text{-}pyr)(pic)_2(CO)_2Cl$ in CD_2Cl_2.

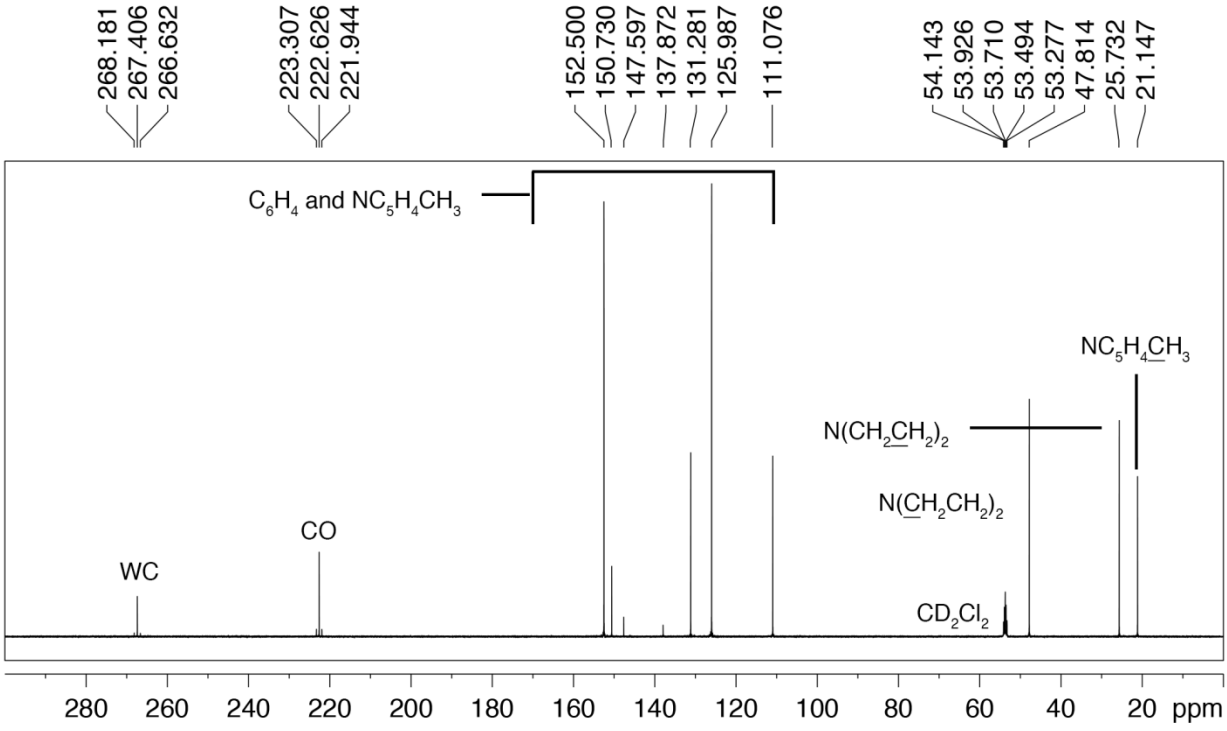

Figure 2.49. $^{13}C\{^{1}H\}$ NMR spectrum of $W(CC_6H_4\text{-}4\text{-}pyr)(pic)_2(CO)_2Cl$ in CD_2Cl_2.

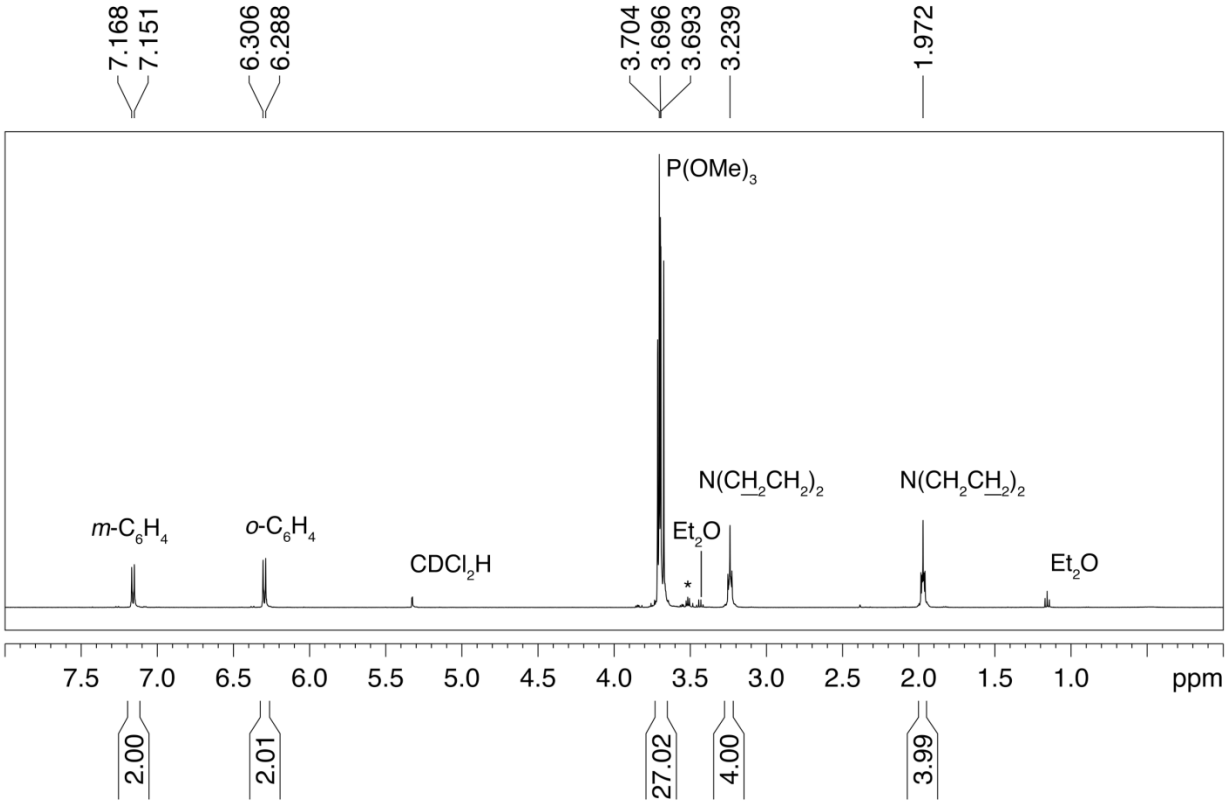

Figure 2.50. ^{1}H NMR spectrum of W(CC_6H_4-4-pyr){$P(OMe)_3$}$_3$(CO)Cl in CD_2Cl_2. The asterisk indicates the resonance attributable to the W(CC_6H_4-4-pyr){$P(OMe)_3$}$_4$Cl impurity in the product.

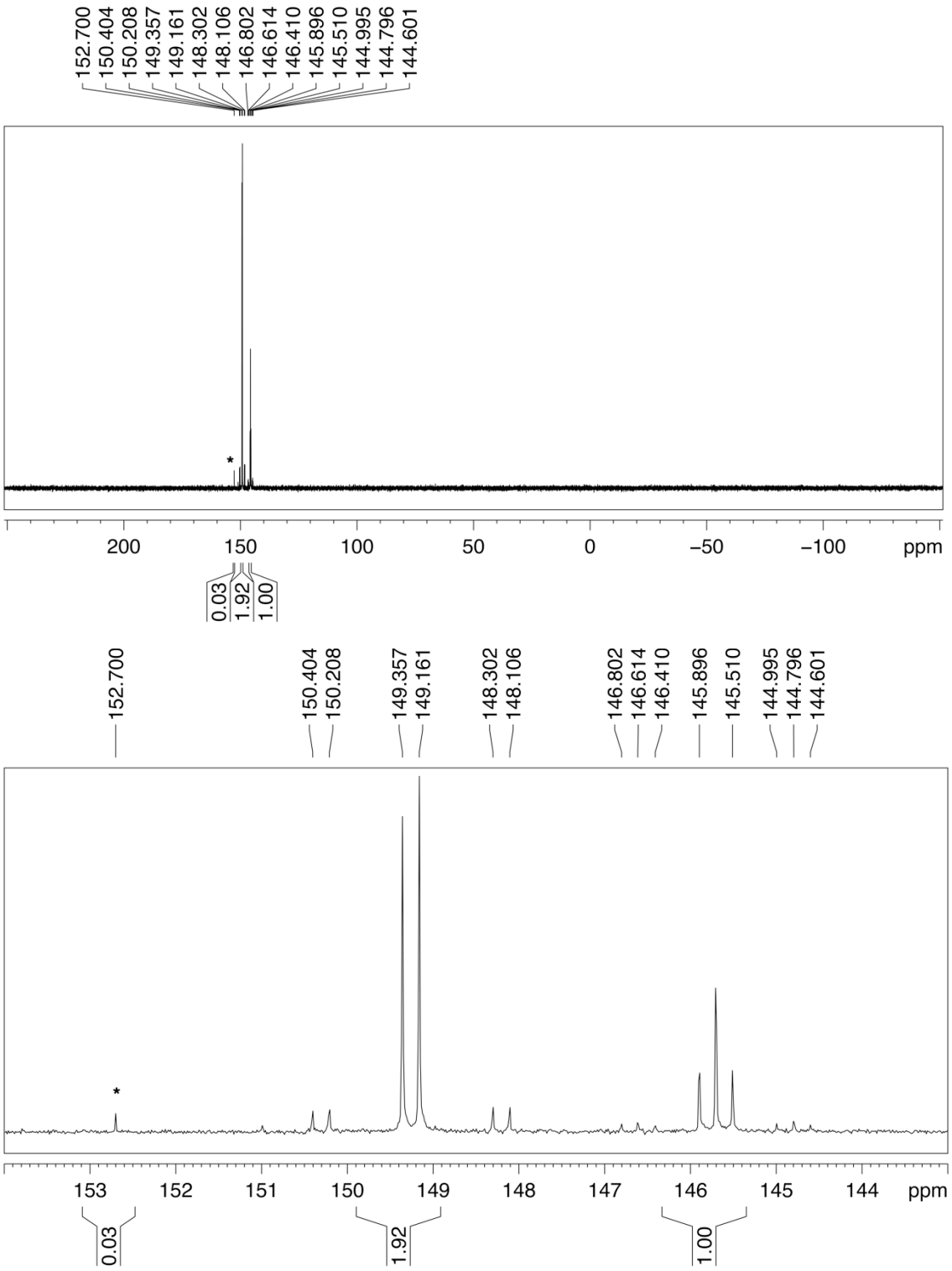

Figure 2.51 $^{31}P\{^{1}H\}$ NMR spectrum of W(CC_6H_4-4-pyr){$P(OMe)_3$}$_3$(CO)Cl in CD_2Cl_2. The bottom spectrum is an expansion of the top spectrum. The asterisk indicates the resonance attributable to the W(CC_6H_4-4-pyr){$P(OMe)_3$}$_4$Cl impurity in the product.

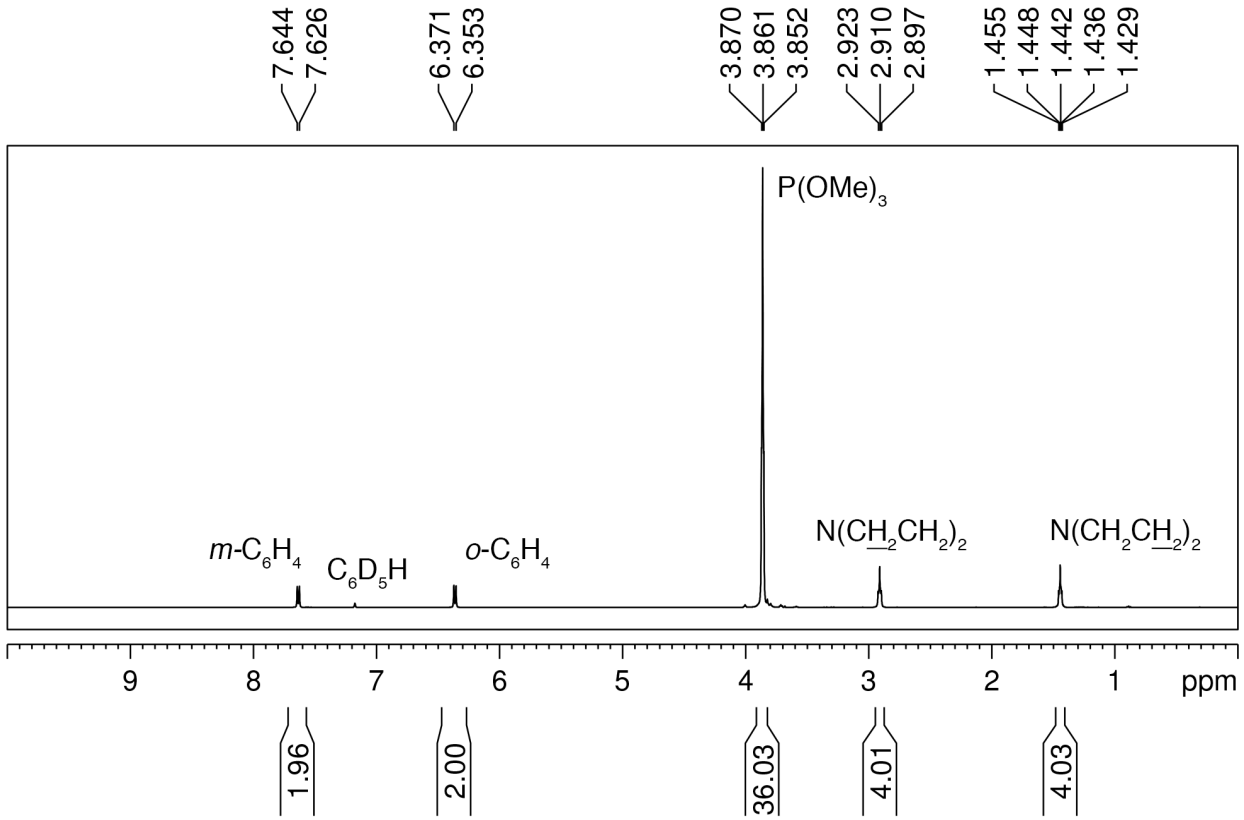

Figure 2.52. ^{1}H NMR spectrum of W(CC$_6$H$_4$-4-pyr){P(OMe)$_3$}$_4$Cl in C$_6$D$_6$.

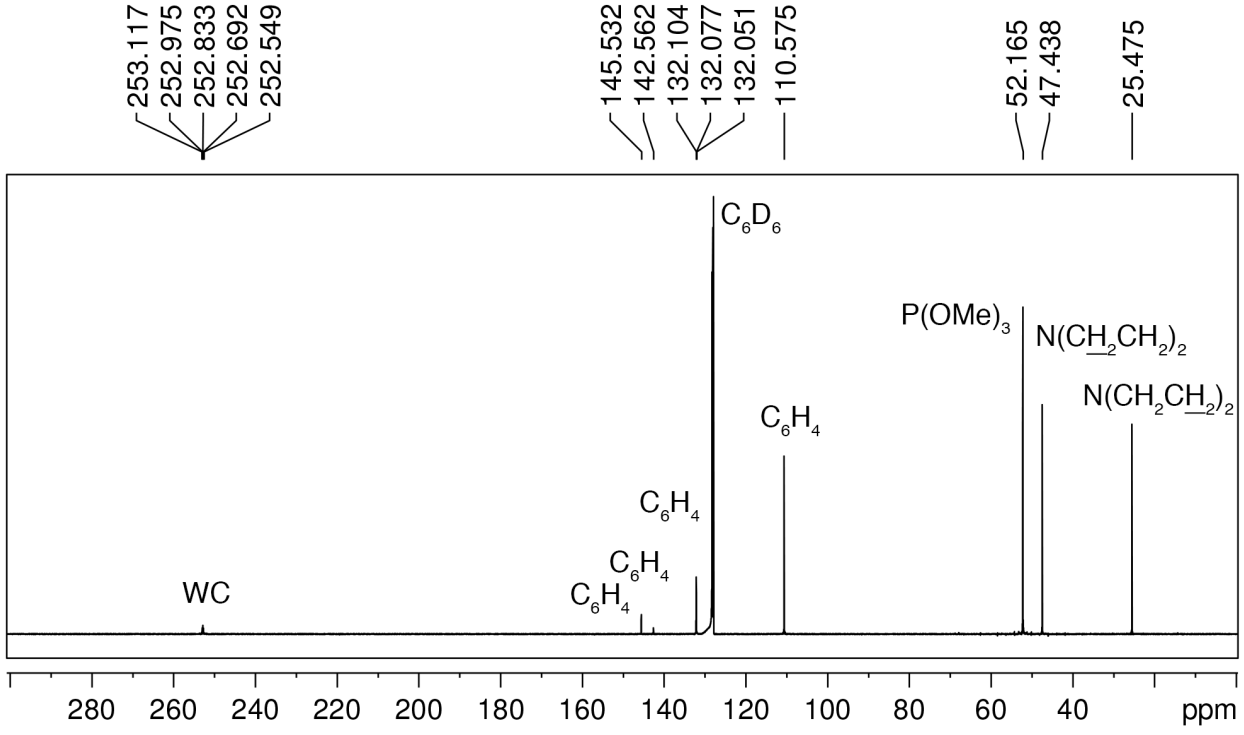

Figure 2.53. ^{13}C{^{1}H} NMR spectrum of W(CC$_6$H$_4$-4-pyr){P(OMe)$_3$}$_4$Cl in C$_6$D$_6$.

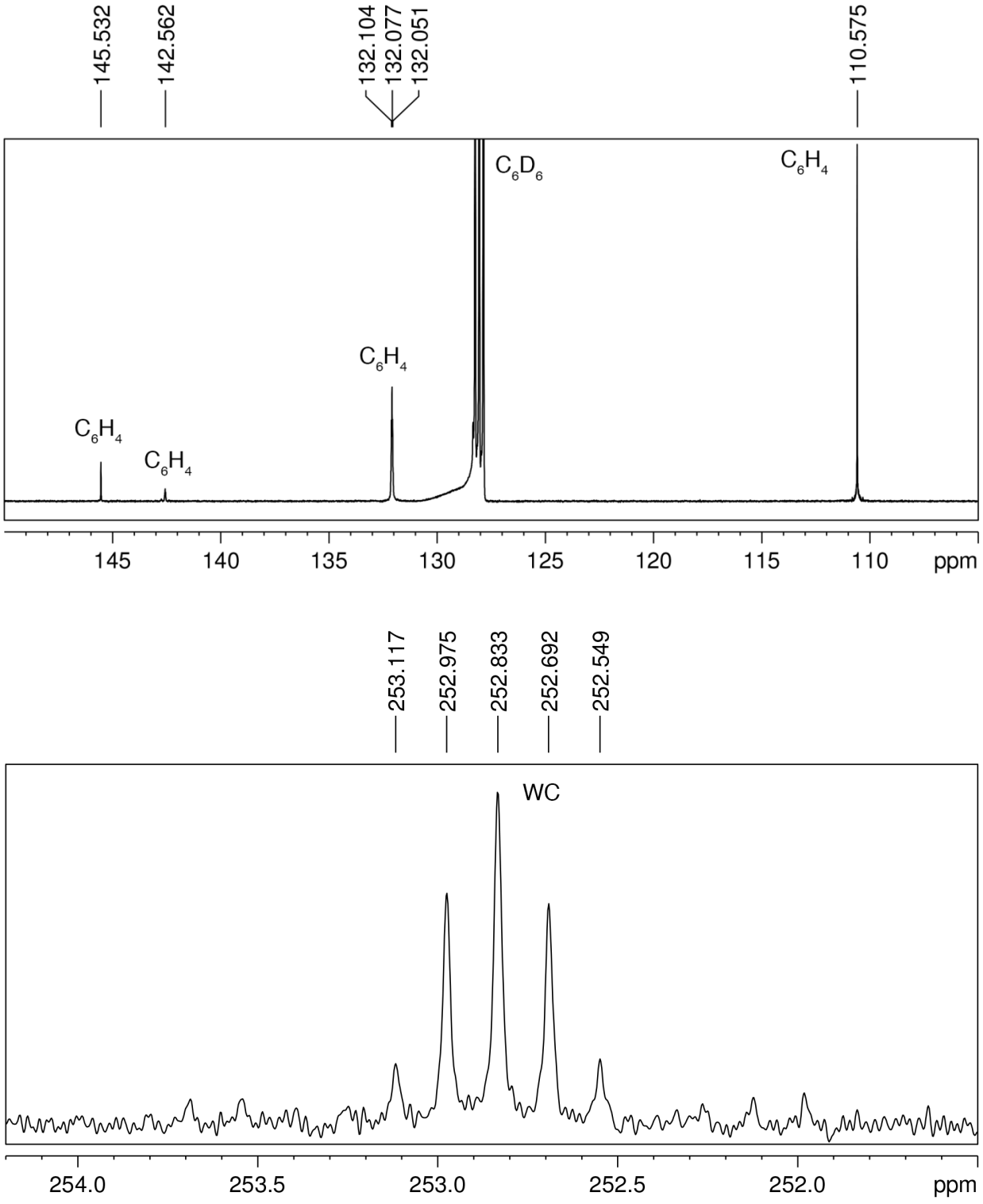

Figure 2.54. Expansions of the $^{13}C\{^{1}H\}$ NMR spectrum of $W(CC_6H_4\text{-}4\text{-}pyr)\{P(OMe)_3\}_4Cl$ in C_6D_6 showing aryl and WC resonances.

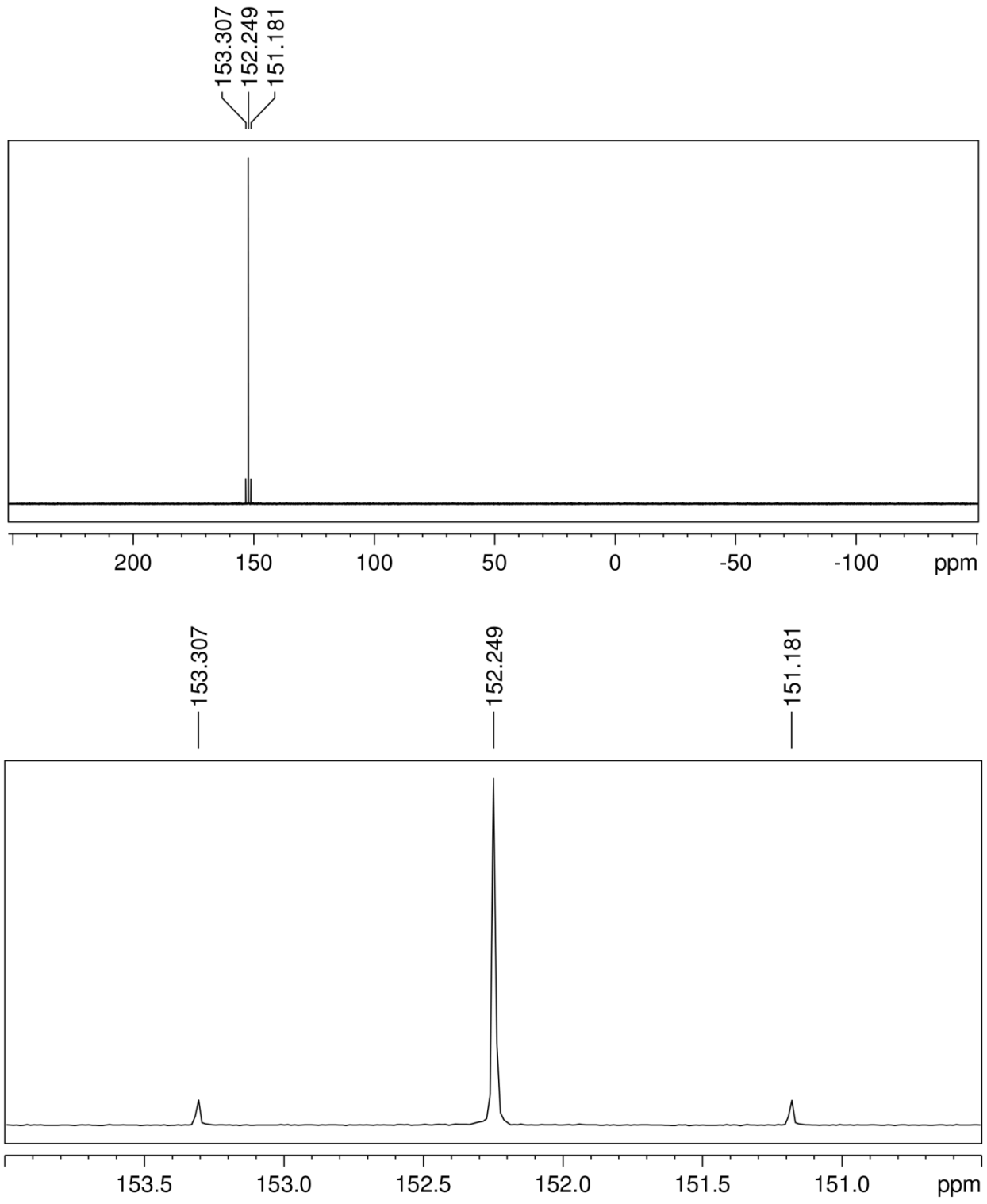

Figure 2.55. $^{31}P\{^{1}H\}$ NMR spectrum of $W(CC_6H_4\text{-}4\text{-}pyr)\{P(OMe)_3\}_4Cl$ in C_6D_6. The bottom spectrum is an expansion of the top spectrum.

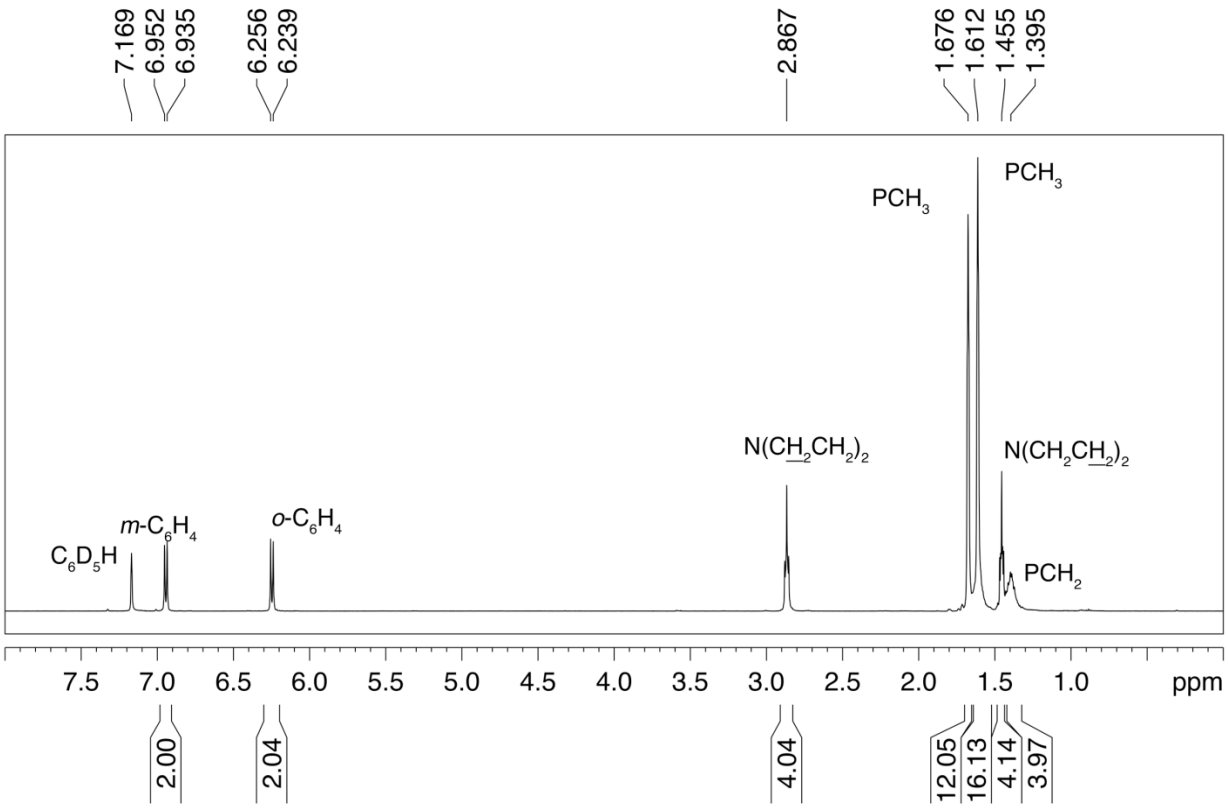

Figure 2.56. ^{1}H NMR spectrum of W(CC$_6$H$_4$-4-pyr)(dmpe)$_2$Cl in C$_6$D$_6$.

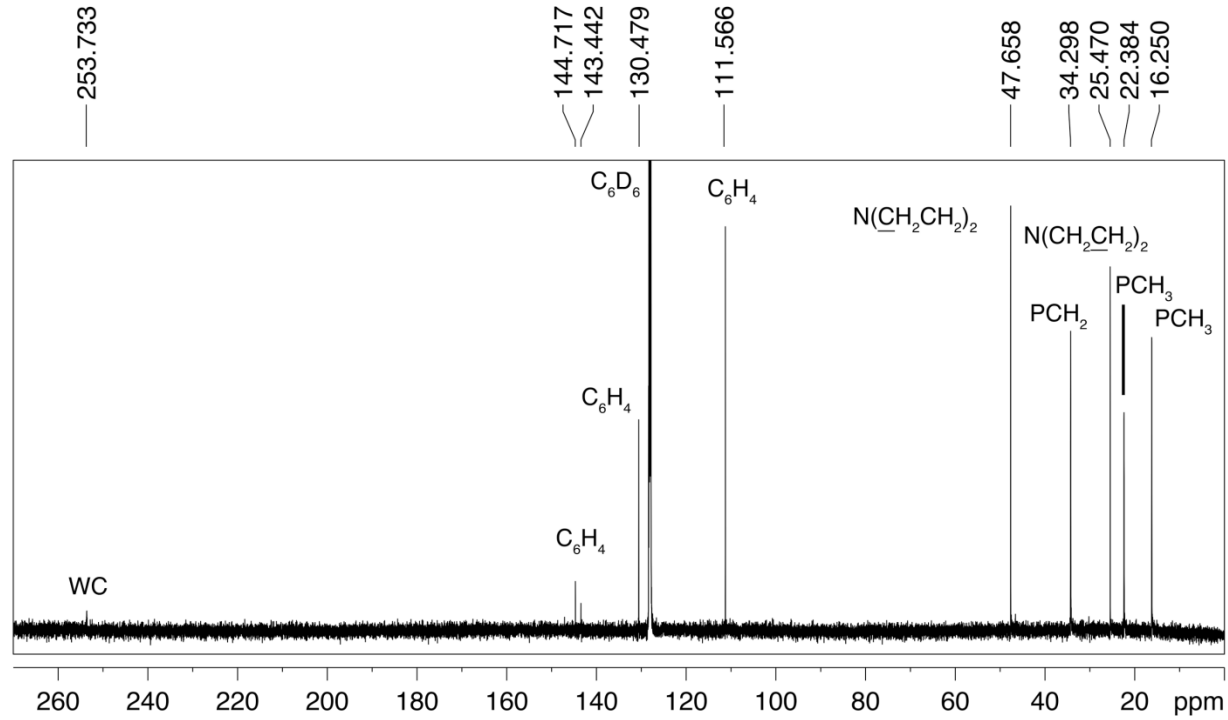

Figure 2.57. ^{13}C{^{1}H,^{31}P} NMR spectrum of W(CC$_6$H$_4$-4-pyr)(dmpe)$_2$Cl in C$_6$D$_6$.

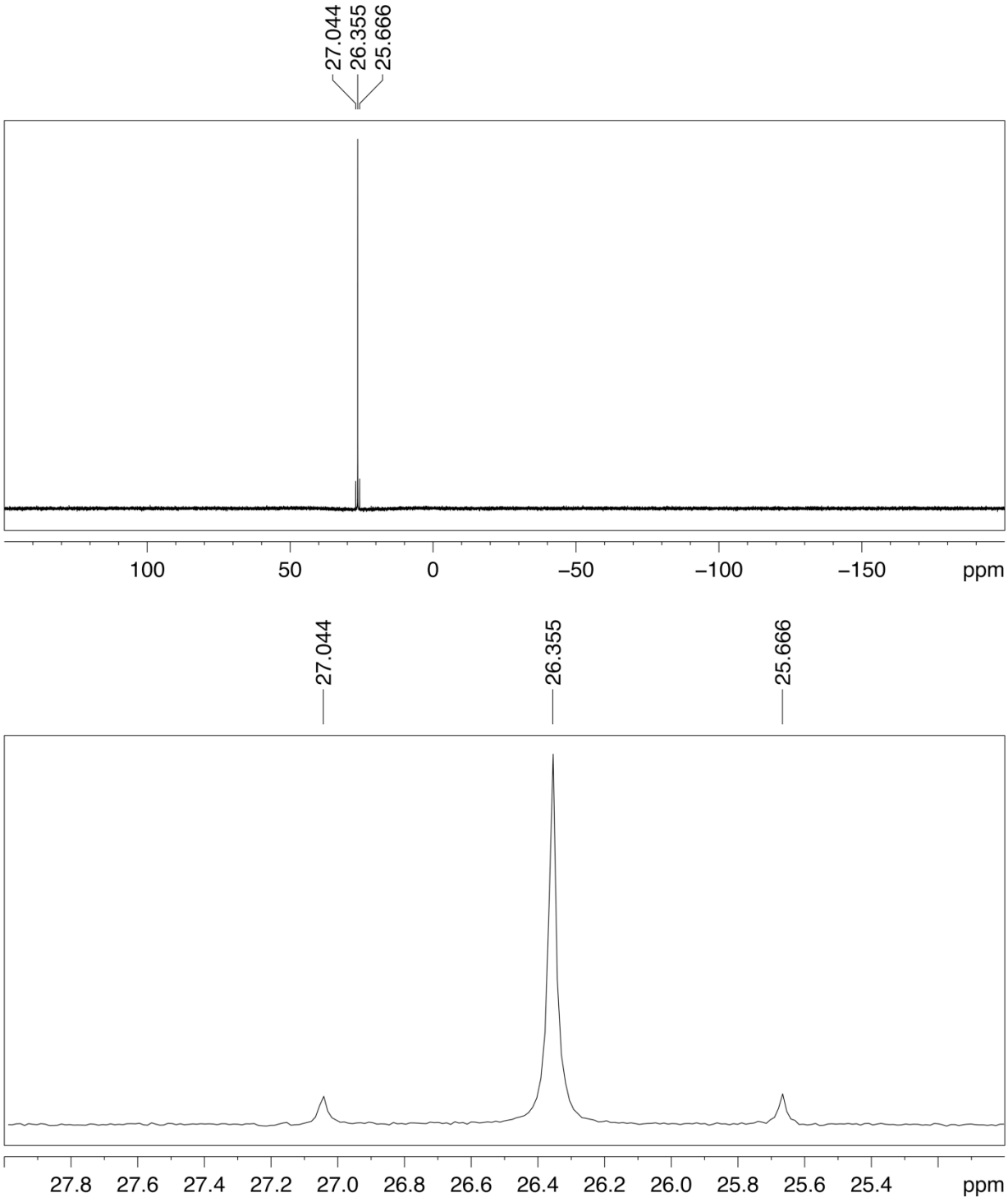

Figure 2.58. $^{31}P\{^{1}H\}$ NMR spectrum of $W(CC_6H_4\text{-}4\text{-}pyr)(dmpe)_2Cl$ in C_6D_6. The bottom spectrum is an expansion of the top spectrum.

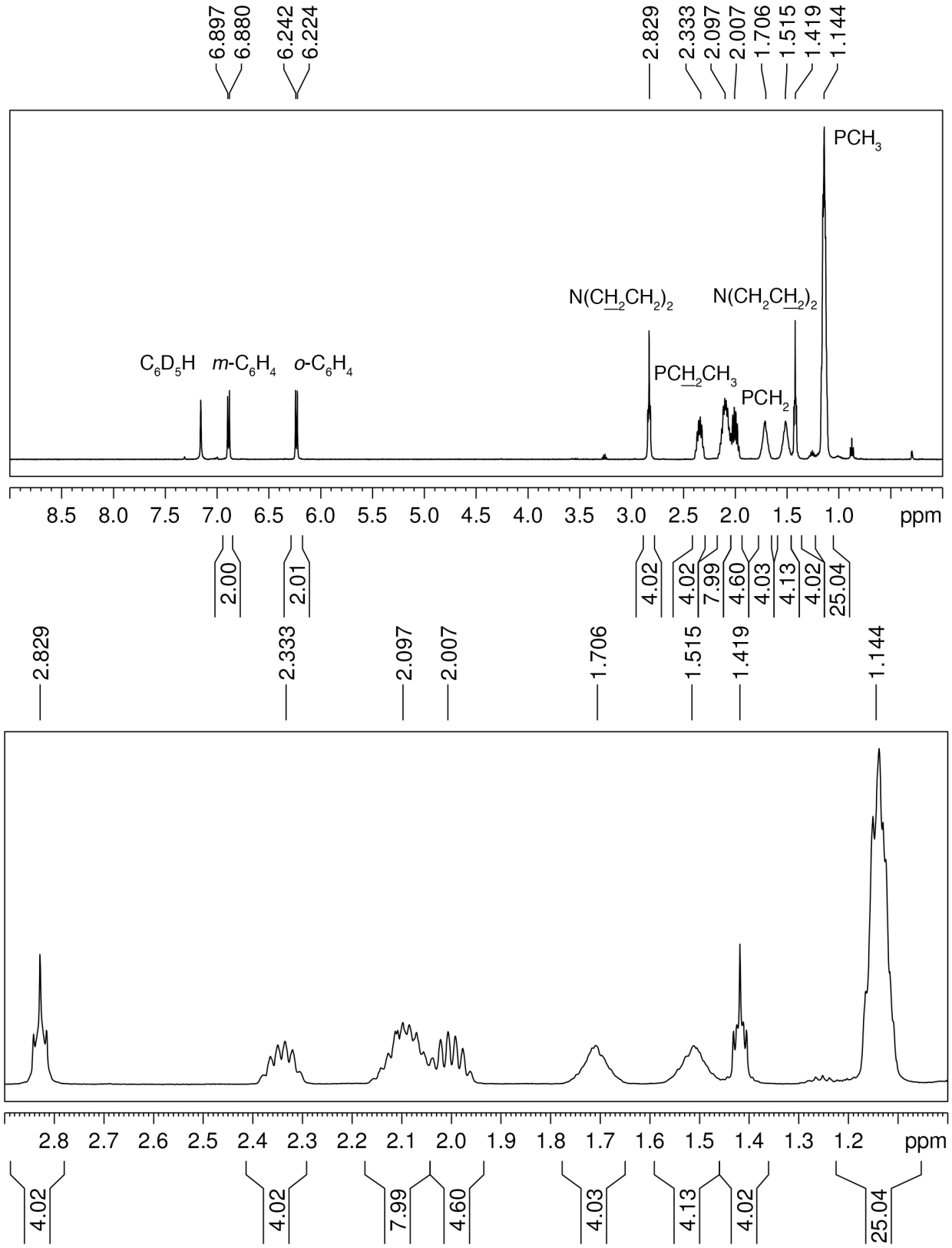

Fig. 2.59. ^{1}H NMR spectrum of W(CC$_6$H$_4$-4-pyr)(depe)$_2$Cl in C$_6$D$_6$. The bottom spectrum is an expansion of the top spectrum.

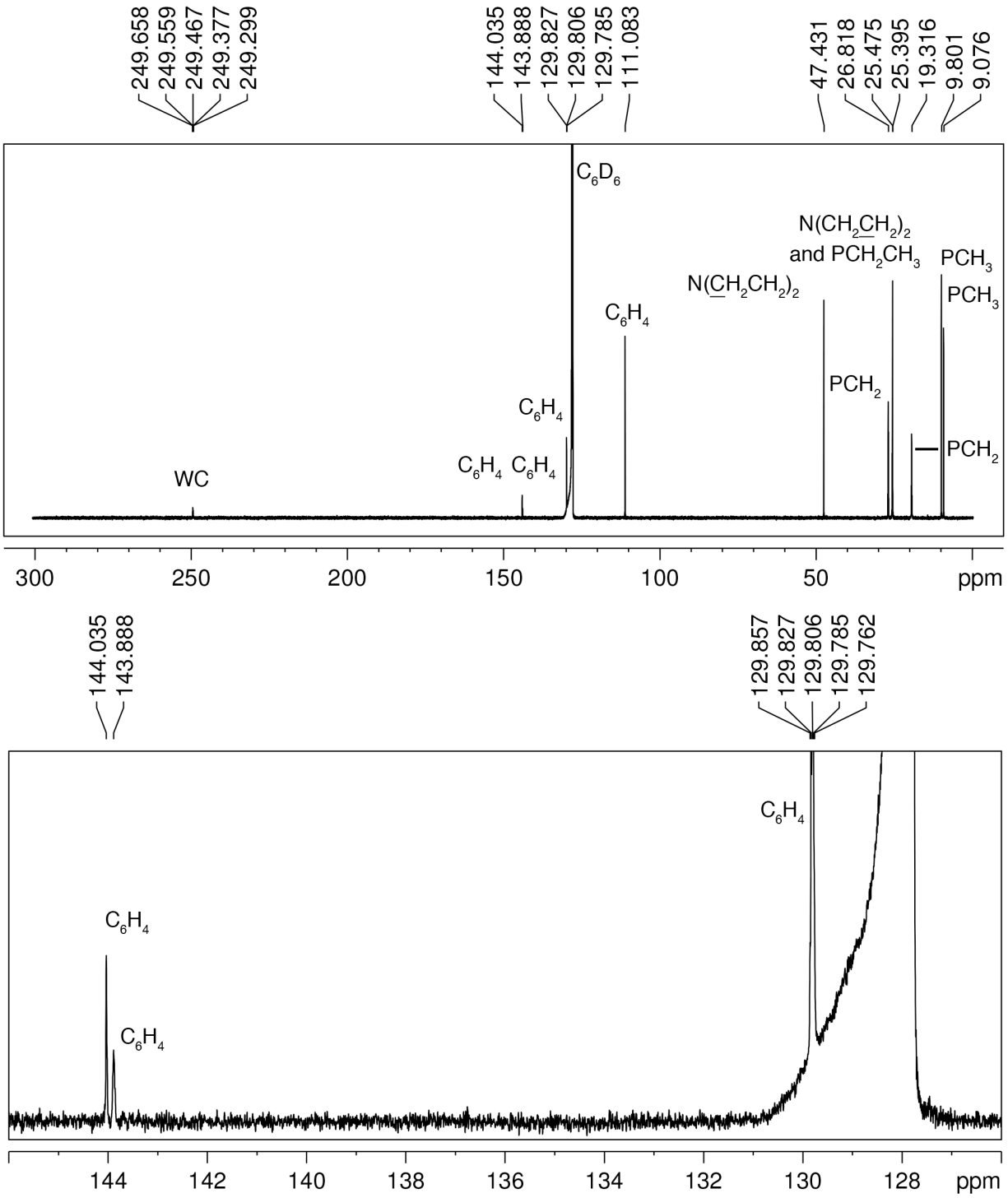

Figure 2.60. $^{13}C\{^{1}H\}$ NMR spectrum of $W(CC_6H_4\text{-}4\text{-}pyr)(depe)_2Cl$ in C_6D_6. The bottom spectrum is an expansion of the top spectrum.

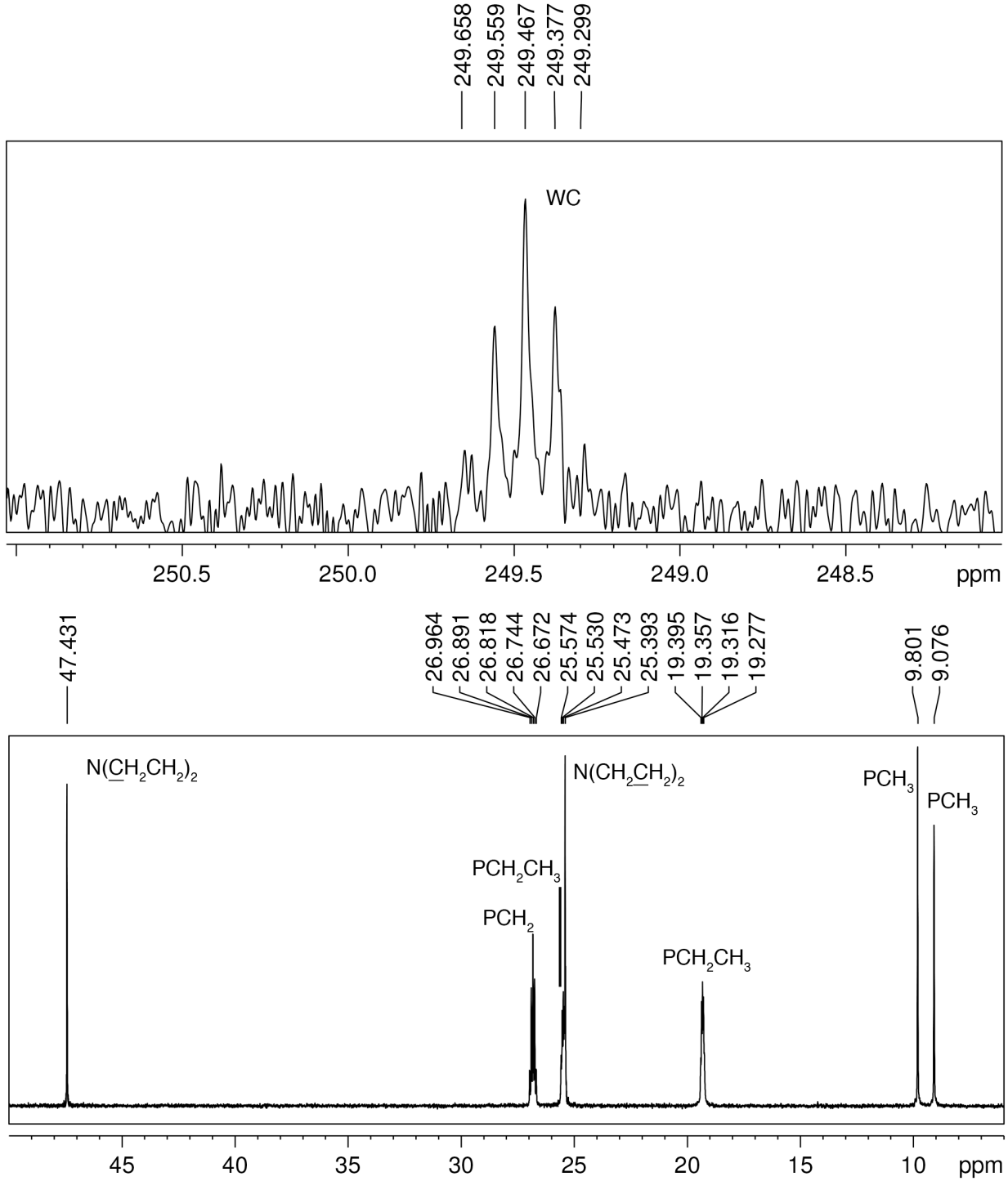

Figure 2.61. Expansions of the $^{13}C\{^{1}H\}$ NMR spectrum of $W(CC_6H_4\text{-}4\text{-}pyr)(depe)_2Cl$ in C_6D_6 showing alkyl and WC resonances.

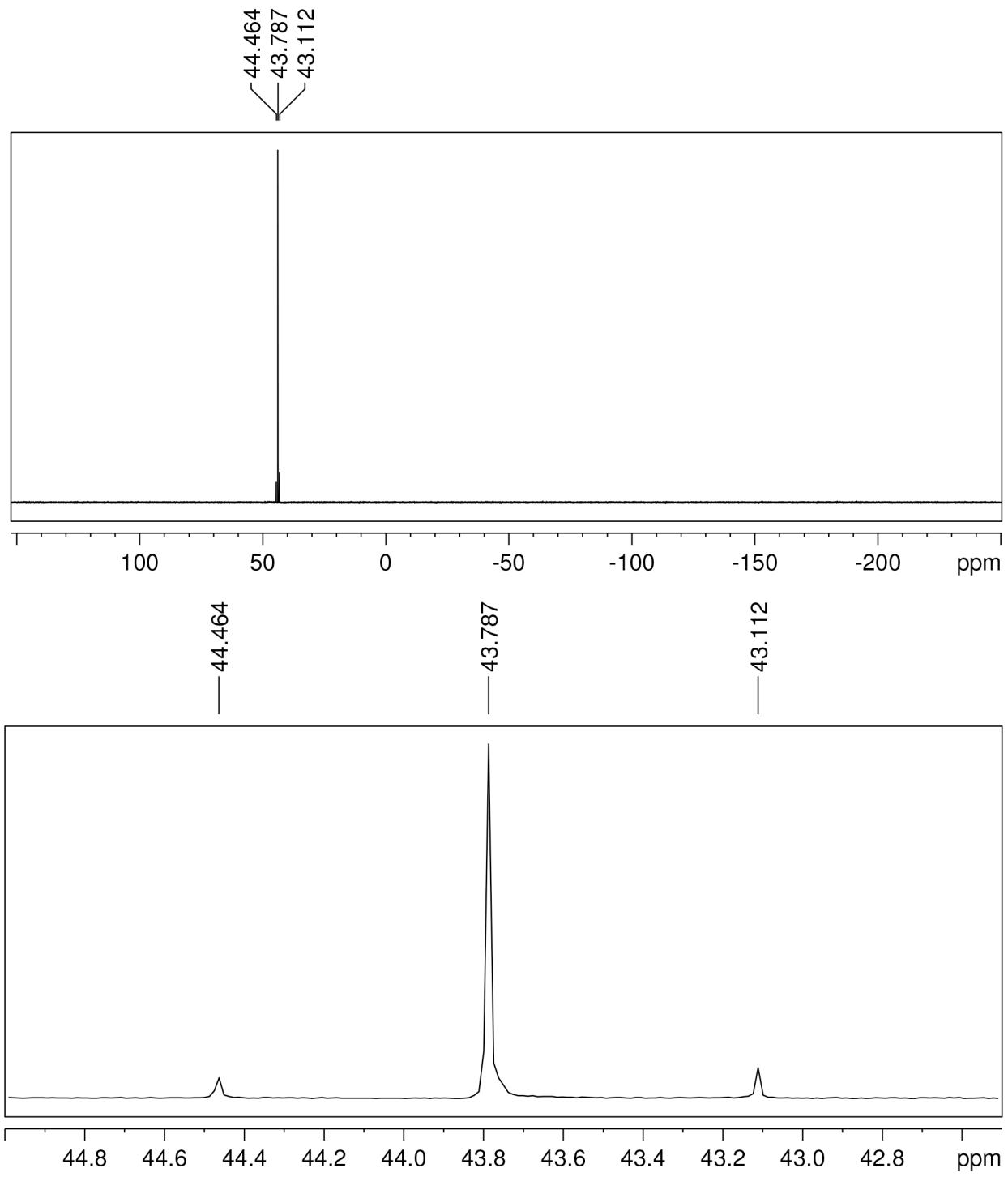

Figure 2.62 $^{31}P\{^{1}H\}$ NMR spectrum of $W(CC_6H_4\text{-}4\text{-}pyr)(depe)_2Cl$ in C_6D_6. The bottom spectrum is an expansion of the top spectrum.

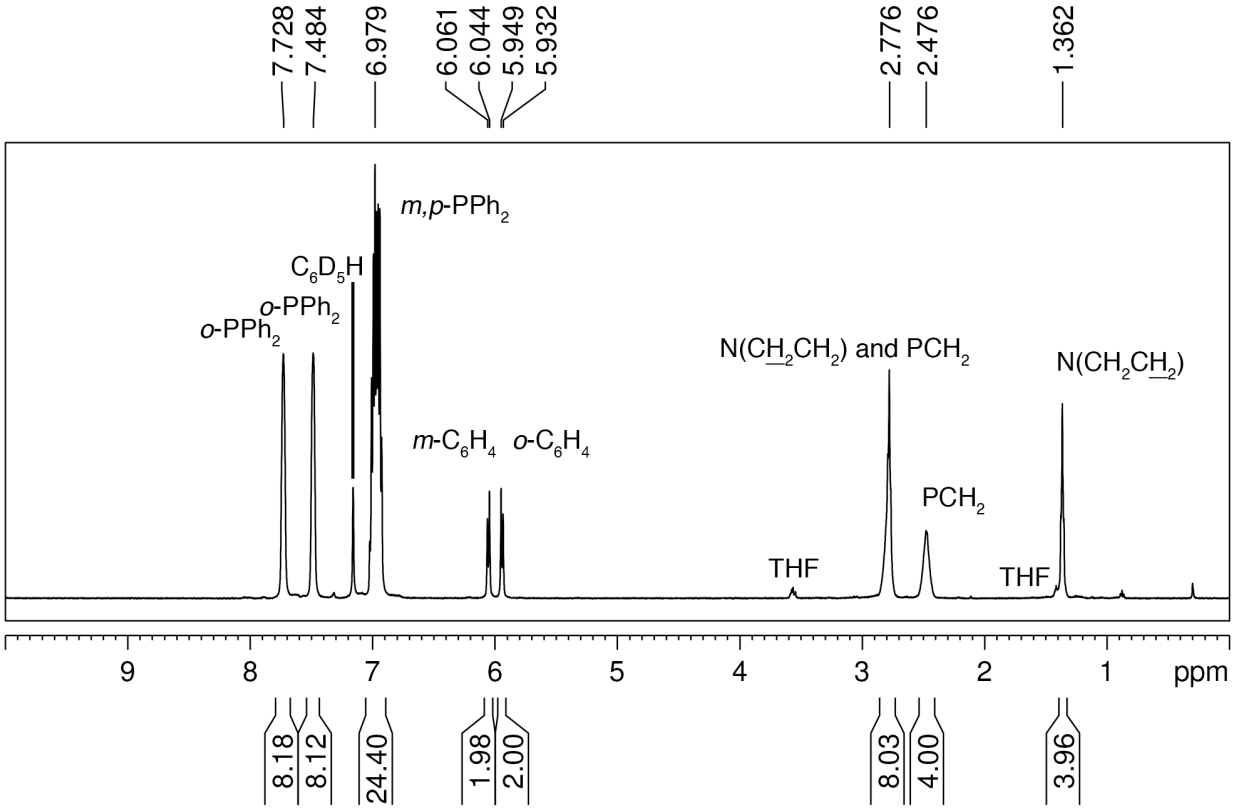

Figure 2.63. ^{1}H NMR spectrum of W(CC$_6$H$_4$-4-pyr)(dppe)$_2$Cl in C$_6$D$_6$.

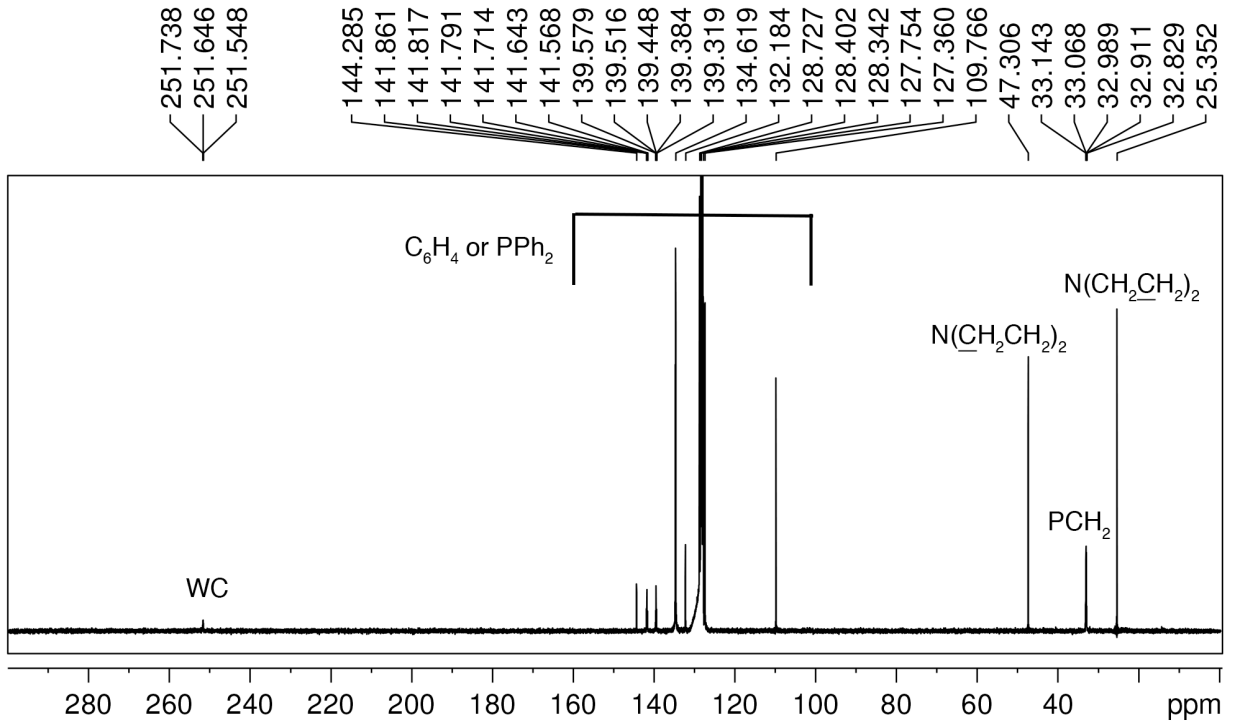

Figure 2.64. ^{13}C{^{1}H} NMR spectrum of W(CC$_6$H$_4$-4-pyr)(dppe)$_2$Cl in C$_6$D$_6$.

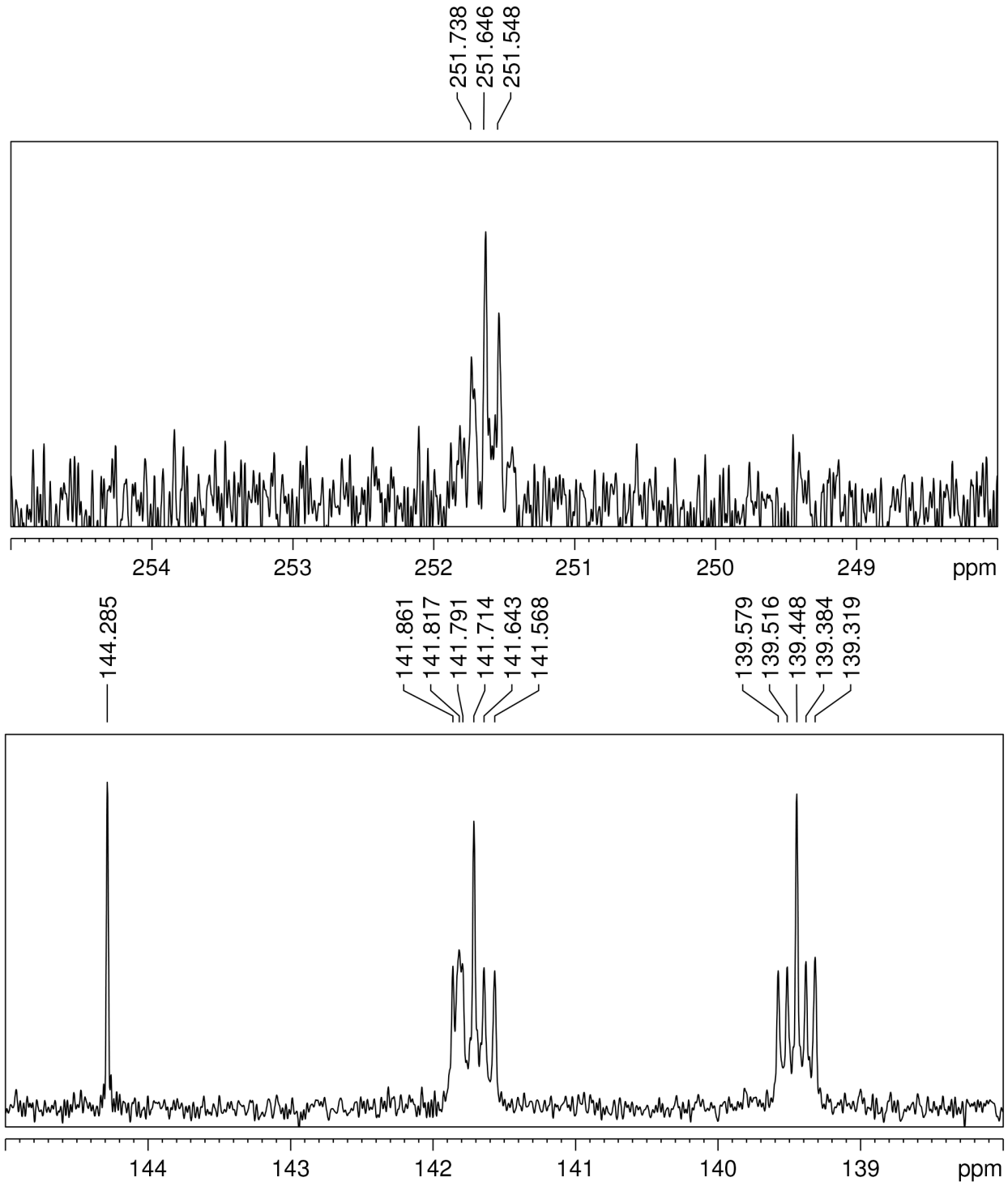

Figure 2.65. Expansions of the $^{13}C\{^{1}H\}$ NMR spectrum of $W(CC_6H_4\text{-}4\text{-}pyr)(dppe)_2Cl$ in C_6D_6 showing aryl and WC resonances.

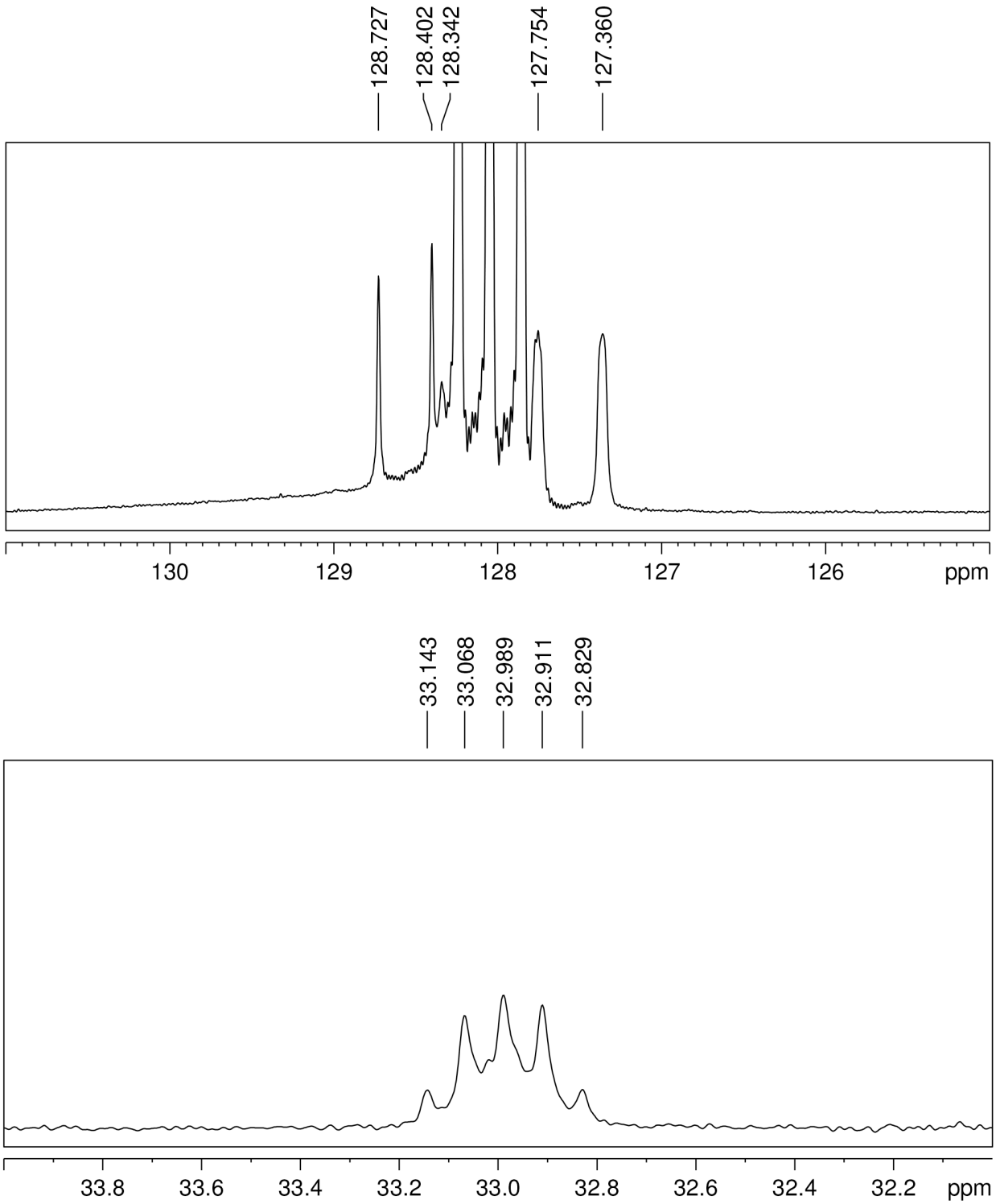

Figure 2.66. Expansions of the $^{13}C\{^{1}H\}$ NMR spectrum of $W(CC_6H_4\text{-}4\text{-}pyr)(dppe)_2Cl$ in C_6D_6 showing alkyl and aryl resonances.

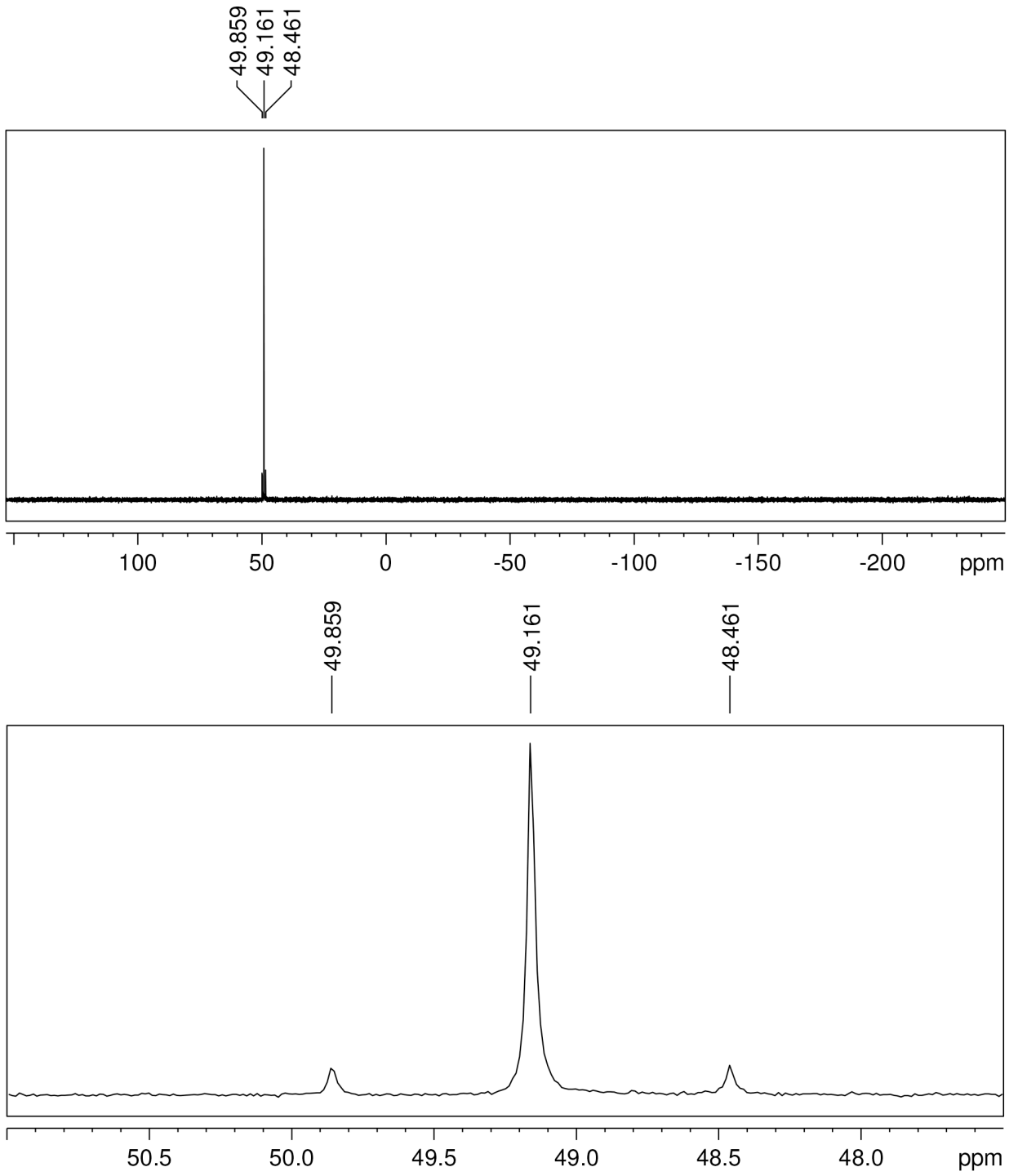

Figure 2.67. $^{31}P\{^{1}H\}$ NMR spectrum of $W(CC_6H_4\text{-}4\text{-}pyr)(dppe)_2Cl$ in C_6D_6. The bottom spectrum is an expansion of the top spectrum.

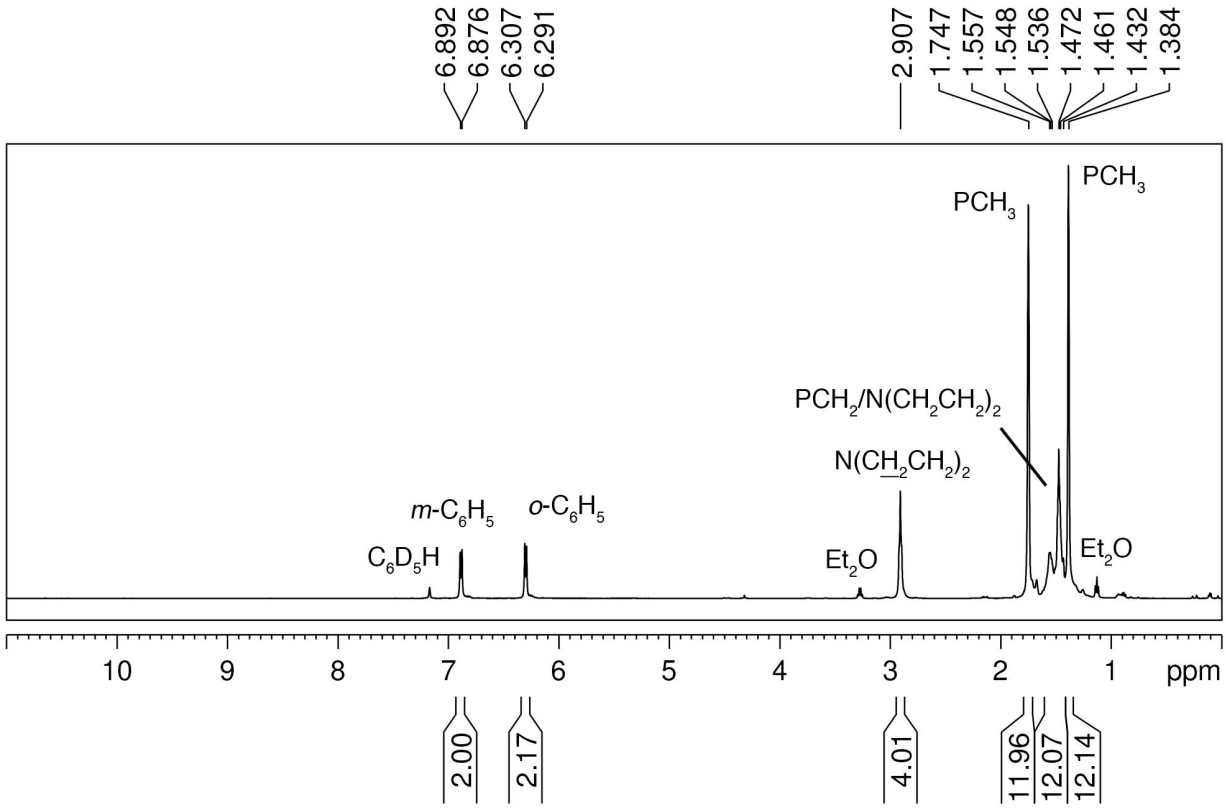

Figure 2.68. ^{1}H NMR spectrum of $W(CC_6H_4\text{-}4\text{-}pyr)(dmpe)_2F$ in C_6D_6.

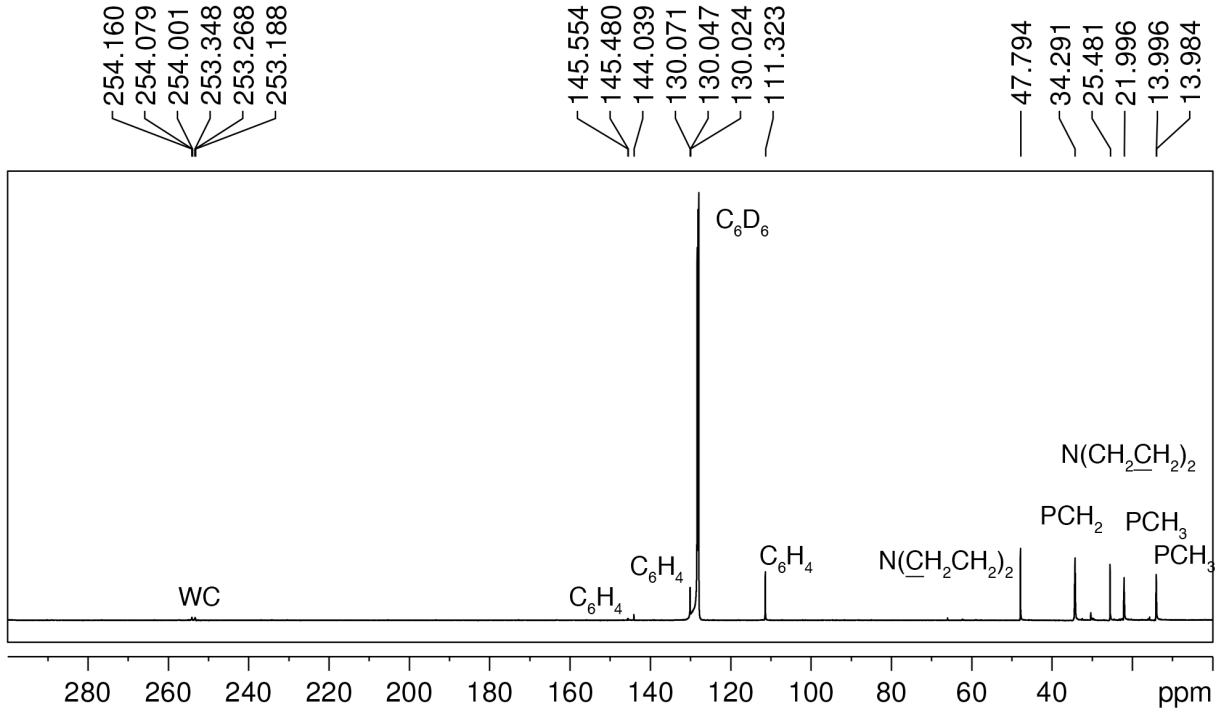

Figure 2.69. $^{13}C\{^{1}H\}$ NMR spectrum of $W(CC_6H_4\text{-}4\text{-}pyr)(dmpe)_2F$ in C_6D_6.

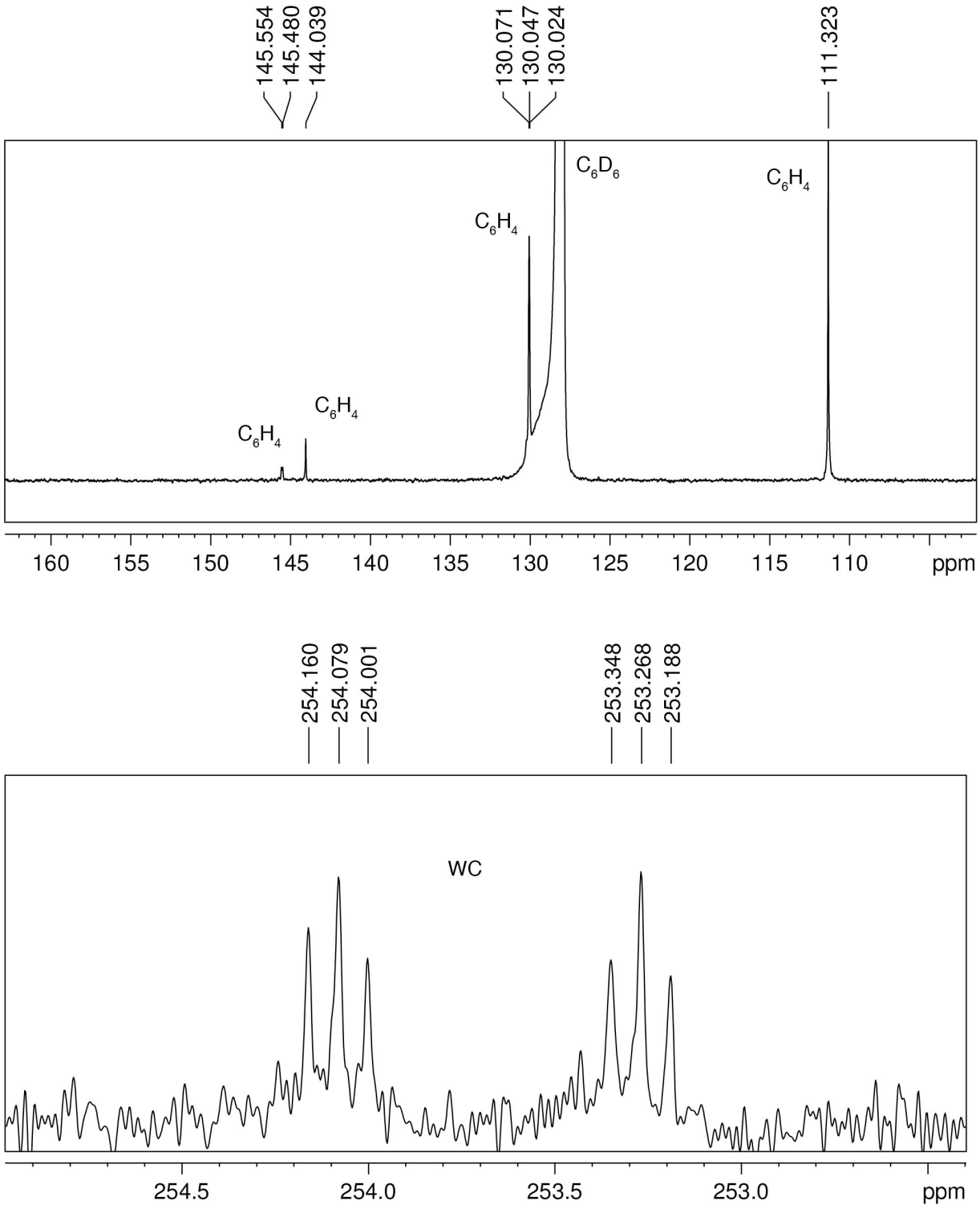

Figure 2.70. Expansions of the $^{13}C\{^{1}H\}$ NMR spectrum of $W(CC_6H_4\text{-}4\text{-}pyr)(dmpe)_2F$ in C_6D_6 showing aryl and WC resonances.

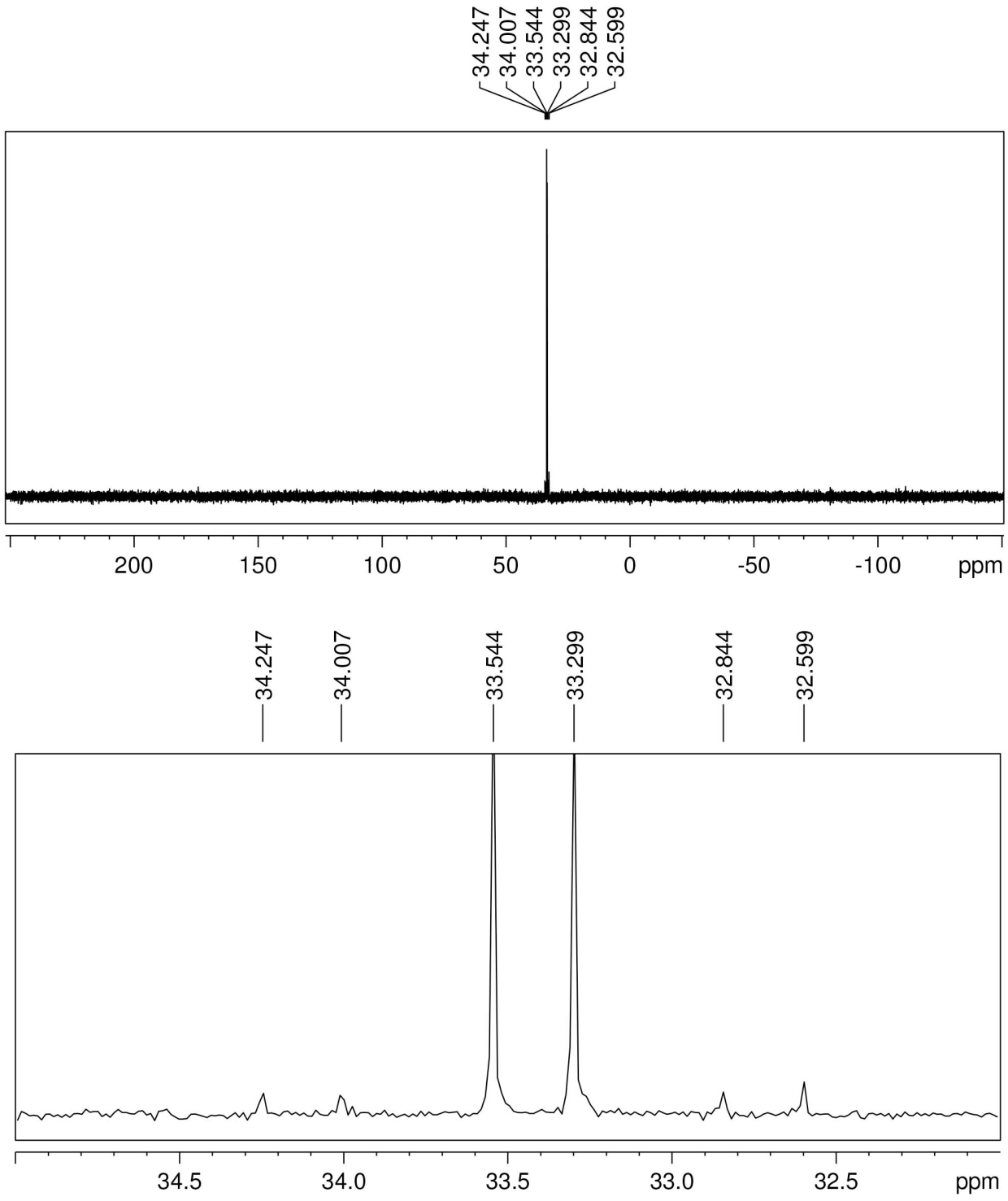

Figure 2.71. $^{31}P\{^{1}H\}$ NMR spectrum of $W(CC_6H_4\text{-}4\text{-}pyr)(dmpe)_2F$ in C_6D_6. The bottom spectrum is an expansion of the top spectrum.

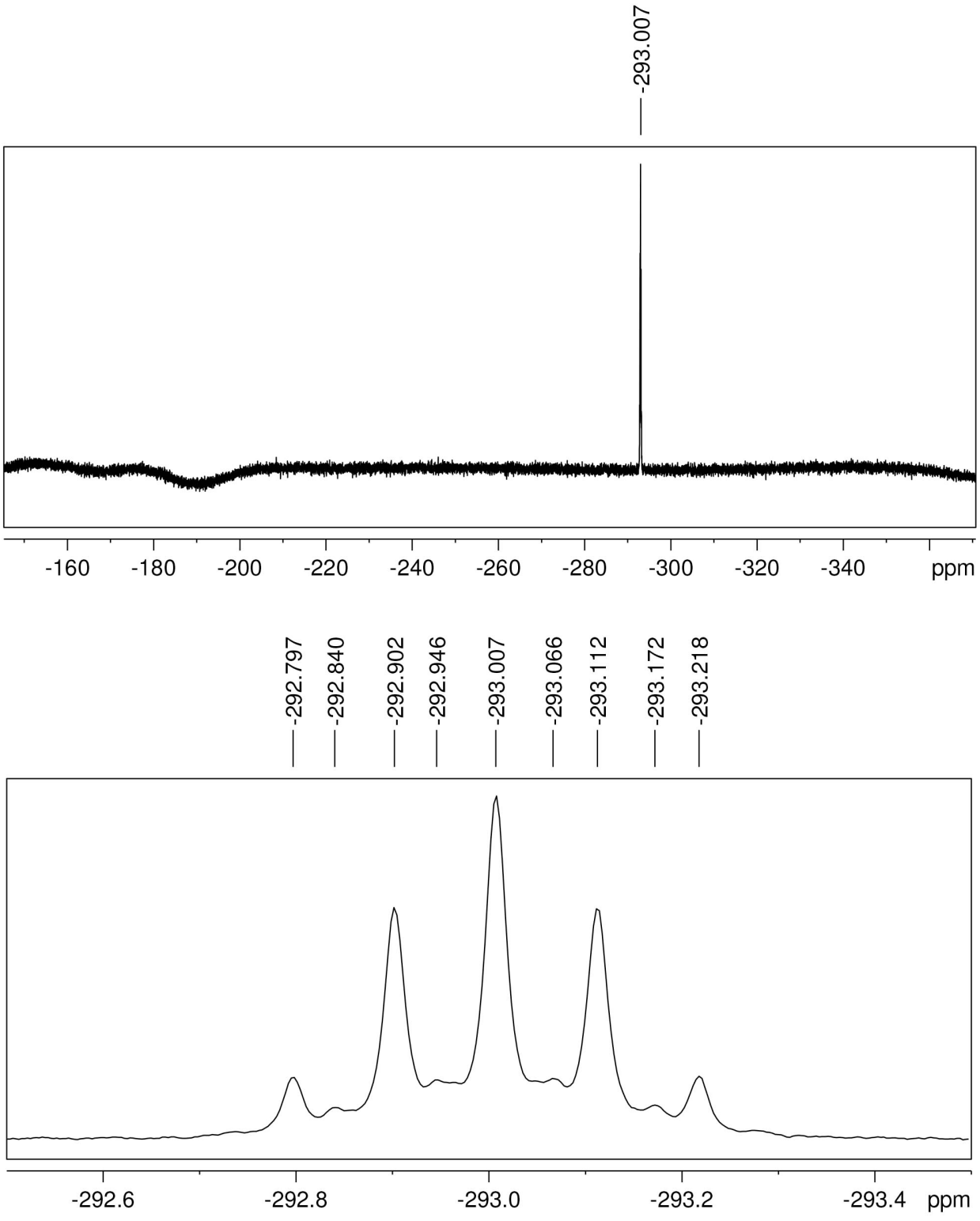

Figure 2.72. ^{19}F NMR spectrum of W(CC_6H_4-4-pyr)$(dmpe)_2F$ in C_6D_6. The bottom spectrum is an expansion of the top spectrum.

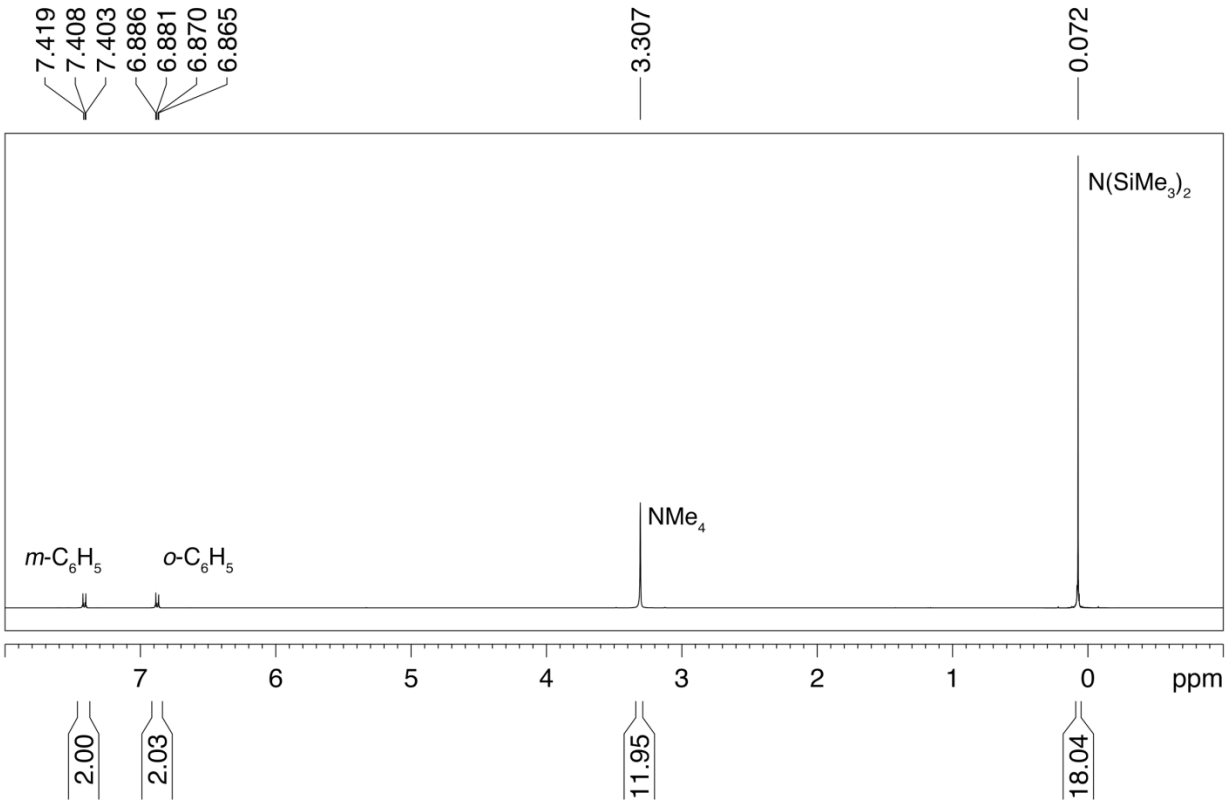

Figure 2.73. ^{1}H NMR spectrum of $NMe_4[W(C(O)C_6H_4\text{-}4\text{-}NH_2)(CO)_5]$ in CD_2Cl_2.

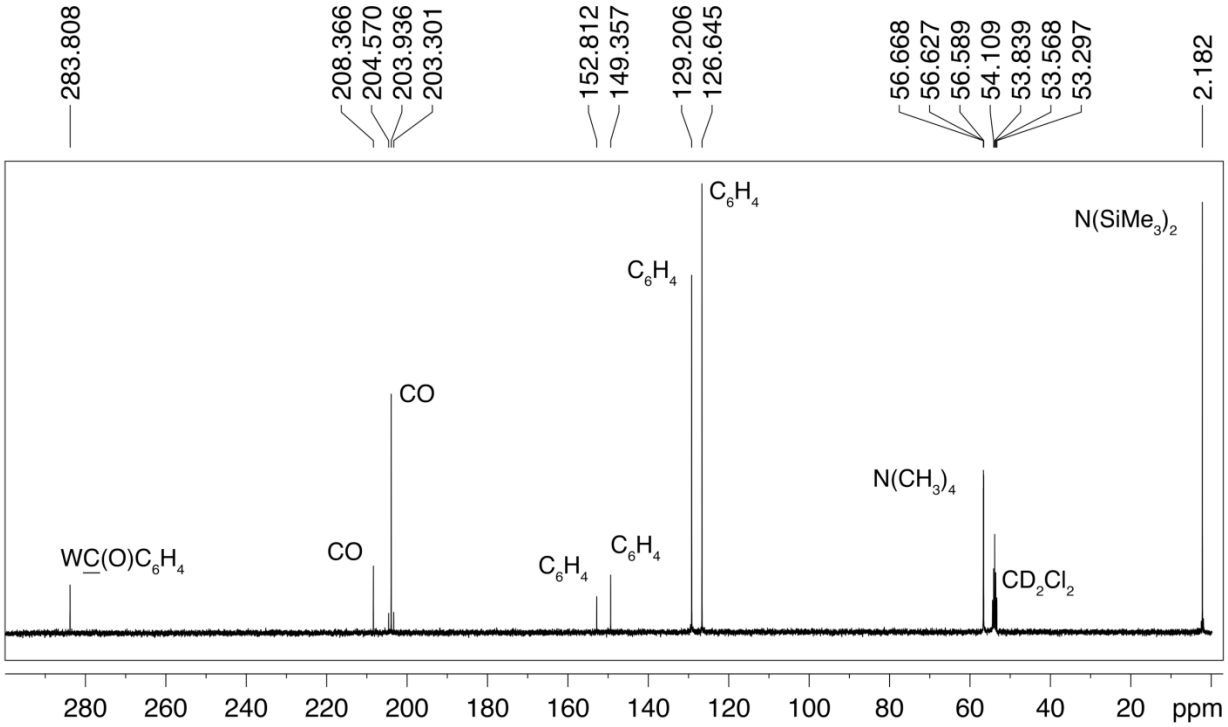

Figure 2.74. $^{13}C\{^{1}H\}$ NMR spectrum of $NMe_4[W(C(O)C_6H_4\text{-}4\text{-}NH_2)(CO)_5]$ in CD_2Cl_2.

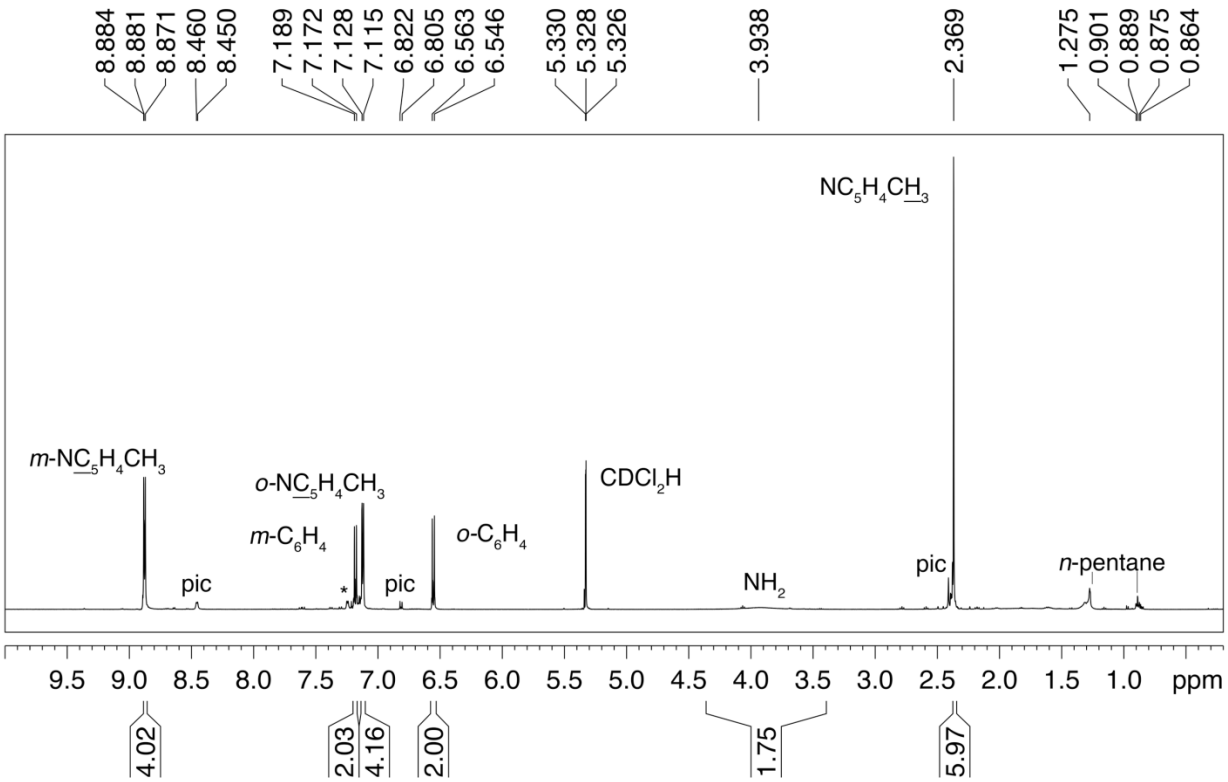

Figure 2.75. ^{1}H NMR spectrum $W(CC_6H_4\text{-}4\text{-}NH_2)(pic)_2(CO)_2Cl$ in CD_2Cl_2.

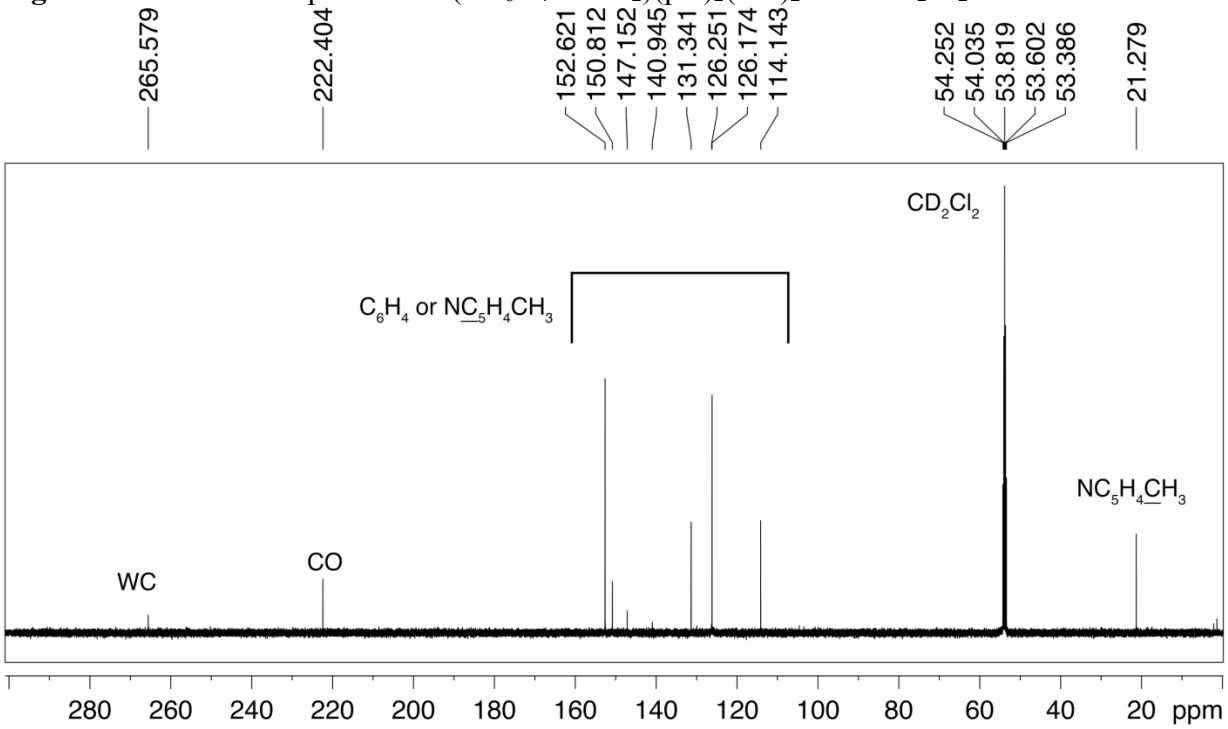

Figure 2.76. $^{13}C\{^{1}H\}$ NMR spectrum $W(CC_6H_4\text{-}4\text{-}NH_2)(pic)_2(CO)_2Cl$ in CD_2Cl_2.

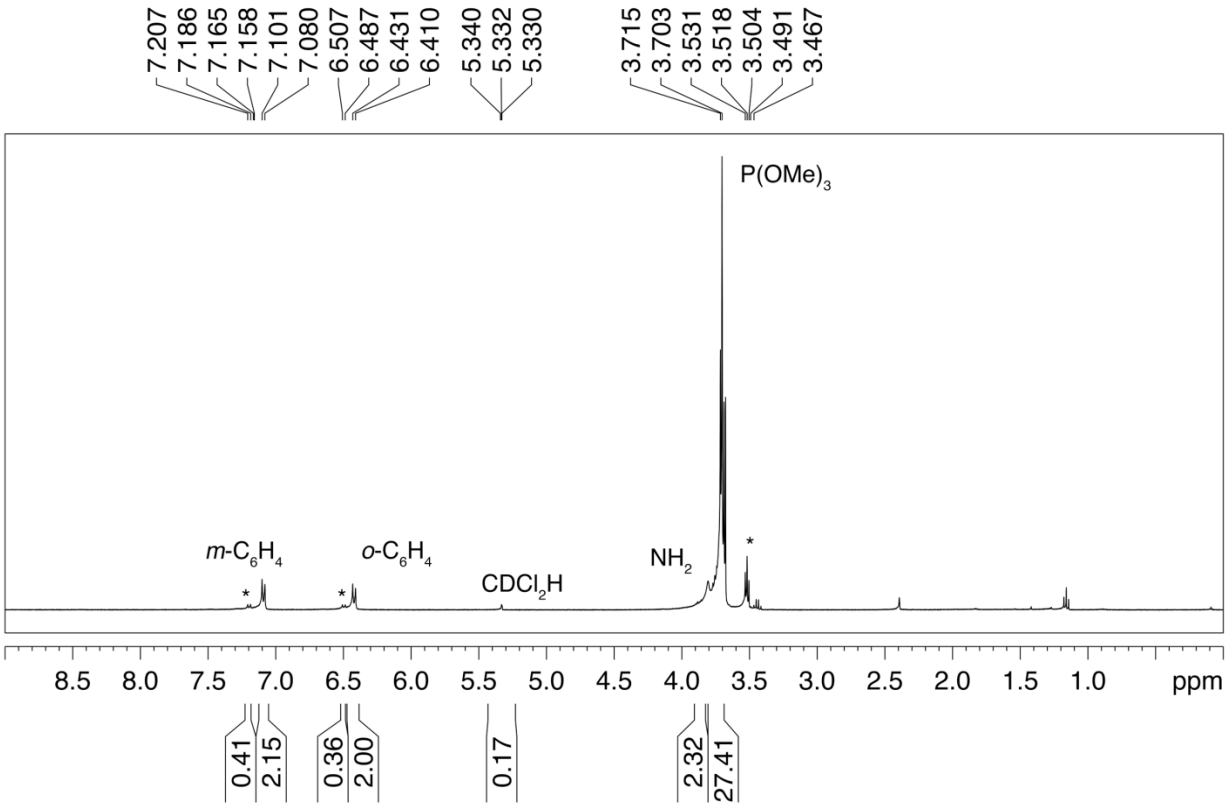

Figure 2.77. ^{1}H NMR spectrum of $W(CC_6H_4\text{-}4\text{-}NH_2)\{P(OMe)_3\}_3(CO)Cl$ in CD_2Cl_2.

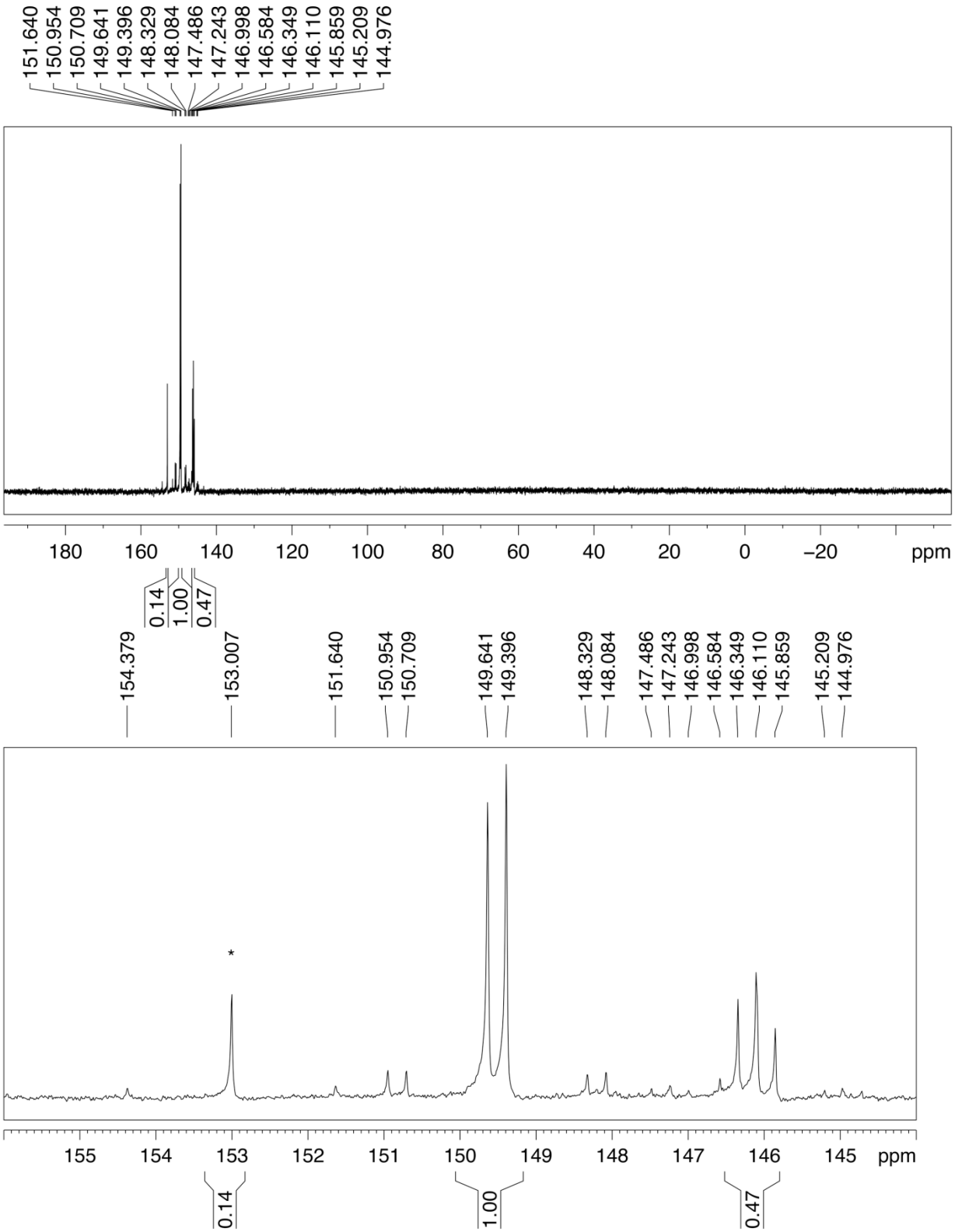

Figure 2.78. $^{31}P\{^{1}H\}$ NMR spectrum of $W(CC_6H_4\text{-}4\text{-}NH_2)\{P(OMe)_3\}_3(CO)Cl$ in CD_2Cl_2. The bottom spectrum is an expansion of the top spectrum. The asterisk indicates the resonance attributable to the $W(CC_6H_4\text{-}4\text{-}NH_2)\{P(OMe)_3\}_4Cl$ impurity in the product.

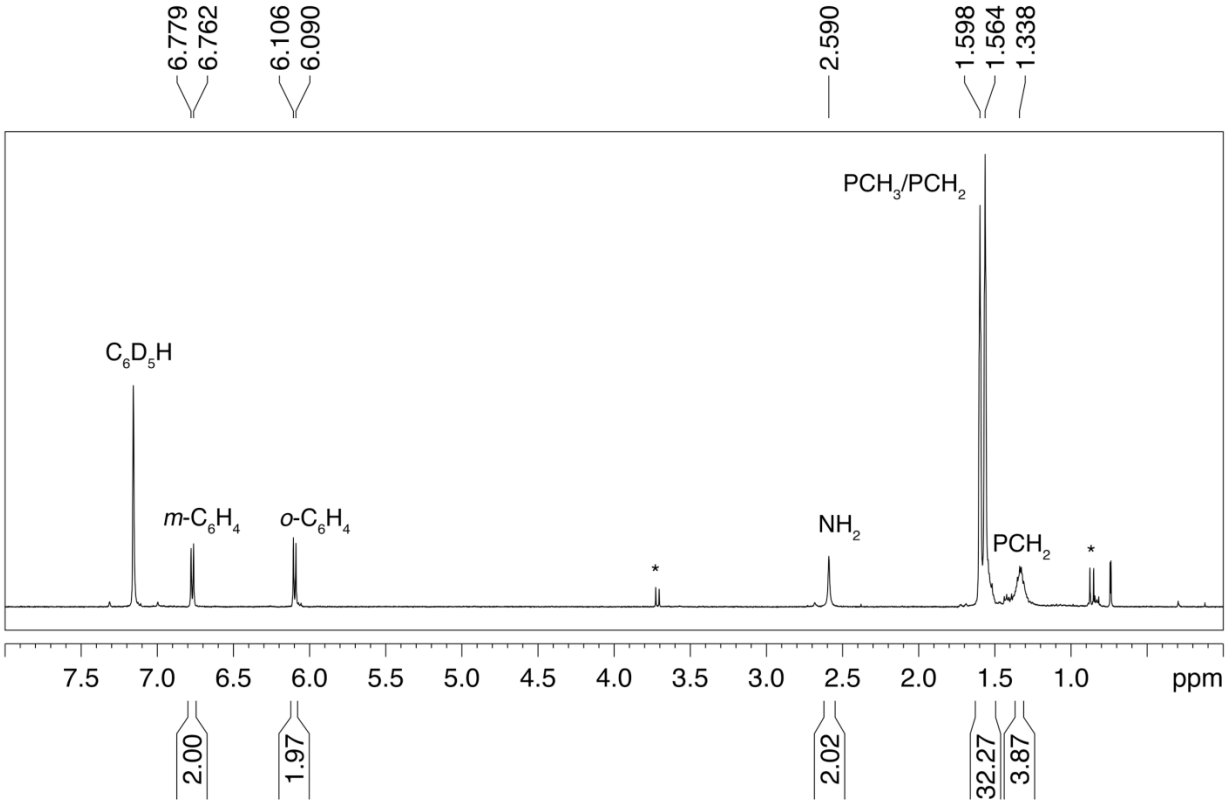

Figure 2.79. ^{1}H NMR spectrum of W(CC_6H_4-4-NH_2)(dmpe)$_2$Cl in C_6D_6. The asterisk indicates impurities that could not be removed from the reaction mixture.

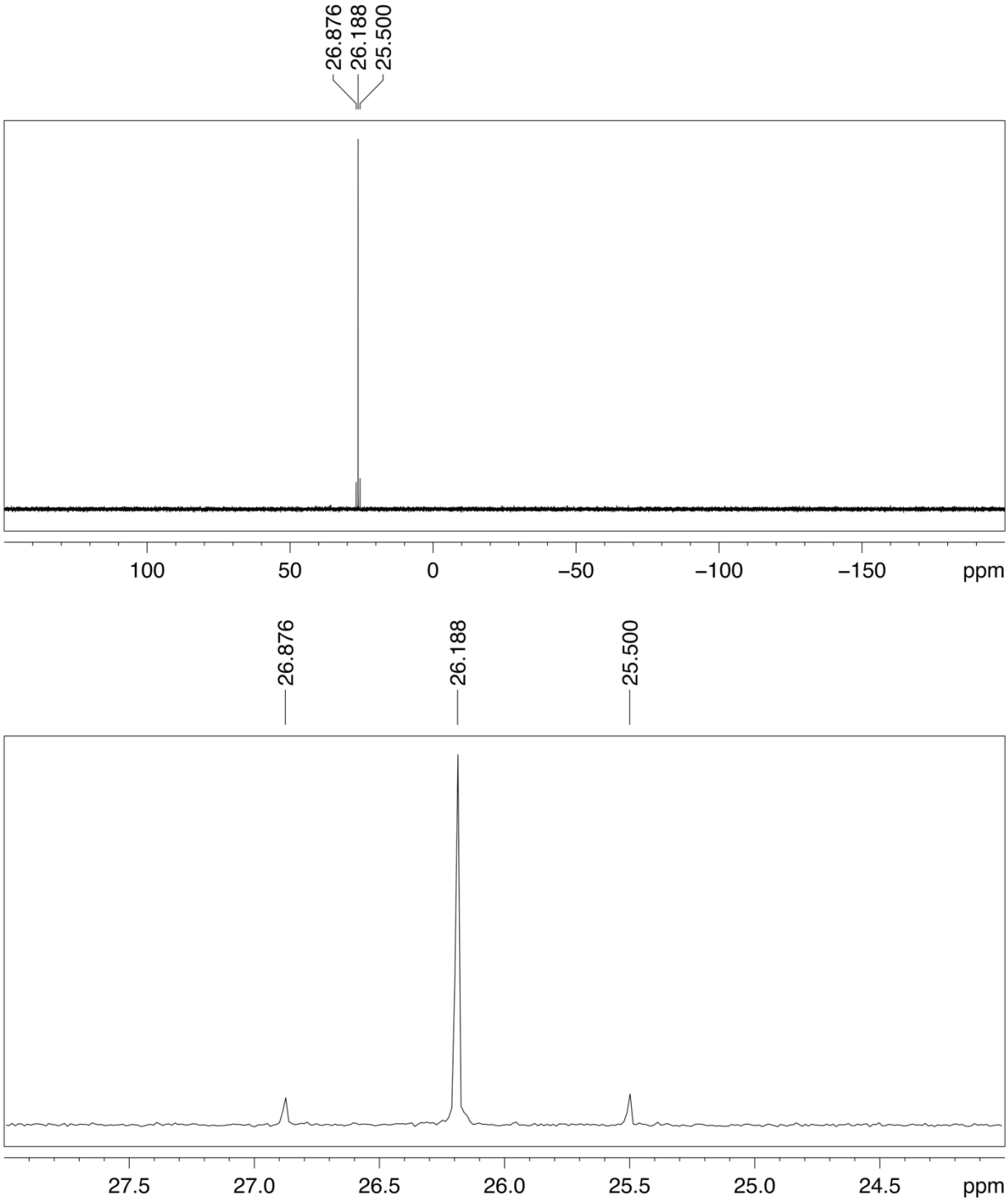

Figure 2.80. $^{31}P\{^{1}H\}$ NMR spectrum of $W(CC_6H_4\text{-}4\text{-}NH_2)(dmpe)_2Cl$ in C_6D_6. The bottom spectrum is an expansion of the top spectrum.

2.4.2. Single crystal X-ray crystallography.

2.4.2.1. General information. Diffraction data were measured at 100 K on a Bruker D8 VENTURE with PHOTON 100 CMOS detector system equipped with a Mo-target X-ray tube (λ = 0.71073 Å). Data were collected using ω scans to survey a hemisphere of reciprocal space. Data reduction and integration were performed with the Bruker APEX 2 (W(CPh)(dmpe)$_2$Cl) or APEX3 (others) software package (Bruker AXS, versions 2014/4, 2015.5-2, or 2017.3-0, 2018). Data were corrected for absorption effects using the numerical scaling as implemented in SADABS (Bruker AXS, version 2014/4, 2014, part of the Bruker APEX2 software package).[34] The structures were solved by SHELXT (Version 2014/5)[35] and refined by a full–matrix least–squares procedure using Bruker SHELXTL (version 6.14)[36] and OLEX2 software packages (XL refinement program version 2014/7).[37]All atoms were refined with anisotropic thermal parameters. Hydrogen atoms were included in idealized positions for structure factor calculations. Crystal structure data and refinement parameters are listed in Table 2.6.

2.4.2.2. Crystal structure of W(CPh)(dmpe)$_2$Cl. Crystals were grown from Et_2O solution at −50 °C. A purple plate (0.08 × 0.20 × 0.34 mm) was mounted with Fluorolube oil on a Dual-Thickness MicroMount (MiTeGen) with 30 μm sample aperture. The structure is shown in Figure 2.14, and selected bond distances and angles are set out in Table 2.3.

2.4.2.3. Crystal structure of W(CPh)(dmpe)$_2$F. Crystals were grown from Et_2O solution at −50 °C. A very small crystal (0.006 × 0.008 × 0.01 mm) was mounted with Fluorolube oil on a Dual-Thickness MicroMount (MiTeGen) with 10 μm sample aperture. The structure is shown in Figure 2.15, and selected bond distances and angles are set out in Table 2.3.

2.4.2.4. Crystal structure of W(CC_6H_4-4-pyr)(dmpe)$_2$Cl. Crystals were grown from a 1:1 THF/pentane solution at −50 °C. A small yellow bipyramid (0.06 × 0.08 × 0.13 mm) was mounted with Fluorolube oil on a Dual-Thickness MicroMount (MiTeGen) with 20 μm sample aperture. One dmpe ligand and interstitial THF are each disordered over two positions. Each disorder was individually modeled. The structure is shown in Figure 2.16, and selected bond distances and angles are set out in Table 2.3.

2.4.2.5. Crystal structure of W(CPh)(depe)$_2$Cl. Crystals were grown from Et_2O solution at −40 °C. A crystal (0.18 × 0.11 × 0.08 mm) was mounted with Fluorolube oil on a Dual-Thickness MicroMount (MiTeGen) with 10 μm sample aperture. The second position showed whole molecule disorder and refined over two orientations (1:1). W and Cl atoms were refined with anisotropic thermal parameters. The structure is shown in Figure 2.17, and selected bond distances and angles are set out in Table 2.3.

Table 2.6. Crystal structure data and refinement parameters

Parameter	W(CPh)(dmpe)$_2$Cl	W(CPh)(dmpe)$_2$F	W(CC$_6$H$_4$-4-pyr)(dmpe)$_2$Cl	W(CPh)(depe)$_2$Cl
Empirical formula	$C_{19}H_{37}ClP_4W$	$C_{19}H_{37}FP_4W$	$C_{27}H_{52}ClNOP_4W$	$C_{27}H_{53}ClP_4W$
Formula weight	608.66	592.21	749.87	720.87
Temperature, K	100(2)	100(2)	100(2)	100(2)
Crystal system	monoclinic	monoclinic	monoclinic	triclinic
Space group	*P*2$_1$/*c*	*C*2/*c*	*P*2$_1$/*n*	*P*-1
a, Å	14.9576(13)	15.7623(15)	13.5317(6)	9.8302(4)
b, Å	11.5926(10)	11.2162(12)	16.7932(7)	17.4963(8)
c, Å	14.3749(13)	13.8591(13)	14.6934(6)	19.9206(9)
α, °	90	90	90	111.0770(10)
β, °	99.279(2)	90.298(3)	95.148(2)	90.810(2)
γ, °	90	90	90	98.5610(10)
Volume, Å^3	2460.0(4)	2450.2(4)	3325.5(2)	3152.8(2)
Z	4	4	4	4
$\rho_{calc,}$ g/cm^3	1.643	1.605	1.498	1.519
μ, mm^{-1}	5.067	4.985	3.766	3.966
F(000)	1208	1176.0	1520.0	1464.0
Crystal size, mm	0.340 × 0.200 × 0.080	0.01 × 0.008 × 0.006	0.13 × 0.08 × 0.06	0.18× 0.11 × 0.08
2Θ range for data collection, °	4.538–55.982	5.168–50.128	4.61–61.092	4.192–54.292
Index ranges	–19 ≤ h ≤ 19 –15 ≤ k ≤ 15 –18 ≤ l ≤ 18	–18 ≤ h ≤ 18 –13 ≤ k ≤ 13 –16 ≤ l ≤ 16	–19 ≤ h ≤ 18 –23 ≤ k ≤ 22 –20 ≤ l ≤ 20	–12 ≤ h ≤ 12 –22 ≤ k ≤ 22 –25 ≤ l ≤ 24
Reflections collected	70124	15490	198766	52471
Independent reflections	5907 [R_{int} = 0.0300]	2184 [R_{int} = 0.0653]	9390 [R_{int} = 0.0455]	13327[R_{int} = 0.0479]
Data / restraints / parameters	5907 / 0 / 234	2184 / 6 / 120	9390 / 253 / 361	13327/24/626
Goodness–of–fit on F^2	1.022	1.120	1.076	1.034
Final *R* indices (*I* > 2σ(*I*))	R1 = 0.0165 wR2 = 0.0381	R1 = 0.0336, wR2 = 0.0551	R1 = 0.0209 wR2 = 0.0338	R1 = 0.0385 wR2 = 0.0702
R indices (all data)	R1 = 0.0196 wR2 = 0.0396	R1 = 0.0451 wR_2 = 0.0579	R1 = 0.0395 wR2 = 0.0370	R1 = 0.0656 wR2 = 0.0771
Largest diff. peak/hole, e•Å^{-3}	1.406/–0.432	1.56/–0.60	0.69/–0.40	1.67/–1.31

2.5. References.

1. Bocarsly, A. B.; Cameron, R. E.; Rubin, H. D.; McDermott, G. A.; Wolff, C. R.; Mayr, A. *Inorg. Chem.* **1985**, *24*, 3976-3978.

2. Tungsten tetrachloride can be purchased from Sigma Aldrich as of 05/10/2018 for approximately $20.0 per gram.

3. Sun, J.; Simpson, C. K.; Hopkins, M. D.; Hock, A. S.; Schrock, R. R. *Inorg. Synth.*; Girolami, G. S., Sattelberger, A. P., Ed.; John Wiley & Sons, Inc.: Hoboken, NJ, 2014; Vol. 36, pp 134-138.

4. Chisholm, M. H.; Martin, J. D.; Hill, J. E.; Rothwell, I. P. *Inorg. Synth.*; Grimes, R. N., Ed.; John Wiley & Sons, Inc.: Hoboken, NJ, 1992; Vol. 29, pp 137-140.

5. Broderick, E. M.; Browne, S. C.; Johnson, M. J. A.; Hitt, T. A.; Girolami, G. S. *Inorg. Synth.*; Girolami, G. S., Sattelberger, A. P., Ed.; John Wiley & Sons, Inc.: Hoboken, NJ, 2014; Vol. 36, pp 95-102.

6. Schrock, R. R.; Listemann, M. L.; Sturgeoff, L. G. *J. Am. Chem. Soc.* **1982**, *104*, 4291-4293.

7. Wengrovius, J. H.; Sancho, J.; Schrock, R. R. *J. Am. Chem. Soc.* **1981**, *103*, 3932-3934.

8. Listemann, M. L.; Schrock, R. R. *Organometallics* **1985**, *4*, 74-83.

9. Stevenson, M. A.; Hopkins, M. D. *Organometallics* **1997**, *16*, 3572-3573.

10. Haines, D. E.; O'Hanlon, D. C.; Manna, J.; Jones, M. K.; Shaner, S. E.; Sun, J.; Hopkins, M. D. *Inorg. Chem.* **2013**, *52*, 9650-9658.

11. Lovaasen, B. M.; Lockard, J. V.; Cohen, B. W.; Yang, S.; Zhang, X.; Simpson, C. K.; Chen, L. X.; Hopkins, M. D. *Inorg. Chem.* **2012**, *51*, 5660-5670.

12. Jones, M. K. Conjugated organometallic materials containing tungsten centers. Ph.D. Dissertation, The University of Chicago, Chicago, IL, 2007.

13. O'Hanlon, D. C.; Cohen, B. W.; Moravec, D. B.; Dallinger, R. F.; Hopkins, M. D. *J. Am. Chem. Soc.* **2014**, *136*, 3127-3136.

14. Fischer, E. O.; Maasböl, A. *Chem. Ber.* **1967**, *100*, 2445-2456.

15. Fischer, H.; Fischer, E. O. *J. Organomet. Chem.* **1974**, *69*, C1-C3.

16. Mayr, A.; McDermott, G. A.; Dorries, A. M. *Organometallics* **1985**, *4*, 608-610.

17. McDermott, G. A.; Dorries, A. M.; Mayr, A. *Organometallics* **1987**, *6*, 925-931.

18. Mayr, A.; Dorries, A. M.; McDermott, G. A.; Van Engen, D. *Organometallics* **1986**, *5*, 1504-1506.

19. Mayr, A.; Asaro, M. F.; Kjelsberg, M. A.; Lee, K. S.; Van Engen, D. *Organometallics* **1987**, *6*, 432-434.

20. Furno, F.; Fox, T.; Schmalle, H. W.; Berke, H. *Organometallics* **2000**, *19*, 3620-3630.

21. Bannwart, E.; Jacobsen, H.; Hübener, R.; Schmalle, H. W.; Berke, H. *J. Organomet. Chem.* **2001**, *622*, 97-111.

22. Yu, M. P. Y.; Mayr, A.; Cheung, K.-K. *J. Chem. Soc., Dalton Trans.* **1998**, 475-481.

23. Jelliss, P. A.; Wampler, K. M.; Siemiarczuk, A. *Organometallics* **2005**, *24*, 707-714.

24. Bastos, C. M.; Lee, K. S.; Kjelsberg, M. A.; Mayr, A.; Van Engen, D.; Koch, S. A.; Franolic, J. D.; Klooster, W. T.; Koetzle, T. F. *Inorg. Chim. Acta* **1998**, *279*, 7-23.

25. Yu, M. P. Y.; Cheung, K.-K.; Mayr, A. *J. Chem. Soc., Dalton Trans.* **1998**, 2373-2378.

26. Gerrard, W.; Lappert, M. F. *Chem. Rev.* **1958**, *58*, 1081-1111.

27. Mayr, A.; Bastos, C. M.; Daubenspeck, N.; McDermott, G. A. *Chem. Ber.* **1992**, *125*, 1583-1588.

28. Heppekausen, J.; Stade, R.; Goddard, R.; Fürstner, A. *J. Am. Chem. Soc.* **2010**, *132*, 11045-11057.

29. Foreman, M. R. S.-J.; Hill, A. F.; White, A. J. P.; Williams, D. J. *Organometallics* **2003**, *22*, 3831-3840.

30. Rudshteyn, B.; Vibbert, H. B.; May, R.; Wasserman, E.; Warnke, I.; Hopkins, M. D.; Batista, V. S. *ACS Catal.* **2017**, *7*, 6134-6143.

31. Pangborn, A. B.; Giardello, M. A.; Grubbs, R. H.; Rosen, R. K.; Timmers, F. J. *Organometallics* **1996**, *15*, 1518-1520.

32. Fulmer, G. R.; Miller, A. J. M.; Sherden, N. H.; Gottlieb, H. E.; Nudelman, A.; Stoltz, B. M.; Bercaw, J. E.; Goldberg, K. I. *Organometallics* **2010**, *29*, 2176-2179.

33. Effenberger, F.; Agster, W.; Fischer, P.; Jogun, K. H.; Stezowski, J. J.; Daltrozzo, E.; Kollmannsberger-Von Nell, G. *J. Org. Chem.* **1983**, *48*, 4649-4658.

34. Krause, L.; Herbst-Irmer, R.; Sheldrick, G. M.; Stalke, D. *J. Appl. Cryst.* **2015**, *48*, 3-10.

35. Sheldrick, G. M. *Acta. Crystallogr., Sect. A: Found. Adv.* **2008**, *A64*, 112-122.

36. Sheldrick, G. M. *Acta. Crystallogr., Sect. A: Found. Adv.* **2015**, *A71*, 3-8.

37. Dolomanov, O. V. B.; Gildea, R. J.; Howard, A. K.; Puschmann, H. *J. Appl. Cryst.* **2009**, *42*, 339-341.

CHAPTER 3

Electronic structure design for W(CAr)L_4X photoredox chromophores

Note: Portions of this work have been published in an alternative format in Rudshetyn, B.; Vibbert, H.B.; May, R.; Wasserman, E.; Warnke, I.; Hopkins, M.D. *ACS Catalysis* **2017**, *7*, 6134-6143.

3.1. Introduction.

Photoredox reactions enable access to highly reactive radical states of molecules that can be used for a multitude of transformations. Few photoredox chromophores combine strongly reducing excited-states with visible-light excitation properties. Among conventional photoredox chromophores, the strongest reductant is [*fac*-Ir(ppy)$_3$]$^-$ (–2.60 V vs $FeCp_2$); this potential is not sufficient to reduce many useful substrates like aryl halides, alkyl halides, or CO_2 (See Chapter 5). One approach towards designing chromophores with more negative potentials than [*fac*-Ir(ppy)$_3$]$^-$ relies on orbital orthogonality, which is shown in Figure 3.1. At its heart, this design scheme relies on the independent control of the HOMO and LUMO energies, which in turn control the redox ($E_{1/2}^{ox}$) and optical properties (E_{00}) of a photoredox chromophore, *via* variation of substituents along the different symmetry axes. While the independent control of redox properties alone does not affect the overall excited-state oxidation potential of a chromophore, independently controlling the ground-state oxidation potential and then controlling the excited-state oxidation potential could produce a chromophore that is highly tunable about its ground and excited-state properties, while maintaining excitation with a convenient, low-energy visible light source (Figure 3.1).

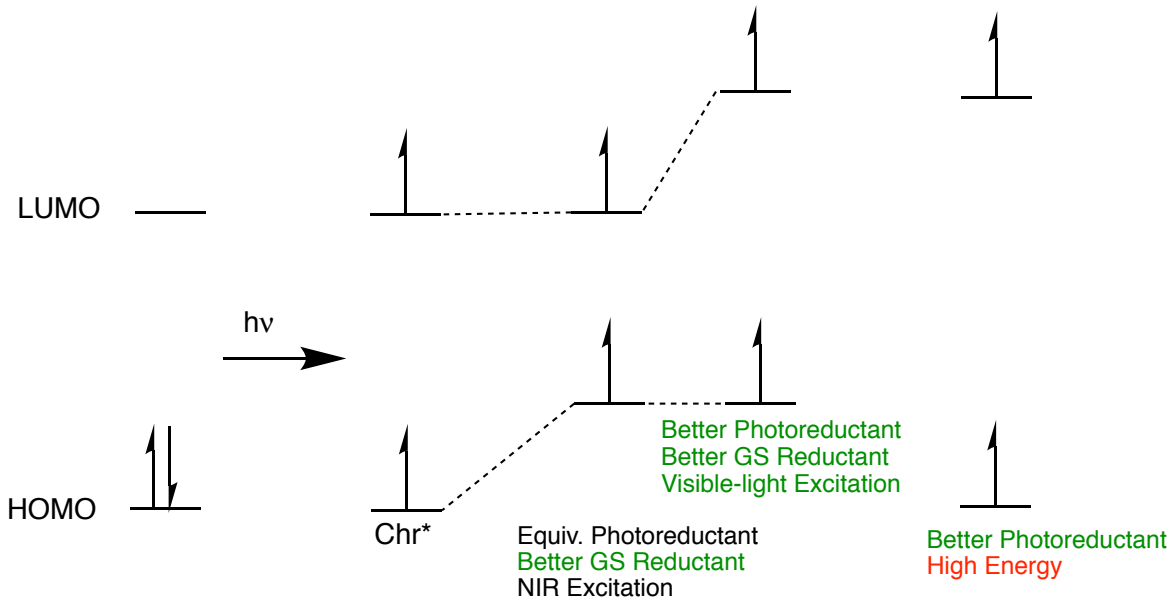

Figure 3.1. Photoredox chromophore design scheme showing the need for orbital orthogonality.

One class of molecules whose HOMO and LUMO are orthogonal are d^2 tungsten-alkylidyne complexes of the type $W(CAr)L_4X$.[1] Tungsten-alkylidyne compounds are highly tunable because of the symmetry of their frontier orbitals. This can be visualized for the metal-methylidyne compound, $M(CH)L_4X$, as shown in Figure 3.2. The orbital energy diagram for the methylidyne compound can be generated by the interaction of a five-coordinate fragment, ML_4X with a CH unit. For tungsten(IV) as M, the HOMO is centered on the metal-d_{xy} orbital and is formally non-bonding (δ-symmetry) with respect to the X and CH ligands and π/π* symmetry with respect to the L ligands, and the LUMO is a degenerate π*(MC) antibonding orbital. Upon replacement of H with Ar in $W(CAr)L_4X$, the LUMO degeneracy is lifted with the LUMO+1 remaining π*(MC) and the LUMO having an out-of-phase combination between a π*(Ar) orbital and π*(MC); this is denoted π*(MCAr). The LUMO is principally sensitive to the nature and substituents of the Ar group and possess weaker interactions with the X and L ligands. The HOMO and LUMO are of different symmetry and mutually orthogonal.

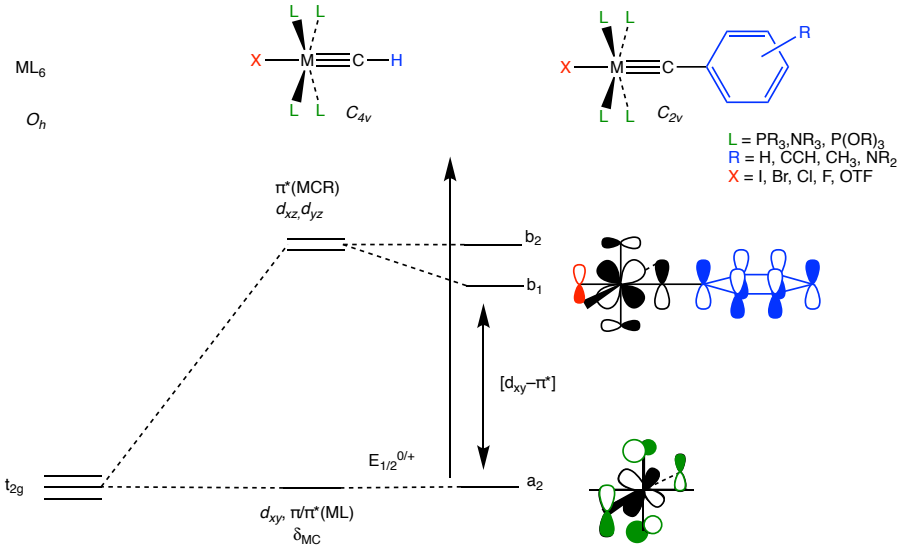

Figure 3.2. Frontier orbital description of metal-alkylidyne compounds.

The properties of importance to the excited-state oxidation potential of a photoredox chromophore are the ground-state oxidation potential and the excited-state energy. The HOMO is the redox orbital for oxidation; thus, the oxidation potential should be a function of the HOMO energy. Because the HOMO energy is primarily influenced by the nature of L, the equatorial ligand, the oxidation potential should be more sensitive to the nature of this ligand than to the CAr and X ligands. Similarly, the excited-state energy should be proportional to the HOMO-LUMO gap and directly relatable to the absorption energy. Modulating the energy of the HOMO-LUMO gap, therefore, should be readily accomplished by variation of L (which sets the HOMO energy) and CAr (which sets the LUMO energy).

Computational chemistry can aid the design of these compounds by providing predictions of orbital energies for compounds with various ligand sets. Recently published results show that DFT calculations provide electronic structures of tungsten-alkylidyne complexes that closely resemble the qualitative pictures discussed above. The calculated HOMO of the representative compound W(CPh)(dmpe)$_2$Cl is a metal-centered d_{xy} orbital (75%) with the remainder due to

π/π* interactions with the dmpe ligands and essentially zero contribution from the CPh and Cl ligands (Figure 3.3).[2, 3] Similarly, the LUMO is π*(WCPh) (69.3%) with the remainder contributing from dmpe and Cl. This suggests that the HOMO and LUMO energies should be controllable in predictable ways through variation of CAr, L, and X.

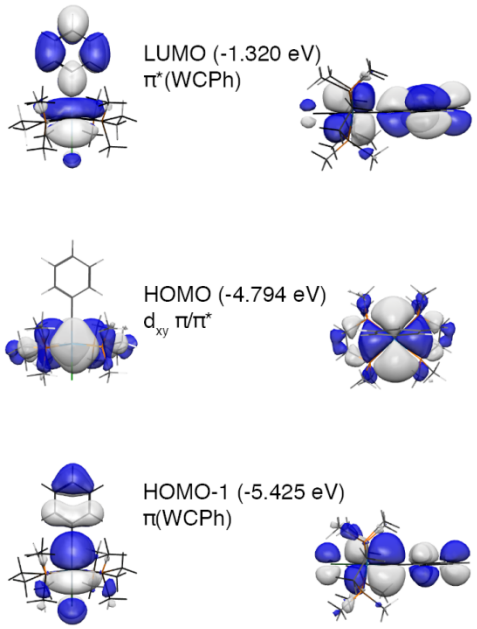

Figure 3.3. DFT computed orbital energies and renderings (isovalue = 0.05) of the frontier orbitals of $W(CPh)(dmpe)_2Cl$. Structure and orbital energies used from Ref. 2.

Consistent with these predictions, the Hopkins group reported previously that the oxidation potentials of these compounds are primarily influenced by the nature of the L ligands, and that they are linearly correlated with the computed HOMO energy (slope $\approx$ 1).[2] This empirical correlation provides a way to predict the oxidation potentials of hypothetical compounds through DFT calculations of their gas-phase HOMO energies. This approach was subsequently refined in a collaboration with the Batista group at Yale, in which DFT calculations were used to calculate the intermediates in a Born-Haber cycle in order to account for effects of

solvation.[4] Again, agreement between theory and experiment was strong, providing a new predictive tool.

This chapter uses computational and empirical methodology developed in prior studies[2, 4] to design tungsten-alkylidyne complexes with desirable ground-state and excited-state properties. Oxidation potentials are shown to conform to a ligand additivity model related to the electrochemical parameters derived by Lever,[5] and the computational methods described above are used to design new compounds that are strong ground-state reductants. An empirical relationship is developed between excited-state energies and calculated HOMO-LUMO gap that can be used to predict the absorption band energies of new compounds. This method is combined with the previous predictor of ground-state oxidation potentials to predict the excited-state redox potentials of tungsten-alkylidyne photoredox chromophores.

3.2. Results and Discussion.

3.2.1. Ligand additive parameters for oxidation potentials. The development of a set of electrochemical ligand parameters that can describe and predict the oxidation potentials of compounds is a useful goal, but requires that the compounds exhibit ligand-modular redox potentials. We set out to determine if ligand additivity relationships existed for $W(CAr)L_4X$ complexes or if the ligand effects were more complicated. Because the symmetry of tungsten-alkylidyne compounds is less than O_h, a model that defines parameters describing equal contributions upon substitution to different positions, such as the one Lever developed for ruthenium(II) complexes, will not provide fruitful results for $W(CAr)L_4X$ compounds.[5-9] The model described here relies on three parameters (ρ_L, ρ_R, and ρ_X) for the equatorial (L) and axial (R, X) components (Figure 3.4) derived using a subset of tungsten-alkylidyne compounds that are sufficient to establish ligand additivity. This model is somewhat akin to the ligand additivity

developed by Bursten,[10] which provides a description of orbital energies for d^6 complexes with L and L′ ligands of different π-acceptor ability. Contained in Table 3.1 are relevant oxidation-potential data for tungsten-alkylidyne complexes with variable L, R, and X substituents.[4]

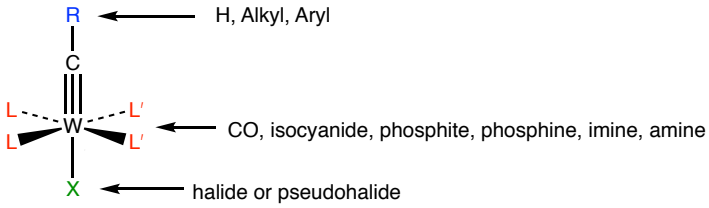

Figure 3.4. Depiction of the ligand parameter space for $W(CR)L_4X$ compounds.

The method used to calculate the ligand additivity parameters is thoroughly developed in Section 3.4. The parameters are shown in Tables 3.2–3.5. Inspection of the electrochemical potentials shows that the largest ρ-values are those for the L ligands, consistent with the fact that the redox orbital interacts with L but is nonbonding to CAr and X. The most electron-donating ligand is tmeda ($\rho_L = -0.05$) and CO is the most electron-withdrawing ligand used (+0.67), with alkyl phosphines, dppe, and $P(OMe)_3$ possessing intermediate values. Among the other ligands, ρ_R-values span a narrow range of –0.09 (C^tBu and CC_6H_4-4-pyr) to +0.06 (CC_6H_4-4-$CCSiPr^i_3$), and ρ_X values range from –0.14 (^{n}Bu) to +0.17 (OTf). Estimated oxidation potentials are provided by these parameters *via* Equation 3.4. These values are compared to the experimentally measured oxidation potentials in Figure 3.5. Over this range of data, the calculated and experimental values correlate with a slope of approximately 1 and intercept of approximately 0. Clearly, this demonstrates that the electrochemical first oxidation potentials of this family are modular with respect to their electronic properties, and that the ligand additivity parameters have predictive power.

Table 3.1. Tungsten-alkylidyne compounds and oxidation potentials used to establish electrochemical ligand additivity.

#	**Compound**	$E_{1/2}^{0/+}$ (V vs $FeCp_2$)[a]
1	$W(CH)(dmpe)_2F$	−0.91[b]
2	$W(CH)(dmpe)_2Cl$	−0.84
3	$W(CH)(dmpe)_2Br$	−0.82
4	$W(CH)(dmpe)_2I$	−0.73
5	$W(CH)(dmpe)_2(OTf)$	−0.68
6	$W(CH)(dmpe)_2(CN)$	−0.78
7	$W(CH)(dmpe)_2(OSiMe_3)$	−0.94[b]
8	$W(CH)(dmpe)_2(Bu^n)$	−0.98[c]
9	$W(CH)(PMe_3)_4Cl$	−0.85
10	$W(CBu^t)(dmpe)_2Cl$	−0.93
11	$W(CBu^t)(PMe_3)_4Cl$	−0.93
12	$W(CPh)(dmpe)_2Cl$	−0.82
13	$W(CPh)(dmpe)_2Br$	−0.78
14	$W(CPh)(dmpe)_2I$	−0.72
15	$W(CPh)(dmpe)_2(OTf)$	−0.65
16	$W(CPh)(dmpe)_2(OPh)$	−0.89[d]
17	$W(CPh)(PMe_3)_4Cl$	−0.85
18	$W(CPh)(PMe_3)_4Br$	−0.80
19	$W(CPh)(PMe_3)_4I$	−0.76
20	$W(CPh)(depe)_2Cl$	−0.84
21	$W(CPh)(dppe)_2Cl$	−0.58
22	$[W(CPh)(dppe)_2(CH_3CN)]^+$	−0.24
23	$W(CC_6H_4\text{-}4\text{-}CCH)(dmpe)_2Cl$	−0.79
24	$W(CC_6H_4\text{-}4\text{-}CCSiPr^i_3)(dmpe)_2Cl$	−0.78
25	$W\{CCHC(c\text{-}C_4H_8)\}(triphos)(CO)Cl$	−0.03[e]
26	$W(CPh)\{P(OMe)_3\}_4Cl$	−0.24[f]
27	$W(CPh)(dppe)(CO)_2Cl$	0.66[b]
28	$W(CPh)(tmeda)(CO)_2Cl$	0.41[c]
29	$W(CPh)(tmeda)(CO)_2Br$	0.43[c]
30	$W(CPh)(CNBu^t)_2(CO)_2Br$	0.62[c]
31	$W(CPh)(py)_2(CO)_2Br$	0.42[b]
32	$W(CCCPh)(CO)_4Cl$	>1.1
33	$W(CPh)(dmpe)_2F$	−0.91
34	$W(CMes)(dmpe)_2Cl$	−0.87
35	$W(CC_6H_4\text{-}4\text{-}pyr)(dmpe)_2Cl$	−0.93

[a] Potentials are found in Ref. 4; [b] Quasi-reversible; [c] Irreverisble; [d] Measured in CH_2Cl_2; [e] Measured in CH_3CN with 0.2 M $[^nBu_4N]BF_4$[11]; [f] Irreversible at room temperature, reversible at −15 °C (See Chapter 4).

Table 3.2. Electrochemical parameters (ρ_X) such that ρ_X(Cl) = 0.[a]

X	Complex	Ref. Complex	$\Delta E_{1/2}$ (V)	ρ_X
Br	W(CH)(dmpe)$_2$Br	W(CH)(dmpe)$_2$Cl	+0.02	+0.04
Br	W(CPh)(dmpe)$_2$Br	W(CPh)(dmpe)$_2$Cl	+0.04	
Br	W(CPh)(PMe$_3$)$_4$Br	W(CPh)(PMe$_3$)$_4$Cl	+0.05	
I	W(CH)(dmpe)$_2$I	W(CH)(dmpe)$_2$Cl	+0.11	+0.10
I	W(CPh)(dmpe)$_2$I	W(CPh)(dmpe)$_2$Cl	+0.10	
I	W(CPh)(PMe$_3$)$_4$I	W(CPh)(PMe$_3$)$_4$Cl	+0.09	
F	W(CH)(dmpe)$_2$F	W(CH)(dmpe)$_2$Cl	–0.07	–0.08
F	W(CPh)(dmpe)$_2$F	W(CPh)(dmpe)$_2$Cl	–0.09	
OTf	W(CH)(dmpe)$_2$(OTf)	W(CH)(dmpe)$_2$Cl	+0.16	+0.17
OTf	W(CPh)(dmpe)$_2$(OTf)	W(CPh)(dmpe)$_2$Cl	+0.17	
CN	W(CH)(dmpe)$_2$(CN)	W(CH)(dmpe)$_2$Cl	+0.06	+0.06*
OSiMe$_3$	W(CH)(dmpe)$_2$(OSiMe$_3$)	W(CH)(dmpe)$_2$Cl	–0.10	–0.10*
^{n}Bu	W(CH)(dmpe)$_2$(^{n}Bu)	W(CH)(dmpe)$_2$Cl	–0.14	–0.14*
OPh	W(CPh)(dmpe)$_2$(OPh)	W(CPh)(dmpe)$_2$Cl	–0.07	–0.07*

[a] Parameters derived from one measured value are denoted with a *.

Table 3.3. Electrochemical parameters (ρ_L) such that ρ_L(dmpe) = 0.[a]

L	Complex	Ref. Complex	$\Delta E_{1/2}$ (V)	ρ_L
PMe$_3$	W(CH)(PMe$_3$)$_4$Cl	W(CH)(dmpe)$_2$Cl	–0.0025	–0.005
PMe$_3$	W(C^{t}Bu)(PMe$_3$)$_4$Cl	W(C^{t}Bu)(dmpe)$_2$Cl	0	
PMe$_3$	W(CPh)(PMe$_3$)$_4$Cl	W(CPh)(dmpe)$_2$Cl	–0.0075	
PMe$_3$	W(CPh)(PMe$_3$)$_4$Br	W(CPh)(dmpe)$_2$Br	–0.005	
PMe$_3$	W(CPh)(PMe$_3$)$_4$I	W(CPh)(dmpe)$_2$I	–0.01	
depe	W(CPh)(depe)$_2$Cl	W(CPh)(dmpe)$_2$Cl	–0.005	–0.005*
dppe	W(CPh)(dppe)$_2$Cl	W(CPh)(dmpe)$_2$Cl	+0.06	+0.06*
P(OMe$_3$)	W(CPh){P(OMe)$_3$}$_4$Cl	W(CPh)(dmpe)$_2$Cl	+0.145	+0.145*

[a] Parameters derived from one measured value are denoted with a *.

Table 3.4. Electrochemical parameters (ρ_R) such that ρ_R(CH) = 0.[a]

R	Complex	Ref. Complex	$\Delta E_{1/2}$ (V)	ρ_R
CPh	W(CPh)(dmpe)$_2$Cl	W(CH)(dmpe)$_2$Cl	+0.02	+0.03
CPh	W(CPh)(PMe$_3$)$_4$Cl	W(CH)(PMe$_3$)$_4$Cl	+0.03	
CPh	W(CPh)(dmpe)$_2$Br	W(CH)(dmpe)$_2$Br	+0.04	
CPh	W(CPh)(dmpe)$_2$I	W(CH)(dmpe)$_2$I	+0.01	
CPh	W(CPh)(dmpe)$_2$(OTf)	W(CH)(dmpe)$_2$(OTf)	+0.03	
C^{t}Bu	W(C^{t}Bu)(dmpe)$_2$Cl	W(CH)(dmpe)$_2$Cl	–0.09	–0.09
C^{t}Bu	W(C^{t}Bu)(PMe$_3$)$_4$Cl	W(C^{t}Bu)(PMe$_3$)$_4$Cl	–0.08	
CC$_6$H$_4$-4-CCH	W(CC$_6$H$_4$-4-CCH)(dmpe)$_2$Cl	W(CH)(dmpe)$_2$Cl	+0.05	+0.05*
CC$_6$H$_4$-4-CCSiPr$^i_3$	W(CC$_6$H$_4$-4-CCSiPr$^i_3$)(dmpe)$_2$Cl	W(CH)(dmpe)$_2$Cl	+0.06	+0.06*
CMes	W(CMes)(dmpe)$_2$Cl	W(CH)(dmpe)$_2$Cl	–0.03	–0.03*
CC$_6$H$_4$-4-pyr	W(CC$_6$H$_4$-4-pyr)(dmpe)$_2$Cl	W(CH)(dmpe)$_2$Cl	–0.09	–0.09*

[a] Parameters derived from one measured value are denoted with a *.

Table 3.5. Electrochemical parameters for W(CR)L$_2$(CO)$_2$X compounds.[a]

L	L′	Complex	Ref. Complex	$\Delta E_{1/2}$ (V)	ρ_L*	$\rho_{L'}$*
dppe	CO	W(CPh)(dppe)(CO)$_2$Cl	W(CPh)(dppe)$_2$Cl	+1.22	+0.06	+0.67
tmeda	CO	W(CPh)(tmeda)(CO)$_2$Cl	W(CPh)(dppe)(CO)$_2$Cl	–0.25	–0.05	+0.67
tmeda	CO	W(CPh)(tmeda)(CO)$_2$Br	W(CPh)(dppe)(CO)$_2$Cl	–0.23		
CN^{t}Bu	CO	W(CPh)(CN^{t}Bu)(CO)$_2$Br	W(CPh)(dppe)(CO)$_2$Cl	–0.04	+0.06	+0.67
py	CO	W(CPh)(py)$_2$(CO)$_2$Cl	W(CPh)(dppe)(CO)$_2$Cl	–0.24	–0.04	+0.67

[a] Parameters derived from one measured value are denoted with a *.

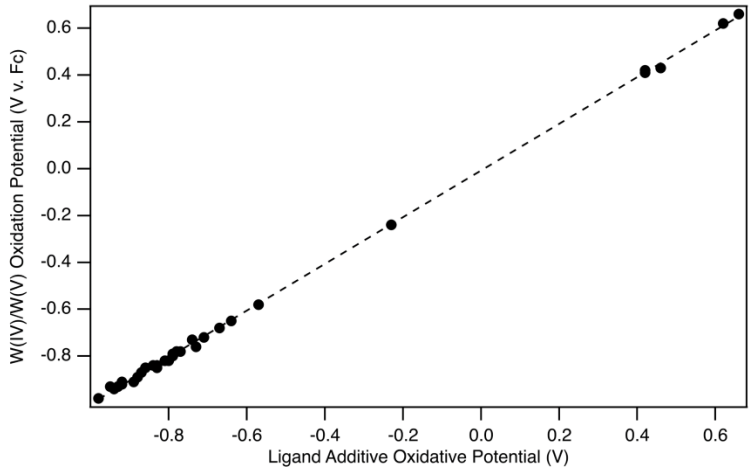

Figure 3.5. Comparison between calculated oxidation potentials *via* ligand additive parameters and experimental oxidation potentials, for those parameters derived from more than one experimental value. Fit: f(x) = 0.933x –0.05, $r^2 = 0.98$.

The calculated ρ-values for L are similar to those parameters derived by Lever (Table 3.6, Figure 3.6). Those quantities are related with a slope of approximately 1, as might be expected for an orbital that is directly interacting with the redox orbital, such as is the case for the t_{2g} set of orbitals for ruthenium(II) compounds.[5] However, the ρ_X values do not closely follow the Lever parameters (Table 3.7), particularly for I, F, and OTf. The Lever parameters are larger than the ρ_X values, because while the X ligands can mix by symmetry with the redox orbitals under O_h symmetry, they are orthogonal in W(CAr)L_4X compounds. Thus, these ligands perturb the redox potential through inductive electronic effects.

Table 3.6. Comparison of ρ_L derived quantities with Lever parameters.

L	E_L (v. NHE)[a]	ΔE_L (Rel. to dmpe)	ρ_L
dmpe	+0.28	0	0
dppe	+0.36	+0.08	+0.06
PMe_3	+0.33	+0.05	–0.005
$P(OMe)_3$	+0.42	+0.14	+0.145
CO	+0.99	+0.71*	+0.67*
pyridine	+0.25	–0.03*	–0.04*

[a]Ref. 5. The asterisk indicates ρ_L values with only one measurement.

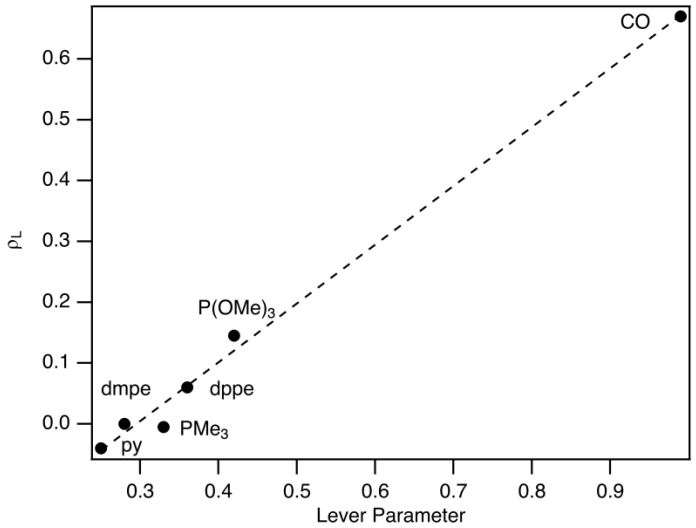

Figure 3.6. Comparison between Lever parameters and ρ_L parameters. f(x) =0.96x –0.28; r^2 = 0.993

Table 3.7. Comparison of ρ_X derived quantities with Lever parameters.

X	E_L (v. NHE)[a]	ΔE_L (Rel. to Cl)	ρ_X
Cl	–0.24	0	0
F	–0.42	–0.18	–0.09
I	–0.24	0	+0.10
Br	–0.22	+0.02	+0.04
CN	+0.02	+0.26	+0.06
OTf	+0.13	+0.37	+0.17

[a]Ref. 5.

3.2.2. Computationally predicted ground-state oxidation potentials for complexes with new L, CAr, and X ligands. The observed linear correlation between E_{HOMO} (DFT) and $E_{1/2}^{0/+}$ (experimental) observed for W(CAr)L_4X complexes provides a simple method by which to easily computationally screen hypothetical complexes for those with desirable ground-state oxidation potentials. These computational screens focused on the variation of L, CAr, and X. The DFT methods used for these studies are described in Section 3.4.

The first set of computational screens explored X ligands that have not previously been employed in experimental studies of photoredox chromophores (Table 3.8). The reference compound was W(CPh)(dmpe)$_2$Cl, where Cl was substituted with ligands that are stronger

electron donors. These X ligands provide predicted oxidation potentials that lie in the order Cl (0) > SMe (–0.06 V) > F (–0.09 V) > OMe (–0.14 V) > CH_3 (–0.18 V) > H (–0.19 V). Given the known high reactivity of hydride ligands[12] and alkyl ligands[13] there is little incentive to use these instead of OMe or F if a chromophore with a strongly reducing ground state is required.

Table 3.8. Computed orbital energies (eV) and predicted oxidation potentials (V vs $FeCp_2$) of selected $W(CPh)(dmpe)_2X$ compounds.

Compound	HOMO-1(eV)	HOMO	LUMO	Pred. $E_{1/2}$[a]
$W(CPh)(dmpe)_2Cl$	−5.4296	−4.7974	−1.3215	−0.78
$W(CPh)(dmpe)_2F$	−5.0900	−4.7156	−1.0255	−0.87
$W(CPh)(dmpe)_2OCH_3$	−4.7668	−4.6642	−1.0193	−0.92
$W(CPh)(dmpe)_2SCH_3$	−4.9166	−4.7434	−1.4529	−0.84
$W(CPh)(dmpe)_2H$	−5.2273	−4.6018	−1.1490	−0.97
$W(CPh)(dmpe)_2CH_3$	−5.2000	−4.6261	−1.1549	−0.95

[a]Predicted using Ref. 9; value is in V vs $FeCp_2$. [b]Ref. 14.

Computational screens varying L were explored with phosphines and tmeda (tetramethylenediamine) (Table 3.9). These equatorial ligands provide predicted oxidation potential values that track with the electron donor strength, such that (Calc. $E_{1/2}$) tmeda < dipe ~ depe < dmpe ~ PMe_3 < dppe < dppbz < $P(OMe)_3$. The computed oxidation potentials are similar to experiment for compounds with dmpe equatorial ligands (Table 3.9). More complicated equatorial ligands like dppe or depe perform less well in direct comparisons.[2] One possible explanation for this behavior is that the oxidation potentials, as calculated *via* Koopmans' theorem analysis, do not take solvation into consideration. Calculation of solvation energies was accomplished by Born-Haber analysis for the tungsten-alkylidyne complexes.[4] As calculated, the total solvation energy is 4 kcal mol^{-1} (0.17 eV) more positive for $W(CPh)(depe)_2Cl$ than for $W(CPh)(dmpe)_2Cl$. The difference of 0.17 eV could account for the error between that of the computational correlation and that of experimental measurements (ΔE = –0.11 V).

Table 3.9. Computed orbital energies (eV), predicted, and experimentally determined oxidation potentials (V vs $FeCp_2$) of selected $W(CPh)L_4Cl$ compounds.

Compound	HOMO-1	HOMO	LUMO	Calc. $E_{1/2}$[a]	Expt. $E_{1/2}$[b]
$W(CPh)\{P(OMe)_3\}_4Cl$	−5.7560	−5.5780	−1.5860	−0.02	–0.24
$W(CPh)(PMe_3)_4Cl$	−5.3640	−4.7530	−1.4850	−0.83	–0.85
$W(CPh)(dmpe)_2Cl$	−5.4297	−4.7975	−1.3215	−0.79	–0.82
$W(CPh)(dppe)_2Cl$	−5.5690	−4.8960	−1.5860	−0.69	–0.58
$W(CPh)(dppbz)_2Cl$	−5.5820	−5.0170	−1.7820	−0.57	NA
$W(CPh)(depe)_2Cl$	−5.3270	−4.6260	−1.2440	−0.95	–0.84
$W(CPh)(dipe)_2Cl$	−5.3933	−4.5535	−1.4144	−1.02	NA
$W(CPh)(tmeda)_2Cl$	−4.7925	−3.1258	−0.7548	−2.40	NA

[a] V vs $FeCp_2$ [b] Electrochemical potentials are shown in Table 3.1. NA = not available

The strongest electron-donating equatorial ligand was tmeda, as evidenced by the profoundly shifted ground-state oxidation potential of $W(CPh)(tmeda)_2Cl$ ($E_{1/2}$ calc. = –2.40 V) relative to $W(CPh)(dmpe)_2Cl$ ($E_{1/2}$ calc. = –0.79 V). The electronic structure of this complex is typical for $W(CAr)L_4X$ compounds (Figure 3.7) with a d_{xy} HOMO and π*(WCAr) LUMO. Thus, this compound is an interesting synthetic target.

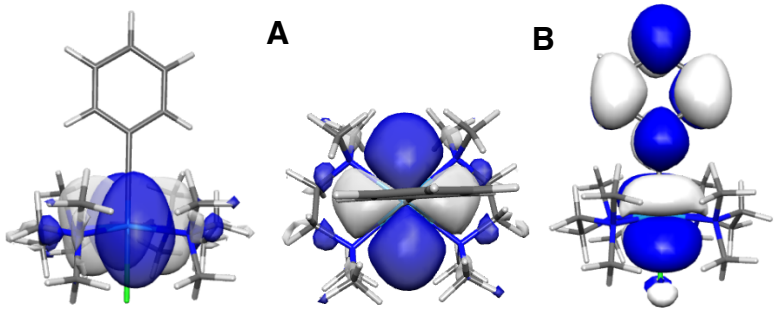

Figure 3.7. Computed connectivity and electronic structure of $W(CPh)(tmeda)_2Cl$ (isovalue = 0.05). (A) HOMO; (B) LUMO.

Computational screens of CAr ligands within compounds of the type $W(CC_6H_4\text{-}4\text{-}R)(dmpe)_2Cl$ show modest effects on the HOMO orbital energy (Table 3.10). The R groups explored were R = CH_3, OMe, SMe, NH_2, NMe_2, N-pyrrolidyl, and N-piperidyl. The methods predict that the -4-pyrrolidyl (-4-pyr) group produces the most reducing ground state. The electronic structure and molecular connectivity of the compound is shown in Figure 3.8. (A

single crystal X-ray structure is shown and analyzed in Chapter 2.) Among the features of this complex are that the amine lies nearly co-planar with the alkylidyne ring, indicating it can act as a strong electron donor. This serves to raise both the HOMO and LUMO orbital energy. The electronic structure of this complex is typical of that for the alkylidyne compounds: the HOMO–1 is π(WCAr), the HOMO is primarily of metal-centered d_{xy} parentage, and the LUMO is π^*(WCAr).

Table 3.10. Computed orbital energies (eV) of selected W(CAr)(dmpe)$_2$Cl compounds.

Compound	HOMO-1(eV)	HOMO	LUMO	Pred. $E_{1/2}$[a]
W(CPh)(dmpe)$_2$Cl	−5.4296	−4.7974	−1.3215	−0.78
W(CC$_6$H$_4$-4-CH$_3$)(dmpe)$_2$Cl	−5.3330	−4.7589	−1.2360	−0.82
W(CC$_6$H$_2$-2,4,6-CH$_3$)(dmpe)$_2$Cl	−5.2677	−4.7410	−1.0383	−0.84
W(CC$_6$H$_4$-4-SCH$_3$)(dmpe)$_2$Cl	−5.2397	−4.7804	−1.2944	−0.80
W(CC$_6$H$_4$-4-OCH$_3$)(dmpe)$_2$Cl	−5.2087	−4.7263	−1.0764	−0.86
W(CC$_6$H$_2$-3,4-5-OCH$_3$)(dmpe)$_2$Cl	−5.3015	−4.8081	−1.2005	−0.78
W(CC$_6$H$_4$-4-NH$_2$)(dmpe)$_2$Cl	−5.0447	−4.6593	−0.9631	−0.92
W(CC$_6$H$_4$-4-N(CH$_3$)$_2$)(dmpe)$_2$Cl	−4.9172	−4.6161	−0.8993	−0.96
W(CC$_6$H$_4$-4-pyr)(dmpe)$_2$Cl	−4.8057	−4.5689	−0.7983	−1.01
W(CC$_6$H$_4$-4-pip)(dmpe)$_2$Cl	−5.0228	−4.6606	−1.0222	−0.92

[a] V vs $FeCp_2$

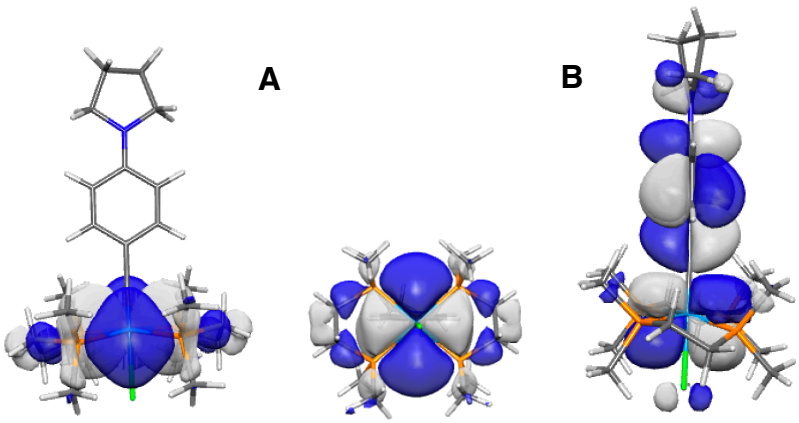

Figure 3.8. Connectivity and electronic structure (isovalue = 0.05) of W(CC$_6$H$_4$-4-pyr)(dmpe)$_2$Cl for the (A) HOMO and (B) LUMO.

Table 3.11. Computed orbital energies (eV) and predicted oxidation potentials (V vs $FeCp_2$) of $W(CAr)L_4X$ compounds with mixed substitutions.

Compound	HOMO-1	Symmetry	HOMO	Symmetry	LUMO	Sym.	Calc. $E_{1/2}$
$W(CPh)\{P(OMe)_3\}_4Cl$	−5.7560	π(WCAr)	−5.5780	d_{xy}	−1.5860	π*(WCAr)	−0.03
$W(CC_6H_4\text{-}4\text{-}OCH_3)\{P(OMe)_3\}_4Cl$	−5.5360	π(WCAr)	−5.5114	d_{xy}	−1.3501	π*(WCAr)	−0.09
$W(CC_6H_4\text{-}4\text{-}pyr)\{P(OMe)_3\}_4Cl$	−5.3768	d_{xy}	−5.1009	π(WCAr)	−1.1015	π*(WCAr)	−0.22
$W(CPh)(dppe)_2Cl$	−5.6461	π(WCAr)	-4.9174	d_{xy}	−1.5767[a]	π*(WCAr)	−0.67
$W(CC_6H_4\text{-}4\text{-}OCH_3)(dppe)_2Cl$	−5.4312	π(WCAr)	-4.8551	d_{xy}	−1.3887	Mixed[b]	−0.73
$W(CC_6H_4\text{-}4\text{-}pyr)(dppe)_2Cl$	−5.0374	π(WCAr)	-4.7383	d_{xy}	−1.2615	π*(dppe)[c]	−0.84
$W(CPh)(dmpe)_2Cl$	−5.4296	π(WCAr)	-4.7974	d_{xy}	−1.3215	π*(WCAr)	−0.78
$W(CC_6H_4\text{-}4\text{-}pyr)(dmpe)_2F$	−4.5191	π(WCAr)	-4.4888	d_{xy}	−0.5119	π*(WCAr)	−1.09
$W(CPh)(depe)_2Cl$	−5.3270	π(WCAr)	-4.6260	d_{xy}	−1.2440	π*(WCAr)	−0.95
$W(CC_6H_4\text{-}4\text{-}pyr)(depe)_2Cl$	−4.7360	π(WCAr)	-4.4118	d_{xy}	−0.7341	π*(WCAr)	−1.16

[a] LUMO+1 (−1.3660 eV) is orbital of π*(dppe)-symmetry. [b] Mixed symmetry between π*(WCAr) and π*(dppe); an orbital with π*(dppe) symmetry is located at LUMO+1 (−1.3489 eV). [c] An orbital of π*(WCAr) symmetry is located at LUMO+2 (−1.1726 eV).

3.2.3. Computationally predicted ground-state oxidation potentials for $[W(CAr)L_4X]^-$ compounds. We were interested in studying the properties of anionic tungsten-alkylidyne complexes of the form $[W(CAr)L_4X]^-$, in which the negative charge is localized on an Ar substituent or the X ligand (Figure 3.9A), because we hypothesized that this could have profound impacts on the HOMO and/or LUMO orbital energy. Because gas-phase DFT calculations, such as those used in earlier empirical correlations for neutral compounds,[2] will not be suitable for extension to charged compounds, we used the computational Born-Haber approach from the collaboration with the Batista group (Figure 3.9B).[4] The computational methodology is described in Section 3.4.

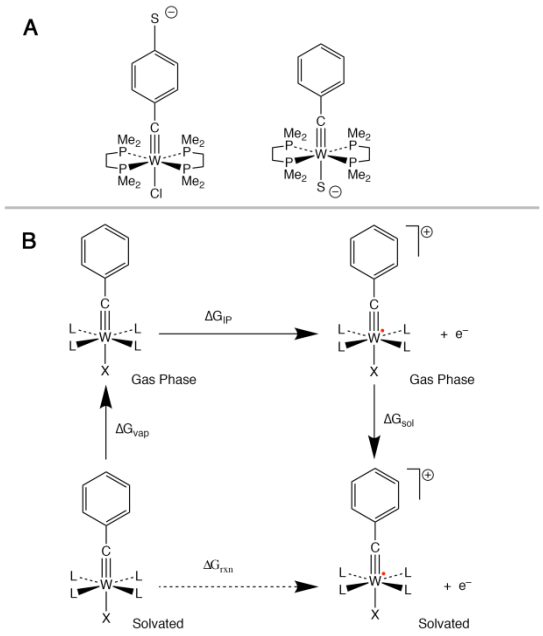

Figure 3.9. (A) Anionic d^2 tungsten-benzylidyne compounds studied in this section; (B) Born-Haber scheme used in these calculations.

The calculated thermodynamic quantity ΔG_{ox} is determined as the sum of the calculated gas-phase ionization potential, enthalpy of solvation, and enthalpy of vaporization. The difference between this free energy and that calculated for the reference compound

W(CPh)(dmpe)$_2$Cl is then applied to the experimental value of $E_{1/2}^{0/+}$ for W(CPh)(dmpe)$_2$Cl to provide the calculated oxidation potential. The results of these calculations are shown in Table 3.12. The utility of this approach for charged compounds is indicated by the fact that the calculated and experimental oxidation potentials of [W(CPh)(dppe)$_2$(NCMe)]$^+$ differ by only 0.04 V.[4] The hypothetical anionic tungsten-alkylidyne compounds studied were [W(CC$_6$H$_4$-4-S)(dmpe)$_2$Cl]$^-$ ($E_{1/2}^{calc}$ = –1.09 V) and [W(CPh)(dmpe)$_2$S]$^-$ ($E_{1/2}^{calc}$ = –1.75 V), which are envisioned products of deprotonation of W(CC$_6$H$_4$-4-SH)(dmpe)$_2$Cl and W(CPh)(dmpe)$_2$(SH), respectively. Both are substantially stronger reductants than W(CPh)(dmpe)$_2$Cl. For X = S$^-$, the local negative charge from the S$^-$ ligand is much closer to the d_{xy} redox orbital than for the 4-S$^-$ substituent. This accounts for the large difference in oxidation potentials between the two compounds.

Table 3.12. Calculated ΔG (kcal mol^{-1}) terms and oxidation potentials (V vs FeCp$_2$) for tungsten-alkylidyne compounds.

Chromophore	ΔG_{IP}[a]	ΔG_{vap}[a]	ΔG_{sol}[a]	$E_{1/2}$ (calc.)[b]	$E_{1/2}$ (expt)[c]
W(CPh)(dmpe)$_2$Cl	118.638	14.246	−44.464	N/A	−0.82
[W(CPh)(dppe)$_2$(NCMe)]$^+$	167.810	57.720	−124.590	−0.28[d]	−0.24
[W(CC$_6$H$_4$-4-S)(dmpe)$_2$Cl]$^-$	47.354	52.326	−17.436	−1.09	N/A
[W(CPh)(dmpe)$_2$S]$^-$	35.784	44.427	−13.257	−1.75	N/A

[a] ΔG_{IP} = Ionization potential, ΔG_{sol} = Free energy of solvation, ΔG_{vap} = Free energy of vaporization; [b] Calculated using the method outlined in Ref. 4; $\Delta G_{rxn} = \Delta G_{IP} + \Delta G_{sol} + \Delta G_{vap}$; $E_{1/2}(calc) = \Delta G_{rxn} - \Delta G_{WCPhdmpe2Cl} - 0.82$; [c] Measured in Ref. 2; [d] From Ref. 4; Replicated in these studies to ensure method validity.

3.2.4 Computational prediction of absorption and luminescence band energies *via* low-level descriptors. While simple computational approaches have been shown to accurately predict the oxidation potentials of W(CAr)L$_4$X compounds, correspondingly simple methods for predicting the electronic-spectroscopic properties of these compounds have not been explored. Standard methods for calculating excited-state energies involve multi-reference methodologies such as time-dependent density-functional theory (TD-DFT) or coupled cluster methods (TD-

CC).[15] These methods are typically computationally expensive and laborious. In many instances, solvent interactions must also be considered, which increases the cost. In contrast to those methods, a semi-empirical approach that uses a simple computational descriptor would find great utility in the design of further tungsten-alkylidyne molecules. Of particular relevance to photoredox properties are the absorption maximum, emission maximum, and photoredox excited-state energies.

Simplistically, the energy of the characteristic $^1[d_{xy}\rightarrow\pi^*(WCAr)]$ (HOMO→LUMO) band of $W(CAr)L_4X$ complexes[1] should be related to the HOMO–LUMO energy gap provided by a gas-phase DFT calculation of the type used for predictions of the oxidation potential. The relationship is, of course, more complicated because of the state energy is influenced by electron-pairing terms, as evidenced by the fact that the corresponding triplet state lies lower in energy, but these might be constant within a series of related complexes. The compounds used in the attempted correlation, along with their absorption energies and calculated HOMO-LUMO gaps, are shown in Table 3.13. The correlation between the observed energy of the $^1[d_{xy}\rightarrow\pi^*(WCAr)]$ band maximum and calculated d_{xy}–π^*(WCAr) HOMO-LUMO energy gap is shown in Figure 3.10. The band energies were found to correlate linearly with the HOMO-LUMO gap across a wide array of functionalities (L, CAr, or X) from 17 tungsten-alkylidyne compounds (slope = 1.37 intercept = 0.19, $r^2 = 0.96$). The correlation is in excellent agreement over a 0.93 V range of absorption energies. The methodology appears to also work well for a charged molecule, $[W(CPh)(dppe)_2(CH_3CN)]^+$. The correlation also includes $W(CC_6H_4\text{-}4\text{-}pyr)\{P(OMe)_3\}_4Cl$, for which the d_{xy} orbital was determined to be the HOMO–1 and the HOMO is π(WCAr), which is the reverse of all other compounds.

Table 3.13. Experimental $^1[d_{xy}\rightarrow\pi^*(WCAr)]$ absorption band maxima and computed d_{xy}–$\pi^*(WCAr)$ HOMO-LUMO gap (ΔE) for tungsten-alkylidyne compounds.

#	Compound	λ_{abs} (nm)[a]	$E_{max,abs}$ (eV)	ΔE (calc, eV)
36	$W(CC_6H_4\text{-}4\text{-pyr})\{P(OMe)_3\}_4Cl$	409	3.03	4.275
37	$W(CC_6H_4\text{-}4\text{-}OCH_3)\{P(OMe)_3\}_4Cl$	428	2.90	4.161
26	$W(CPh)\{P(OMe)_3\}_4Cl$	449	2.76	3.992
38	$W(CC_6H_4\text{-}4\text{-pyr})(dmpe)_2F$	455	2.72	3.977
35	$W(CC_6H_4\text{-}4\text{-pyr})(dmpe)_2Cl$	485	2.56	3.771
39	$W(CC_6H_4\text{-}4\text{-pyr})(depe)_2Cl$	492	2.52	3.678
33	$W(CPh)(dmpe)_2F$	500	2.48	3.481
34	$W(CMes)(dmpe)_2Cl$	505	2.46	3.703
40	$W(CC_6H_4\text{-}4\text{-}OCH_3)(dmpe)_2Cl$	503	2.46	3.649
41	$W(CC_6H_4\text{-}4\text{-}OCH_3)(dppe)_2Cl$	505	2.45	3.466
21	$W(CPh)(dppe)_2Cl$	531	2.34	3.310
12	$W(CPh)(dmpe)_2Cl$	535	2.32	3.476
20	$W(CPh)(depe)_2Cl$	545	2.27	3.382
22	$[W(CPh)(dppe)_2(CH_3CN)]^+$	550[b]	2.25	3.156
17	$W(CPh)(PMe_3)_4Cl$	550	2.25	3.268
24	$W(CC_6H_4\text{-}4\text{-}CCSi^iPr_3)(dmpe)_2Cl$	595[c]	2.08	3.038
23	$W(CC_6H_4\text{-}4\text{-}CCH)(dmpe)_2Cl$	596[c]	2.09	3.066
42	$W(CC_6H_4\text{-}4\text{-}CCPh)(dppe)_2Cl$	604[d]	2.05	2.729
43	$W(CC_6H_4\text{-}4\text{-}CCC_6H_4\text{-}4\text{-}CCPh)(dppe)_2Cl$	623[d]	1.99	2.411

[a] UV-vis spectra shown in Section 4.4, these values were recorded in toluene solution. [b] Ref. 16 [c] Ref. 17 [d] Ref. 18.

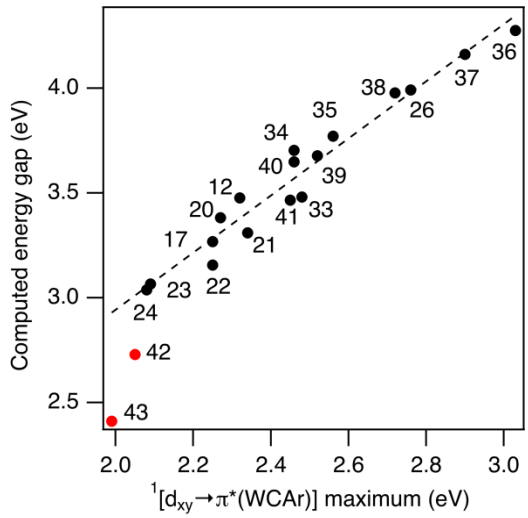

Figure 3.10. Correlation between measured absorption maxima, $^1[d_{xy}\rightarrow\pi^*(WCAr)]$, and the computed HOMO–LUMO gap. The red dots, two measurements of *oligo*-phenylene-ethynylene compounds from Ref. 18 were not included in the fit. Fit equation: $f(x) = 1.36x + 0.21$; $r^2 = 0.95$.

The model overestimates the predicted absorption band energies of compounds with extended *oligo*-phenylene-ethynylene CAr substituents.[18] We do not understand these deficiencies at present. However, with this exception the model should allow the absorption band maxima of hypothetical chromophores of this general type to be predicted.

A second important property with regard to photoredox processes is the excited-state energy, which is estimated in this work (Chapter 4) as being the wavelength at which the emission intensity along the blue flank of the band reaches 10% of its maximum value. A linear correlation between the calculated HOMO-LUMO gap and that of the $^3[d_{xy}\leftarrow\pi^*(WCAr)]$ emission maximum or onset emission energy is also plausible, based on the arguments and observations for the $^1[d_{xy}\rightarrow\pi^*(WCAr)]$ band above. The calculated and experimental values are shown in Table 3.14 and a plot of their correlation is shown in Figure 3.11. This correlation was found to be substantially worse than that of the $^1[d_{xy}\rightarrow\pi^*(WCAr)]$ vs HOMO-LUMO gap correlation. Several noteworthy outliers are $W(CMes)(dmpe)_2Cl$ and all of the dppe-containing complexes. Given this finding, the dppe-containing complexes were extracted and plotted separately. This plot is shown in Figure 3.12. The compounds with dppe equatorial ligands form a reasonable line ($r^2 = 0.98$), albeit one defined by few points. The dmpe equatorial ligands do not correlate as well as the dppe ligands. Because of these problems, and substantial differences between the emission band widths of these compounds, the onset emission energies correlate only weakly with the calculated HOMO-LUMO gap. Thus, the correlations in this section seem best suited to predicting the energy of the $^1[d_{xy}\rightarrow\pi^*(WCAr)]$ absorption bands of these complexes. This is still valuable, as it allows prediction of the excitation wavelength needed for photoredox experiments.

Table 3.14. Experimental $^3[d_{xy}\leftarrow\pi^*(WCAr)]$ emission band energies and computed d_{xy}–π^*(WCAr) HOMO-LUMO gap for tungsten-alkylidyne compounds. Emission spectra shown in Chapter 4.

#	Compound	E_{em} (max, eV)[a]	E_{00} (eV)[b]	ΔE (calc, eV)
43	$W(CC_6H_4\text{-}4\text{-}CCC_6H_4\text{-}4\text{-}CCPh)(dppe)_2Cl$	1.54[c]	*N/A*	2.411
42	$W(CC_6H_4\text{-}4\text{-}CCPh)(dppe)_2Cl$	1.60[c]	*N/A*	2.729
34	$W(CMes)(dmpe)_2Cl$	1.68	2.12	3.703
17	$W(CPh)(PMe_3)_4Cl$	1.70	1.91	3.268
20	$W(CPh)(depe)_2Cl$	1.78	2.00	3.382
12	$W(CPh)(dmpe)_2Cl$	1.78	1.98	3.476
33	$W(CPh)(dmpe)_2F$	1.82	2.06	3.481
21	$W(CPh)(dppe)_2Cl$	1.86	2.07	3.311
40	$W(CC_6H_4\text{-}4\text{-}OCH_3)(dmpe)_2Cl$	1.87	2.11	3.649
39	$W(CC_6H_4\text{-}4\text{-}pyr)(depe)_2Cl$	1.87	2.14	3.678
38	$W(CC_6H_4\text{-}4\text{-}pyr)(dmpe)_2F$	1.89	2.24	3.977
44	$W(CC_6H_4\text{-}4\text{-}pyr)(dppe)_2Cl$	1.91	2.22	3.477
41	$W(CC_6H_4\text{-}4\text{-}OCH_3)(dppe)_2Cl$	1.92	2.17	3.466
26	$W(CPh)\{P(OMe)_3\}_4Cl$	1.93	2.27	3.992
35	$W(CC_6H_4\text{-}4\text{-}pyr)(dmpe)_2Cl$	1.97	2.25	3.771
36	$W(CC_6H_4\text{-}4\text{-}pyr)\{P(OMe)_3\}_4Cl$	1.98	2.24	4.275
37	$W(CC_6H_4\text{-}4\text{-}OCH_3)\{P(OMe)_3\}_4Cl$	2.06	2.38	4.161

[a] Emission maxima recorded in toluene solution, calculated by first conversion to cm^{-1} (correcting for monochromator) and then converting to eV; [b] E_{00} is taken to be the energy at which the intensity along the blue flank of the emission band is 10% of the maximum band intensity; [c] Ref. 18.

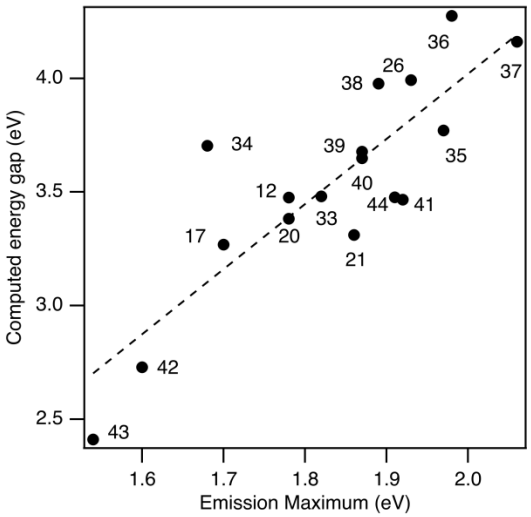

Figure 3.11. Correlation between 17 experimentally observed emission maxima, $^3[d_{xy}\leftarrow\pi^*(WCAr)]$, and the computed HOMO–LUMO gap. Fit equation: $f(x) = 2.87x - 1.71$; $r^2 = 0.72$.

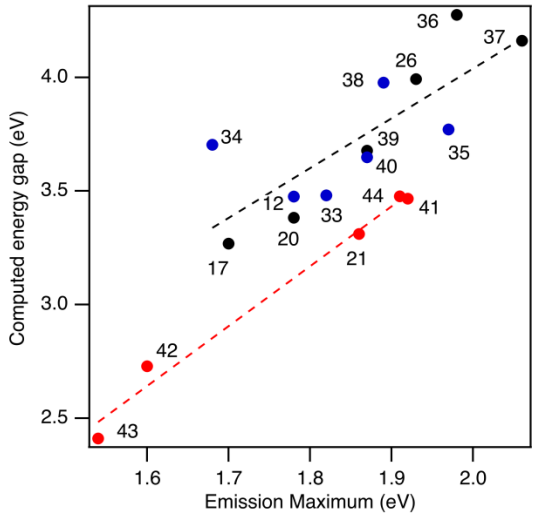

Figure 3.12. Correlation between emission maxima, $^3[d_{xy} \leftarrow \pi^*(WCAr)]$, and the computed HOMO–LUMO gap for dppe-containing compounds and all other compounds. The red dots are complexes with dppe equatorial ligands, the blue dots are compounds with dmpe equatorial ligands, and the black dots are other tungsten-alkylidyne complexes. Fit for dppe ligands: f(x) = 2.63x −1.57, r^2 = 0.98; other ligands: f(x) = 2.19x −0.34, r^2 = 0.64.

3.2.5. Predicting $E^{*/ox}$ *via* computational methods. The use of simple DFT calculations and empirical correlations to predict ground state oxidation potentials and absorption band energies of W(CAr)L_4X complexes prompted the question of whether the excited-state oxidation potential could also be predicted, which would greatly aid the design of these complexes. The simple equation tested was $E^{*/ox}(calc.) = E_{1/2}(calc.) - \Delta E(\pi^*(WCAr)–d_{xy})$, where the calculated values would be referenced to a standard chromophore (W(CPh)$(dmpe)_2$Cl). The calculated values for a selected set of tungsten-alkylidyne complexes were found to be similar to those obtained from experimental measurements, especially for complexes containing dmpe or depe ligands (Table 3.15). For the dmpe-containing complexes, those Ar = Ph and C_6H_4-4-OCH_3 substitutions agree closely with experimental observations. Those complexes containing L = dmpe with the Ar = C_6H_4-4-pyr substitution, however, perform less well, especially as the compounds become more reducing. For example, the measured

excited-state oxidation potential for W(CC_6H_4-4-pyr)(dmpe)$_2$Cl is –3.18 V; the computed value is –3.32 V. This deviation of 0.14 V is significantly higher than that for W(CC_6H_4-4-OCH_3)(dmpe)$_2$Cl (−3.05 V calc. vs −3.01 V experimental).

Table 3.15. Comparison between calculated and experimentally measured $E^{*/ox}$ values (V vs $FeCp_2$).

Compound	Calc. $E_{1/2}$ (V)	ΔE (eV)[a]	Calc. $E^{*/ox}$ (V)	Expt. $E^{*/ox}$ (V)	$E^{*/ox}$(expt.) –$E^{*/ox}$(calc.) (V)
W(CPh)(dmpe)$_2$Cl	−0.79	3.476	—	–2.80	—
W(CPh){P(OMe)$_3$}$_4$Cl	−0.03	3.992	−2.56	−2.51	0.05
W(CC_6H_4-4-pyr){P(OMe)$_3$}$_4$Cl	−0.22	4.275	−3.04	−2.58	0.46
W(CPh)(dppe)$_2$Cl	−0.69	3.310	−2.54	−2.65	0.11
W(CC_6H_4-4-OCH_3){P(OMe)$_3$}$_4$Cl	−0.09	4.161	−2.80	−2.68	0.12
W(CPh)(PMe_3)$_4$Cl	−0.83	3.268	−2.64	−2.71	–0.07
W(CC_6H_4-4-OCH_3)(dppe)$_2$Cl	−0.73	3.467	−2.74	−2.78	–0.04
W(CPh)(depe)$_2$Cl	−0.95	3.382	−2.87	−2.84	0.03
W(CC_6H_4-4-pyr)(dppe)$_2$Cl	−0.85	3.477	−2.86	−2.88	–0.02
W(CPh)(dmpe)$_2$F	−0.92	3.481	−2.94	−2.97	–0.03
W(CMes)(dmpe)$_2$Cl	−0.84	3.703	−3.08	−2.99	0.09
W(CC_6H_4-4-OCH_3)(dmpe)$_2$Cl	−0.86	3.649	−3.05	−3.01	0.04
W(CC_6H_4-4-pyr)(depe)$_2$Cl	−1.16	3.678	−3.38	−3.10	0.28
W(CC_6H_4-4-pyr)(dmpe)$_2$Cl	−1.01	3.771	−3.32	−3.18	0.14
W(CC_6H_4-4-pyr)(dmpe)$_2$F	−1.09	3.977	−3.60	−3.26	0.34

[a] $\Delta E = \pi^*(WCAr)$ (calc., eV) – d_{xy} (calc., eV).

The excited-state oxidation potential can be readily predicted for nearly all of the tungsten-alkylidyne compounds which are known to perform adequately in the ground-state oxidation potential correlation. The group of complexes that were screened for ground-state oxidation potentials can now be screened for their excited-state oxidation potentials *via* application of this inexpensive computational descriptor. Even though all of the correlations are not in perfect agreement with experiment, this low-level technique provides a good screening technique for the development of other photoredox chromophores. Selected compounds that were screened for $E^{*/ox}$ are shown in Table 3.16.

Table 3.16. Computational screen of $E^{*/ox}$ for tungsten-alkylidyne complexes (V vs $FeCp_2$).

Compound	$E_{1/2}^{calc}$ (V)	ΔE (V)[a]	$E^{*/ox}$ (calc., V)
$W(CPh)(dmpe)_2OCH_3$	−0.92	3.645	−3.10
$W(CPh)(dmpe)_2SCH_3$	−0.84	3.291	−2.67
$W(CPh)(dmpe)_2H$	−0.98	3.453	−2.97
$W(CPh)(dmpe)_2CH_3$	−0.95	3.471	−2.96
$W(CPh)(dppbz)_2Cl$	−0.57	3.381	−2.49
$W(CPh)(dipe)_2Cl$	−1.02	3.139	−2.70
$W(CPh)(tmeda)_2Cl$	−2.41	2.371	−3.32
$W(CC_6H_4\text{-}4\text{-}CH_3)(dmpe)_2Cl$	−0.78	3.522	−2.89
$W(CC_6H_4\text{-}4\text{-}NH_2)(dmpe)_2Cl$	−0.92	3.696	−3.16
$W(CC_6H_4\text{-}4\text{-}N(CH_3)_2)(dmpe)_2Cl$	−0.96	3.717	−3.22
$W(CC_6H_4\text{-}4\text{-}pip)(dmpe)_2Cl$	−0.92	3.638	−3.10

[a] $\Delta E = \pi^*(WCAr)$ (calc., eV) – d_{xy} (calc., eV).

None of the complexes studied were predicted to be significantly more reducing than $W(CC_6H_4\text{-}4\text{-}pyr)(dmpe)_2Cl$. The complex predicted to be the most reducing in the ground state, $W(CPh)(tmeda)_2Cl$, is also computed to have an exceptionally reducing excited-state. However, the energy of the excited state is also predicted to be exceptionally low in energy. This low-energy excited-state may be a problem for compounds whose luminescence properties obey the energy-gap law, where $\Delta E \propto \ln(k_{nr})$. The energy gap may be so low for this complex that either the lifetime is very short or the complex is not luminescent.

3.3. Conclusions.

These computational methods have enabled the understanding and design of a large number of $W(CAr)L_4X$ compounds. Ground-state oxidation potentials of these chromophores have been studied by extensions of methods developed by the Hopkins group and others. It was shown that the oxidation potentials of these compounds are additive about their positions and can be approximated easily using physical parameters. The ground-state oxidation potentials can be easily approximated using both a low-level computational descriptor (the HOMO orbital energy)

or by calculating the ΔG for the oxidation reaction. Each method, as outlined, has utility in different aspects of the design of photoredox chromophores. The HOMO orbital correlation was instrumental in the design photoredox chromophores as a mechanism to easily screen potential synthesis candidates. The Born-Haber approach provides a more accurate picture and tolerates tungsten-alkylidyne molecules with more unusual properties (e.g. anionic, etc.). Furthermore, the development of a computational method to screen the excited-state oxidation potentials of these complexes by application of two computational descriptors (HOMO energy and HOMO-LUMO gap) that provide insight into the excited-state oxidation potentials of a large number of tungsten-alkylidyne compounds was discussed. Hopefully, this work will be the first in a line of attempts to continue to optimize the excited-state oxidation potentials and properties of these compounds, and that application of these computational descriptors that are readily accessible aids to the design of even more reducing photoredox chromophores.

3.4. Experimental Section.

3.4.1 Methodology for ligand additive parameters. Electrochemical parameters (ρ_L, ρ_R, and ρ_X) are calculated relative to a standard L, R, and X ligand. The ligand selected was based on the number of available substituents. The standard L ligand is 1,2-bis(dimethylphosphino)ethane (dmpe), the standard R ligand is C–H, and Cl is the standard for X. Parameters ρ_L, ρ_R, and ρ_X were calculated based on oxidation potential and compositional differences between compounds as expressed by Equations 3.1–3.3:

$$\rho_L(L) = \frac{\left(E_L - E_{dmpe}\right)}{B} \quad (3.1)$$

$$\rho_R(R) = E_R - E_{CH} \quad (3.2)$$

$$\rho_X(X) = E_X - E_{Cl} \quad (3.3)$$

where E is the redox potential and B is the number of times the ligand appears. For example, the only difference between $W(CH)(dmpe)_2Cl$ and $W(CPh)(dmpe)_2Cl$ is in the R parameter. Subtraction of the oxidation potential for $W(CPh)(dmpe)_2Cl$ from $W(CH)(dmpe)_2Cl$ provides the parameter ρ_R (CPh). The calculated oxidation potential of a tungsten-alkylidyne compound is the sum of the ligand parameters multiplied by the number of times that ligand appears (*B)* (Equation 3.4),

$$E_{calc} = A + \sum_{m}^{n} B_n(\rho_n) = A + B_L\rho_L + B_R\rho_R + B_X\rho_X \quad (3.4)$$

where $B_R = B_X = 1$ and A is –0.84 V. The electrochemical parameters were determined or used from previously reported oxidation potentials (Table 3.1). Parameters with multiple measurements were averaged to obtain a single value. Electrochemical parameters with only one measured value were calculated for comparison purposes only and are denoted with an asterisk (ρ^*). For the dicarbonyl derivatives, calculations referenced ρ^*_L(dppe) obtained from $W(CPh)(dppe)_2Cl$ per equation 3.5:

$$\rho_L^*(CO) = \frac{\Delta E + 2\rho_L^*(dppe)}{2} \quad (3.5)$$

The ρ^*_L values for the remainder of the $W(CR)L_2(CO)_2X$ compounds were determined relative to $W(CPh)(dppe)(CO)_2Cl$ by using Equation 3.5. The derived parameters for ρ^*_L, ρ^*_R, and ρ^*_X are shown in Tables 3.2 – 3.5.

3.4.2. Computational methodology. DFT calculations were performed using Gaussian 09[19] or Gaussian 16.[20] Calculations employed the B3P86 functional, which according to benchmarks ranks among the best functionals for predicting the molecular structures of third-row transition-metal complexes.[21] Geometries were optimized without symmetry constraints (**nosymm** keyword). No imaginary frequencies were obtained in subsequent vibrational

calculations, confirming that the optimized structures reside at potential-surface minima. Atoms H–Cl were optimized using Dunning double-ζ potentials with polarizations on p and d.[22, 23] Atoms with mass greater than Cl were described using the LANL2DZ basis set and effective core potential. Calculations utilizing the Born-Haber methodology were optimized using the B3LYP functional. Atoms H, C, and P were optimized using 6-311G(p,d). Atoms W, S, and Cl were described using the LANL2DZ basis set and effective core potential.

Calculation of the local minimum energy structure of $W(CAr)L_4X$ compounds proceeded *via* incremental modification of parent $W(CAr)(L)_4X$ calculated structures. After calculation of the minimum energy structure, as confirmed by a vibrational analysis, a single point calculation using the keyword **pop=full** provided the molecular orbital energy levels; rendering of the orbitals was affected by the creation of a formatted checkpoint file (.fchk); command **formchk -2 programname.chk**. Visualization of the molecular orbitals was affected in IQmol (www.iqmol.org). Typical symmetries of the HOMO–1, HOMO, and LUMO are shown in Figure 3.3 for $W(CPh)(dmpe)_2Cl$. Atomic parentages were calculated using AOMix, version 6.94b (http://www.sg-chem.net/aomix/).

3.4.3. Computational prediction of $E^{*/ox}$. In this method, the ground-state oxidation potential of a tungsten-alkylidyne compound is predicted from the equation $E_{pred} = -0.97E_{dxy} - 5.44$,[2] the calculated energy gap ($E_{\pi^*} - E_{dxy}$) is subtracted from the calculated potential, and the resulting value is are corrected using $W(CPh)(dmpe)_2Cl$ as a calibration standard ($E^{*/ox} = -2.80$ V).

3.5. References.

1. Da Re, R. E.; Hopkins, M. D. *Coord. Chem. Rev.* **2005**, *249*, 1396-1409.

2. Haines, D. E.; O'Hanlon, D. C.; Manna, J.; Jones, M. K.; Shaner, S. E.; Sun, J.; Hopkins, M. D. *Inorg. Chem.* **2013**, *52*, 9650-9658.

3. Orbital parentages were calculated using AOMix, version 6.94b.

4. Rudshteyn, B.; Vibbert, H. B.; May, R.; Wasserman, E.; Warnke, I.; Hopkins, M. D.; Batista, V. S. *ACS Catal.* **2017**, *7*, 6134-6143.

5. Lever, A. B. P. *Inorg. Chem.* **1990**, *29*, 1271-1285.

6. Pombeiro, A. J. L. *J. Organomet. Chem.* **2005**, *690*, 6021-6040.

7. Pombeiro, A. J. L. *Eur. J. Inorg. Chem.* **2007**, 1473-1482.

8. Masui, H.; Lever, A. B. P. *Inorg. Chem.* **1993**, *32*, 2199-2201.

9. Fielder, S. S.; Osborne, M. C.; Lever, A. B. P.; Pietro, W. J. *J. Am. Chem. Soc.* **1995**, *117*, 6990-6993.

10. Bursten, B. E. *J. Am. Chem. Soc.* **1982**, *104*, 1299-1304.

11. Zhang, L.; Gamasa, M. P.; Gimeno, J.; da Silva, M.; Pombeiro, A. J. L.; Graiff, C.; Lanfranchi, M.; Tiripicchio, A. *Eur. J. Inorg. Chem.* **2000**, 1707-1715.

12. Furno, F.; Fox, T.; Schmalle, H. W.; Berke, H. *Organometallics* **2000**, *19*, 3620-3630.

13. Manna, J.; Geib, S. J.; Hopkins, M. D. *Angew. Chem., Int. Ed. Engl.* **1993**, *32*, 858-861.

14. Hansch, C.; Leo, A.; Taft, R. W. *Chem. Rev.* **1991**, *91*, 165-195.

15. Adamo, C.; Jacquemin, D. *Chem. Soc. Rev.* **2013**, *42*, 845-856.

16. Lovaasen, B. M.; Lockard, J. V.; Cohen, B. W.; Yang, S.; Zhang, X.; Simpson, C. K.; Chen, L. X.; Hopkins, M. D. *Inorg. Chem.* **2012**, *51*, 5660-5670.

17. John, K. D. Electronic materials based on metal-acetylide complexes. Ph.D. Dissertation, University of Pittsburg, Pittsburg, PA, 1998.

18. O'Hanlon, D. C.; Cohen, B. W.; Moravec, D. B.; Dallinger, R. F.; Hopkins, M. D. *J. Am. Chem. Soc.* **2014**, *136*, 3127-3136.

19. M. J. Frisch, G. W. T., H. B. Schlegel, G. E. Scuseria, M. A. Robb, J. R. Cheeseman, G. Scalmani, V. Barone, G. A. Petersson, H. Nakatsuji, X. Li, M. Caricato, A. Marenich, J. Bloino, B. G. Janesko, R. Gomperts, B. Mennucci, H. P. Hratchian, J. V. Ortiz, A. F. Izmaylov, J. L.

Sonnenberg, D. Williams-Young, F. Ding, F. Lipparini, F. Egidi, J. Goings, B. Peng, A. Petrone, T. Henderson, D. Ranasinghe, V. G. Zakrzewski, J. Gao, N. Rega, G. Zheng, W. Liang, M. Hada, M. Ehara, K. Toyota, R. Fukuda, J. Hasegawa, M. Ishida, T. Nakajima, Y. Honda, O. Kitao, H. Nakai, T. Vreven, K. Throssell, J. A. Montgomery, Jr., J. E. Peralta, F. Ogliaro, M. Bearpark, J. J. Heyd, E. Brothers, K. N. Kudin, V. N. Staroverov, T. Keith, R. Kobayashi, J. Normand, K. Raghavachari, A. Rendell, J. C. Burant, S. S. Iyengar, J. Tomasi, M. Cossi, J. M. Millam, M. Klene, C. Adamo, R. Cammi, J. W. Ochterski, R. L. Martin, K. Morokuma, O. Farkas, J. B. Foresman, and D. J. Fox *Gaussian 09*, Revision A.02; Gaussian, Inc.: 2016.

20. Frisch, M. J. T., G. W.; Schlegel, H. B.; Scuseria, G. E.; Robb, M. A.; Cheeseman, J. R.; Scalmani, G.; Barone, V.; Petersson, G. A.; Nakatsuji, H.; Li, X.; Caricato, M.; Marenich, A. V.; Bloino, J.; Janesko, B. G.; Gomperts, R.; Mennucci, B.; Hratchian, H. P.; Ortiz, J. V.; Izmaylov, A. F.; Sonnenberg, J. L.; Williams-Young, D.; Ding, F.; Lipparini, F.; Egidi, F.; Goings, J.; Peng, B.; Petrone, A.; Henderson, T.; Ranasinghe, D.; Zakrzewski, V. G.; Gao, J.; Rega, N.; Zheng, G.; Liang, W.; Hada, M.; Ehara, M.; Toyota, K.; Fukuda, R.; Hasegawa, J.; Ishida, M.; Nakajima, T.; Honda, Y.; Kitao, O.; Nakai, H.; Vreven, T.; Throssell, K.; Montgomery, J. A., Jr.; Peralta, J. E.; Ogliaro, F.; Bearpark, M. J.; Heyd, J. J.; Brothers, E. N.; Kudin, K. N.; Staroverov, V. N.; Keith, T. A.; Kobayashi, R.; Normand, J.; Raghavachari, K.; Rendell, A. P.; Burant, J. C.; Iyengar, S. S.; Tomasi, J.; Cossi, M.; Millam, J. M.; Klene, M.; Adamo, C.; Cammi, R.; Ochterski, J. W.; Martin, R. L.; Morokuma, K.; Farkas, O.; Foresman, J. B.; Fox, D. J. *Gaussian 16*, Gaussian, Inc.: Wallingford, CT, 2016.

21. Bühl, M.; Reimann, C.; Pantazis, D. A.; Bredow, T.; Neese, F. *J. Chem. Theory Comput.* **2008**, *4*, 1449-1459.

22. Dunning, T. H.; Hay, P. J. *Methods of Electronic Structure Theory*; Schaefer, H. F., Ed.; Plenum Press: New York, 1977; Vol. 2.

23. Magnusson, E.; Schaefer, H. F. I. *J. Chem. Phys.* **1985**, *83*, 5721-5726.

CHAPTER 4

Ground- and excited-state properties of tungsten-alkylidyne complexes

Note: Portions of this work have been published in an alternative format in Rudshetyn, B.; Vibbert, H.B.; May, R.; Wasserman, E.; Warnke, I.; Hopkins, M.D. *ACS Catalysis* **2017**, *7*, 6134-6143.

4.1. Introduction.

Since tungsten-alkylidyne complexes were first recognized as luminescent in fluid solution,[1] their ground- and excited-state properties have served as active components in conjugated molecular wires[2] and assemblies for artificial photosynthesis.[3, 4] These prior studies suggested that $W(CAr)L_4X$ molecules could serve as highly reducing photoredox chromophores, based on measurements of their ground-state redox potentials and excited-state energies, but no prior work had characterized the ability of $W(CAr)L_4X$ complexes to serve as sensitizers in bimolecular photoredox reactions. The recent renaissance of photoredox catalysis in organic synthesis suggested that a more in-depth study of the electrochemical and photophysical properties of these chromophores, relevant to their potential photocatalytic activity was warranted.

Key quantities that determine the potential applications of a photoredox chromophore are its excited-state oxidation ($E^{*/ox}$) or reduction ($E^{*/red}$) potentials. For $E^{*/ox}$, which is the quantity relevant to the present work, a reasonable estimate can typically be provided from measurements of the ground-state oxidation potential (E^{ox}) and excited-state energy (E_{00}) *via* the equation $E^{*/ox} = E^{ox}–E_{00}$. More rigorously, the excited-state oxidation potential can be determined by analysis

of the free-energy relationship for electron-transfer quenching rate constants. Thus, systematic measurement of the ground-state oxidation potentials, excited-state energies, and electron-transfer rate constants of $W(CAr)L_4X$ complexes are required to fully assess their excited-state oxidation potentials.

Electronic-absorption, emission band profiles, maxima, excited-state lifetimes, and quantum efficiencies are also important quantities for characterizing photoredox chromophores. A general reaction scheme of relevant photoredox excitation and electron-transfer events is shown in Figure 4.1. The lowest absorption band determines the longest wavelengths of light required to access the reactive excited state, the emission band profile provides an estimate of the excited-state energy, and the excited-state lifetime and quantum yield set limits on the minimum rate constant possible for a bimolecular electron-transfer event and characterize the efficiency of nonradiative decay channels.

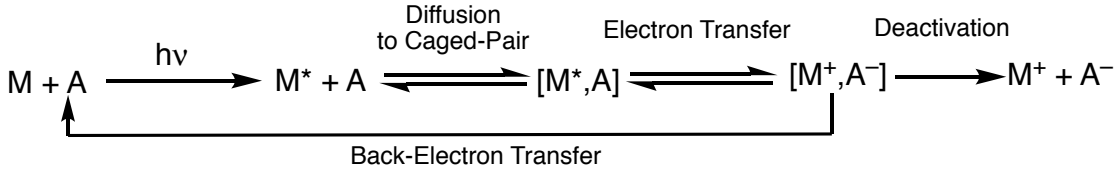

Figure 4.1. General process for a productive photoinduced electron-transfer reaction.

This chapter describes the characterization of these fundamental properties of a class of $W(CAr)L_4X$ complexes. Specifically, ground-state oxidation potentials were measured and interpreted, electronic absorption and emission spectra and photophysical properties were studied in non-polar and polar solvents, and excited-state oxidation potentials were estimated from the quantities derived from these. Additionally, the excited-state oxidation potentials of two chromophores are determined from analysis of kinetic data provided by electron-transfer quenching experiments. It was found that the measured values of $E^{*/ox}$ are in good agreement with those estimated from the ground-state oxidation potential and excited-state energy. The

results show that $W(CAr)L_4X$ photoredox chromophores are the most powerful reductants that can be activated using visible-light excitation.

4.2. Results and Discussion.

4.2.1. Ground-state oxidation potentials of $W(CR)L_4X$ compounds. An earlier study in our group reported the oxidation potentials of 32 complexes of the general form $W(CR)L_2L'_2X$, and found that these potentials were correlated linearly with the calculated energy of the d_{xy} HOMO (and redox orbital) provided by DFT.[5] One goal of the present project was to investigate the effects of axial CR and X substitution that were not encompassed in the prior study.[5] The compounds studied were divided into three main categories: (i) $W(CR)(PP)_2Cl$ (PP = bidentate phosphine); (ii) $W(CAr)\{P(OMe)_3\}_4Cl$; and (iii) $W(CPh)L_2(CO)_2Cl$. The potentials were measured by cyclic voltammetry (CV) and/or differential pulse voltammetry (DPV); for the former, the electrochemical reversibility of the process was quantified by Randles-Sevcik analysis. The $W(CAr)(PP)_2Cl$ complexes were found to possess reversible oxidations. The data for $W(CPh)(dmpe)_2Cl$, recorded in THF solution, is shown in Figure 4.2 as a representative example for the class of reversible compounds. The Randles-Sevcik plots are characterized by good linear fits ($r^2 > 0.98$) with slopes nearly always equal but opposite in sign. Those compounds of the types $W(CAr)\{P(OMe)_3\}_4Cl$ and $W(CPh)L_2(CO)_2Cl$ were found to exhibit either irreversible or quasi-reversible reduction potentials at room temperature. Data for all compounds in this study are shown in Section 4.4 (Figures 4.10-4.27) and the oxidation potentials are set out in Table 4.1. The entries include a few compounds from the earlier study that were remeasured to check for consistency.

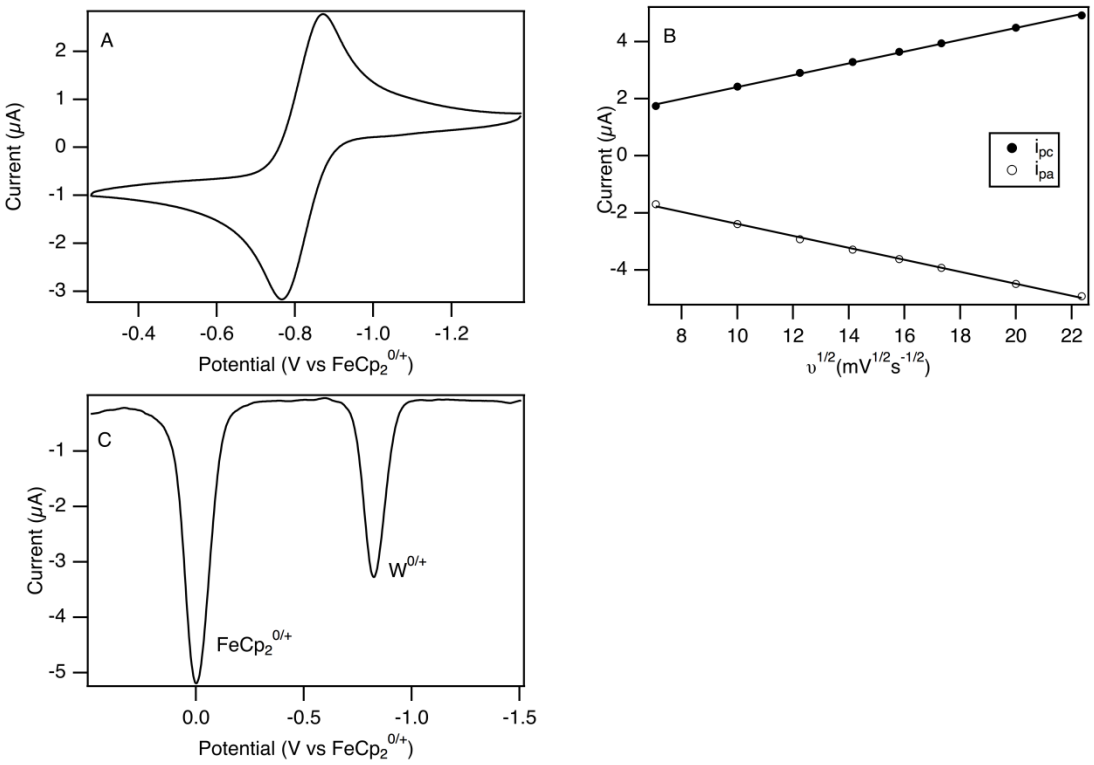

Figure 4.2. Electrochemical data for W(CPh)(dmpe)$_2$Cl in THF solution with 0.1 M [^{n}Bu$_4$N][PF$_6$]: (A) CV (200 mV s^{-1}); (B) Randles-Sevcik plot: i_{pc}, f(x) = 0.21x + 0.34, r^2 = 0.99; ip_a, f(x) = –0.21x – 0.28, r^2 = 0.99; (C) DPV.

The expanded range of W(CAr)L$_4$X compounds provided new insights into the substituent-dependence of the oxidation potentials. Several W(CAr)L$_4$Cl (L = ½ dmpe, ½ dppe, P(OMe)$_3$) compounds included CAr ligands bearing electron-donor groups (Ar = Ph, Mes, C$_6$H$_4$-4-OCH$_3$, and C$_6$H$_4$-4-pyr). These compounds were observed to possess oxidation potentials lower than the parent benzylidyne compounds and lie in an order consistent with the relative electron-donating ability of the substituent. Two W(CAr)(dmpe)$_2$F compounds were measured. Both possess electrochemically reversible oxidation potentials, in contrast to the quasi-reversible oxidation observed in the earlier study for W(CH)(dmpe)$_2$F.[5] Their potentials are shifted negative of those of the chloro derivatives by –0.09 V, consistent with it being a stronger electron donor. The oxidation potential of W(CPh)(dmpe)$_2$Cl was measured in acetonitrile and dichloromethane to determine their differences from THF. The differences were small: THF = –

0.82 V vs $FeCp_2^{0/+}$, CH_3CN = –0.84 V, CH_2Cl_2 = –0.86 V. Thus, values of $E^{*/ox}$ determined from measurements in THF will be good approximations of those in other solvents.

Table 4.1. Ground-state oxidation potentials of $W(CR)L_4X$ compounds (V vs $FeCp_2$).[a]

Compound	$E_{1/2}^{0/+}$	Figure
$W(CBu^t)(PMe_3)_4Cl$	–0.93	4.10
$W(CPh)(pic)_2(CO)_2Cl$	0.32[b]	4.11
$W(CPh)(dppe)(CO)_2Cl$	0.68[c]	4.12
$W(CPh)(tmeda)(CO)_2Cl$	0.40[c]	4.13
$W(CPh)\{P(OMe)_3\}_4Cl$	–0.24[c]	4.14
$W(CC_6H_4\text{-}4\text{-}OCH_3)\{P(OMe)_3\}_4Cl$	–0.30[c]	4.15
$W(CC_6H_4\text{-}4\text{-}pyr)\{P(OMe)_3\}_4Cl$	–0.34[c]	4.16
$W(CPh)(dmpe)_2Cl$	–0.82	4.2
$W(CPh)(dmpe)_2Cl$ (CH_3CN solution)	–0.84	4.17
$W(CPh)(dmpe)_2Cl$ (DCM solution)	–0.86	4.18
$W(CMes)(dmpe)_2Cl$	–0.86	4.20
$W(CC_6H_4\text{-}4\text{-}OCH_3)(dmpe)_2Cl$	–0.90	4.21
$W(CC_6H_4\text{-}4\text{-}pyr)(dmpe)_2Cl$	–0.93	4.23
$W(CC_6H_4\text{-}4\text{-}NH_2)(dmpe)_2Cl$	–0.92	4.27
$W(CPh)(depe)_2Cl$	–0.84	Ref. 5
$W(CC_6H_4\text{-}4\text{-}pyr)(depe)_2Cl$	–0.95	4.24
$W(CPh)(dppe)_2Cl$	–0.58	Ref. 5
$W(CC_6H_4\text{-}4\text{-}OCH_3)(dppe)_2Cl$	–0.61	4.22
$W(CC_6H_4\text{-}4\text{-}pyr)(dppe)_2Cl$	–0.66	4.25
$W(CPh)(dmpe)_2F$	–0.91	4.19
$W(CC_6H_4\text{-}4\text{-}pyr)(dmpe)_2F$	–1.02	4.26

[a] Potentials recorded in 0.1 M $[^nBu_4N]PF_6$ THF solution unless otherwise noted. Redox couples were observed to be reversible from 50 mV s^{-1} to 500 mV s^{-1} and determined by CV, unless otherwise noted. [b] Quasi-reversible, potential determined by DPV; [c] Irreversible, potential determined by DPV.

4.2.2. Electronic spectroscopy and photophysical properties. The electronic spectra and luminescence properties of $W(CAr)L_4X$ complexes were measured to determine if they fulfill the criteria for useful photoredox chromophores and to understand the factors that control these properties. The absorption and emission spectra of one representative complex, $W(CPh)(dmpe)_2Cl$ in toluene solution, is shown in Figure 4.3. Plots of the other studied compounds are shown in Section 4.4 (Figures 4.28-4.52). Band maxima are set out in Table 4.2. The lowest-energy electronic absorption band of these complexes has been previously identified

as arising from the $^1[d_{xy}\rightarrow\pi^*(WCAr)]$ (HOMO→LUMO) transition (λ_{max} = 535 nm for $W(CPh)(dmpe)_2Cl$).[6] To higher energy is the much stronger $^1[\pi(WCAr)\rightarrow\pi^*(WCAr)]$ band (338 nm). The luminescence has been assigned to the $^3[d_{xy}\leftarrow\pi^*(WCAr)]$ transition. It overlaps with the $^1[d_{xy}\rightarrow\pi^*(WCAr)]$, as expected for a transition between the same orbitals.

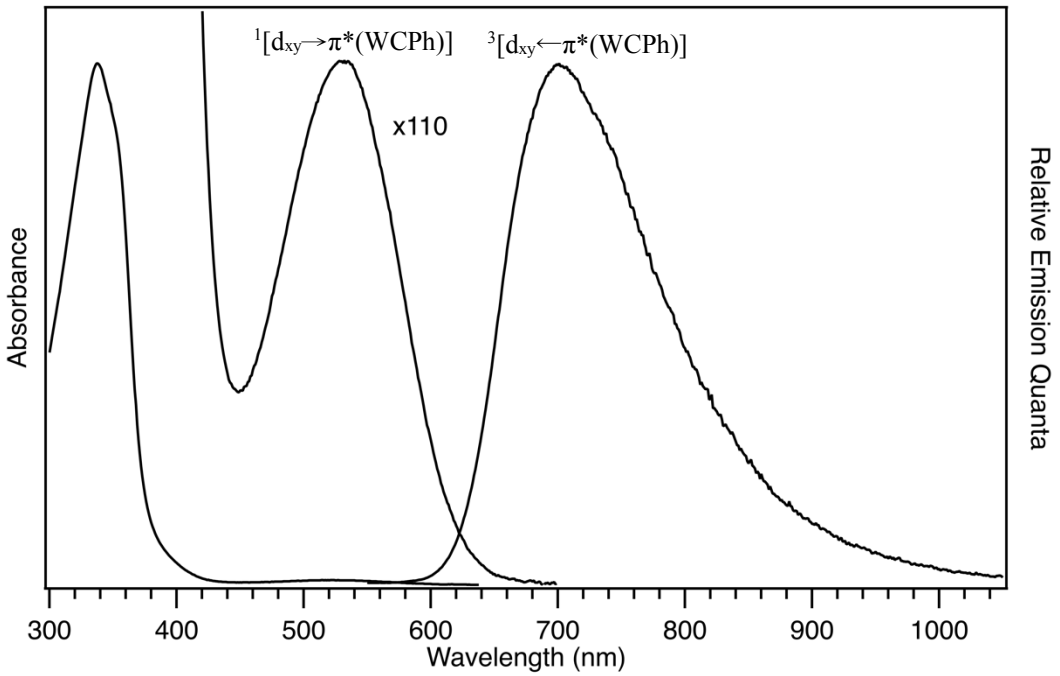

Figure 4.3. Electronic absorption and emission spectra of $W(CPh)(dmpe)_2Cl$ in toluene solution.

As outlined in Chapter 3, the energy of the d_{xy} HOMO and π*(WCAr) LUMO principally depend on the nature of the L ligands (HOMO) and CAr and X substituents (LUMO).[5] Changing L and/or CAr, therefore, affects the energy of the $^1[d_{xy}\rightarrow\pi^*(WCAr)]$ band. For instance, the band is observed to shift to higher energy (shorter wavelength) as the π-acceptor ability of the equatorial ligands is increased: $P(OMe)_3$ (449 nm) > dppe (531 nm) > dmpe (535 nm) ≅ PMe_3 (550 nm) (Table 4.2). Among these phosphines alone, the absorption band can be shifted over nearly a 100 nm range (449–550 nm). The substitution of X = F for Cl and of *para*-CAr substituents with varying π-donor strengths can also exert a degree of fine-tuning over the

absorption energy. For example, the $^1[d_{xy} \rightarrow \pi^*(WCAr)]$ band maximum shifts from 535 nm for $W(CPh)(dmpe)_2Cl$ to 485 nm for $W(CC_6H_4\text{-}4\text{-}pyr)(dmpe)_2Cl$, and to 500 nm for $W(CPh)(dmpe)_2F$. These variations allow the absorption bands of $W(CAr)L_4X$ compounds to tuned over an extremely wide range of wavelengths (Figure 4.4), allowing them to be tailored for specific photoredox applications.

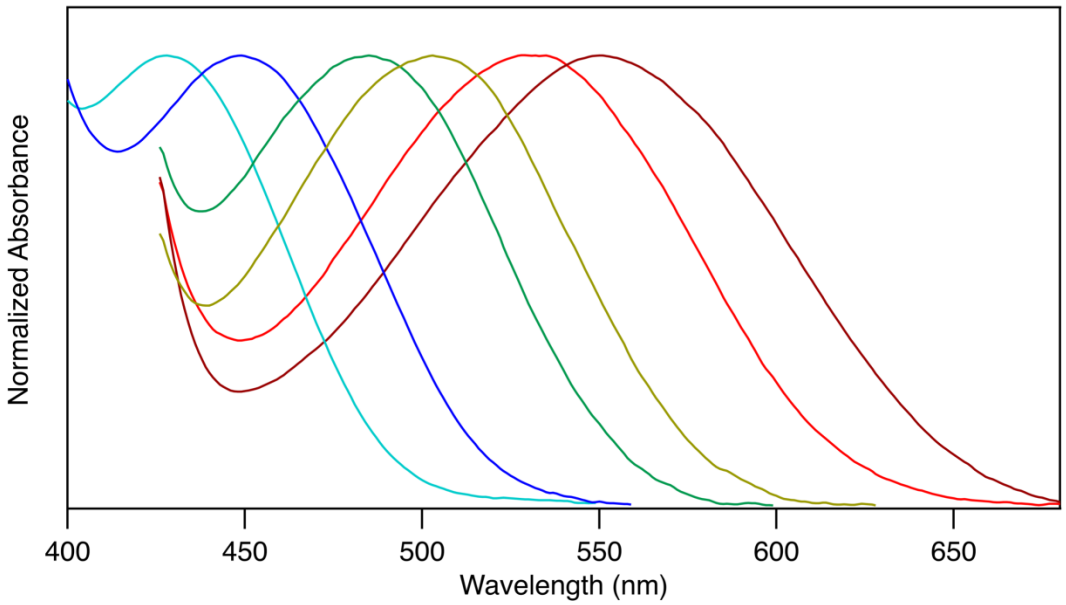

Figure 4.4. Absorbance overlap for selected tungsten-alkylidyne complexes depicting the range of available excitation wavelengths. Key: $W(CC_6H_4\text{-}4\text{-}OCH_3)\{P(OMe)_3\}_4Cl$; $W(CPh)\{P(OMe)_3\}_4Cl$; $W(CC_6H_4\text{-}4\text{-}pyr)(dmpe)_2Cl$; $W(CC_6H_4\text{-}4\text{-}OCH_3)(dmpe)_2Cl$; $W(CPh)(dmpe)_2Cl$; $W(CPh)(PMe_3)_4Cl$.

Table 4.2. Electronic, spectroscopic, and photophysical data for W(CAr)L_4X and related complexes in toluene solution.

Compound (Figure)	$^1[\pi\rightarrow\pi^*(WCAr)]$ (nm)	$^1[d_{xy}\rightarrow\pi^*(WCAr)]$ (nm)	$^3[d_{xy}\leftarrow\pi^*(WCAr)]$ (nm)	FWHM[a] (cm^{-1})	E_{00}[b] (eV)	τ (μs)
W(CPh)L_2(CO)$_2$Cl Complexes						
W(CPh)(pic)$_2$(CO)$_2$Cl (4.28)	340	488sh	669	3667	2.20	NR
W(CPh)(bpy)(CO)$_2$Cl (4.29)	340[c]	430[c]	NA	NA	NA	NA
W(CAr)L_4X Complexes						
W(CPh){P(OMe)$_3$}$_4$Cl (4.30)	328	449	643	4115	2.27	1.2
W(CC_6H_4-4-OCH$_3$){P(OMe)$_3$}$_4$Cl (4.32)	326	428	600	4399	2.38	2.3
W(CC_6H_4-4-pyr){P(OMe)$_3$}$_4$Cl (4.33)	350	409	626[d]	3705	2.24	5.8
W(CPh)(PMe$_3$)$_4$Cl (4.34)	351	550	725	2835	1.91	0.48
W(CPh)(dmpe)$_2$Cl (4.3)	338	535	700	2974	1.98	0.41
W(CMes)(dmpe)$_2$Cl (4.36)	335	505	740	2208	2.12	0.02
W(CC_6H_4-4-OCH$_3$)(dmpe)$_2$Cl (4.37)	335	503	668	3081	2.11	0.88
W(CC_6H_4-4-pyr)(dmpe)$_2$Cl (4.38)	352	485	630	3380	2.25	1.9
W(CC_6H_4-4-NH$_2$)(dmpe)$_2$Cl (4.40)	341	498	651	3404	2.18	1.1
W(CPh)(dmpe)$_2$F (4.41)	343	500	685	3292	2.06	0.08
W(CC_6H_4-4-pyr)(dmpe)$_2$F (4.42)	353	455	655	3569	2.24	0.95
W(CPh)(dmpe)$_2$(OTf) (4.43)	328	530	710	3216	2.02	0.02[h]
W(CPh)(depe)$_2$Cl (4.44)	340	545	700	2459	2.00	0.34
W(CC_6H_4-4-pyr)(depe)$_2$Cl (4.47)	352	492	659	3268	2.14	1.0
W(CPh)(dppe)$_2$Cl (4.49)	339	531[e]	680	3084	2.07	0.30
W(CC_6H_4-4-OCH$_3$)(dppe)$_2$Cl (4.51)	338	505[f]	634	2962	2.17	0.01[h]
W(CC_6H_4-4-pyr)(dppe)$_2$Cl (4.52)	360	NA[g]	641	3380	2.22	0.01[h]

[a] Full width at half maximum intensity of emission band. [b] Approximated to be the energy at which the intensity along the blue flank of the emission band is 10% of the maximum intensity. [c] Additional bands attributable to $[d_{xy}\rightarrow\pi^*(bpy)]$ and $[\pi(bpy)\rightarrow\pi^*(bpy)]$ observable at 310 and 550 nm. [d] Shoulder present at 575 nm. [e] Additional shoulder present at 430 nm. [f] Band position obtained *via* spectral deconvolution; additional shoulder present at 430 nm. [g] No visible $d_{xy}\rightarrow\pi^*$ band for spectral deconvolution; shoulder present at 460 nm. [h] Upper bound for lifetime; signal observed was highly convoluted with instrumental response function. NA = not available; NR = not recorded.

The absorption spectra of the dppe-containing molecules were observed to be more complicated than those of the dmpe- or depe-containing molecules. Each exhibited an additional, unassigned shoulder on the higher-lying $^1[\pi(WCAr)\rightarrow\pi^*(WCAr)]$ transition. This obscured the $^1[d_{xy}\rightarrow\pi^*(WCAr)]$ band, the position of which was found by deconvolution for the Ar = Ph[2] and C_6H_4-4-OCH_3 derivatives and was not observable at all in the case of the Ar = C_6H_4-4-pyr compound.

The $^3[d_{xy}\leftarrow\pi^*(WCAr)]$ luminescent bands of the $W(CAr)L_4X$ compounds exhibit maxima that mostly track with the $^1[d_{xy}\rightarrow\pi^*(WCAr)]$ absorption bands. Exceptions are the compounds $W(CAr)(dppe)_2Cl$ and $W(CAr)\{P(OMe)_3\}_4Cl$, for which the band maxima of the $^1[d_{xy}\rightarrow\pi^*(WCAr)]$ absorption bands lie in the expected energy ordering Ar = C_6H_4-4-pyr > C_6H_4-4-OMe > Ph but the $^3[d_{xy}\leftarrow\pi^*(WCAr)]$ emission bands lie in the order C_6H_4-4-OMe > C_6H_4-4-pyr > Ph. The anomalous behavior of the –pyr derivatives may be explained by DFT calculations (Section 3.2), which for $W(CC_6H_4\text{-}4\text{-pyr})\{P(OMe)_3\}_4Cl$ indicate that the HOMO and HOMO–1 are the π(WCAr) and d_{xy} orbitals, respectively, which is reversed from other compounds, while for $W(CC_6H_4\text{-}4\text{-pyr})(dppe)_2Cl$ the LUMO is an orbital with π^*(dppe) character rather than the normal π^*(WCAr).

The electronic spectra of several compounds were also measured in THF and acetonitrile to determine how excited-state energies will change in polar solvents relative to photoredox reactions. The band shifts in THF (Table 4.3) are fairly small, with the $^1[d_{xy}\rightarrow\pi^*(WCAr)]$ band typically shifting to shorter wavelength in THF by $\leq$ 10 nm and the shifts in emission bands ranging from –3 to +26 nm. The derivatives containing depe were sufficiently soluble in CH_3CN to record electronic absorption and emission spectra (Table 4.4). Absorption band shifts were again $\leq$ 10 nm, but emission bands were more strongly red-shifted ($\geq$40 nm). This means that

estimates of E_{00} based on emission band profiles in toluene may not apply straightforwardly to acetonitrile solution.

Table 4.3. Absorption and emission band maxima and emission lifetimes of W(CAr)L_4X compounds in THF and toluene solution.

Compound (Figure)	$^1[d_{xy}\rightarrow\pi^*(WCAr)]$ (nm)	$^1[\pi(WCAr)\rightarrow\pi^*(WCAr)]$ (nm)	λ_{em} (nm)	τ (μs)
	Toluene Solution			
W(CPh){P(OMe)$_3$}$_4$Cl (4.30)	449	328	643	1.2
W(CPh)(dmpe)$_2$Cl (4.3)	535	338	700	0.41
W(CC_6H_4-4-pyr)(dmpe)$_2$Cl (4.38)	485	352	630	1.9
W(CPh)(depe)$_2$Cl (4.44)	545	340	700	0.34
W(CPh)(dppe)$_2$Cl (4.49)	531	339	680	0.30
	THF Solution			
W(CPh){P(OMe)$_3$}$_4$Cl (4.31)	441	328	640	0.47
W(CPh)(dmpe)$_2$Cl (4.35)	525	337	720	0.23
W(CC_6H_4-4-pyr)(dmpe)$_2$Cl (4.39)	475	350	635[a]	1.3
W(CPh)(depe)$_2$Cl (4.45)	538	337	726	0.22
W(CPh)(dppe)$_2$Cl (4.50)	510	339	685	0.21

[a] Vibronic shoulder at 580 nm.

Table 4.4. Absorption and emission band maxima and emission lifetimes of W(CAr)(depe)$_2$Cl compounds in CH_3CN and toluene solution.

Compound (Figure)	$^1[d_{xy}\rightarrow\pi^*(WCAr)]$ (nm)	$^1[\pi(WCAr)\rightarrow\pi^*(WCAr)]$ (nm)	λ_{em} (nm)	τ (μs)
	Toluene Solution			
W(CPh)(depe)$_2$Cl (4.44)	545	340	700	0.34
W(CC_6H_4-4-pyr)(depe)$_2$Cl (4.47)	492	352	659	1.0
	CH_3CN Solution			
W(CPh)(depe)$_2$Cl (4.46)	550	337	775	0.04
W(CC_6H_4-4-pyr)(depe)$_2$Cl (4.48)	483	353	698	0.20[a]

[a] Biexponential lifetime decay with one process shorter than the instrument response function. The lifetime reported is the longer of the two lifetimes.

The excited-state lifetimes of W(CAr)L_4X complexes were measured to determine which compounds would be suitable for participating in bimolecular electron-transfer reactions and to understand their structure/property relationships. The lifetimes are generally observed to lie in the range of hundreds of nanoseconds to a few microseconds in toluene solution (Table 4.2).

Except for one case, which will be discussed in greater detail, the emission-intensity vs time data from which lifetimes were derived were observed to adhere to a first-order exponential decay, which could be fit to approximately 3τ and were reproducible at several wavelengths across the emission band.[6] The compound with the longest emission lifetime, $W(CC_6H_4\text{-}4\text{-}pyr)\{P(OMe)_3\}_4Cl$, was observed to possess a concentration-dependent and laser-power-dependent lifetime. This is consistent with a self-quenching process, which can be either due to triplet-triplet annihilation or to bimolecular ground-state/excited-state interactions. In order to assess the nature of the interaction the lifetime of the chromophore was measured at constant laser power with different concentrations of chromophore (Figure 4.53). The reported lifetime (5.8 μs) was determined by extrapolation to the hypothetical zero-concentration. Similar experiments for chromophores with the next longest lifetimes, $W(CC_6H_4\text{-}4\text{-}OCH_3)\{P(OMe)_3\}_4Cl$ (2.3 μs) and $W(CC_6H_4\text{-}4\text{-}pyr)(dmpe)_2Cl$ (1.9 μs) did not show evidence for self-quenching, thus suggesting that triplet-triplet annihilation is a likely mechanism of deactivation.

Emission quantum yields (ϕ_{em}) of selected tungsten-alkylidyne compounds were measured in toluene solution to allow assessment of the radiative and nonradiative decay rates (Table 4.5). The quantum yields range from 0.4–5.8%. The radiative rate constants for these compounds ($k_r = \phi_{em}/\tau$) are on the order *ca.* 10^4 s^{-1}, consistent with the fact that prior measurements of extinction coefficients of related compounds show that they vary little across substituent space ($\varepsilon \sim 10^2$ $M^{-1}cm^{-1}$).[6] Non-radiative rates were found to be on the order of 10^6 s^{-1}. The latter were observed to largely follow the energy gap law.[7] A strong correlation ($r^2 = 0.97$) was observed between the emission maximum and non-radiative rate constant for the tungsten-alkylidyne complexes when $W(CPh)(dmpe)_2F$ and $W(CPh)(dppe)_2Cl$ were excluded from the linear regression analysis (Figure 4.5). Nonradiative decay rates are often difficult to interpret,

and this strong relationship with the energy-gap law is unusually straightforward. The strong relationship for all but two tungsten-alkylidyne complexes suggests that the deactivating mode or modes are similar. It is not understood why W(CPh)(dmpe)$_2$F is an outlier. Interestingly, a previous analysis for W{C(C$_6$H$_4$-4-CC)$_n$Ph}(dppe)$_2$Cl compounds, which were studied as photoactive molecular wires, demonstrated that the compound, W(CPh)(dppe)$_2$Cl, was also an outlier against that series, again, for unknown reasons.[2]

Table 4.5. Quantum yields of selected W(CAr)L$_4$X compounds.

Compound (Figure)	E_{em} (cm^{-1})	τ (μs)	ϕ_{em}	k_r (s^{-1})	k_{nr} (s^{-1})	τ_{nat} (μs)
W(CPh){P(OMe)$_3$}$_4$Cl (4.61)	15337	1.2	0.015[a]	1.3×10^4	8.2×10^5	80
W(CPh)(dppe)$_2$Cl (Ref. 8)	14577	0.30	0.017[b]	5.7×10^4	3.3×10^6	18
W(CPh)(PMe$_3$)$_4$Cl (4.61)	14006	0.48	0.028[c]	5.8×10^4	2.0×10^6	17
W(CPh)(dmpe)$_2$Cl (4.60)	14025	0.41	0.021[a]	5.1×10^4	2.4×10^6	20
W(CC$_6$H$_4$-4-OCH$_3$)(dmpe)$_2$Cl (4.60)	14749	0.88	0.040[a]	4.6×10^4	1.1×10^6	22
W(CC$_6$H$_4$-4-pyr)(dmpe)$_2$Cl (4.60)	15601	1.9	0.058[a]	3.1×10^4	5.0×10^5	33
W(CPh)(dmpe)$_2$F (4.60)	14144	0.08	0.004[c]	5.0×10^4	1.3×10^7	20
W(CPh)(depe)$_2$Cl (4.61)	13736	0.34	0.040[a]	1.1×10^5	2.8×10^6	15

[a] Recorded in toluene solution relative to an external standard of [Ru(bpy)$_3$](PF$_6$)$_2$ in de-aerated CH$_3$CN; ϕ_{em} of standard was determined in Ref. 9 . [b] Recorded in toluene solution relative to an external standard of [Ru(bpy)$_3$]Cl$_2$ in de-aerated H$_2$O (ϕ_{em} = 0.063), Ref. 8. [c] Recorded in toluene solution relative to an external standard of W(CPh)(dmpe)$_2$Cl (ϕ_{em} = 0.021).

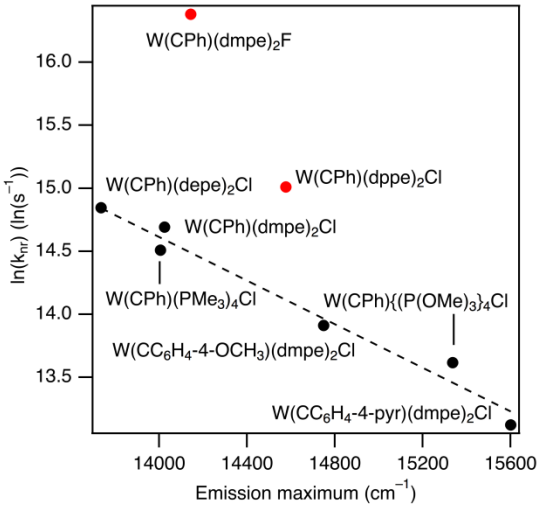

Figure 4.5. Energy-gap-law plot for W(CAr)L$_4$X compounds. The points in black were used to generate the line of fit. The red points, W(CPh)(dmpe)$_2$F and W(CPh)(dppe)$_2$Cl, were omitted from the line of fit. Fit: f(x) = −0.0009x + 26.71, r^2 = 0.97.

4.2.3. Electron-transfer quenching experiments. While the approximation $E^{*/ox} = E^{ox} - E_{00}$ is often valid for transition-metal chromophores, we wished to determine if it applied to $W(CAr)L_4X$ complexes. Thus, the excited-state oxidation potentials of two photoredox chromophores, $W(CPh)(dppe)_2Cl$ and $W(CPh)(dmpe)_2Cl$, were measured through a free-energy analysis of their electron-transfer quenching rate constants. This procedure first requires measurements of quenching rate constants (k_q) *via* Stern-Volmer analysis for a series of quenchers of known redox potential.

The approximate excited-state oxidation potentials of $W(CPh)(dppe)_2Cl$ and $W(CPh)(dmpe)_2Cl$ are –2.65 V and –2.80 V respectively. Thus, organic quenchers are required that possess reduction potentials negative of –2.5 V, and span a range to produce both endergonic and exergonic reactions. Second, they should possess triplet energies > 2.4 eV, based on the fact that $E_{00} \leq 2.1$ eV for the chromophores in question. This eliminates energy transfer quenching as a viable pathway. Among the most promising candidates were benzophenone derivatives.[10, 11] The reduction potentials of benzophenones have been extensively studied during the past fifty years. The molecules are suitably difficult to reduce in aprotic media such as THF, DMF, or CH_3CN. Their potential can be tuned by substitution,[12] although[11] the potentials are extremely sensitive to the small presence of protic impurities that stabilize the generated ketyl intermediate,[13] requiring that solvents and reagents are rigorously pure. Five benzophenone quenchers were selected to react with the tungsten-alkylidyne chromophore candidates. Those quenchers and their relevant parameters are outlined in Table 4.6. Those quenchers span a range in reduction potentials from –2.38 to –2.80 V.

Table 4.6. Benzophenone quenchers.

Molecule	$E_{1/2}^{0/-a}$	E_T (eV)	Ref.
4-trifluoromethylbenzophenone	−2.38	2.95	14
benzophenone	−2.59	3.00	14, 15
4,4′-dimethylbenzophenone	−2.64	3.01	16
4,4′ -dimethoxybenzophenone	−2.70	3.05	14
4,4′-bis(dimethylamino)benzophenone	−2.80	2.70	10

a Potentials measured in THF solution vs $FeCp_2^{0/+}$ in 0.1 M [^{n}Bu$_4$N][PF$_6$] THF solution as outlined in 4.2.

Stern-Volmer emission quenching experiments using the selected benzophenone quenchers were conducted with W(CPh)(dppe)$_2$Cl and W(CPh)(dmpe)$_2$Cl. These experiments were consistent with a purely dynamic quenching process. A representative Stern-Volmer plot is shown for W(CPh)(dmpe)$_2$Cl and benzophenone in Figure 4.6. Other Stern-Volmer quenching experiments are set forth in Section 4.4 (Figures 4.62-4.70). The quenching rate constant was observed to decrease as the reduction potential for the organic species became more negative. For W(CPh)(dppe)$_2$Cl, for instance, no quenching was observed with 4,4′-dimethylaminobenzophenone (estimated ΔG = 0.15 V). For quenchers with the least negative reduction potentials, quenching rate constants approach the diffusion limit. The quenching rate constants are set out in Table 4.7.

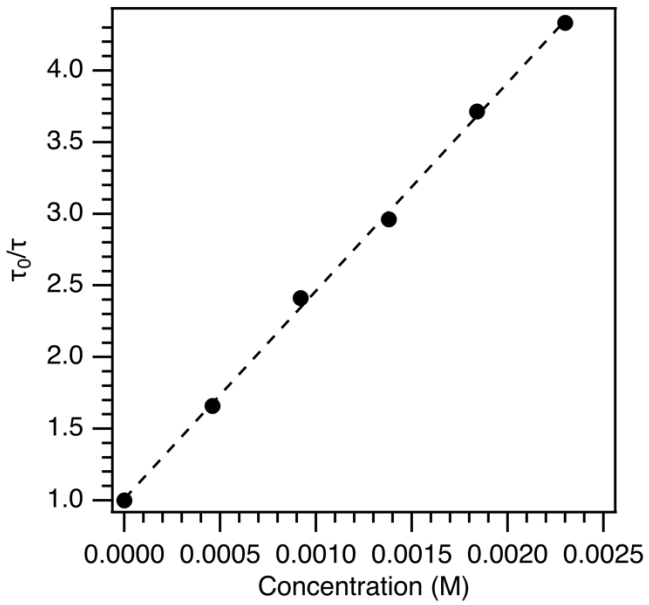

Quencher concentration (M)	Lifetime (ns)
0	234
4.6×10^{-4}	141
9.2×10^{-4}	97
1.4×10^{-3}	79
1.8×10^{-3}	63
2.3×10^{-3}	54

Figure 4.6. Stern–Volmer experiment with W(CPh)(dmpe)$_2$Cl and benzophenone. Linear regression: f(x) = 1452.2x + 1.01; $r^2 = 0.999$. The quenching rate constant is listed in Table 4.7.

Table 4.7. Electron-transfer quenching (Stern–Volmer) rate constants for tungsten–alkylidyne complexes with organic acceptors.

Chromophore	Acceptor	k_q ($M^{-1}s^{-1}$)	Figure
W(CPh)(dppe)$_2$Cl	4-trifluoromethylbenzophenone	6.58×10^9	4.61
	benzophenone	3.72×10^9	4.62
	4,4′-dimethylbenzophenone	1.42×10^9	4.63
	4,4′-dimethoxybenzophenone	2.71×10^8	4.64
W(CPh)(dmpe)$_2$Cl	4-trifluoromethylbenzophenone	6.86×10^9	4.65
	benzophenone	6.20×10^9	4.66
	4,4′-dimethylbenzophenone	5.50×10^9	4.67
	4,4′-dimethoxybenzophenone	3.42×10^9	4.68
	4,4′-(dimethylamino)benzophenone	2.45×10^8	4.69
W(CPh)(dmpe)$_2$F	4,4′-(dimethylamino)benzophenone	4.44×10^9	4.70

The determination of $E^{*/ox}$ from these quenching rate constant data required that they be fit to a free-energy relationship, the details of which are outlined in Section 4.4. That equation allows one to relate ΔG of an electron-transfer reaction with the observed quenching rate constants from that reaction (Figure 4.7). The curve fitting procedure derived in Section 4.4 was observed to fit the experimentally measured data very well. A comparison of the ΔG values

obtained by addition and those obtained *via* electron-transfer quenching can be found in Figure 4.9. The procedure measures the excited-state oxidation potential $E^{*/ox}$ as –2.61 V for W(CPh)(dppe)$_2$Cl, as compared to −2.64 V estimated from $E^{*/ox} = E^{ox} - E_{00}$, and –2.74 V for W(CPh)(dmpe)$_2$Cl as compared to the estimated –2.80 V. The excellent agreement between the values measured *via* quenching experiments and those predicted from E^{ox} and E_{00} negated the need to use electron-transfer quenching for future experiments.

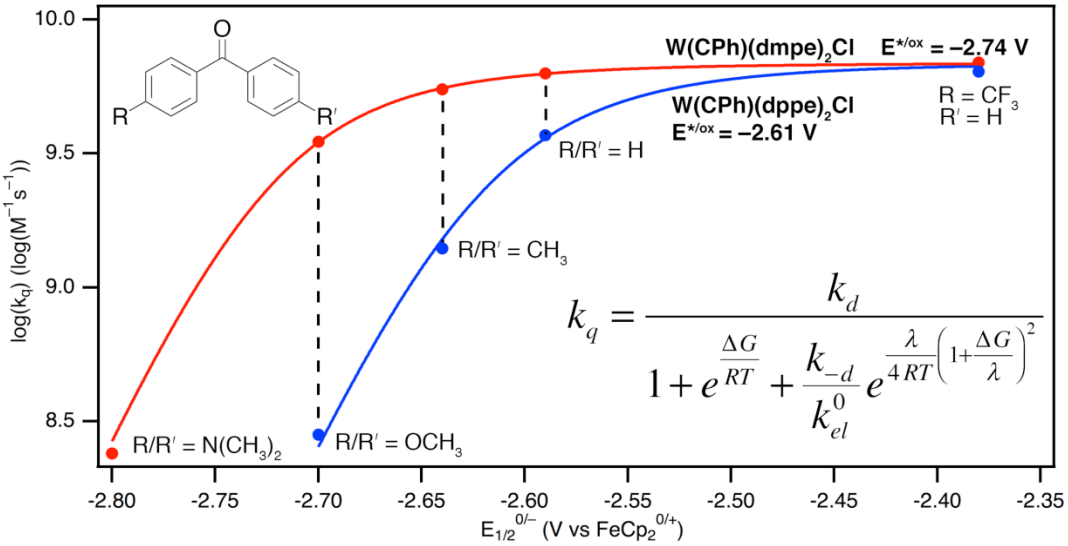

Figure 4.7. Rehm-Weller plot for the reaction between W(CPh)(dppe)$_2$Cl (blue), W(CPh)(dmpe)$_2$Cl (red), and substituted benzophenones. The points are measured values from Stern-Volmer quenching experiments and the solid line is the fit of the points using the equation in the figure.

4.2.4. Estimation of excited-state oxidation potentials. Due to the good agreement found between the measured and estimated excited-state oxidation potentials, the excited-state oxidation potentials of the other W(CAr)L$_4$X chromophores were estimated (Table 4.8). These potentials were found to span a range from –2.5 V to –3.3 V vs FeCp$_2$—bridging a potential space that is bookended by conventional photoredox chromophores and alkali metal reductants.[17]

Table 4.8. Excited-state oxidation potentials (V vs $FeCp_2$) of selected tungsten-alkylidyne photoredox chromophores.

Chromophore	$E_{1/2}^{0/+}$ (V)	$^1[d_{xy} \rightarrow \pi^*(WCAr)]$ (nm)	E_{00} (eV)[c]	$E^{*/ox}$ (V)
$W(CC_6H_4\text{-}4\text{-}pyr)(dmpe)_2F$	−1.02	455	2.24	−3.26
$W(CC_6H_4\text{-}4\text{-}pyr)(dmpe)_2Cl$	−0.93	485	2.25	−3.18
$W(CC_6H_4\text{-}4\text{-}pyr)(depe)_2Cl$	−0.95	492	2.14	−3.09
$W(CC_6H_4\text{-}4\text{-}OCH_3)(dmpe)_2Cl$	−0.90	503	2.11	−3.01
$W(CMes)(dmpe)_2Cl$	−0.86	505	2.12	−2.98
$W(CPh)(dmpe)_2F$	−0.91	500	2.06	−2.97
$W(CC_6H_4\text{-}4\text{-}pyr)(dppe)_2Cl$	−0.66	460[b]	2.22	−2.88
$W(CPh)(depe)_2Cl$	−0.84	545	2.00	−2.84
$W(CPh)(dmpe)_2Cl$	−0.82	535	1.98	−2.80
$W(CC_6H_4\text{-}4\text{-}OCH_3)(dppe)_2Cl$	−0.61	505	2.17	−2.78
$W(CPh)(PMe_3)_4Cl$	−0.85	550	1.91	−2.76
$W(CC_6H_4\text{-}4\text{-}OCH_3)\{P(OMe)_3\}_4Cl$	−0.30	410	2.38	−2.68
$W(CPh)(dmpe)_2(OTf)$	−0.65[a]	530	2.02	−2.67
$W(CPh)(dppe)_2Cl$	−0.58[a]	531	2.07	−2.65
$W(CC_6H_4\text{-}4\text{-}pyr)\{P(OMe)_3\}_4Cl$	−0.34	428	2.24	−2.58
$W(CPh)\{P(OMe)_3\}_4Cl$	−0.24	449	2.27	−2.51

[a] Ref. 5. [b] Observable shoulder. [c] E_{00} is taken to be the energy at which the intensity along the blue flank of the emission band is 10% of the maximum emission band intensity.

4.3. Conclusions.

The electrochemical and photophysical measurements of $W(CAr)L_4X$ compounds were described. These properties enabled the characterization of the excited-state oxidation potentials of these complexes. The excited-state oxidation potentials of $W(CPh)(dppe)_2Cl$ and $W(CPh)(dmpe)_2Cl$ were measured by electron-transfer quenching and found to be close to the values predicted by addition of the ground-state oxidation potential and onset emission energy approximated at room temperature. These chromophores were found to be highly reducing; they were found to span a range of potentials from –2.5 V to –3.3 V.

4.4. Experimental Section.

4.4.1 Electrochemical methods. Electrochemical measurements were performed at room temperature in a nitrogen-filled glovebox using a Bioanalytical Systems 100 B/W Electrochemical Workstation. A three-electrode configuration was used, which consisted of a working electrode (Bioanalytical Systems, platinum disk, area = 0.2 cm^2), auxiliary electrode (Bioanalytical Systems, platinum disk, area = 0.2 cm^2), and a quasi-reference electrode (silver wire). Electrodes were polished prior to each experiment. Samples ranged in concentration from (0.3–2.0) × 10^{-3} M analyte in THF containing 0.1 M [Bu^n_4N][PF_6]. The electrochemical reversibility of redox couples was established via Randles-Sevcik plots of cyclic-voltammetry (CV) data. Peak currents in CV experiments were determined from scans in which the switching potential was at least 0.30 V beyond the peak potentials. Differential pulse voltammetry (DPV) was conducted using a scan rate of 20 mV s^{-1}, a pulse amplitude of 50 mV, a sampling width of 17 ms, a pulse width of 50 ms, and a pulse period of 200 ms. Electrode potentials are referenced to the $FeCp_2^{0/+}$ couple; this was used as an internal electrode-potential standard for CV and DPV experiments.[17] For compounds whose waveforms overlapped with that of $FeCp_2$, the internal standards $FeCp^*_2$ or [$CoCp_2^+$][PF_6] were used; the potentials of these standards relative to $FeCp_2$ were then measured separately under identical experimental conditions.[17] Under the conditions of the CV experiments, the internal electrode-potential standard exhibited $i_{pc}/i_{pa} \cong 1$ and ΔE_p = 0.09−0.27 V. THF for electrochemical measurements was HPLC grade and passed through activated alumina under N_2 prior to use. $FeCp_2$ was recrystallized three times from 95% ethanol and then sublimed under vacuum. [Bu^n_4N][PF_6] was recrystallized three times from 95% ethanol and dried under vacuum at 80 °C for 24 h.[18]

4.4.2. General procedures for electronic absorption and emission measurements. Solution samples for electronic spectroscopy were prepared under N_2 in sealable cuvettes of path length 1 cm or 1 mm, degassed with 3 freeze–pump–thaw cycles using a vacuum line, and sealed under purified N_2. Solvents (THF and toluene) were purified by stirring over NaK for at least 24 h. Absorption spectra were recorded with a Cary 300 UV-vis spectrophotometer. Emission spectra were recorded with a PTI QuantMaster fluorimeter equipped with a Peltier-cooled R928 photomultiplier-tube (PMT) and InGaAs detectors. The emission monochromator was wavelength-calibrated using the emission lines of an Ar lamp; the accuracy is < 0.5 nm over the detection range. Emission spectra that spanned the wavelength ranges of the two detectors (PMT, $\lambda \leq 750$ nm; InGaAs, $\lambda \geq 700$ nm) were collected using both detectors, individually corrected for instrument response, intensity normalized in the overlapping wavelength region (700–750 nm) and merged into a single spectrum.

4.4.3. General procedures for emission lifetime measurements. Samples were prepared in the same manner as those for electronic spectroscopy. The optical density at the excitation wavelength was ≤ 0.15 absorbance units. Data for these experiments were collected with an automated, LabView-controlled instrument in which the excitation source was an integrated Nd:YAG-optical-parametric-oscillator pulsed laser (Opotek Vibrant 355 LD, 10 Hz repetition rate, 10-ns pulse width, 0.5–1.5 mJ/pulse energy at the sample) that produced tunable output between 410–710 nm. The laser beam sent to the sample was not focused. From the sample, luminescence (for lifetime measurements) was focused onto the input slit of a monochromator (Horiba Scientific iHR320), the output of which was detected by a six-stage Hamamatsu R928 photomultiplier tube and processed with a digital oscilloscope (Tektronix TDS 3032C). The resulting time-resolved signal-intensity data were analyzed using Igor Pro software

(version 6.37 or 7.04). Emission decay (lifetime) data for all compounds were found to be well fit using a single-exponential decay function over a minimum of 3τ. For each compound, lifetimes were measured at wavelengths across the emission band (50 nm intervals) and of different samples; for compounds with only one lifetime component, these were observed to agree within 5%.

4.4.4. General Procedure for Electron-Transfer Quenching Experiments. A stock solution of a tungsten–alkylidyne chromophore in THF (25 mL) was prepared such that the absorbance of the sample was approximately 0.15 at the excitation wavelength (1 cm path length). To a 10-mL portion of the stock solution was added a quantity of an organic electron acceptor (quencher). A series of independent samples spanning a range of quencher concentrations were prepared by mixing aliquots from the two stock solutions. Each sample was sealed in a 1-cm path length quartz cuvette, degassed via three freeze–pump–thaw cycles on a vacuum line, and sealed under purified N_2. The emission lifetime was recorded for each sample, including that which did not contain quencher. The electron-transfer quenching rate constant was determined from a linear fit of these data to the Stern–Volmer equation (Equation 4.1).[19]

$$\frac{\tau_0}{\tau} = 1 + k_q[Q]\tau_0 \qquad (4.1)$$

In Equation 4.1, τ_0 is the emission lifetime of the chromophore in the absence of quencher, τ is the emission lifetime of the chromophore in the presence of a given concentration of quencher [Q], and k_q is the electron-transfer quenching rate constant (units $M^{-1}s^{-1}$). The goodness-of-fit was found to be $r^2 \geq 0.994$ across all experiments. Results from these analyses are used, by application of a fitting equation derived in Section 4.4.5, to determine the excited-state oxidation potential.

4.4.5. Excited-state oxidation potential fit equation.

4.4.5.1. Derivation of fit equation. The kinetic expression used here relates the ΔG of reaction to the observed quenching rate constant (k_q) by the Stern-Volmer relation.[20] In this equation it is important to assume that no net photochemistry occurs.

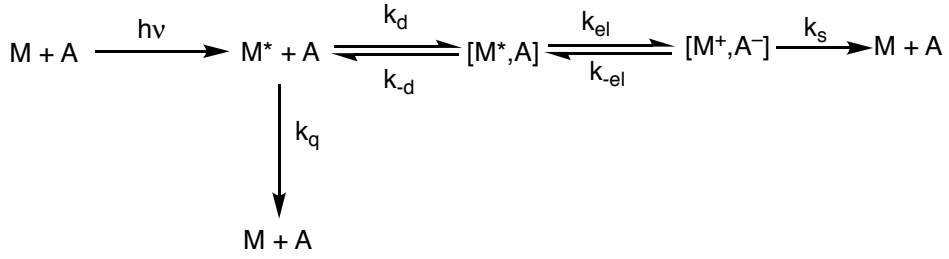

Figure 4.8. Schematic representation of a photoinduced electron-transfer reaction with associated rate constants.

Assume the development of a bimolecular solution pair, M and A as shown in Figure 4.8. One key assumption is that M and A must undergo a diffusional process to be in the same solvent cage, and it is within that solvent cage where outer-sphere electron transfer occurs. In Figure 4.8, $k_{d/-d}$ are the forward and back-diffusion rate constant. The rate constants k_{el}/k_{-el} are the forward and backward electron-transfer rate. Finally, k_q is the quenching rate constant (the quantity observed from the experiment) and k_s is the sum of rate constants that deactivate a charge separated pair. Solving for the concentration of $[M^+, A^-]$ using the steady-state approximation provides Equations 4.2 and 4.3.

$$\frac{d[M^+,A^-]}{dt} = 0 = k_{el}[M^*,A] - k_{-el}[M^+,A^-] - k_s[M^+,A^-] \quad (4.2)$$

$$[M^+,A^-] = \frac{k_{el}[M^*,A]}{k_{-el} + k_s} \quad (4.3)$$

Solving for the cage-activated pair prior to electron transfer provides Equations 4.4 and 4.5.

$$\frac{d[M^*,A]}{dt} = 0 = k_d[M^*][A] - k_{-d}[M^*,A] - k_{el}[M^*,A] + k_{-el}[M^+,A^-] \quad (4.4)$$

$$[\mathrm{M}^{*},\mathrm{A}] = \frac{k_d[M^*][A] + k_{-el}[M^+, A^-]}{k_{-d} + k_{el}} \quad (4.5)$$

Substituting the results obtained for the solution of $[M^+,A^-]$ (Equation 4.3) into the derived equation for $[M^*, A]$ (Equation 4.5) provides Equation 4.6.

$$[M^*, A] = \frac{k_d[M^*][A]}{(k_{-d} + k_{el}) - k_{el}\frac{k_{el}}{k_{-el} + k_s}} \quad (4.6)$$

Finally, the solution found in Equation 4.6 can be integrated into a kinetic expression relating the quenching rate constant to that of the diffusion rate constants (Equations 4.7 and 4.8).

$$k_q[M^*][A] = k_d[M^*][A] - k_{-d}[M^*, A] \quad (4.7)$$

$$k_q = \frac{k_d}{1 + \frac{k_{-d}}{k_s} + \frac{k_{-d}}{k_s}\frac{k_{el}}{k_{-el}}} \quad (4.8)$$

A kinetic development of the processes encompassing the observation of the quenching rate constant is shown in Equations 4.7 and 4.8. Substitution of the results for $[M^*, A]$ (Equation 4.6) into Equation 4.7 provides a form of k_q (Equation 4.8), which can be related in only terms of k_d/k_{-d} k_{el}/k_{-el} or k_s. Finally, the solutions from absolute rate theory

($k_{el} = k_{el}^0 e^{\frac{-\Delta G^\dagger}{RT}}$ and $k_{-el} = k_{el}^0 e^{\frac{\Delta G}{RT}}$) provide an equation in terms of ΔG and $\Delta G^\dagger$.

$$k_q = \frac{k_d}{1 + \frac{k_{-d}}{k_s}e^{\Delta G/RT} + \frac{k_{-d}}{k_{el}^0}e^{\Delta G^\dagger/RT}} \quad (4.9)$$

Provided that the rates of back-diffusion transfer (k_{-d}) and the sum of deactivation electron transfer (k_s) are similar, Equation 4.9 provides a more amenable expression for

evaluation. Substitution of the results with Marcus theory for $\Delta G^{\dagger}$ provides the final expression (Equation 4.10) that can be used for curve fitting.

$$k_q = \frac{k_d}{1 + e^{\Delta G/RT} + \frac{k_{-d}}{k_{el}^0} e^{\lambda\left(1+\frac{\Delta G}{\lambda}\right)^2 / 4RT}} \quad (4.10)$$

4.4.5.2. Approximations to determine excited-state oxidation potentials *via* electron-transfer quenching. In order to determine the excited-state oxidation potential from Equation 4.10, the values of the diffusion rate constants and the reorganization energy must be approximated. There are standard approaches to each approximation, as described below. Common to both is treatment of the chromophore and quencher as hard spheres that entirely encompass each molecule and whose radii (r_a, r_b) determine their interaction distance. The radii of the benzophenone-derived quenchers were assumed to be identical to that of benzophenone (0.47 nm), the value for which has been estimated in previously reported kinetic analyses of its electrochemical reduction.[21] The hard-sphere radii for W(CPh)(dmpe)$_2$Cl (0.48 nm) and W(CPh)(dppe)$_2$Cl (0.70 nm) were determined from the longest intramolecular non-bonded contacts found in their crystal structures.[8, 22]

The values of the diffusion rate constants k_d and k_{-d} were approximated from the Debye-Smoluchowski equation (Equation 4.11) and the Eigen equation (Equation 4.12), respectively.[23] In these equations, R is the gas constant, T is the temperature, η is viscosity in Poise, k_B is the Boltzman constant, and r_{ab} is the critical interaction distance ($r_{ab} = r_a + r_b$). Using the radii above, Equation 4.11 provides $k_d = 1.4 \times 10^{10}$ $M^{-1}s^{-1}$ for both W(CPh)(dppe)$_2$Cl and W(CPh)(dmpe)$_2$Cl, and Equation 4.12 provides $k_{-d} = 1.0 \times 10^{10}$ s^{-1} for W(CPh)(dppe)$_2$Cl and 1.1×10^{10} s^{-1} for W(CPh)(dmpe)$_2$Cl.

$$k_d = \frac{2RT}{3000\eta}\left(2 + \frac{r_a}{r_b} + \frac{r_b}{r_a}\right) \quad (4.11)$$

$$k_{-d} = \frac{3k_BT}{6\pi\eta d^2}\left(\frac{1}{r_a} + \frac{1}{r_b}\right) \quad (4.12)$$

The total reorganization energy λ of the reaction pair is the sum of their outer-sphere (λ_o) and inner-sphere reorganization energies (λ_i). The outer-sphere reorganization energy (λ_o) was approximated using the dielectric continuum model (Equation 4.13),[24] where Δe is the charge transferred, D_{op} is the optical dielectric constant (square of the refractive index; D_{op}(THF) = 1.979), and D_s is the static dielectric constant of the solvent (D_s(THF) = 7.58). Equation 4.13 provides λ_o = 0.35 eV (W(CPh)(dppe)$_2$Cl) and 0.40 eV (W(CPh)(dmpe)$_2$Cl).

$$\lambda_o = (\Delta e)^2\left[\frac{1}{2r_a} + \frac{1}{2r_b} - \frac{1}{r_{ab}}\right]\left[\frac{1}{D_{op}} - \frac{1}{D_s}\right] \quad (4.13)$$

The inner-sphere reorganization energy was assumed to be zero (that is, λ_i negligible relative to λ_o) on the following grounds. For benzophenone, previously reported analyses of the experimentally determined rate constant for the electrochemical reduction of benzophenone demonstrated that $\lambda \cong \lambda_o$, that is, that λ_i can be ignored.[21] For the W(CR)L$_4$X complexes, λ_i was assumed to be zero because this is the standard approximation for pseudo-octahedral metal complexes whose redox orbital is of t_{2g}-parentage.[25, 26] This is supported by previously reported X-ray crystallographic structural data for W(CPh)(dppe)$_2$Cl and its one-electron-oxidized congener (the same redox pair present in the excited-state electron-transfer quenching experiments), which demonstrated the essentially non-bonding character of the redox orbital via the small differences observed between their bond lengths (Δd(WC)$^{0/+}$ = –0.007 Å, Δd(WP$_{avg}$)$^{0/+}$ = 0.08 Å , Δd(WCl)$^{0/+}$ = –0.02 Å).[8] The approximate total reorganization energy of λ = 0.35 eV

($W(CPh)(dppe)_2Cl$) and 0.40 eV ($W(CPh)(dmpe)_2Cl$) is very similar to that obtained in a previously reported analysis of the excited-state oxidation potential of $W(CPh)(Cp)\{P(OMe)_3\}(CO)$ ($\lambda = 0.40$).[27]

4.4.5.3. Nonlinear fitting of quenching rate constant data with Equation 4.10. The dependence of the experimentally determined quenching rate constants (k_q) for tungsten–alkylidyne chromophores upon the reduction potential of the benzophenone quenchers was fit using Equation 4.10. In the fitting process, the values of λ, k_d, and k_{-d} were fixed and k^0_{el} and ΔG were allowed to vary. Fits for both compounds converged within 8 iterations with a χ^2-tolerance of 1×10^{-9}. Plots of the resulting fits are displayed in Figure 4.9. Figure 4.9 sets out measured and predicted rate constants for each quencher. $W(CPh)(dppe)_2Cl$ was found to possess $E^{*/ox} = -2.61$ V and $W(CPh)(dmpe)_2Cl$ was found to possess $E^{*/ox} = -2.74$ V v. $FeCp_2^{0/+}$.

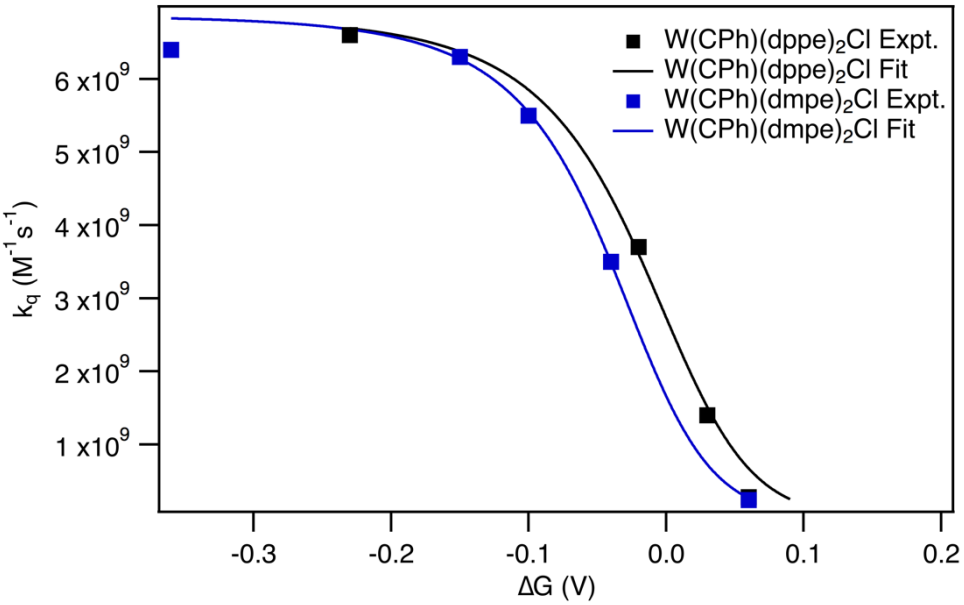

	W(CPh)(dppe)$_2$Cl			W(CPh)(dmpe)$_2$Cl		
Quencher	Expt k_q[a]	Pred k_q[a]	ΔG (V)	Expt k_q[a]	Pred k_q[a]	ΔG (V)
A	6.6×10^9	6.7×10^9	–0.23	6.4×10^9	6.8×10^9	–0.36
B	3.7×10^9	3.6×10^9	–0.02	6.3×10^9	6.3×10^9	–0.15
C	1.4×10^9	1.5×10^9	0.03	5.5×10^9	5.5×10^9	–0.10
D	2.8×10^8	6.4×10^8	0.06	3.5×10^9	3.5×10^9	–0.04
E	Not Obs.	N/A	0.16	2.4×10^8	2.6×10^8	0.06

[a] $M^{-1}s^{-1}$

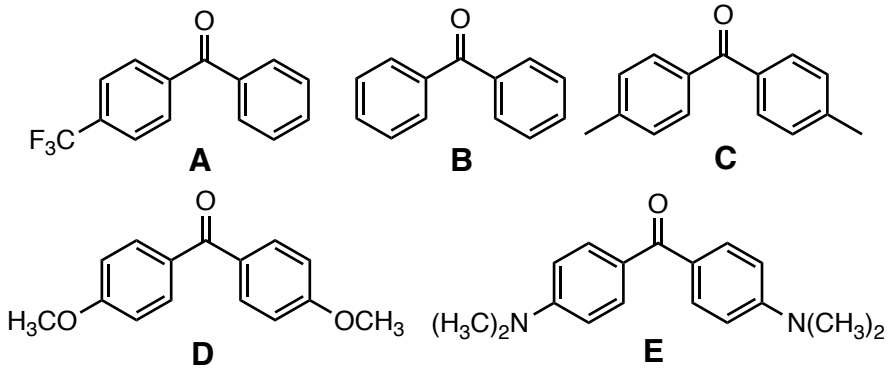

Figure 4.9. Plots of ΔG using experimentally determined $E^{*/ox}$ value vs experimental and simulated quenching rate constant.

4.4.5.4. Robustness of Non-linear Curve Fit. To test the sensitivity of the fit to the approximation that $\lambda = \lambda_o$, curves were calculated using fixed, reasonable values for k_d, k_{-d}, k_{el}^0, and $E^{*/ox}$ ($k_d = 1.4 \times 10^{10}$; $k_{-d} = 1.1 \times 10^{10}$; $k_{el}^0 = 1.4 \times 10^{11}$; $E^{*/ox} = -2.71$ V) with variation of λ across the range 0–2 eV. These curves were found to be essentially indistinguishable relative to their fit to the data, suggesting that the approximation $\lambda = \lambda_o$ is valid. For $\lambda > 2$ eV, the curve shape becomes highly dependent on the nature of λ.

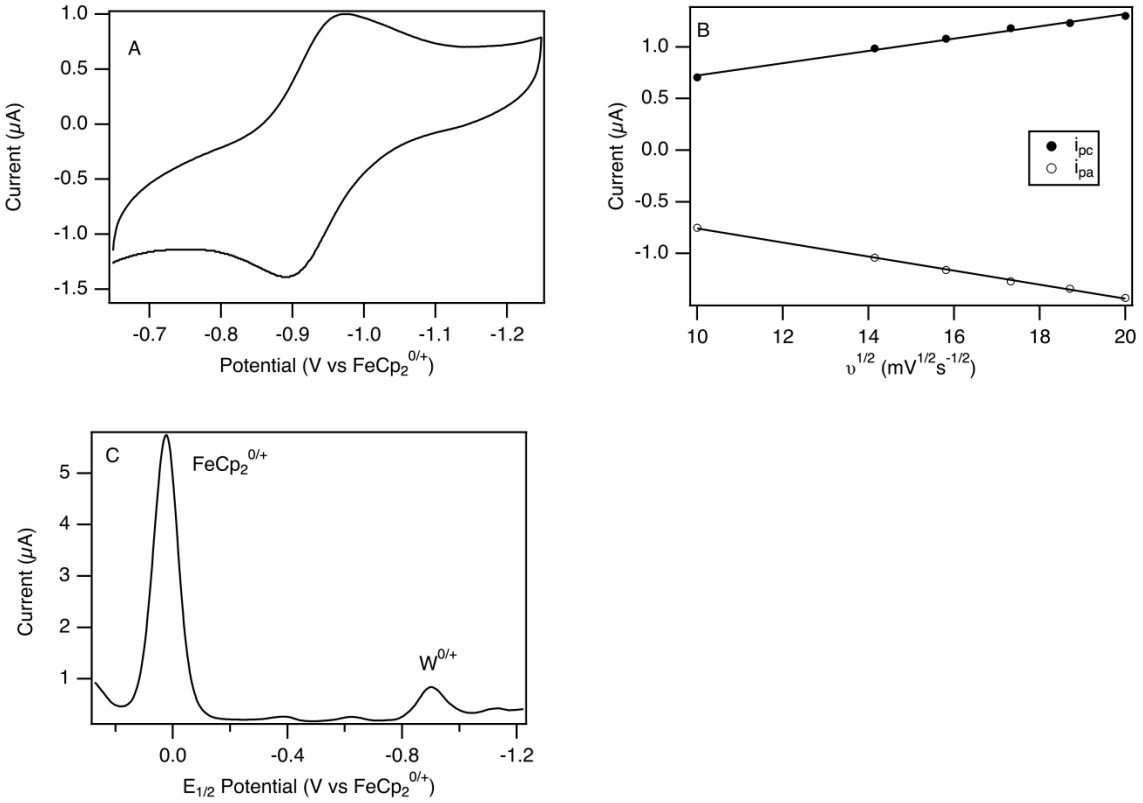

Figure 4.10. Electrochemical data for $W(CBu^t)(PMe_3)_4Cl$: (A) CV (200 mV s^{-1}) in THF with 0.1 M $[Bu^n_4N][PF_6]$; (B) Randles-Sevcik plot: i_{pc} f(x) =0.059x + 0.13, r^2 = 0.99; i_{pa} f(x) = -0.068x - 0.075, r^2 = 0.99; (C) DPV. **Note:** It was previously reported that $E_{1/2}^{0/+}$ = –0.87 V vs $FeCp_2^{0/+}$ (ref. [28]); the present data change this to $E_{1/2}^{0/+}$ = –0.93 V.

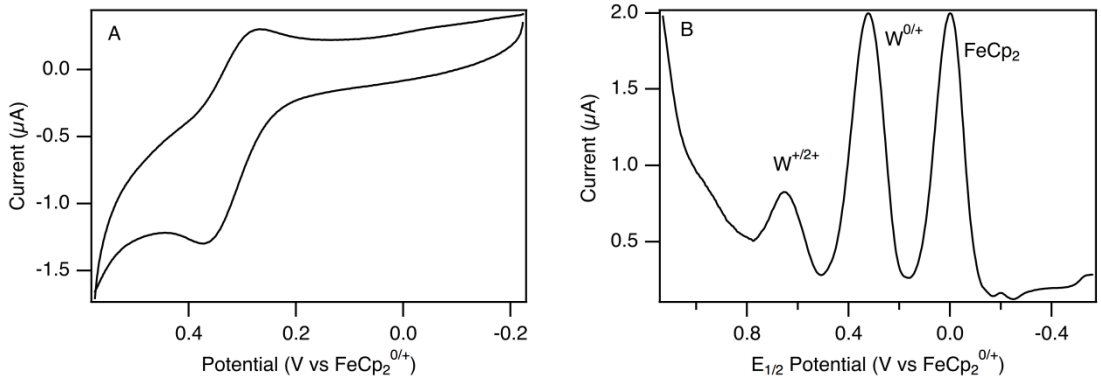

Figure 4.11. Electrochemical data for $W(CPh)(pic)_2(CO)_2Cl$: (A) CV (200 mV s^{-1}) in THF with 0.1 M $[Bu^n_4N][PF_6]$; (B) DPV.

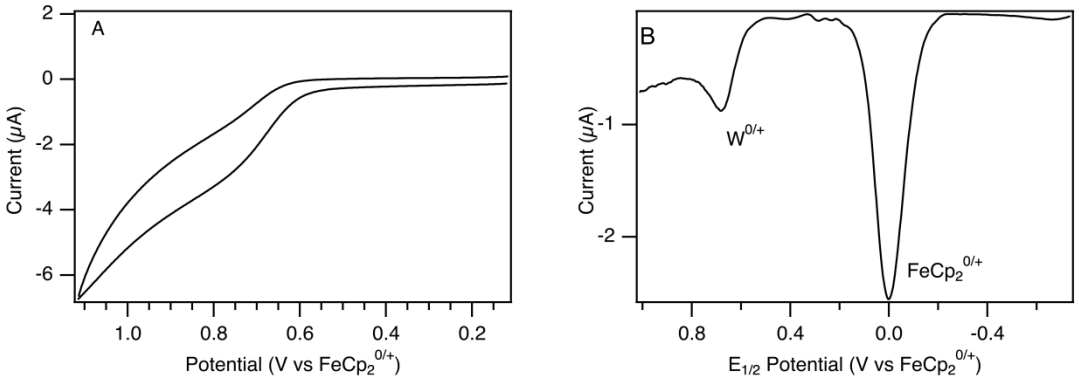

Figure 4.12. Electrochemical data for W(CPh)(dppe)$(CO)_2$Cl in THF with 0.1 M [Bu^n_4N][PF_6]: (A) CV (200 mV s^{-1}); (B) DPV.

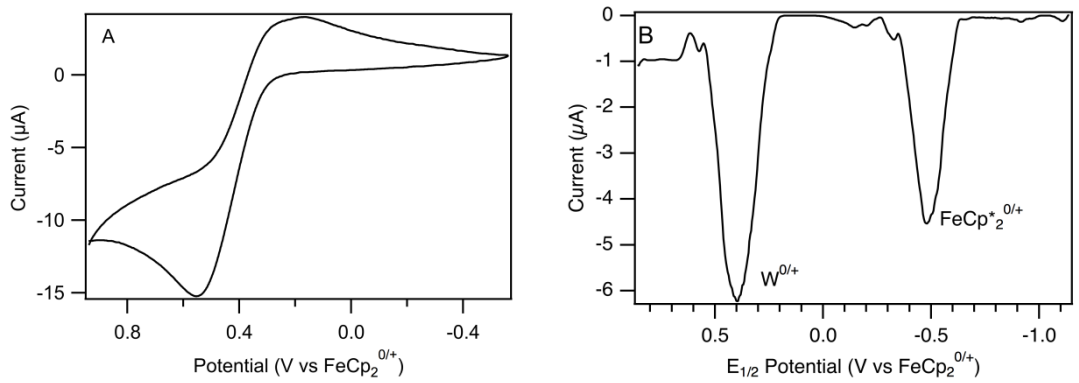

Figure 4.13. Electrochemical data for W(CPh)(tmeda)$(CO)_2$Cl in THF with 0.1 M [Bu^n_4N][PF_6]: (A) representative CV (200 mV s^{-1}); (B) DPV ($FeCp^*_2$ internal reference).

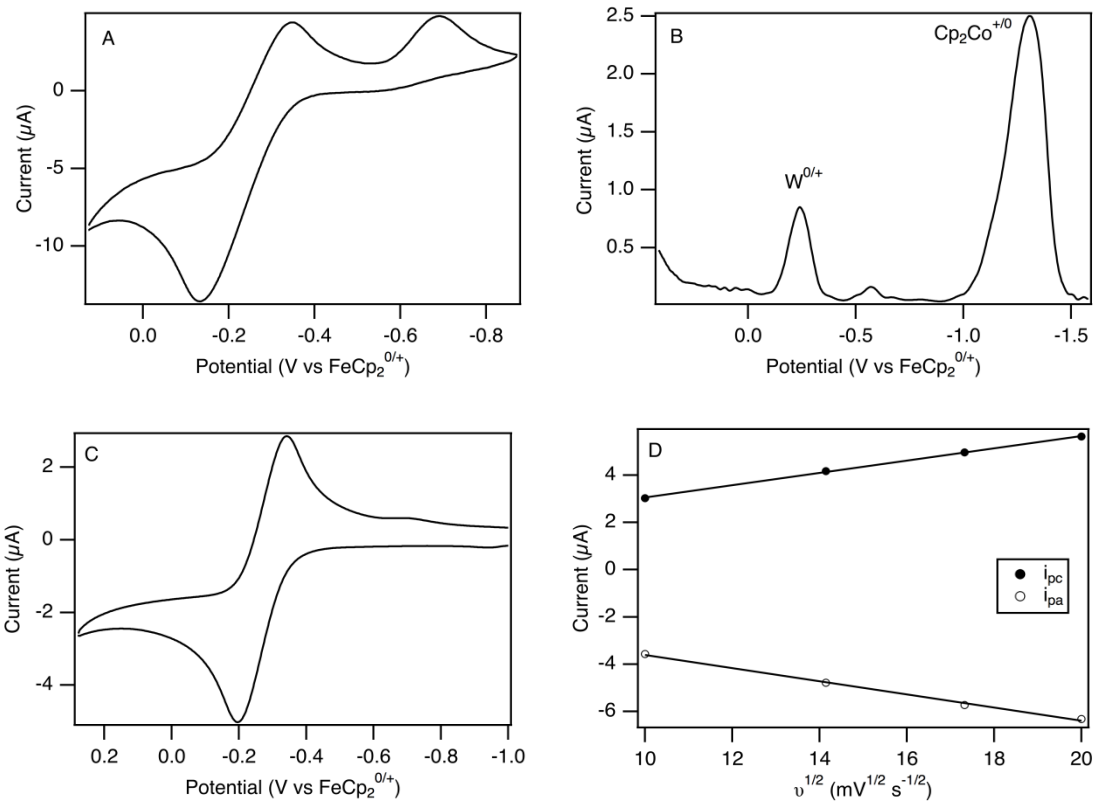

Figure 4.14. Electrochemical data for W(CPh){P(OMe)$_3$}$_4$Cl in THF with 0.1 M [Bu$^n_4$N][PF$_6$]: (A) Room-temperature CV (200 mV s^{-1}); (B) Room-temperature DPV; (C) –15°C CV (200 mV s^{-1}); (D) –15°C Randles-Sevcik plot.

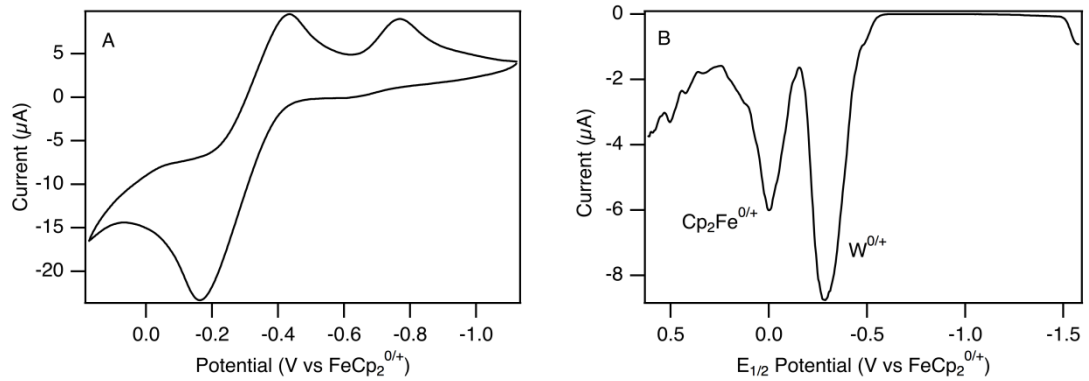

Figure 4.15. Electrochemical data for W(CC$_6$H$_4$-4-OCH$_3$){P(OMe)$_3$}$_4$Cl in THF solution with 0.1 M [^{n}Bu$_4$N][PF$_6$]: (A) CV (200 mV s^{-1}); (B) DPV.

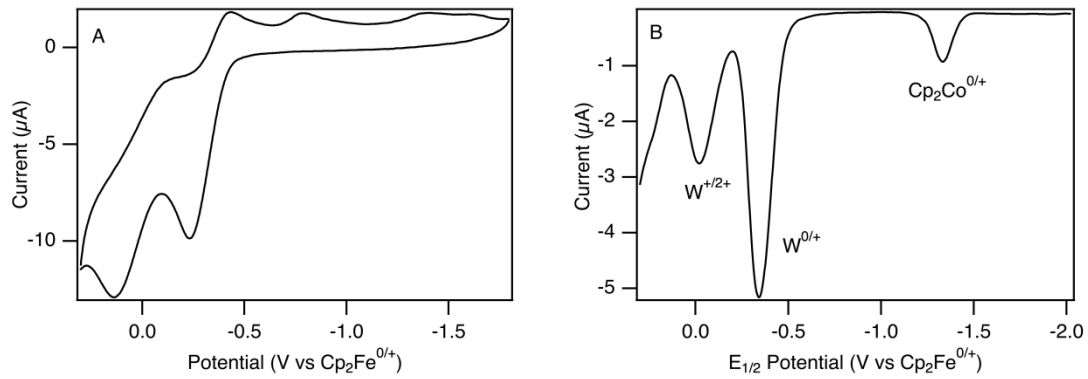

Figure 4.16. Electrochemical data for $W(CC_6H_4\text{-}4\text{-}pyr)\{P(OMe)_3\}_4Cl$ in THF solution with 0.1 M $[^nBu_4N][PF_6]$: (A) CV (200 mV s^{-1}); (B) DPV.

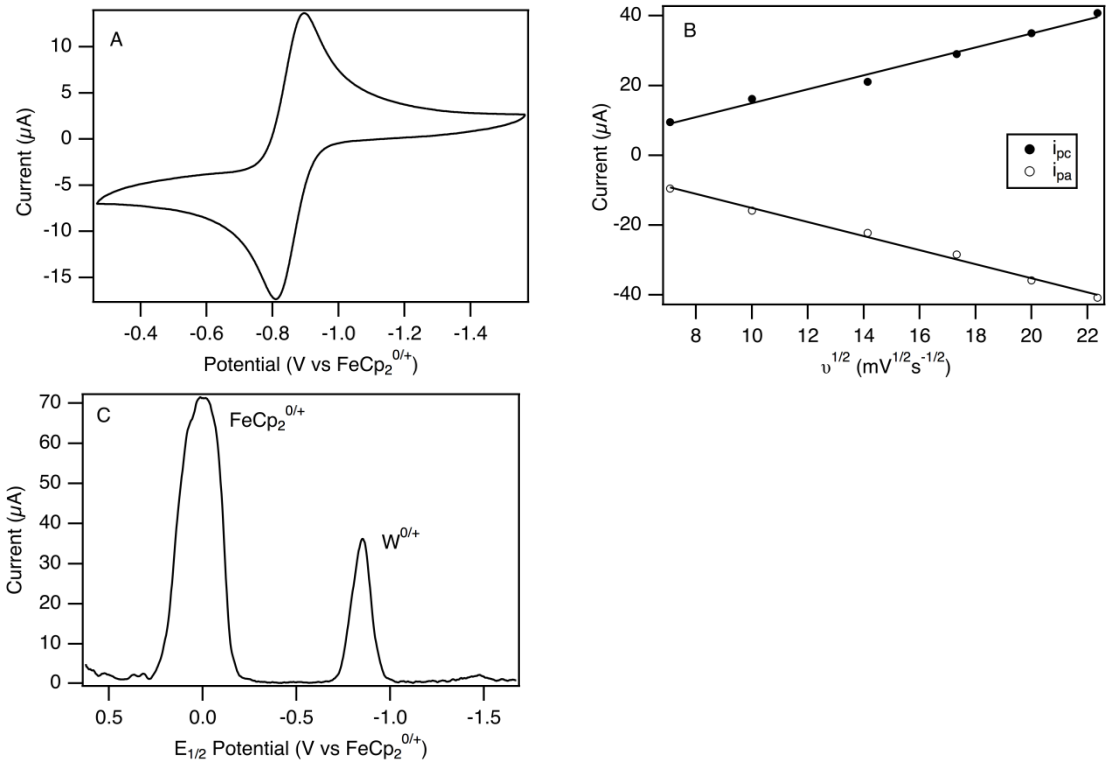

Figure 4.17. Electrochemical data for $W(CPh)(dmpe)_2Cl$ in CH_3CN solution with 0.1 M $[^nBu_4N][PF_6]$: (A) CV(200 mV s^{-1}); (B) Randles-Sevcik plot: i_{pc}, f(x) = 1.99x +5.01, $r^2 = 0.99$; ip_a, f(x) = –2.01x – 5.04, $r^2 = 0.99$; (C) DPV.

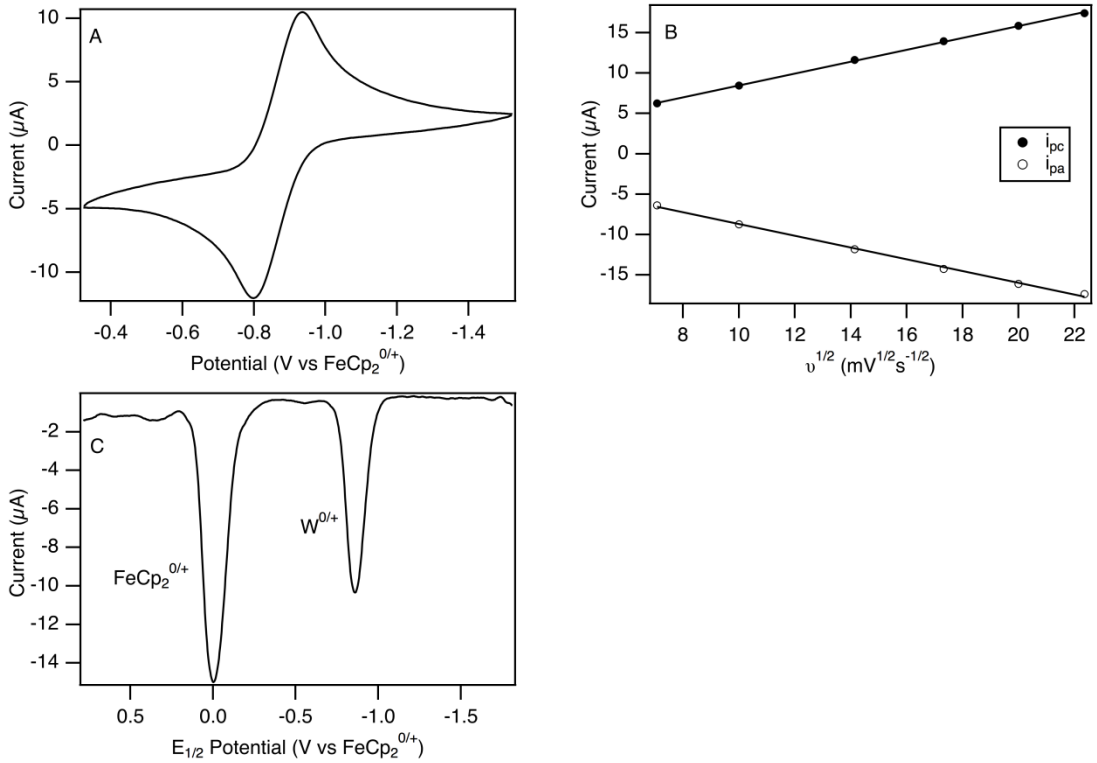

Figure 4.18. Electrochemical data for W(CPh)(dmpe)$_2$Cl in CD_2Cl_2 solution with 0.1 M [^{n}Bu$_4$N][PF$_6$]: (A) Representative CV at 200 mV s^{-1}; (B) Randles-Sevcik plot: i_{pc}, f(x) = 0.73x + 1.11, r^2 = 0.99; ip_a, f(x) = –0.73x – 1.42, r^2 = 0.99; (C) DPV.

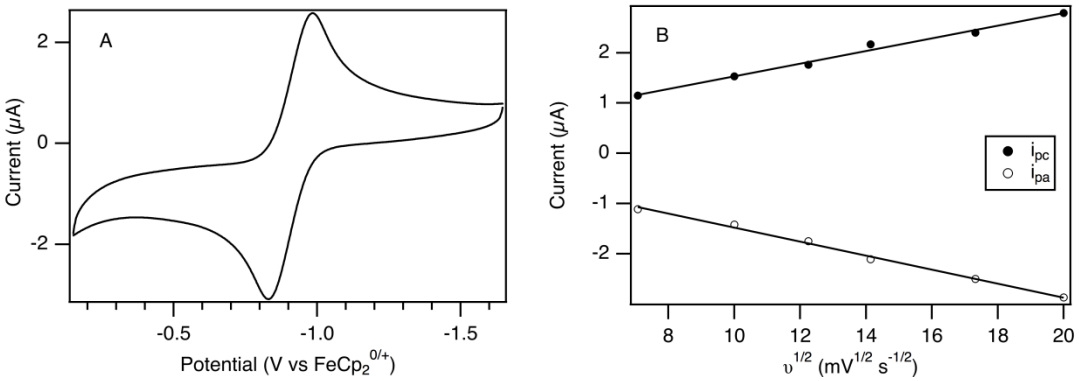

Figure 4.19. Electrochemical data for W(CPh)(dmpe)$_2$F in THF with 0.1 M [Bu^n$_4$N][PF$_6$]: (A) CV (200 mV s^{-1}); (B) Randles-Sevcik plot: i_{pc}, f(x) = 0.13x + 0.26, r^2 = 0.99; ip_a, f(x) = –0.14x – 0.08, r^2 = 0.99.

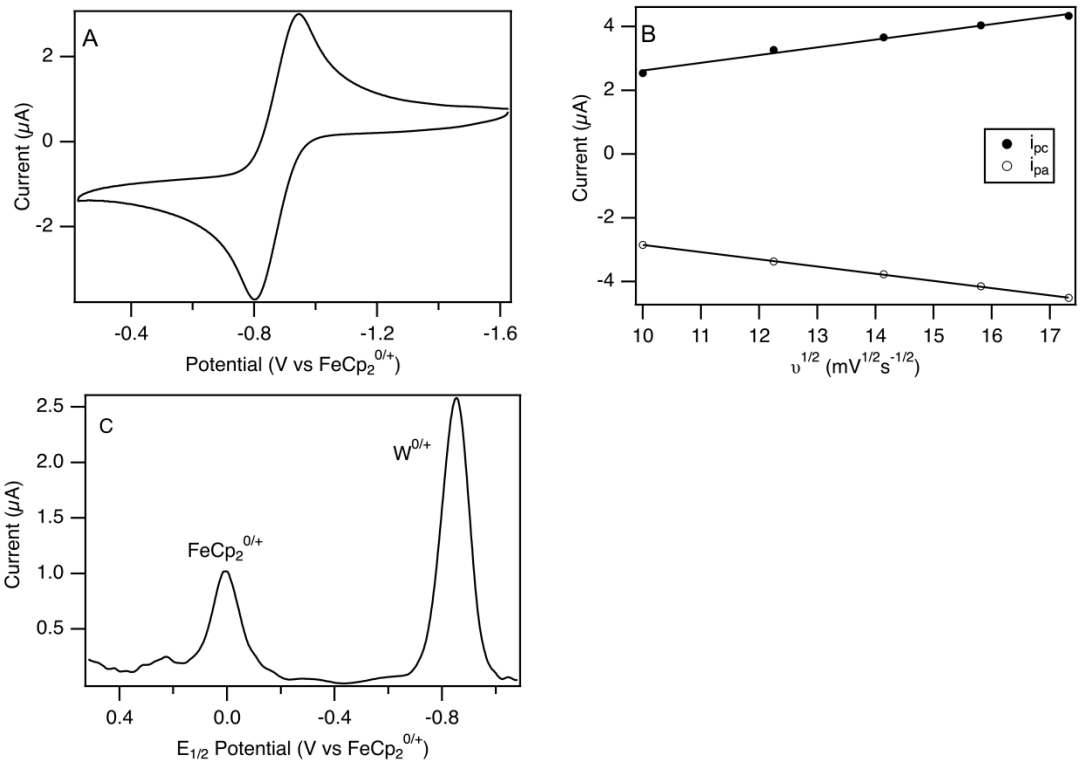

Figure 4.20. Electrochemical data for W(CMes)(dmpe)$_2$Cl in THF with 0.1 M [Bu$^n_4$N][PF$_6$]: (A) CV (200 mV s^{-1}); (B) Randles-Sevcik plot: i_{pc}, f(x) = 0.24x + 0.21, r^2 = 0.99; ip_a, f(x) = – 0.23x – 0.60, r^2 = 0.99; (C) DPV.

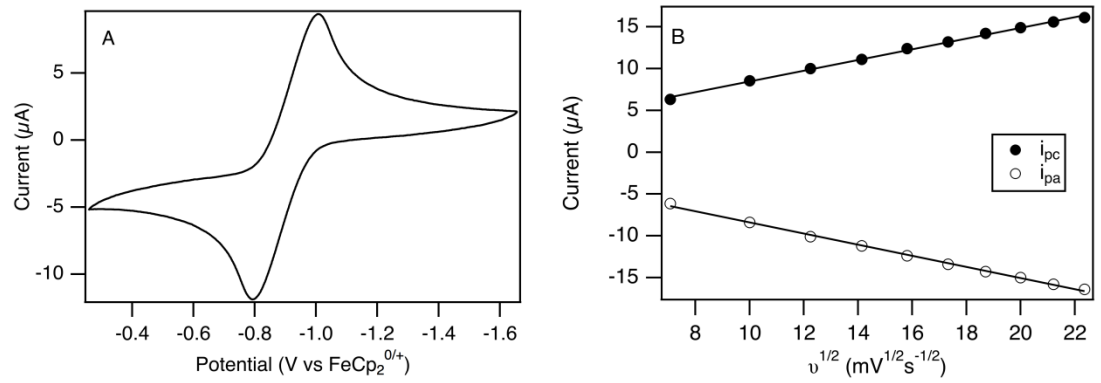

Figure 4.21. Electrochemical data for $W(CC_6H_4\text{-}4\text{-}OCH_3)(dmpe)_2Cl$ in THF solution with 0.1 M $[^nBu_4N][PF_6]$: (A) Representative CV at 200 mV s^{-1}; (B) Randles-Sevcik plot: i_{pc}, f(x) = 0.64x + 2.05, $r^2 = 0.99$; ip_a, f(x) = –0.66x – 1.73, $r^2 = 0.99$.

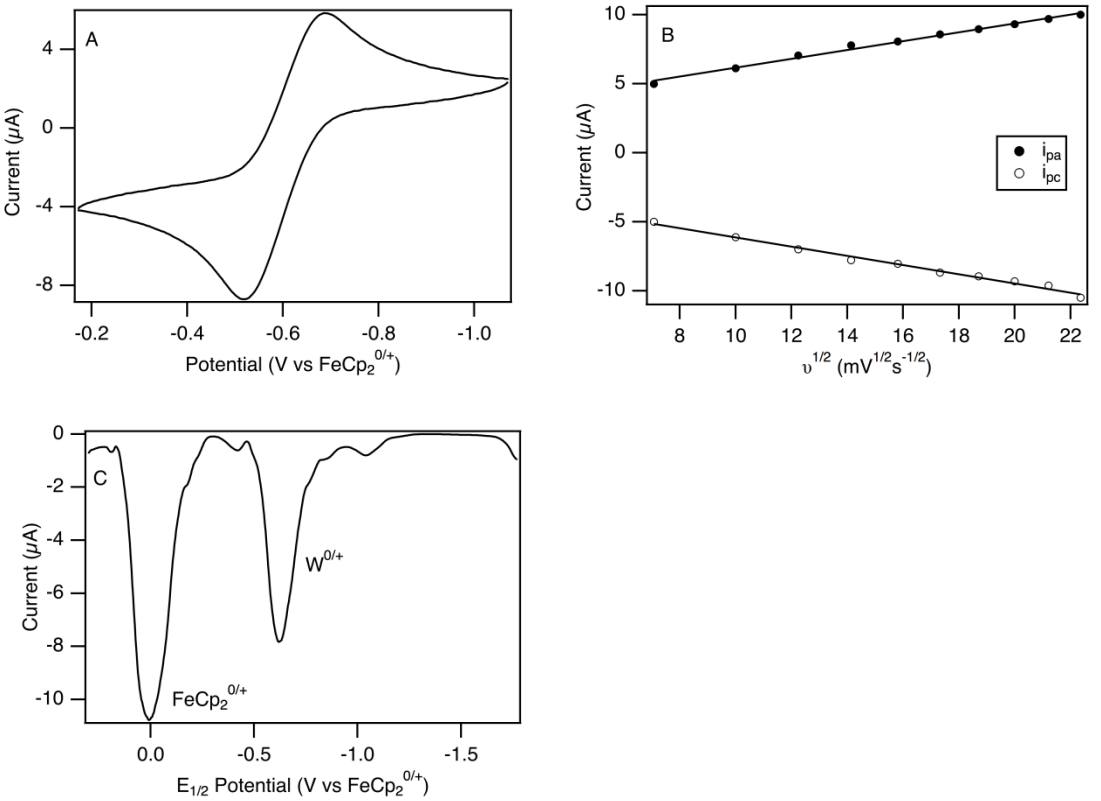

Figure 4.22. Electrochemical data for $W(CC_6H_4\text{-}4\text{-}OCH_3)(dppe)_2Cl$ in THF solution with 0.1 M $[^nBu_4N][PF_6]$: (A) Representative CV at 200 mV s^{-1}; (B) Randles-Sevcik plot: i_{pc}, f(x) = 0.32x + 2.96, $r^2 = 0.99$; ip_a, f(x) = –0.33x – 2.79, $r^2 = 0.99$; (C) DPV.

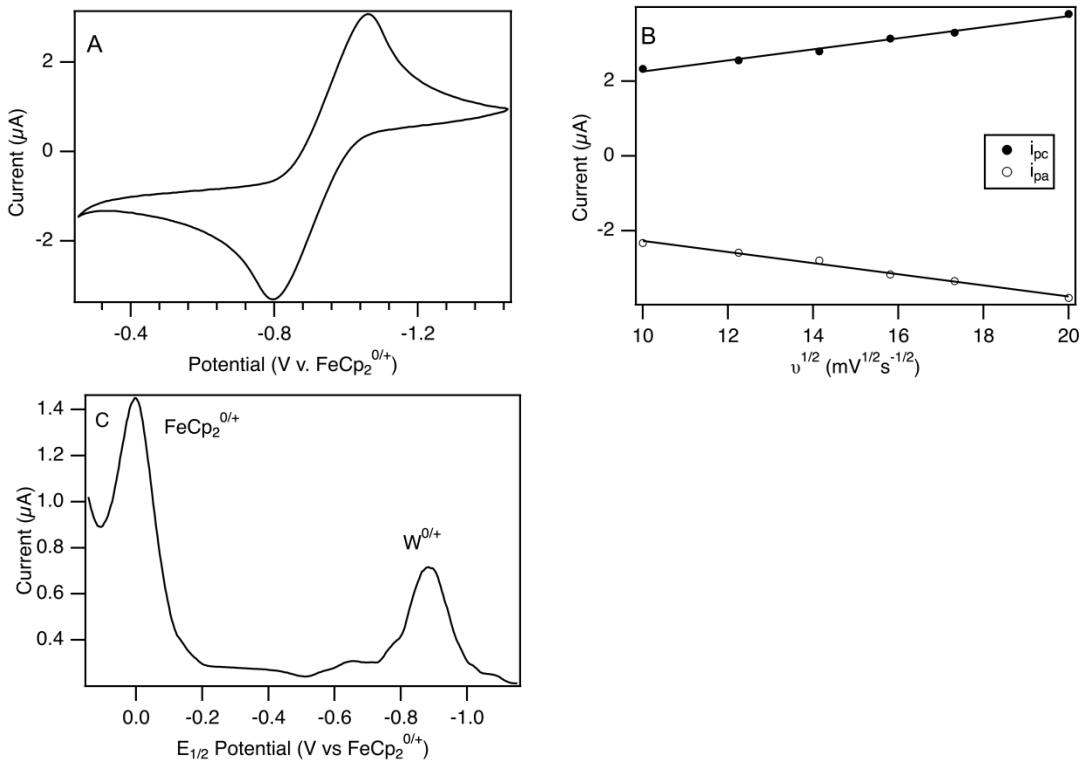

Figure 4.23. Electrochemical data for $W(CC_6H_4\text{-}4\text{-}pyr)(dmpe)_2Cl$ in THF with 0.1 M $[Bu^n{}_4N][PF_6]$: (A) CV (200 mV s^{-1}); (B) (B) Randles-Sevcik plot: i_{pc}, $f(x) = 0.15x + 0.78$, $r^2 = 0.99$; ip_a, $f(x) = –0.15x – 0.79$, $r^2 = 0.99$; (C) DPV.

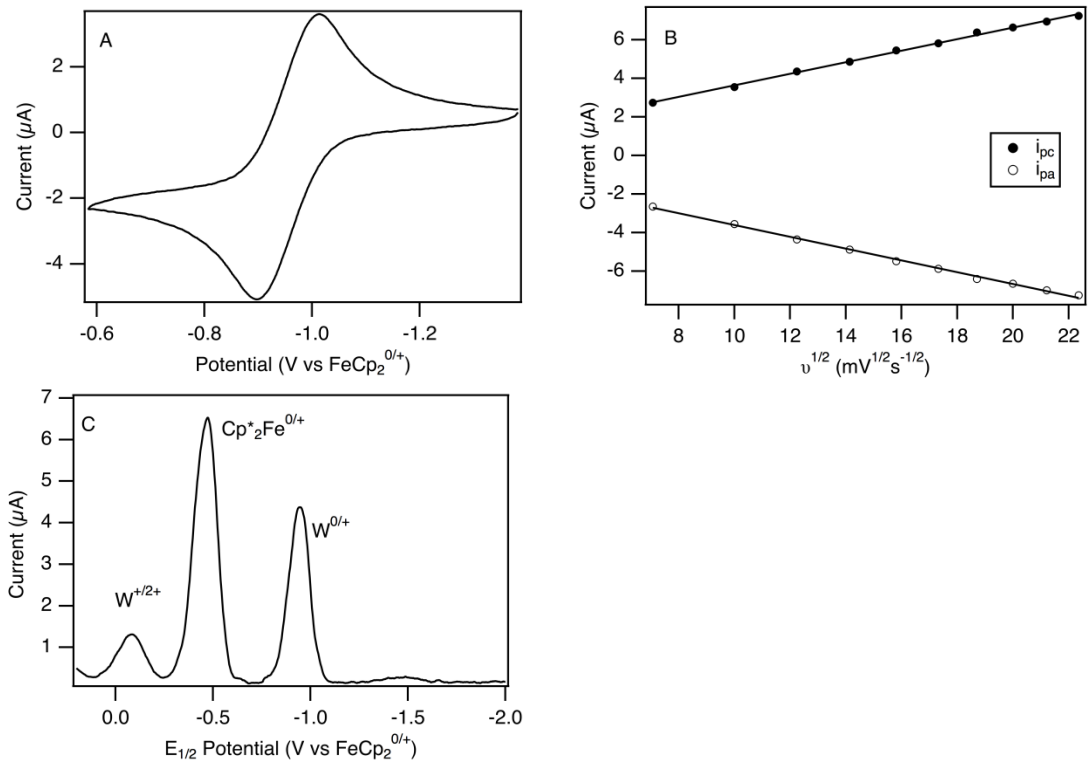

Figure 4.24. Electrochemical data for $W(CC_6H_4\text{-}4\text{-}pyr)(depe)_2Cl$ in THF solution with 0.1 M $[^nBu_4N][PF_6]$: (A) Representative CV at 200 mV s^{-1}; (B) Randles-Sevcik plot: i_{pc}, $f(x) = 0.30x + 0.64$, $r^2 = 0.99$; ip_a, $f(x) = -0.30x - 0.55$, $r^2 = 0.99$; (C) DPV.

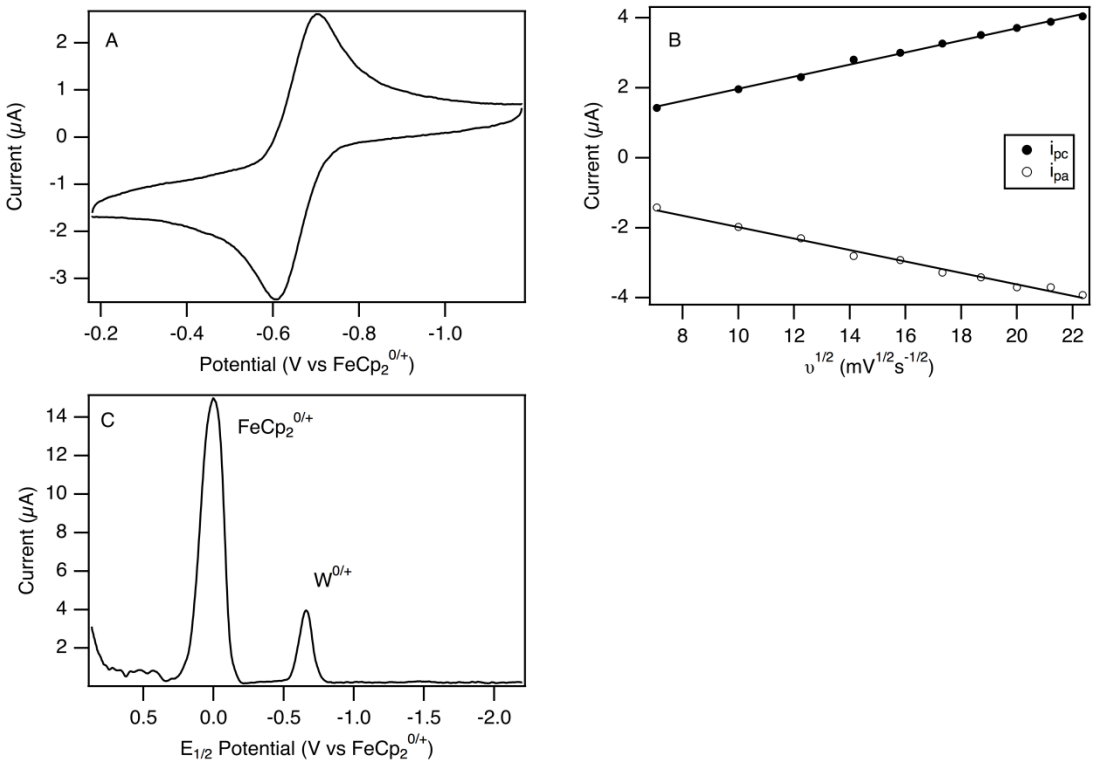

Figure 4.25. Electrochemical data for $W(CC_6H_4\text{-}4\text{-}pyr)(dppe)_2Cl$ in THF solution with 0.1 M $[^nBu_4N][PF_6]$: (A) Representative CV at 200 mV s^{-1}; (B) Randles-Sevcik plot: i_{pc}, $f(x) = 0.17x + 0.24$, $r^2 = 0.99$; ip_a, $f(x) = -0.16x - 0.34$, $r^2 = 0.99$; (C) DPV.

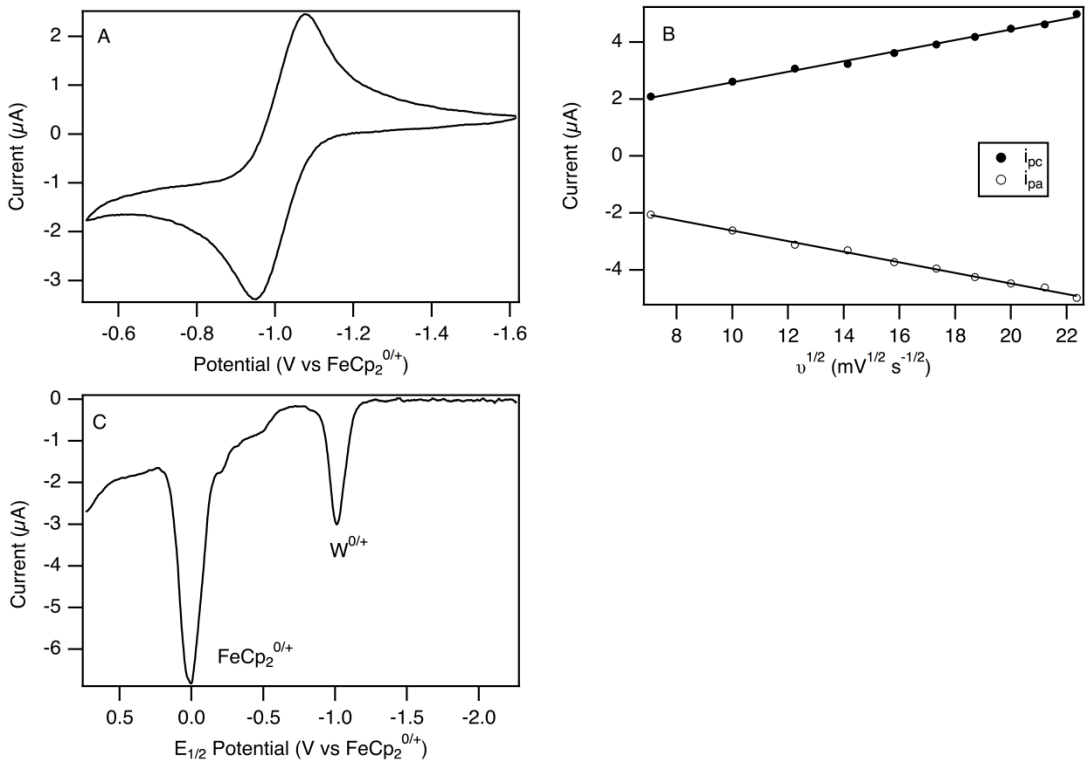

Figure 4.26. Electrochemical data for $W(CC_6H_4\text{-}4\text{-}pyr)(dmpe)_2F$ in THF solution with 0.1 M [^{n}Bu$_4$N][PF$_6$]: (A) Representative CV at 200 mV s^{-1}; (B) Randles-Sevcik plot: ip_c, $f(x) = 0.19x + 0.73$, $r^2 = 0.99$; ip_a, $f(x) = -0.19x - 0.75$, $r^2 = 0.99$; (C) DPV.

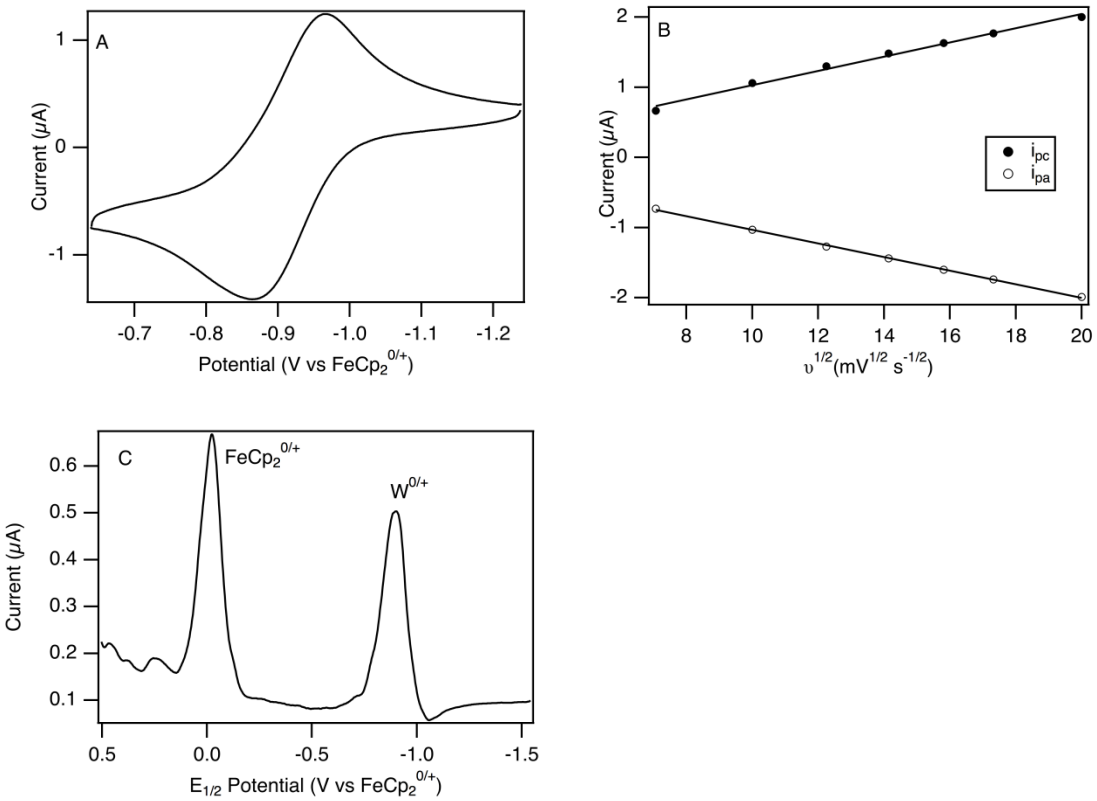

Figure 4.27. Electrochemical data for $W(CC_6H_4\text{-}4\text{-}NH_2)(dmpe)_2Cl$ in THF solution with 0.1 M [^{n}Bu$_4$N][PF$_6$]. (A) Representative CV at 200 mV s^{-1}; (B) Randles-Sevcik plot: ip_c, f(x) = 0.10x + 0.01, r^2 = 0.99; ip_a, f(x) = –0.09x – 0.06, r^2 = 0.99; (C) DPV.

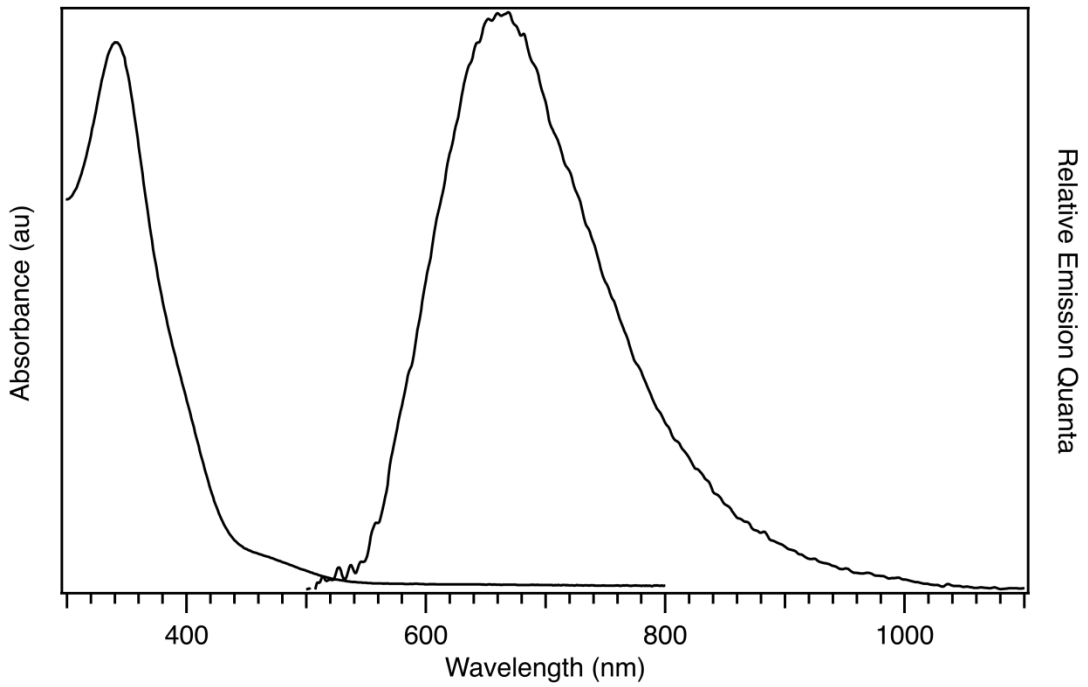

Figure 4.28. Electronic absorption and emission spectra of $W(CPh)(pic)_2(CO)_2Cl$ in toluene solution.

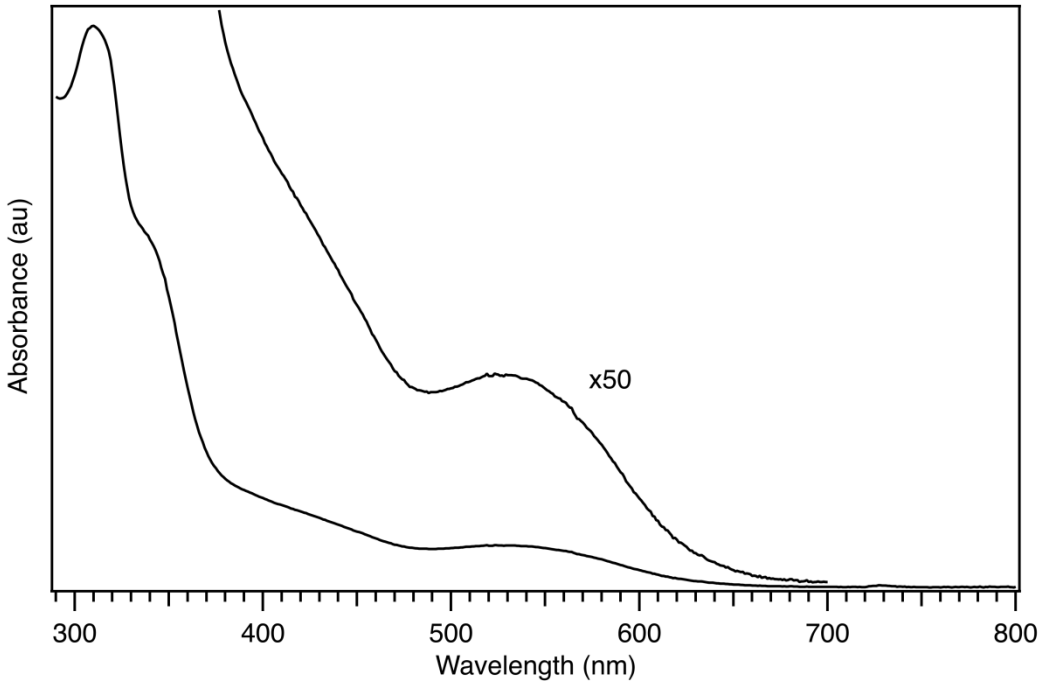

Figure 4.29. Electronic absorption and emission spectra of $W(CPh)(bpy)(CO)_2Cl$ in toluene solution.

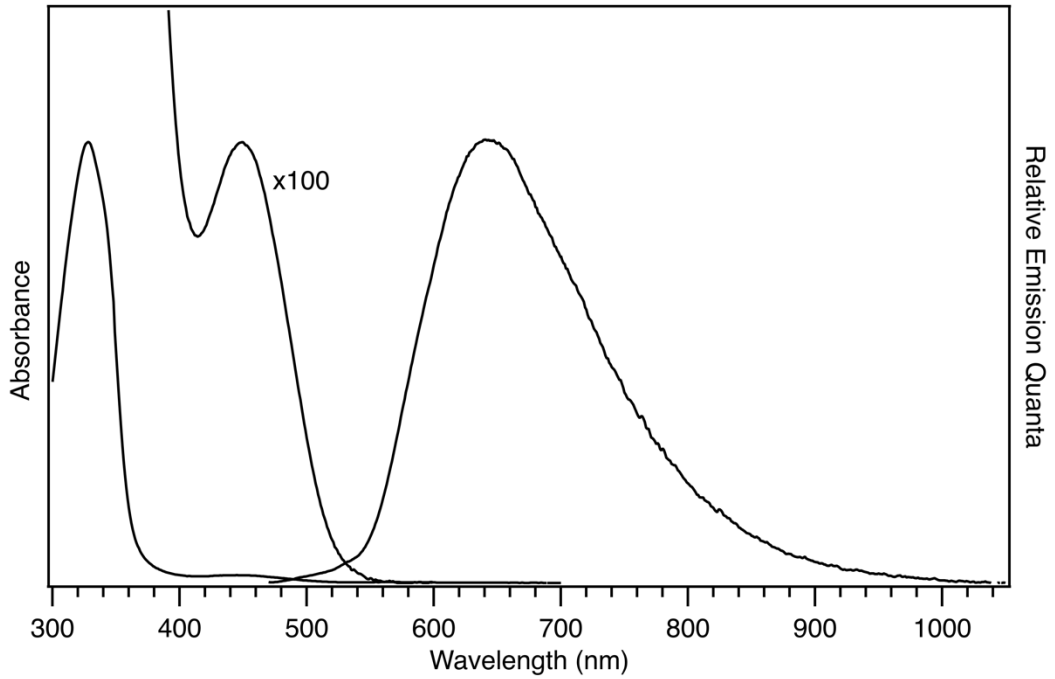

Figure 4.30. Electronic absorption and emission spectra of W(CPh){P(OMe)$_3$}$_4$Cl in toluene solution.

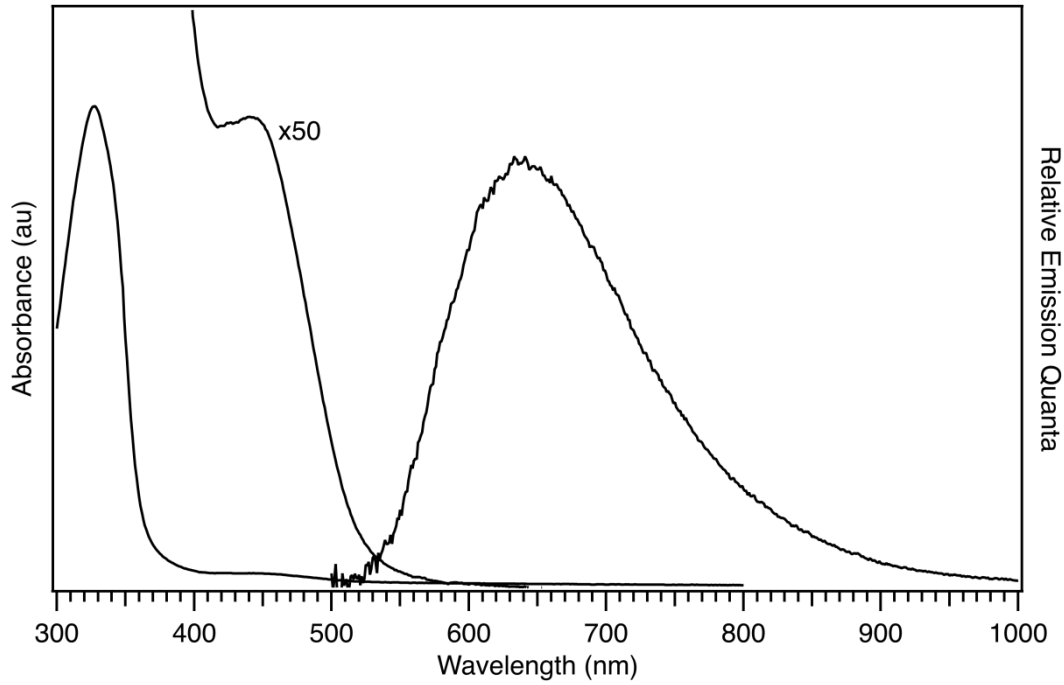

Figure 4.31. Electronic absorption and emission spectra of W(CPh){P(OMe)$_3$}$_4$Cl in THF solution.

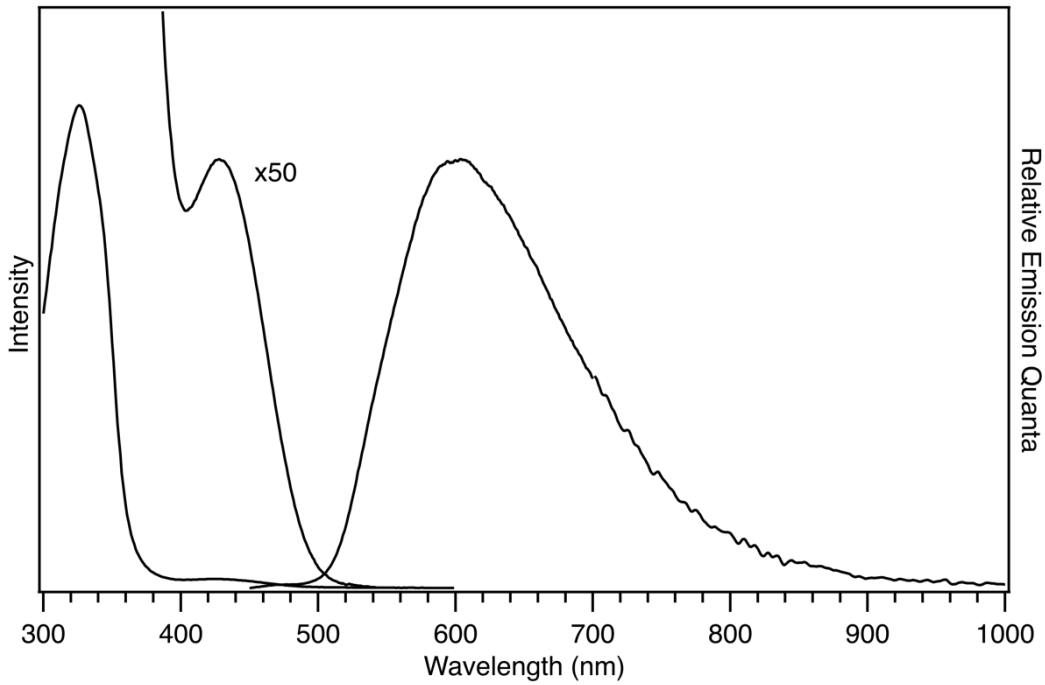

Figure 4.32. Electronic absorption and emission spectra of $W(CC_6H_4\text{-}4\text{-}OCH_3)\{P(OMe)_3\}_4Cl$ in toluene solution.

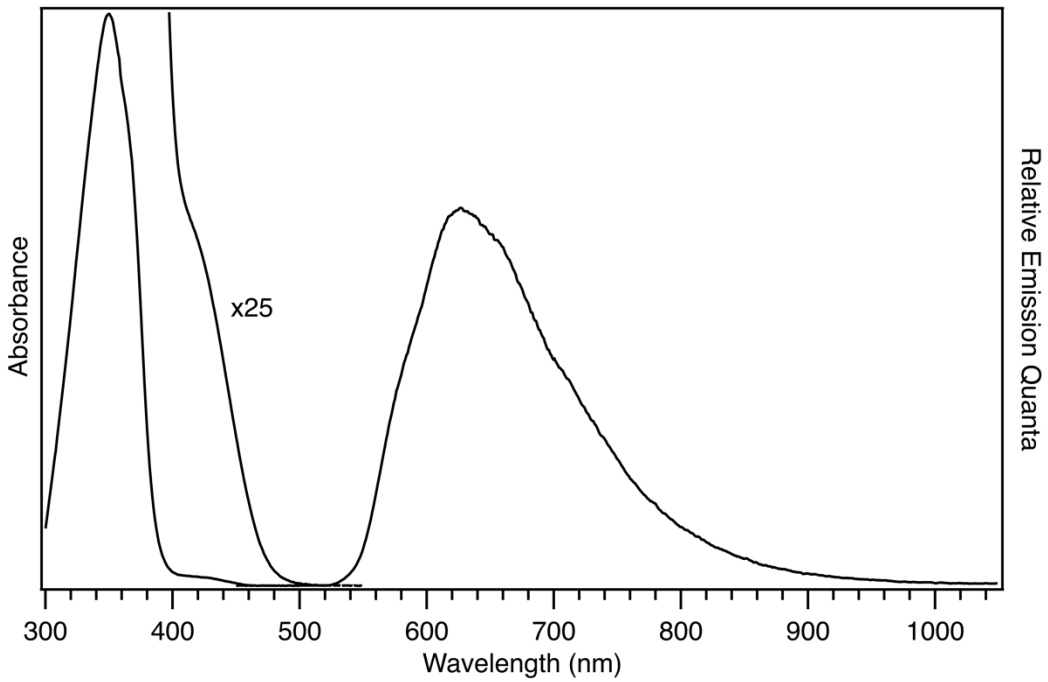

Figure 4.33. Electronic absorption and emission spectra of $W(CC_6H_4\text{-}4\text{-}pyr)\{P(OMe)_3\}_4Cl$ in toluene solution.

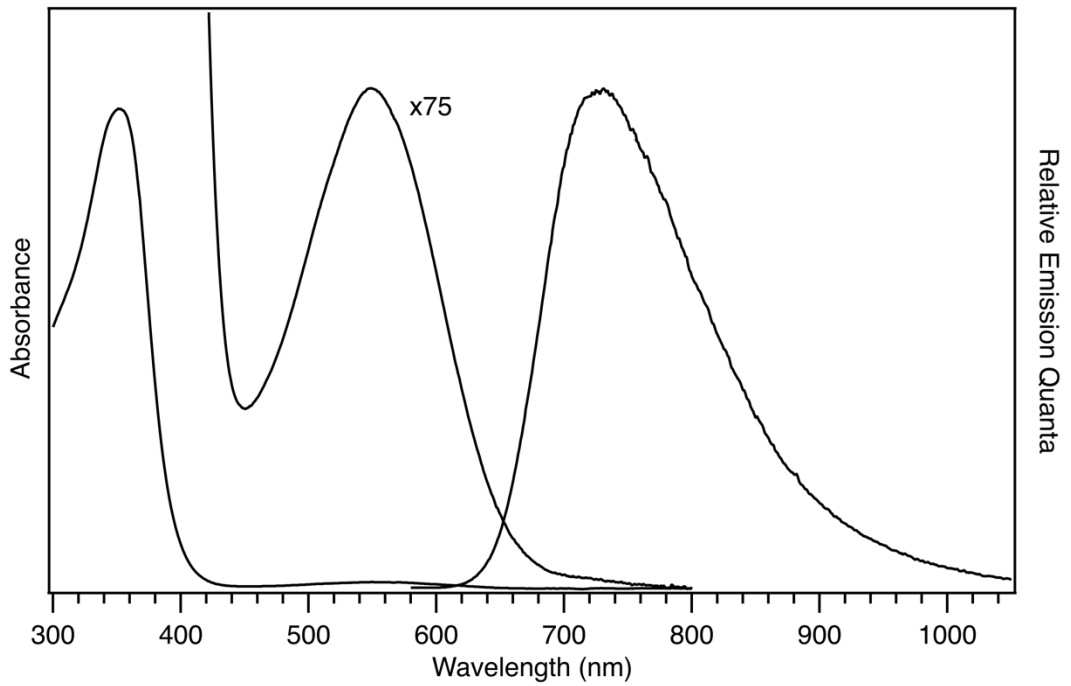

Figure 4.34. Electronic absorption and emission spectra of W(CPh)(PMe_3)$_4$Cl in toluene solution.

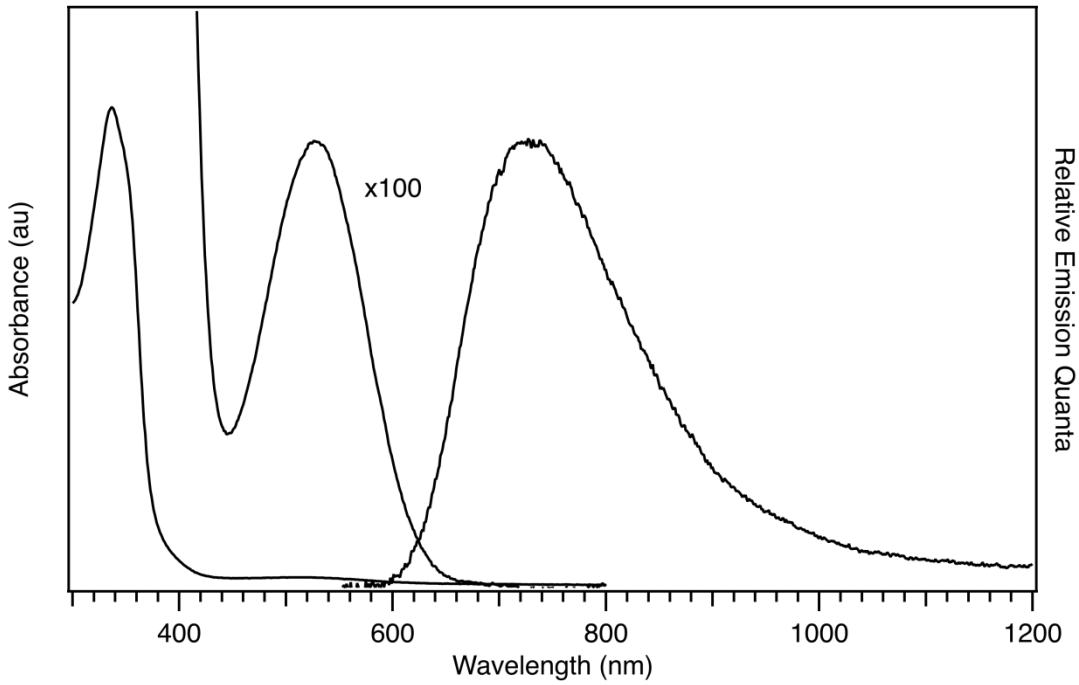

Figure 4.35. Electronic absorption and emission spectra of W(CPh)(dmpe)$_2$Cl in THF solution.

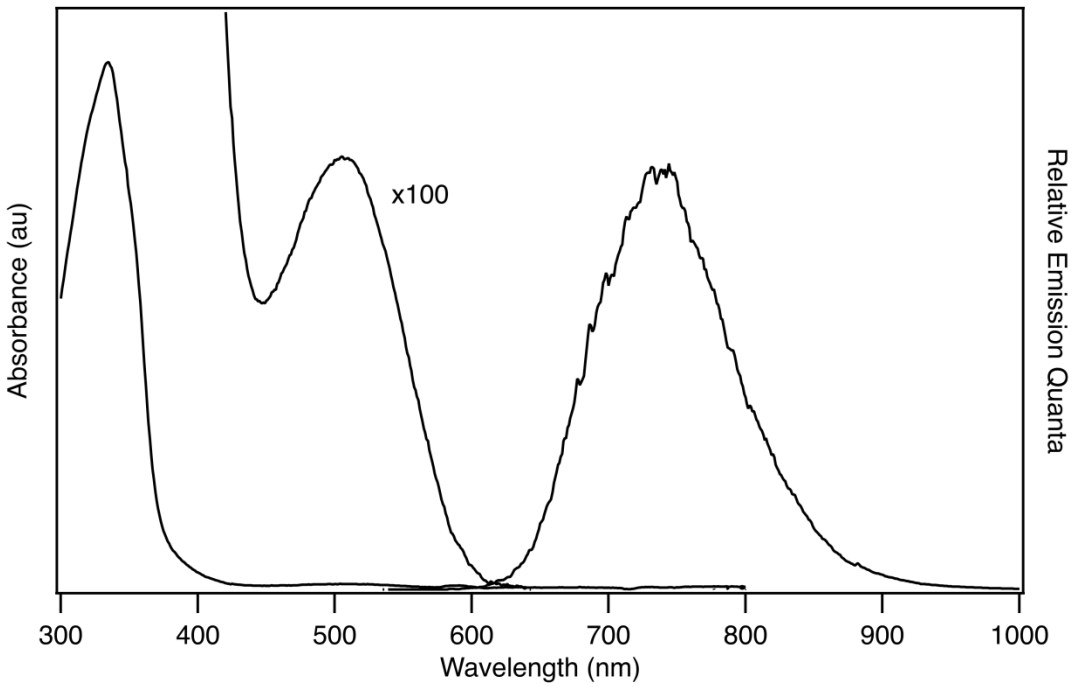

Figure 4.36. Electronic absorption and emission spectra of W(CMes)(dmpe)$_2$Cl in toluene solution.

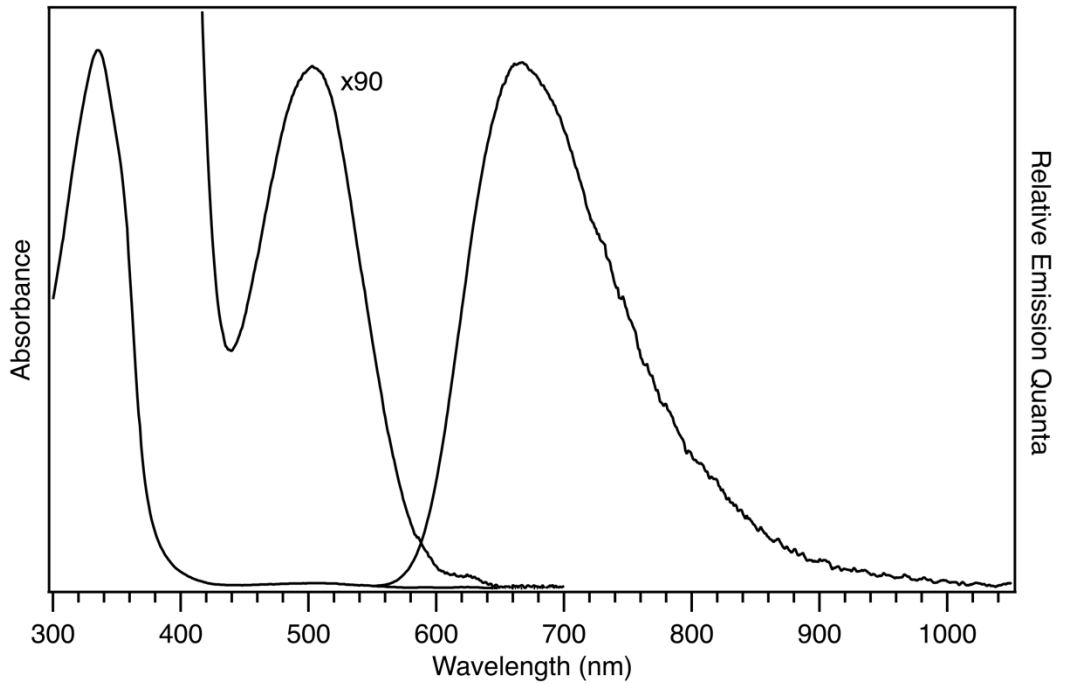

Figure 4.37. Electronic absorption and emission spectra of W(CC_6H_4-4-OCH_3)(dmpe)$_2$Cl in toluene solution.

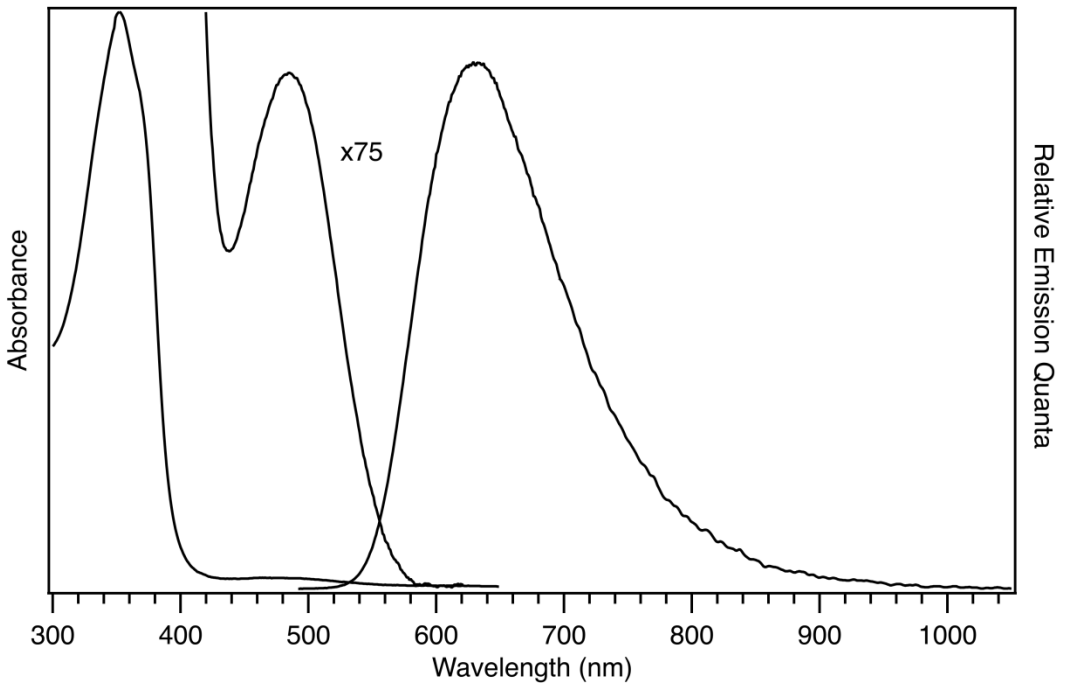

Figure 4.38. Electronic absorption and emission spectra of $W(CC_6H_4\text{-}4\text{-}pyr)(dmpe)_2Cl$ in toluene solution.

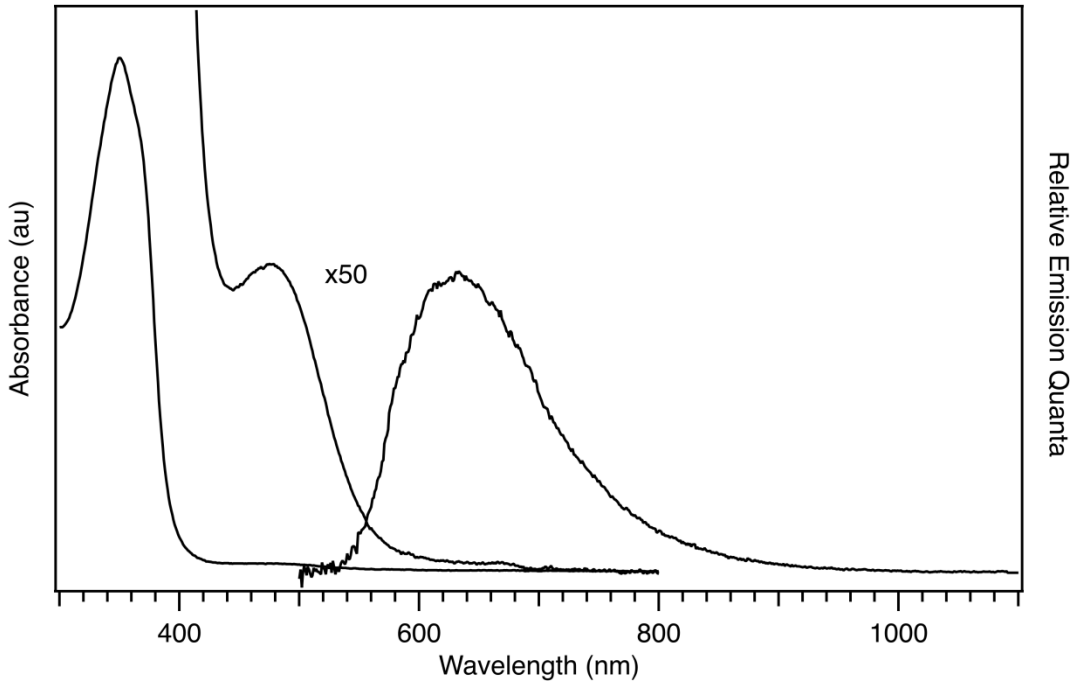

Figure 4.39. Electronic absorption and emission spectra of $W(CC_6H_4\text{-}4\text{-}pyr)(dmpe)_2Cl$ in THF solution.

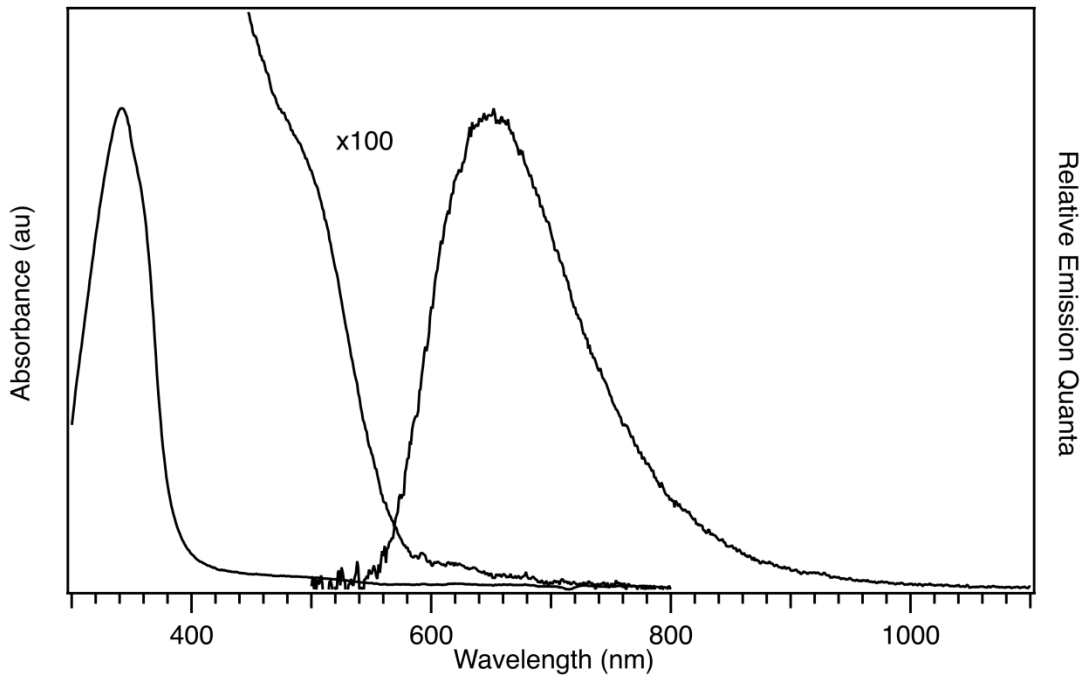

Figure 4.40. Electronic absorption and emission spectra of $W(CC_6H_4\text{-}4\text{-}NH_2)(dmpe)_2Cl$ in toluene solution.

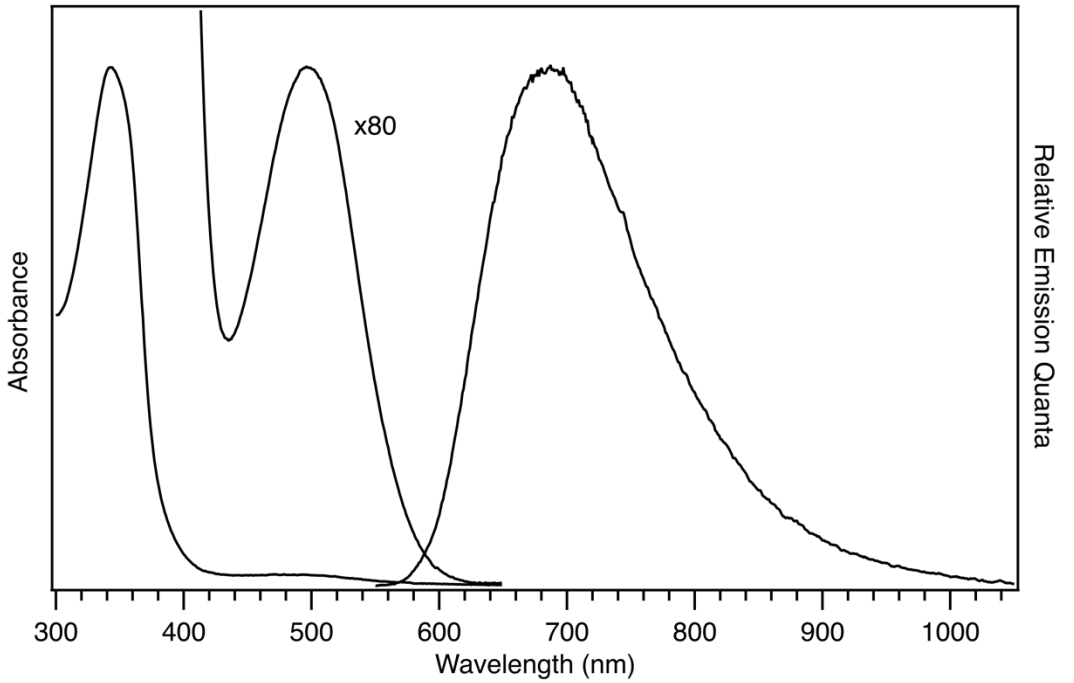

Figure 4.41. Electronic absorption and emission spectra of $W(CPh)(dmpe)_2F$ in toluene solution.

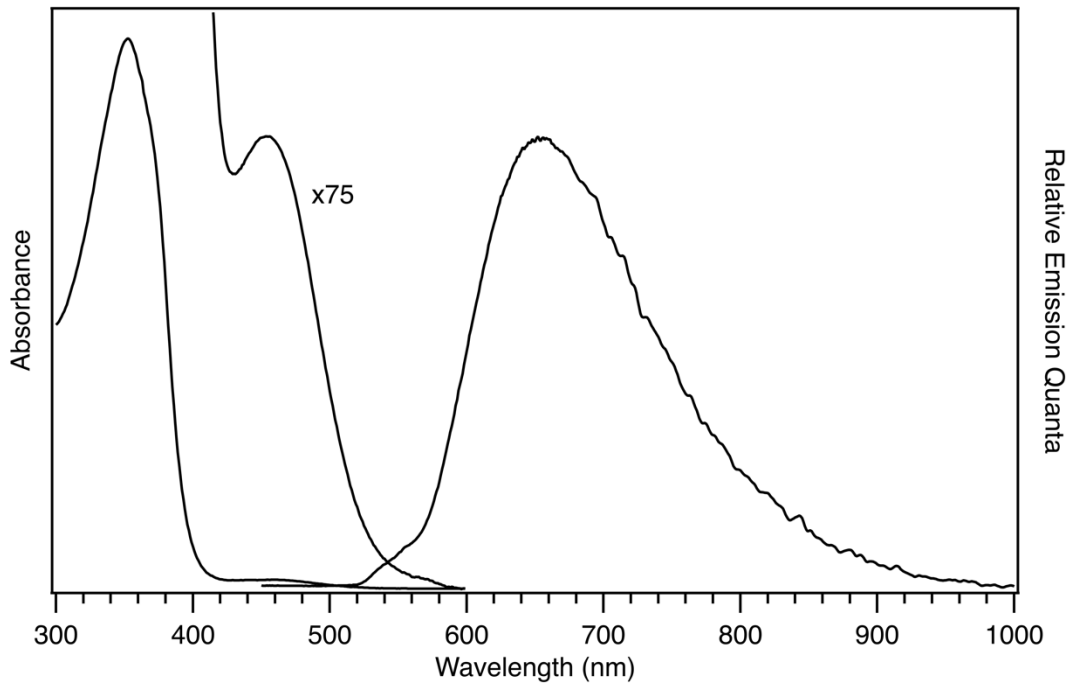

Figure 4.42. Electronic absorption and emission spectra of $W(CC_6H_4\text{-}4\text{-}pyr)(dmpe)_2F$ in toluene solution.

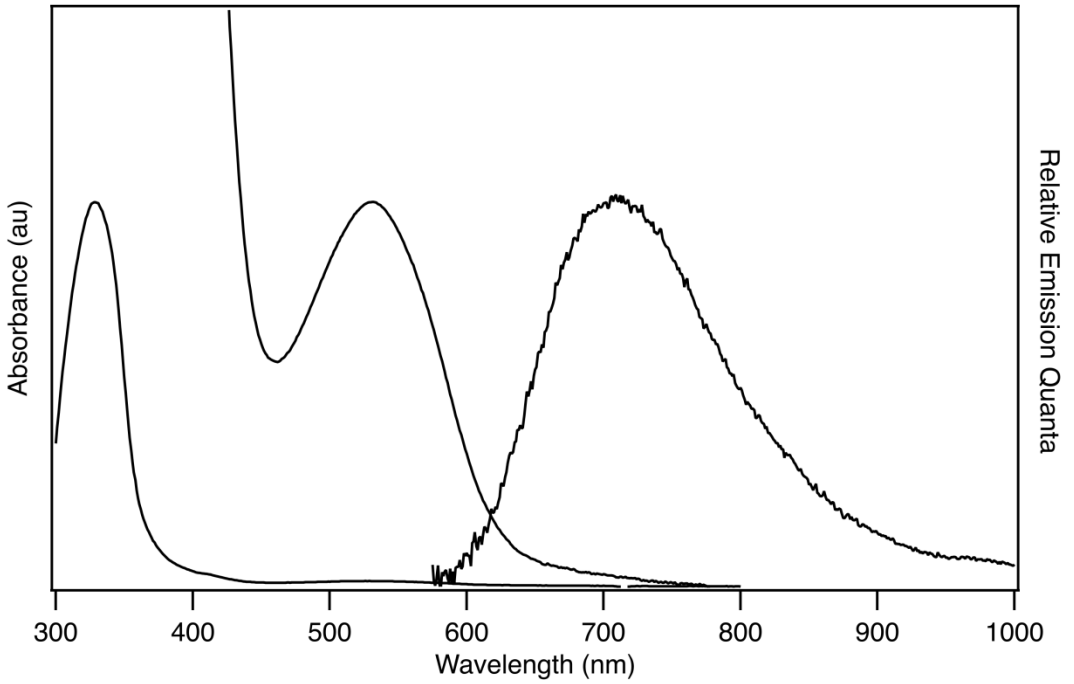

Figure 4.43. Electronic absorption and emission spectrum of $W(CPh)(dmpe)_2(OTf)$ in toluene solution.

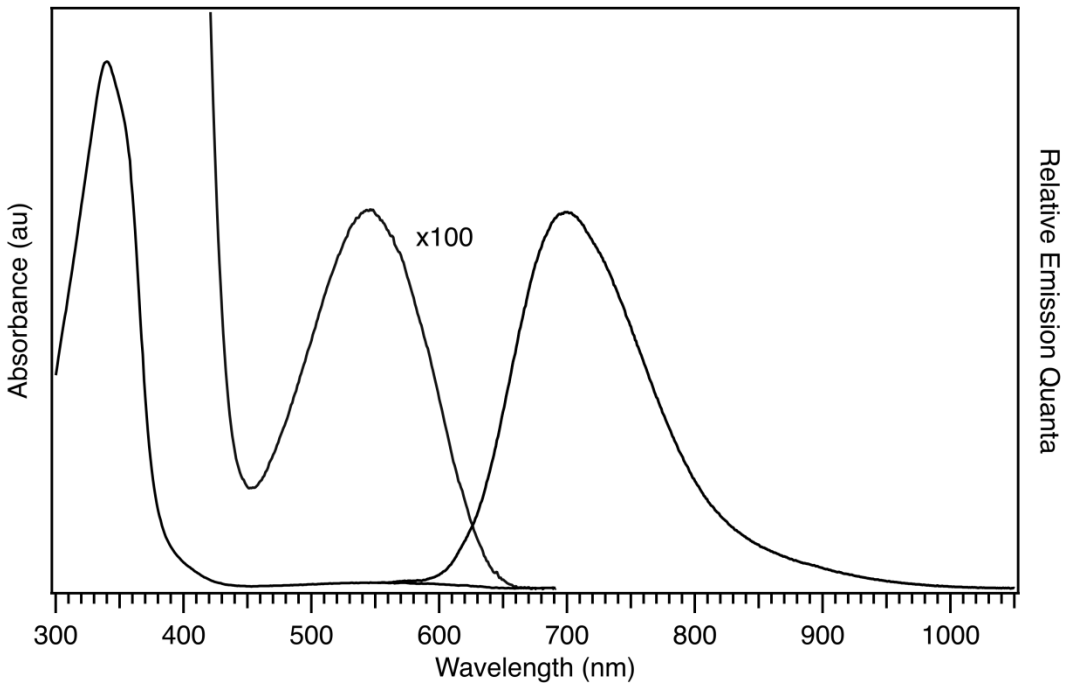

Figure 4.44. Electronic absorption and emission spectra of W(CPh)(depe)$_2$Cl in toluene solution.

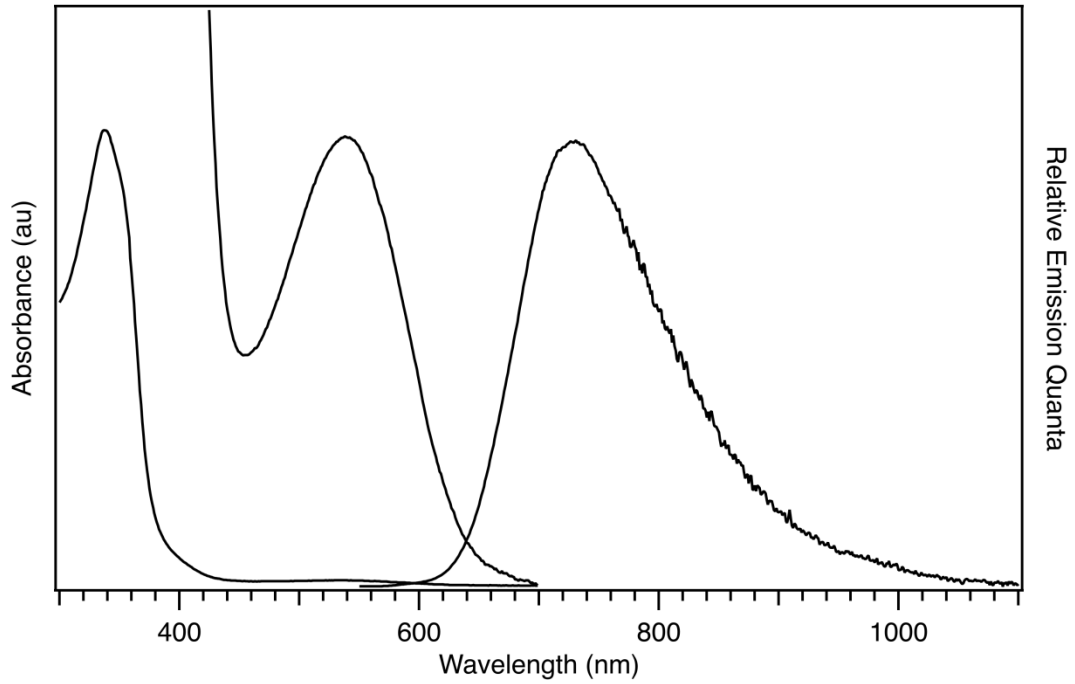

Figure 4.45. Electronic absorption and emission spectra of W(CPh)(depe)$_2$Cl in THF solution.

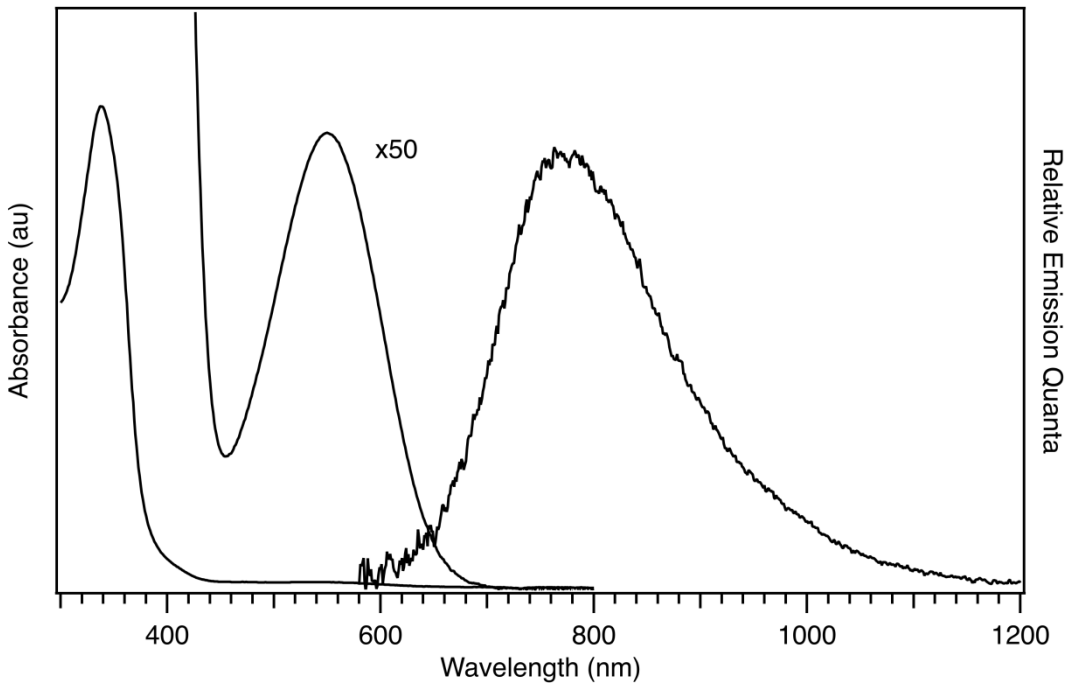

Figure 4.46. Electronic absorption and emission spectra of W(CPh)(depe)$_2$Cl in CH_3CN solution.

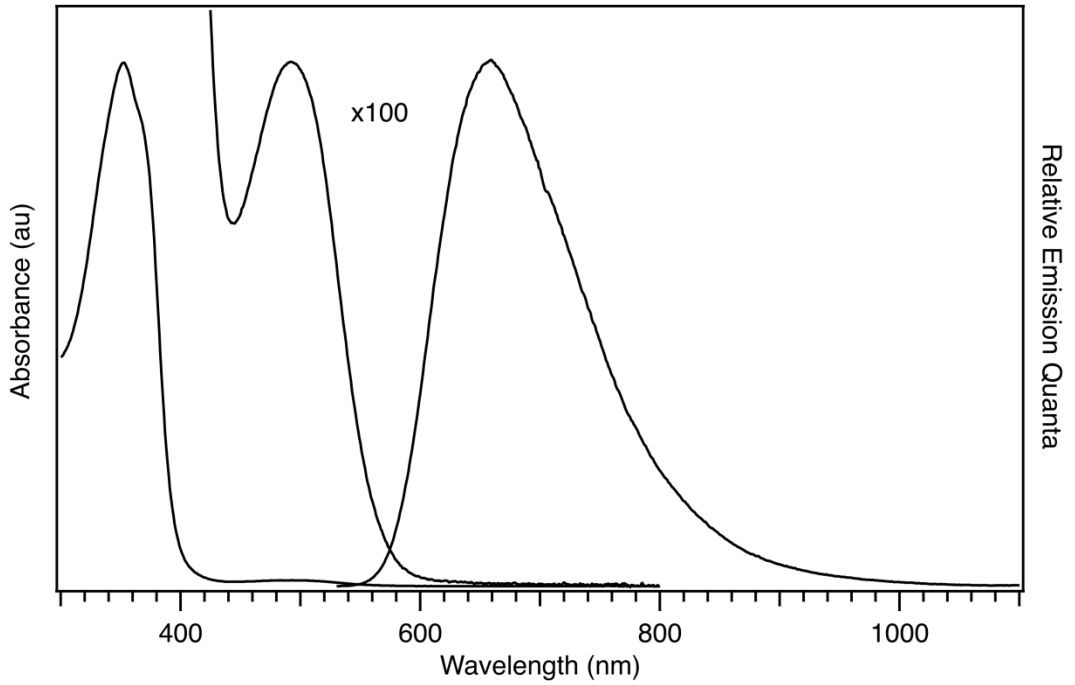

Figure 4.47. Electronic absorption and emission spectra of W(CC_6H_4-4-pyr)(depe)$_2$Cl in toluene solution.

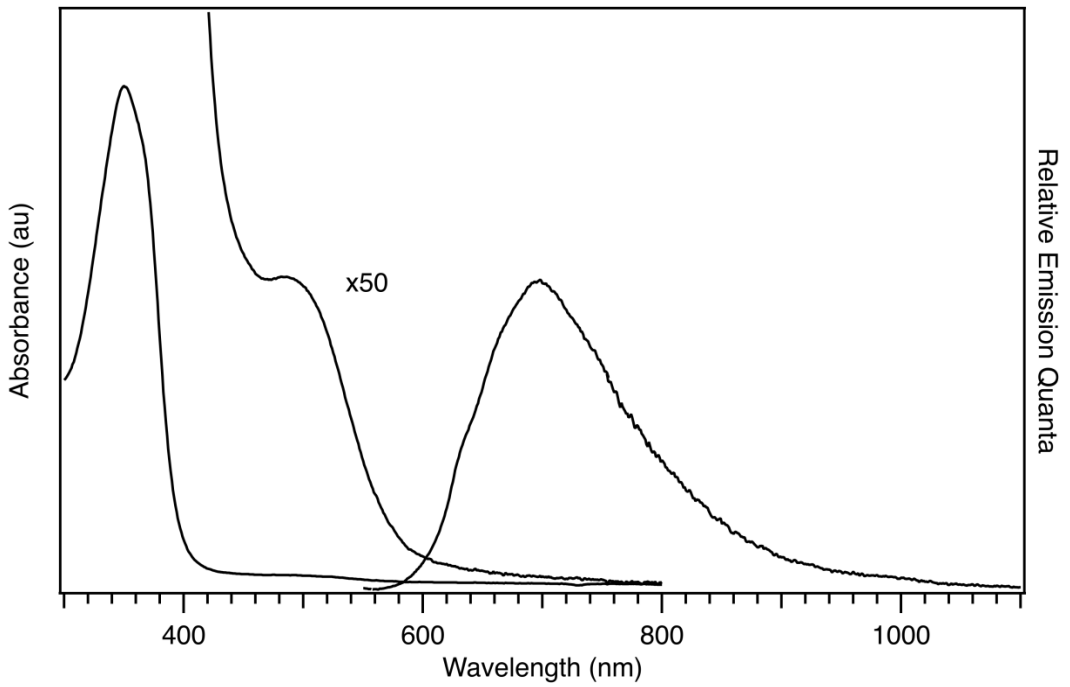

Figure 4.48. Electronic absorption and emission spectra of $W(CC_6H_4\text{-}4\text{-}pyr)(depe)_2Cl$ in CH_3CN solution.

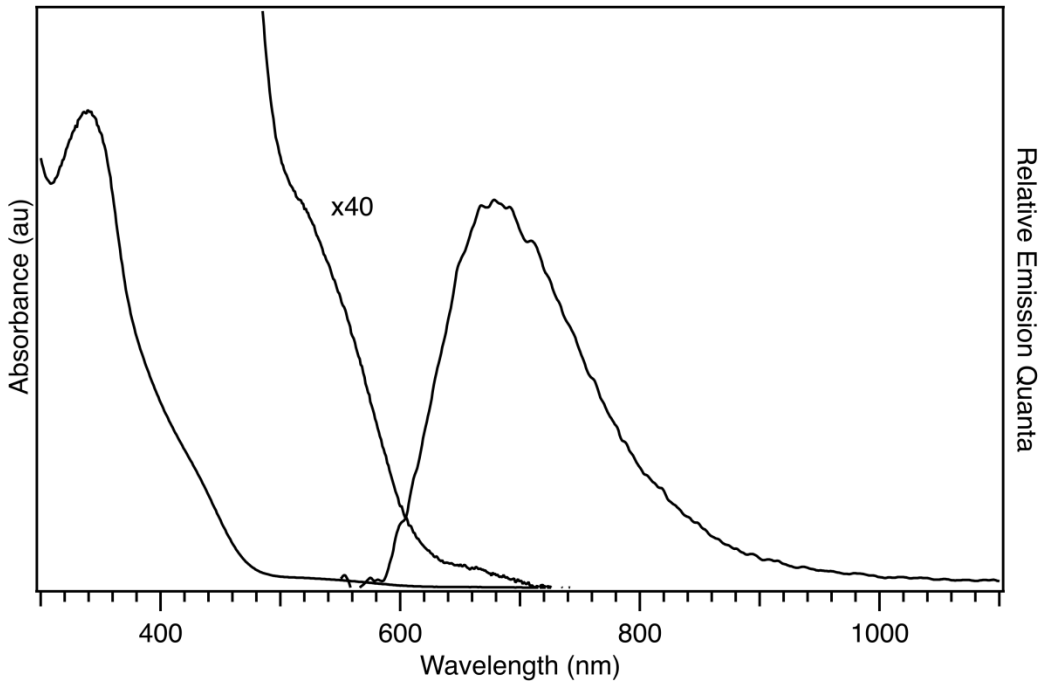

Figure 4.49. Electronic absorption and emission spectra of $W(CPh)(dppe)_2Cl$ in toluene solution.

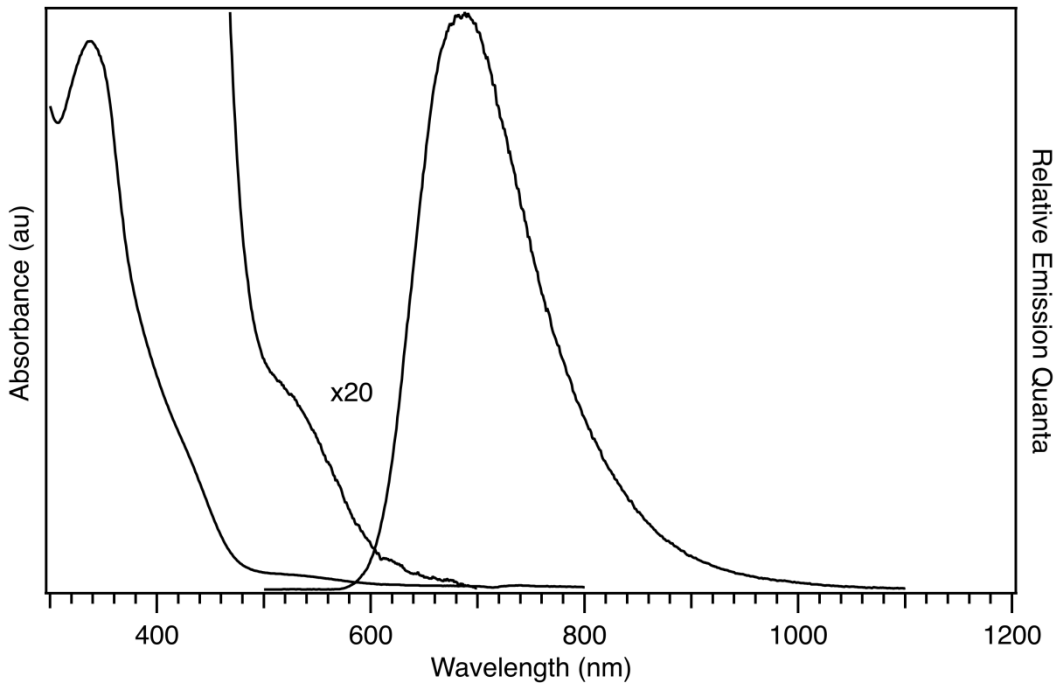

Figure 4.50. Electronic absorption and emission spectra of W(CPh)(dppe)$_2$Cl in THF solution.

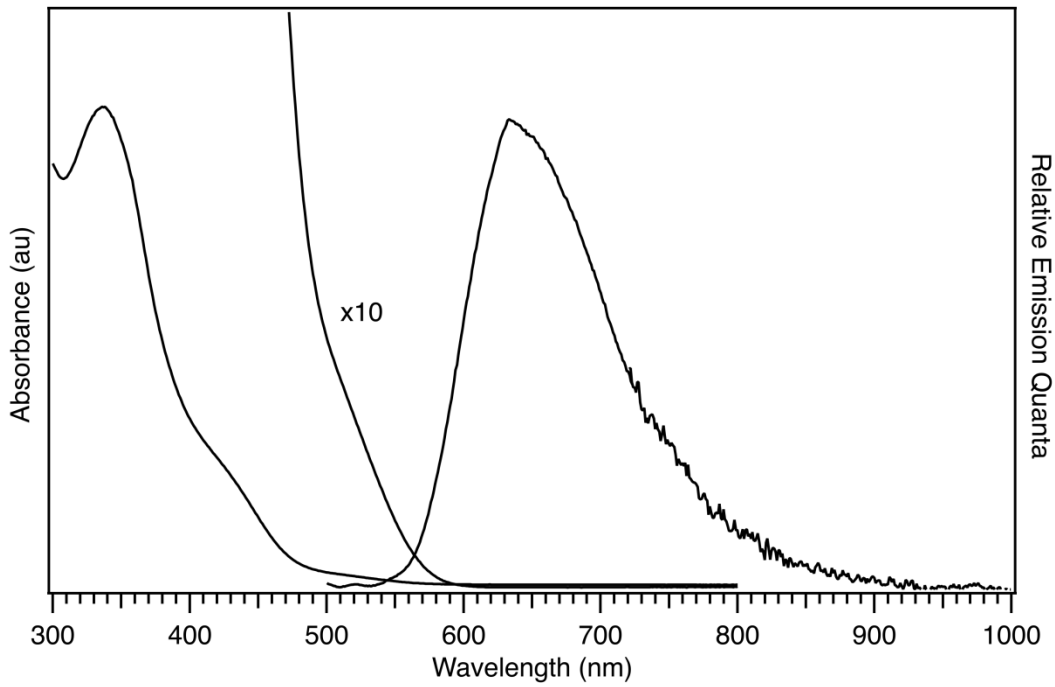

Figure 4.51. Electronic absorption and emission spectra of W(CC$_6$H$_4$-4-OCH$_3$)(dppe)$_2$Cl in toluene solution.

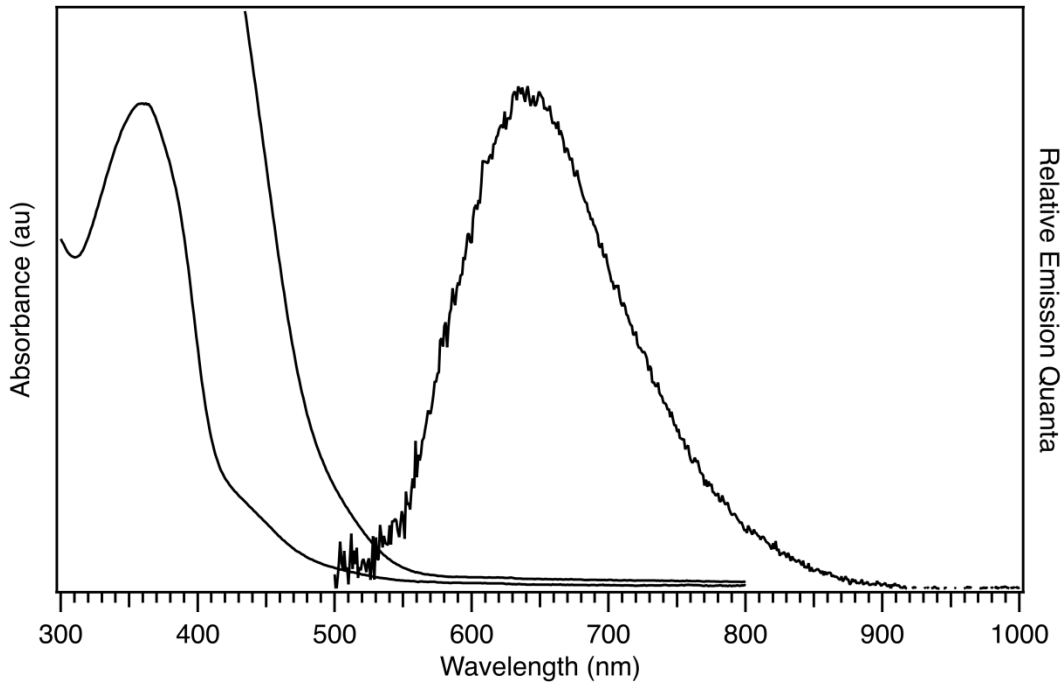

Figure 4.52. Electronic absorption and emission spectra of $W(CC_6H_4\text{-}4\text{-}pyr)(dppe)_2Cl$ in toluene solution.

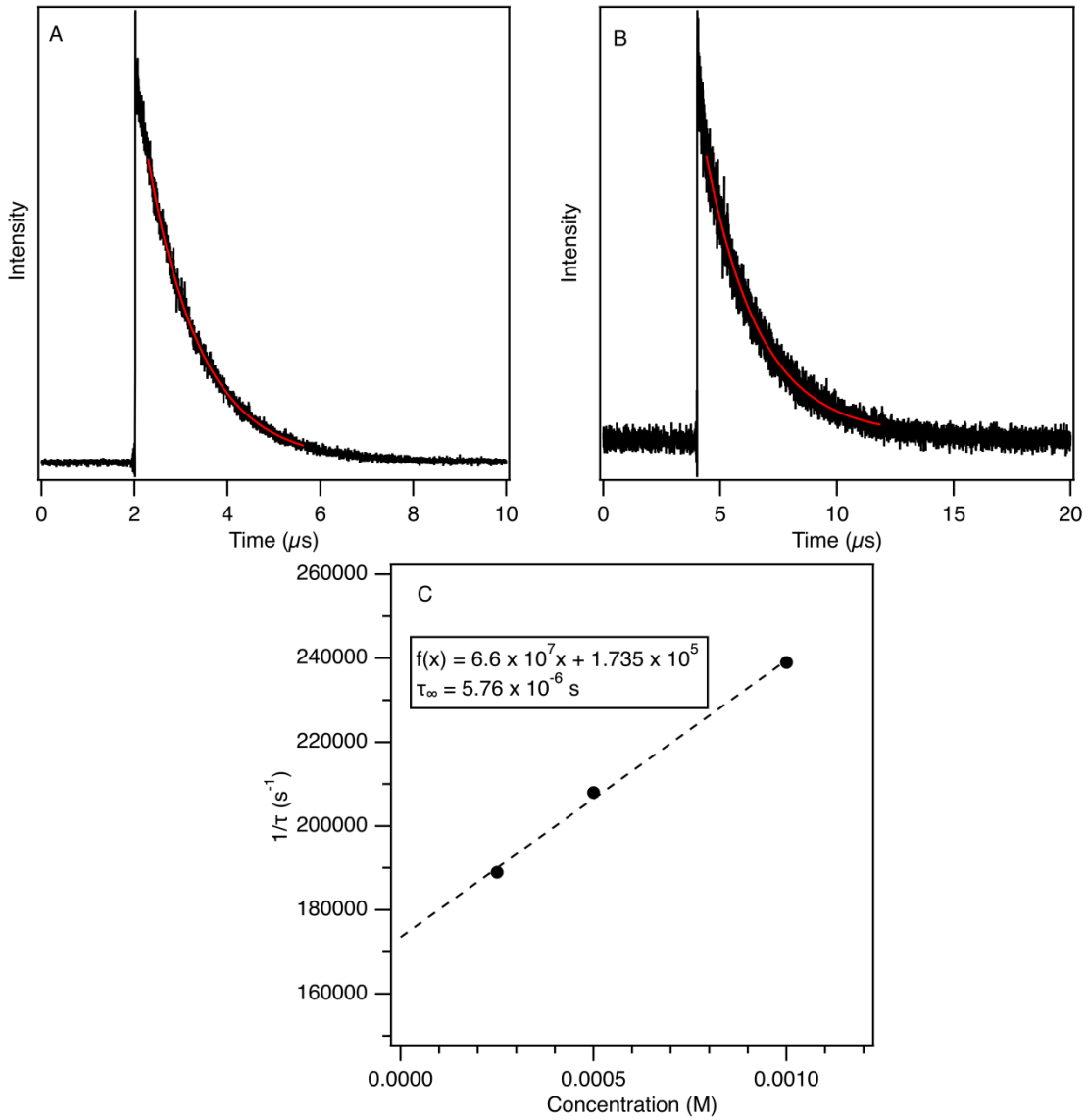

Figure 4.53. Excited-state lifetime in toluene solution of: (A) W(CPh){P(OMe)$_3$}4Cl; (B) W(CC$_6$H$_4$-4-OCH$_3$){P(OMe)$_3$}4Cl; (C) W(CC$_6$H$_4$-4-pyr){P(OMe)$_3$}$_4$Cl; Dependence of W(CC$_6$H$_4$-4-pyr){P(OMe)$_3$}$_4$Cl concentration at constant laser power.

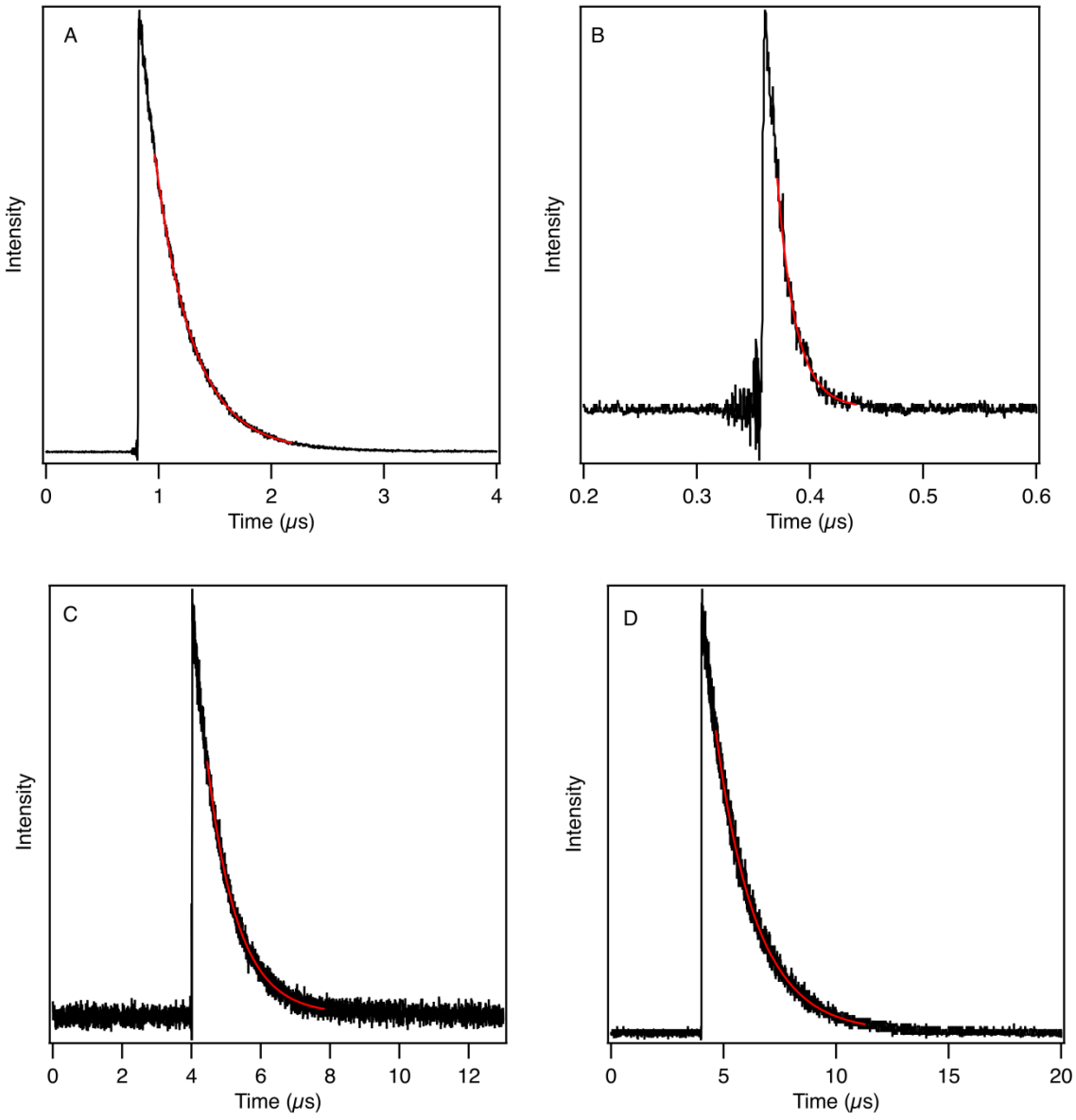

Figure 4.54. Excited-state lifetime in toluene solution of: (A) W(CPh)(dmpe)$_2$Cl (B) W(CMes)(dmpe)$_2$Cl; (C) W(CC$_6$H$_4$-4-OCH$_3$)(dmpe)$_2$Cl; (D) W(CC$_6$H$_4$-4-pyr)(dmpe)$_2$Cl.

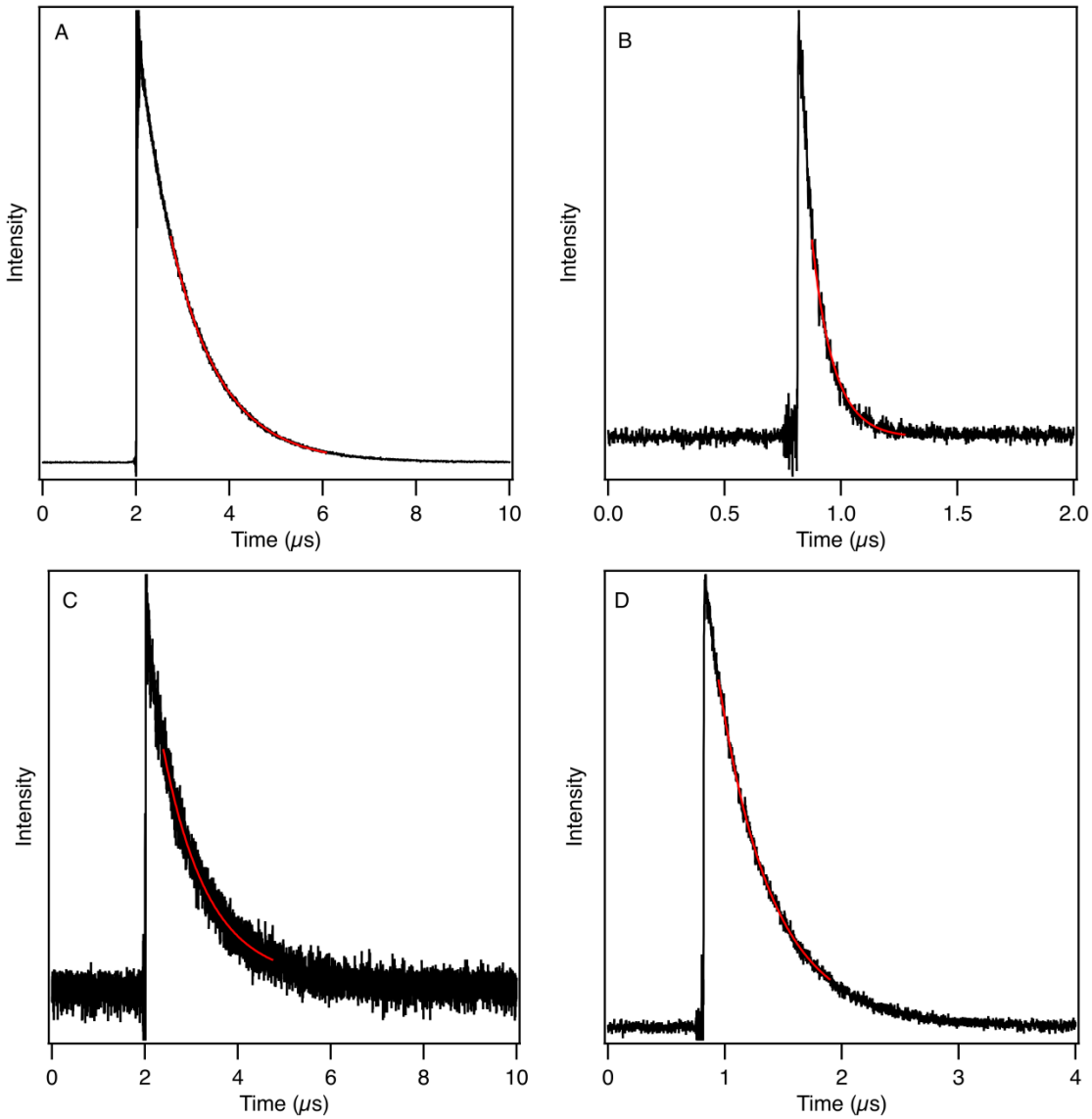

Figure 4.55. Excited-state lifetime in toluene solution of: (A) $W(CC_6H_4\text{-}4\text{-}NH_2)(dmpe)_2Cl$; (B) $W(CPh)(dmpe)_2F$; (C) $W(CC_6H_4\text{-}4\text{-}pyr)(dmpe)_2F$; (D) $W(CPh)(PMe_3)_4Cl$.

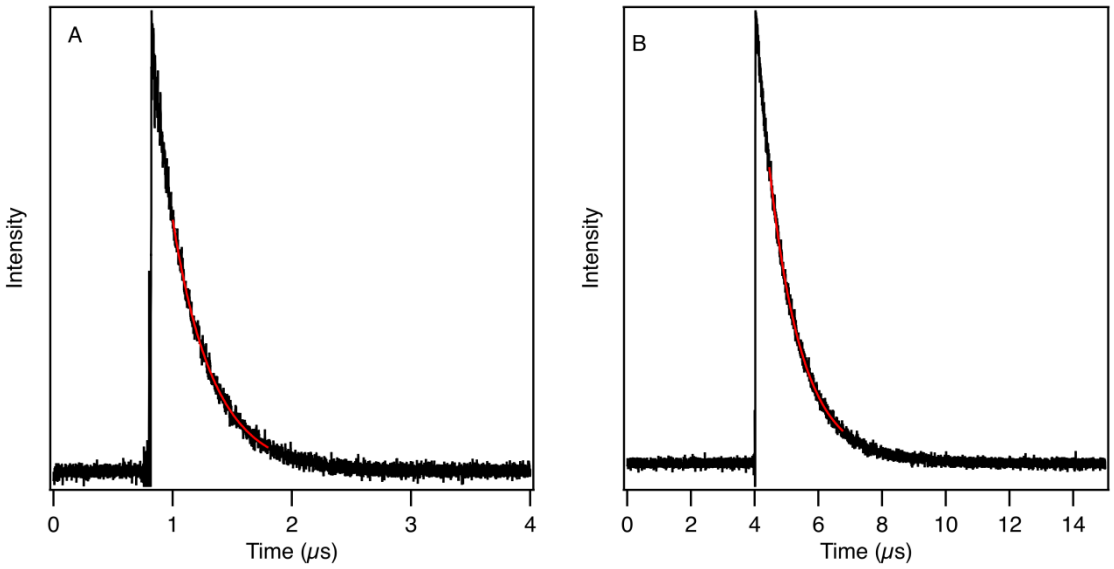

Figure 4.56. Excited-state lifetime in toluene solution of: (A) W(CPh)(depe)$_2$Cl; (B) W(CC$_6$H$_4$-4-pyr)(depe)$_2$Cl.

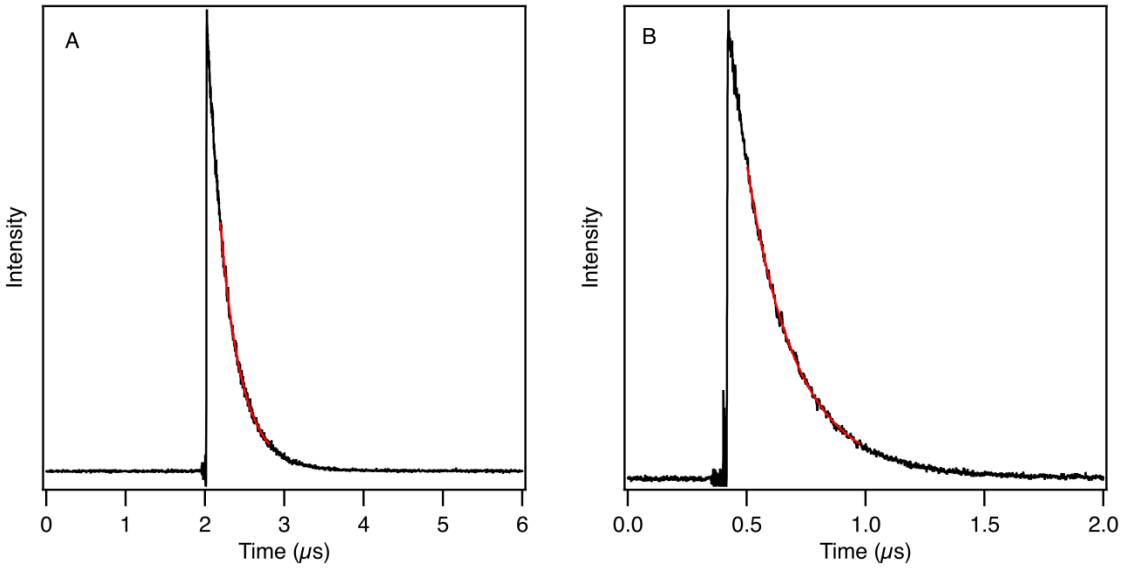

Figure 4.57. Excited-state lifetime of W(CPh)(dppe)$_2$Cl in: (A) toluene solution; (B) THF solution.

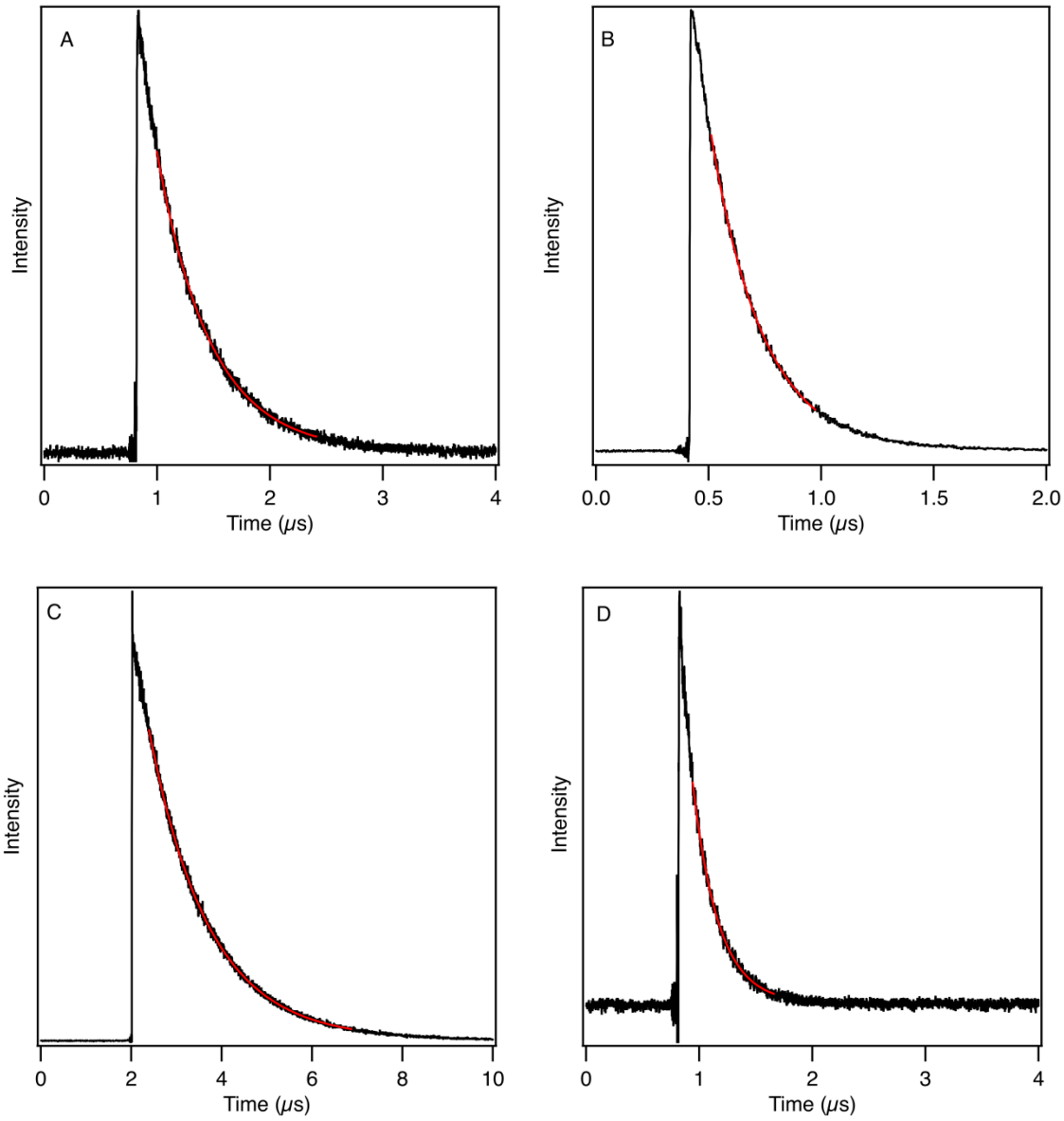

Figure 4.58. Excited-state lifetime in THF solution of: (A) W(CPh){P(OMe)$_3$}$_4$Cl; (B) W(CPh)(dmpe)$_2$Cl; (C) W(CC$_6$H$_4$-4-pyr)(dmpe)$_2$Cl; (D) W(CPh)(depe)$_2$Cl.

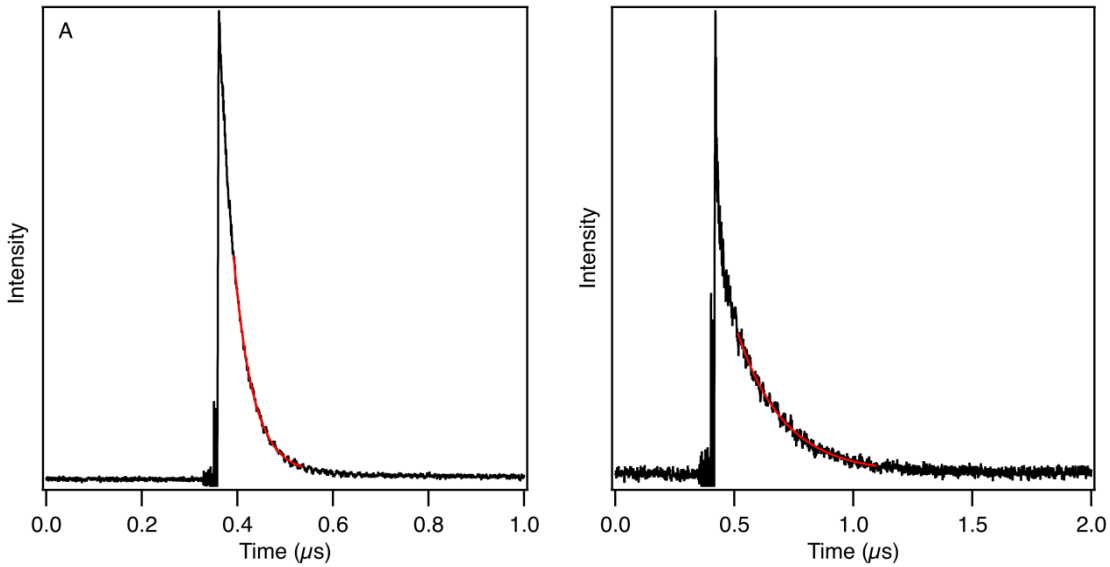

Figure 4.59. Excited-state lifetime in CH_3CN solution of: (A) $W(CPh)(depe)_2Cl$; (B) $(WCC_6H_4$-4-pyr$)(depe)_2Cl$.

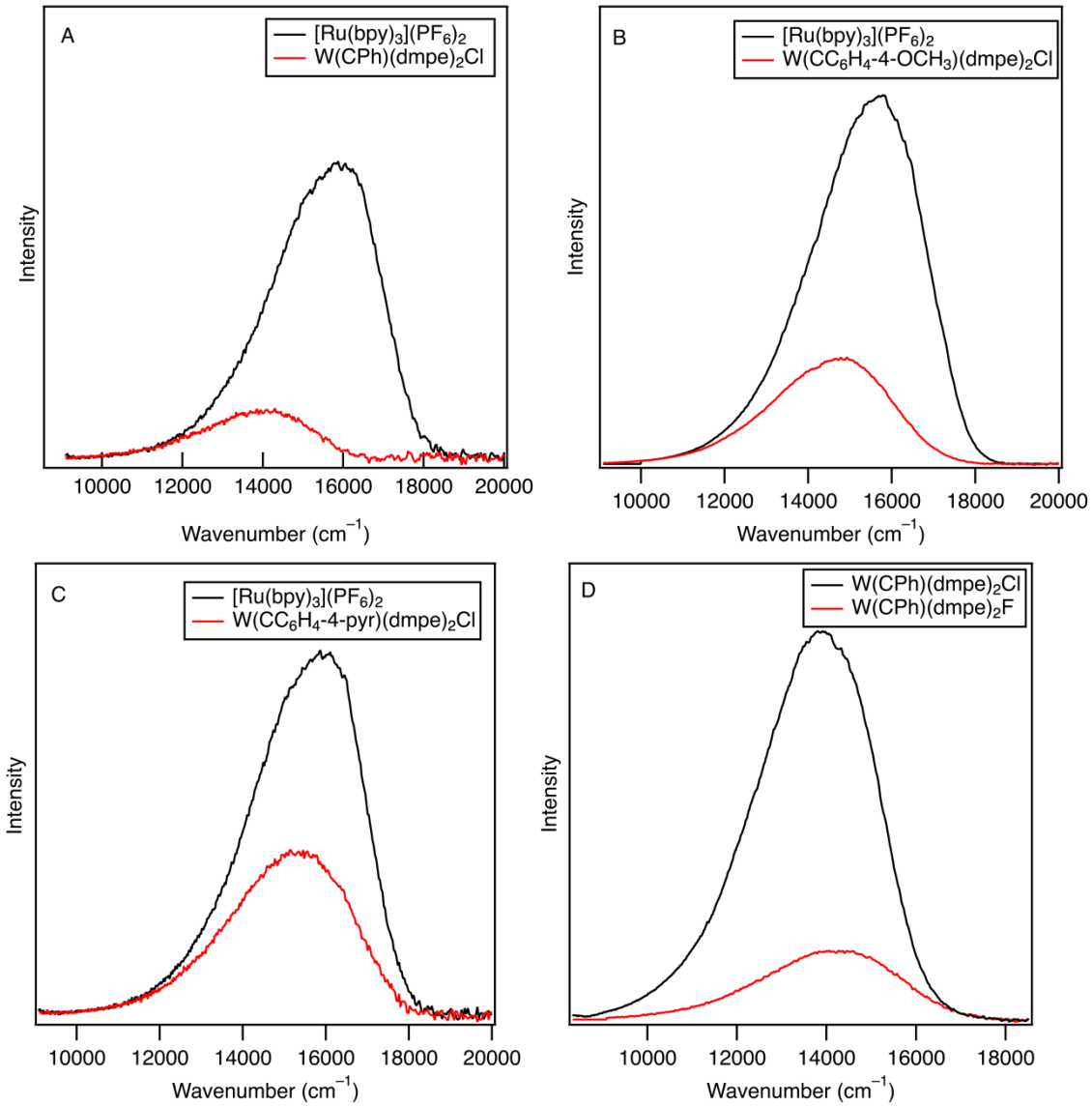

Figure 4.60. Quantum yield of: (A) $W(CPh)(dmpe)_2Cl$ recorded relative to $[Ru(bpy)_3](PF_6)_2$ (CH_3CN; λ_{ex} = 480 nm); (B) $W(CC_6H_4\text{-}4\text{-}OCH_3)(dmpe)_2Cl$ recorded relative to $[Ru(bpy)_3](PF_6)_2$ (CH_3CN; λ_{ex} = 480 nm); (C) $W(CC_6H_4\text{-}4\text{-}pyr)(dmpe)_2Cl$ recorded relative to $[Ru(bpy)_3](PF_6)_2$ (CH_3CN; λ_{ex} = 470 nm); (D) $W(CPh)(dmpe)_2F$ recorded relative to $W(CPh)(dmpe)_2Cl$ (Tol, λ_{ex} = 515 nm).

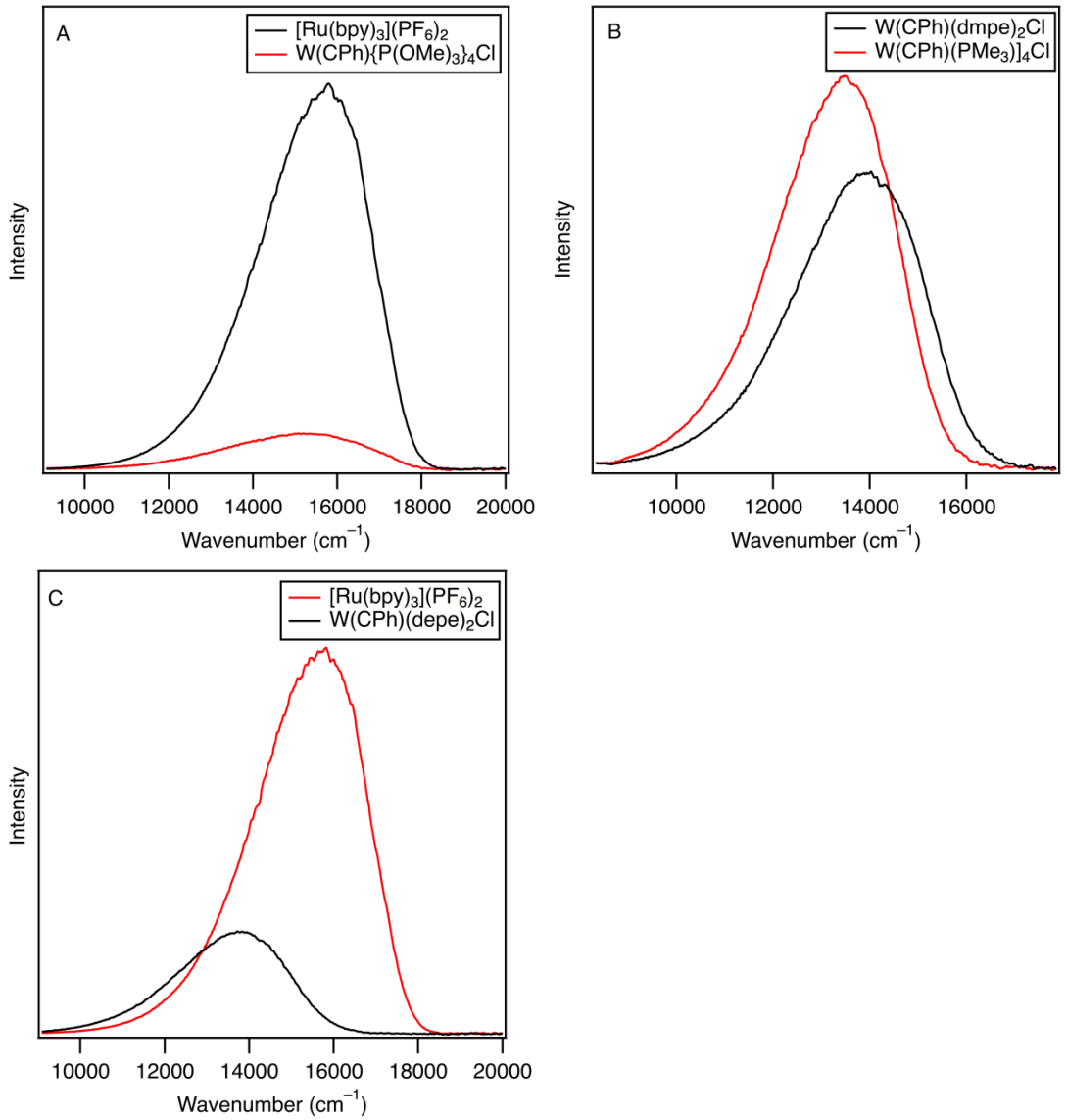

Figure 4.61. Quantum yield of: (A) W(CPh){P(OMe)$_3$}$_4$Cl recorded relative to [Ru(bpy)$_3$](PF$_6$)$_2$ (CH$_3$CN; λ_{ex} = 470 nm); (B) W(CPh)(PMe$_3$)$_4$Cl recorded relative to W(CPh)(dmpe)$_2$Cl (Tol; λ_{ex} = 545 nm); (C) W(CPh)(depe)$_2$Cl recorded relative to [Ru(bpy)$_3$](PF$_6$)$_2$ (CH$_3$CN; λ_{ex} = 425 nm).

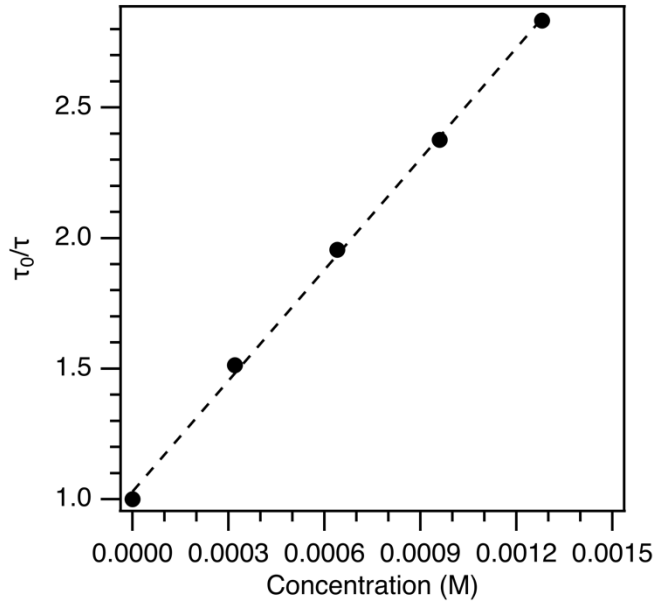

Quencher concentration (M)	Lifetime (ns)
0	215
3.2×10^{-4}	153
6.4×10^{-4}	111
9.6×10^{-4}	96
1.3×10^{-3}	81

Figure 4.62. Stern–Volmer experiment with $W(CPh)(dppe)_2Cl$ and 4-trifluoromethylbenzophenone. Linear regression: $f(x) = 1415.4x + 1.018$; $r^2 = 0.994$. The quenching rate constant is listed in Table 4.7.

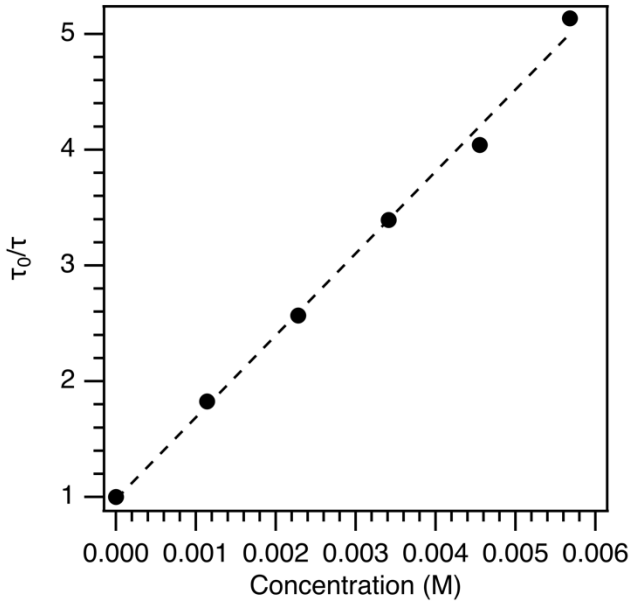

Quencher concentration (M)	Lifetime (ns)
0	190
1.1×10^{-3}	104
2.2×10^{-3}	74
3.4×10^{-3}	56
4.5×10^{-3}	47
5.6×10^{-3}	37

Figure 4.63. Stern–Volmer experiment with $W(CPh)(dppe)_2Cl$ and benzophenone. Linear regression: $f(x) = 707.9x + 0.981$; $r^2 = 0.996$. The quenching rate constant is listed in Table 4.7.

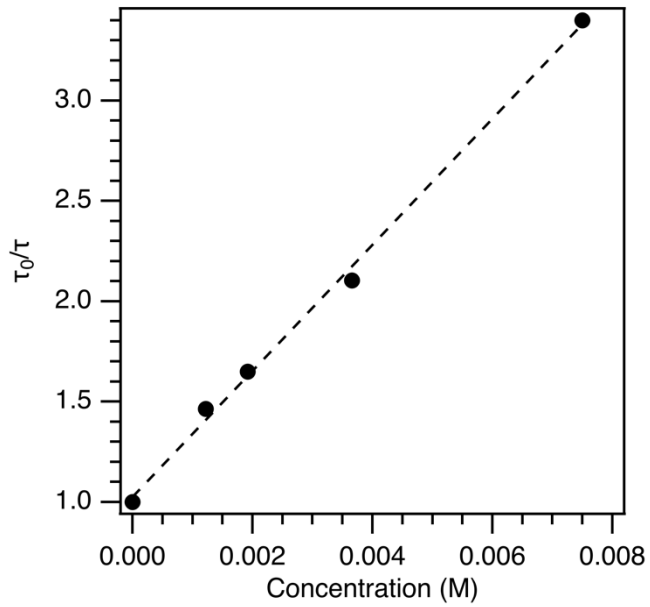

Quencher concentration (M)	Lifetime (ns)
0	221
1.2×10^{-3}	151
1.9×10^{-3}	134
3.7×10^{-3}	105
7.5×10^{-3}	65

Figure 4.64. Stern–Volmer experiment with W(CPh)(dppe)$_2$Cl and 4,4′-dimethylbenzophenone. Linear regression: f(x) = 313.93x + 1.026; r^2 = 0.997. The quenching rate constant is listed in Table 4.7.

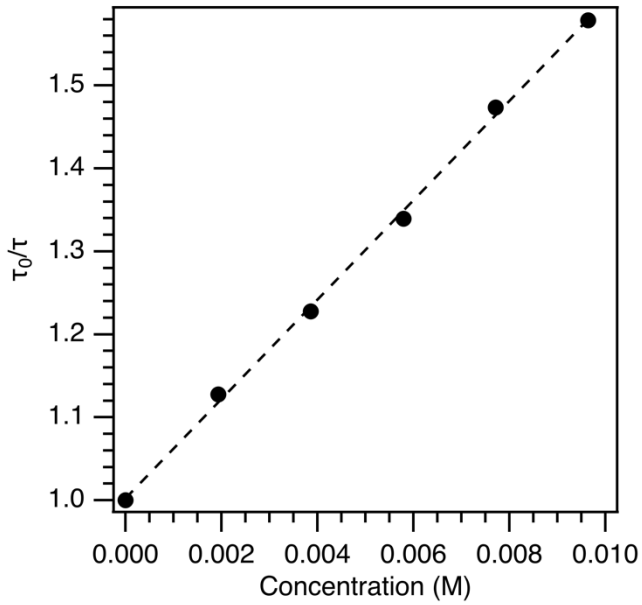

Quencher concentration (M)	Lifetime (ns)
0	221
1.9×10^{-3}	196
3.9×10^{-3}	180
5.8×10^{-3}	165
7.7×10^{-3}	150
9.6×10^{-3}	140

Figure 4.65. Stern–Volmer experiment with W(CPh)(dppe)$_2$Cl and 4,4′-dimethoxybenzophenone. Linear regression: f(x) = 59.90x + 1.00; r^2 = 0.999. The quenching rate constant is listed in Table 4.7.

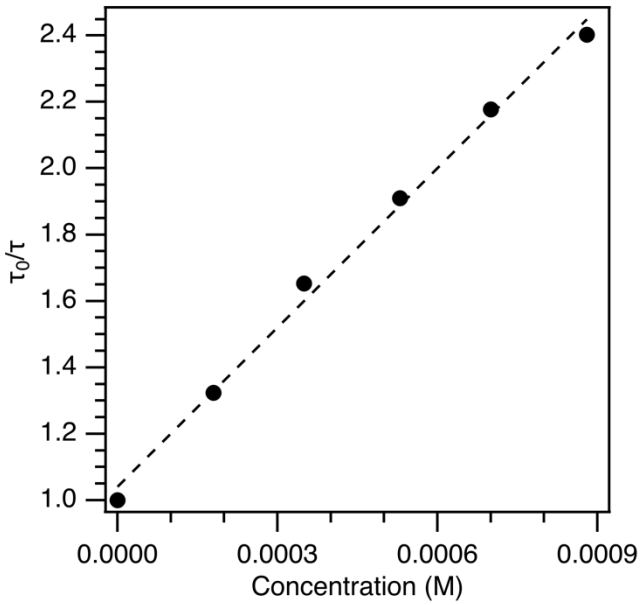

Quencher concentration (M)	Lifetime (ns)
0	233
1.8×10^{-4}	176
3.5×10^{-4}	141
5.3×10^{-4}	122
7.0×10^{-4}	107
8.8×10^{-4}	97

Figure 4.66. Stern–Volmer experiment with $W(CPh)(dmpe)_2Cl$ and 4-trifluoromethylbenzophenone. Linear regression: $f(x) = 1600.5x + 1.04$; $r^2 = 0.995$. The quenching rate constant is listed in Table 4.7.

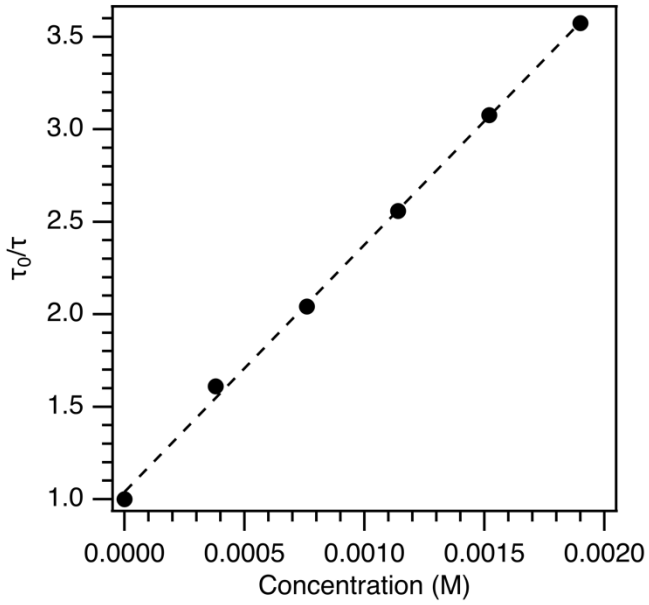

Quencher concentration (M)	Lifetime (ns)
0	243
3.8×10^{-4}	151
7.6×10^{-4}	119
1.1×10^{-3}	95
1.5×10^{-3}	79
1.9×10^{-3}	68

Figure 4.67. Stern–Volmer experiment with W(CPh)(dmpe)$_2$Cl and 4,4′-dimethylbenzophenone. Linear regression: f(x) = 1337.1x + 1.04; r^2 = 0.999. The quenching rate constant is listed in Table 4.7.

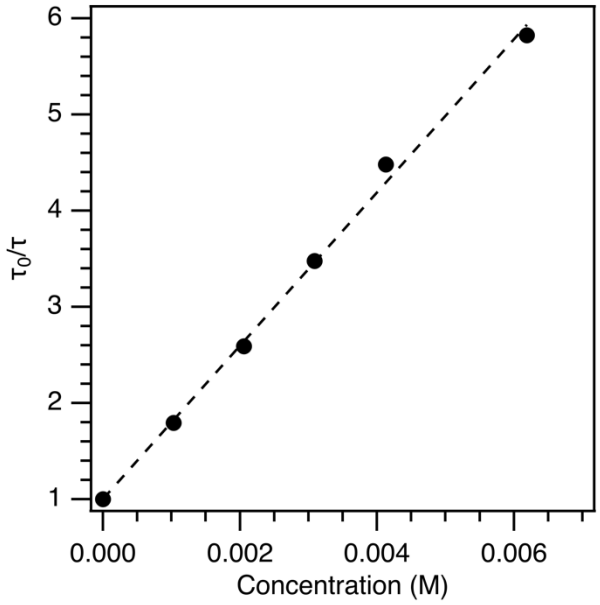

Quencher concentration (M)	Lifetime (ns)
0	233
1.0×10^{-3}	130
2.1×10^{-3}	90
3.1×10^{-3}	67
4.1×10^{-3}	52
6.2×10^{-3}	40

Figure 4.68. Stern–Volmer experiment with W(CPh)(dmpe)$_2$Cl and 4,4′-dimethoxybenzophenone. Linear regression: f(x) = 796.2x + 1.00; r^2 = 0.997. The quenching rate constant is listed in Table 4.7.

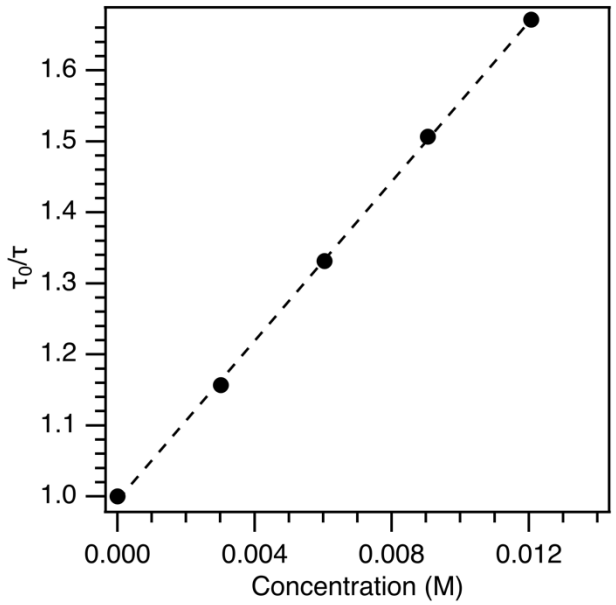

Quencher concentration (M)	Lifetime (ns)
0	229
3.0×10^{-3}	198
6.0×10^{-3}	172
9.1×10^{-3}	152
1.2×10^{-2}	137

Figure 4.69. Stern–Volmer experiment with $W(CPh)(dmpe)_2Cl$ and 4,4′-dimethylaminobenzophenone. Linear regression: $f(x) = 56.1x + 0.995$; $r^2 = 0.999$. The quenching rate constant is listed in Table 4.7.

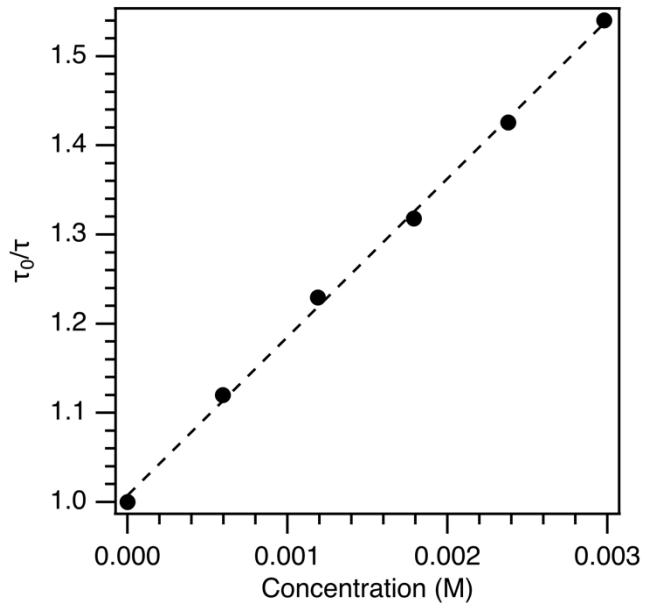

Quencher concentration (M)	Lifetime (ns)
0	40
6.0×10^{-4}	36
1.2×10^{-3}	33
1.8×10^{-3}	31
2.4×10^{-3}	28
3.0×10^{-3}	26

Figure 4.70. Stern–Volmer experiment with $W(CPh)(dmpe)_2F$ and 4,4′-dimethylaminobenzophenone. Linear regressions: $f(x) = 177.8x + 1.00$; $r^2 = 0.999$. The quenching rate constant is listed in Table 4.7.

4.5. References.

1. Bocarsly, A. B.; Cameron, R. E.; Rubin, H. D.; McDermott, G. A.; Wolff, C. R.; Mayr, A. *Inorg. Chem.* **1985**, *24*, 3976-3978.

2. O'Hanlon, D. C.; Cohen, B. W.; Moravec, D. B.; Dallinger, R. F.; Hopkins, M. D. *J. Am. Chem. Soc.* **2014**, *136*, 3127-3136.

3. Moravec, D. B.; Hopkins, M. D. *Chem. Eur. J* **2013**, *19*, 17082-17091.

4. Cohen, B. W.; Lovaasen, B. M.; Simpson, C. K.; Cummings, S. D.; Dallinger, R. F.; Hopkins, M. D. *Inorg. Chem.* **2010**, *49*, 5777-5779.

5. Haines, D. E.; O'Hanlon, D. C.; Manna, J.; Jones, M. K.; Shaner, S. E.; Sun, J.; Hopkins, M. D. *Inorg. Chem.* **2013**, *52*, 9650-9658.

6. Da Re, R. E.; Hopkins, M. D. *Coord. Chem. Rev.* **2005**, *249*, 1396-1409.

7. Caspar, J. V.; Meyer, T. J. *J.Phys. Chem.* **1983**, *87*, 952-957.

8. Lovaasen, B. M.; Lockard, J. V.; Cohen, B. W.; Yang, S.; Zhang, X.; Simpson, C. K.; Chen, L. X.; Hopkins, M. D. *Inorganic Chemistry* **2012**, *51*, 5660-5670.

9. Suzuki, K.; Kobayashi, A.; Kaneko, S.; Takehira, K.; Yoshihara, T.; Ishida, H.; Shiina, Y.; Oishi, S.; Tobita, S. *Phys. Chem. Chem. Phys.* **2009**, *11*, 9850-9860.

10. Timpe, H.-J.; Kronfeld, K.-P.; Lammel, U.; Fouassier, J.-P.; Lougnot, D.-J. *J. Photochem. Photobiol. A* **1990**, *52*, 111-122.

11. Farran, H.; Hoz, S. *Organic Letters* **2008**, *10*, 4875-4877.

12. Jaworski, J. S.; Malik, M.; Kalinowski, M. K. *J. Phys. Org. Chem.* **1992**, *5*, 590-594.

13. Michielli, R. F.; Elving, P. J. *J. Am. Chem. Soc.* **1968**, *90*, 1989-1995.

14. Rajadurai, S.; Bhattacharyya, K.; Das, P. K. *Chem. Phys. Lett.* **1986**, *129*, 244-252.

15. Park, S. M.; Bard, A. J. *J. Am. Chem. Soc.* **1975**, *97*, 2978-2985.

16. Leigh, W. J.; Arnold, D. R. *J. Chem. Soc., Chem. Commun.* **1980**, 406-408.

17. Connely, N. G.; Geiger, W. E. *Chem. Rev.* **1996**, *96*, 877-910.

18. Creager, S., In *Handbook of Electrochemistry*, Zoski, C. G., Ed. Elsevier: 2007; pp 70-71.

19. Turro, N. J.; Ramamurthy, V.; Scaiano, J. C. *Modern Molecular Photochemistry of Organic Molecules*. University Science Books: 2010.

20. Balzani, V.; Bolletta, F.; Scandola, F. *J. Am. Chem. Soc.* **1980**, *102*, 2152-2163.

21. Fawcett, W. R.; Fedurco, M. J. *J. Phys. Chem.* **1993**, *97*, 7075-7080.

22. Rudshteyn, B.; Vibbert, H. B.; May, R.; Wasserman, E.; Warnke, I.; Hopkins, M. D.; Batista, V. S. *ACS Catal.* **2017**, *7*, 6134-6143.

23. Meyer, T. J. *Prog. Inorg. Chem.* **1983**, *30*, 389-440.

24. Marcus, R. A.; Sutin, N. *Biochem. Biophys. Acta* **1985**, *811*, 265-322.

25. Brunschwig, B.; Creutz, C.; Macartney, D. H.; Sham, T.-K.; Sutin, N. *Faraday Discuss. Chem. Soc.* **1982**, *74*, 113-127.

26. Creutz, C.; Keller, A. D.; Sutin, N.; Zipp, A. P. *J. Am. Chem. Soc.* **1982**, *104*, 3618-3627.

27. Cavalheiro, C. C. S.; Torraca, K. E.; Schanze, K. S.; McElwee-White, L. *Inorg. Chem.* **1999**, *38*, 3254-3257.

28. Haines, D. E.; O'Hanlon, D. C.; Manna, J.; Jones, M. K.; Shaner, S. E.; Sun, J.; Hopkins, M. D. *Inorg. Chem.* **2013**, *52*, 9650-9658.

CHAPTER 5

Photoredox synthesis of organic compounds using W(CAr)L_4X chromophores

5.1. Introduction.

Visible-light photoredox catalysis is a powerful technique to construct and break chemical bonds through the generation of reactive radicals. Although the power of visible-light photoredox catalysis has been apparent in the inorganic community since the mid 1970s,[1] the recent realization in the organic community that these photoredox chromophores could catalyze formation of C–C, C–N, C–S, and C–O bonds has stimulated a renewed interest in the field. Photoredox catalysis can enable transformations that are either inaccessible to or highly difficult for thermal catalysts.

The generation of aryl radicals by photoredox methods is challenging because most conventional photoredox chromophores do not possess the required ground-state or excited-state redox potentials to reduce desirable precursors. The most desirable starting substrates are aryl halides and aryl triflates (Figure 5.1), because many derivatives are easily prepared or are commercially available and are stable under ambient conditions. Aryl triflates are common precursors in cross-coupling reactions and are conveniently prepared from phenols. However, the parent phenyl halides and triflates are difficult-to-reduce; even iodobenzene, which possesses the least negative reduction potential among them (–2.69 V vs $FeCp_2$), is inaccessible to conventional photoredox chromophores.[2] One approach to activating aryl halides is to append them with electron withdrawing groups to lower their reduction potentials.[3-8] More commonly, halides are replaced by less desirable cleavable groups to modulate the reduction potential (Figure 5.1). Aryl diazonium compounds, for instance, are easily reduced (*ca* −0.5 V),[9] but many

are thermally unstable and must be prepared immediately prior to use. Diaryliodonium salts are also readily reduced and are reported to be stable under ambient conditions, but their preparation requires the use of harsh reagents that often limit the scope of molecules that can be prepared.[10] Despite these limitations, photoredox-generated aryl radicals have been utilized in a number of interesting ways, including reductive dehalogenation,[11, 12] C–H arylation reactions,[13] thiolation,[14] amino acid synthesis,[15] and hydroarylation[16] reactions among other fundamental methods. Stephenson *et al.* reported that *fac*-Ir(ppy)$_3$ ($E^{*/ox}$ = –2.13 V; $E_{1/2}^{0/-}$ = –2.59 V, See Chapter 1) was observed, in a reaction with tributylamine (E_{ox} = 0.52 V) and formic acid or Hantzsch ester to reductively dehalogenate various aryl iodides.[11, 12 17]

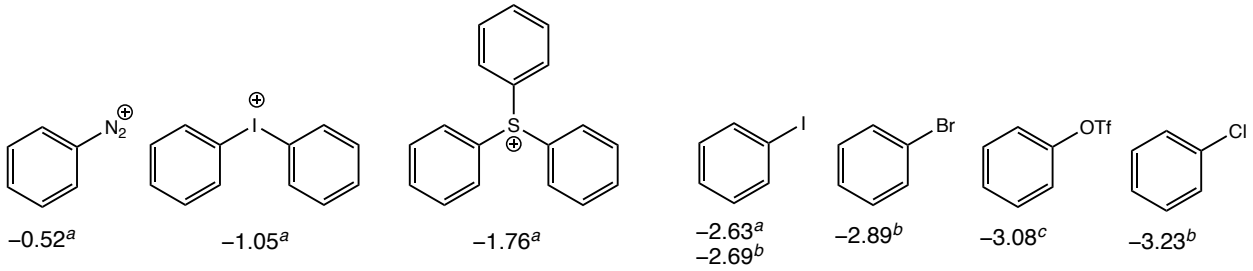

Figure 5.1. Precursors for generation of aryl radicals *via* reductive bond scission. Potentials are referenced vs $FeCp_2$ using the conversion in Ref. 18. [a] Ref. 9; potentials recorded in 0.1 M [^{n}Bu$_4$N][BF$_4$] acetonitrile solution vs SCE; [b] Ref. 2; potentials recorded in 0.1 M [^{n}Bu$_4$N][BF$_4$] DMF solution vs SCE; [c] Ref. 19; potentials recorded in 0.1 M [^{n}Bu$_4$N][BF$_4$] DMF solution vs SCE.

The steps that lead to generation of aryl radicals following the reduction of aryl halides are relevant processes for the application of photoredox chromophores. Under electrochemical conditions, Savéant *et al.* have shown[9, 20] that one-electron reduction of ArX generates a high energy π*-type radical intermediate ($ArX^{\cdot-}$) that quickly converts to a σ*-type radical accompanied by the loss of halide. This radical is reduced at potentials positive of ArX. In electrochemical experiments, the applied potential reduces the radical to an aryl radical anion.[20] This second reduction process is not relevant under photoredox conditions unless the

chromophore has a ground-state potential negative of *ca.* –1 V. Under photoredox conditions, photo-initiated electron transfer produces the ArX^{-} radical and an oxidized chromophore. In order for productive aryl-radical chemistry to occur, Ar–X bond scission from ArX^{-} must out-compete back-electron transfer to reform ArX and the ground state of the chromophore. Thus, an important consideration is the fragmentation rate for aryl iodide, bromide, and chloride molecules. In general, the rate is governed by whether fragmentation occurs by a stepwise mechanism, in which the ArX^{-} radical is a discrete intermediate,[21] or a concerted mechanism, in which reduction and Ar–X cleavage are concomitant. Fragmentation rate constants (k_f) have been determined by a number of means (Table 5.1). The fragmentation rates of Ar–X molecules vary widely from 10^{-2}–10^{10} s^{-1} (Table 5.1).[22, 23] In general, these fragmentation rates are a marker of the stability of the generated aryl halide radical anion and track with the observed reduction potential of the molecule such that more difficult-to-reduce Ar–X molecules exhibit generally faster fragmentation rates.

Table 5.1. Selected Ar–X fragmentation rate constants and reduction potentials recorded in DMF solution.

Molecule	k_f (s^{-1})	$E_{1/2}$ (V vs Cp_2Fe)[a]	Ref.
Aryl and Heteroaryl Bromide Molecules			
3-bromobiphenyl	1.3×10^9	−2.83	22
4-bromobiphenyl	3.2×10^{10}	−2.88	22
2-bromopyridine	2.81×10^9	−2.71	22
3-bromopyridine	3.16×10^9	−2.68	22
2-bromonaphthalene	1.77×10^{10}	−2.66	22
Aryl and Heteroaryl Chloride Molecules			
2-chloronitrobenzene	0.01	−1.44	22
3-chlorobenzophenone	44	-2.09	22
Ethyl 4-chlorobenzoate	1.25×10^7	-2.47	22
2-chlorobiphenyl	7×10^{10}	−3.04	22
4-chlorobiphenyl	4.5×10^8	−2.88	22
2-chloronaphthalene	1.00×10^8	−2.75	22
3-chloropyridine	3.16×10^9	−2.81	22
2-chloropyridine	4.2×10^9	−2.82	23

[a] From Refs. 22, 23 ; recorded vs SCE in DMF solution, corrected vs $FeCp_2$ using Ref. 18.

The remarkably negative excited-state oxidation potentials for $W(CAr)L_4X$ complexes ($E^{*/ox}$ = –2.5 to –3.3 V, Chapter 4) suggest that many derivatives could be used to reduce aryl halide molecules with reduction potentials far beyond those accessible to conventional photoredox chromophores. Conveniently, many aryl bromide and chloride molecules with highly negative redox potentials also possess very fast halide fragmentation rate constants (~10^{10} s^{-1}, Table 5.1), suggesting that fragmentation can compete with back-electron transfer (Figure 5.2). On the other hand, the photoredox production of aryl radicals also will yield an oxidized tungsten(V)-alkylidyne complex. Because the W(IV)/W(V) potential of these compounds is typically < –0.5 V, conventional sacrificial donors such as alkyl amines cannot be used to close catalytic photoredox cycles. Closure of such cycles will require careful reaction design, as outlined in this chapter. The tungsten–alkylidyne photoredox reactions in this chapter will be grouped into three sections. The first section will focus on the photoredox kinetics and spectroscopic signatures of difficult-to-reduce molecules that form bound radical ions upon reduction. In the second section, stoichiometric photoredox reactions of aryl halides are elaborated. The third section will describe reactions of such substrates that are photocatalytic.

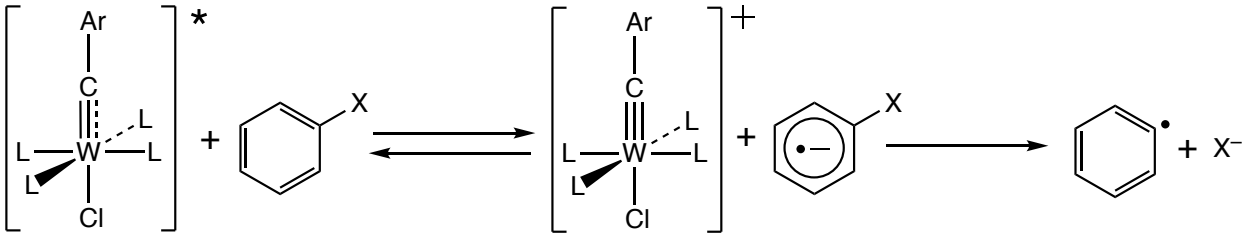

Figure 5.2. Diagram depicting steps required to generate an aryl radical using tungsten-alkylidyne complexes.

5.2. Results and Discussion.

5.2.1. Generation of bound radical ions. $W(CC_6H_4\text{-}4\text{-}pyr)(dmpe)_2Cl$ ($E^{*/ox}$ = –3.18 V, Chapter 4) was used to generate radical anions of substituted benzenes bearing useful functional groups, according to the general scheme shown in Figure 5.3. The substrates studied were benzaldehyde, acetophenone, diphenylacetylene, phenylacetylene, ethyl benzoate, naphthalene, styrene, and α,α,α-trifluorotoluene. In general, reduction of these substrates requires pulse radiolysis or treatment with sodium at low temperature,[24, 25] as indicated by the fact that they possess reduction potentials in the range –2.4 to –3.1 V (Figure 5.3). These unusual radical anions have the potential to be synthetically elaborated by dimerization, radical-initiated oligomerization, or by trapping with electrophiles.

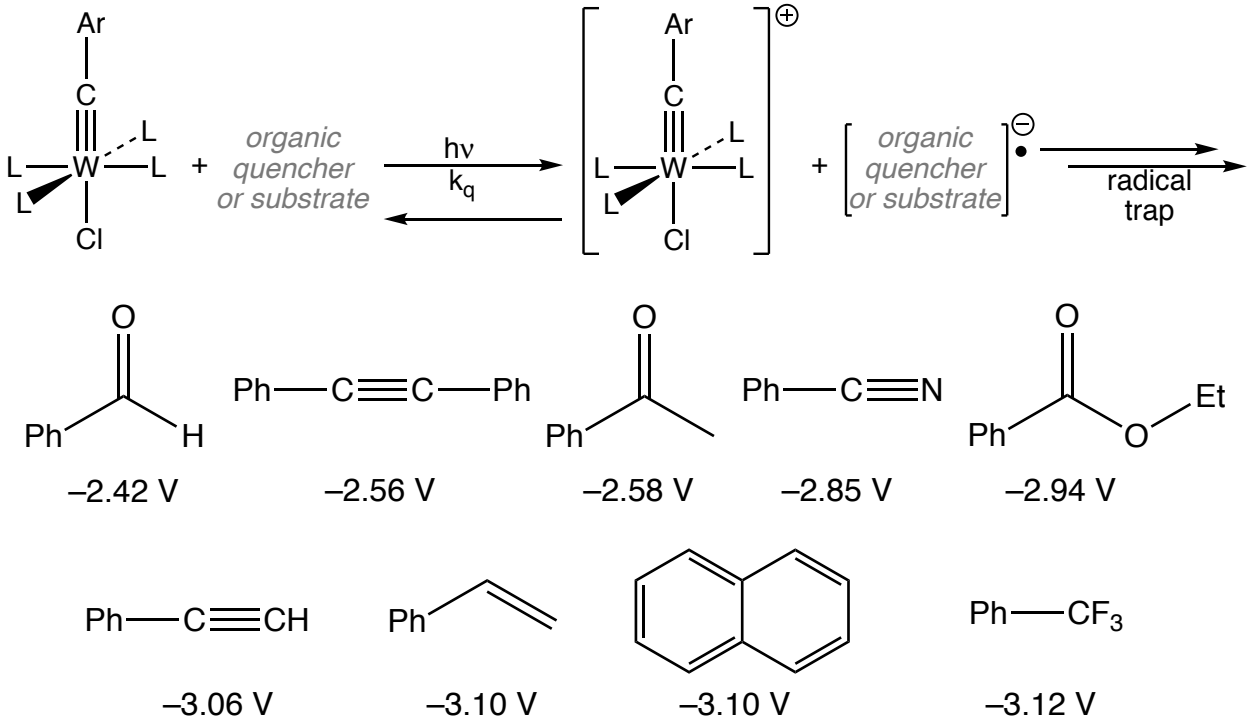

Figure 5.3. (Top) General reaction scheme used to generate bound radical anions. (Bottom) Substrates studied. Electrochemical potential for PhCCPh determined in Ref. 26. All other reduction potentials determined in 0.3 M [^{n}Bu$_4$N][PF$_6$] THF solution with Au working and auxiliary electrodes.

These arenes are found to oxidatively quench the excited state of W(CC_6H_4-4-pyr)(dmpe)$_2$Cl ($E^{*/ox}$ = –3.18 V) to form their corresponding radical anions and the oxidized chromophore. Because trapping reagents were absent in the experiments, the radical decayed *via* back-electron transfer to the oxidized chromophore (Figure 5.3). The emission lifetime varied with quencher concentration according to the Stern-Volmer relationship (Figures 5.28 – 5.35), which allowed determination of the quenching rate constant (Table 5.2). These rate constants were observed to vary appropriately with reaction driving force.

Table 5.2. Electron-transfer quenching rate constants for W(CC_6H_4-4-pyr)(dmpe)$_2$Cl.

Acceptor	k_q ($M^{-1}s^{-1}$)	ΔG (V)	Figure
benzaldehyde	1.76×10^{10}	−0.76	5.28
acetophenone	1.38×10^{10}	−0.60	5.29
benzonitrile	5.59×10^{8}	−0.33	5.30
ethyl benzoate	5.21×10^{9}	−0.24	5.31
phenyl acetylene	8.13×10^{6}	−0.12	5.32
naphthalene	7.04×10^{6}	−0.08	5.33
α,α,α-trifluorotoluene	4.71×10^{6}	−0.06	5.34
styrene	3.53×10^{6}	−0.08	5.35

To verify that the quenching reactions involved electron transfer, transient absorption (TA) spectra were recorded for the photochemical reaction of W(CC_6H_4-4-pyr)(dmpe)$_2$Cl with two quenchers for which the spectra of their radical anions are known: diphenylacetylene and naphthalene. Both experiments were conducted in THF solution containing 0.1 M [^{n}Bu$_4$N][PF_6] to aid the cage escape of charged intermediates.[27] Diphenylacetylene anion ($E^{0/-}$ = −2.56 V)[26] is reported to possess a broadly absorbing transient signature from *ca*. 700–1000 nm.[28, 29] The TA data (Figure 5.4) show the quick in-growth of a strong signal that was observed to live for *ca*. 8 μs before it completely dissipates. A TA spectrum generated by temporal integration of the data from 1-2 μs after laser excitation shows a rising absorption that closely matches that reported in the literature for [PhCCPh]$^-$ (Figure 5.4).[29] In the original report of the TA spectrum, which was

obtained under different conditions than that reported here (γ-radiation), the diphenylacetylene radical anion was observed to slowly add to a molecule of neutral diphenylacetylene.[28] This was not observed under our conditions.

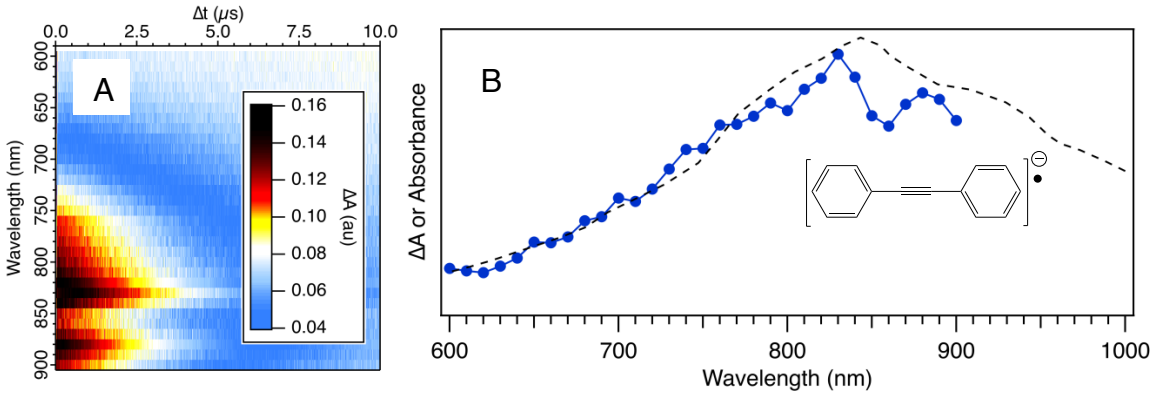

Figure 5.4. (A) 3D Representation of the TA data recorded for the reduction of diphenylacetylene using W(CC$_6$H$_4$-4-pyr)(dmpe)$_2$Cl (λ_{ex} = 485 nm) in THF solution (5 mL) with 0.1 M [^{n}Bu$_4$N][PF$_6$] and 0.03 g diphenylacetylene; (B) Temporally integrated (1-2 μs after laser excitation) spectrum of diphenylacetylene radical anion (blue) overlaid with the literature spectrum (black, digitized from Ref. 29).

The TA data for the photoinduced reaction of W(CC$_6$H$_4$-4-pyr)(dmpe)$_2$Cl with naphthalene shows rapid growth of signals from *ca.* 600–1000 nm (Figures 5.5). At short times following excitation (≤ 200 ns) the emission of W(CC$_6$H$_4$-4-pyr)(dmpe)$_2$Cl is observed as a dip at *ca*. 630 nm (cf. λ_{em} = 635 nm, Chapter 4). After this time the emission was observed to decay, and a weak absorbance was observed to grow (Figure 5.6). From 0.9–1 μs after excitation, a signal is observable that corresponds to naphthalene radical anion. This is demonstrated by the temporally integrated spectrum shown in Figure 5.7, which can be seen to match the spectrum of naphthalene radical anion produced from γ-irradiation.[29]

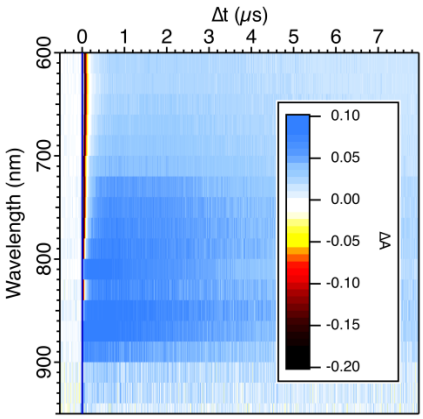

Figure 5.5. 3-D Representation of the raw TA data obtained from the reaction of W(CC_6H_4-4-pyr)(dmpe)$_2$Cl (λ_{ex} = 490 nm) in THF solution (5mL) with 0.1 M [^{n}Bu$_4$N][PF_6] and 0.50 g naphthalene .

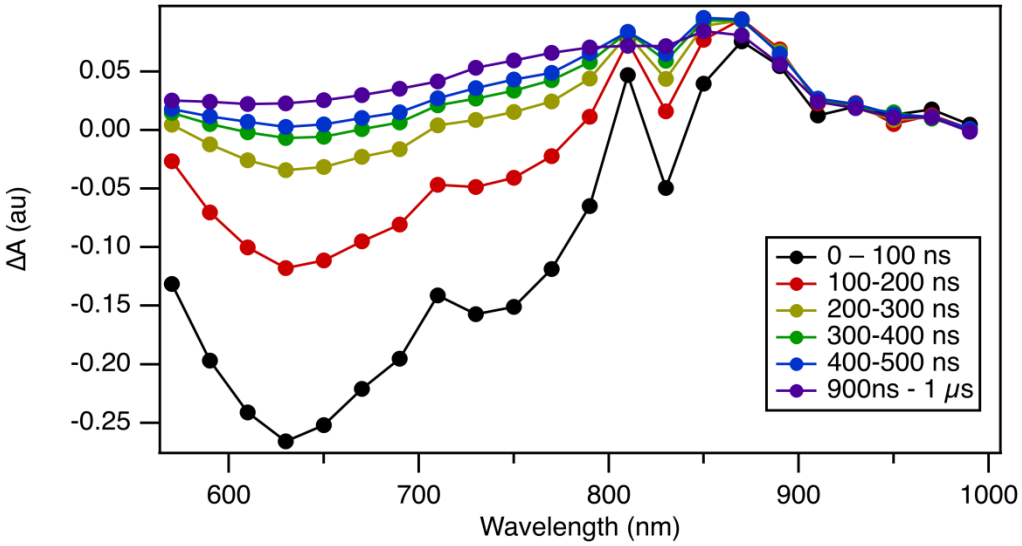

Figure 5.6. Evolution of the TA spectrum for the photoreaction of W(CC_6H_4-4-pyr)(dmpe)$_2$Cl with naphthalene.

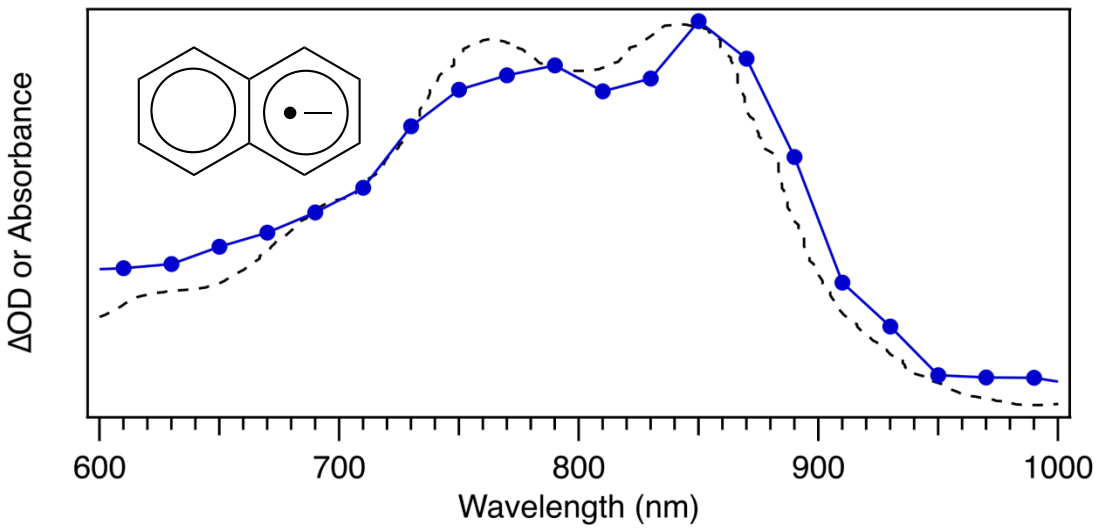

Figure 5.7. Transient absorption spectrum showing naphthalene radical anion, temporally integrated between 1.5 –5.5 μs after laser excitation of W(CC6H4-4-pyr)(dmpe)2Cl. The blue line and points are recorded via TA spectroscopy. The black line is digitized from Ref. 29.

Using the reported molar absorptivity of the diphenylacetylene[28] and naphthalene[29] radical anions, the kinetics of the back-electron transfer processes were characterized. These processes followed second-order kinetics, as expected (Figures 5.8 and 5.9). For diphenylacetylene, the rate constant is on the order of 10^{11} $M^{-1}s^{-1}$. For naphthalene, the back-electron transfer rate constant is 1.4×10^{10} $M^{-1}s^{-1}$, which is in good agreement with the predicted values from the Eigen equation (Equation 4.12, $k_{-d} = 1.1\times 10^{10}$ $M^{-1}s^{-1}$ for $W(CPh)(dmpe)_2Cl$).

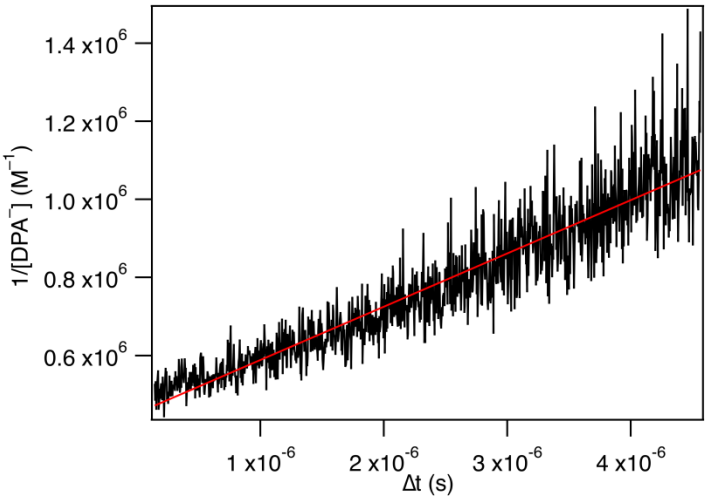

Figure 5.8. Kinetics of back-electron transfer for the reaction between W(CC_6H_4-4-pyr)$(dmpe)_2Cl$ and diphenylacetylene at 800 nm. Fit: $f(x) = 1.37 \times 10^{11}x + 4.205 \times 10^5$; $r^2 = 0.86$.

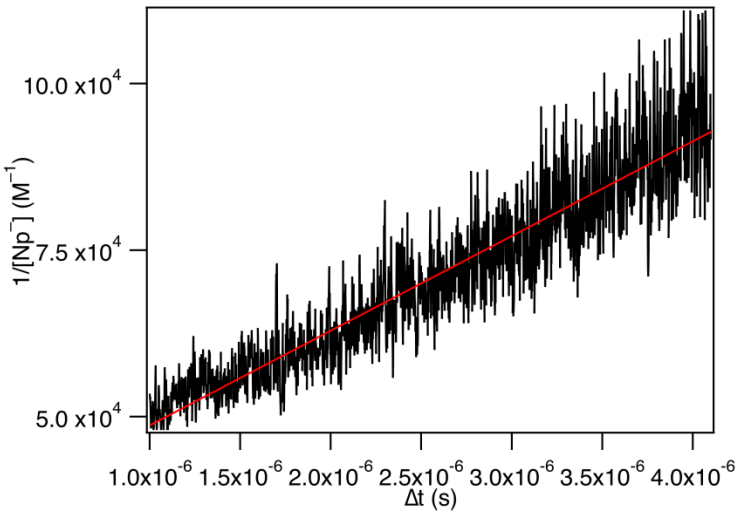

Figure 5.9. Kinetics of back-electron transfer for the reaction between W(CC_6H_4-4-pyr)$(dmpe)_2Cl$ and naphthalene at 750 nm. Fit: $f(x) = 1.42 \times 10^{10}x + 34469$; $r^2 = 0.87$.

5.2.2. Stoichiometric C–C bond forming reactions. As a first step towards exploring the net photoredox chemistry of tungsten-alkylidyne compounds, a series of screening reactions were conducted that employed stoichiometric quantities of chromophore relative to substrate. In the first of these, the chromophore, W(CPh)$(dmpe)_2Cl$, was used to stoichiometrically photoreduce benzyl bromide. The aim of this experiment was to initiate coupling between two benzyl radicals (Figure 5.10). In this reaction, photoexcitation of the chromophore generates the

excited-state ($E^{*/ox}$ = –2.80 V), which is expected to reduce benzyl bromide ($E_{1/2}^{0/-}$ = –2.16 V, ΔG = –0.64 V),[30] with concerted loss of bromide, to generate benzyl radical. Dimerization of benzyl radical to bibenzyl is rapid.[31] Benzyl radical generation has previously been accomplished by conventional photoredox chromophores in polar solvents.[32, 33] Given the high driving force possible with tungsten-alkylidyne chromophores, it was decided to explore the reactivity of the tungsten-alkylidyne compounds in non-polar solution (pentane) as a demonstration of their potentially unusual applications. Photolysis of a solution of benzyl bromide (2 eq) and $W(CPh)(dmpe)_2Cl$ in pentane using a green LED (apparatus described in Section 5.4) for 24 h resulted in consumption of the photoredox chromophore, as indicated by bleaching of the color of the solution and observation of a tan precipitate. GC/MS analysis of the reaction mixture provided a 97% yield of bibenzyl relative to tungsten. A $^{31}P\{^1H\}$ NMR spectrum of the reaction mixture showed the presence of free dmpe, indicating decomposition of the chromophore. Nevertheless, this result demonstrates that the chromophores can participate in productive photoredox chemistry.

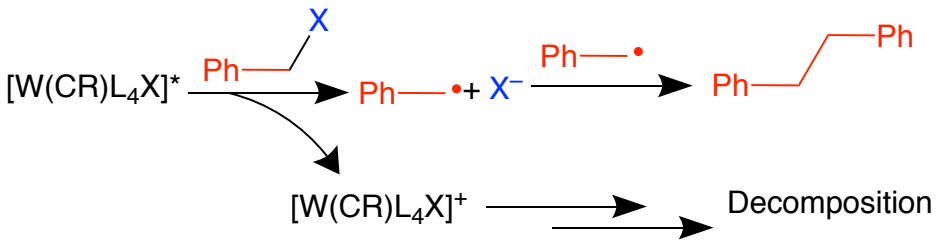

Figure 5.10. Dimerization of benzyl bromide (X = Br) (λ_{ex} = 530 nm).

A second photoredox screening reaction employed the chromophore, $W(CPh)(dppe)_2Cl$ ($E^{*/ox}$ = –2.65 V) with PhI ($E^{0/-}$ = –2.71 V, THF), in the presence of excess toluene (100 eq), to determine whether reduction of PhI and formation of phenyl radical substrate led to C–H arylation (Figure 5.11). Consistent with this photoredox reaction being slightly uphill, photolysis of these mixtures in CD_3CN resulted in slow changes to the ^1H and $^{31}P\{^1H\}$ NMR spectra of the

reaction mixture. Interestingly, after 2 d the ^{1}H NMR spectrum showed a quintet resonance characteristic of the hydride ligand of previously reported $[HW(CPh)(dppe)_2Cl]^+$.[34] One possible explanation for the formation of the hydride compound is outlined in Figure 5.12. Here, the photoredox-produced phenyl radical adds to toluene to form an ene-yl radical, which can be rearomatized upon loss of a proton and electron to generate the biaryl. We surmised that the oxidized chromophore formed following the photoredox reaction, $[W(CPh)(dppe)_2Cl]^+$, served as the oxidant, and that the chromophore served as the base. Prior work in our group showed that the $W(CPh)(dppe)_2Cl$ is a strong base (pK_a $[HW(CPh)(dppe)_2Cl]^+$ = 16.8 in THF solution).[35, 36]

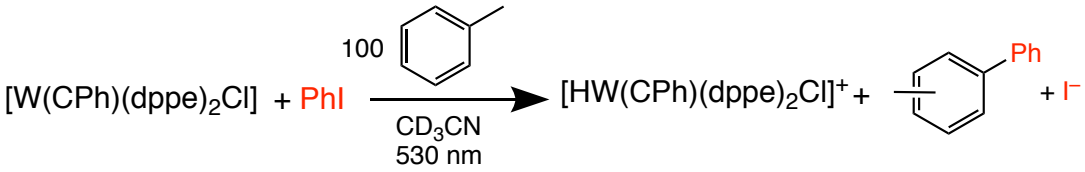

Figure 5.11. Photosensitized reduction of iodobenzene using $W(CPh)(dppe)_2Cl$.

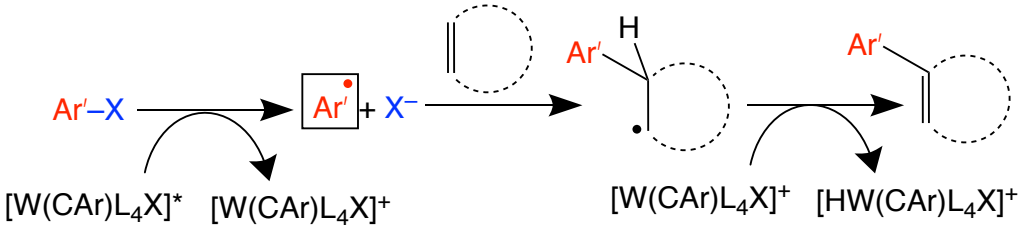

Figure 5.12. Schematic diagram depicting possible formation of hydride *via* stoichiometric photoredox chemistry.

The observed formation of $[HW(CPh)(dppe)_2Cl]^+$ stimulated an extensive study of photocatalytic C–H arylation chemistry with these chromophores, which is detailed in the next section. But before this was undertaken, a refinement of the preliminary experiment was explored. This employed the stronger photoreductant $W(CPh)(dmpe)_2Cl$ ($E^{*/ox}$ = –2.80 V vs $FeCp_2$), a simpler addition substrate (C_6H_6), which was also used as the solvent, and 3-iodobenzonitrile as the reduction substrate. Scaiano *et al.*[37] previously reported the radical addition rate of phenyl radical to benzene (4×10^5 $M^{-1}s^{-1}$). Photolysis of this mixture with a

green LED for 24 h led to formation of 3-cyanobiphenyl and a fine white precipitate (Figure 5.13). The GC/MS trace (Figure 5.13) clearly shows 3-cyanobiphenyl; no other products were observed. The amount of precipitate was too small to allow accurate NMR analysis, but its identity was determined by HR-ESI-MS (at 0 applied voltage) to be $[HW(CPh)(dmpe)_2Cl]^+$, based on comparison to the simulation (Figure 5.14).

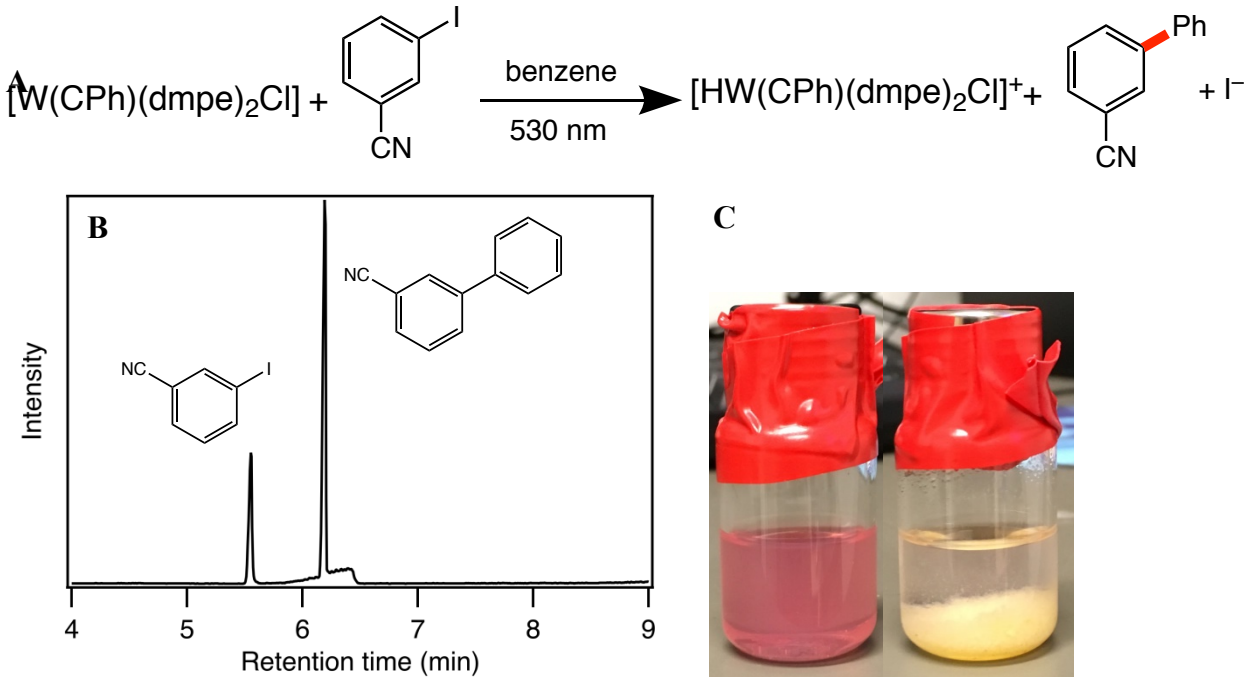

Figure 5.13. (A) Reaction scheme for the photosensitized reduction of 3-iodobenzonitrile using $W(CPh)(dmpe)_2Cl$; (B) Representative GC/MS trace for stoichiometric photoredox reactions (3-iodobenzonitrile); (C) Picture of the reaction mixture before and after photolysis. The GC/MS was recorded on the Varian instrument.

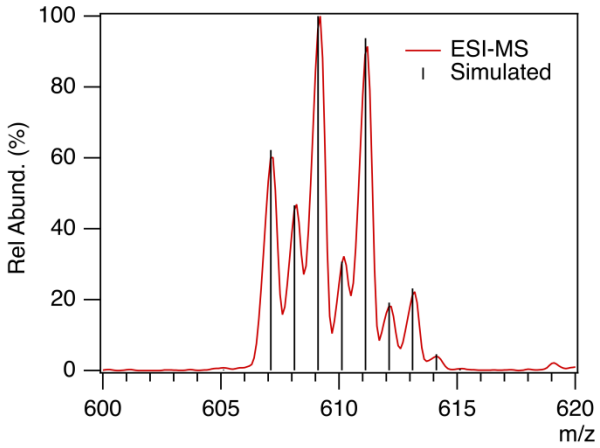

Figure 5.14. High-resolution mass spectrum of the white powder obtained in the photoreduction of 3-iodobenzonitrile (CH_2Cl_2, 0V).

A final stoichiometric C–H arylation screening reaction employed $W(CPh)(dmpe)_2Cl$, iodobenzene (1 μL, 8.9 μmol), and a white light excitation source in benzene solvent, which provided biphenyl in good yields (90% relative to tungsten) after 48 h of photolysis (Figures 5.15-5.16). To test for the possibility that this product arose from direct coupling of two phenyl radicals, a similar experiment in C_6D_6 solvent was performed. After 48 h of photolysis, the GC/MS data showed that the product C_6H_5–C_6D_5 is formed exclusively (Figure 5.17).

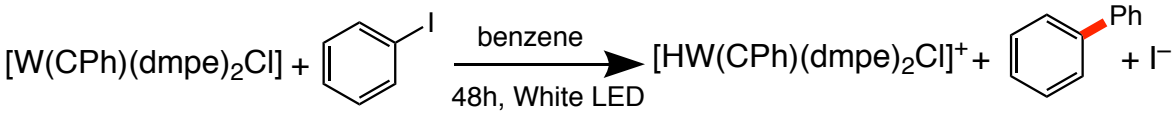

Figure 5.15. Photosensitized reduction of iodobenzene with $W(CPh)(dmpe)_2Cl$.

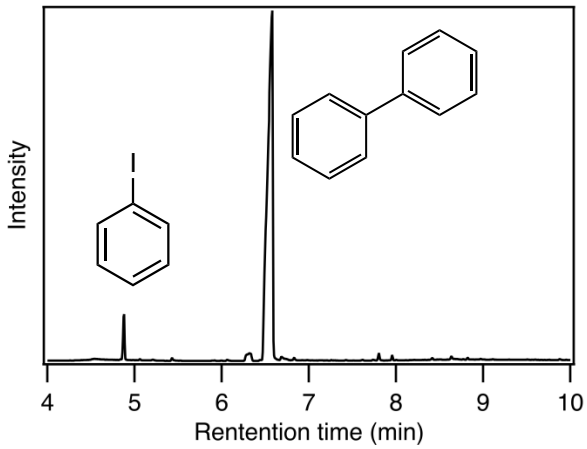

Figure 5.16. GC/MS trace for the reduction of iodobenzene using a white LED after 48 h of photolysis. GC/MS was recorded on the Agilent instrument.

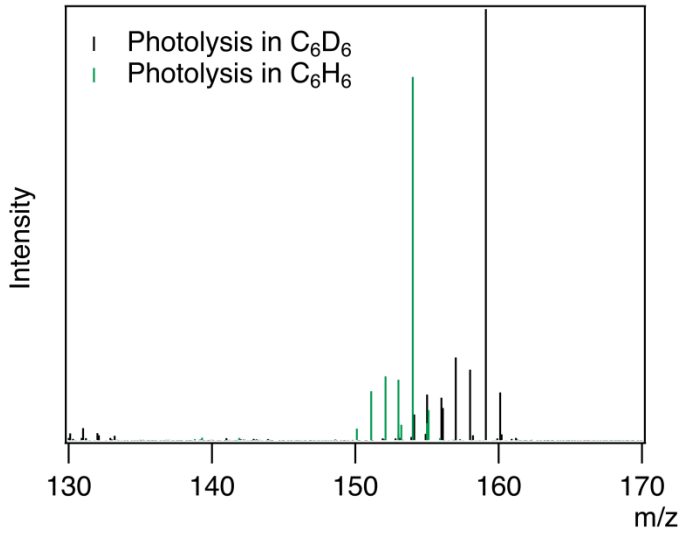

Figure 5.17. Comparison of the mass spectrum results for the photolysis of iodobenzene in C_6H_6 and C_6D_6. C_6H_6 = 154.1 m/z; C_6D_6 = 159.1 m/z.

5.2.3. Photocatalytic C–C bond forming reactions. The stoichiometric C–H arylation reactions described above rely on the presence of the tungsten chromophore to act as an oxidant and base toward the transient en-yl radical. Protonation of the tungsten chromophore consumes it, eliminating the possibility of catalytic photoredox chemistry. This suggested that the addition of a stoichiometric base could preserve the chromophore and enable photocatalysis. Several common organic bases (DBU, N^iPr_2Et, and tetramethylguanidine (TMG)) were investigated in screening reactions.

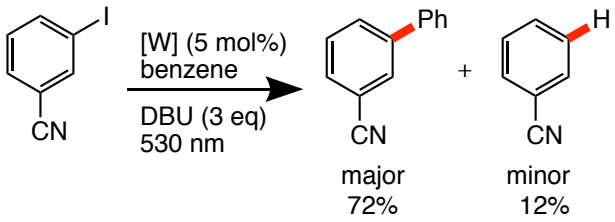

Figure 5.18. Initial catalytic C–H arylation experiments using W(CPh)(dmpe)$_2$Cl (5 mol%), 3-iodobenzonitrile, and DBU(3 eq).

Three test photoredox reactions using DBU as a base (3 eq. relative to aryl halide) were conducted using a catalytic amount of the W(CPh)(dmpe)$_2$Cl chromophore (5 mol%) and 3-iodobenzonitrile with benzene as the solvent and radical trap (Figure 5.18). This reaction was found to provide the C–H arylated product in good yields overnight, corresponding to multiple turnovers for the tungsten-benzylidyne complex. Interestingly, GC/MS traces of the reaction with 3-iodobenzonitrile using DBU as a base showed the presence of benzonitrile, the product of reductive dehalogenation (Figure 5.19). This side product either requires the presence of the cyanophenyl anion (from a process that results in the two-electron reduction of iodobenzonitrile), which would form benzonitrile *via* deprotonation (e.g., of [HDBU]$^+$), or operation of a H-atom transfer pathway with cyanophenyl radical. Because the two-electron reduction pathway seemed unlikely, we favored the latter. One possibility for its operation could be that [HDBU]$^+$ is redox active and could oxidatively quench the excited state of the chromophore.

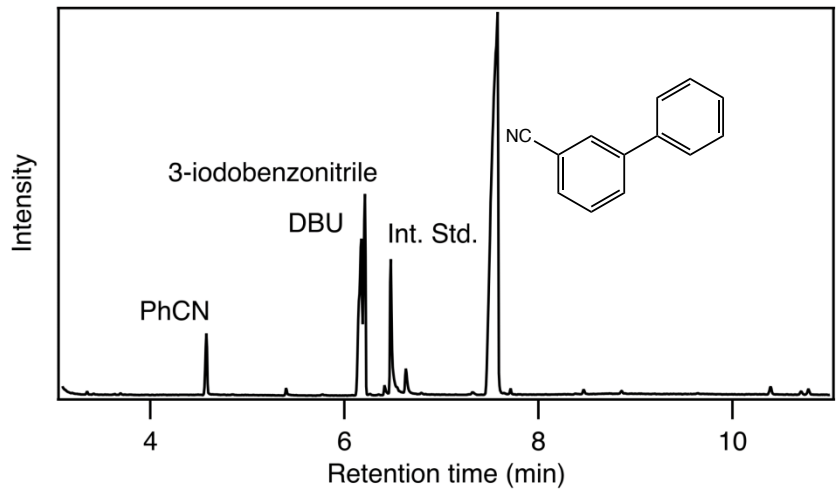

Figure 5.19. Representative GC/MS trace for the reaction of W(CPh)(dmpe)$_2$Cl, DBU (3 eq) and 3-iodobenzonitrile in benzene solution photolyzed with a green LED (530 nm) for 18h. Tetradecane was used as an internal standard. The GC/MS was recorded on the Agilent instrument.

Several approaches were taken to attempt to eliminate reductive dehalogenation side product in the photoredox activation of 3-iodobenzonitrile. Again, the chromophore was W(CPh)(dmpe)$_2$Cl (2 mol%) and solvent and radical trap was benzene. First, the amount of DBU was decreased from 3 to 1.1 equiv. As before, DBU was observed to form 3-cyanobiphenyl in moderate yields during 7 h of photolysis (56%). A smaller amount of benzonitrile was also formed (3%, Table 5.3) compared to the experiment utilizing 3 eq. DBU. Second, the bulky base N^{i}Pr$_2$Et was used because, unlike DBU, its conjugate acid is not redox active. It is too bulky to deprotonate [HW(CPh)(dmpe)$_2$Cl]$^+$, should this be an intermediate in the photoredox reaction. Using N^{i}Pr$_2$Et, the yield of 3-cyanobiphenyl was very poor (2%); indeed, this amount of product matches the quantity of chromophore, which might indicate the latter is being consumed stoichiometrically. The third base used was TMG, which provided the desired 3-cyanobiphenyl product in a yield similar to that obtained with DBU but with only a trace of the undesirable benzonitrile reductive dehalogenation side product. Thus, TMG was employed as the base in all subsequent studies.

Table 5.3. Base optimization for catalysis with 3-iodobenzonitrile and benzene (% yield).[a]

Base	3-Cyanobiphenyl (%)	Benzonitrile (%)
DBU	56	3
N^iPr_2Et	2	0
TMG	62	<1

[a] Yields determined by GC/MS using tetradecane as an internal standard. GC/MS data recorded on the Agilent instrument.

Use of benzene as both a radical trap and solvent is advantageous in screening reactions because its maximal concentration minimizes radical decomposition pathways. However, for practical syntheses translating these photoredox reactions to polar solvents became a priority. The use of polar, unreactive solvents would allow reduction of more challenging substrates and, additionally, allow selection of a more diverse set of radical traps. In particular, generating C–C bonds between pyrroles and arenes or heteroarenes was of interest. Functionalized pyrroles are constituents in a wide variety of natural products and widespread components in pharamaceuticals.[38] Utilizing photoredox catalysis as a method to functionalize pyrrolic rings could allow for the construction of molecules containing substituents that could be difficult to synthesize by conventional thermal methods.

A large number of photoredox reactions of the type shown in Figure 5.20A were explored and found to be successful in this solvent. Standard reaction conditions employed a low loading of chromophore with sufficient excited-state potential to accomplish the reduction of the aryl halide (chromophore, 2 mol%), and the base TMG. These were excited with white light at room temperature. The substrate scope is shown in Figure 5.20C. For reactions with pyrrole and *N*-methylpyrrole, the coupling products could generally be produced in 85% or greater yield; Figure 5.21 shows a representative GC trace. The general scheme envisioned for catalytically accomplishing these reactions is shown in Figure 5.20B. Photoinitiated reduction of the

(hetero)aryl-halide (Ar–X) by the chromophore results in dissociation of halide to form a neutral aryl radical (Ar•), together with the oxidized chromophore. Reaction of the aryl radical with the pyrrole *via* C–C bond formation provides a transient ene-yl radical, which is rearomatized by deprotonation with TMG and oxidation by the spent chromophore, regenerating the latter.

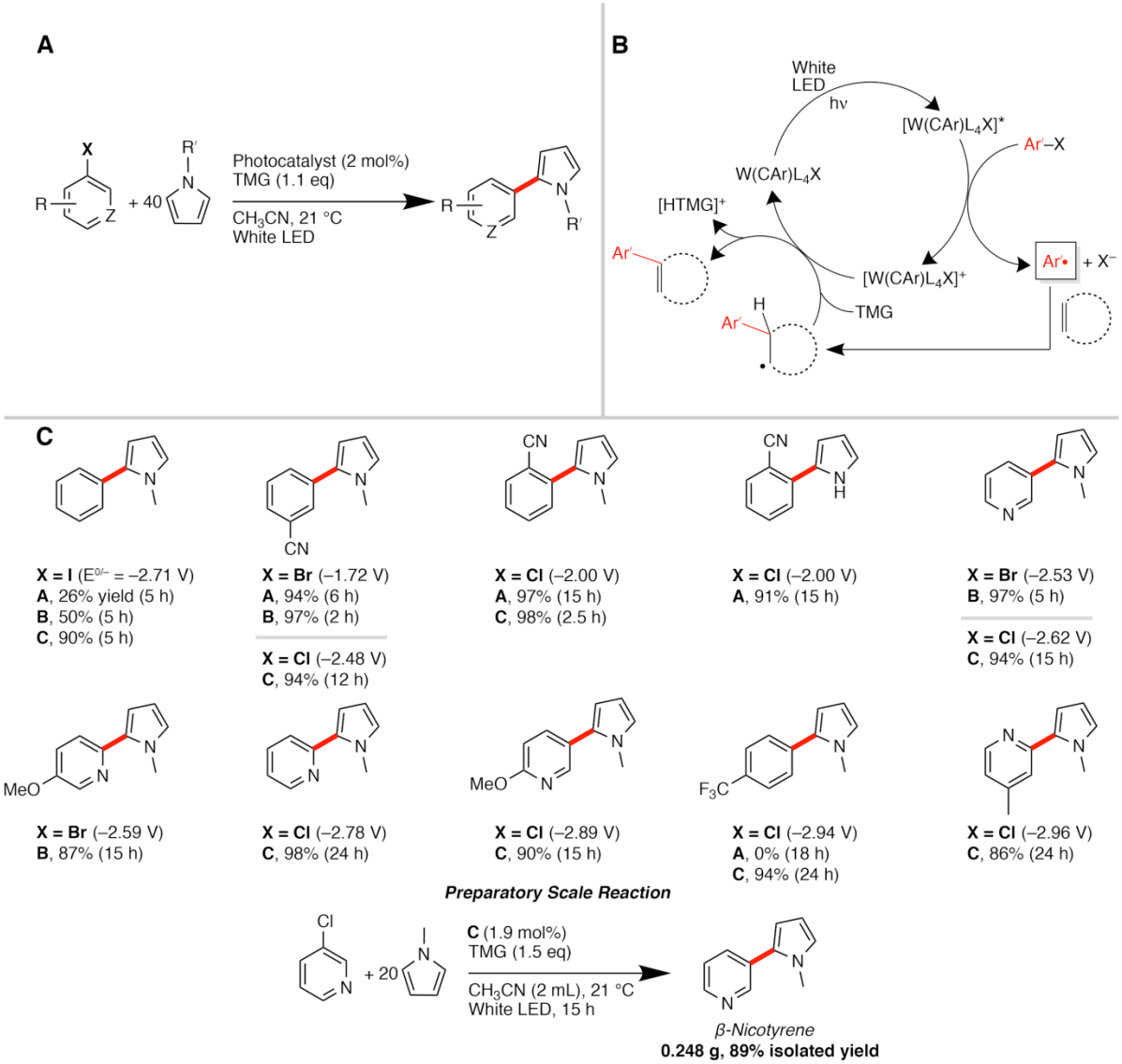

Figure 5.20. (A) Reaction scheme; (B) Proposed Mechanism; (C) Substrate scope with pyrroles and preparatory scale reaction A = $W(CPh)(dmpe)_2Cl$, B = $W(CC_6H_4\text{-}4\text{-}OCH_3)(dmpe)_2Cl$; C = $W(CC_6H_4\text{-}4\text{-}pyr)(dmpe)_2Cl$.

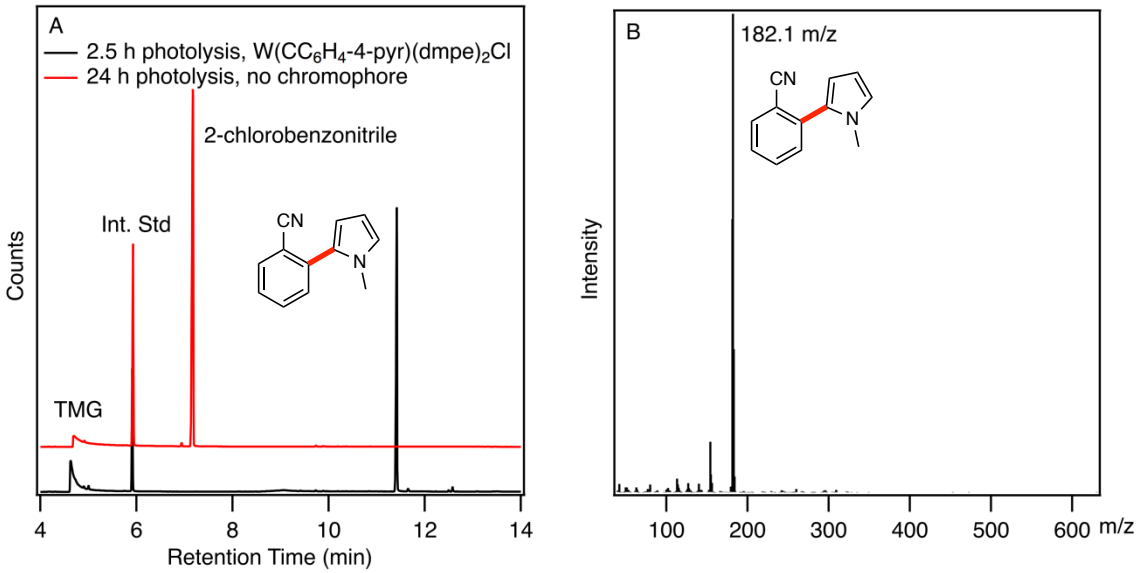

Figure 5.21 (A) Representative GC/MS chromatogram of a reaction mixture following photolysis. (B) Mass spectrum of GC peak in (A) at RT = 11.4 min; calc. m/z = 182.08, obs. = 182.1. GC/MS data was recorded on the Varian instrument.

For a given reaction, the excited-state electron-transfer driving force (which is governed by the choice of chromophore) affects the rate at which the reaction proceeds. For example, with the substrate PhI ($E^{0/-}$ = –2.71 V) the aryl-pyrrole product was produced using W(CC_6H_4-4-pyr)(dmpe)$_2$Cl ($E^{*/+}$ = –3.18 V) in 90% yield in 5 h, whereas W(CC_6H_4-4-OCH_3)(dmpe)$_2$Cl ($E^{*/ox}$ = –3.01 V) and W(CPh)(dmpe)$_2$Cl ($E^{*/ox}$ = –2.80 V) provided yields of 50% and 26%, respectively, after the same reaction time. The attempted reduction of 4-chloro-α,α,α-trifluorotoluene by W(CPh)(dmpe)$_2$Cl (ΔG = 0.14 V) was observed to provide no product, consistent with it being significantly uphill, whereas productive reactions were observed for the chromophores W(CC_6H_4-4-OCH_3)(dmpe)$_2$Cl and W(CC_6H_4-4-pyr)(dmpe)$_2$Cl; this suggests the possibility of targeting specific redox-cleavable groups in multifunctionalized substrates with specific chromophores. To demonstrate that photoredox-catalyzed C–H arylation reactions can be accomplished on a synthetic scale, the compound β-nicotyrene was prepared on a quarter-gram scale in 89% purified yield from the photoredox-catalyzed reaction between 3-

chloropyridine and *N*-methylpyrrole, using the chromophore $W(CC_6H_4\text{-}4\text{-}pyr)(dmpe)_2Cl$. Both the commercial availability of starting materials and reaction conditions of this method compare favorably to other means of synthesis of β-nicotyrene. These often use non-commercial starting materials (lithiated pyrroles) and highly elevated temperatures (>80 °C) (Figure 5.22).[39-41]

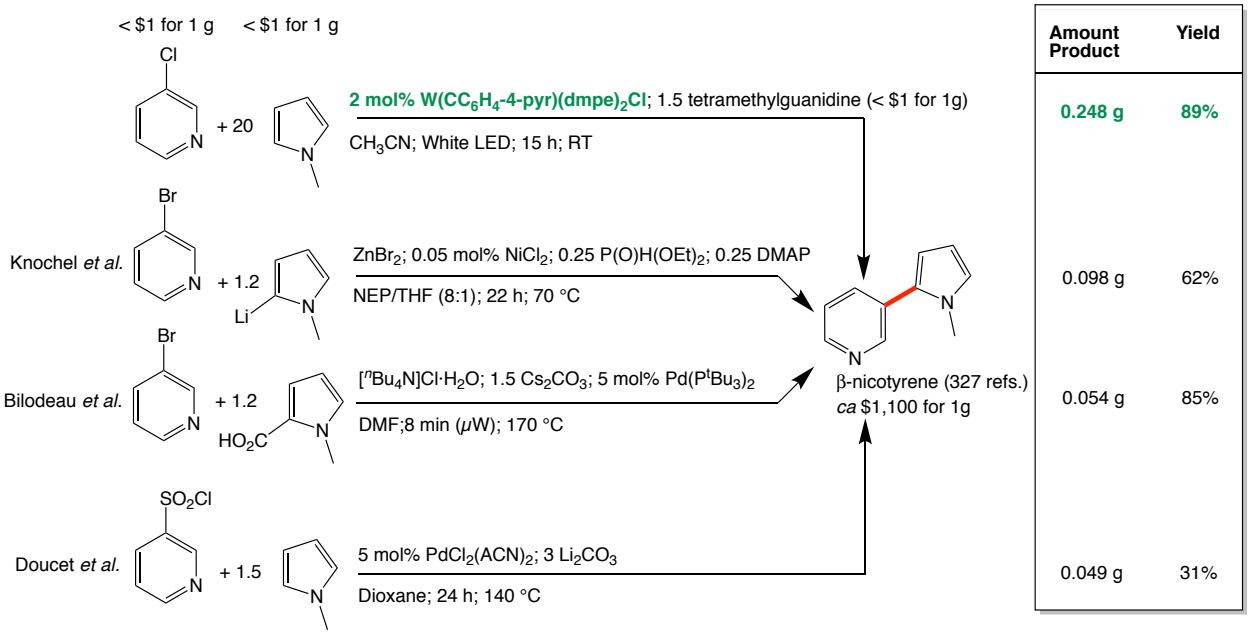

Figure 5.22. Comparison of the photochemical synthesis of β-nicotyrene to thermal methods found in Refs. 39-41.

The initial reactions discussed in this section were stoichiometric C–C bond formation reactions in benzene solution. With the optimized conditions, the scope of these reactions could be expanded to derivatives of biphenyl by photoredox catalysis. Biaryl derivatives are a common motif in pharmacological settings; the ability to generate bi-aryl and -heteroaryl molecules cleanly using only chromophore and base could also enable the synthesis of new types of biologically active molecules.[29] However, nonpolar media are generally not used for electron-transfer reactions because their poor stabilization of charged compounds and intermediates substantially raises the thermodynamic barrier to electron-transfer reactions. An example of a

nonpolar solvent/substrate is benzene, which has provided modest yields as a coupling substrate in photoredox C–H arylation reactions with aryl halides when conducted in polar solvents.[42] White-light excitation of photoredox catalyst, W(CPh)(dmpe)$_2$Cl, in benzene solution containing TMG and (hetero)aryl-iodide substrates provided the corresponding (hetero)aryl–phenyl products in yields of ~50–90% (Figure 5.23), suggesting this as an approach to photoredox-catalyzed C–H arylation reactions with less efficient radical traps. In this experiment, the reaction time for 3-iodobenzonitrile was optimized to allow for maximal yield. This time optimization was noted to raise the yield from 62% (7 h photolysis) to 89% (12 h photolysis). The three molecules examined were 3-iodobenzonitrile, 2-iodopyridine, and 4-iodotrifluorotoluene. In each case, reactions were observed to be rather sluggish with W(CPh)(dmpe)$_2$Cl requiring over 12 h of reaction time. Yields were observed in a general trend corresponding to the relative reduction potential of the substrate.

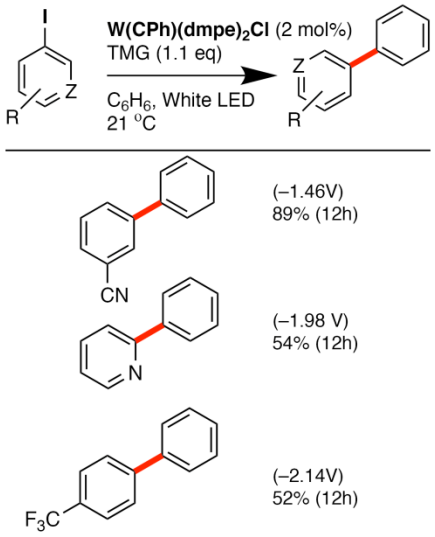

Figure 5.23. Reaction scheme for C–H arylation reactions with benzene; (B) Substrates incorporated into the reactions using W(CPh)(dmpe)$_2$Cl as the photoredox chromophore.

5.3. Conclusions.

In this chapter, the use of tungsten-benzylidyne photoredox chromophores as catalysts for organic transformations have been described. Initially, we focused on understanding the reduction kinetics of organic molecules that oxidatively quench the chromophore to produce bound radical anions. It was found that a variety of substituted benzenes oxidatively quench $W(CC_6H_4\text{-}4\text{-}pyr)(dmpe)_2Cl$ with rate constants that vary appropriately with driving force, and shown by TA specifically for naphthalene and diphenylacetylene that their radical anions are produced. Additionally, the stoichiometric reductive photochemical reactions of $W(CAr)L_4X$ chromophores with organic halides were shown to form reactive organic radicals, e.g., the formation and dimerization of benzyl radicals generated from the reduction of benzyl bromide. Finally, catalytic photoredox C–H arylation reactions of pyrroles using aryl and heteroaryl substrates were found to proceed in high yields and cleanly. The compound β-nicotyrene was synthesized on a quarter-gram scale, in 89% purified yield. This demonstrates that these methods have the capability to be scaled reasonably and that these complexes are excellent photoredox chromophores for future applications in synthetic organic chemistry.

5.4. Experimental Section.

5.4.1. General Procedures. General procedures for this section are the same as elaborated in Section 2.4.

5.4.2. Procedures for emission lifetime measurements and transient absorption spectroscopy. Solution samples for electronic spectroscopy were prepared under N_2 in sealable cuvettes of path length 1 cm or 1 mm, degassed with three freeze–pump–thaw cycles using a

vacuum line, and sealed under purified N_2. Solvents (THF and toluene) were purified by stirring over NaK for at least 24 h. The optical density at the excitation wavelength was ≤ 0.15 absorbance units. Data for these experiments were collected with an automated, LabView-controlled instrument in which the excitation source was an integrated Nd:YAG-optical-parametric-oscillator pulsed laser (Opotek Vibrant 355 LD, 10 Hz repetition rate, 10-ns pulse width, 0.5–1.5 mJ/pulse energy at the sample) that produced tunable output between 410–710 nm. The laser beam sent to the sample was not focused. From the sample, luminescence (for lifetime measurements) or the transmitted probe beam (for transient-absorption spectroscopy) was focused onto the input slit of a monochromator (Horiba Scientific iHR320), the output of which was detected by a six-stage Hamamatsu R928 photomultiplier tube and processed with a digital oscilloscope (Tektronix TDS 3032C). The resulting time-resolved signal-intensity data were analyzed using Igor Pro software (version 6.37). Emission decay (lifetime) data for all compounds were found to be well fit using a single-exponential decay function over a minimum of 3τ. For each compound, lifetimes were measured at wavelengths across the emission band (50 nm intervals) and of different samples; these were observed to agree within 5%. Transient-absorption spectra were measured using a white-light probe beam provided by a 75-W xenon lamp (PTI A1010) that was passed through a 1250 nm short-pass filter and a 550 nm long-pass filter. The toroidal-shaped probe beam was focused onto the sample with a concave mirror; the transmitted light was focused onto the input slit of the monochromator with a second concave mirror. Laser excitation was collinear with and counter propagating to the probe beam, passing through holes in the centers of the concave mirrors (where lamp intensity was zero); this allowed overlap of the laser and focused probe beams in the sample. Transient decay traces at each

wavelength were averaged over 2048 laser pulses; these were analyzed to determine the transient lifetime and transient absorbance (ΔOD).

5.4.3. Procedure for electron-transfer quenching experiments. A stock solution of a tungsten–alkylidyne chromophore in THF (25 mL) was prepared such that the absorbance of the sample was approximately 0.15 at the excitation wavelength (1 cm path length). To a 10-mL portion of the stock solution was added a quantity of an organic electron acceptor (quencher). A series of independent samples spanning a range of quencher concentrations were prepared by mixing aliquots from the two stock solutions. Each sample was sealed in a 1-cm path length quartz cuvette, degassed via three freeze–pump–thaw cycles on a vacuum line, and sealed under purified N_2. The emission lifetime was recorded for each sample, including that which did not contain quencher. The electron-transfer quenching rate constant was determined from a linear fit of these data to the Stern–Volmer equation (Equation 5.1).[43]

$$\frac{\tau_0}{\tau} = 1 + k_q[Q]\tau_0 \qquad (5.1)$$

In Equation 5.1, τ_0 is the emission lifetime of the chromophore in the absence of quencher, τ is the emission lifetime of the chromophore in the presence of a given concentration of quencher [Q], and k_q is the electron-transfer quenching rate constant (units $M^{-1}s^{-1}$). The goodness-of-fit was found to be $r^2 \geq 0.994$ across all experiments.

5.4.4. Photochemical reactions.

5.4.4.1 Green-light photolysis apparatus. A green LED (530 nm, 350 mW, Part Number: M530L3, THOR Scientific) was used as one illumination source. Samples were positioned 10 cm from the LED and irradiated while stirring. A photograph of the apparatus is shown in Figure 5.24.

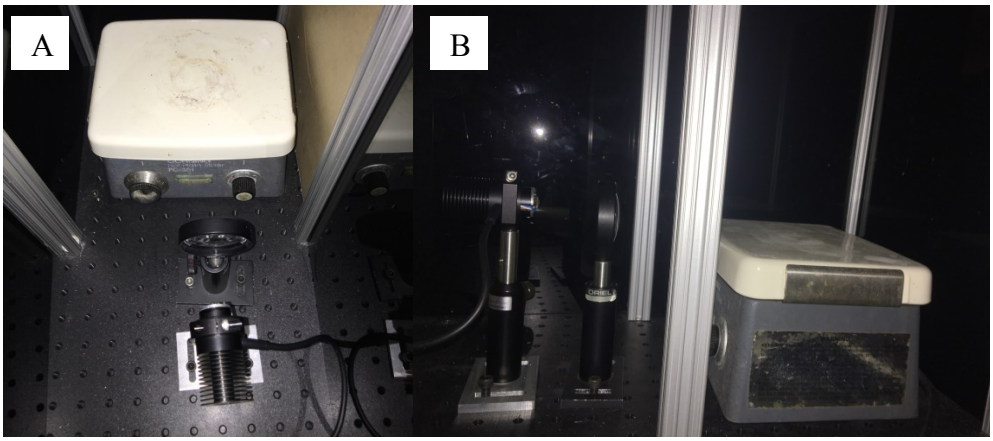

Figure 5.24. Green LED illumination apparatus. (A) Top view; (B) Side view.

5.4.4.2. White photolysis apparatus. For those experiments which could be excited using white light, a strip of white LEDs (superbriteleds.com model 4NFLS-xH24-24V-CL, λ_{ex} = 420–570 nm) was placed inside a 20 cm diameter crystallizing dish with the LEDs facing inwards, and the dish placed atop a magnetic stirrer. The photolysis sample was placed in the center of the dish. A fan was placed above the dish to provide continuous turnover of the air within it; a thermocouple gauge within this air space indicated that the temperature was constant at 21 °C (Figure 5.25).

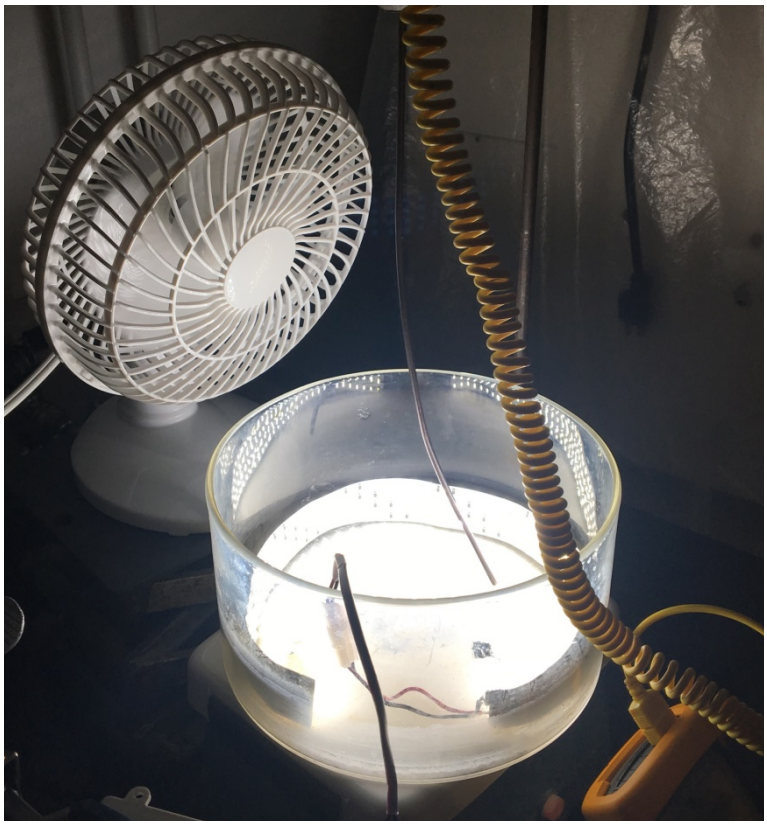

Figure 5.25. White LED illumination apparatus.

5.4.4.3. General procedure for photochemical reactions in acetonitrile. Samples prepared in screw-cap vials were prepared under N_2 in a glove box. Each sample contained haloarene (0.096 mmol, 1 eq), tetramethylguanidine (TMG, 13 μL, 0.105 mmol, 1.1 eq), *N*-methylpyrrole (3.84 mmol, 40 eq), and chromophore (1.92 μmol, 2 mol%) in acetonitrile (3 mL). The sample was then photolyzed (white LEDs) at room temperature with stirring using the apparatus described above. After the photolysis was terminated, each vial was opened in air, its contents were diluted with acetonitrile to 10 mL, and the solution passed through a 0.2-μm filter. Acetophenone (10 μL) was added as an internal GC standard. One aliquot (1.5 mL) from each sample was then analyzed by GC/MS.

5.4.4.4. General procedure for photochemical reactions in benzene. Samples prepared in screw-cap vials were prepared under N_2 in a glove box. Each sample contained haloarene

(0.096 mmol, 1 eq), tetramethylguanidine (TMG, 13 μL, 0.105 mmol, 1.1 eq), and chromophore (1.92 μmol, 2 mol%) in benzene (3 mL). The sample was then photolyzed (white LEDs) at room temperature with stirring using the apparatus described above. After the photolysis was terminated, each vial was opened in air, its contents were diluted with acetonitrile to 10 mL, and the solution passed through a 0.2 μm filter. Acetophenone (10 μL) was added as an internal GC standard. One aliquot (1.5 mL) from each sample was then analyzed by GC/MS.

5.4.4.5. Preparative synthesis of β-nicotyrene (1-methyl-2-(3-pyridyl)pyrrole). A solution containing 3-chloropyridine (0.200 g, 1.76 mmol), *N*-methylpyrrole (2.88 g, 35.2 mmol), tetramethylguanidine (0.305 g, 2.64 mmol), and $W(CC_6H_4\text{-}4\text{-}pyr)(dmpe)_2Cl$ (0.023 g, 0.033 mmol, 1.9 mol%) in CH_3CN (2 mL) was prepared under N_2 in a screw top, 20 mL scintillation vial. The dark orange sample was photolyzed at room temperature with stirring using a white LED source for 15 h, during which time the solution darkened slightly. The cap was then removed from the vial, in air, and the solution filtered to remove a fine white precipitate. Volatile contents were removed under vacuum, leaving a dark yellow oil. The oil was purified by column chromatography on silica gel with 1:1 Et_2O/CH_2Cl_2 as the eluent. Removal of solvent left the product as a light yellow viscous liquid (0.248 g, 1.56 mmol, 89% yield). The ^{1}H-NMR (Figure 5.26), $^{13}C\{^1H\}$-NMR (Figure 5.27), and EI-MS data are in excellent agreement with the literature.[39]

5.4.5. GC/MS Method. A Varian Saturn 2000 GC/MS/MS with a CP-3800 gas chromatograph and CP-8400 autosampler or an Agilent GC/MS (7890B GC, 7693 Autosampler, and 5977A SQ MS) equipped with an Agilent 122-4732 column was used for these experiments. For the Varian system, the elution time was set to 16 min with a front oven temperature of 200 °C. The column oven was initially set to 50 °C. The temperature was held at 50 °C for 1 min and

then a temperature gradient of 15 °C/min was introduced. For the Agilent system, the elution time was set to 13 min with a front oven temperature of 250 °C. The column oven was initially set to 50 °C. The temperature was held at 50 °C for 1 min and a temperature gradient of 40 °C/min was introduced. GC yields were calculated using an acetophenone internal standard. Response factors were calculated from measurements made of authentic samples of products.

Table 5.4. Yields for photoredox-catalyzed C–H arylation reactions with Ar–X and *N*-methylpyrrole.

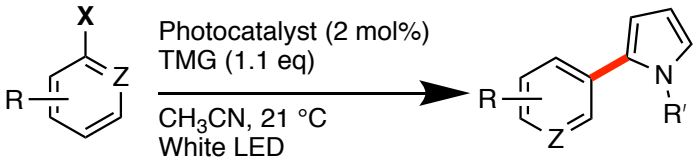

Ar–X	$E_{1/2}^{0/-}$ (V)	Chromophore (Chr)[a]	Time (h)	Yield (%)[b]
iodobenzene	–2.71	**A**	5	26
		B	5	50
		C	5	90
3-bromobenzonitrile	–1.72	None	12	0
		A	12	0[c]
		A	12	tr[d,e]
		A	6	94
		B	2	97
3-bromopyridine	–2.53	**B**	5	97
2-bromo-5-methoxypyridine	–2.59	**B**	15	87
2-chlorobenzonitrile	–2.00	None	24	0
		A	15	91[f]
		A	15	97
		C	2.5	98
3-chlorobenzonitrile	–2.48	**B**	15	55
		C	12	94
4-chlorobenzotrifluoride	–2.94	**A**	18	tr[e]
		B	15	53
		C	24	94
2-chloropyridine	–2.78	**B**	15	50
		C	24	98
3-chloropyridine	–2.62	**B**	15	66
		C	15	94
2-chloro-4-methylpyridine	–2.96	**C**	24	86
2-methoxy-5-chloropyridine	–2.89	**C**	15	90

[a]**A:** W(CPh)(dmpe)$_2$Cl; **B:** W(CC$_6$H$_4$-4-OCH$_3$)(dmpe)$_2$Cl; **C:** W(CC$_6$H$_4$-4-pyr)(dmpe)$_2$F. [b]Yields determined by GC. [c]No light. [d] No TMG. [e] A trace amount of product was visible by GC/MS, but it was below the threshold for accurate integration. [f] C–H arylation substrate was pyrrole instead of *N*-methylpyrrole.

Table 5.5. Yields for photoredox-catalyzed C–H arylation reactions with Ar–I and C_6H_6.

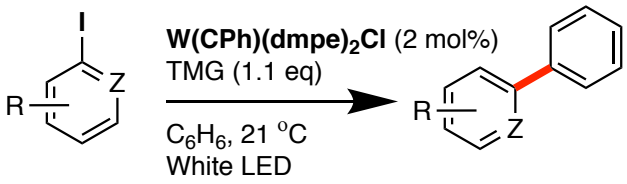

Ar–I	$E_{1/2}^{0/-}$ (V)	Time (h)	Yield (%)[b]
3-iodobenzonitrile	–1.46	12	0
		12	0[c]
		12	tr[d]
		12	89
2-iodopyridine	–1.98	12	54
4-iodobenzotrifluoride	–2.14	12	52

[a]**A:** W(CPh)(dmpe)$_2$Cl. [b] Yields determined by GC. [c] No light [d] No TMG; a trace amount of product was visible by GC/MS, but it was below the threshold for accurate integration.

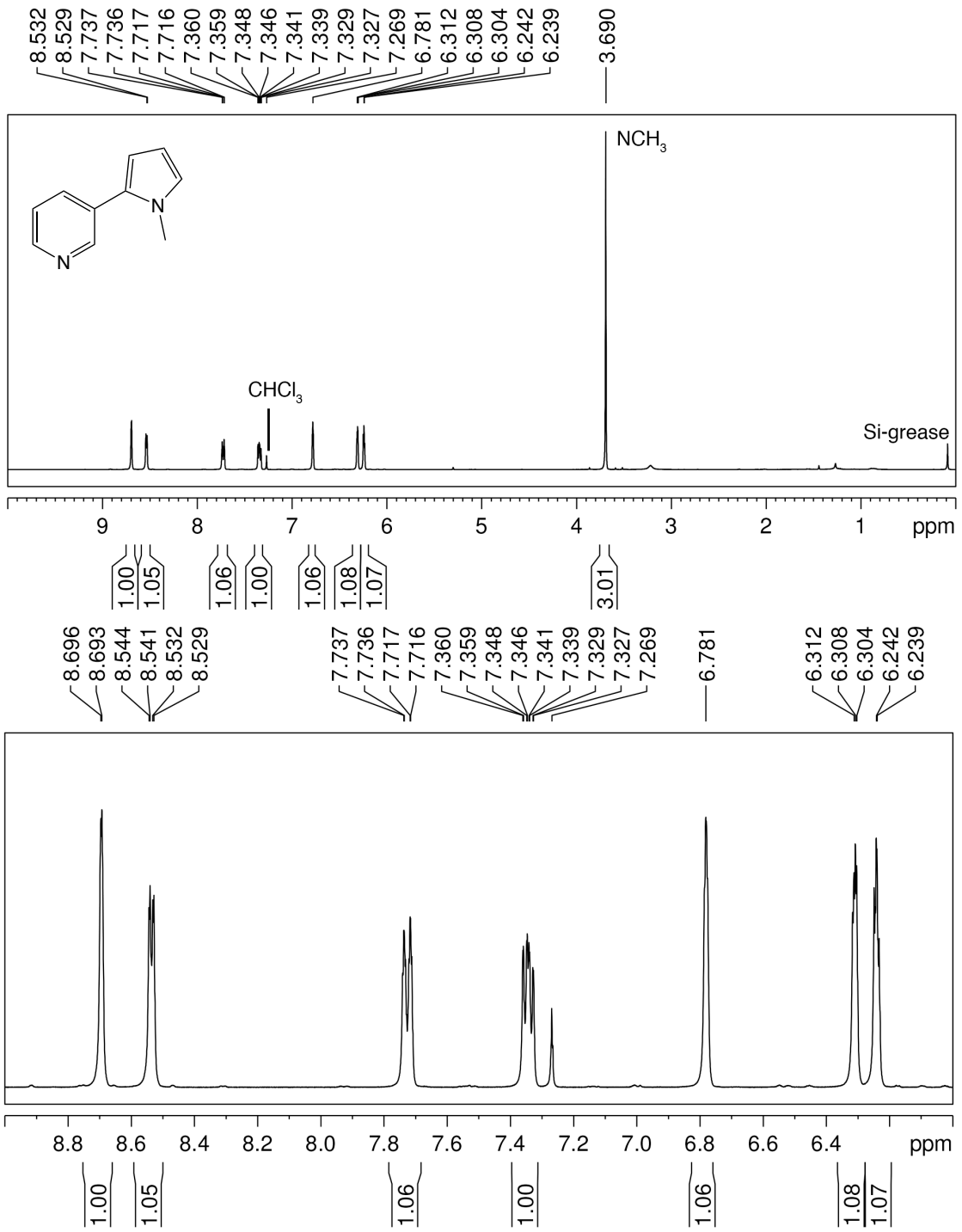

Figure 5.26. ^{1}H NMR spectra of β-nicotyrene in $CDCl_3$. The bottom spectrum is an expansion of the top spectrum.

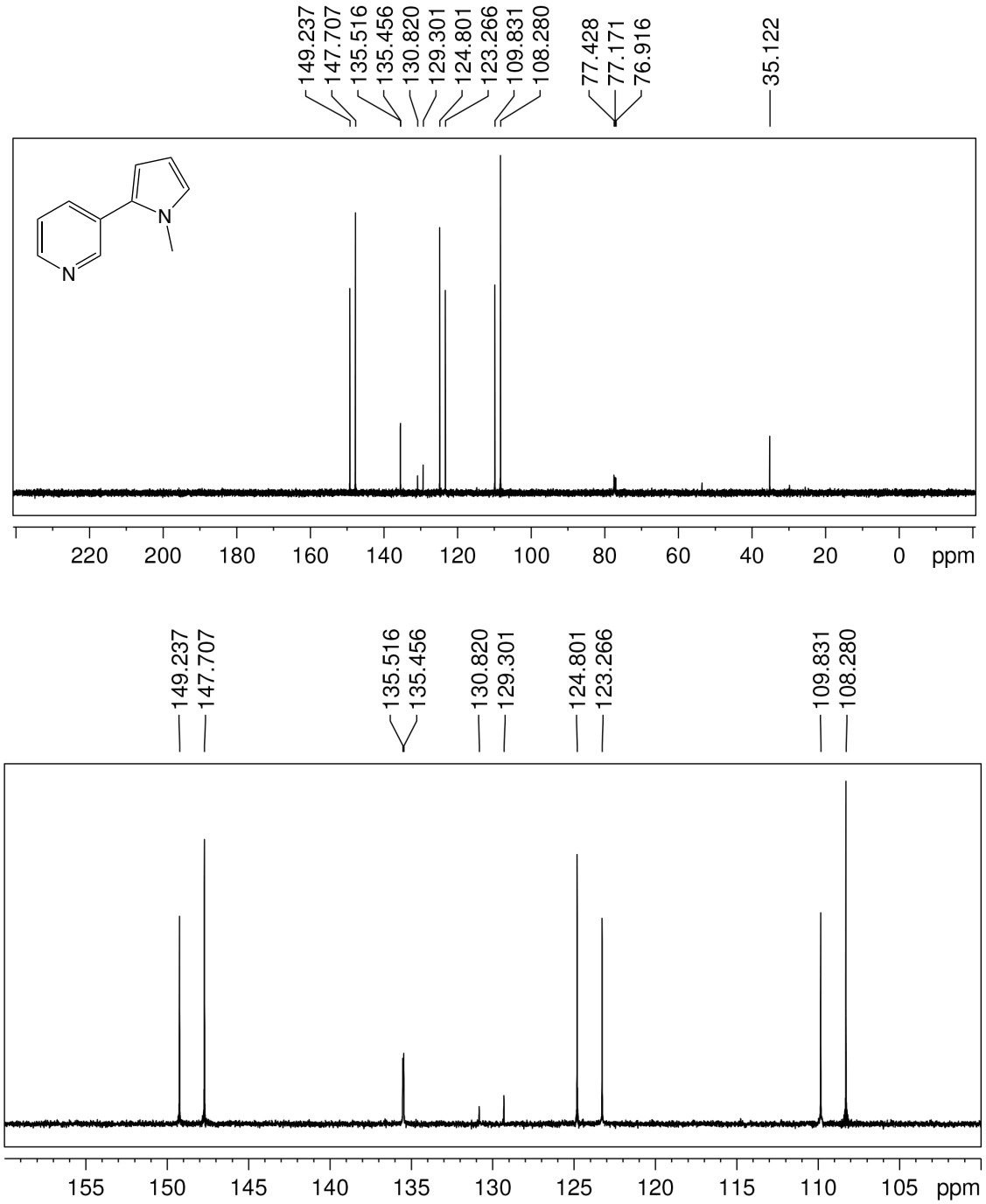

Figure 5.27. $^{13}C\{^{1}H\}$ NMR spectra of β-nicotyrene in $CDCl_3$. The bottom spectrum is an expansion of the top spectrum.

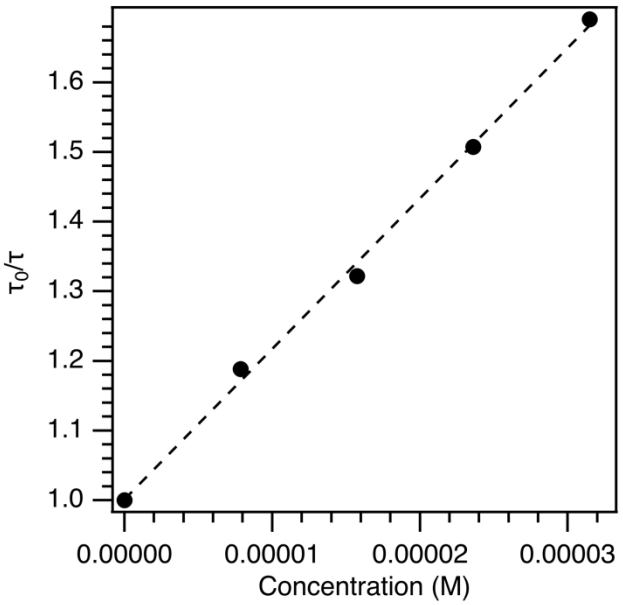

Figure 5.28. Stern–Volmer experiment with $W(CC_6H_4\text{-}4\text{-}pyr)(dmpe)_2Cl$ and benzaldehyde. Linear regression: f(x) = 21603x + 1.00; r^2 = 0.997. The quenching rate constant is listed in Table 5.2.

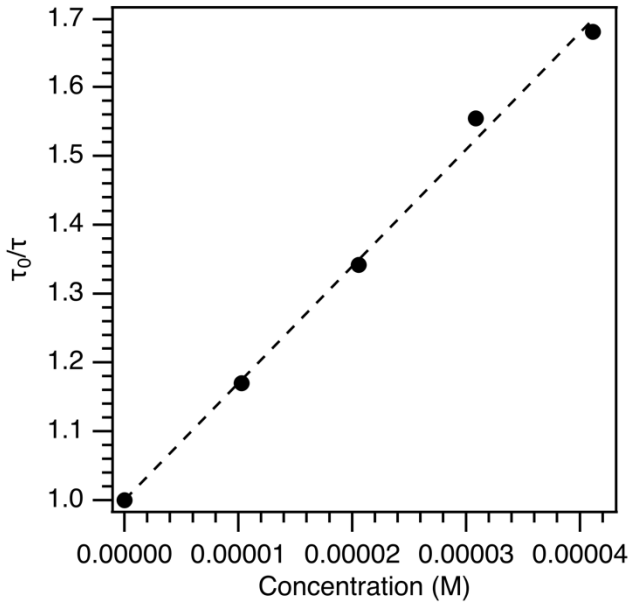

Figure 5.29. Stern–Volmer experiment with $W(CC_6H_4\text{-}4\text{-}pyr)(dmpe)_2Cl$ and acetophenone. Linear regression: f(x) = 16966x + 1.00; r^2 = 0.995. The quenching rate constant is listed in Table 5.2.

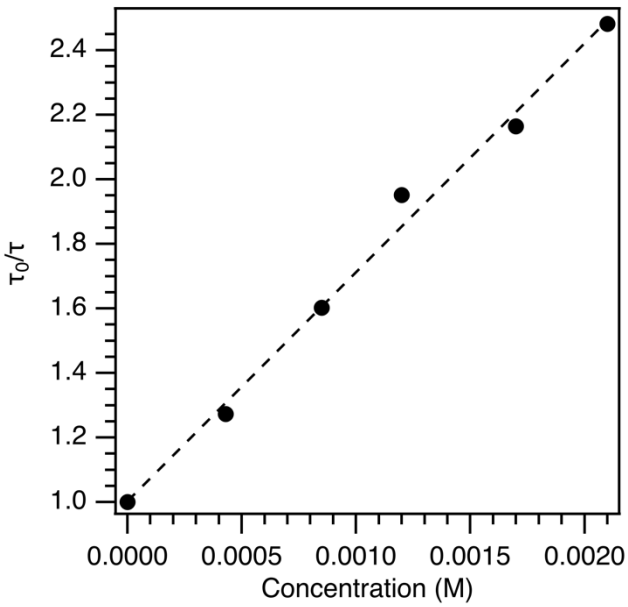

Figure 5.30. Stern–Volmer experiment with $W(CC_6H_4\text{-}4\text{-}pyr)(dmpe)_2Cl$ and benzonitrile. Linear regression: $f(x) = 709.5x + 1.00$; $r^2 = 0.994$. The quenching rate constant is listed in Table 5.2.

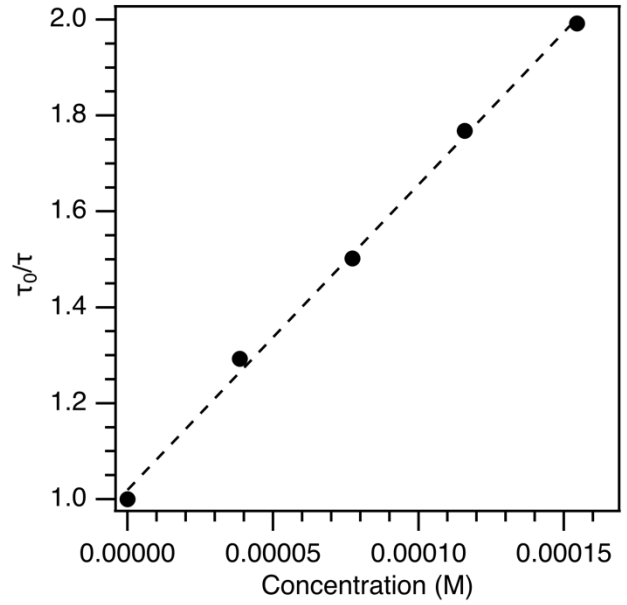

Figure 5.31. Stern–Volmer experiment with $W(CC_6H_4\text{-}4\text{-}pyr)(dmpe)_2Cl$ and ethyl benzoate. Linear regression: $f(x) = 6366x + 1.02$; $r^2 = 0.997$. The quenching rate constant is listed in Table 5.2.

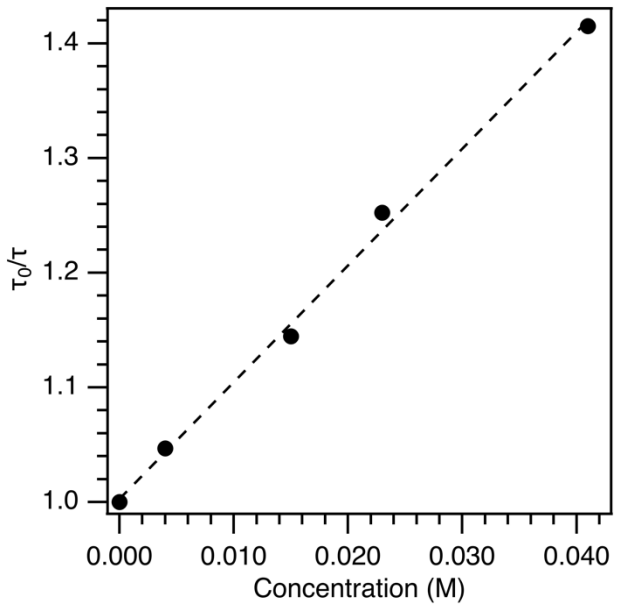

Figure 5.32. Stern–Volmer experiment with $W(CC_6H_4\text{-}4\text{-}pyr)(dmpe)_2Cl$ and phenyl acetylene. Linear regression: $f(x) = 10.18x + 1.00$; $r^2 = 0.996$. The quenching rate constant is listed in Table 5.2.

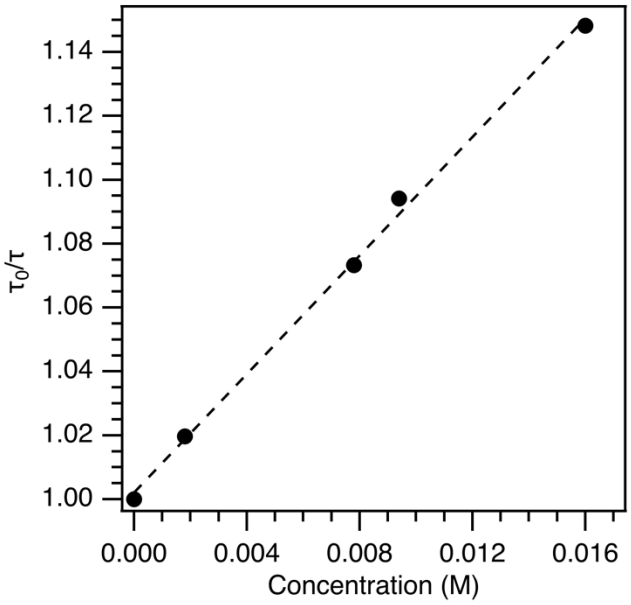

Figure 5.33. Stern–Volmer experiment with $W(CC_6H_4\text{-}4\text{-}pyr)(dmpe)_2Cl$ and naphthalene. Linear regression: $f(x) = 9.28x + 1.00$; $r^2 = 0.998$. The quenching rate constant is listed in Table 5.2.

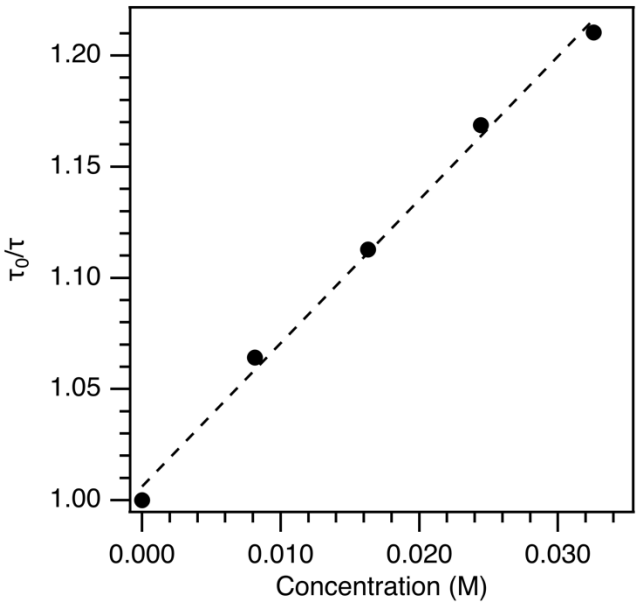

Figure 5.34. Stern–Volmer experiment with $W(CC_6H_4\text{-}4\text{-}pyr)(dmpe)_2Cl$ and α,α,α-trifluorotoluene. Linear regression: $f(x) = 6.45x + 1.01$; $r^2 = 0.996$. The quenching rate constant is listed in Table 5.2.

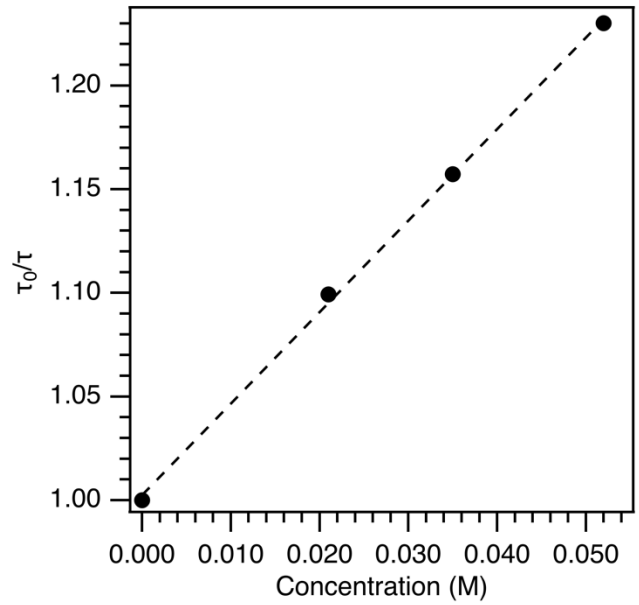

Figure 5.35. Stern–Volmer experiment with $W(CC_6H_4\text{-}4\text{-}pyr)(dmpe)_2Cl$ and styrene. Linear regression: $f(x) = 4.41x + 1.00$; $r^2 = 0.999$. The quenching rate constant is listed in Table 5.2.

5.5. References.

1. Bock, C. R.; Meyer, T. J.; Whitten, D. G. *J. Am. Chem. Soc.* **1974**, *96*, 4710-4712.

2. Pause, L.; Robert, M.; Savéant, J.-M. *J. Am. Chem. Soc.* **1999**, *121*, 7158-7159.

3. Ghosh, I.; Ghosh, T.; Bardagi, J. I.; König, B. *Science* **2014**, *346*, 725-728.

4. Ghosh, I.; König, B. *Angew. Chem. Int. Ed.* **2016**, *55*, 7676-7679.

5. Graml, A.; Ghosh, I.; König, B. *J. Org. Chem.* **2017**, *82*, 3552-3560.

6. Obst, M.; Shaikh, R. S.; König, B. *React. Chem. Eng.* **2017**, *2*, 472-478.

7. Meyer, A. U.; Slanina, T.; Heckel, A.; König, B. *Chem. Eur. J* **2017**, *23*, 7900-7904.

8. Bardagi, J. I.; Ghosh, I.; Schmalzbauer, M.; Ghosh, T.; König, B. *Eur. J. Org. Chem.* **2018**, *2018*, 34-40.

9. Koefoed, L.; Vase, K. H.; Stenlid, J. H.; Brinck, T.; Yoshimura, Y.; Lund, H.; Pedersen, S. U.; Daasbjerg, K. *ChemElectroChem* **2017**, *4*, 3212-3221.

10. Merritt, E. A.; Olofsson, B. *Angew. Chem. Int. Ed.* **2009**, *48*, 9052-9070.

11. Narayanam, J. M. R.; Tucker, J. W.; Stephenson, C. R. J. *J. Am. Chem. Soc.* **2009**, *131*, 8756-8757.

12. Nguyen, J. D.; D'Amato, E. M.; Narayanam, J. M. R.; Stephenson, C. R. J. *Nature Chem.* **2012**, *4*, 854-859.

13. Ghosh, I.; Marzo, L.; Das, A.; Shaikh, R.; König, B. *Acc. Chem. Res.* **2016**, *49*, 1566-1577.

14. Czyz, M. L.; Weragoda, G. K.; Monaghan, R.; Connell, T. U.; Brzozowski, M.; Scully, A. D.; Burton, J.; Lupton, D. W.; Polyzos, A. *Org. Biomol. Chem.* **2018**, *16*, 1543-1551.

15. Aycock, R. A.; Vogt, D. B.; Jui, N. T. *Chem. Sci.* **2017**, *8*, 7998-8003.

16. Boyington, A. J.; Riu, M.-L.; Jui, N. T. *J. Am. Chem. Soc.* **2017**, *139*, 6582-6585.

17. A recent report has shown that Hantzsch ester is capable of second reduction chemistry. Jung, J.; Kim, J.; Park, G.; You,Y.; Cho, E.J. *Adv. Synth. Catal.* **2016**, 358, 74-80.

18. Connelly, N. G.; Geiger, W. E. *Chem. Rev.* **1996**, *96*, 877-910.

19. Jutand, A.; Négri, S. *Eur. J. Org. Chem.* **1998**, 1811-1821.

20. Andrieux, C. P.; Pinson, J. *J. Am. Chem. Soc.* **2003**, *125*, 14801-14806.

21. Costentin, C.; Robert, M.; Savéant, J.-M. *Chem. Phys.* **2006**, *324*, 40-56.

22. Costentin, C.; Robert, M.; Savéant, J.-M. *J. Am. Chem. Soc.* **2004**, *126*, 16051-16057.

23. Enemærke, R. J.; Christensen, T. B.; Jensen, H.; Daasbjerg, K. *J. Chem. Soc., Perkin Trans. 2* **2001**, 1620-1630.

24. Hook, J. M.; Mander, L. N. *Nat. Prod. Rep.* **1986**, *3*, 35-85.

25. Samori, S.; Tojo, S.; Fujitsuka, M.; Ryhding, T.; Fix, A. G.; Armstrong, B. M.; Haley, M. M.; Majima, T. *J. Org. Chem.* **2009**, *74*, 3776-3782.

26. Szostak, M.; Spain, M.; Procter, D. J. *J. Org. Chem.* **2014**, *79*, 2522-2537.

27. Clark, C. D.; Hoffman, M. Z. *J. Phys. Chem.* **1996**, *100*, 7526-7532.

28. Majima, T.; Tojo, S.; Takamuku, S. *J. Phys. Chem. A.* **1997**, *101*, 1048-1055.

29. Shida, T. *Electronic absorption spectra of radical ions*. Elsevier Science Publishers: New York, New York, 1988.

30. Savéant, J.-M. *J. Am. Chem. Soc.* **1992**, *114*, 10595-10602.

31. Park, G.; Yi, S. Y.; Jung, J.; Cho, E. J.; You, Y. *Chem. Eur. J.* **2016**, *22*, 17790-17799.

32. Hironaka, K.; Fukuzumi, S.; Tanaka, T. J. *J. Chem. Soc., Perkin Trans. 2* **1984**, 1705-1709.

33. Kern, J.-M.; Sauvage, J.-P. *J. Chem. Soc., Chem Commun* **1987**, 546-548.

34. Morales-Verdejo, C. A.; Newsom, M. I.; Cohen, B. W.; Vibbert, H. B.; Hopkins, M. D. *Chem. Commun.* **2013**, *49*, 10566-10568.

35. Newsom, M. I. Structure and reactivity of d^2, d^1, and d^0 tungsten-benzylidyne compounds. The University of Chicago, 2010.

36. Hansen, C. B. 1. Tungsten photoredox chromphores containing amine-functionalized diphosphine and *N*-heterocyclic carbene ligands. 2. The chemistry of low-coordinate cobalt compounds supported by *N*-heterocyclic carbenes and bulky amines. The University of Chicago, 2017.

37. Scaiano, J. C.; Stewart, L. C. *J. Am. Chem. Soc.* **1983**, *105*, 3609-3614.

38. Young, I. S.; Thornton, P. D.; Thompson, A. *Nat. Prod. Rep.* **2010**, *27*, 1801-1839.

39. Gavryushin, A.; Kofink, C.; Manolikakes, G.; Knochel, P. *Org. Lett.* **2005**, *7*, 4871-4874.

40. Bilodeau, F.; Brochu, M.-C.; Guimond, N.; Thesen, K. H.; Forgione, P. *J. Org. Chem.* **2010**, *75*, 1550-1560.

41. Saoudi, B.; Debache, A.; Soulé, J.-F.; Doucet, H. *RSC Adv.* **2015**, *5*, 65175-65183.

42. Bardagi, J. I.; Ghosh, I.; Schmalzbauer, M.; Ghosh, T.; König, B. *Eur. J. Org. Chem.* **2018**, 34-40.

43. Turro, N. J.; Ramamurthy, V.; Scaiano, J. C. *Modern Molecular Photochemistry of Organic Molecules*. University Science Books: 2010.

CHAPTER 6

Synthesis, properties, and reactivity of d^3 molybdenum and tungsten-oxo complexes

6.1. Introduction.

The oxo ligand is unparalleled at supporting high oxidation-states of metal centers. Metal-oxo compounds in low oxidation-states, however, are difficult to prepare and examine. In the classical picture developed by Ballhausen and Gray for metal-monooxo compounds residing in tetragonal coordination environments (Figure 6.1),[1-3] the HOMO and LUMO are of t_{2g} parentage, with the HOMO (d_{xy}) being non-bonding (δ-symmetry) with respect to the axial oxygen atom and the LUMO (d_{xz}, d_{yz}) being π*(M–O) in nature. As a consequence, d-electron counts of d^0, d^1, and d^2 result in a formal metal-oxygen bond order of 3. The addition of electrons beyond two, however, populates the LUMO and reduces the M–O bond order by 0.5 for each subsequent electron. This decrease in bond order is accompanied by an increase in the reactivity of the oxo ligand, and the resulting compounds are often unstable and can be difficult to characterize or isolate.

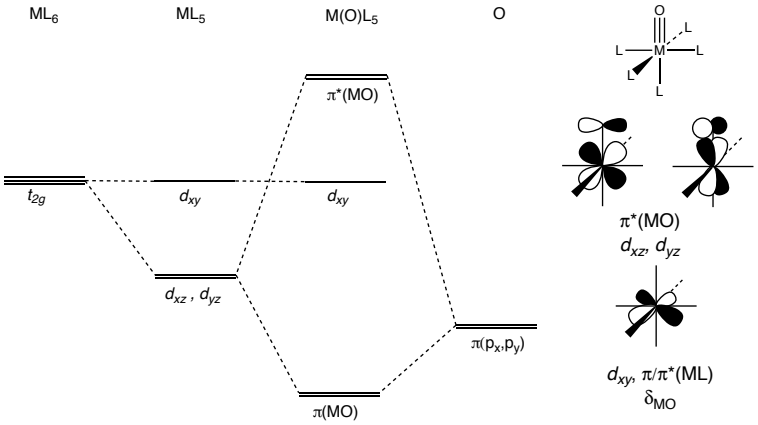

Figure 6.1 . Molecular orbital diagram of the t_{2g} set of orbitals for a general metal-oxo complex of the form $M(O)L_5$. Representations of the d_{xy} and π*(MO) molecular orbitals are shown.

Metal-oxo complexes with d-electron counts greater than two are oxidatively active centers in biological contexts as exemplified by the iron-oxo center of cytochrome P450.[4] Because of this, and the possibility that synthetic analogues might be useful oxidation catalysts, many groups have worked to study low-oxidation state metal-oxo compounds and develop various strategies to stabilize them. One approach is to use ligand sets that enforce trigonal bipyramidal or tetrahedral geometries that possess electronic structures for which higher d-electron counts are allowed without population of π^*(M–O) orbitals.[5-10] Within tetragonal symmetry, the stability of a compound with a given d-electron count is strongly affected by the metal oxidation state. Thus, d^4 ruthenium(IV), iron(IV), and osmium(IV)-oxos are known,[11-16] but among the early metals, with necessarily lower metal oxidation states, few oxo compounds with more than two d-electrons have been reported. No examples are known in group 5. In group 6, electrochemical studies by Pickett *et al.*[17] and Chang and Long *et al.*[18-20] imply the intermediacy of d^3 molybdenum(III)-oxo compounds in catalytic proton or water reduction. One example of a molybdenum-oxo compound described as possessing a d^4 configuration has been recently reported by Trovitch *et al.,*[21] which will be discussed in more detail later.

A potential design approach to group 6 metal-oxo compounds with d-electron counts above d^2 is to employ sterically demanding equatorial ligands that shield the reactive oxo ligand from the surrounding environment. Preliminary evidence supporting this approach is provided by prior electrochemical studies of the d^2 compounds $[Mo(O)(dppbz)_2Cl]^+$ (**2**$^+$, Figure 6.2) and $[Mo(O)(dppe)_2Cl]^+$ (**3**$^+$), for which cyclic voltammograms (CV) are reported to exhibit a reversible reduction that may logically be assigned to the Mo(IV)/Mo(III) couple on the basis of the Ballhausen-Gray model and the absence of low-lying ligand orbitals.[17, 22] To test this hypothesis, we studied the reduction chemistry of the molybdenum(IV) and tungsten(IV)-oxo

complexes $\mathbf{1}^{+}$–$\mathbf{7}^{+}$ (Figure 6.2). The molybdenum compounds possess equatorial ligands that encompass a range of steric profiles. The isocyanide-bearing compound $\mathbf{1}^{+}$ possesses a highly exposed oxo ligand. The alkyl phosphine derivatives $\mathbf{4}^{+}$, $\mathbf{5}^{+}$, and $\mathbf{6}^{+}$ protect the oxo ligand with progressively larger R groups (Me < Et < Cy), while $\mathbf{2}^{+}$ and $\mathbf{3}^{+}$ possess bulky aryl phosphine ligands that are, additionally, slightly electron withdrawing relative to the alkyl phosphines. The tungsten compound $\mathbf{7}^{+}$, which is analogous to $\mathbf{3}^{+}$, is studied to understand how the nature of the metal affects the reduction chemistry. It was found that the stability and reactivity of d^3 molybdenum(III)-oxo compounds are sensitive to the steric bulk of the ligands. The sterically protected d^3 molybdenum(III)-oxo complex **3** was prepared, isolated, and its physical properties and oxo-transfer reaction chemistry studied. In contrast, **4** could be prepared *in-situ* but was too reactive to isolate.

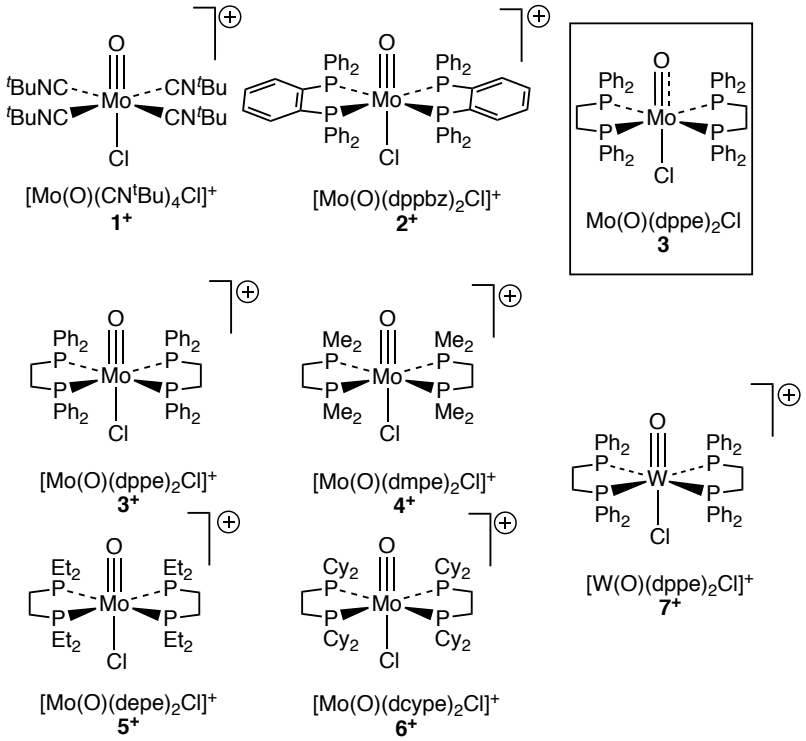

Figure 6.2. Compounds included in this study.

6.2. Results and Discussion.

6.2.1. Synthesis of 5^+ and 6^+. The new d^2 compounds **5**[BPh_4] and **6**[BPh_4] were synthesized as shown in Figure 6.3. As with previously reported $\mathbf{2}^+$, $\mathbf{3}^+$, and $\mathbf{4}^+$, these were prepared *via* ligand substitution of $Mo(O)(PMe_3)_3Cl_2$.[23] The compounds were characterized by ^1H-, $^{13}C\{^1H\}$-, and $^{31}P\{^1H\}$ NMR spectroscopy and HR-ESI-MS (0 V) to confirm purity and identity. In both cases HR-ESI-MS exhibited a clean molecular ion peak with no fragmentation.

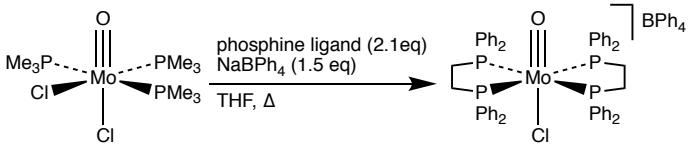

Figure 6.3. Synthesis of **5**[BPh_4] and **6**[BPh_4] (R = Et or Cy).

6.2.2. Electronic structures and spectra of 1^+ – 7^+. The molecular and electronic structures of d^2 $\mathbf{1}^+$–$\mathbf{7}^+$ were calculated using density functional theory (DFT) to ensure that they conform to the classical Ballhausen-Gray model. Benchmarking calculations were performed at the double-ζ and triple-ζ levels on $\mathbf{4}^+$ (Table 6.1); this ion was chosen because its crystal structure does not exhibit O–Mo–Cl orientation disorder,[24] unlike many other molybdenum-oxo complexes. Calculations at the double-ζ level provided core bond lengths and angles in good agreement with experiment; the calculated Mo–O, Mo–P, and Mo–Cl distances are within $\pm 3\sigma$ of the experimental values. Calculations at the triple-ζ level did not greatly improve the agreement but were much more time consuming. Thus, double-ζ level theory was employed for all studies.

Table 6.1. Bond length (Å) and angles (°) for computational benchmarking study of $\mathbf{4}^{+}$.

	$\mathbf{4}$(Cl)·5H$_2$O[a]	Double-ζ[b]	Δ(comp-exp)	Triple-ζ[b]	Δ(comp-exp)
Mo–O	1.690(4)	1.694	0.004	1.683	−0.007
Mo–Cl	2.5606(14)	2.588	0.027	2.550	−0.010
Mo–P(avr)	2.5067 [9]	2.523	0.016	2.523	0.016
O–Mo–Cl	177.89 (14)	178.8	0.91	178.5	0.61
O–Mo–P(avr)	97.26[9]	98.6	1.34	97.5	0.24
P–Mo–P (inner)	79.42[3]	80.3	0.88	79.9	0.48
P–Mo–P (outer)	98.73[5]	97.2	−1.53	98.1	−0.63

[a] Ref. 24; [b] B3P86, LANL2DZ(Mo)**,** 6-31G** (all other atoms); [c] B3P86**:** SDD (Mo)**,** cc-PVTZ (all other atoms).

The calculated molecular structures of $\mathbf{1}^{+}$–$\mathbf{6}^{+}$ provide space-filling models that clearly show the anticipated variation in steric shielding of the oxo ligand (Figure 6.4), which is hypothesized as being important for stabilizing the reduced, d^3 analogs. Specifically, isocyanide derivative $\mathbf{1}^{+}$ is highly exposed, dmpe and depe derivatives $\mathbf{4}^{+}$ and $\mathbf{5}^{+}$ are progressively more protected, and the phenyl- and cyclohexyl-phosphine derivatives $\mathbf{2}^{+}$, $\mathbf{3}^{+}$, and $\mathbf{6}^{+}$ are highly shielded. The core bond distances and angles (Table 6.2) are unremarkable for $\mathbf{1}^{+}$–$\mathbf{5}^{+}$ and $\mathbf{7}^{+}$. In $\mathbf{6}^{+}$, however, the Mo–P bond distance is longer than that for $\mathbf{4}^{+}$ by 0.109 Å and O–Mo–P bond angle is smaller by 6.7°. This presumably reflects the steric pressure within $\mathbf{6}^{+}$ that is exerted by the bulky cyclohexyl groups.

Table 6.2. Calculated core structural bond distances (Å) and angles (°) for $\mathbf{2}^{+}$ – $\mathbf{7}^{+}$ (Å).

	2^{+}	3^{+}	4^{+}	5^{+}	6^{+}	7^{+}
Mo/W–O	1.701	1.700	1.694	1.718	1.696	1.714
Mo/W–Cl	2.483	2.510	2.588	2.580	2.480	2.475
Mo/W–P(avr)	2.552	2.564	2.523	2.583	2.632	2.541
O-Mo/W-P(avr)	94.7	97.1	98.6	96.4	91.9	95.1
P-Mo/W-P(inner)	78.3	80.3	80.3	81.0	79.5	80.2
P-Mo/W-P(outer)	101.0	98.6	97.2	97.8	100.3	99.0

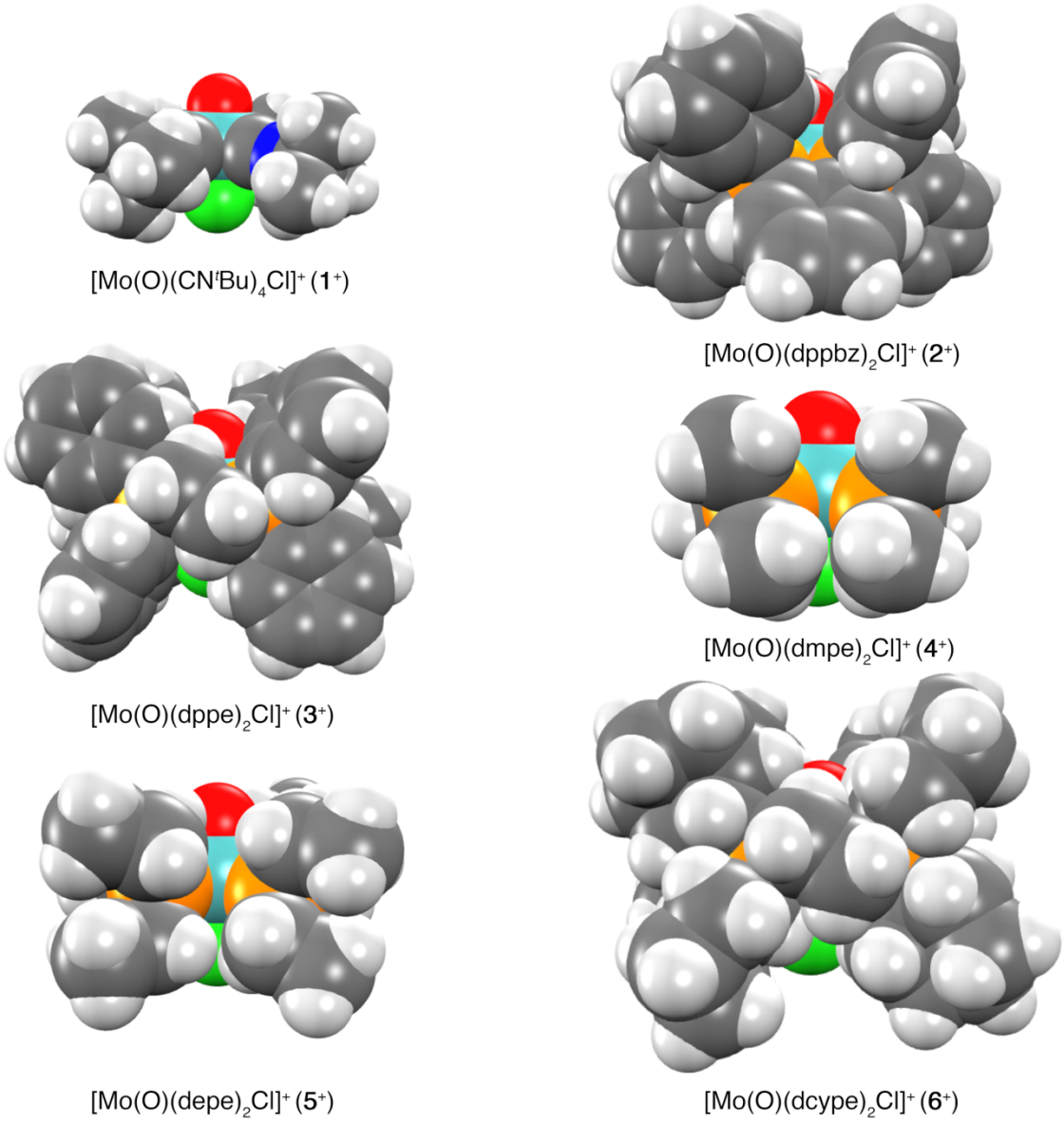

Figure 6.4. DFT-calculated space-filling models of molybdenum(IV)-oxo compounds.

The DFT calculations on **1**$^+$ – **7**$^+$ confirm that they conform to the Balhausen-Gray orbital model (Table 6.3); the HOMO of each is primarily d_{xy} in parentage (70–85%) and contains nearly zero contribution from the axial oxo and chloro ligands, and the LUMO and LUMO+1 are closely spaced and are π*(Mo–O) in nature (Mo = 53-60%; O = 22-24%). Thus, one-electron

reduction of these compounds is expected to populate the π*(Mo–O) orbital, rendering the compounds more reactive.

Table 6.3. Calculated orbital energies and atomic parentages for molybdenum(IV)-oxo and tungsten(IV)-oxo complexes.

Compound	Orbital				Atomic Parentage, %			
	#	Assignment	Type	Energy (eV)	Mo/W	O	4P/C	Cl
[Mo(O)(CN^{t}Bu)$_4$Cl]$^+$ [a]	113	LUMO+1	π*	–5.74	53.29	24.07	9.02	5.57
	112	LUMO	π*	–5.74	53.20	24.05	9.06	5.57
	111	HOMO	d_{xy}	–9.58	72.63	0.03	2.21	0.01
[Mo(O)(dppbz)$_2$Cl]$^+$	255	LUMO+1	π*	–4.91	62.69	21.47	5.08	4.54
	254	LUMO	π*	–5.10	59.26	22.81	6.32	5.04
	253	HOMO	d_{xy}	–8.76	77.32	0.34	5.60	0.46
[Mo(O)(dppe)$_2$Cl]$^+$	231	LUMO+1	π*	–5.03	63.12	21.52	6.36	3.92
	230	LUMO	π*	–5.21	60.62	22.31	7.08	4.14
	229	HOMO	d_{xy}	–8.83	81.43	0.13	4.25	0.27
[Mo(O)(dmpe)$_2$Cl]$^+$	103	LUMO+1	π*	–5.36	61.63	22.64	9.63	2.64
	102	LUMO	π*	–5.57	56.59	23.30	12.11	3.02
	101	HOMO	d_{xy}	–9.49	83.96	0.13	5.77	0.22
[Mo(O)(depe)$_2$Cl]$^+$	135	LUMO+1	π*	–4.07	62.68	22.16	8.58	2.87
	134	LUMO	π*	–5.43	61.06	23.26	7.38	3.45
	133	HOMO	d_{xy}	–9.05	83.89	0.12	4.91	0.05
[Mo(O)(dcype)$_2$Cl]$^+$	255	LUMO+1	π*	–4.91	66.28	22.19	3.87	4.13
	254	LUMO	π*	–5.10	63.67	22.72	4.21	4.50
	253	HOMO	d_{xy}	–8.71	84.30	0.14	5.25	0.35
[W(O)(dppe)$_2$Cl]$^+$	231	LUMO+1	π*	–4.52	60.53	19.87	7.36	4.57
	230	LUMO	π*	–4.77	56.98	21.07	9.02	4.91
	229	HOMO	d_{xy}	–8.50	80.49	0.07	5.23	0.07

[a] Atomic Parentage of N: HOMO (20.03%); LUMO (6.70%); LUMO+1 (6.66%).

The electronic absorption spectra of **1**$^+$–**7**$^+$ were measured to validate the calculated orbital ordering through observation of the characteristic ^{1}[d_{xy}→π*(MoO)] (HOMO→LUMO) band. The spectra are shown in Figure 6.5 and band maxima are set out in Table 6.4. Previous work established assignment of the electronic spectra of **1**$^+$ and **4**$^+$ by single-crystal molecular-axis- polarized electronic-absorption spectroscopy,[24] and the electronic-absorption spectra of **1**[BPh_4],[25] **2**[Cl],[22] **2**[BPh_4],[26] **3**[Cl],[27] **3**[BF_4],[25] **3**[BPh_4],[26] **4**[Cl],[24] and **7**[ClO_4][27] have been

previously reported in various solvents; they were remeasured here in THF, which is the solvent employed for electrochemical studies. The spectra of all ions exhibit the $^1[d_{xy} \rightarrow \pi^*(MoO)]$ band as the lowest-energy feature, in agreement with the calculated orbital ordering. Among the phosphine complexes, the spectrum of $\mathbf{6}^+$ was found to be significantly different than the others; it lies at longer wavelengths and exhibits vibronic features, probably due to the structural differences noted above. The vibronic spacing is 735 cm^{-1}, which is lower than that observed at low temperature for other d^2 compounds (e.g., $\mathbf{4}^+$, 790 cm^{-1}).[24]

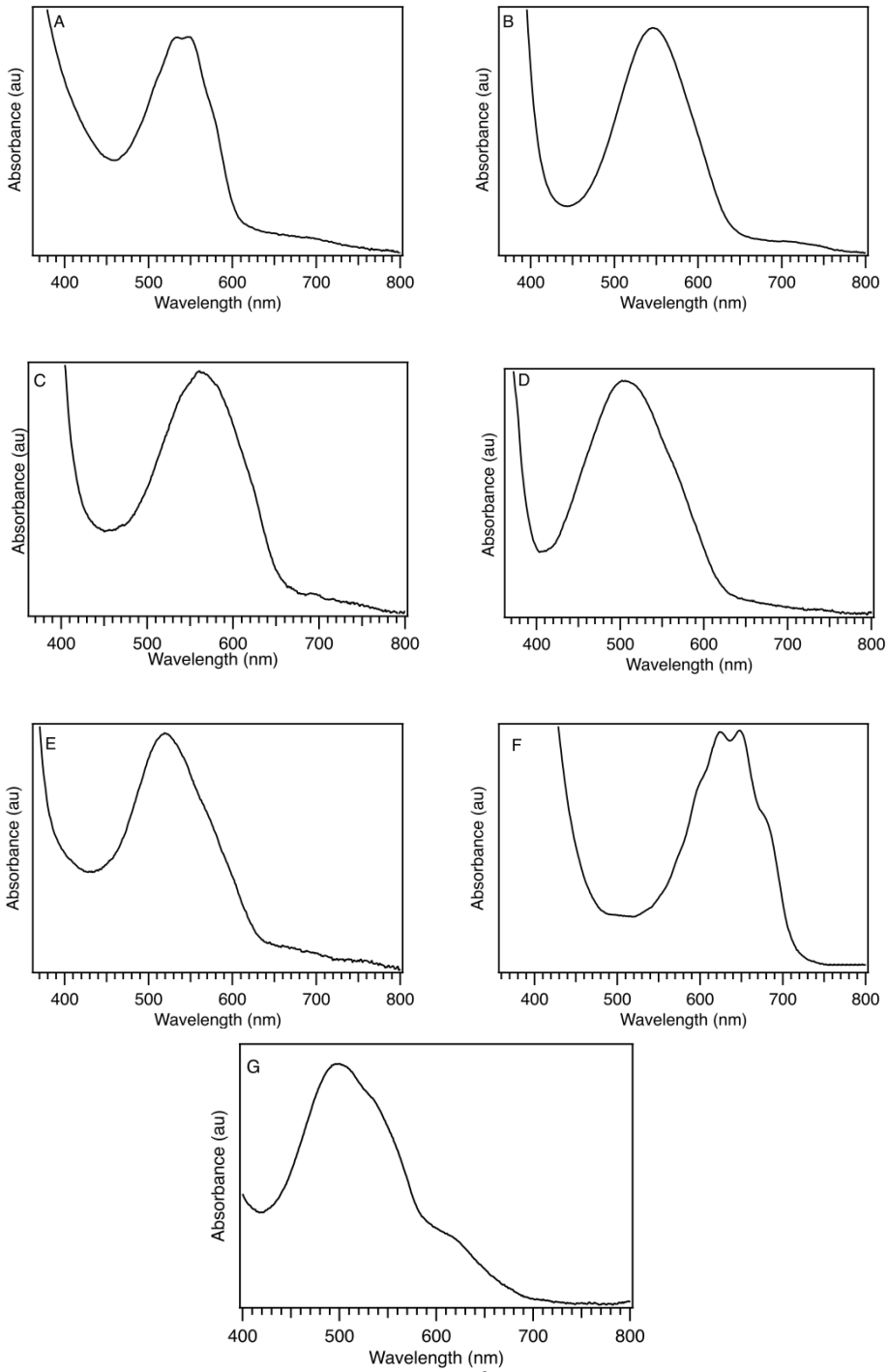

Figure 6.5. UV-vis absorption spectra of d^2 oxo complexes in THF solution; (A) $[Mo(O)(CN^tBu)_4Cl]BPh_4$ (**1**[BPh_4]); (B) $[Mo(O)(dppbz)_2Cl]PF_6$ (**2**[PF_6]); (C) $[Mo(O)(dppe)_2Cl]BF_4$ (**3**[BF_4]); (D) $[Mo(O)(dmpe)_2Cl]PF_6$ (**4**[PF_6]); (E) $[Mo(O)(depe)_2Cl]BPh_4$ (**5**[BPh_4]); (F) $[Mo(O)(dcype)_2Cl]BPh_4$ (**6**[BPh_4]); (G) $[W(O)(dppe)_2Cl]BPh_4$ (**7**[BPh_4]).

Table 6.4. $^1[d_{xy} \rightarrow \pi^*(MO)]$ band maxima in THF solution.

Compound	λ_{max} (nm)[a]
$[Mo(O)(CN^tBu)_4Cl]BPh_4$	542[b]
$[Mo(O)(dppbz)_2Cl]PF_6$	545[c]
$[Mo(O)(dppe)_2Cl]BF_4$	565[d]
$[Mo(O)(dmpe)_2Cl]PF_6$	510[e]
$[Mo(O)(depe)_2Cl]BPh_4$	520
$[Mo(O)(dcype)_2Cl]BPh_4$	636[f]
$[W(O)(dppe)_2Cl]BPh_4$	496[g]

[a] Figure 6.4; [b] Reported in Ref. 25 as 550 nm in CH_2Cl_2; [c] Reported in Ref. 26 as 544 nm in CH_2Cl_2 and Ref. 22 as 546 nm CH_2Cl_2; [d] Reported in Ref. 25 as 567 nm in CH_2Cl_2, Ref. 27 as 566 nm in $CHCl_3$, and Ref. 26 as 564 nm in CH_2Cl_2; [e] Reported in Ref. 24 as 512 nm in CH_2Cl_2; [f] Vibronic spacing *ca.* 735 cm^{-1}; [g] Reported in Ref. 27 as 502 nm in $CHCl_3$.

6.2.3. Electrochemistry of 1^+ – 7^+. The electrochemical properties of 1^+ – 7^+ were studied by cyclic voltammetry (CV) and differential pulse voltammetry (DPV) to assess the nature and potentials of their reduction and oxidation processes. The redox potentials are set out in Table 6.5 and the data are shown in Figures 6.6-6.12. Redox potentials for 1^+ and 2^+ have been reported in prior work;[22, 25] they have been remeasured here in THF for comparison purposes.

Table 6.5. Redox potentials of molybdenum(IV)-oxo and tungsten(IV)-oxo complexes (THF solution vs $FeCp_2^{0/+}$).

Compound	$E_{1/2}^{+/2+}$ (V)[a,b]	$E_{1/2}^{+/0}$ (V)[a,c]	$E_{1/2}^{0/-}$ (V)[a,b]	Fig.
$[Mo(O)(CN^tBu)_4]BPh_4$ ($\mathbf{1}^+$)	0.94[d]	–1.70[e]	Not Observed	6.6
$[Mo(O)(dppbz)_2Cl]PF_6$ ($\mathbf{2}^+$)	1.28[f]	–1.68[f]	–2.90	6.7
$[Mo(O)(dppe)_2Cl]BF_4$ ($\mathbf{3}^+$)	0.91	–1.76[g]	–2.84	6.8
$[Mo(O)(dmpe)_2Cl]PF_6$ ($\mathbf{4}^+$)	0.76	–2.10	–3.18	6.9
$[Mo(O)(depe)_2Cl]BPh_4$ ($\mathbf{5}^+$)	0.77	–2.10	Not Observed	6.10
$[Mo(O)(dcype)_2Cl]BPh_4$ ($\mathbf{6}^+$)	0.85	–2.10	Not Observed	6.11
$[W(O)(dppe)_2Cl]BPh_4$ ($\mathbf{7}^+$)	0.88[h]	–2.06	–3.21[i]	6.12

[a] 0.1 M $[^nBu_4N][PF_6]$ in THF solution, Pt working and auxiliary electrodes; [b] Electrochemically irreversible unless otherwise noted; potential measured by DPV; [c] Electrochemically reversible unless otherwise noted; [d] Measured in Ref. 25 as *ca.* 0.8 V in CH_3CN solution; [e] Irreversible, recorded by DPV; [f] Measured in Ref. 22, E_{pa} = 1.15 and $E_{1/2}^{+/0}$ = –1.17 V vs Ag/AgCl in 0.1 M $[^nBu_4N][PF_6]$ CH_2Cl_2 solution; [g] Controlled-potential electrolysis reported at –1.9 V vs $FeCp_2$ in THF in Ref. 17; [h] Reversible, potential recorded by CV; [i] Irreversible, cathodic peak maximum reported by CV.

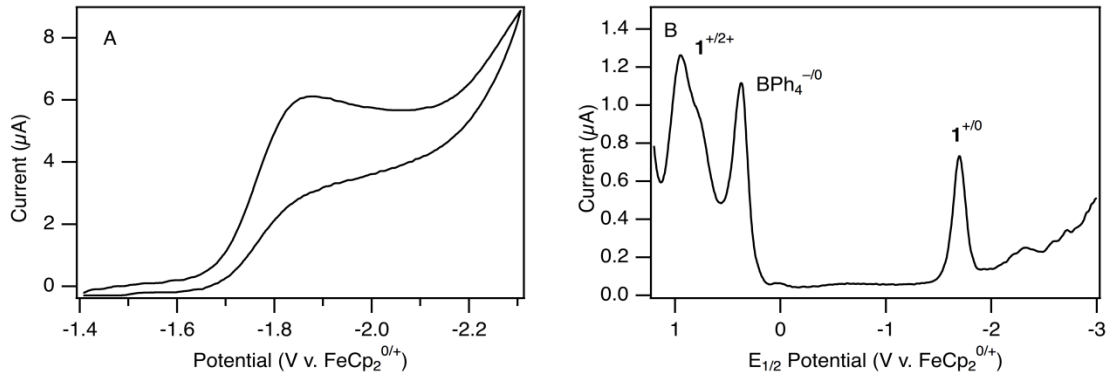

Figure 6.6. Electrochemical data for [Mo(O)(CN^{t}Bu)$_4$Cl]BPh$_4$ (**1**[BPh$_4$]) in THF with 0.1 M [Bu$^n{}_4$N][PF$_6$]: (A) representative CV (200 mV s^{-1}); (B) DPV.

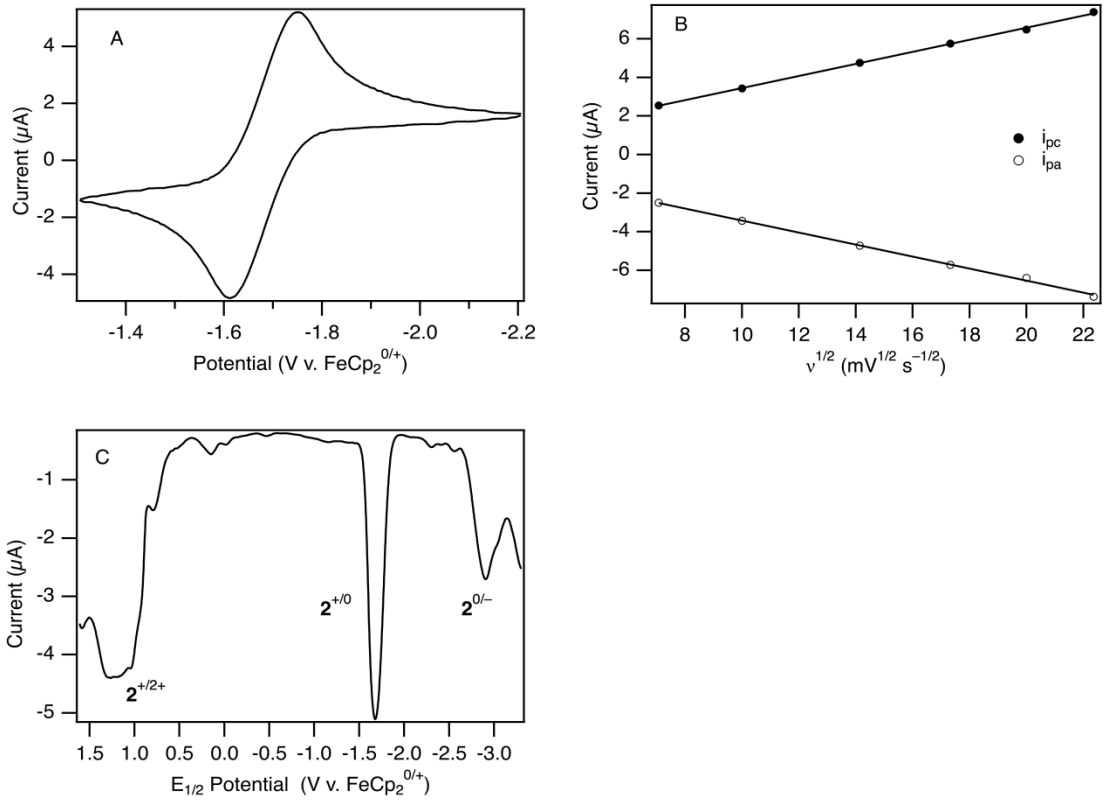

Figure 6.7. Electrochemical data for [Mo(O)(dppbz)$_2$Cl]PF$_6$ (**2**[PF$_6$]) in THF with 0.1 M [Bu$^n{}_4$N][PF$_6$]: (A) CV of the reversible reduction (200 mV s^{-1}); (B) Randles-Sevcik plot: i_{pc}, f(x) = 0.31x + 0.32, r^2 = 0.99; i_{pa}, f(x) = −0.31x − 0.30, r^2 = 0.99; (C) DPV.

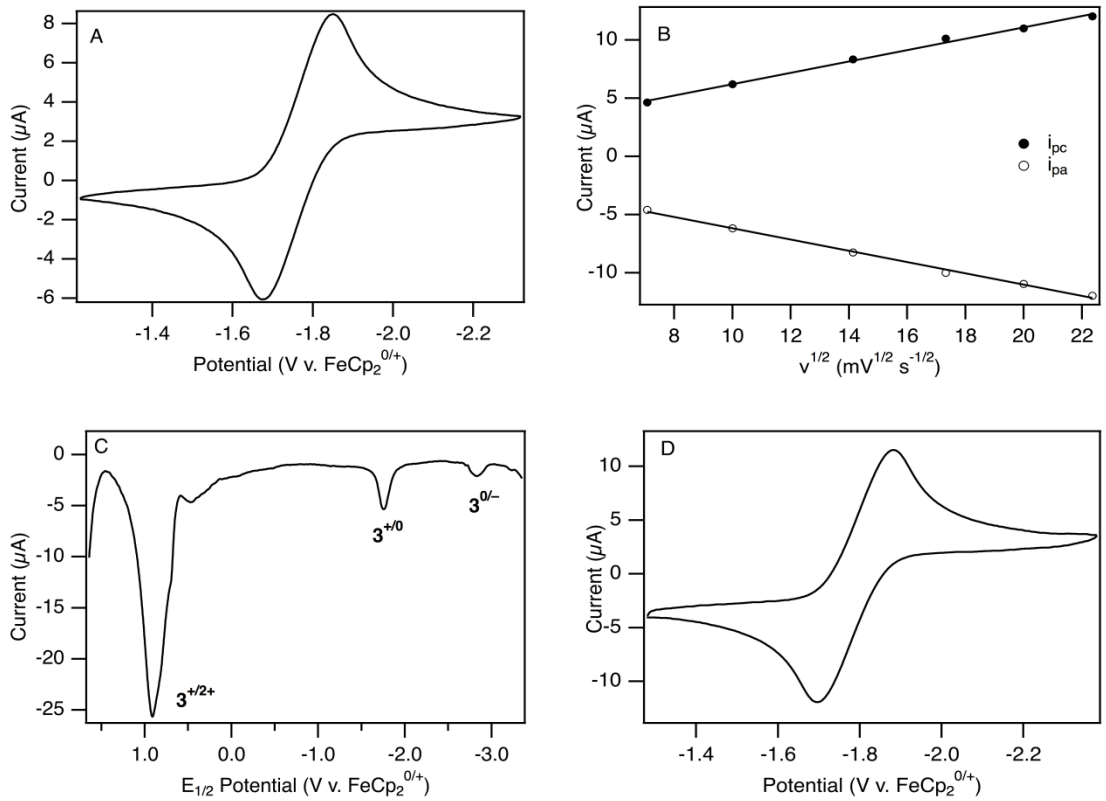

Figure 6.8. Electrochemical data for $[Mo(O)(dppe)_2Cl]BF_4$ (**3**$[BF_4]$) in THF with 0.1 M $[Bu^n{}_4N][PF_6]$: (A) CV of the reversible reduction (200 mV s^{-1}); (B) Randles-Sevcik plot: i_{pc}, f(x) = 0.48x + 1.33, $r^2 = 0.99$; i_{pa}, f(x) = −0.48x − 1.32, $r^2 = 0.99$; (C) DPV. (D) CV (200 mV s^{-1}) of the electrochemical oxidation for $Mo(O)(dppe)_2Cl$ (**3**).

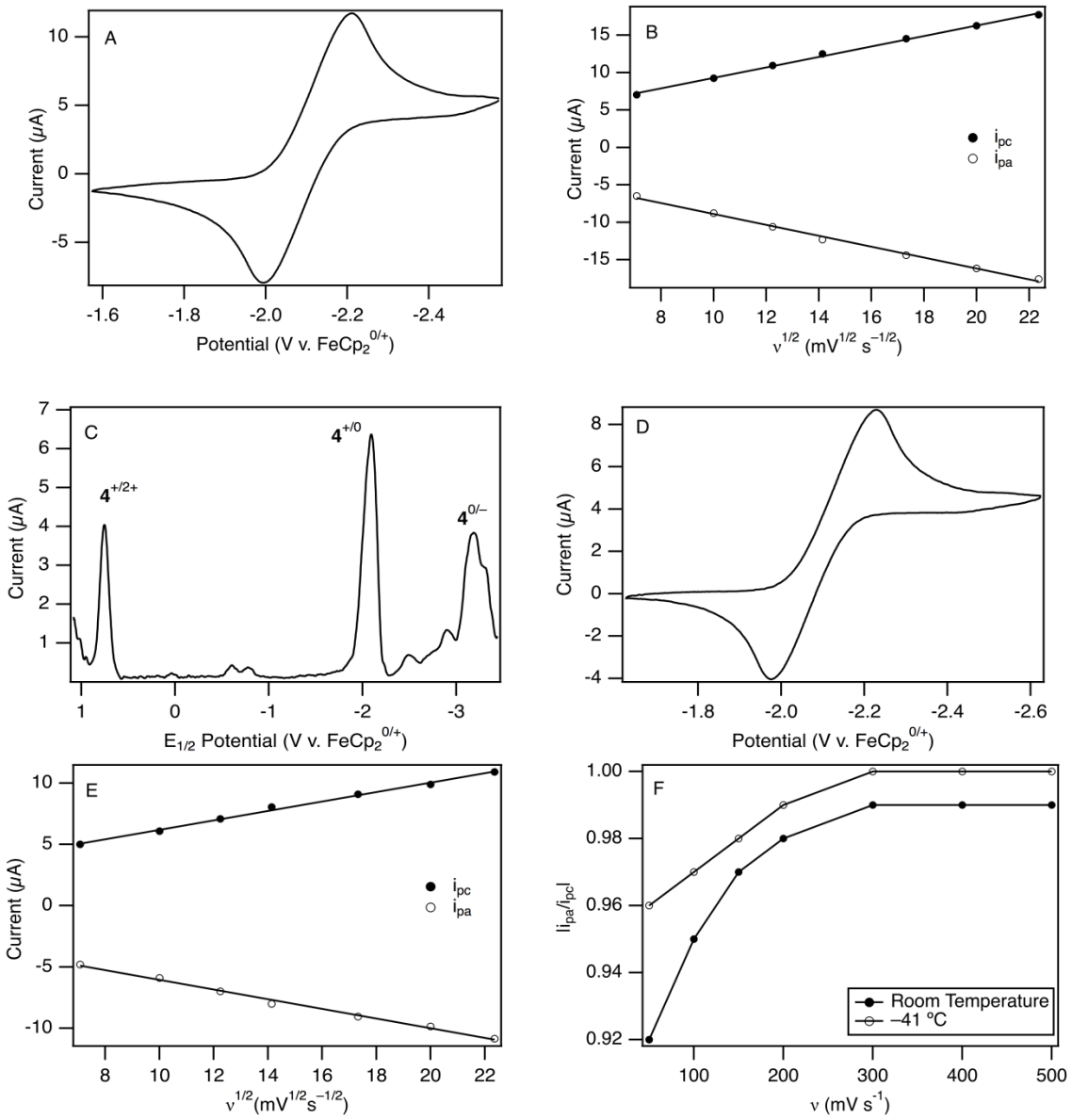

Figure 6.9. Electrochemical data for $[Mo(O)(dmpe)_2Cl]PF_6$ (**4**$[PF_6]$) in THF with 0.1 M $[Bu^n_4N][PF_6]$: (A) CV of the reduction (200 mV s^{-1}); (B) Randles-Sevcik plot: i_{pc}, f(x) = 0.70x + 2.32, r^2 = 0.99; i_{pa}, f(x) = −0.73x − 1.60, r^2 = 0.99; (C) DPV; (D) CV of the reduction (200 mV s^{-1}) at –41 °C (dry ice/acetonitrile); (E) Randles-Sevcik plot for CV at –41 °C: i_{pc}, f(x) = 0.39x + 2.34, r^2 = 0.99; i_{pa}, f(x) = −0.39x − 2.11, r^2 = 0.99; (F) Plot of $|i_{pa}/i_{pc}|$ versus scan rate at room temperature and –41 °C.

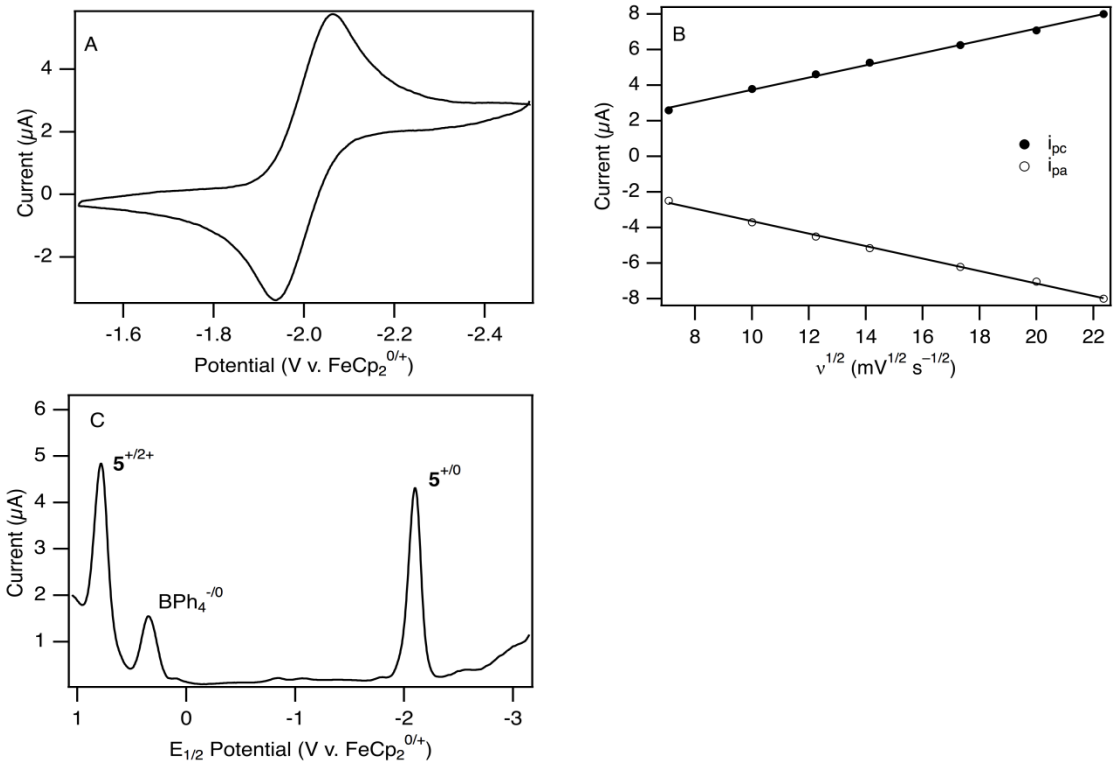

Figure 6.10. Electrochemical data for $[Mo(O)(depe)_2Cl]PF_6$ (**5**$[BPh_4]$) in THF with 0.1 M $[Bu^n_4N][PF_6]$: (A) CV of the reversible reduction (200 mV s^{-1}); (B) Randles-Sevcik plot: i_{pc}, f(x) = 0.34x + 0.23, $r^2 = 0.99$; i_{pa}, f(x) = −0.35x − 0.13, $r^2 = 0.99$; (C) DPV.

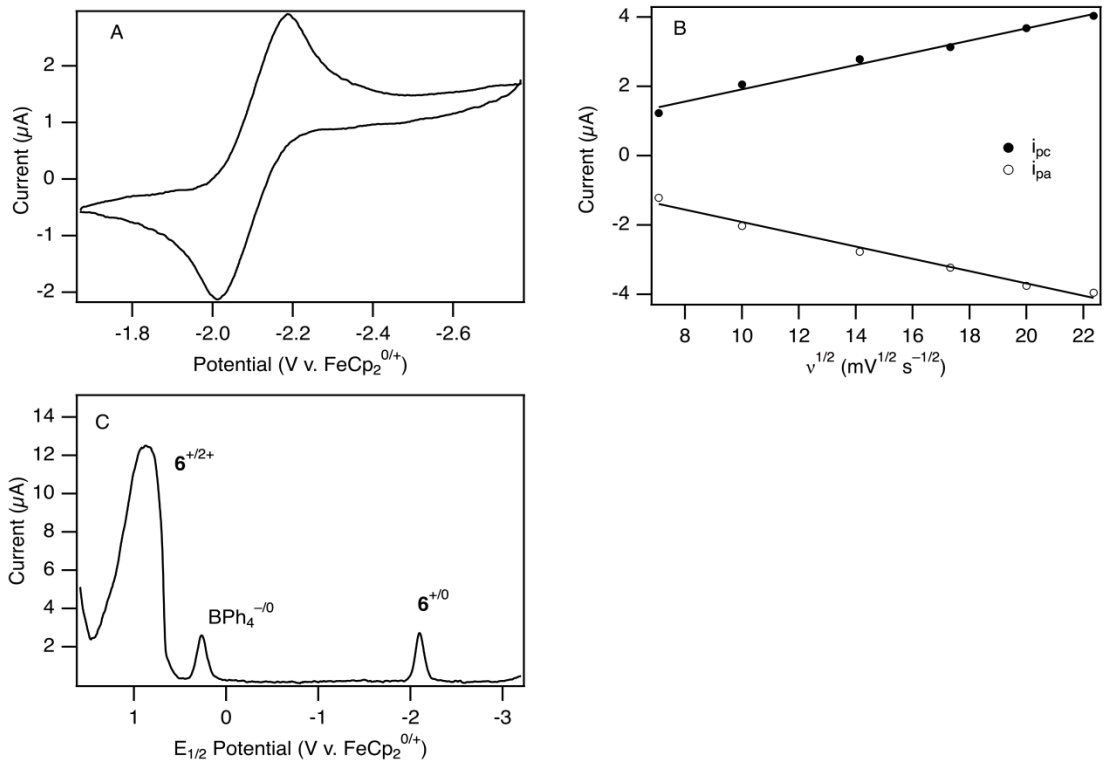

Figure 6.11. Electrochemical data for $[Mo(O)(dcype)_2Cl]BPh_4$ (**6**$[BPh_4]$) in THF with 0.1 M $[Bu^n_4N][PF_6]$: (A) representative CV (200 mV s^{-1}); (B) Randles-Sevcik plot: i_{pc}, f(x) = 0.18x + 0.15, $r^2 = 0.98$; i_{pa}, f(x) = −0.18x − 0.14, $r^2 = 0.98$; (C) DPV.

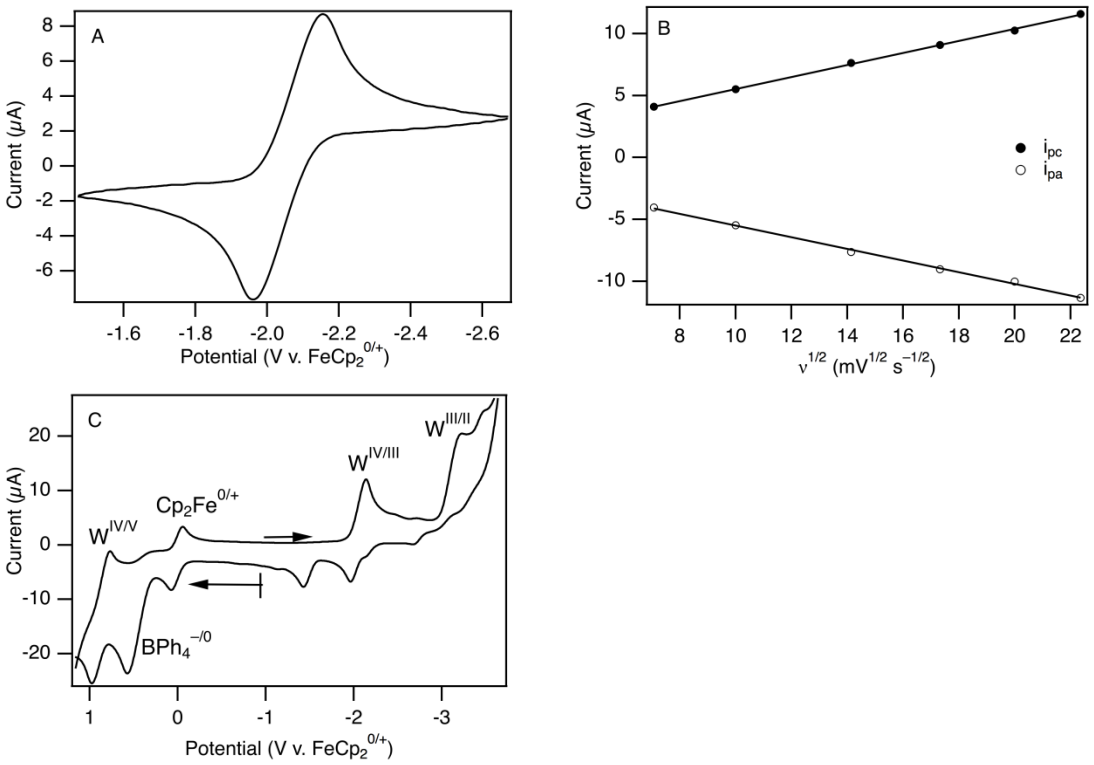

Figure 6.12. Electrochemical data for $[W(O)(dppe)_2Cl]BPh_4$ (**7**(BPh_4)) in THF with 0.1 M $[Bu^n_4N][PF_6]$: (A) representative CV (200 mV s^{-1}); (B) Randles-Sevcik plot: i_{pc}, f(x) = 0.48x + 0.67, $r^2 = 0.99$; i_{pa}, f(x) = −0.47x − 0.78, $r^2 = 0.99$; (C) Representative full range CV (200 mV s^{-1}).

The CV and DPV data for each compound exhibit an oxidation assigned to the M(IV)/M(V) couple. For the molybdenum compounds (**1**$^+$–**6**$^+$) the oxidation is electrochemically irreversible whereas for tungsten compound **7**$^+$ it is reversible. Complexes **1**$^+$ and **5**$^+$–**7**$^+$ were also observed to possess an irreversible oxidation between 0.3–0.5 V that is assigned to oxidation of BPh_4^-.[28] Of more relevance to the present work are the reduction processes. For isocyanide derivative **1**$^+$ (Figure 6.6), the reduction is completely irreversible, indicating the d^3 complex decomposes rapidly on the CV timescale whereas for the phosphine derivatives **2**$^+$–**7**$^+$ the reduction is (or is nearly) reversible. This is evidenced qualitatively by the appearance of their CVs at a scan rate of 200 mV s^{-1} and, more quantitatively, by the fact that their Randles-Sevcik plots are linear with slopes that are equal but opposite in sign for the anodic and cathodic

processes. As expected, the reduction potentials of the alkyl phosphine derivatives ($\mathbf{4}^+$–$\mathbf{6}^+$) are negative of those of the aryl phosphine derivatives $\mathbf{2}^+$ and $\mathbf{3}^+$ (by *ca*. 0.4 V), and that of tungsten compound $\mathbf{7}^+$ is negative of its molybdenum analog $\mathbf{3}^+$ (by –0.30 V).

Further analysis of the reduction processes shows that there are very subtle deviations from reversibility for some compounds. This is indicated by a plot of the ratio of the anodic and cathodic peak currents as a function of CV scan rate (Figure 6.13). For a reversible couple, the ratio should equal 1 (within experimental error) at all scan rates. This behavior is observed for $\mathbf{2}^+$, $\mathbf{3}^+$, and $\mathbf{6}^+$, which possess bulky phosphine ligands ($|i_{pa}/i_{pc}| \geq 0.98$). In contrast, $\mathbf{4}^+$ and $\mathbf{5}^+$, which possess the smaller dmpe and depe ligands, respectively, exhibit a small but experimentally significant decrease in the current ratio at lower scan rates, indicating that a chemical reaction is consuming the Mo(III) product. At 50 mVs^{-1}, the ratio for $\mathbf{5}^+$ is 0.96 and that for $\mathbf{4}^+$ is 0.92. Performing the CV experiment for $\mathbf{4}^+$ at –41 °C (Figure 6.9) led to a slightly higher ratio at 50 mV s^{-1}, indicating slow decomposition of the reduction product even at this temperature. The decrease in reversibility of the reduction with decreasing steric bulk of the phosphine supports the hypothesis underlying this study.

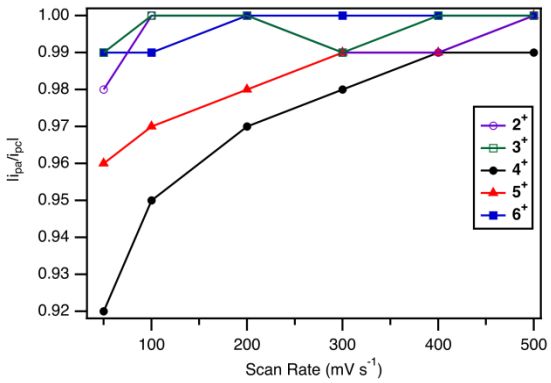

Figure 6.13. Comparison of the anodic (i_{pa}) and cathodic (i_{pc}) ratios (($|i_{pa}/i_{pc}|$) recorded from CV measurements for $\mathbf{2}^+$, $\mathbf{3}^+$, $\mathbf{4}^+$, $\mathbf{5}^+$, and $\mathbf{6}^+$ from 50 mV s^{-1} to 500 mV s^{-1}.

6.2.4. Synthesis of 3 and 7 and attempted synthesis of 4. The surprising electrochemical reversibility of the reduction for certain molybdenum(IV)-oxo phosphine derivatives led us to attempt to synthesize and isolate a molybdenum(III)-oxo compound. Preliminary experiments demonstrated that an Ar atmosphere is required to provide pure products during recrystallization. Prior work by Pickett showed that the controlled reductive electrolysis of $\mathbf{3}^{+}$ in the presence of PhOH under a N_2 atmosphere cleanly provided $Mo(N_2)_2(dppe)_2$.[17] In our initial attempts to synthesize **3** and **7** under N_2, the products were found to contain small amounts of $M(N_2)_2(dppe)_2$ (by X-ray crystallography). Accordingly, further experiments were performed using Schlenk techniques under an Ar atmosphere. Solid samples were handled under N_2 for physical measurements but stored under an Ar atmosphere.

The reduction reactions were first explored *in-situ* using UV-visible spectroscopic monitoring of samples containing a d^2 complex and Na/Hg ($E_{1/2}^{0/+}$ = –2.36 V vs $FeCp_2$)[29] as the reductant in Ar-saturated THF solution at room temperature. The evolution of the reduction reaction for $\mathbf{3}^{+}$ is shown in Figure 6.14. The pale blue solution quickly darkened and the characteristic $^1[d_{xy} \rightarrow \pi^*(Mo–O)]$ band was observed to broaden considerably. The UV-vis spectrum remained essentially unchanged after 30 min. Exposing the dark green solution to air resulted in a rapid color change, providing again a blue solution that exhibited the original $^1[d_{xy} \rightarrow \pi^*(Mo–O)]$ band. This indicates that $\mathbf{3}^{+}$ can be chemically reduced to form **3**, which is stable and can be reoxidized to $\mathbf{3}^{+}$. A similar experiment for $\mathbf{7}^{+}$ (Figure 6.14) also showed reversible chemical reduction and oxidation over the timescale of this experiment, although the spectrum of the reduced product **7** was affected by scattering of Na/Hg particles in solution. These findings are consistent with the observed electrochemical reversibility of the reductions of $\mathbf{3}^{+}$ and $\mathbf{7}^{+}$.

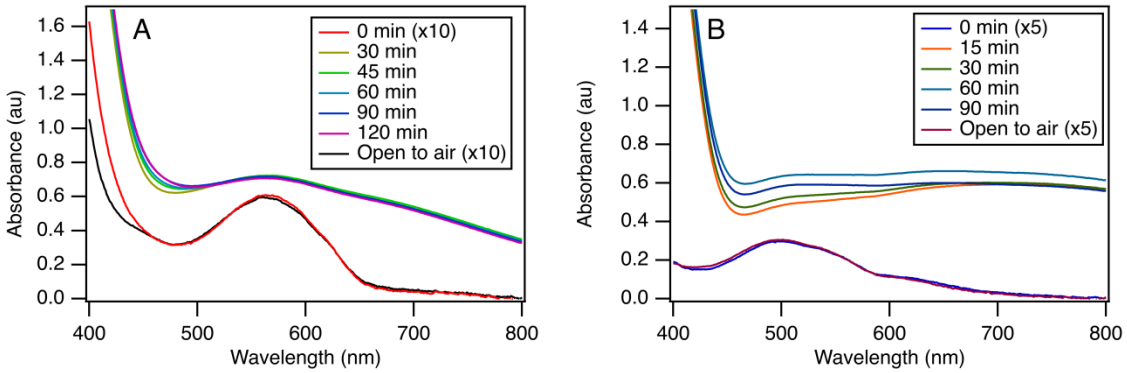

Figure 6.14. UV-vis monitoring of the *in-situ* reduction and reoxidation of $\mathbf{3}^{+}$ (A) and $\mathbf{7}^{+}$ (B).

Corresponding experiments for compounds $\mathbf{4}^{+}$ and $\mathbf{6}^{+}$ gave different results from those for $\mathbf{3}^{+}$ and $\mathbf{7}^{+}$ (Figure 6.15). Those for $\mathbf{6}^{+}$ were inconclusive. Upon reduction of $\mathbf{6}^{+}$ the bands of the reduced species evolved somewhat, and after exposure to air the band of $\mathbf{6}^{+}$ was clearly evident, but there was a sloping baseline that could be consistent with a scattering background due to Na/Hg or to slow decomposition. In the case of $\mathbf{4}^{+}$, however, the differences from the behavior of $\mathbf{3}^{+}$ and $\mathbf{7}^{+}$ were marked. Here, the spectrum of the reduced product evolved continuously and oxidation did not reform $\mathbf{4}^{+}$. (Figure 6.15). This indicates that **4** is less stable (more reactive) than **3**, consistent with the observed deviation of the reduction from full electrochemical reversibility and the smaller steric encumbrance of the ligands.

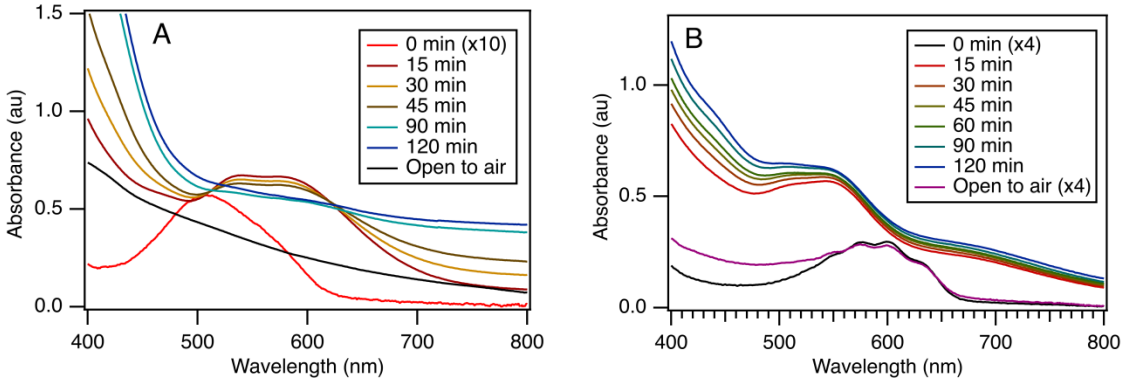

Figure 6.15. UV-vis monitoring of the *in-situ* reduction and re-oxidation of $\mathbf{4}^{+}$ (A) and $\mathbf{6}^{+}$ (B).

In view of these results, the d^3 compounds **3** and **7** were targeted for synthesis and isolation. Chemical synthesis of **3** was achieved through addition of Na/Hg (0.4% w/w) to $\mathbf{3}^{+}$ in

THF at 0 °C under Ar. Upon stirring, the dark blue solution converted to a dark green suspension accompanied by the formation of a fine white precipitate. Purification and recrystallization provided dark green crystals in 51% yield that was suitable for single crystal X-ray crystallography. The CV of **3** (Figure 6.8D) shows a reversible oxidation that is indistinguishable from the reversible reduction observed for $\mathbf{3}^+$ (Figure 6.8A). Compound **7** was synthesized under similar conditions.

6.2.5. Magnetic properties of 3. The magnetic moment of **3** was determined in solution by the Evans method, which provided a solution magnetic moment of 1.55 μ_B. Magnetic moments of similar magnitude have been observed for the d^1 Mo(V)–O compounds (1.5 μ_B – 1.7 μ_B).[23, 26, 30] This indicates that the ground-state spin of **3** is S = ½, consistent with the electron configuration $(d_{xy})^2(\pi^*(MoO))^1$.

The X-band EPR spectrum of **3** at low temperature in THF (Figure 6.15) provides g_{eff} = 1.89, consistent with the S = ½ spin state found for this complex. The first-derivative spectrum is fairly complex (Figure 6.16A and B), so the second derivative spectrum was calculated with the hope that it would accentuate some underlying hyperfine coupling (Figure 6.16C). Three distinct coupling constants could be measured: A_1 = 47G; A_2 = 10G; A_3 = 25G. One possible explanation for this complexity is that it arises from small inequivalences in Mo–P bond distances. Prior work on d^9 $[Ni(P_2N_2)_2]^+$ complexes demonstrated that small variations in Ni–P bond distances have profound impacts on the hyperfine coupling constants;[31] for instance, differences in bond lengths of less than 0.1 Å dispersed phosphorus hyperfine coupling constants by 50 MHz. This level of variation in Mo–P bond lengths is found in the structure of **3** (see next section).

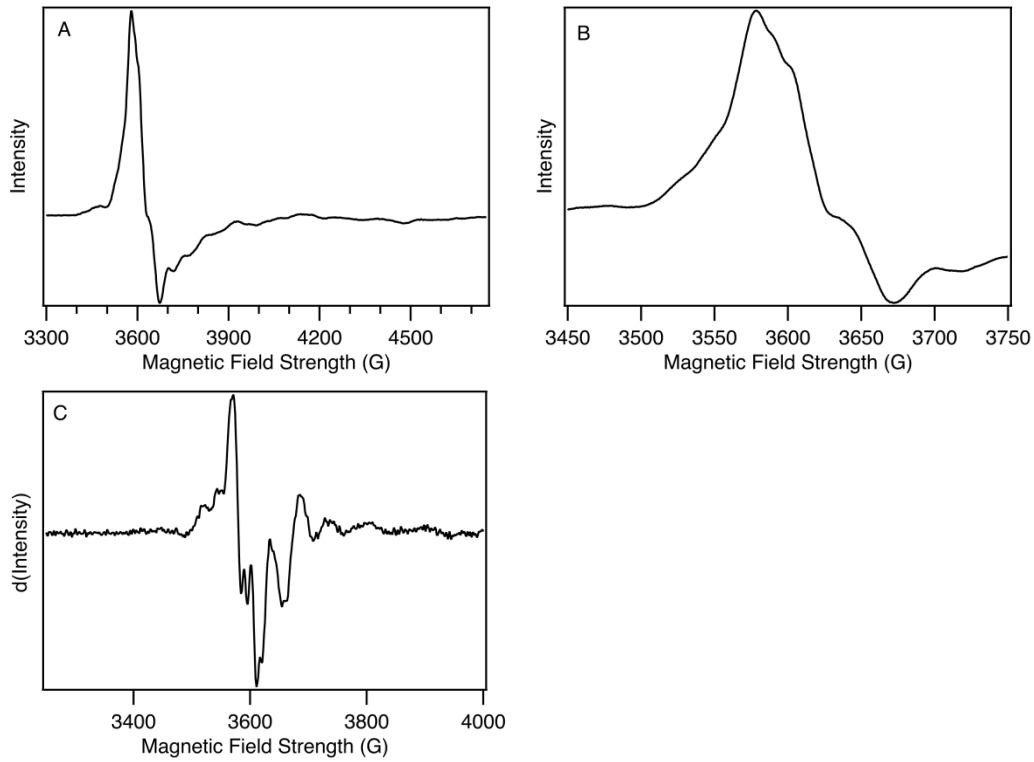

Figure 6.16. X-band EPR spectrum of 3 in THF at 15K. Microwave frequency: 9.63 GHz; microwave power: 4.0 mW, g_{eff} = 1.89. (A) Full spectrum (first-derivative plot shown); (B) Expansion of region from 3450 – 3750 G; (C) Second-derivative plot calculated using central differences; A_1 = 47G; A_2 = 10G; A_3 = 25G.

6.2.6. Molecular structure of 3. The molecular structures of $\mathbf{3}^+$ and **3** were determined by X-ray crystallography to assess structural differences between the $(d_{xy})^2$ and $(d_{xy})^2(\pi^*(MoO))^1$ electron configurations . Both compounds exhibit a pseudo-octahedral geometry with axial oxo and chloride ligands and equatorial dppe ligands (Figure 6.17). Both structures are complicated by the presence of disorder between the oxo and chloro ligands; this was well modeled by crystallographic criteria, but additional experiments were performed to confirm the Mo–O bond lengths (*vide infra*). The core bond lengths for **3** and $\mathbf{3}^+$ are set out in Table 6.6; full metrical data are reported in Section 6.4. The MoO bond length of $\mathbf{3}^+$ is 1.662 Å, consistent with a triple bond. This is confirmed by benchmarks for such compounds from the Cambridge Structural Database (*vide infra*). The MoO bond length of **3** (1.809(5) Å) is 0.147 Å longer than that of $\mathbf{3}^+$,

consistent with population by one electron of the π*(MoO) orbital and reduction of the MoO bond order from 3 to 2.5. Additionally, the Mo–P(avr) bond distance of 3 was found to 0.071 Å shorter than that of $\mathbf{3}^{+}$, consistent with greater Mo→P π-backbonding for Mo(III) than for Mo(IV).[32]

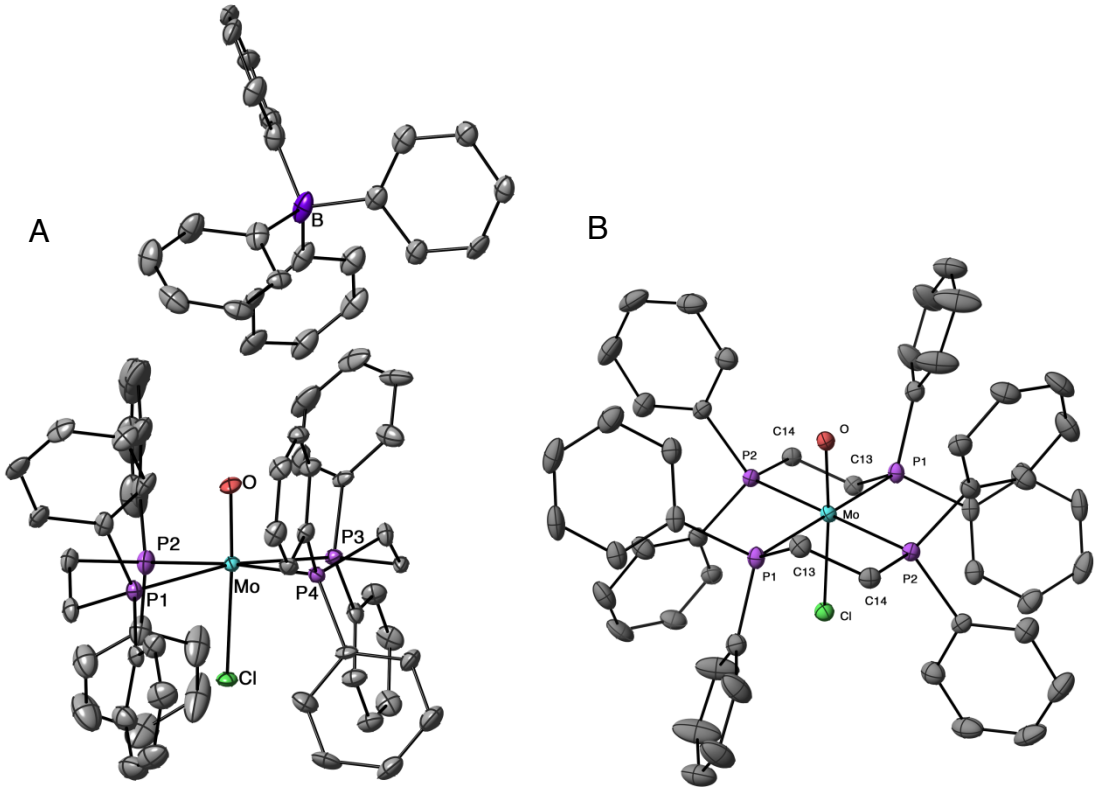

Figure 6.17. (A) Molecular structure of $[Mo(O)(dppe)_2Cl]BPh_4$ ($\mathbf{3}^{+}$) as determined by X-ray crystallography (50% probability ellipsoids). Hydrogen atoms, O-Mo-Cl disorder, and interstitial solvent are not shown to enhance clarity. (B) Molecular structure of $[Mo(O)(dppe)_2Cl]$ (**3**) as determined by single crystal X-ray crystallography (50% probability ellipsoids). Hydrogen atoms, O-Mo-Cl disorder, and interstitial solvent are not shown to enhance clarity.

Table 6.6. Core bond lengths for **3** and $\mathbf{3}^+$ (Å).[a]

	$\mathbf{3}^{+b}$	$\mathbf{3}^c$	$\Delta(\mathbf{3}\text{-}\mathbf{3}^+)$
Mo–O	1.662(15)	1.809(5)	0.147
Mo–Cl	2.461(5)	2.5155(17)	0.054
Mo–P(1)	2.531(3)	2.4845(7)	−0.046
Mo–P(2)	2.577(3)	2.4952(7)	−0.082
Mo–P(3)	2.593(3)	2.4845(7)	−0.108
Mo–P(4)	2.544(3)	2.4952(7)	−0.049
Mo–P(avg)	2.561[3]	2.4898[7]	−0.071

[a] Values in parentheses are the estimated standard deviation and those in square brackets are the mean standard deviation for the related set of bond distances. [b] Disordered 66:34 over two O–Mo–Cl orientations; metrical data given for the major-occupancy orientation. [c] Disordered 1:1 over two O–Mo–Cl orientations.

Because of concern that the crystallographic O–Mo–Cl disorder present in $\mathbf{3}^+$ and **3** might affect the measured Mo–O bond lengths, the structural differences between $\mathbf{3}^+$ and **3** were probed by complementary techniques. First, vibrational spectroscopy was used to determine the M–O vibrational frequencies (Table 6.7). Those for d^2 $\mathbf{1}^+$–$\mathbf{7}^+$ are generally found between 940–960 cm^{-1}, consistent with prior reports for such compounds.[24-27, 33] The ^{18}O-labeled compound $\mathbf{3}^+$***** (50% ^{16}O/50% ^{18}O) was also prepared and studied; its frequency (894 cm^{-1}) is within 2 cm^{-1} of that predicted by the diatomic oscillator approximation from the frequency of $\mathbf{3}^+$ (see Table 6.8 and Section 6.4). The Raman spectra of **3** and **3*** were also measured (Figure 6.18 and Table 6.7). The MoO frequency of **3** (792 cm^{-1}) is substantially lower than that of $\mathbf{3}^+$ (943 cm^{-1}), consistent with a weaker bond for the d^3 compound, and the frequencies for **3** (792 cm^{-1}) and **3*** (751 cm^{-1}) are also found to differ by the amount predicted by the diatomic oscillator approximation (Table 6.8). The Raman spectrum of **7** (Figure 6.19) exhibits a WO frequency of 790 cm^{-1}, very similar to that of **3**).

Table 6.7. M–O vibrational frequencies for $\mathbf{1}^+ - \mathbf{7}^+$.

Compound	$\tilde{\nu}$ (M–O) (cm^{-1})[a]
$[Mo(O)(CN^tBu)_4Cl]^+$ ($\mathbf{1}^+$)	953[b]
$[Mo(O)(dppbz)_2Cl]^+$ ($\mathbf{2}^+$)	941[c]
$[Mo(O)(dppe)_2Cl]^+$ ($\mathbf{3}^+$)	943[d]
$[Mo(^{18}O)(dppe)_2Cl]^+$ ($\mathbf{3*}^+$)	894
$[Mo(O)(dppe)_2Cl]$ (**3**)	792[e]
$[Mo(^{18}O)(dppe)_2Cl]$ (**3***)	751
$[Mo(O)(dmpe)_2Cl]^+$ ($\mathbf{4}^+$)	951[f]
$[Mo(O)(depe)_2Cl]^+$ ($\mathbf{5}^+$)	948
$[Mo(O)(dcype)_2Cl]^+$ ($\mathbf{6}^+$)	947
$[W(O)(dppe)_2Cl]^+$ ($\mathbf{7}^+$)	955[g]
$[W(O)(dppe)_2Cl]$ (**7**)	790[e]

[a] Recorded on a solid sample using ATR; [b] Reported in Ref. 25 as 952 cm^{-1} (KCl disk); [c] Reported in Ref. 26 as 939 cm^{-1} (Nujol); [d] Reported in Ref. 27 as 943 cm^{-1} (KBr disk); [e] Reported on a solid sample using confocal Raman. [f] Reported in Ref. 33 as 950 cm^{-1} (Nujol); [g] Reported in Ref. 27 as 952 cm^{-1} (KBr disk);

Table 6.8. M–O vibrational frequencies of ^{18}O labeled compounds (cm^{-1}).

Compound	Measured	Predicted[a]
$[Mo(^{18}O)(dppe)_2Cl]^+$ ($\mathbf{3*}^+$)	894	896
$[Mo(^{18}O)(dppe)_2Cl]$ (**3***)	751	753

[a] Predicted *via* Equation 6.2 using values from ^{16}O compounds in Table 6.7.

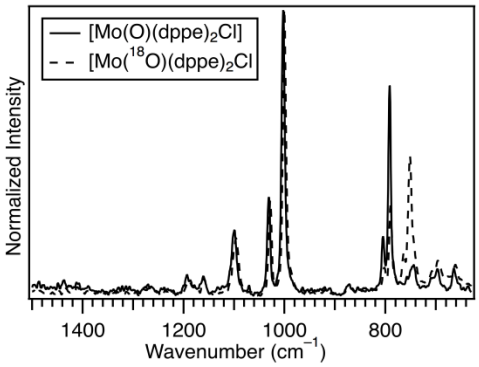

Figure 6.18. Raman spectra of **3** and **3*** (Solid sample, λ = 633 nm).

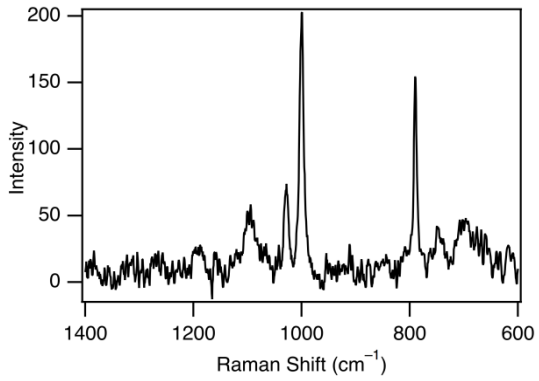

Figure 6.19. Raman spectroscopy of 7 from 600 – 1400 cm^{-1} (Solid sample, λ = 633 nm).

The MoO vibrational frequencies for **3**$^{+}$ and **3** allow validation of the crystallographically determined MoO bond lengths *via* Badger's-rule like frequency/bond-length correlations. Hardcastle *et al.*,[34] observed strong empirical correlations between the Mo–O vibrational frequencies, bond length, and bond order for molybdenum oxide compounds.[34] The bond-length/frequency correlation is shown in Equation 6.1, where *R* is the bond distance in Å. Application to the vibrational frequencies for **3** and **3**$^{+}$ predicts Mo–O bond lengths of 1.69 Å (**3**$^{+}$) and 1.80 Å (**3**). The value obtained for **3** is within ±3σ of the measured bond length from the single crystal X-ray crystallography data (Table 6.9).

$$\tilde{\nu}_i = 32895e^{-2073R} \quad (6.1)$$

Table 6.9. Measured vs predicted bond length (Å).

Compound	Measured	Predicted[a]	Δ(Pred-Meas.)
[Mo(O)(dppe)$_2$Cl]$^{+}$ (**3**$^{+}$)	1.662(15)	1.71	0.048(15)
[Mo(O)(dppe)$_2$Cl] (**3**)	1.809(5)	1.80	–0.009(5)

[a]Predicted *via* Equation 6.1.

The MoO bond lengths from X-ray crystallography were also corroborated for **3** by a DFT calculation (LANL2DZ, 6-31G**). The structure of **3** was reproduced when ground-state spin was set as S = ½ (Table 6.10). The Mo–O bond length was measured to be within 0.023 Å and the Mo–P(avr) distance was reproduced within 0.038 Å. A mixed double/triple-ζ calculation also reproduced the structure, but was not significantly better than just the double-ζ level alone.

Computational costs of the spin unrestricted calculations prevented calculation at full triple-ζ theory. The double-ζ calculation also provided spin densities for **3**, predicting it to be fully localized on molybdenum (72%) and oxygen (27%) (Figure 6.20 and Table 6.11). This is consistent with the π*(MoO) nature of the SOMO.

Table 6.10. Bond length (Å) and angles (°) for computational study of **3**.

Bond Length/ Bond Angle	Exptl (XRD) [a]	Double-ζ[b]	Δ(calc-exp)	Mixed[c]	Δ(calc-exp)
Mo–O	1.809(5)	1.786	−0.023	1.787	−0.022
Mo–Cl	2.5155(17)	2.602	0.086	2.586	0.071
Mo–P(avr)	2.4898[7]	2.523	0.038	2.517	0.027
O–Mo–P(avr)	95.70[13]	93.8	−1.9	93.6	−2.1
P –Mo–P(outer)	100.95[2]	100.25	−0.7	100.35	−0.6
P –Mo–P(inner)	79.05[2]	79.4	0.35	79.4	0.35

[a] The values in parentheses are the estimated standard deviation and those in square brackets are the mean standard deviation for the related set of bond distances. Structure refinement parameters are shown in Section 6.4. [b] B3P86: LANL2DZ (Mo), 6-31G** (all other atoms); [c] B3P86: SDD (Mo), 6-31G** (all other atoms).

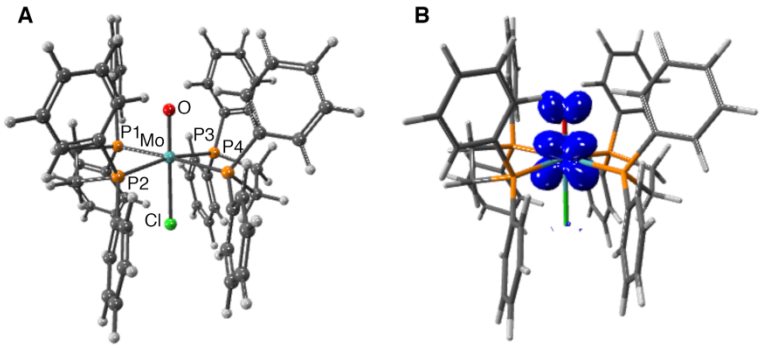

Figure 6.20. Calculated structure (A) and spin density distribution (isovalue = 0.004) for **3**.

Table 6.11. Mulliken spin density for selected molybdenum(III)-oxo complexes.

	Spin Density			
Compound	Mo	O	4P	Cl
$[Mo(O)(dppe)_2Cl]$	0.722	0.269	–0.025	0.008
$[Mo(O)(dmpe)_2Cl]$	0.650	0.312	0.005	0.006

The collective structural, spectroscopic, and computational data point clearly to **3** possessing a $(d_{xy})^2(\pi^*MoO)^1$ ground-state electron configuration, which corresponds to a formal

MoO bond order of 2.5. This 2.5 bond order is also found for d^2 compounds in the low-lying $(d_{xy})^1(\pi^*\ MoO)^1$ excited state, which has been probed for related molybdenum(IV)-oxo complexes by molecular-axis polarized electronic-absorption spectroscopy.[24] Strikingly, the MoO frequency previously observed for the excited state of **4** (790–800 cm^{-1}) is the same as that observed for the ground state of **3** (790 cm^{-1}), demonstrating the strong correspondence between the MoO bond orders for these compounds. This is because the d_{xy}-orbital is non-bonding with respect to the oxo ligand; thus, the MoO bond length (and vibrational frequency) is independent of the electron count of this orbital, to a first approximation.

Confirmation of the single crystal X-ray crystallography data by vibrational spectroscopy and DFT calculations allow comparison of the Mo–O bond length of **3** to those of other molybdenum-oxo complexes in the Cambridge Structural Database.[35] A search for terminal molybdenum-oxo complexes in all oxidation states using the criteria $r_{int} < 0.1$, and disregarding. structures that possess highly elongated thermal ellipsoids on oxygen that may indicate unresolved disorder affecting the bond length, provided 264 examples that possessed Mo–O bond distances lying from 1.605 – 1.802 Å (Table 6.12). Among those 264 samples, 61 were observed to be Mo(VI), 145 were Mo(V), 57 were Mo(IV), and one was reported to have more than two d-electrons. Distributions are shown in Figure 6.21 and statistical parameters are set out in Table 6.12. Very few examples have bond lengths > 1.75 Å. The MoO bond length of **3** is clearly statistically different from those of Mo(VI), Mo(V), and Mo(IV) complexes.

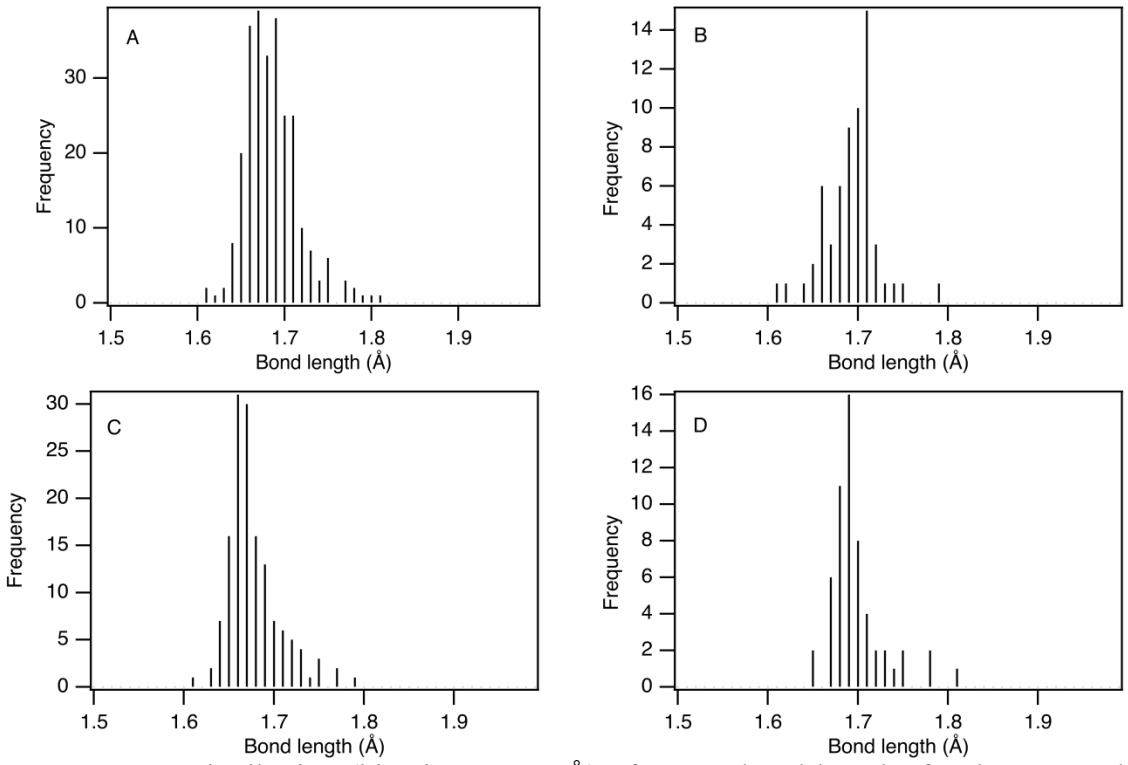

Figure 6.21. Distribution (bin size = 0.01 Å) of Mo–O bond lengths for the 264 molybdenum-oxo compounds studied (A) Full distribution; (B) Mo(VI)-oxo; (C) Mo(V)-oxo; (D) Mo(IV)-oxo.

Table 6.12. Bond length statistics (Å).

Oxidation State	Avg. Bond Length	95% CI	Median
All	1.68(3)	1.68 – 1.74	1.68
VI	1.69(3)	1.69 – 1.74	1.69
V	1.67(3)	1.67 – 1.73	1.67
IV	1.69(3)	1.69 – 1.75	1.69

The one complex that is reported to possess a comparable Mo–O bond length to **3** was recently described by Trovitch *et al.,*[21] who reported that reduction of $[Mo(O)(PDI^{Ph2PPr})]^{2+}$ using two equivalents of $K[C_{10}H_8]$ provided a compound formulated as a molybdenum(II)–oxo. The bond lengths of that compound are compared to those of **3** in Figure 6.22. Given the close similarity between the MoO bond lengths (1.809(5) Å **3**, 1.797(3) Å Trovitch), we believe that the Trovitch compound is instead a molybdenum(III)-oxo with a PDI-localized radical.

Additionally, the bond elongation observed in the Trovitch compound upon reduction (0.104 Å) is close to that found for **3** (0.147 Å).

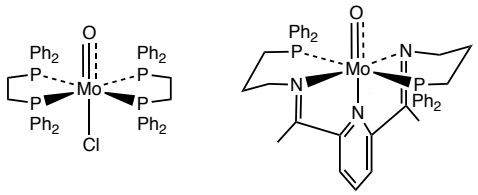

d^3 Mo–O (Å)	1.809(5)	1.797(3)
d^2 Mo–O (Å)	1.662(15)	1.693(2)

Figure 6.22. Comparison of the d^3 molybdenum-oxo compound obtained in this study with that of Ref. 21.

6.2.7. Reactivity studies. The differences between the electrochemical reversibility of the reductions of $\mathbf{3}^+$ and $\mathbf{4}^+$ and corresponding instability of *in-situ* prepared samples of **4** suggested that the reactivity of molybdenum(III)-oxo compounds might also be controlled by the steric bulk of the equatorial phosphine ligand (Figure 6.4). This was probed by examining oxygen atom transfer of the d^3 complexes with phosphines, which is a classical test of reactivity for reduced metal-oxo compounds.[36] The d^2 complexes $\mathbf{3}^+$ and $\mathbf{4}^+$ did not react with PMe_2Ph (equimolar ratio, 1 mmol) during the course of two days (Figure 6.23). In contrast, **3** reacts with PMe_2Ph (50 eq) to provide $OPMe_2Ph$, identified by GC/MS, in good yield (72%, Table 6.13). The compound does not react with PPh_3, possibly due to steric constraints

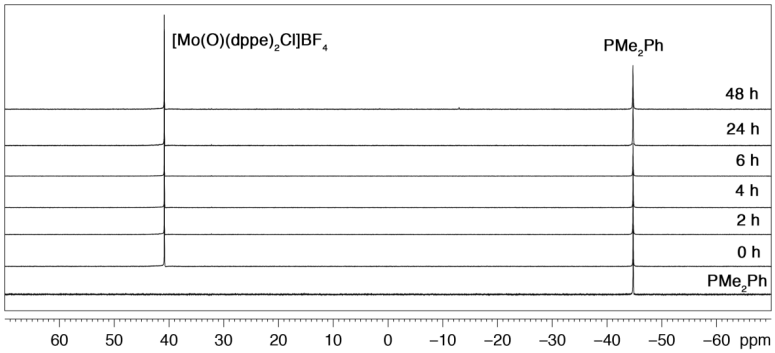

Figure 6.23. $^{31}P\{^1H\}$ NMR spectra recorded in CD_3CN showing that PMe_2Ph does not react with $[Mo(O)(dppe)_2Cl]BF_4$ ($\mathbf{3}^+$).

Table 6.13. GC analysis of oxygen atom transfer reactions.

Compound	Substrate	GC Yield of OPR_3 (%)
$[Mo(O)(dppe)_2Cl]BF_4$ (**3**$^+$)	PMe_2Ph	0
	PPh_3	0
$Mo(O)(dppe)_2Cl$ (**3**)	PMe_2Ph	72
	PPh_3	0

In order to test the hypothesis that the reactivity of **4** should be enhanced relative to that of **3**, the reactions of electrochemically generated **3** and **4** with PMe_2Ph were studied under identical conditions. Specifically, the CVs of the compounds were recorded in THF in the absence and presence of PMe_2Ph (100 equiv). At a scan rate of 50 mV s^{-1} the reduction wave of **3**$^+$ is identical with and without substrate, whereas for **4**$^+$ the anodic feature disappears when PMe_2Ph is present (Figure 6.24-6.25). This indicates reduction of **4**$^+$ to **4** is followed by a chemical reaction between **4** and PMe_2Ph that is fast on this time scale, whereas **3** is unreactive on this time scale. This suggests that both stability and reactivity of d^3 oxo compounds can be sterically controlled.

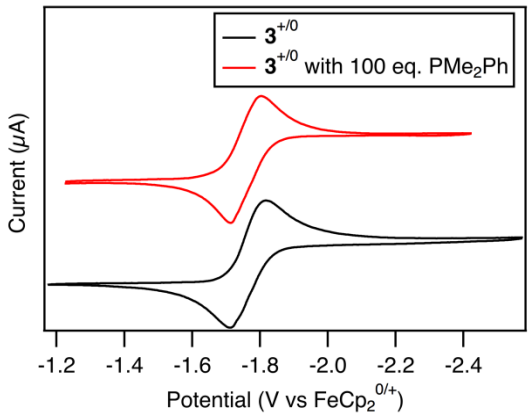

Figure 6.24. Electrochemical reduction of $[Mo(O)(dppe)_2Cl]BF_4$ (**3**$^+$) in the absence and presence of 100 eq. PMe_2Ph (Scan rate = 50 mV s^{-1}). **Note:** Recorded potentials are externally referenced to $FeCp_2$.

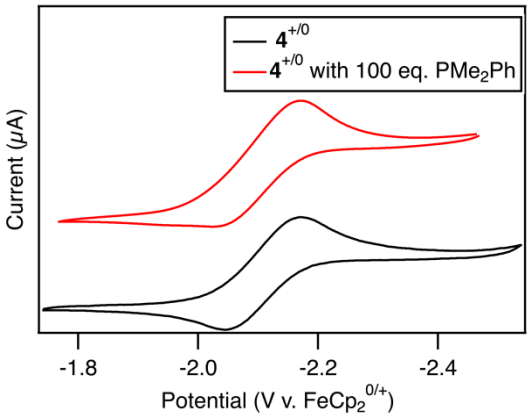

Figure 6.25. Electrochemical reduction of $[Mo(O)(dmpe)_2Cl]PF_6$ ($\mathbf{4}^+$) in the absence and presence of 100 eq. PMe_2Ph (Scan rate = 50 mV s^{-1}). **Note:** Recorded potentials are externally referenced to $FeCp_2$.

6.3. Conclusions.

The initial synthesis and characterization of a family of molybdenum(III)-oxo compounds whose reactivity can be controlled through the application of equatorial phosphine ligands with different steric profiles is reported. A molybdenum(III)-oxo compound has been characterized by electrochemistry, single-crystal X-ray crystallography, magnetic measurements, and computational chemistry. Electrochemical measurements suggest that one stabilizing factor of **3** is the steric bulk around the molybdenum-oxo ligand. Utilizing compounds with less steric bulk than **3** were observed to be highly reactive and not isolable in solution. The d^3 compound **3** was observed to react slowly with phosphines, suggesting that the inclusion of less sterically demanding groups could further heighten the reactivity of these molybdenum-oxo compounds.

6.4. Experimental Section.

6.4.1. General synthesis procedures. Unless otherwise noted, all manipulations were performed under a nitrogen atmosphere using standard Schlenk and glovebox techniques. Solvents used for synthesis and electrochemistry were HPLC grade and purified by passing them under nitrogen pressure through an anaerobic stainless-steel system consisting of either 4.5 in ×

24 in (1 gal) columns of activated A2 alumina (CH_3CN, Et_2O, CH_2Cl_2, THF) or one column of activated A2 alumina and one column of activated BASF R3-11 catalyst (toluene, pentane).[37] Solvents used for NMR spectroscopy (C_6D_6, CD_2Cl_2) were stored in air. All other reagents were procured from commercial sources and used as received. The compounds $[Mo(O)(CN^tBu)_4Cl]BPh_4$ (**1**[BPh_4]),[25] $[Mo(O)(dppe)_2Cl]BPh_4$ (**3**[BPh_4]),[26] and $[Mo(O)(dmpe)_2Cl]Cl$ (**4**[Cl])[24, 33] were synthesized by standard procedures. ^{1}H-, $^{13}C\{^1H\}$-, and $^{31}P\{^1H\}$-NMR spectra were measured at room temperature with a Bruker AF-500 or DRX-400 NMR spectrometer. Chemical shifts were measured relative to solvent resonances (^{1}H, ^{13}C)[38] or external standards (^{31}P, 85% v/v H_3PO_4, ^{19}F, C_6F_6). The ^{1}H NMR spectrum of $\mathbf{2}^+$ was assigned by ^{1}H-^{1}H COSY NMR spectroscopy. HRA-MS were measured with an Agilent 6224 TOF High Resolution Mass Spectrometer in positive ion mode. Infrared spectra were measured with a Thermo Nicolet iS50 FT-IR. Raman spectra were recorded on a Horiba LabRAM HR Evolution analytical Raman microscope (λ_{ex} = 633 nm). Solid samples for Raman spectroscopy were prepared in the glovebox by inserting a small amount of the analyte into a 1mm pathlength sealable, non-precision cuvette. Elemental analyses were performed by Robertson Microlit Laboratories (Ledgewood, NJ).

6.4.2. Electrochemical measurements. Electrochemical measurements were performed at room temperature in a nitrogen-filled glovebox using a Bioanalytical Systems 100 B/W Electrochemical Workstation. A three-electrode configuration was used, which consisted of a working electrode (Bioanalytical Systems, platinum disk, area = 0.2 cm^2), auxiliary electrode (Bioanalytical Systems, platinum disk, area = 0.2 cm^2), and quasi-reference electrode (silver wire). Electrodes were polished prior to each experiment. Samples ranged in concentration from (0.3–2.0) × 10^{-3} M analyte in THF solution with 0.1 M $[Bu^n_4N][PF_6]$. Peak currents in cyclic

voltammetry experiments were determined from scans in which the switching potential was at least 0.30 V beyond the peak potentials. Electrochemical reversibility of redox couples, when applicable, was established by Randles-Sevcik plots. Differential pulse voltammetry (DPV) was conducted using a scan rate of 20 mV s^{-1}, a pulse amplitude of 50 mV, a sampling width of 17 ms, a pulse width of 50 ms, and a pulse period of 200 ms. Electrode potentials are referenced to the $FeCp_2^{0/+}$ couple; this was used as an internal electrode-potential standard for CV and DPV experiments. THF for electrochemical measurements was HPLC grade and passed through activated alumina under N_2 prior to use. Ferrocene was recrystallized three times from 95% ethanol and then sublimed under vacuum. $[Bu^n_4N][PF_6]$ was recrystallized three times from 95% ethanol and dried under vacuum at 80 °C for 24 h.

6.4.3. Electronic absorption spectroscopy. Solution samples for electronic spectroscopy were prepared under N_2. THF was purified by stirring over NaK for at least 24 h. Absorption spectra were recorded with a Cary 300 UV-vis spectrophotometer.

6.4.4. *In-situ* reduction measurements. To a sealable synthesis cuvette (pathlength = 1 cm) under nitrogen was added a THF solution (5 mL) of molybdenum(IV)-oxo complex (15 mg, $\mathbf{3}^+$; 5 mg $\mathbf{4}^+$), Na/Hg (1 eq Na, 0.4% w/w), and a stir bar. The solution was degassed by on a vacuum line *via* three freeze-pump-thaw cycles and left under vacuum.

6.4.5. GC/MS procedure. An Agilent GC/MS (7890B GC, 7693 Autosampler, and 5977A SQ MS) equipped with an Agilent 122-4732 column was used for these experiments. The elution time was set to 25.25 min with a front oven temperature of 250 °C. The column oven was initially set to 160 °C. The temperature was held at 160 °C for 1 min and then a temperature gradient of 40 °C/min was introduced until a temperature of 300 °C was reached. That temperature was held for 20.75 min. Yields were calculated from measurements made of

authentic samples of products. Samples prepared in screw-cap vials were initially loaded under N_2 in a glove box. Each sample contained **3**/**3**$^+$ (0.017 g, 18 μmol), phosphine (0.9 mmol, 50 eq.), and a stir bar. The sample was sealed, removed from the glovebox, sparged with Ar for 10 min, and then CH_3CN (Ar saturated, 3 mL) was added *via* syringe. The sample was allowed to stir at room temperature for 18 h after which time the sample was removed to the N_2 glovebox and analyzed by GC/MS.

6.4.6. Diatomic approximation calculations. The relationship for a single isotopically linked diatom pair, with same force constant k, can be described in Equation 6.2. There, μ and μ_i are the reduced masses of Mo–O (13.7) and Mo–^{18}O (15.1), respectively.

$$\tilde{\nu}_i = \tilde{\nu}\sqrt{\frac{\mu}{\mu_i}} \qquad (6.2)$$

6.4.7. Density functional theory (DFT) calculations. DFT calculations were performed with Gaussian 16.[39] Calculations employed the B3P86 functional, which has been demonstrated to be suitable for 2nd row transition metal complexes.[40] Geometries were optimized without symmetry constraints. No imaginary frequencies were observed upon subsequent vibrational calculations, confirming that the structures reside at a potential-surface minima. For atoms H through Cl the 6-31G(d,p) basis set was used. The LANL2DZ double-ζ basis set and effective core potentials (ECP) were used for Mo.[41, 42] Orbital parentages were calculated using AOMix (version 6.94b, www.sg-chem.net).[43] Mulliken atomic spin densities were calculated in Gaussian 16.[39] For benchmarking studies, double-ζ and triple-ζ quality basis sets of the same functional (B3P86) were compared with the solid-state X-ray structure.

6.4.8. Single crystal X-ray crystallography measurements. The diffraction data were measured at 100 K on a Bruker D8 VENTURE diffractometer with a PHOTON 100 CMOS

detector system equipped with a Mo–target X–ray tube (λ = 0.71073 Å). Data were collected using ω scans to survey a hemisphere of reciprocal space. Data reduction and integration were performed with the APEX3 software package (Bruker AXS, versions 2014/4 or 2015.5–2). Data were scaled and corrected for absorption effects using the multi-scan procedure as implemented in SADABS (Bruker AXS, version 2014/5, 2015, part of Bruker APEX3 software package). The structures were solved by SHELXT (Version 2014/7)[44] and refined by a full–matrix least–squares procedure using Bruker SHELXTL (version 6.14)[45] and OLEX2 software packages (XL refinement program version 2014/7).[44, 46]All atoms were refined with anisotropic thermal parameters. Hydrogen atoms were included in idealized positions for structure factor calculations. Crystallographic data and details of the data collection and structure refinement are listed in Table 6.14.

6.4.8.1. Crystal structure of [Mo(O)(dppe)$_2$Cl][BPh$_4$]. A purple prism (0.10 × 0.12 × 0.32 mm^3) was mounted on a Dual-Thickness MicroMount^{tm} (MiTeGen) with 30 µm sample aperture with Fluorolube™ oil. All atoms were refined with anisotropic thermal parameters. The [O-Mo-Cl] moiety was found to be disordered over two orientations as was previously observed in similar systems.[24, 47] This disorder was modeled without application of any geometric restraints to provide a 66:34 occupancies ratio. The molybdenum atom is displaced from the midpoint of the O-Mo-Cl bonds toward the oxygen atom. The thermal parameters of nearly superimposed O1 and Cl1A and Cl1 and O1A were constrained to be the same (EADP). No other restraints were used to model this disorder. The structure is shown in Figure 6.16, and selected bond distances, angles, and occupancy ratios are set out in Tables 6.15-6.17.

6.4.8.2. Crystal structure of Mo(O)(dppe)$_2$Cl. A green plate (0.09 × 0.21 × 0.32 mm^3) was mounted on a Dual-Thickness MicroMount^{tm} (MiTeGen) with 30 µm sample aperture with

Fluorolube™ oil. The [O-Mo-Cl] moiety was found to be disordered over two orientations (1:1) as was previously observed in similar systems.[24, 47] This disorder was modelled without any additional restraints. The C–C distances of the solvent benzene molecule were each restrained to be the same distance. The structure is shown in Figure 6.16, and selected bond distances and angles are set out in Tables 6.18 and 6.19.

6.4.9. Synthetic procedures.

Synthesis of [Mo(O)(dppbz)$_2$Cl][PF$_6$] (**2**[PF$_6$]). The synthesis of **2**[BPh$_4$][26] and **2**[PF$_6$][22] have been described previously by a different method than that described here. The $^{31}P\{^1H\}$ NMR chemical shift was found to match that reported in Ref. 22. To a stirred, room temperature solution of Mo(O)(PMe$_3$)$_3$Cl$_2$[48] (0.470 g, 1.06 mmol) in anhydrous ethanol (120 mL) was added 1,2-bis(diphenylphosphino)benzene (dppbz, 1.00 g, 2.24 mmol). A reflux condenser was affixed to the flask and the green suspension was refluxed for 15 h. During this time, the green suspension converted to a dark purple solution. The reaction flask was opened to air, allowed to cool to room temperature, and the volatile components were removed under vacuum. The resulting dark purple film was extracted into MeOH (50 mL) and the resulting solution filtered through Celite and concentrated under vacuum to 20 mL. To the dark purple solution was added a solution of KPF$_6$ (1.0 g, 5.43 mmol) in methanol (20 mL). Immediately, a dark pink powder precipitated. This was collected by filtration and washed with toluene (3 x 10 mL), hexane (3 x 5 mL), and H$_2$O (3 x 10 mL), and dried overnight under vacuum (0.703 g, 0.593 mmol, 56% yield). ^1H NMR (500.13 MHz, CD_2Cl_2, Figure 6.27): δ 7.69 (br s, 8H, C_6H_4); 7.44 (br t, 4H, *p*-PPh$_2$); 7.38 (br t, 4H, *p*-PPh$_2$); 7.23 (br s, 16H, *o*,*m*-PPh$_2$); 7.12 (br t, 8H, *m*-PPh$_2$); 6.65 (br s, 8H, *o*-PPh$_2$). $^{13}C\{^1H\}$ NMR (125.75 MHz, CD_2Cl_2, Figure 6.28): δ 141.92 (quin, J_{CP} = 11 Hz, PPh$_2$); 135.85 (quin, J_{CP} = 4 Hz, C_6H_4); 133.97 (quin, J_{CP} = 3 Hz, PPh$_2$); 133.74 (quin, J_{CP} = 3

Hz, PPh_2); 132.72 (C_6H_4); 131.80 (PPh_2); 131.32 (PPh_2); 129.31 (quin, J_{CP} = 10 Hz, C_6H_4); 129.13 (quin, J_{CP} = 3 Hz, PPh_2); 128.67 (quin, J_{CP} = 3 Hz, PPh_2). $^{31}P\{^1H\}$ NMR (202.45 MHz, CD_2Cl_2, Figure 6.29): δ 48.89; –144.04 (sept, $^1J_{PF}$ = 710 Hz, PF_6^-). IR (ATR, cm^{-1}): 941(ν_{Mo-O}). HR-ESI-MS (CH_2Cl_2, 298 K): *m/z* 1041.119 (M^+, rel. int. 100, calc. 1041.14).

[Mo(O)(dppe)$_2$Cl]BF$_4$ (**3**[BF_4])**.**[25] Additional characterization data: HRA-ESI-MS (CH_2Cl_2, 298 K): *m/z* 945.125 (M^+, rel. int. 100, calc. 945.14); IR (ATR, 298 K, cm^{-1}): 943 (ν_{Mo-O}).

[Mo(^{18}O)(dppe)$_2$Cl]BF$_4$ (**3***[BF_4]). The compound was synthesized analogously to **3**(BF_4)[25] using Mo(^{18}O)(PMe_3)$_3$Cl as a starting material. It contains *ca*. 50% of the ^{16}O isotopomer. The observed ^1H- and $^{31}P\{^1H\}$-NMR data agree with that reported for [Mo(O)(dppe)$_2$Cl]BF_4[25]. Additional characterization data: IR (ATR, 298 K, cm^{-1}): 943 (Mo-O); 894 (Mo-^{18}O). HR-ESI-MS (CH_2Cl_2, 298 K): *m/z* 945.125 (M^+, rel. int. 97.5, calc. 945.14); 947.125 ($M(^{18}O)^+$, rel. int. 100, calc. 947.14).

Mo(O)(dppe)$_2$Cl (**3**). In a N_2 glovebox, [Mo(O)(dppe)$_2$Cl]BF_4 (0.200g, 0.193 mmol) and Na/Hg (0.086 mL, 0.4% w/w, 0.203 mmol Na) were added to a Schlenk flask equipped with a stir bar. The flask was removed from the N_2 glovebox and purged for 15 min with Ar while cooling with an ice water bath. To the flask was added THF (20 mL, Ar sparged) *via* cannula. The [Mo(O)(dppe)$_2$Cl]BF_4 dissolved to produce a pale blue solution over Na/Hg. The Na/Hg was agitated by stirring for 1 h, during which time the pale blue suspension converted to a dark green suspension with a fine white precipitate. The volatile components of the suspension were removed under vacuum, and the remaining solid was extracted into C_6H_6 (20 mL, Ar sparged) and filtered by cannula into a new Schlenk flask. The volatile components of the green solution were removed under vacuum and recrystallized from a layered solution of benzene/pentane (1:1).

The dark green solid was collected by filtration and dried under vacuum (0.099 g, 0.104 mmol, 51 % yield). Solution magnetic moment (C_6D_6): 1.55 μ_B. Raman (solid, λ_{ex} = 633 nm, cm^{-1}): 792 (Mo-O). Mo(^{18}O)(dppe)$_2$Cl (**3***) was prepared analogously from [Mo(^{18}O)(dppe)$_2$Cl]BF_4 (**3***(BF_4)). Raman (solid, λ_{ex}=633 nm, cm^{-1}): 792 (Mo-O); 751 (Mo-^{18}O).

[Mo(O)(dmpe)$_2$Cl]PF_6 (**4**[PF_6]). To a solution of [Mo(O)(dmpe)$_2$Cl]Cl[24, 33] prepared without purification from Mo(O)(PMe_3)$_3Cl_2$[33] (0.300 g, 0.730 mmol) in methanol (25 mL) was added KPF_6 (0.5 g, 2.72 mmol) in methanol (10 mL), which immediately resulted in the precipitation of a fine maroon powder. The powder was collected by filtration, washed with toluene (3 x 5 mL), hexane (3 x 5 mL), and H_2O (3 x 5 mL), and dried overnight under vacuum to provide a fine maroon powder (0.198 g, 0.334 mmol, 46% yield). The compound can be stored and handled in air. ^{1}H NMR (400.13 MHz, CD_2Cl_2, Figure 6.35): δ 2.18 (br m, PCH_2, 8H); 1.80 (s, PCH_3, 12H); 1.70 (s, PCH_3, 12H).^{13}C{^{1}H} NMR (125.76 MHz, CD_2Cl_2, Figure 6.36): δ 28.55 (PCH_2); 15.51 (PCH_3); 13.89 (PCH_2). ^{31}P{^{1}H} NMR (161.97, CD_2Cl_2, Figure 6.37): δ 29.76; –143.13 (sept, $^1J_{PF}$ = 710 Hz, PF_6^-). IR (ATR, 298 K, cm^{-1}): 951 ($\nu_{Mo–O}$). HR-ESI-MS (CH_2Cl_2, 298 K): *m/z* 449.006 (M^+, rel. int. 100, calc. 449.01).

[Mo(O)(depe)$_2$Cl]BPh_4 (**5**[BPh_4]). To a stirred room temperature solution of Mo(O)(PMe_3)$_3Cl_2$[48] (0.300 g, 0.730 mmol) in THF (40 mL) was added 1,2-bis(diethylphosphino)ethane (depe, 0.315 g, 1.53 mmol) and $NaBPh_4$ (0.375 g, 1.10 mmol). The reaction mixture was refluxed for 18 h. During this time, the solution converted from light green to magenta. The reaction mixture was allowed to cool to room temperature and the volatile components were removed under vacuum. The resulting magenta film was extracted into CH_2Cl_2 (3 x 10 mL) and the resulting solution filtered through Celite. Addition of pentane resulted in precipitation of a magenta powder. This was collected by filtration, washed with toluene, and

dried overnight under vacuum (0.295 g, 0.336 mmol, 46% yield). The complex can be stored and handled in air. ^{1}H NMR (CD_2Cl_2, 500.13 MHz, Figure 6.38): δ 7.38 (br m, 8H, *o*-BPh_4); 7.09 (t, 8H, *m*-BPh_4); 6.94 (t, 4H, *o*-BPh_4); 2.05 (br overlapping m, 24H, $PC\underline{H}_2CH_3$ and PCH_2); 1.31 (quin, 12H, $PCH_2C\underline{H}_3$); 1.23 (quin, 12H, $PCH_2C\underline{H}_3$). $^{13}C\{^{1}H\}$ NMR (CD_2Cl_2, 125.75 MHz, Figure 6.39): δ 164.40 (m, $^{1}J_{CB}$ = 50 Hz, BPh_4); 136.25 (BPh_4); 125.95 (m, $^{1}J_{CB}$ = 3 Hz, BPh_4); 122.06 (BPh_4); 20.82 (quin, $^{1}J_{CP}$ = 10 Hz, PCH_2); 19.40 (quin, $^{1}J_{CP}$ = 5 Hz, $P\underline{C}H_2CH_3$); 18.46 (quin, $^{1}J_{CP}$ = 6 Hz, $PCH_2\underline{C}H_3$) 8.69 (PCH_2CH_3); 7.69 (PCH_2CH_3). $^{31}P\{^{1}H\}$ NMR (CD_2Cl_2, 202.45 MHz, Figure 6.40): 45.95. IR (ATR, cm^{-1}): 948(ν_{Mo-O}). HR-ESI-MS (CH_2Cl_2, 298 K): *m/z* 561.131(M^+, rel. int. 100, calc. 561.14).

[Mo(O)(dcype)$_2$Cl]BPh$_4$ (**6**[BPh_4]). To a stirred room temperature solution of Mo(O)(PMe_3)$_3$$Cl_2$[48] (0.300 g, 0.730 mmol) in THF (40 mL) was added 1,2-bis(dicyclohexylphosphino)ethane (dcype, 0.650 g, 1.53 mmol) and $NaBPh_4$ (0.375 g, 1.10 mmol). The reaction mixture was stirred at 50 °C overnight. During this time, the green solution converted to a dark blue solution. The reaction mixture was cooled to room temperature and the volatile components were removed under vacuum. The resulting dark blue film was extracted into CH_2Cl_2 (3 x 10 mL), and the resulting solution was filtered through Celite. Addition of pentane resulted in the precipitation of a light blue powder. This was collected by filtration, washed with toluene, and dried overnight under vacuum, providing a light blue powder (0.532 g, 0.406 mmol, 56% yield). This product can be handled and stored in the air. ^{1}H NMR (CD_2Cl_2, 500.13 MHz, Figure 6.41-6.42): δ 7.32 (br s, *o*-BC_6H_5, 8H); 7.04 (t, *m*-BC_6H_5, 8 H); 6.89 (t, *p*-BC_6H_5, 4H); 2.31 (br t, H_A, 4H); 2.15 (overlapping d, H_C, 16H); 1.89 (m, H_E, H_B, 24H); 1.75 (d, H_B, 8H); 1.57 (m, H_A, 4H); 1.45 (m, PCH_2, 8H); 1.27 (m, H_D, H_F, H_G, 32H). $^{13}C\{^{1}H\}$ NMR (CD_2Cl_2, 125.75 MHz, Figure 6.43): 164.44 (m, $^{1}J_{CB}$ = 50 Hz, BPh_4); 136.28 (BPh_4); 125.96 (m,

$^1J_{CB}$ = 3 Hz, BPh_4); 122.06 (BPh_4); 36.84 (quin, J_{CP} = 3 Hz, cy); 35.39 (quin, J_{CP} = 3 Hz, cy) ; 29.63 (cy); 29.56 (cy); 29.14 (cy); 28.70 (cy); 28.07 (cy); 27.95 (cy); 27.80 (cy); 27.68 (cy); 26.32 (cy); 26.25 (cy); 18.45 (quin, $^1J_{CP}$ = 8 Hz, PCH_2). $^{31}P\{^1H\}$ NMR (CD_2Cl_2, 161.97 MHz, Figure 6.44): 46.22. IR (ATR, cm^{-1}): 947 (ν_{Mo-O}). HR-ESI-MS (CH_2Cl_2, 298 K): *m/z* 993.497 (M^+, rel. int. 100, calc. 993.52). Anal. Calc. (Found) for $C_{76}H_{116}BClOMoP_4$: C 69.58 (69.63); H 8.91 (8.99).

[W(O)(dppe)$_2$Cl]BPh$_4$ (7[BPh$_4$]).[49] Additional characterization data: ^1H NMR (CD_2Cl_2, 500.13 MHz, Figure 6.45) δ 7.46 (m, *o,p*-PC_6H_5, 12H); 7.36 (t, PC_6H_5, 4H); 7.34 (m, *m*-PC_6H_5 and *o*-BPh_4, 16H); 7.11 (t, *m*-PC_6H_5, 8H); 7.00 (t, *m*-BPh_4, 8H); 6.93 (m, *o*-PC_6H_5, 8H); 6.85 (t, *p*-BPh_4, 4H) . $^{13}C\{^1H\}$ NMR (CD_2Cl_2, 125.75 MHz, Figure 6.46): 164.52 (BPh_4); 136.27 (BPh_4); 133.67 (PC_6H_5); 133.21 (PC_6H_5); 132.06 (PC_6H_5); 131.38 (PC_6H_5); 129.35 (PC_6H_5); 128.96 (PC_6H_5); 125.96 (BPh_4); 122.06 (BPh_4); 32.24 (PCH_2). $^{31}P\{^1H\}$ NMR (CD_2Cl_2, 161.97 MHz, Figure 6.47): 24.99 (s with ^{183}W-satellites, $^1J_{WP}$ = 313 Hz). HRA-ESI-MS (CH_2Cl_2, 298 K): *m/z* 1031.167 (M^+, rel. int. 100, calc. 1031.19).

[W(O)(dppe)$_2$Cl] (7). In a N_2 glovebox, [W(O)(dppe)$_2$Cl]BPh_4 (0.500g, 0.369 mmol) and Na/Hg (0.172 mL, 0.4% w/w, 0.406 mmol Na) were added to a Schlenk flask equipped with a stir bar. To the flask was added THF (20 mL) *via* cannula. Upon addition the [W(O)(dppe)$_2$Cl]BPh_4 was observed to dissolve, leaving a pink solution over Na/Hg. The Na/Hg was agitated by stirring for 1 h during which time the pink suspension converted to a dark yellow-green suspension. The volatile components of the suspension were removed by vacuum, and the resulting dark yellow-green film was extracted into C_6H_6 (20 mL) and filtered into a new Schlenk flask. The volatile components of the green solution were removed by vacuum and

collected to produce a black solid (0.360 g, 0.350 mmol, 94 % crude yield). Raman (solid, λ_{ex}=633 nm, cm^{-1}): 790 (W-O).

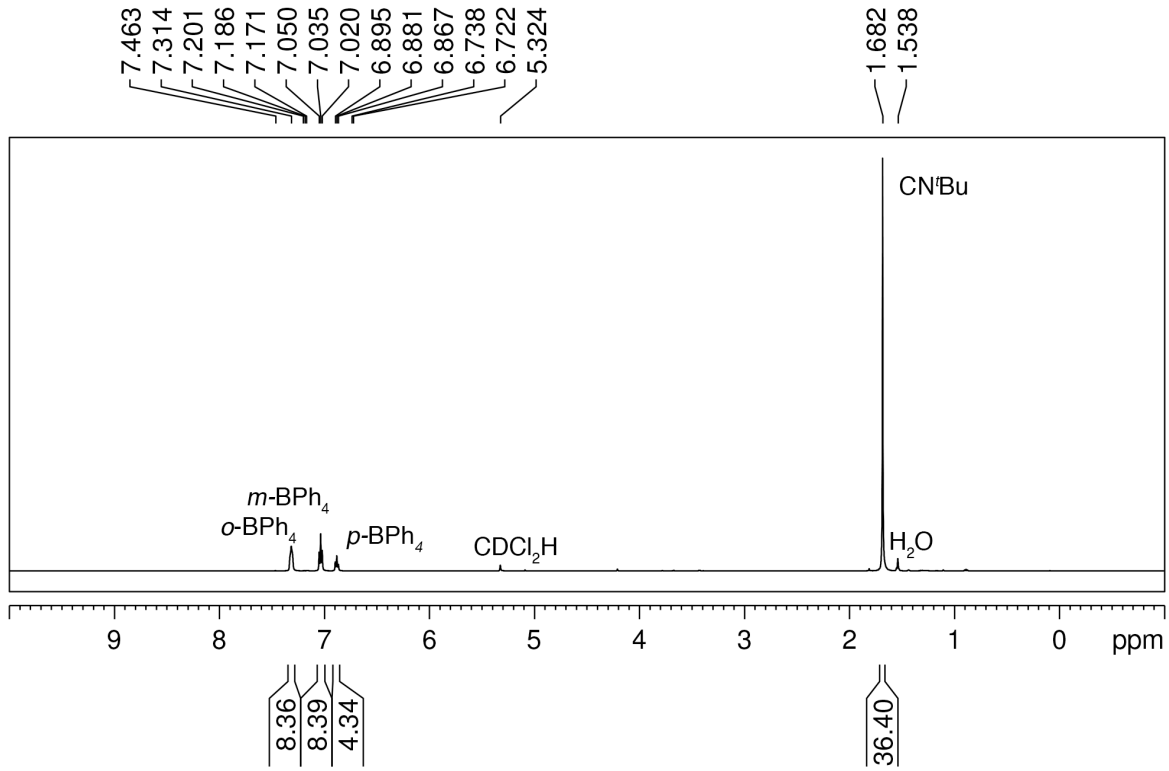

Figure 6.26. ^{1}H NMR spectrum of $[Mo(O)(CN^{t}Bu)_4Cl]BPh_4$ (**1**[BPh_4]) in CD_2Cl_2. Note: the residual water observed in this sample was also recorded in a blank NMR spectrum.

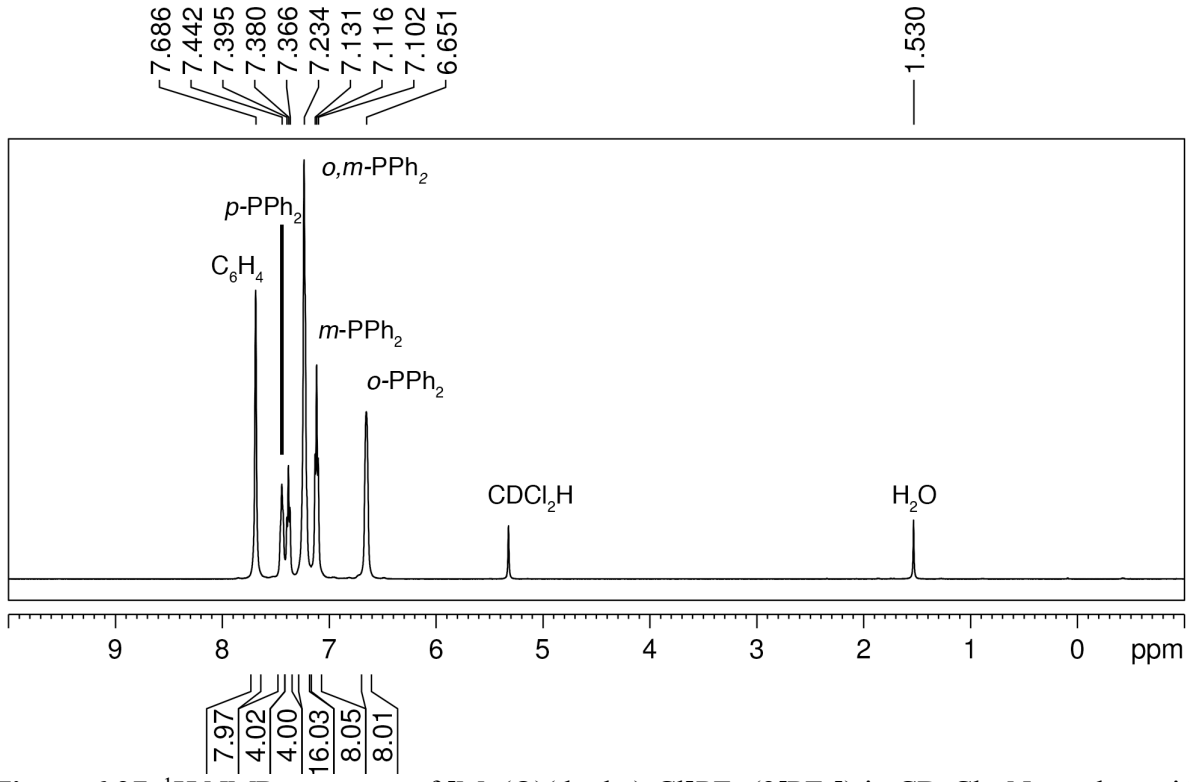

Figure 6.27. ^{1}H NMR spectrum of [Mo(O)(dppbz)$_2$Cl]PF$_6$ (**2**[PF$_6$]) in CD_2Cl_2. Note: the residual water observed in this sample was also recorded in a blank NMR spectrum.

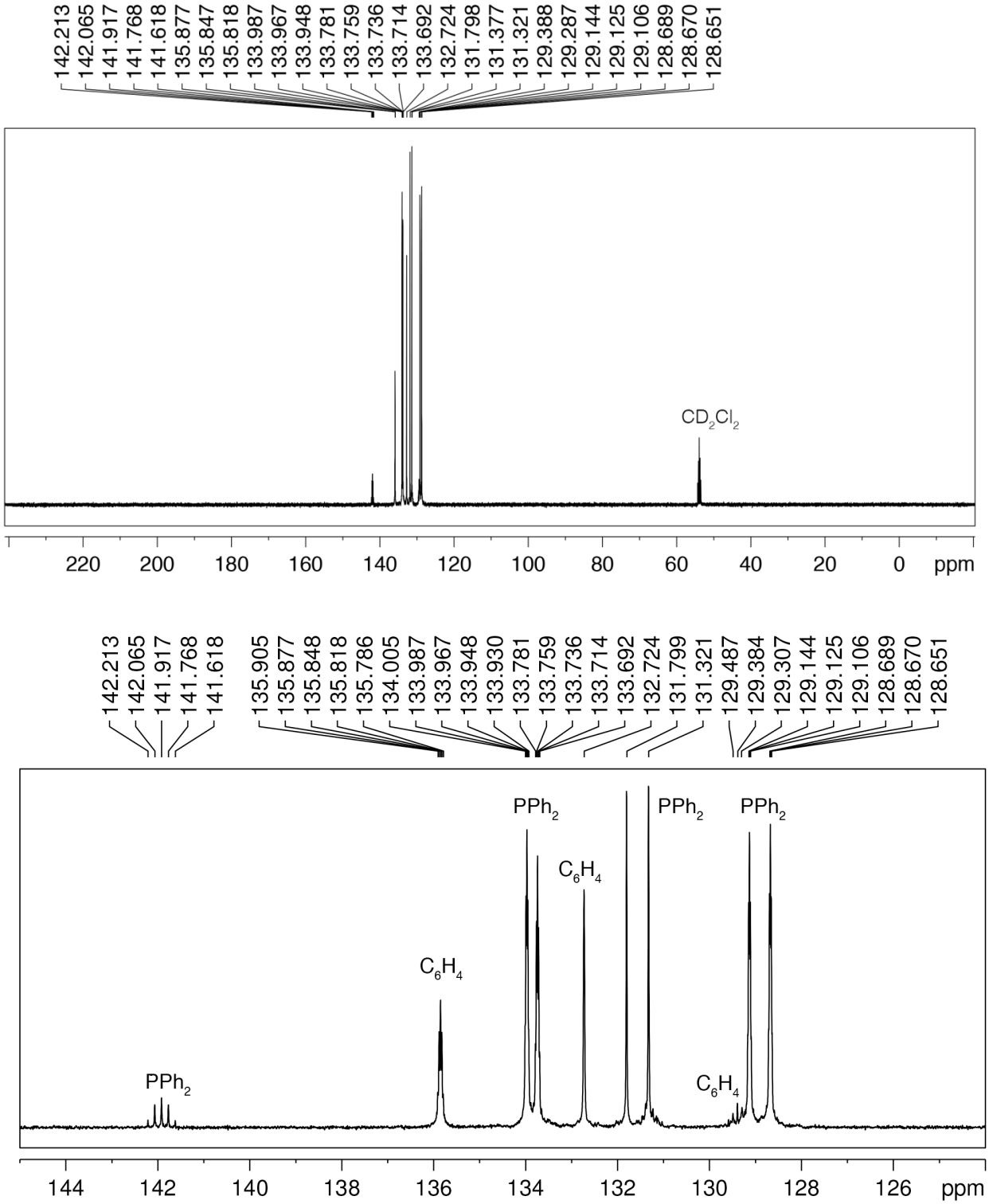

Figure 6.28. $^{13}C\{^{1}H\}$ NMR spectrum of $[Mo(O)(dppbz)_2Cl]PF_6$ (**2**$[PF_6]$) in CD_2Cl_2. The bottom spectrum is an expansion of the top spectrum.

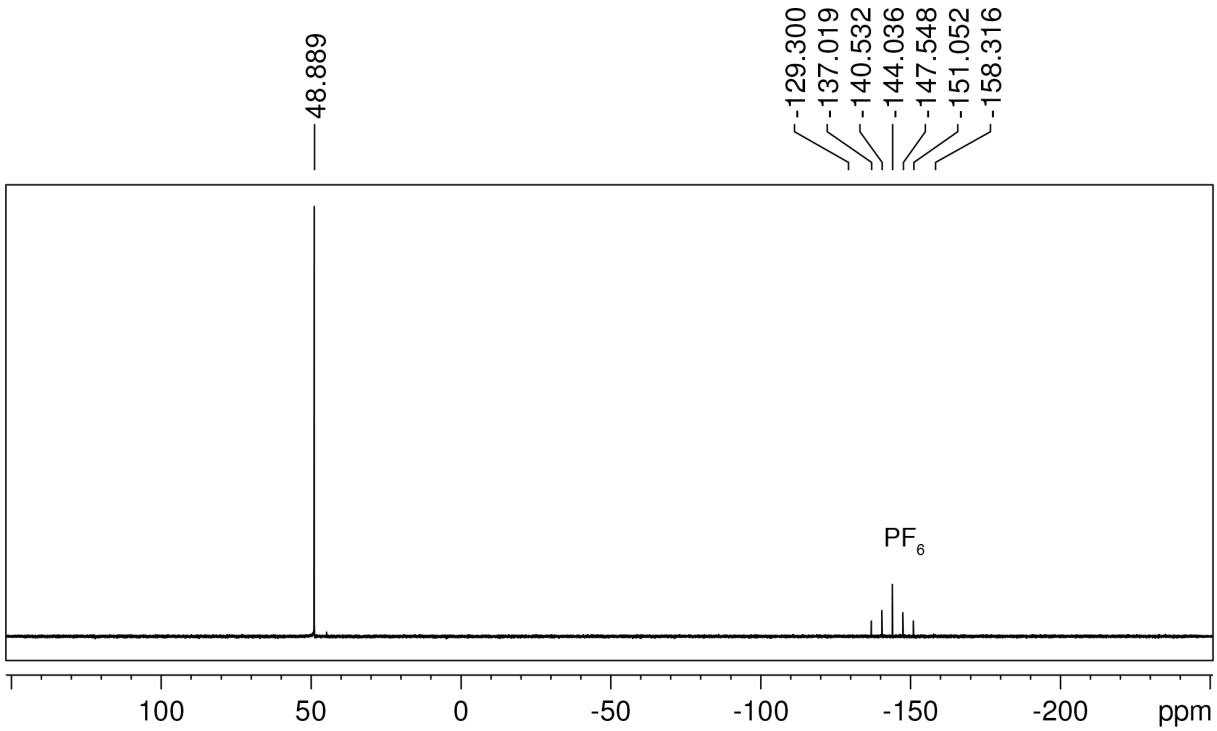

Figure 6.29. $^{31}P\{^{1}H\}$ NMR spectrum of $[Mo(O)(dppbz)_2Cl]PF_6$ (**2**$[PF_6]$) in CD_2Cl_2.

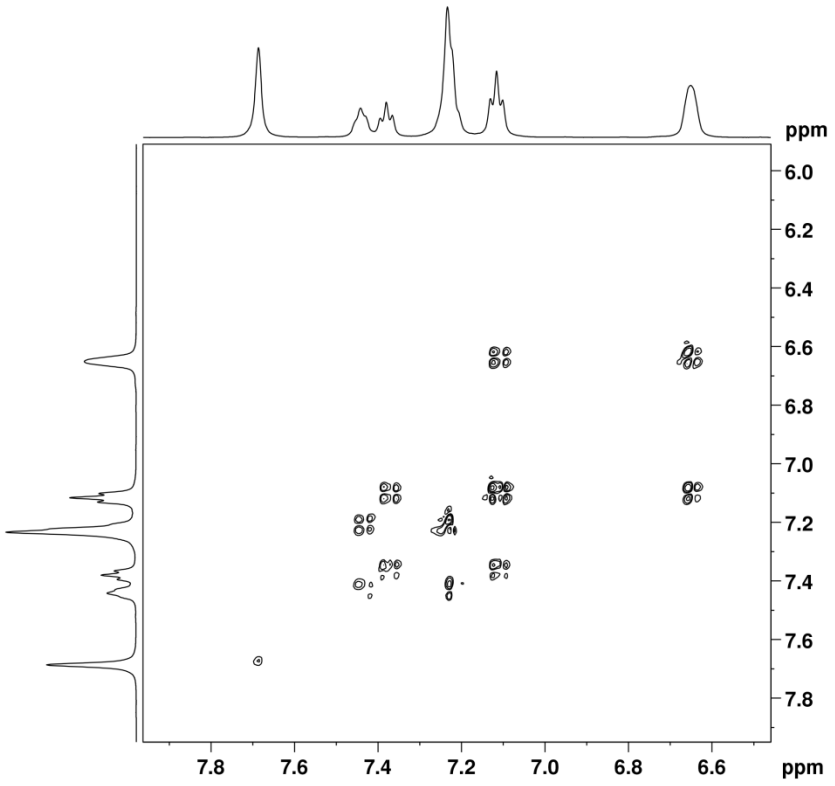

Figure 6.30. $^{1}H–^{1}H$ COSY NMR spectrum of $[Mo(O)(dppbz)_2Cl]PF_6$ (**2**$[PF_6]$) in CD_2Cl_2.

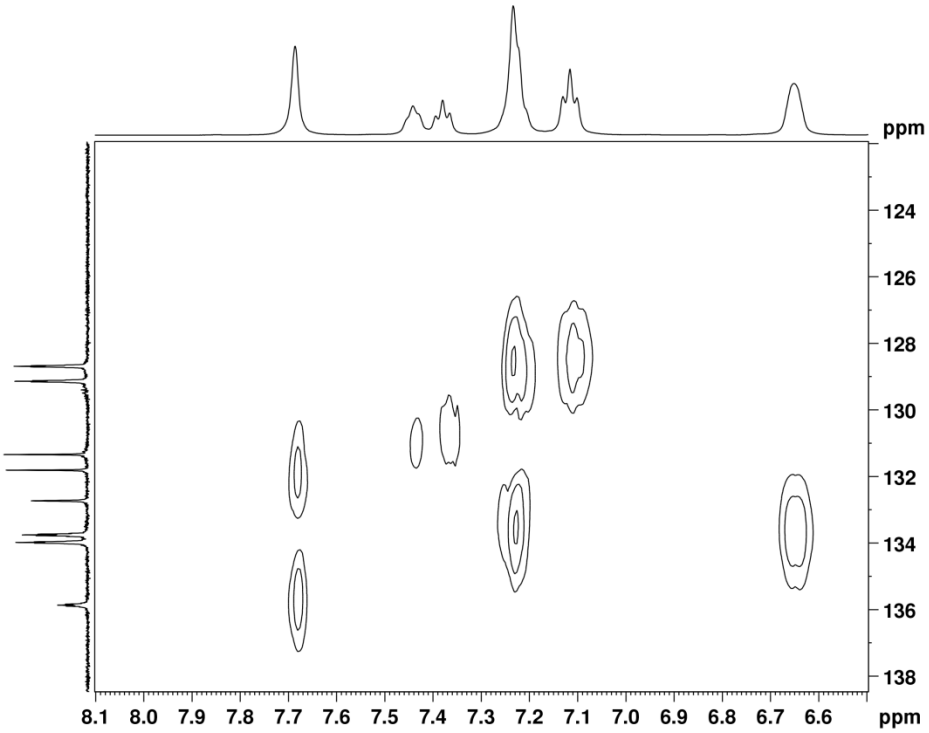

Figure 6.31. $^{1}H–^{13}C\{^{1}H\}$ HMQC NMR spectrum of $[Mo(O)(dppbz)_2Cl]PF_6$ (**2**$[PF_6]$) in CD_2Cl_2.

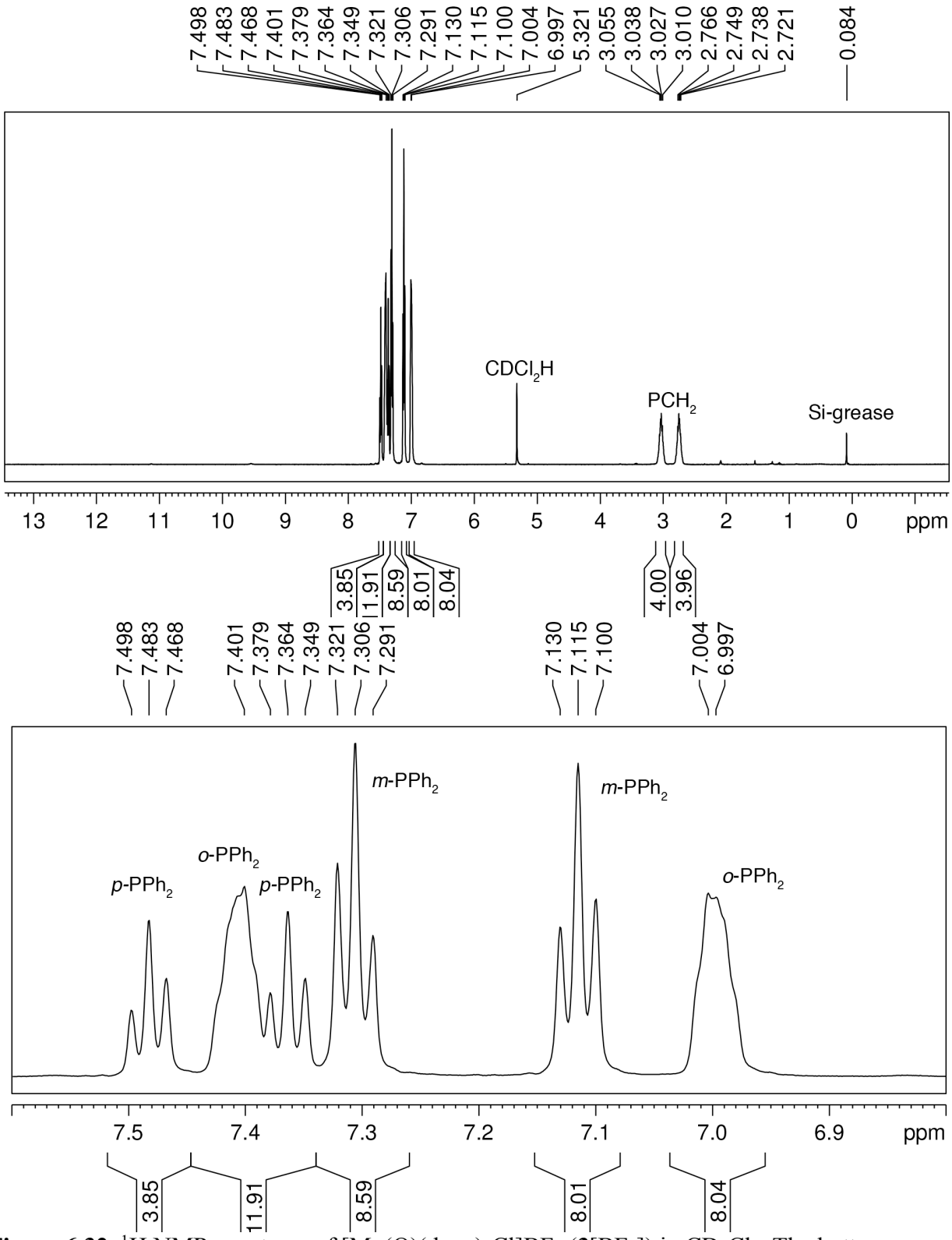

Figure 6.32. ^{1}H NMR spectrum of $[Mo(O)(dppe)_2Cl]BF_4$ (**3**$[BF_4]$) in CD_2Cl_2. The bottom spectrum is an expansion of the top spectrum.

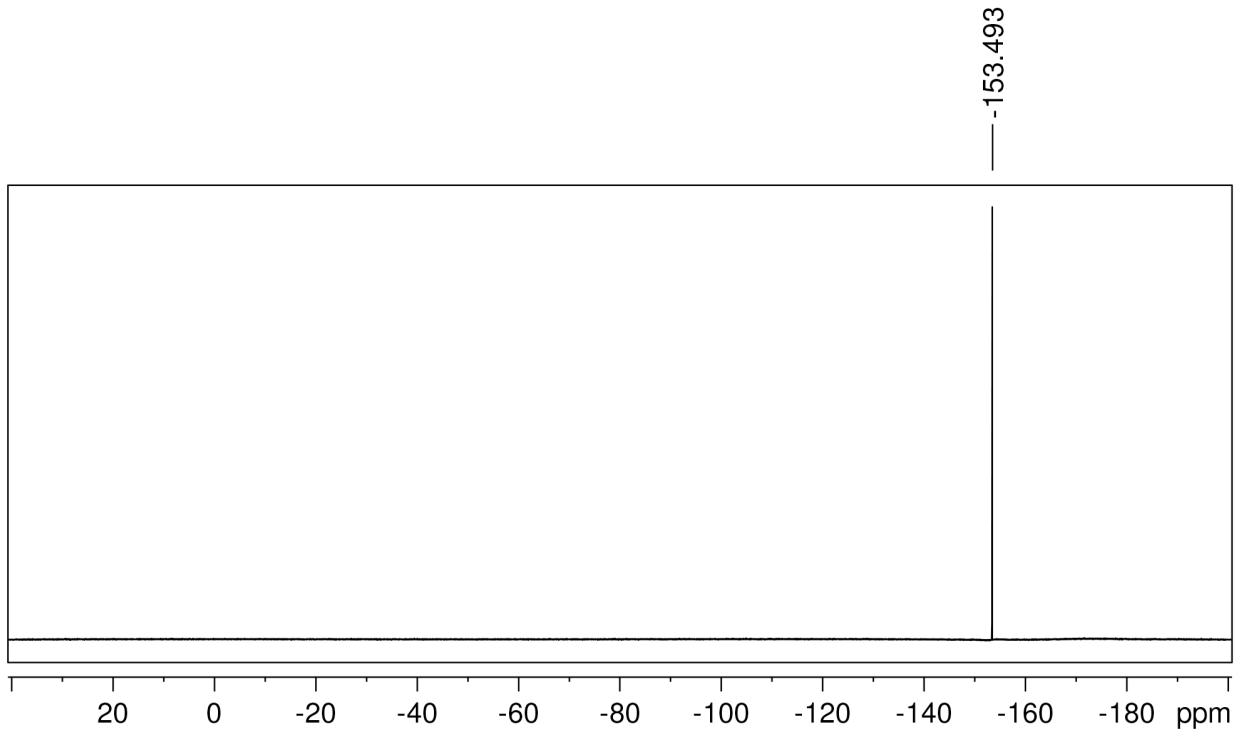

Figure 6.33. ^{19}F NMR spectrum of $[Mo(O)(dppe)_2Cl]BF_4$ (**3**$[BF_4]$) in CD_2Cl_2.

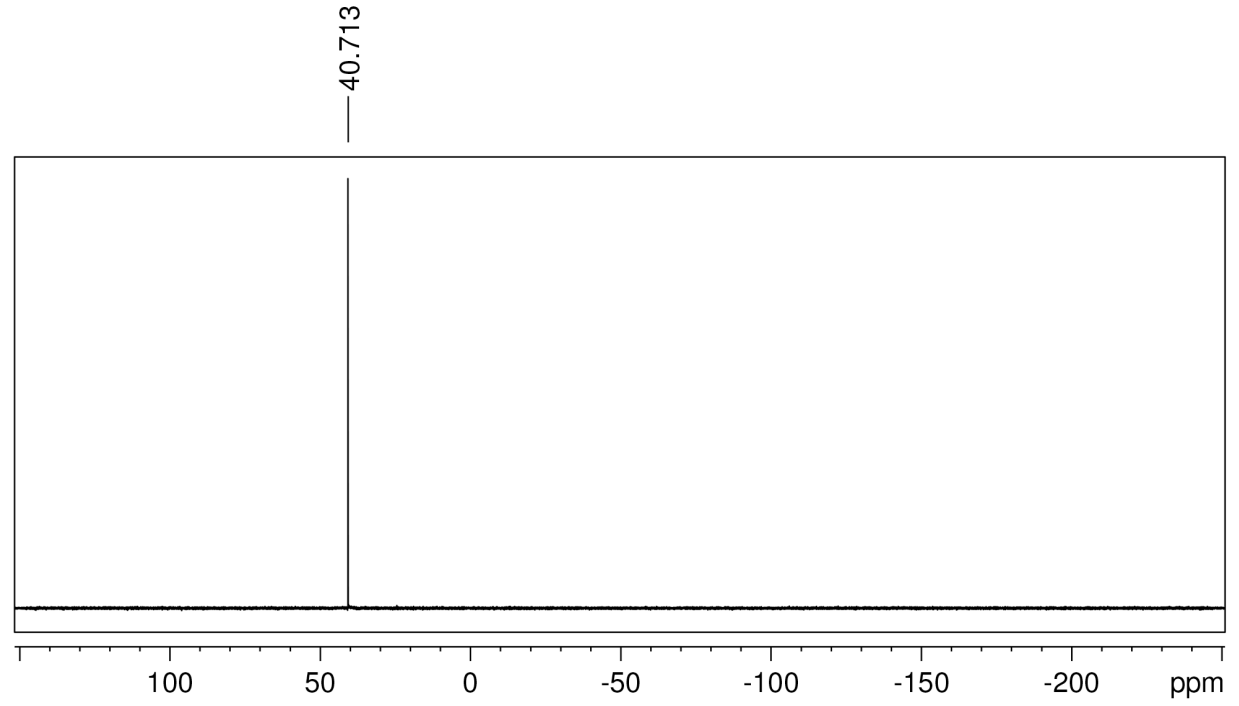

Figure 6.34. $^{31}P\{^1H\}$ NMR spectrum of $[Mo(O)(dppe)_2Cl]BF_4$ (**3**$[BF_4]$) in CD_2Cl_2.

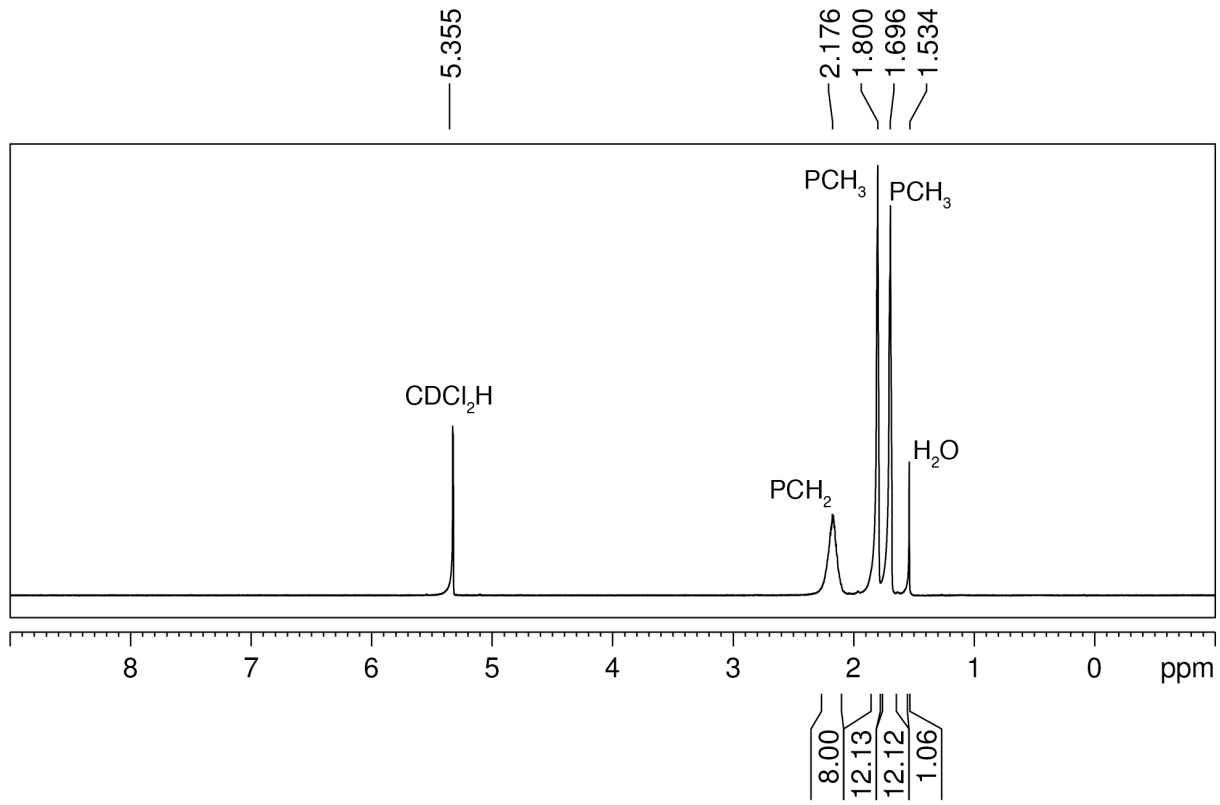

Figure 6.35. ^{1}H NMR spectrum of $[Mo(O)(dmpe)_2Cl]PF_6$ (**4**$[PF_6]$) in CD_2Cl_2. Note: the residual water observed in this sample was also recorded in a blank NMR spectrum.

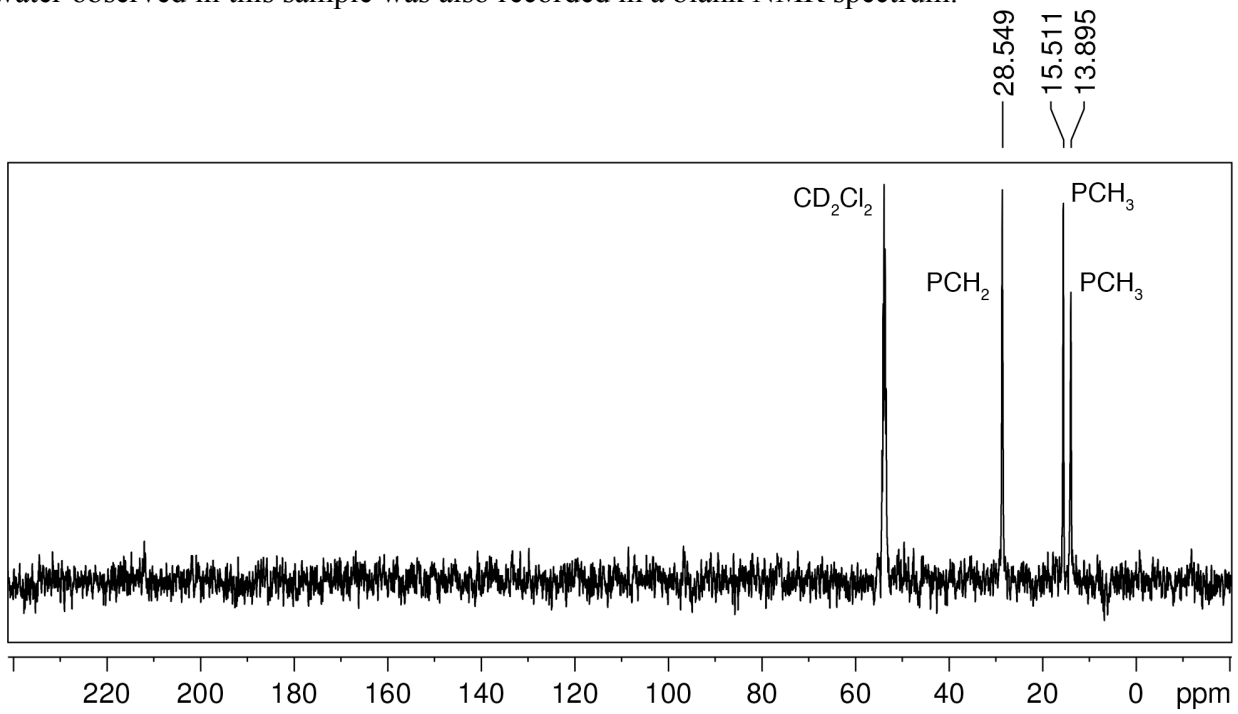

Figure 6.36. $^{13}C\{^{1}H\}$ NMR spectrum of $[Mo(O)(dmpe)_2Cl]PF_6$ (**4**$[PF_6]$) in CD_2Cl_2.

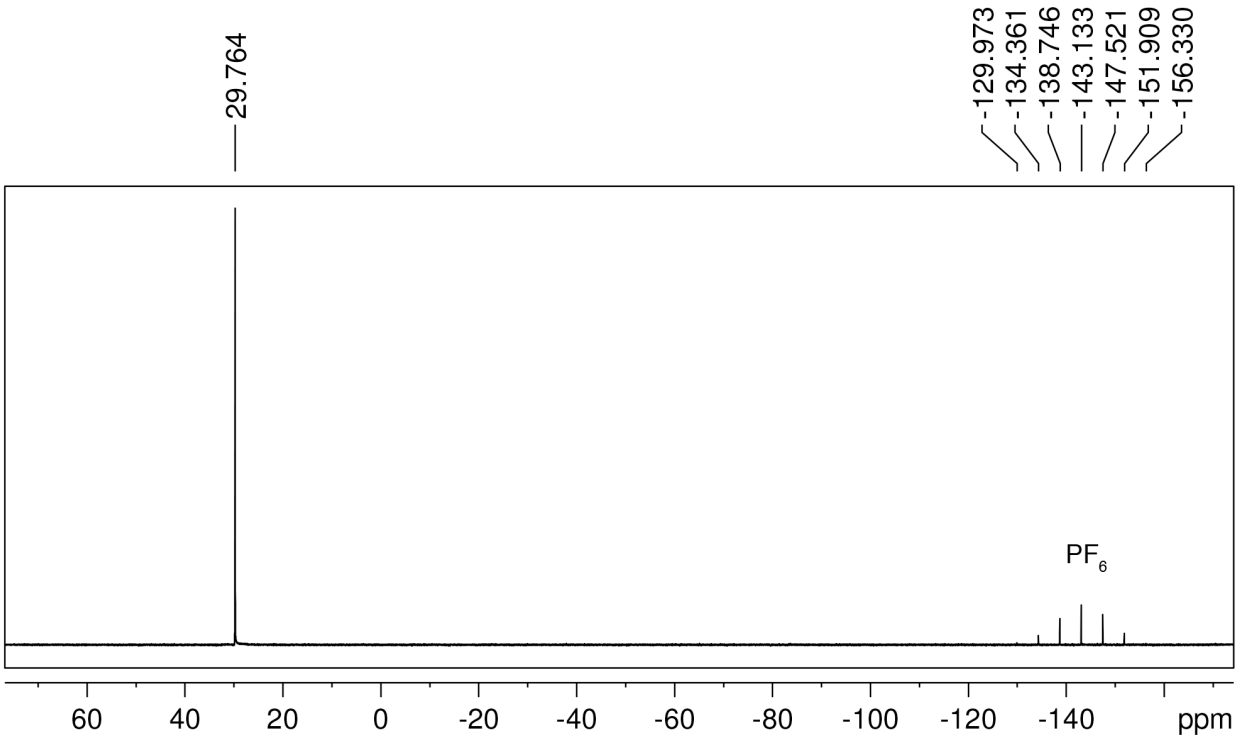

Figure 6.37. $^{31}P\{^{1}H\}$ NMR spectrum of $[Mo(O)(dmpe)_2Cl]PF_6$ (**4**$[PF_6]$) in CD_2Cl_2.

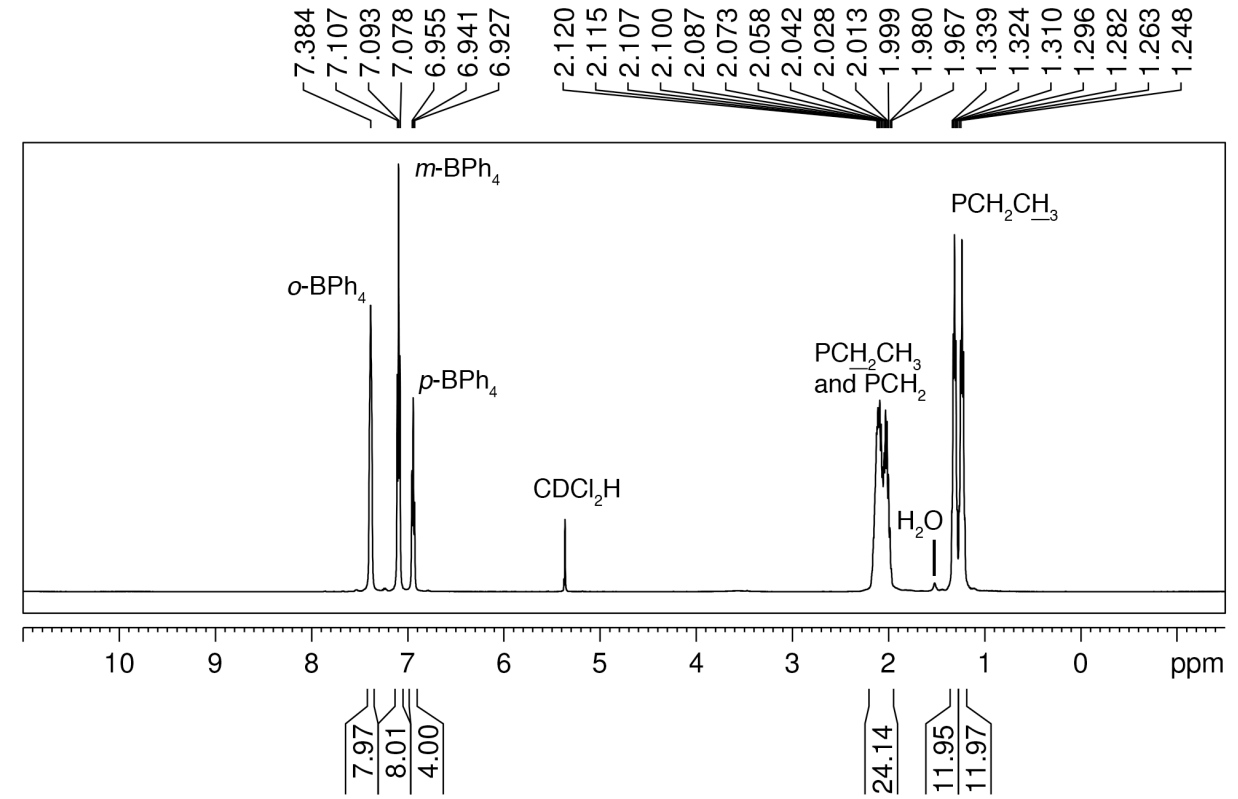

Figure 6.38. ^{1}H NMR spectrum of $[Mo(O)(depe)_2Cl]BPh_4$ (**5**$[BPh_4]$) in CD_2Cl_2. Note: the residual water observed in this sample was also recorded in a blank NMR spectrum.

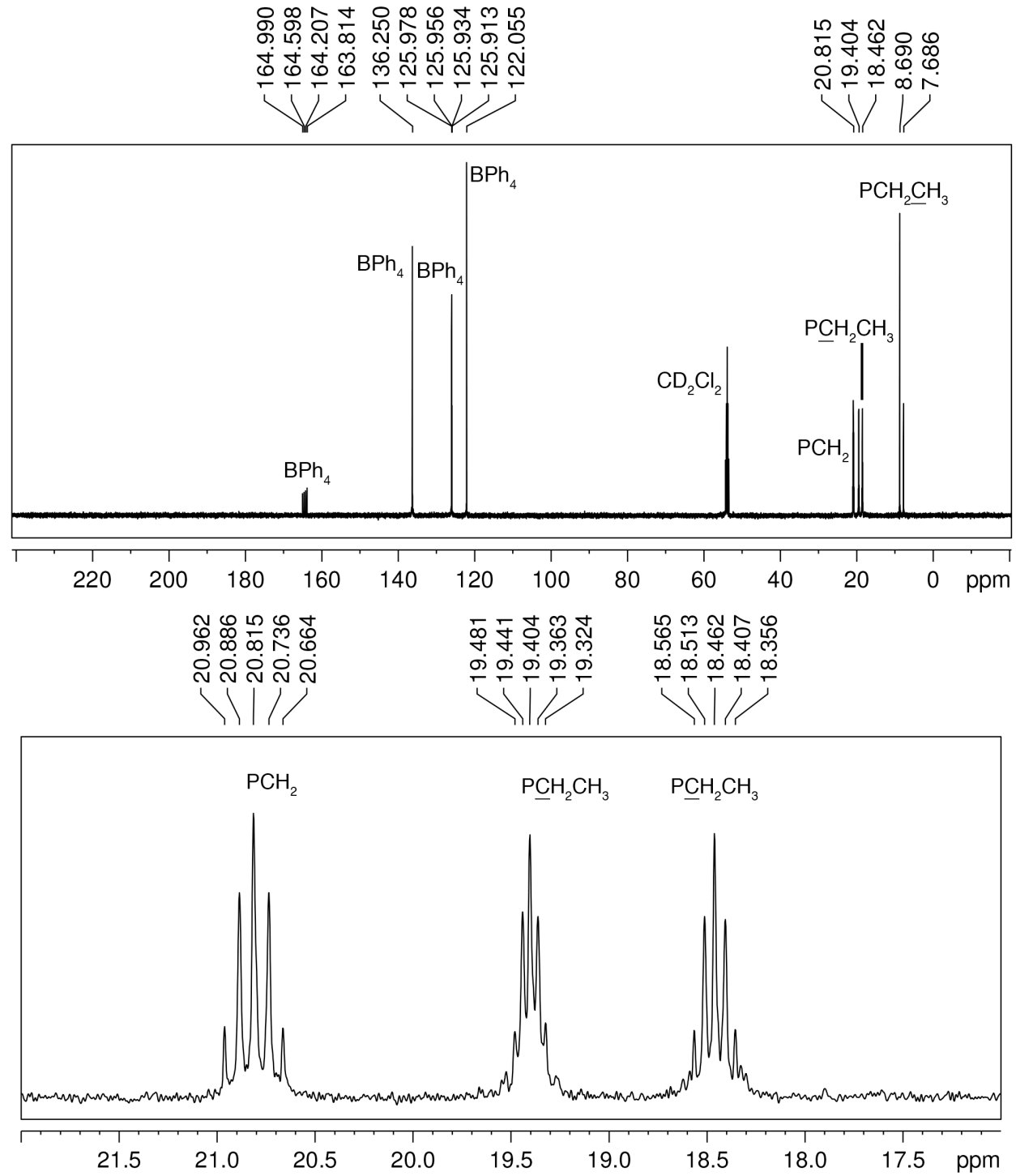

Figure 6.39. $^{13}C\{^{1}H\}$ NMR spectrum of $[Mo(O)(depe)_2Cl]BPh_4$ (**5**$[BPh_4]$) in CD_2Cl_2. The bottom spectrum is an expansion of the top spectrum.

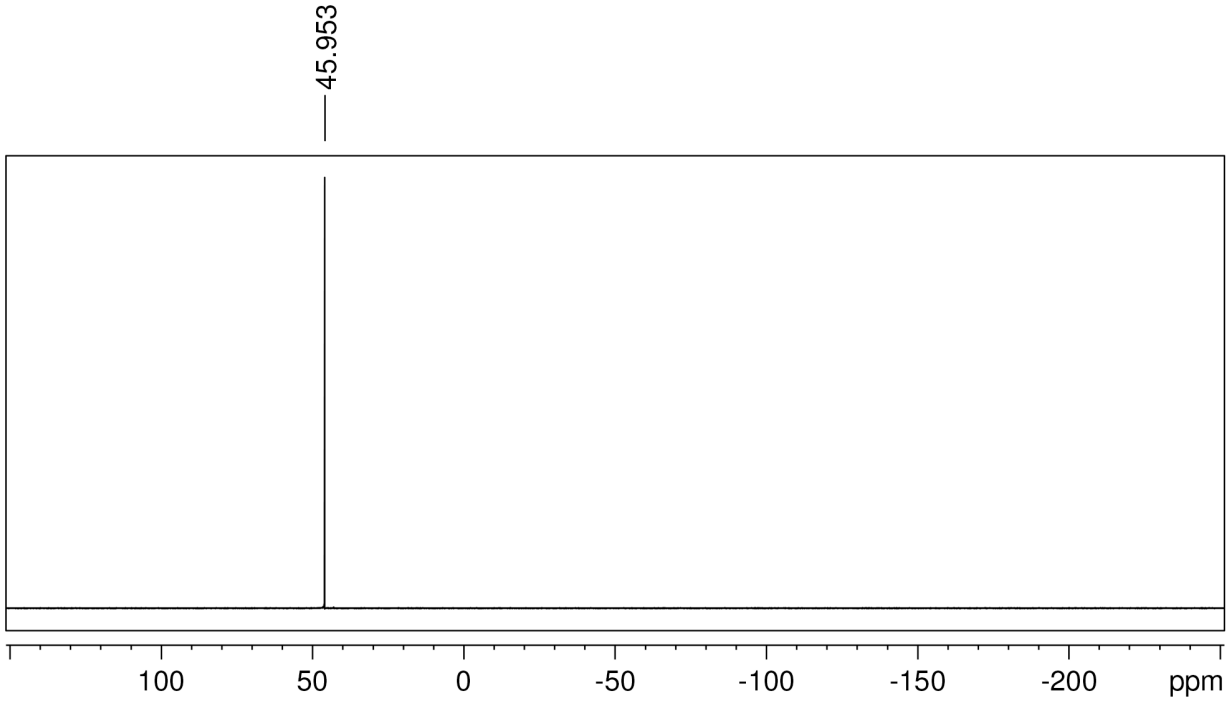

Figure 6.40. $^{31}P\{^{1}H\}$ NMR spectrum of $[Mo(O)(depe)_2Cl]BPh_4$ (**5**$[BPh_4]$) in CD_2Cl_2.

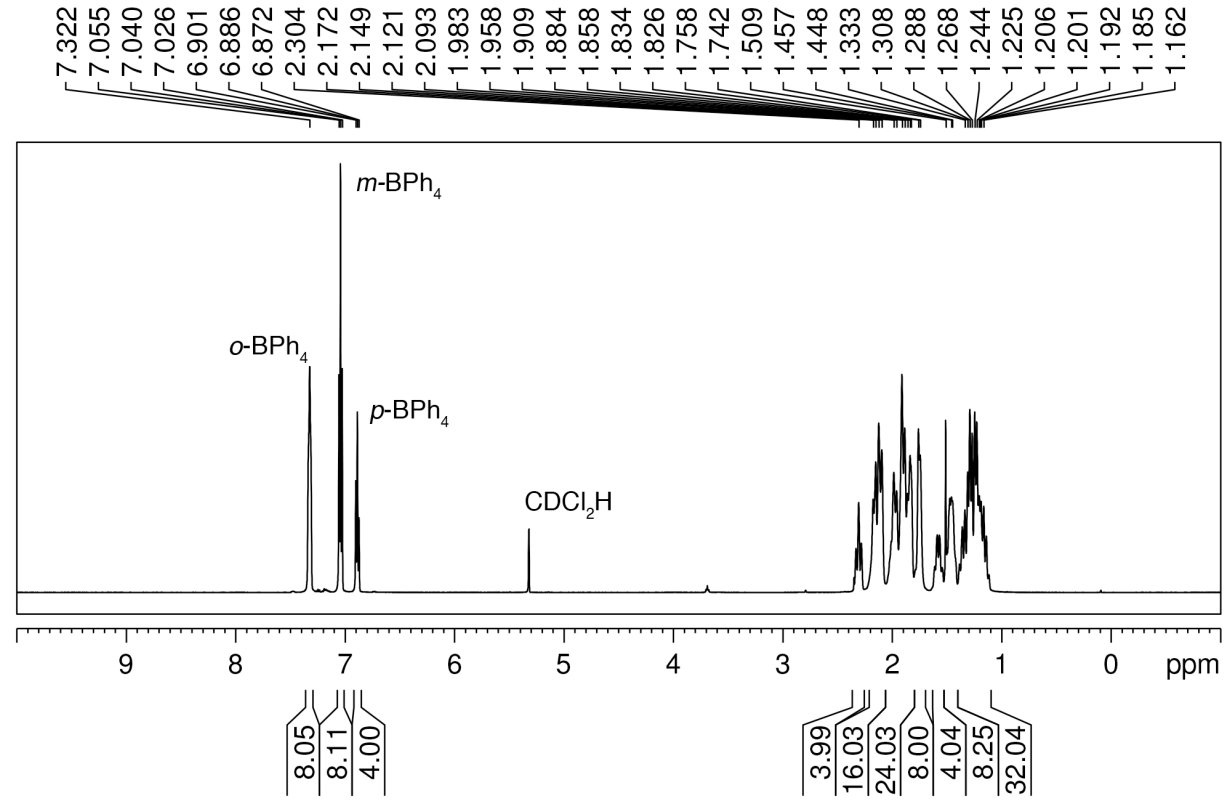

Figure 6.41. ^{1}H NMR spectrum of $[Mo(O)(dcype)_2Cl]BPh_4$ (**6**$[BPh_4]$) in CD_2Cl_2. Note: the residual water observed in this sample was also recorded in a blank NMR spectrum.

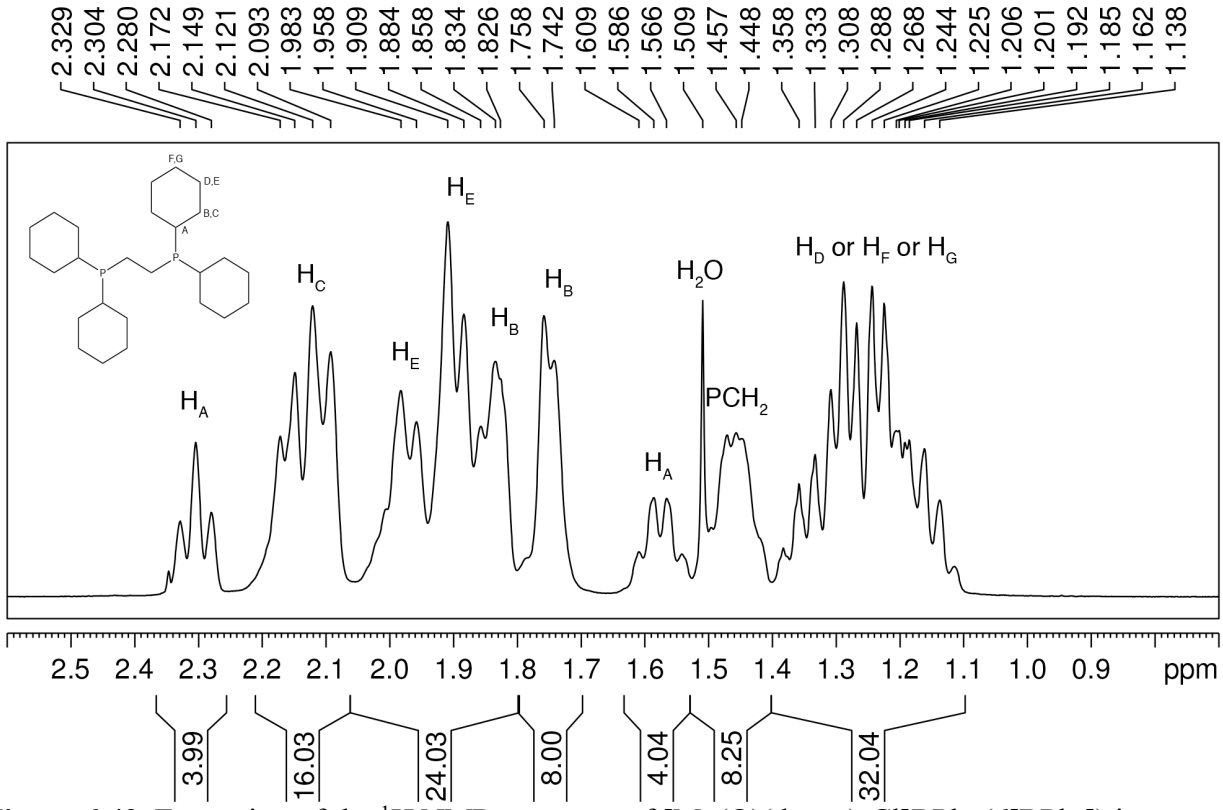

Figure 6.42. Expansion of the ^{1}H NMR spectrum of $[Mo(O)(dcype)_2Cl]BPh_4$ (**6**$[BPh_4]$) in CD_2Cl_2. Note: the residual water observed in this sample was also recorded in a blank NMR spectrum. Assignments by analogy to prior work in the group.[50]

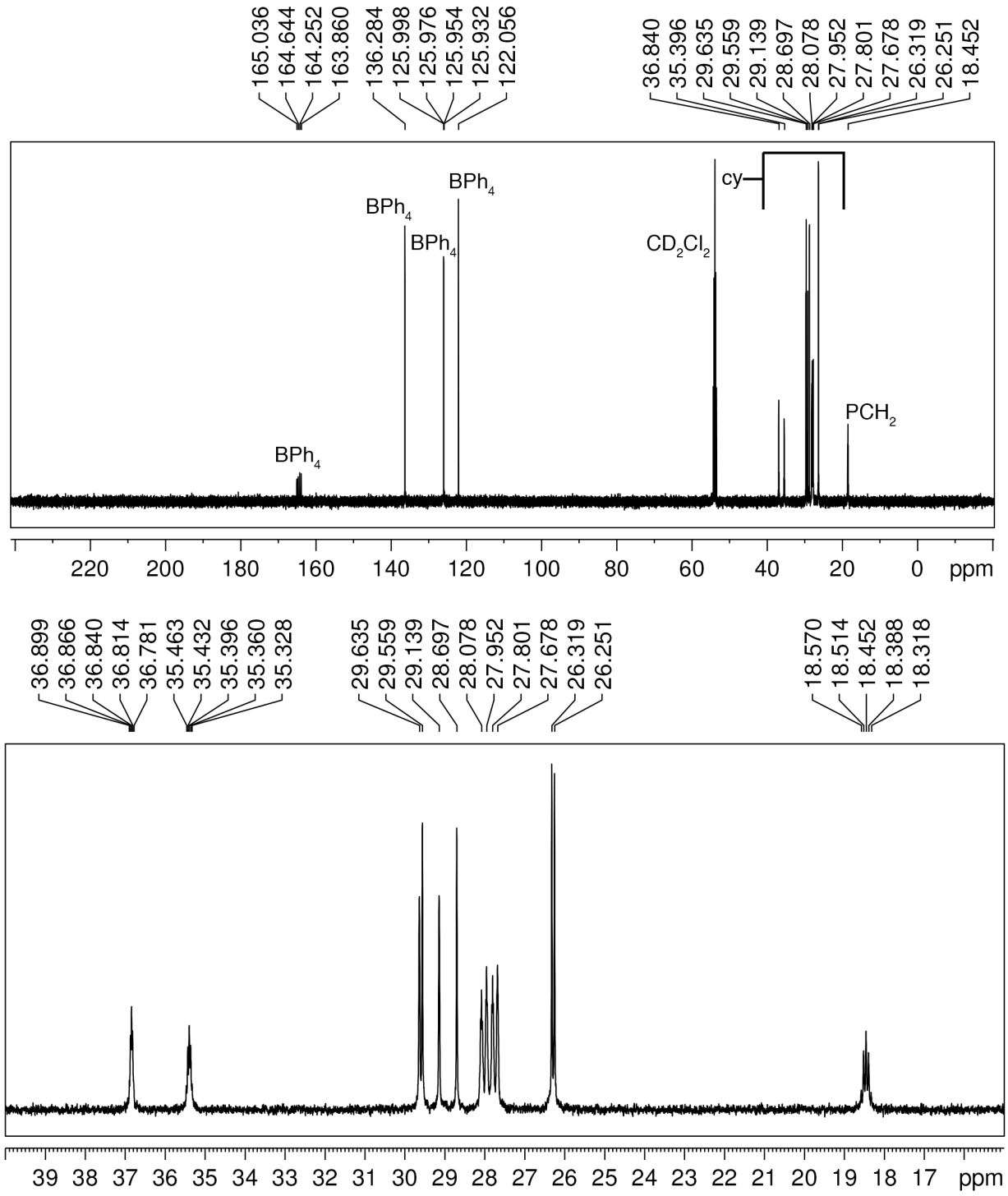

Figure 6.43. $^{13}C\{^{1}H\}$ NMR spectrum of $[Mo(O)(dcype)_2Cl]BPh_4$ (**6**[BPh_4]) in CD_2Cl_2. The bottom spectrum is an expansion of the top spectrum.

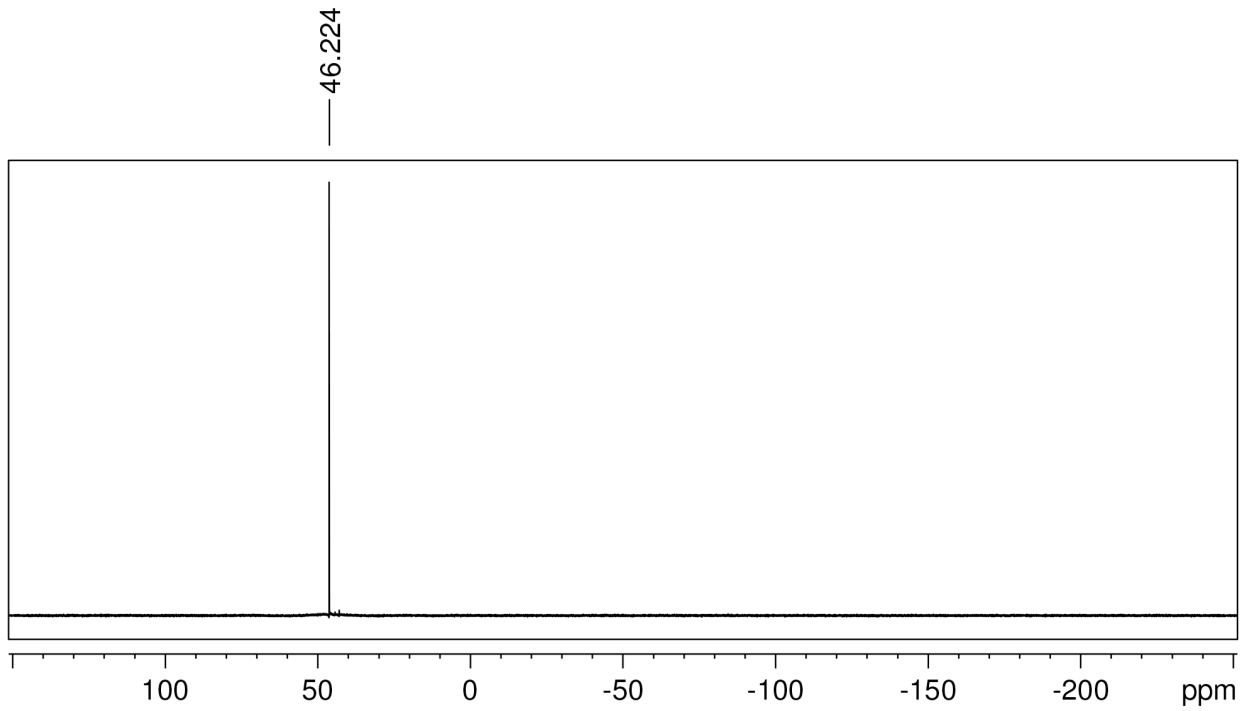

Figure 6.44. $^{31}P\{^{1}H\}$ NMR spectrum of $[Mo(O)(dcype)_2Cl]BPh_4$ (**6**$[BPh_4]$) in CD_2Cl_2.

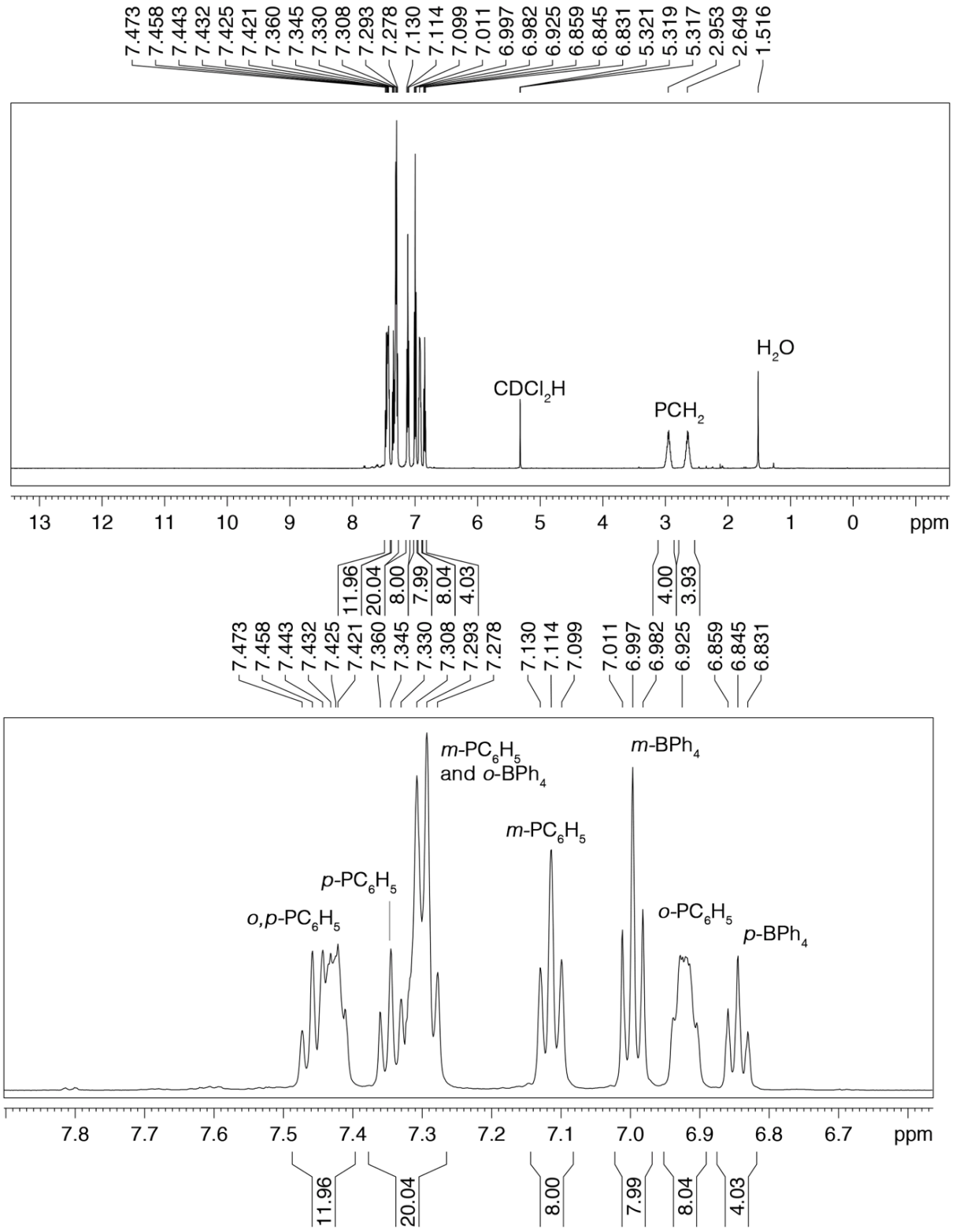

Figure 6.45. ^{1}H NMR spectrum of [W(O)(dppe)$_2$Cl]BPh$_4$ (**7**[BPh$_4$]) in CD_2Cl_2. The bottom spectrum is an expansion of the top spectrum. Note: the residual water observed in this sample was also recorded in a blank NMR spectrum.

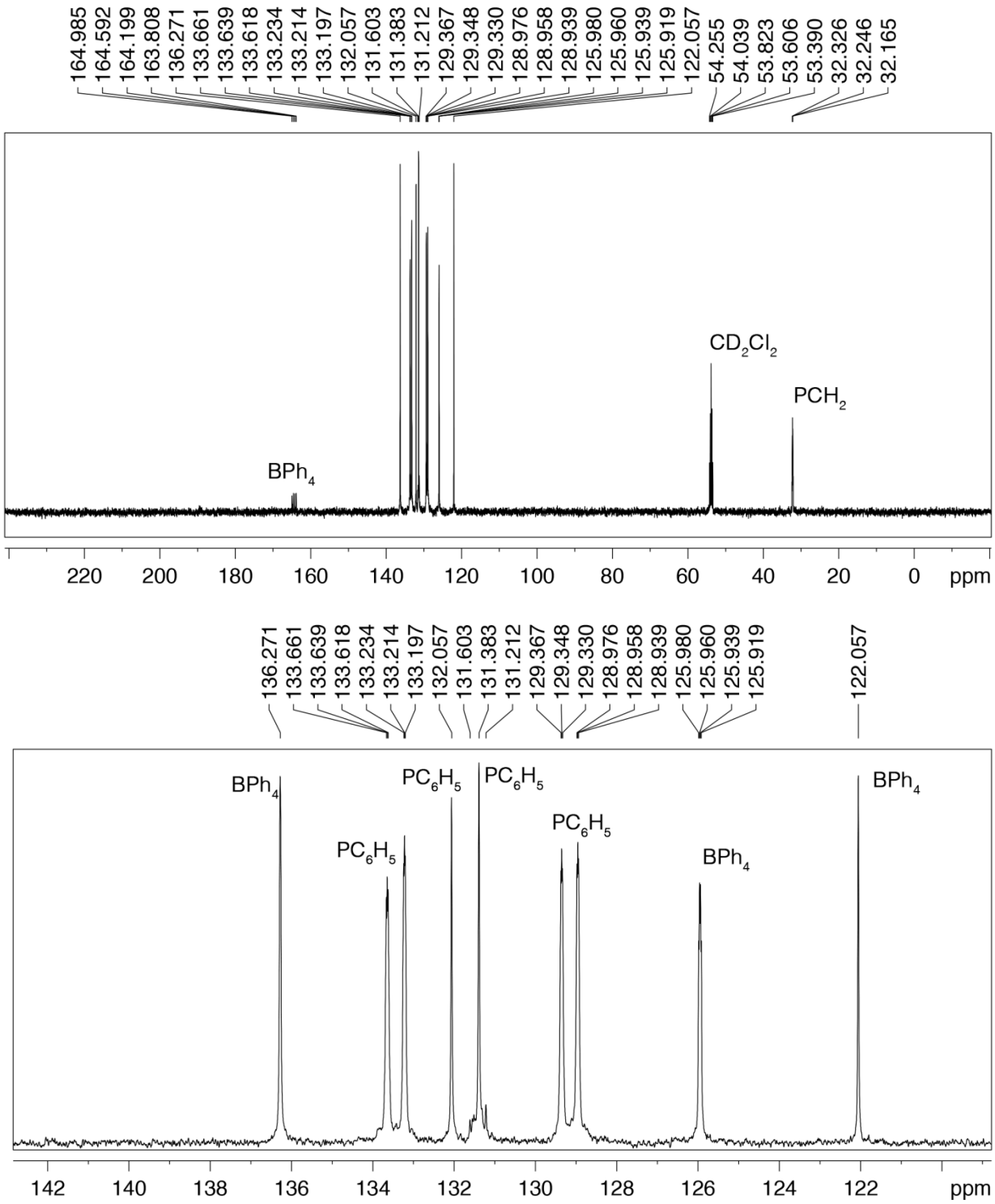

Figure 6.46. $^{13}C\{^{1}H\}$ NMR spectrum of $[W(O)(dppe)_2Cl]BPh_4$ (**7**[BPh_4]) in CD_2Cl_2. The bottom spectrum is an expansion of the top spectrum.

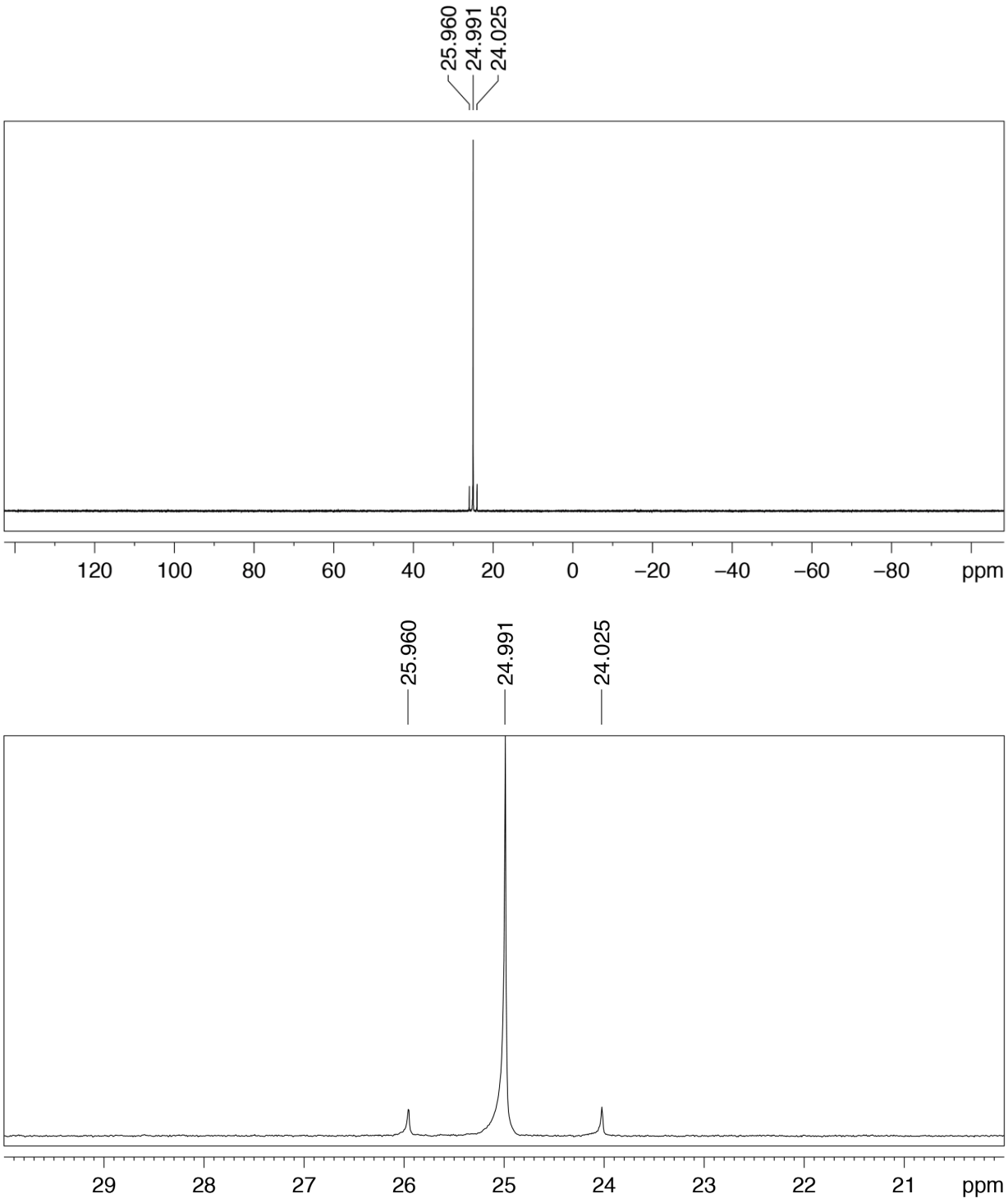

Figure 6.47. $^{31}P\{^{1}H\}$ NMR spectrum of $[W(O)(dppe)_2Cl]BPh_4$ (**7**$[BPh_4]$) in CD_2Cl_2. The bottom spectrum is an expansion of the top spectrum.

Table 6.14. Crystal data and structure refinement parameters.

Parameter	**3**(BPh_4)	**3**
Empirical formula	$C_{78}H_{72}BCl_3MoOP_4$	$C_{58}H_{54}ClMoOP_4$
Formula weight	1362.33	1022.28
Temperature, K	100(2)	100(2)
Crystal system	orthorhombic	monoclinic
Space group	$P2_12_12_1$	$C2/c$
*a,*Å	25.717(2)	27.707(3)
*b,*Å	13.0278(11)	14.1205(11)
*c,*Å	19.729(3)	12.866(4)
α,°	90	90
β,°	90	104.866(4)
γ,°	90	90
Volume, $Å^3$	6609.8(12)	4863.2(7)
Z	4	4
ρ_{calc} , g/cm^3	1.369	1.396
μ, mm^{-1}	0.463	0.498
F(000)	2824.0	2116.0
Crystal size, mm^3	0.32 × 0.12 × 0.1	0.32 × 0.21 × 0.09
Radiation	MoKα (λ = 0.71073)	MoKα (λ = 0.71073)
2Θ range for data collection/°	4.422 – 57.588	4.892 – 55.866
Index ranges	–34 ≤ h ≤ 34	–36≤ h ≤ 36
	–17 ≤ k ≤ 17	–18 ≤ k ≤ 18
	–26 ≤ l ≤ 25	–16 ≤ l ≤ 16
Reflections collected	150649	52581
Independent reflections	16680	5791
	R_{int} = 0.0645	R_{int} = 0.0488
	R_{sigma} = 0.0483	R_{sigma} = 0.0369
Data / restraints / parameters	16680 / 36 / 809	5791 / 6 / 304
Goodness–of–fit on F^2	1.023	1.178
Final *R* indexes ($I \geq 2\sigma(I)$)	R_1 = 0.0606	R_1 = 0.0451
	wR_2 = 0.1372	wR_2 = 0.0911
Final *R* indexes (all data)	R_1 = 0.0760	R_1 = 0.0625
	wR_2 = 0.1436	wR_2 = 0.0957
Largest diff. peak/hole, e• $Å^{-3}$	1.00/–0.71	1.03/–0.42

$R_{int} = \Sigma \mid F_o^2 - \langle F_o^2 \rangle \mid / \Sigma \mid F_o^2 \mid$

$R1 = \Sigma \mid \mid F_o \mid - \mid F_c \mid \mid / \Sigma \mid F_o \mid$

$wR2 = [\Sigma [w (F_o^2 - F_c^2)^2] / \Sigma [w (F_o^2)^2]]^{1/2}$

Goodness–of–fit = $[\Sigma [w (F_o^2 - F_c^2)^2] / (n-p)^{1/2}$; n = no. indep. refl.; p = no. refined parameters

Table 6.15. Selected bond lengths (Å) for **3**(BPh_4).

Atom	Atom	Length	Atom	Atom	Length
Mo1	O1	1.662(15)	C32	C33	1.365(11)
Mo1	Cl1	2.461(5)	C33	C34	1.395(10)
Mo1	P1	2.531(3)	C35	C36	1.531(8)
Mo1	P2	2.577(3)	C37	C38	1.400(8)
Mo1	P3	2.593(3)	C37	C42	1.387(8)
Mo1	P4	2.544(3)	C38	C39	1.383(9)
Mo1A	Cl1A	2.415(14)	C39	C40	1.380(9)
Mo1A	O1A	1.70(2)	C40	C41	1.396(10)
Mo1A	P1	2.558(5)	C41	C42	1.372(9)
Mo1A	P2	2.553(5)	C43	C44	1.382(10)
Mo1A	P3	2.566(5)	C43	C48	1.396(10)
Mo1A	P4	2.606(5)	C44	C45	1.395(10)
P1	C15	1.820(6)	C45	C46	1.395(14)
P1	C21	1.826(7)	C46	C47	1.375(13)
P1	C27	1.834(6)	C47	C48	1.367(10)
P2	C1	1.824(7)	C49	C50	1.398(8)
P2	C7	1.823(7)	C49	C54	1.388(9)
P2	C28	1.842(6)	C50	C51	1.383(9)
P3	C36	1.831(6)	C51	C52	1.391(10)
P3	C37	1.825(6)	C52	C53	1.393(9)
P3	C43	1.825(6)	C53	C54	1.389(9)
P4	C29	1.825(6)	C55	C56	1.405(11)
P4	C35	1.823(6)	C55	C60	1.396(9)
P4	C49	1.828(6)	C55	B1	1.634(11)
C1	C2	1.402(12)	C56	C57	1.385(10)
C1	C6	1.394(11)	C57	C58	1.383(10)
C2	C3	1.380(11)	C58	C59	1.364(12)
C3	C4	1.344(17)	C59	C60	1.388(11)
C4	C5	1.378(18)	C61	C62	1.402(10)
C5	C6	1.401(14)	C61	C66	1.412(9)
C7	C8	1.397(10)	C61	B1	1.635(10)
C7	C12	1.375(10)	C62	C63	1.376(10)
C8	C9	1.394(12)	C63	C64	1.391(12)
C9	C10	1.382(14)	C64	C65	1.380(11)
C10	C11	1.369(13)	C65	C66	1.396(9)
C11	C12	1.385(12)	C67	C68	1.427(9)
C15	C16	1.388(9)	C67	C72	1.400(10)
C15	C20	1.387(10)	C67	B1	1.647(10)
C16	C17	1.374(10)	C68	C69	1.377(10)
C17	C18	1.365(12)	C69	C70	1.368(10)
C18	C19	1.376(12)	C70	C71	1.412(9)
C19	C20	1.397(11)	C71	C72	1.396(10)
C21	C22	1.392(8)	C73	C74	1.390(10)

Table 6.15 continued. Selected bond lengths (Å) for **3**(BPh_4).

C21	C26	1.394(9)	C73	C78	1.386(10)
C22	C23	1.411(9)	C73	B1	1.675(11)
C23	C24	1.372(11)	C74	C75	1.390(9)
C24	C25	1.378(10)	C75	C76	1.393(10)
C25	C26	1.386(9)	C76	C77	1.389(10)
C27	C28	1.526(9)	C77	C78	1.396(10)
C29	C30	1.380(9)	Cl2	C79	1.777(8)
C29	C34	1.394(9)	Cl3	C80	1.739(8)
C30	C31	1.394(10)	C79	C80	1.496(11)
C31	C32	1.387(11)			

Table 6.16. Selected bond angles (˚) for **3**(BPh_4).

Atom	Atom	Atom	Angle	Atom	Atom	Atom	Angle
O1	Mo1	Cl1	176.7(7)	C17	C18	C19	119.2(7)
O1	Mo1	P1	98.0(8)	C18	C19	C20	121.1(8)
O1	Mo1	P2	94.1(7)	C15	C20	C19	119.1(7)
O1	Mo1	P3	91.8(8)	C22	C21	P1	121.5(5)
O1	Mo1	P4	90.4(7)	C22	C21	C26	119.3(6)
Cl1	Mo1	P1	79.99(13)	C26	C21	P1	118.8(5)
Cl1	Mo1	P2	82.92(13)	C21	C22	C23	119.4(7)
Cl1	Mo1	P3	90.25(12)	C24	C23	C22	120.4(6)
Cl1	Mo1	P4	92.57(12)	C23	C24	C25	119.9(6)
P1	Mo1	P2	79.24(9)	C24	C25	C26	120.5(7)
P1	Mo1	P3	170.17(15)	C25	C26	C21	120.4(6)
P1	Mo1	P4	99.82(10)	C28	C27	P1	109.3(4)
P2	Mo1	P3	100.90(10)	C27	C28	P2	109.0(4)
P4	Mo1	P2	175.48(15)	C30	C29	P4	119.7(5)
P4	Mo1	P3	79.25(8)	C30	C29	C34	119.8(6)
Cl1A	Mo1A	P1	86.3(4)	C34	C29	P4	120.4(5)
Cl1A	Mo1A	P2	81.5(4)	C29	C30	C31	120.1(7)
Cl1A	Mo1A	P3	84.5(4)	C32	C31	C30	119.8(6)
Cl1A	Mo1A	P4	84.0(4)	C33	C32	C31	120.2(6)
O1A	Mo1A	Cl1A	178.1(9)	C32	C33	C34	120.6(7)
O1A	Mo1A	P1	92.2(9)	C29	C34	C33	119.5(7)
O1A	Mo1A	P2	97.0(9)	C36	C35	P4	109.4(4)
O1A	Mo1A	P3	97.0(8)	C35	C36	P3	111.0(4)
O1A	Mo1A	P4	97.4(9)	C38	C37	P3	117.9(4)
P1	Mo1A	P3	170.3(3)	C42	C37	P3	123.1(5)
P1	Mo1A	P4	97.51(17)	C42	C37	C38	119.0(5)
P2	Mo1A	P1	79.20(15)	C39	C38	C37	119.8(6)
P2	Mo1A	P3	102.29(18)	C40	C39	C38	121.1(6)
P2	Mo1A	P4	165.3(3)	C39	C40	C41	118.7(6)
P3	Mo1A	P4	78.61(14)	C42	C41	C40	120.7(6)
C15	P1	Mo1	120.4(2)	C41	C42	C37	120.7(6)

Table 6.16 continued. Selected bond angles (˚) for **3**(BPh_4).

C15	P1	Mo1A	114.1(2)	C44	C43	P3	118.9(5)
C15	P1	C21	103.7(3)	C44	C43	C48	118.0(6)
C15	P1	C27	105.5(3)	C48	C43	P3	123.1(6)
C21	P1	Mo1	113.8(2)	C43	C44	C45	121.3(8)
C21	P1	Mo1A	123.4(3)	C44	C45	C46	118.9(8)
C21	P1	C27	105.0(3)	C47	C46	C45	120.2(7)
C27	P1	Mo1	107.2(2)	C48	C47	C46	120.1(8)
C27	P1	Mo1A	103.5(2)	C47	C48	C43	121.5(8)
C1	P2	Mo1	118.1(3)	C50	C49	P4	120.3(5)
C1	P2	Mo1A	125.6(3)	C54	C49	P4	119.7(5)
C1	P2	C28	101.9(3)	C54	C49	C50	119.9(6)
C7	P2	Mo1	118.0(2)	C51	C50	C49	120.3(6)
C7	P2	Mo1A	108.7(3)	C50	C51	C52	120.1(6)
C7	P2	C1	105.7(4)	C51	C52	C53	119.5(6)
C7	P2	C28	105.6(3)	C54	C53	C52	120.6(6)
C28	P2	Mo1	105.6(2)	C49	C54	C53	119.6(6)
C28	P2	Mo1A	107.8(2)	C56	C55	B1	122.8(6)
C36	P3	Mo1	106.6(2)	C60	C55	C56	114.2(7)
C36	P3	Mo1A	107.2(2)	C60	C55	B1	123.0(7)
C37	P3	Mo1	124.9(2)	C57	C56	C55	122.8(6)
C37	P3	Mo1A	116.1(3)	C58	C57	C56	120.1(8)
C37	P3	C36	102.0(3)	C59	C58	C57	119.4(8)
C43	P3	Mo1	111.8(2)	C58	C59	C60	119.7(7)
C43	P3	Mo1A	120.0(3)	C59	C60	C55	123.8(8)
C43	P3	C36	105.0(3)	C62	C61	C66	113.5(6)
C43	P3	C37	104.6(3)	C62	C61	B1	122.3(6)
C29	P4	Mo1	121.7(2)	C66	C61	B1	123.4(6)
C29	P4	Mo1A	112.4(3)	C63	C62	C61	124.7(7)
C29	P4	C49	103.2(3)	C62	C63	C64	119.7(7)
C35	P4	Mo1	103.6(2)	C65	C64	C63	118.6(7)
C35	P4	Mo1A	106.1(2)	C64	C65	C66	120.5(7)
C35	P4	C29	104.7(3)	C65	C66	C61	122.9(6)
C35	P4	C49	102.7(3)	C68	C67	B1	119.6(6)
C49	P4	Mo1	118.6(2)	C72	C67	C68	115.5(6)
C49	P4	Mo1A	125.7(2)	C72	C67	B1	124.9(6)
C2	C1	P2	119.6(6)	C69	C68	C67	122.1(7)
C6	C1	P2	122.1(7)	C70	C69	C68	121.4(6)
C6	C1	C2	118.3(8)	C69	C70	C71	118.8(6)
C3	C2	C1	120.5(9)	C72	C71	C70	119.7(7)
C4	C3	C2	121.7(12)	C71	C72	C67	122.5(7)
C3	C4	C5	118.8(11)	C74	C73	B1	122.7(6)
C4	C5	C6	121.8(11)	C78	C73	C74	116.3(7)
C1	C6	C5	118.8(11)	C78	C73	B1	121.0(6)
C8	C7	P2	115.3(6)	C73	C74	C75	122.2(7)

Table 6.16 continued. Selected bond angles (˚) for **3**(BPh_4).

C12	C7	P2	124.0(6)	C74	C75	C76	120.6(7)
C12	C7	C8	120.5(7)	C77	C76	C75	118.1(6)
C9	C8	C7	118.6(8)	C76	C77	C78	120.1(7)
C10	C9	C8	120.5(8)	C73	C78	C77	122.6(7)
C11	C10	C9	119.9(8)	C55	B1	C61	108.7(6)
C10	C11	C12	120.7(8)	C55	B1	C67	109.0(5)
C7	C12	C11	119.7(7)	C55	B1	C73	109.5(6)
C16	C15	P1	120.1(5)	C61	B1	C67	111.2(5)
C20	C15	P1	120.6(5)	C61	B1	C73	109.4(5)
C20	C15	C16	119.0(6)	C67	B1	C73	108.9(6)
C17	C16	C15	120.8(7)	C80	C79	Cl2	112.3(6)
C18	C17	C16	120.8(8)	C79	C80	Cl3	114.0(6)

Table 6.17. Atomic occupancy for **3**(BPh_4).

Atom	Occupancy	Atom	Occupancy	Atom	Occupancy
Mo1	0.662(10)	O1	0.662(10)	Cl1	0.662(10)
Mo1A	0.338(10)	Cl1A	0.338(10)	O1A	0.338(10)

Table 6.18. Selected bond distances (Å) for **3**.

Atom	Atom	Length	Atom	Atom	Length
Mo1	Cl1[1]	2.5155(17)	C8	C9	1.385(5)
Mo1	Cl1	2.5155(17)	C9	C10	1.378(5)
Mo1	O1	1.809(5)	C10	C11	1.369(5)
Mo1	O1[1]	1.809(5)	C11	C12	1.378(5)
Mo1	P1	2.4845(7)	C13	C14	1.526(4)
Mo1	P1[1]	2.4845(7)	C15	C16	1.394(4)
Mo1	P2[1]	2.4952(7)	C15	C20	1.397(4)
Mo1	P2	2.4952(7)	C16	C17	1.383(4)
P1	C1	1.837(3)	C17	C18	1.380(5)
P1	C7	1.821(3)	C18	C19	1.385(5)
P1	C13	1.838(3)	C19	C20	1.389(4)
P2	C14	1.860(3)	C21	C22	1.393(4)
P2	C15	1.825(3)	C21	C26	1.389(4)
P2	C21	1.830(3)	C22	C23	1.393(4)
C1	C2	1.391(4)	C23	C24	1.376(5)
C1	C6	1.386(4)	C24	C25	1.360(5)
C2	C3	1.389(4)	C25	C26	1.386(4)
C3	C4	1.371(5)	C27	C27[2]	1.373(4)
C4	C5	1.376(5)	C27	C28	1.371(4)
C5	C6	1.385(4)	C28	C29	1.365(4)
C7	C8	1.380(5)	C29	C29[2]	1.363(4)
C7	C12	1.387(4)			

[1]3/2-X,1/2-Y,1-Z; [2]1-X,+Y,3/2-Z

Table 6.19. Selected bond angles (°) for **3**.

Atom	Atom	Atom	Angle	Atom	Atom	Atom	Angle
Cl1[1]	Mo1	Cl1	180.0	C6	C1	C2	118.9(3)
O1	Mo1	P1	83.53(13)	C3	C2	C1	119.9(3)
O1[1]	Mo1	P1	96.48(13)	C4	C3	C2	120.7(3)
O1[1]	Mo1	P2[1]	85.08(13)	C3	C4	C5	119.9(3)
O1	Mo1	P2[1]	94.92(13)	C4	C5	C6	120.1(3)
O1	Mo1	P2	85.08(13)	C5	C6	C1	120.6(3)
O1[1]	Mo1	P2	94.92(13)	C8	C7	P1	118.0(2)
P1	Mo1	Cl1[1]	93.52(4)	C8	C7	C12	117.9(3)
P1	Mo1	Cl1	86.48(4)	C12	C7	P1	124.0(2)
P1[1]	Mo1	Cl1[1]	86.48(4)	C7	C8	C9	121.2(3)
P1[1]	Mo1	Cl1	93.52(4)	C10	C9	C8	119.6(3)
P1	Mo1	P1[1]	180.0	C11	C10	C9	119.8(3)
P1[1]	Mo1	P2	100.95(2)	C10	C11	C12	120.2(3)
P1	Mo1	P2[1]	100.95(2)	C11	C12	C7	121.0(3)
P1	Mo1	P2	79.05(2)	C14	C13	P1	108.84(18)
P1[1]	Mo1	P2[1]	79.05(2)	C13	C14	P2	112.32(18)
P2	Mo1	Cl1	83.04(4)	C16	C15	P2	121.6(2)
P2[1]	Mo1	Cl1[1]	83.04(4)	C16	C15	C20	118.6(3)
P2	Mo1	Cl1[1]	96.96(4)	C20	C15	P2	119.5(2)
P2[1]	Mo1	Cl1	96.96(4)	C17	C16	C15	120.7(3)
P2	Mo1	P2[1]	180.0	C18	C17	C16	120.3(3)
C1	P1	Mo1	118.70(9)	C17	C18	C19	119.8(3)
C1	P1	C13	104.78(12)	C18	C19	C20	120.2(3)
C7	P1	Mo1	118.74(9)	C19	C20	C15	120.3(3)
C7	P1	C1	102.88(13)	C22	C21	P2	123.6(2)
C7	P1	C13	104.61(13)	C26	C21	P2	117.6(2)
C13	P1	Mo1	105.54(9)	C26	C21	C22	118.7(3)
C14	P2	Mo1	109.29(9)	C21	C22	C23	119.9(3)
C15	P2	Mo1	113.82(9)	C24	C23	C22	120.2(3)
C15	P2	C14	104.87(12)	C25	C24	C23	120.3(3)
C15	P2	C21	103.94(13)	C24	C25	C26	120.3(3)
C21	P2	Mo1	122.61(9)	C25	C26	C21	120.6(3)
C21	P2	C14	100.27(12)	C28	C27	C27[2]	119.2(2)
C2	C1	P1	122.3(2)	C29	C28	C27	121.0(4)
C6	C1	P1	118.4(2)	C29[2]	C29	C28	119.7(2)

[1]3/2-X,1/2-Y,1-Z; [2]1-X,+Y,3/2-Z

6.5. References.

1. Ballhausen, C. J.; Gray, H. B. *Inorg. Chem.* **1962**, *1*, 111-122.

2. Gray, H. B.; Hare, C. R. *Inorg. Chem.* **1962**, *1*, 363-368.

3. Winkler, J. R.; Gray, H. B., Electronic structures of oxo-metal ions. In *Molecular Electronic Structures of Transition Metal Complexes. I. Structure and Bonding*, Mingos, D., Day, P., Dahl, J., Eds. Springer: Berlin, Heidelberg, 2011; Vol. 142, pp 17-28.

4. Denisov, I. G.; Makris, T. M.; Sligar, S. G.; Schlichting, I. *Chem. Rev.* **2005**, *105*, 2253-2278.

5. Parsell, T. H.; Behan, R. K.; Green, M. T.; Hendrich, M. P.; Borovik, A. S. *J. Am. Chem. Soc.* **2006**, *128*, 8728-8729.

6. MacBeth, C. E.; Golombek, A. P.; Young, V. G.; Yang, C.; Kuczera, K.; Hendrich, M. P.; Borovik, A. S. *Science* **2000**, *289*, 938-941.

7. Hill, E. A.; Weitz, A. C.; Onderko, E.; Romero-Rivera, A.; Guo, Y.; Swart, M.; Bominaar, E. L.; Green, M. T.; Hendrich, M. P.; Lacy, D. C.; Borovik, A. S. *J. Am. Chem. Soc.* **2016**, *138*, 13143-13146.

8. Gupta, R.; Taguchi, T.; Lassalle-Kaiser, B.; Bominaar, E. L.; Yano, J.; Hendrich, M. P.; Borovik, A. S. *Proc. Natl. Acad. Sci.* **2015**, *112*, 5319-5324.

9. Bigi, J. P.; Harman, W. H.; Lassalle-Kaiser, B.; Robles, D. M.; Stich, T. A.; Yano, J.; Britt, R. D.; Chang, C. J. *J. Am. Chem. Soc.* **2012**, *134*, 1536-1542.

10. Halbach, R. L.; Gygi, D.; Bloch, E. D.; Anderson, B. L.; Nocera, D. G. *Chem. Sci.* **2018**, *9*, 4524-4528.

11. Rohde, J.-U.; In, J.-H.; Lim, M. H.; Brennessel, W. W.; Bukowski, M. R.; Stubna, A.; Münck, E.; Nam, W.; Que, L. *Science* **2003**, *299*, 1037-1039.

12. Marshman, R. W.; Shapley, P. A. *J. Am. Chem. Soc.* **1990**, *112*, 8369-8378.

13. Marmion, M. E.; Takeuchi, K. J. *J. Am. Chem. Soc.* **1986**, *108*, 510-511.

14. Lim, M. H.; Rohde, J.-U.; Stubna, A.; Bukowski, M. R.; Costas, M.; Ho, R. Y. N.; Münck, E.; Nam, W.; Que, L. *Proc. Natl. Acad. Sci.* **2003**, *100*, 3665-3670.

15. Barthazy, P.; Wörle, M.; Mezzetti, A. *J. Am. Chem. Soc.* **1999**, *121*, 480-481.

16. Barthazy, P.; Wörle, M.; Rüegger, H.; Mezzetti, A. *Inorg. Chem.* **2000**, *39*, 4903-4912.

17. Hughes, D. L.; Mohammed, M. Y.; Pickett, C. J. *J. Chem. Soc., Chem. Commun.* **1988**, 1481-1482.

18. Karunadasa, H. I.; Chang, C. J.; Long, J. R. *Nature* **2010**, *464*, 1329-1333.

19. Sundstrom, E. J.; Yang, X.; Thoi, V. S.; Karunadasa, H. I.; Chang, C. J.; Long, J. R. *J. Am. Chem. Soc.* **2012**, *134*, 5233-5242.

20. Thoi, S. V.; Karunadasa, H. I.; Surendranath, Y.; Long, J. R.; Chang, C. J. *Energy Environ. Sci.* **2012**, *5*, 7762-7770.

21. Pal, R.; Laureanti, J. A.; Groy, T. L.; Jones, A. K.; Trovitch, R. J. *Chem. Commun.* **2016**, *52*, 11555-11558.

22. Bakir, M.; Cotton, F. A.; Cudahy, M. M.; Simpson, C. Q.; Smith, T. J.; Vogel, E. F.; Walton, R. A. *Inorg. Chem.* **1988**, *27*, 2608-2612.

23. Butcher, A. V.; Chatt, J. *J. Chem. Soc. A* **1971**, 2356-2358.

24. Da Re, R. E.; Hopkins, M. D. *Inorg. Chem.* **2002**, *41*, 6973-6985.

25. Isovitsch, R. A.; Beadle, A. S.; Fronczek, F. R.; Maverick, A. W. *Inorg. Chem.* **1998**, *37*, 4258-4264.

26. Levason, W.; McAuliffe, C. A.; Sayle, B. J. *J. Chem. Soc., Dalton Trans.* **1976**, 1177-1181.

27. Bendix, J.; Bøgevig, A. *Inorg. Chem.* **1998**, *37*, 5992-6001.

28. Pal, P. K.; Chowdhury, S.; Drew, M. G. B.; Datta, D. *New J. Chem.* **2002**, *26*, 367-371.

29. Connelly, N. G.; Geiger, W. E. *Chem. Rev.* **1996**, *96*, 877-910.

30. McAuliffe, C. A.; McCullough, F. P.; Parrott, M. J.; Rice, C. A.; Sayle, B. J.; Levason, W. *J. Chem. Soc., Dalton Trans.* **1977**, 1762-1766.

31. Niklas, J.; Westwood, M.; Mardis, K. L.; Brown, T. L.; Pitts-McCoy, A. M.; Hopkins, M. D.; Poluektov, O. G. *Inorg. Chem.* **2015**, *54*, 6226-6234.

32. Orpen, A. G.; Connelly, N. G. *Organometallics* **1990**, *9*, 1206-1210.

33. Carmona, E.; Galindo, A.; Guille-Photin, C.; Sanchez, L. *Polyhedron* **1988**, *7*, 1767-1771.

34. Hardcastle, F. D.; Wachs, I. E. *J. Raman Spectrosc.* **1990**, *21*, 683-691.

35. Groom, C. R.; Bruno, I. J.; Lightfoot, M. P.; Ward, S. C. *Acta Cryst.* **2016**, *B72*, 171-179.

36. Holm, R. H. *Chem. Rev.* **1987**, *87*, 1401-1449.

37. Pangborn, A. B.; Giardello, M. A.; Grubbs, R. H.; Rosen, R. K.; Timmers, F. J. *Organometallics* **1996**, *15*, 1518-1520.

38. Fulmer, G. R.; Miller, A. J. M.; Sherden, N. H.; Gottlieb, H. E.; Nudelman, A.; Stoltz, B. M.; Bercaw, J. E.; Goldberg, K. I. *Organometallics* **2010**, *29*, 2176-2179.

39. Frisch, M. J.; Trucks, G. W.; Schlegel, H. B.; Scuseria, G. E.; Robb, M. A.; Cheeseman, J. R.; Scalmani, G.; Barone, V.; Petersson, G. A.; Nakatsuji, H.; Li, X.; Caricato, M.; Marenich, A. V.; Bloino, J.; Janesko, B. G.; Gomperts, R.; Mennucci, B.; Hratchian, H. P.; Ortiz, J. V.; Izmaylov, A. F.; Sonnenberg, J. L.; Williams; Ding, F.; Lipparini, F.; Egidi, F.; Goings, J.; Peng, B.; Petrone, A.; Henderson, T.; Ranasinghe, D.; Zakrzewski, V. G.; Gao, J.; Rega, N.; Zheng, G.; Liang, W.; Hada, M.; Ehara, M.; Toyota, K.; Fukuda, R.; Hasegawa, J.; Ishida, M.; Nakajima, T.; Honda, Y.; Kitao, O.; Nakai, H.; Vreven, T.; Throssell, K.; Montgomery Jr., J. A.; Peralta, J. E.; Ogliaro, F.; Bearpark, M. J.; Heyd, J. J.; Brothers, E. N.; Kudin, K. N.; Staroverov, V. N.; Keith, T. A.; Kobayashi, R.; Normand, J.; Raghavachari, K.; Rendell, A. P.; Burant, J. C.; Iyengar, S. S.; Tomasi, J.; Cossi, M.; Millam, J. M.; Klene, M.; Adamo, C.; Cammi, R.; Ochterski, J. W.; Martin, R. L.; Morokuma, K.; Farkas, O.; Foresman, J. B.; Fox, D. J. *Gaussian 16*, Gaussian, Inc.: Wallingford, CT, 2016.

40. Waller, M. P.; Braun, H.; Hojdis, N.; Bühl, M. *J. Chem. Theory Comput.* **2007**, *3*, 2234-2242.

41. Hay, P. J.; Wadt, W. R. *J. Chem. Phys.* **1985**, *82*, 270-283.

42. Hay, P. J.; Wadt, W. R. *J. Chem. Phys.* **1985**, *82*, 284-298.

43. Gorelsky, S. I.; Lever, A. B. P. *J. Organomet. Chem.* **2001**, *635*, 187-196.

44. Sheldrick, G. M. *Acta Crystallogr., Sect. A: Found. Adv.* **2015**, *A71*, 3-8.

45. Dolomanov, O. V.; Bourhis, L. J.; Gildea, R. J.; Howard, J. A. K.; Puschmann, H. J. *J. Appl. Crystallogr.* **2009**, *42*, 339-341.

46. Sheldrick, G. M. *Acta Crystallogr., Sect. A: Found. Adv.* **2008**, *A64*, 112-122.

47. Parkin, G. *Chem. Rev.* **1993**, *93*, 887-911.

48. Carmona, E.; Galindo, A.; Sanchez, L.; Nelson, A. J.; Wilkinson, G. *Polyhedron* **1984**, *3*, 347-352.

49. Levason, W.; McAuliffe, C. A.; McCullough, F. P. *Inorg. Chem.* **1977**, *16*, 2911-2916.

50. Hansen, C. B. 1. Tungsten photoredox chromphores containing amine-functionalized diphosphine and *N*-heterocyclic carbene ligands. 2. The chemistry of low-coordinate cobalt compounds supported by *N*-heterocyclic carbenes and bulky amines. Ph.D. Dissertation, The University of Chicago, 2017.